3D PRINTING FOR IMPLANTABLE MEDICAL DEVICES: FROM SURGICAL RECONSTRUCTION TO TISSUE/ORGAN REGENERATION

EDITED BY: Julien Georges Didier Barthès, Christophe A. Marquette and Luciano Vidal

PUBLISHED IN: Frontiers in Bioengineering and Biotechnology

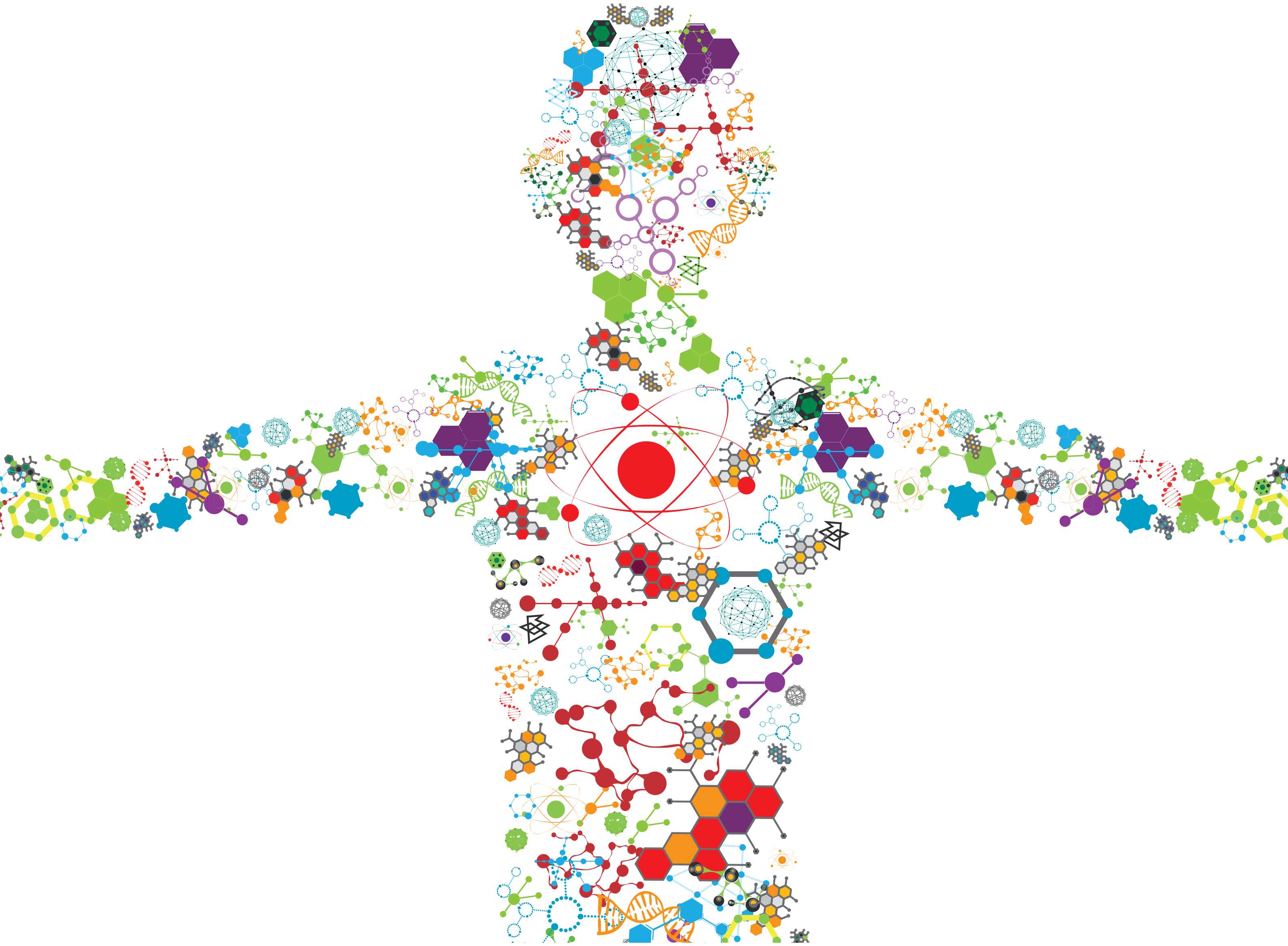

frontiers Research Topics

About Frontiers

Frontiers is more than just an open-access publisher of scholarly articles: it is a pioneering approach to the world of academia, radically improving the way scholarly research is managed. The grand vision of Frontiers is a world where all people have an equal opportunity to seek, share and generate knowledge. Frontiers provides immediate and permanent online open access to all its publications, but this alone is not enough to realize our grand goals.

Frontiers Journal Series

The Frontiers Journal Series is a multi-tier and interdisciplinary set of open-access, online journals, promising a paradigm shift from the current review, selection and dissemination processes in academic publishing. All Frontiers journals are driven by researchers for researchers; therefore, they constitute a service to the scholarly community. At the same time, the Frontiers Journal Series operates on a revolutionary invention, the tiered publishing system, initially addressing specific communities of scholars, and gradually climbing up to broader public understanding, thus serving the interests of the lay society, too.

Dedication to Quality

Each Frontiers article is a landmark of the highest quality, thanks to genuinely collaborative interactions between authors and review editors, who include some of the world's best academicians. Research must be certified by peers before entering a stream of knowledge that may eventually reach the public - and shape society; therefore, Frontiers only applies the most rigorous and unbiased reviews.
Frontiers revolutionizes research publishing by freely delivering the most outstanding research, evaluated with no bias from both the academic and social point of view. By applying the most advanced information technologies, Frontiers is catapulting scholarly publishing into a new generation.

What are Frontiers Research Topics?

Frontiers Research Topics are very popular trademarks of the Frontiers Journals Series: they are collections of at least ten articles, all centered on a particular subject. With their unique mix of varied contributions from Original Research to Review Articles, Frontiers Research Topics unify the most influential researchers, the latest key findings and historical advances in a hot research area! Find out more on how to host your own Frontiers Research Topic or contribute to one as an author by contacting the Frontiers Editorial Office: frontiersin.org/about/contact

ISSN 1664-8714
ISBN 978-2-88966-509-9
DOI 10.3389/978-2-88966-509-9

3D PRINTING FOR IMPLANTABLE MEDICAL DEVICES: FROM SURGICAL RECONSTRUCTION TO TISSUE/ORGAN REGENERATION

Topic Editors:
Julien Georges Didier Barthès, Protip Medical, France
Christophe A. Marquette, UMR5246 Institut de Chimie et Biochimie Moléculaires et Supramoléculaires (ICBMS), France
Luciano Vidal, Ecole Centrale de Nantes, France

Dr. Julien Barthes is Collaborative Project Manager at PROTiP MEDICAL SAS. All other Topic Editors declare no competing interests with regards to the Research Topic subject.

Citation: Barthès, J. G. D., Marquette, C. A., Vidal, L., eds. (2021). 3D Printing for Implantable Medical Devices: From Surgical Reconstruction to Tissue/Organ Regeneration. Lausanne: Frontiers Media SA. doi: 10.3389/978-2-88966-509-9

Table of Contents

frontiers in Bioengineering and Biotechnology

ORIGINAL RESEARCH
published: 19 November 2019
doi: 10.3389/fbioe.2019.00348

Three Dimensional Printing Bilayer Membrane Scaffold Promotes Wound Healing

Shoubao Wang[1†], *Yao Xiong*[1†], *Jingting Chen*[1], *Abdulsamad Ghanem*[1], *Yinmin Wang*[1], *Jun Yang*[1*] *and Binbin Sun*[2*]

[1] Department of Plastic and Reconstructive Surgery, Shanghai Ninth People's Hospital, Shanghai Jiao Tong University School of Medicine, Shanghai, China, *[2] Department of Orthopaedics, Shanghai Ninth People's Hospital, Shanghai Jiao Tong University School of Medicine, Shanghai, China*

OPEN ACCESS

Edited by:
Julien Georges Didier Barthès,
Protip Medical, France

Reviewed by:
Saeid Kargozar,
Mashhad University of Medical Sciences, Iran
Lia Rimondini,
University of Eastern Piedmont, Italy
Gilson Khang,
Chonbuk National University, South Korea

***Correspondence:**
Jun Yang
yangj1580@163.com
Binbin Sun
sunbinbin1992@163.com

† These authors have contributed equally to this work

Specialty section:
This article was submitted to Biomaterials, a section of the journal Frontiers in Bioengineering and Biotechnology

Received: *28 August 2019*
Accepted: *06 November 2019*
Published: *19 November 2019*

Citation:
Wang S, Xiong Y, Chen J, Ghanem A, Wang Y, Yang J and Sun B (2019) Three Dimensional Printing Bilayer Membrane Scaffold Promotes Wound Healing. Front. Bioeng. Biotechnol. 7:348. doi: 10.3389/fbioe.2019.00348

Full-thickness skin wounds are common and could be a heavy physical and economic burden. With the development of three dimensional (3D) printing technology, skin-like constructs have been fabricated for skin wound healing and regeneration. Although the 3D printed skin has great potential and enormous advantages before vascular networks can be well-constructed, living cells are not recommended for 3D skin printing for *in vivo* applications. Herein, we designed and printed a bilayer membrane (BLM) scaffold consisting of an outer poly (lactic-co-glycolic acid) (PLGA) membrane and a lower alginate hydrogel layer, which respectively mimicked the skin epidermis and dermis. The multi-porous alginate hydrogel of the BLM scaffolds promoted cell adhesion and proliferation *in vitro*, while the PLGA membrane prevented bacterial invasion and maintained the moisture content of the hydrogel. Skin regeneration using the bilayer scaffold was compared with that of PLGA, alginate hydrogel and the untreated defect *in vivo*. Tissue samples were analyzed using histopathological and immunohistochemical staining of CD31. In addition, mRNA expression levels of collagen markers [collagen type 1 alpha 1 (COL1a1) and collagen type 3 alpha 1 (COL3a1)] and inflammatory markers [interleukin-1β (IL-1β), as well as tumor necrosis factor (TNF-α)] were measured. Conclusively, the application of BLM scaffold resulted in highest levels of best skin regeneration by increasing neovascularization and boosting collagen I/III deposition. Taken together, the 3D-printed BLM scaffolds can promote wound healing, and are highly suitable for a wide range of applications as wound dressings or skin substitutes.

Keywords: three dimensional printing, bilayer membrane scaffold, wound healing, alginate, poly (lactic-co-glycolic acid)

INTRODUCTION

Skin is the largest organ and the outermost protective sheath of the human body (Iii et al., 2000; Sun and Mao, 2012). It is highly susceptible to wounds, which are commonly caused by trauma, burns, skin diseases etc. Patients with full-thickness skin wounds suffer physical, psychological and economical burdens. Wound healing involves the coordination of many distinct but spatiotemporally overlapping physiological processes, including hemostasis, inflammation, epithelial cell proliferation, and tissue remodeling (Sabine and Richard, 2003; Eming et al., 2014; Sorg et al., 2017). Various natural and synthetic tissue engineering materials have been developed to accelerate wound healing, such as electrospun film, hydrogels, sponges etc. (Seo et al., 2012; Anisha et al., 2013; Dong et al., 2014; Catanzano et al., 2015; Zhao et al., 2017), which create a multi-porous and moist matrix that aids tissue regeneration. However, most scaffolds are composed of a single material, and therefore cannot simulate the functions of the full-thickness skin.

Three-dimensional printing is a personalized, flexible and accurate technology that is particularly suitable for wound healing (Murphy and Atala, 2014; Seol et al., 2014; Gu et al., 2015). Recent studies have reported *in vitro* fabrication of 3D simulated skin with dermis and epidermis-like structures through printing multiple layers of cells on various matrices (Lee et al., 2009, 2014; Skardal et al., 2012; Stefanie et al., 2013; Koch et al., 2015). In the absence of a vascular network, the 3D-printed skin relies solely on molecular diffusion and mechanical perfusion *in vivo*, which significantly reduces its viability since the diffusion range is generally limited to 100–200 μm (Tran and Wen, 2014;). Therefore, tissue construction by direct deposition or aggregation of living cells is not suitable for *in vivo* applications until microvascular networks can also be well-printed.

PLGA, the copolymer of poly (glycolic acid) and poly (lactic acid), is a biodegradable and biocompatible material that is used for tissue repair and reconstruction and drug delivery (Ueno et al., 2001; Danhier et al., 2012; Hudson and Margaritis, 2014). Since PLGA films are stiff, hydrophobic and semi-permeable, they do not have the capacity to absorb exudates or provide a moist microenvironment to accelerate wound healing (Ueno et al., 2001). These very characteristics however make PLGA a suitable outer layer that can separate a hydrogel matrix from the external environment, and retain the moisture content in the former. Furthermore, the nanofibers of the PLGA membrane are highly dense and can prevent bacterial invasion. Alginate, an anionic linear polysaccharide composed of (1,4)-linked β-D-mannuronic acid (M) and α-L-guluronic acid (G) blocks, is typically obtained from brown seaweed and is widely used in wound healing on account of its high histocompatibility, low toxicity, good bioresorption and low cost (Ueno et al., 2001; Boateng and Catanzano, 2015). It forms a hydrogel in the presence of divalent cations that cross-link with the G-blocks (Goh et al., 2012). Alginate hydrogels limit wound secretions and minimize bacterial contamination through super absorbance (Lee and Mooney, 2012). Furthermore, the multi-porous structure of these hydrogels promote cell invasion and neovascularization (Sun et al., 2018), and provide a physiologically moist microenvironment for wound healing (Boateng et al., 2014). Another major advantage of alginate hydrogel in the context of tissue reconstruction is the ease of 3D printing (Jahangir et al., 2018). Studies show that alginate wound dressings maintain a physiologically moist microenvironment, reduce bacterial infection at the wound site, and promote wound healing (Lee and Mooney, 2012).

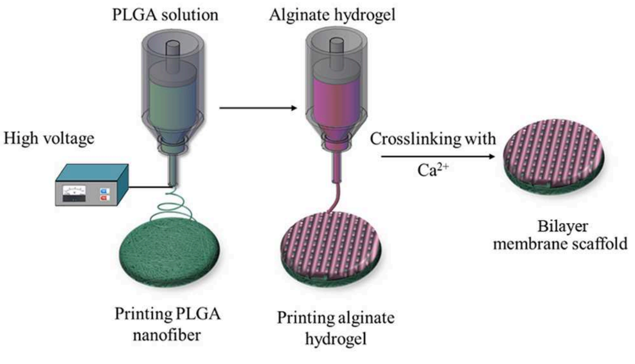

FIGURE 1 | Schematic diagram. The schematic diagram of the bilayer membrane scaffold by 3D printing.

To this end, we used the 3D printing technology to create an BLM scaffold, with PLGA membrane as the superior layer and alginate membrane as inferior layer that, respectively, mimic the epidermis and dermis. Briefly, the first layer of PLGA nanofiber membrane was prepared using high voltage printing, while the second layer was fabricated by printing alginate hydrogel on the surface of PLGA nanofiber membrane. The schematic diagram of BLM fabrication is shown in **Figure 1**. The BLM scaffold provided an isolated and moist micro-environment that promoted inflammation, facilitated rapid vascularization and collagen deposition, and ultimately accelerated wound healing.

RESULTS AND DISCUSSION

Characteristics of the BLM Scaffold

SEM images of the BLM scaffold revealed a dense outer layer of nano-sized PGLA fibers of diameter 857.02 ± 211.81 nm, and a loose microporous alginate hydrogel underneath. The thickness of the PLGA and alginate hydrogel layer were 20 and 100 μm, respectively. The FTIR results of the samples are shown in **Figure 2**. The spectrum of raw PLGA data shows absorbance peaks at wavelengths of 753 (CH-bend), 1,082 and 1,170 (CO stretch), 1,388 (CH-bend), 1,750 (CO ester), and 2,847 (CH_2-bend) cm^{-1} (**Figure 2E**), while all spectrum peaks were observed in the PLGA nanofiber layer in BLM. Raw alginate produced a peak at 3,400 cm^{-1} indicating the presence of hydroxyl groups. Asymmetric and symmetric –COO groups are indicated by the peaks at a wavelength of 1,597 and 1,407 cm^{-1}, respectively. The CO group is indicated by the peak at a wavelength of 1,027 cm^{-1}. For alginate hydrogel layer in BLM, peaks were observed at the same sites (**Figure 2F**). The FTIR results showed that the preparation process does not affect the chemical properties of PLGA and alginate. The moisture retention and vapor transmission rates of the PLGA, alginate hydrogel and BLM scaffold are shown in **Figure 3**. While the hydrogel alone showed poor moisture retention and lost most of the water within 24 h, the BLM scaffold retained its moisture for 72 h (**Figure 3A**). Consistent with this, the PLGA nanofiber and BLM scaffolds had lower vapor transmission rates compared to that of alginate hydrogel (**Figure 3B**). Thus, the PLGA nanofiber membrane reduces evaporation from the alginate hydrogel. This is critical for wound healing since adequate moisture not only reduces the epithelial cell death but also promotes their migration and proliferation, and helps in tissue regeneration. Furthermore, while only 20% of the PLGA nanofiber degraded within 4 weeks,

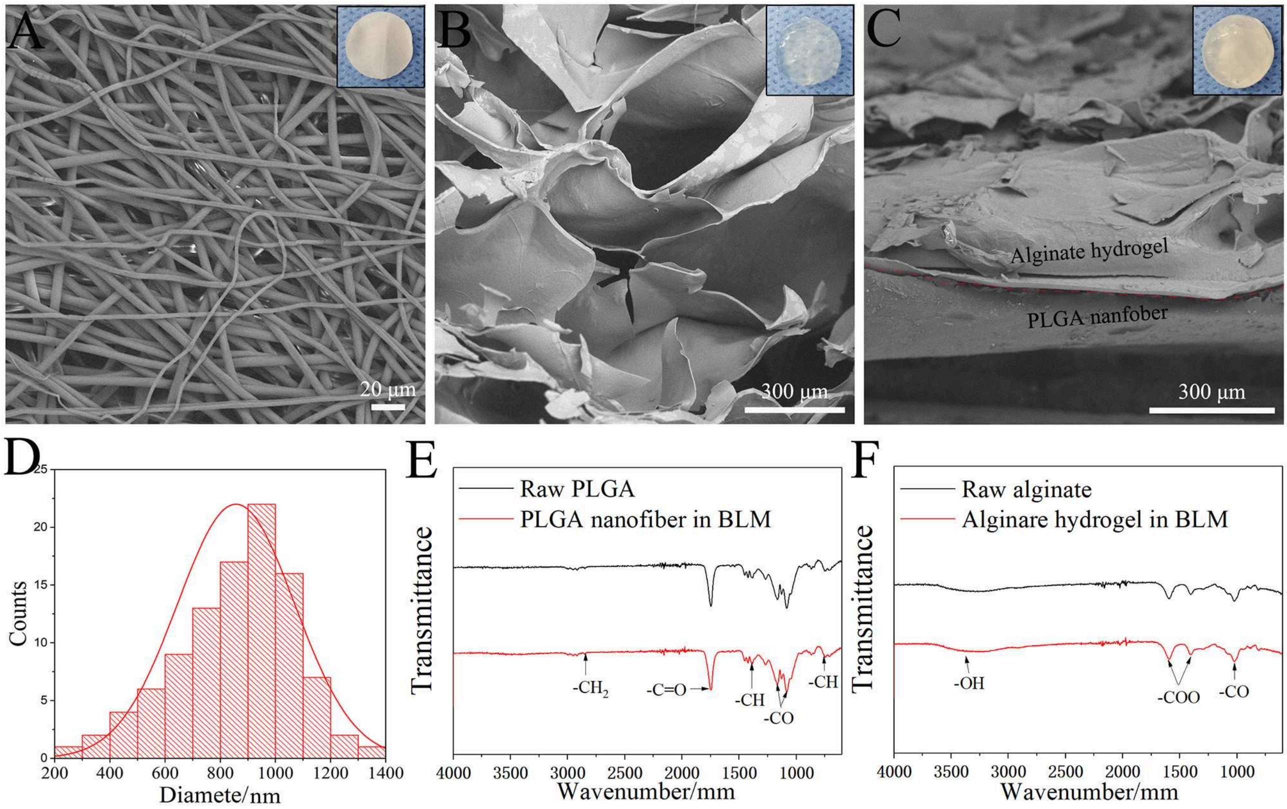

FIGURE 2 | Morphology and structure. SEM image of PLGA nanofiber layer **(A)**, Alginate hydrogel layer **(B)** and BLM scaffold **(C)** (the top right-hand corner images are the corresponding digital photograph of each samples). **(D)** Nanofiber diameter distribution of PLGA nanofiber layer. FTIR results of raw PLGA and PLGA nanofiber in BLM **(E)**, and raw alginate and alginate hydrogel in BLM **(F)**.

the degradation rate of alginate was slow in the first 2 weeks, and accelerated to 80% thereafter (**Figure 3C**), which is consistent with previous reports (Danhier et al., 2012; Lee and Mooney, 2012). The degradation rate of the BLM scaffold was intermediate to that of PLGA and alginate hydrogel. The rapid degradation of the hydrogel layer, which was designed to be in direct contact with the damaged area, is necessary for skin cell growth and tissue regeneration. In contrast, the outer PLGA membrane was designed to cover the wound for an extended period of time in order to prevent wound infection. The mechanical properties of the skin scaffold are critical for wound healing. The tensile stress, elongation at break, and Young's modulus of alginate were 231.51 ± 10.41 KPa, 139.18 ± 12.02% and 24.93 ± 2.45 KPa, respectively, which increased to 2753.58 ± 92.25 KPa, 304.28 ± 15.74% and 531.11 ± 12.64 KPa with the addition of the outer PGLA layer (**Figure 3D**). Taken together, the PLGA nanofiber layer has high tensile strength and can protect hydrogel while the latter aids in tissue regeneration.

BLM Scaffold Resists Bacterial Invasion and Is Cyto-Compatible

In addition to desirable mechanical properties and the ability to retain the moisture of the hydrogel, PGLA also acted as a barrier to bacterial invasion. As shown in **Figures 4A–C**, *S. aureus* was seeded onto the surface of three scaffolds. After the culture, it was found that the bacteria could infiltrate into the alginate hydrogel, but not into PLGA nanofiber or BLM scaffold. This indicates that the bacteria are able to penetrate into the hydrogel, but not into the PLGA layer, probably due to the high density nanofiber structure. This result provides evidence that the PLGA nanofiber layer can resist bacterial invasion. Furthermore, **Figure 4D** shows that murine fibroblasts are able to adhere to both the PLGA nanofibers and BLM scaffold regardless of their water content. In contrast, the alginate hydrogel and BLM scaffold had more cells adhered to them, compared with the PLGA nanofibers within the first 12 h. This demonstrates the stronger cell adhesion ability of alginate hydrogel, when it is moist. Therefore, it is essential to prevent water evaporation from the hydrogel to optimize cell adhesion during wound healing. In this regard, the BLM scaffold was more conducive to cell adhesion compared to pure hydrogel due to the protective PLGA layer. The biocompatibility of the different materials was tested by culturing murine L929 cells on the respective surfaces for 1, 3, 5, and 7 days. The cells spread and proliferated rapidly on all materials, indicating their biocompatibility (**Figures 5A–D**). However, after 5 and 7 days of incubation, the proliferative rate of the L929 cells growing on the alginate hydrogel and BLM scaffold were significantly higher compared to that cultured on the PLGA nanofibers, likely due to

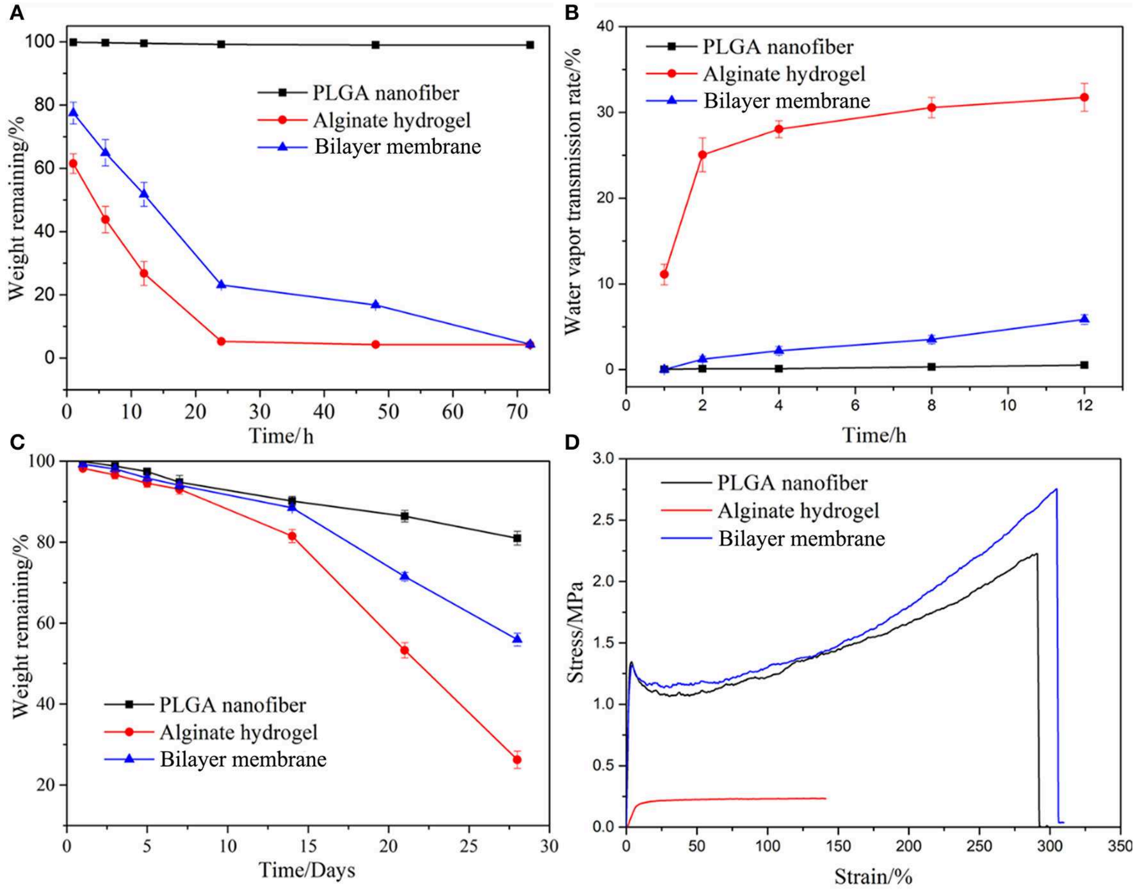

FIGURE 3 | Properties characterization. The moisturizing **(A)**, water vapor transmission rate **(B)**, degradation **(C)**, and mechanical properties of PLGA nanofiber, alginate hydrogel and bilayer membrane scaffolds. **(D)** Stress-strain curves of three samples.

the higher biocompatibility, micro-porosity and water content of the hydrogel.

BLM Scaffold Accelerated *in vivo* Wound Healing

In vivo wound healing was tested by implanting the respective biomaterials in full thickness wounds made in a rat model. All the animals survived, and showed gradual wound healing without infection, although the BLM scaffold induced the fastest wound closure. As shown in **Figure 5A**, the wound sizes were similar in the control, PLGA and alginate hydrogel groups after 4 days, whereas the BLM scaffold reduced wound size by 20.8% in the same time period (**Figures 6A,B**). On day 8 post wounding, the BLM and alginate hydrogel scaffolds resulted in 47.8 and 72.2% wound closure, respectively, whereas only 11.5 and 15.2% wound closure was observed in the control and PLGA groups (**Figures 6A,B**). The wounds treated with BLM scaffolds were completely healed by day 12, while 8.8, 28.5, and 33.7% of the wounds remained unhealed in the alginate hydrogel, PLGA and the control groups, respectively (**Figures 6A,B**). Histological examination revealed granulation tissue in the wound bed in all groups on the 4th day after the operation (**Figure 6C**), which was gradually replaced with new tissue in the BLM and alginate hydrogel-treated groups by day 8 (**Figure 6C**). On the 12th day, continuous and regular epithelial formation was seen on the alginate and BLM-treated wounds (**Figure 6C**), with a thicker epidermis thickness in the latter. In contrast, no continuous mature epithelial layer was seen in the control and PLGA groups. Taken together, the soft and porous structure of the alginate hydrogel accelerated wound healing by supporting cell adhesion, proliferation and migration (Lee and Mooney, 2012). In contrast, the hydrophobicity of PGLA prevents cell adhesion and migration (Danhier et al., 2012), which translated to poor wound healing in the absence of a supportive hydrogel layer.

BLM Promotes Inflammation, Vascularization, and Collagen Deposition in the Wound

Wound healing is a complex process which is initiated with the clotting cascade and platelet activation, with the latter releasing pro-inflammatory cytokines like IL-1β and TNF-α. Senapati et al. and Ganeshkumar et al. showed that increased expression of pro-inflammatory cytokines in the early stages promoted wound healing (Senapati et al., 2011;

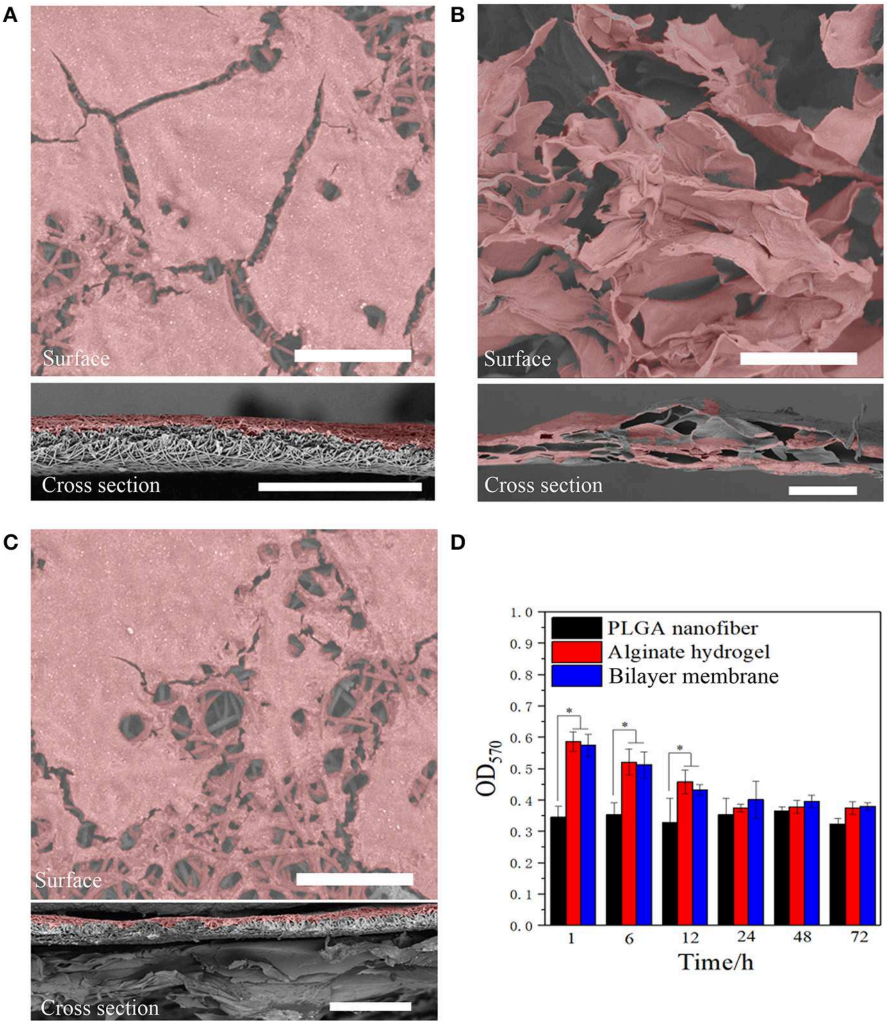

FIGURE 4 | Anti-bacterial invasion and cell adhesion. SEM images of *Staphylococcus* bacterial on **(A)** PLGA nanofiber, **(B)** alginate hydrogel, and **(C)** bilayer membrane scaffold surface and cross section (the bacterial were labeled with pseudo-color, scare bar = 80 μm). **(D)** The cell adhesion results on three samples (*$P < 0.05$).

Ganeshkumar et al., 2012) by recruiting leukocytes and activating fibroblasts, thereby promoting neovascularization and collagen deposition (Ganeshkumar et al., 2012). Consistent with this, IL-1β and TNF-α mRNAs were detected at all time points after surgery. The expression of IL-1β and TNF-α were significantly higher in the BLM and alginate hydrogel-treated groups compared to the PLGA and control groups on the 4th day (**Figures 6D,E**), and opposite trends were seen on the 8th and 12th day (**Figures 6D,E**).

Vascularization is critical for wound healing since that delivers nutrients and oxygen to the newly-formed tissues. In addition, neovascularization accelerates the migration of cellular and humoral factors to the wound (Eming et al., 2014), which in turn promote wound healing via formation of granulation tissue and collagen synthesis (Eming et al., 2014). We observed an increase in CD31-expressing endothelial cells in the BLM and alginate hydrogel-treated wounds on day 4 compared to the untreated control and PLGA-treated groups (**Figures 6F,G**). On day 8, the mean number of CD31+ cells in the wounds of the BLM, alginate hydrogel, PLGA and control groups were 9.66, 6.34, 1.36, and 1.5%, respectively (**Figures 6F,G**). Furthermore, the blood vessel density was significantly higher in the BLM and hydrogel-treated wounds compared to the untreated and PLGA-treated wounds (**Figures 6F,H**). The capacity of BLM and alginate hydrogel to stimulate neovascularization in the early stages of wound healing may be attributed to the 3D porous alginate scaffold. Interestingly, the CD31+ cells and blood vessel density was higher in the BLM-treated compared to the alginate hydrogel group on the 12th day after surgery (**Figures 6F–H**), possibly due to the PLGA membrane in the former which maintained the moist microenvironment of the hydrogel and accelerated neovascularization.

Collagen synthesis and deposition play a vital role in wound healing by providing mechanical support to the tissues, and promoting cell adhesion, proliferation and differentiation (Eming et al., 2014). Masson's trichrome staining showed

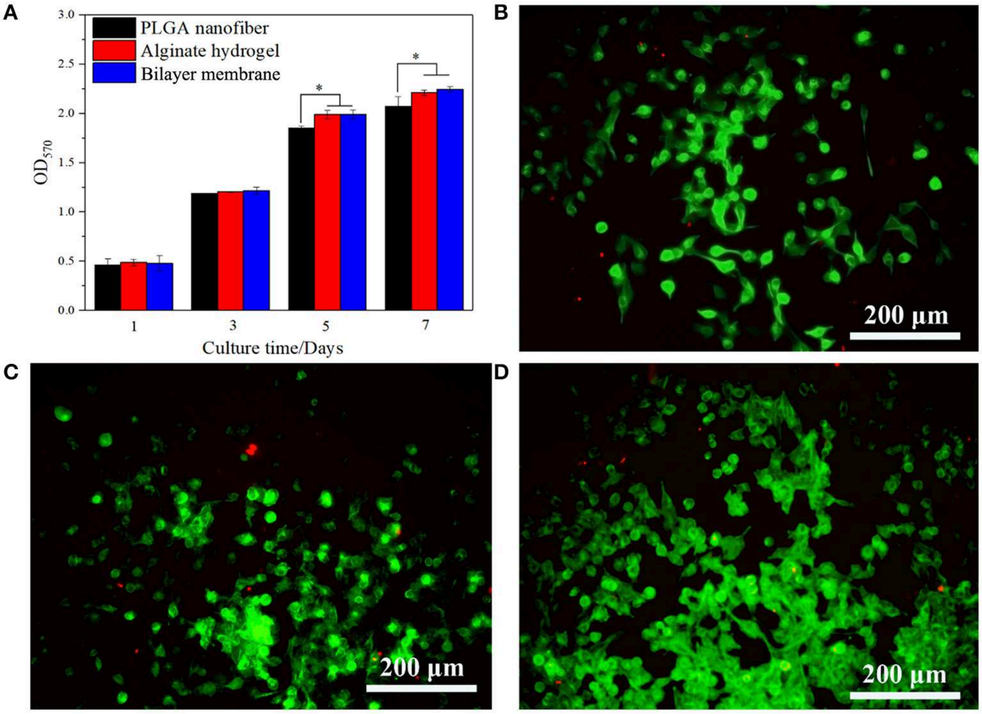

FIGURE 5 | Cells viability and proliferation. **(A)** CCK-8 assay of L929 cells proliferation after incubation for 5 days on PLGA nanofiber, alginate hydrogel and bilayer membrane. **(B–D)** Live/Dead staining of L929 cells on PLGA nanofiber, alginate hydrogel and bilayer membrane on day 5. Living cells are labeled as green fluorescence, while dead cells are labeled as red fluorescence ($^{*}P < 0.05$).

relatively sparse and disordered collagen fibers in the control and PLGA groups, while that in the BLM and alginate hydrogel groups were bundled and neatly arranged on day 4 (**Figures 7A,B**). With gradual wound healing, the deposition of collagen fibers increased in all groups. On the 8th and 12th days post wounding, the collagen fibers in the BLM and alginate hydrogel-treated groups were significantly denser compared to that in the control and PLGA groups (**Figures 7A,B**). Consistent with this, the relative expression of Col1α1 and Col3α1 were significantly higher in the BLM-treated wounds compared to the untreated and PLGA-treated wounds on days 8 and 12 (**Figures 7C–E**). Furthermore, the BLM-treated wounds had higher collagen content compared to the alginate-treated wounds (**Figures 7A,B**). The greater capacity of BLM scaffold to promote collagen deposition was likely related to the 3D porous alginate scaffold, as well as the outer protective PLGA membrane. Taken together, the BLM scaffold accelerates wound healing by promoting inflammation in the early stages, neovascularization and collagen synthesis.

CONCLUSION

For this study, the BLM scaffold was created using 3D printing technology to mimic the skin structure, with PLGA nanofiber as the superior "epidermal" layer and alginate as the inferior "dermal" layer. The porous alginate hydrogel promoted cell adhesion and proliferation, compared with PLGA, whereas the BLM scaffold with a PLGA layer was able to prevent bacterial invasion and retain the humidity of the underlying hydrogel *in vitro*. Moreover, compared with the control, the PLGA and alginate hydrogel groups, the BLM scaffold displayed the strongest ability to promote inflammation, neovascularization and collagen I/III deposition, after implantation in the dorsal wound of rats, and ultimately accelerated wound healing. In conclusion, the above findings indicate that the 3D-printed BLM scaffold is optimal for wound healing *in vivo*. We found that the 3D-printed BLM scaffold is a highly promising type of wound dressing and skin substitute. Furthermore, the results obtained from this *in vivo* study can help make a thicker BLM scaffold that is suitable for use in prospective clinical studies on human wound healing.

Materials

PLGA (Mw = 70–88 kDa, LA: GA = 50:50) was purchased from Jinan Daigang Co. Ltd. (China), and 1,1,1,3,3,3-Hexafluoro-2-propanol (HFIP) from Alfa Aesar Company (Ward Hill, MA, USA). Analytical grade sodium alginate and calcium chloride were obtained from Aladdin Co. Ltd (China).

Fabrication of BLM Scaffold by 3D Printing

To prepare the PLGA nanofiber layer, the copolymer was dissolved in HFIP [w/v(%) = 15%] with constant stirring at room temperature for 4 h. The PLGA solution was placed in a barrel loaded in syringe pump and operated at a speed of 1.5 mL/h via the 3D printer (Tongli micro-nano technology Co., Ltd., Shenzhen, China). A high voltage of 12 kV was

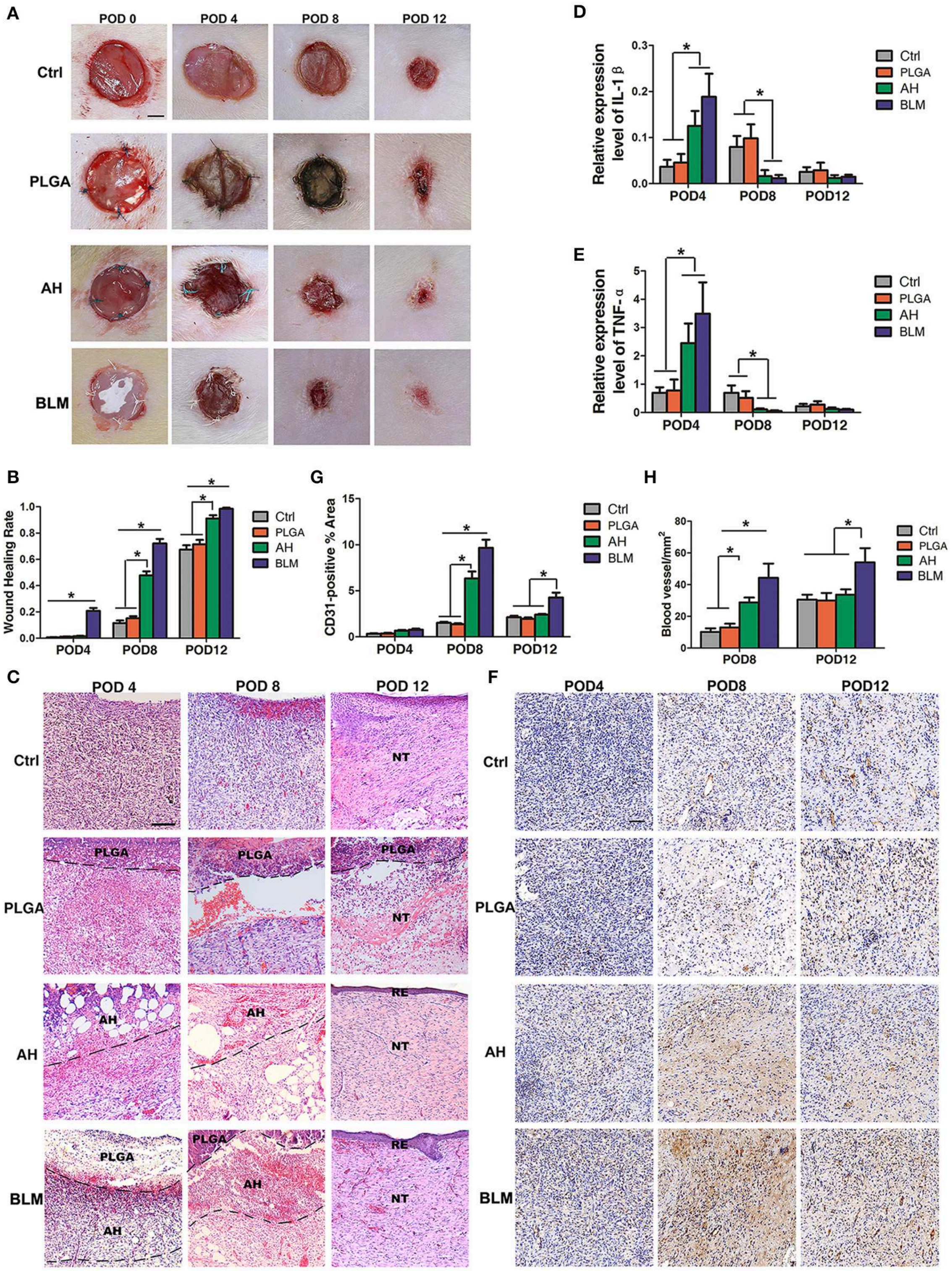

FIGURE 6 | *In vivo* wound healing and staining. **(A)** *In vivo* wound healing of blank control, PLGA, alginate hydrogel (AH), and BLM scaffold on PODs 0, 4, 8, and 12; NT, new tissue; RE, re-epithelization (Scale bar 250 μm). **(B)** Analysis of wound healing rates in different groups. **(C)** H&E staining of control, PLGA, AH, and BLM scaffold on PODs 4, 8, and 12 (Scale bar 50 μm). **(D)** Q-PCR analysis of IL-1β in different groups on PODs 4, 8, and 12. **(E)** Q-PCR analysis of TNF-α in different groups on PODs 4, 8, and 12. **(F)** Immunohistochemical staining of different groups on PODs 4, 8, and 12 (Scale bar 5 μm). The red arrow indicate the vessels. **(G)** Quantification of blood vessel density in CD31-stained tissue sections. **(H)** Quantitative analysis of CD31-positive area (*$P < 0.05$).

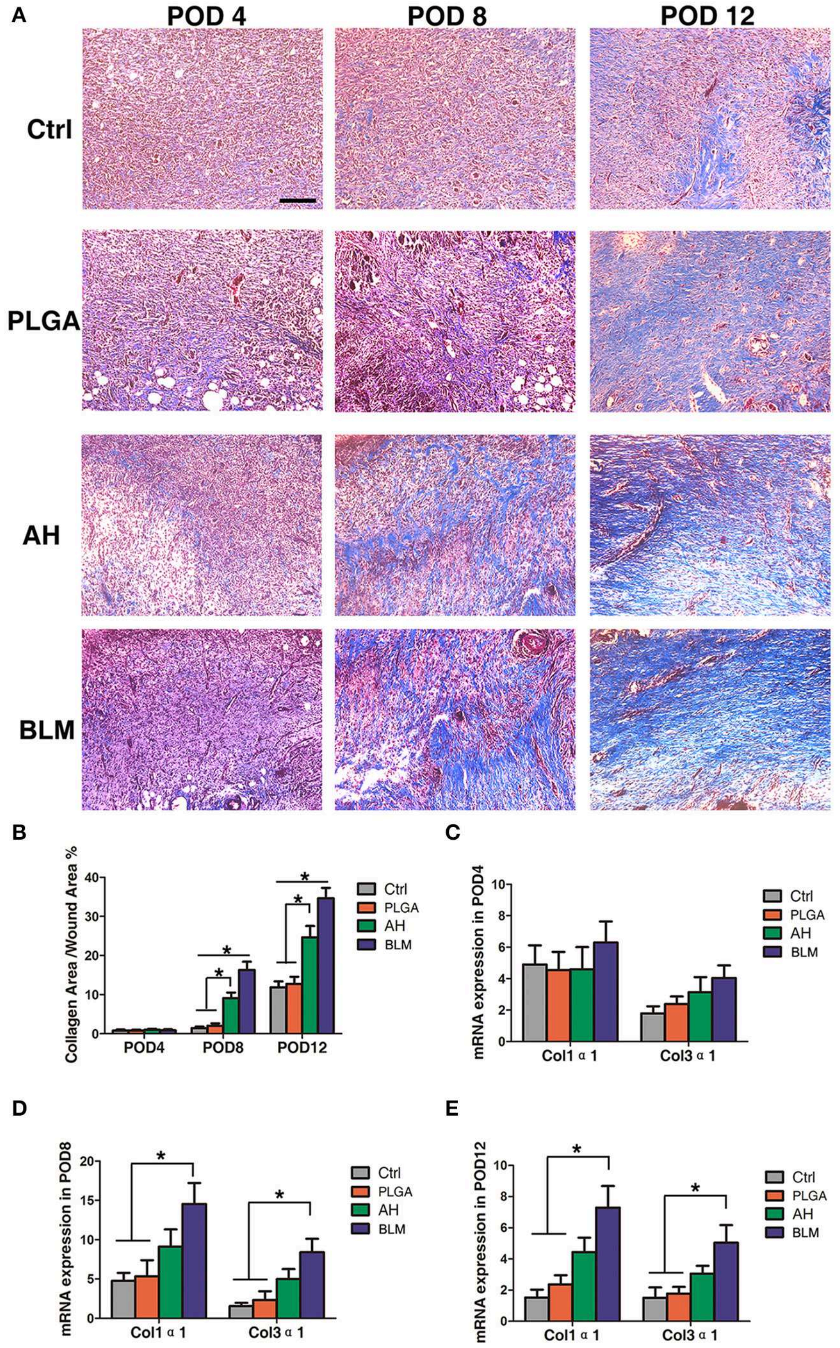

FIGURE 7 | Collagen deposition. **(A)** Masson's staining of wounds in each group on PODs 4, 8, and 12 after operation. Scale bar, 5 μm. The red arrow indicates collagen fibers. **(B)** Quantification of trichrome blue stained area. **(C)** Q-PCR analysis of Col1α1 and Col3α1 in each group on POD4. **(D)** Q-PCR analysis of Col1α1 and Col3α1 in each group on POD8. **(E)** Q-PCR analysis of Col1α1 and Col3α1 in each group on POD12 ($^*P < 0.05$).

generated and connected to the printed needle site. The distance between the needle and the collector was 5–6 cm. The printing needle was set in a circular motion at the speed of 1 mm/s, and the layer height was set to 0.05 μm. PLGA nanofiber membranes of 10 mm diameter and 2 μm thickness were obtained.

The second hydrogel layer was prepared by dissolving sodium alginate in water with constant stirring at 40°C for 4 h. The hydrogel was placed in another barrel which was loaded in air compressor and operated at 0.05 MPa using the same 3D printer. The printing speed was 10 mm/s, and the layer height was set to 100 μm. The hydrogel layer was printed on the surface of the PLGA nanofibers membrane to obtain the BLM scaffold. The latter was then immersed into 5% (w/v) calcium chloride solution for 5 min to crosslink the alginate hydrogel, and then in sterile PBS for hydration. All 3D printing steps were performed under aseptic conditions at 25°C and 40% relative humidity. The equipment was UV-sterilized before 3D printing, and all biomaterials were sterilized through a 0.22 μm filter.

Characterization of BLM Scaffold

The BLM scaffold was freeze-dried for 3 days, and its structure and surface morphology were observed under a scanning electron microscope (SEM, Hitachi TM-100, Japan) fitted with a digital camera (Cannon-50D, Japan). The raw PLGA, raw alginate, PLGA nanofiber layer in BLM scaffold, and alginate hydrogel layer in BLM scaffold were characterized using Fourier transform infrared spectroscopy (FTIR, Avatar 380 FTIR spectrometer). To analyze the moisture retention capacity, alginate hydrogel and BLM scaffold samples were weighed and dried at 37°C for 1, 6, 12, 24, 48, and 72 h in 24-well plates. The dried samples were weighed again, and the residual mass of samples was calculated according to the following formula:

$$\text{Weight remaining }\% = 100\% \times \frac{W_m}{W_i} \tag{1}$$

W_m is the mass of samples after evaporation (g), W_i is the initial mass of samples (g).

To determine the water vapor transmission rate, the pre-weighed samples were sealed and fixed on a utensil. The latter was then placed in a water-filled vessel and incubated at 37°C for 1, 2, 4, 8, and 12 h. The dried samples were weighed and water vapor transmission rate was calculated by the following formula:

$$\text{Water vapor trasmission rate }\% = 100\% \times \frac{W_t}{W_0} \tag{2}$$

W_t is the residual mass after evaporation (g), W_i is the initial mass (g).

The degradation of the alginate hydrogel, PLGA nanofiber and BLM scaffold *in vitro* was also measured by the loss of weight method. The pre-weighed samples were immersed in PBS containing 0.02 % (w/v) sodium azide and incubated at 37°C for 1, 3, 5, 7, 14, 21, and 28 days. The samples were weighed after the incubation period, and the residual mass (weight remaining %) of the samples degraded over time was calculated by the following formula:

$$\text{Weight remaining }\% = 100\% \times \frac{W_f}{W_i} \tag{3}$$

W_f is the mass of samples after degradation (g), W_i is the initial mass of samples (g). The above assays were repeated three times.

The mechanical strength of the samples ($n = 5$) was measured on a universal materials tester (HY-940FS, China) at room temperature and 60% humidity with stretching speed set at 10 mm per min. The stress-strain curve of each sample was observed, and the corresponding Young's modulus was calculated.

Anti-bacterial Barrier and Mammalian Cell Support Function

BLM samples were fixed on nylon net supports that were then placed into petri dishes. Fifty microliters *Staphylococcus aureus* suspension containing 1×10^8 colony-forming units (CFU)/ml was dropped on the center of each BLM sample, and the latter were immersed in culture medium. After incubating at 37°C for 24 h, the samples were fixed with 4% paraformaldehyde for 2 h, and dehydrated through an ethanol gradient (50, 70, 90, 95, and 100%). Bacterial invasion was observed by SEM, and the images were pseudo-colored using Photoshop CS 5.0.

To evaluate the surface adhesion of mammalian cells on the different materials, PLGA nanofiber, alginate hydrogel and BLM scaffold were dried for 1, 6, 12, 24, 48, and 72 h, and inoculated with 1×10^5 murine fibroblast L929 cells. After 6 h of incubation, the non-adherent cells were removed with fresh medium, and then the number of adherent cells were counted using the Cell Counting Kit-8 (CCK-8 Beyotime, China). Cell proliferation was also analyzed on days 1, 3, 5 and 7 of culture. Briefly, 10 μL CCK-8 solution was added to each well and incubated for 2 h, and the absorbance was measured at 450 nm using a micro-plate reader. Viability was measured on day 5 using the LIVE/DEAD Viability/Cytotoxicity Kit (Life Technologies) according to the manufacturer's instructions.

Establishment of Rat Dorsal Model of Wound Healing

Seventy-two 10-weeks old female Sprague-Dawley (SD) rats weighing 300–350 g were purchased from Xipu'er-bikai Experimental Animal Co. Ltd. (Shanghai, China). The animals were housed in specific pathogen-free conditions and had *ad libitum* access to food and water. All protocols were approved by the Animal Care and Use Committee of Shanghai Ninth People's Hospital Affiliated to Shanghai Jiaotong University School of Medicine approval no. SH9H-2019-A612-1. The rats were randomized into the untreated control, PLGA, alginate hydrogel and BLM scaffold groups ($n = 18$ each) prior to wound induction. Anesthesia in rats was induced using isoflurane, while the rats were in a chamber (isoflurane/oxygen: 5%).Thereafter the rats were placed in a prone position and allowed to breathe spontaneously through a nasal cone (isoflurane/oxygen: 1.5–2.0%). The backs of the rats were sterilized and shaved prior to surgery. Thereafter, three 10 mm biopsy punch wounds were made on each side of the dorsal midline, and the epidermis, dermis and perichondrium were removed to expose the underlying muscle tissue, as previously described previously (Gilmartin et al., 2016). The respective scaffolds were stitched to the edge of wounds using a 5-0 suture (Polypropylene suture (Ethicon U.S) for PLGA, Green Braided Polyester suture (Tevdek U.S) for alginate hydrogel and Gore-Tex suture (W.L. Gore & Associates U.S) for BLM, and the animals were placed on a 37°C heating plate for recovery.

Wound Healing Evaluation

The wound area was measured on days 0, 4, 8, and 12 after operation ($n = 6$) using a sterile ruler, and the wound healing rate was calculated as the ratio of the areas of the healed and original wounds. Six animals from each group were sacrificed on days 4, 8, and 12 days after operation, and the wound tissue along with a 5 mm margin of surrounding intact tissue were removed. The tissues were fixed in 4% paraformaldehyde for 24 h and embedded in paraffin, sectioned, and stained with hematoxylin-eosin (H&E), Masson's trichrome and immuno-histochemical reagents (Song et al., 2018).

Quantitative RT-PCR

Total RNA was extracted from the wound tissues, and reverse transcribed with Prime Script^{TM} RT reagent Kit (RR037A, TaKaRa). Quantitative RT-PCR was performed using SYBR Green mixture on a QuantStudio^{TM} 7 Flex Real-time PCR system (Applied Biosystems). The primers are listed in the table below.

Gene	Primer sequences
IL-1β	Sense: 5′-CAGGCTTCGAGATGAACAACAA-3′ Antisense: 5′-ATCACTTGAGAGGTGGTCCCA-3′
TNF-α	Sense: 5′-CCCACGTCGTAGCAAACCACCA-3′ Antisense: 5′-CCATTGGCCAGGAGGGCGTTG-3′
Col1α1	Sense: 5′-CTCAAGATGTGCCACTCTGACT-3′ Antisense: 5′-GAGGGAGTTTACAGGAAGCAGAC-3′
Col3α1	Sense: 5′-TGGCGGCTTTTCACCATATT-3′ Antisense: 5′-ACTCTCTATTTGTCCGTTAACAGACTTG-3′
Gapdh	Sense: 5′-CCTTCATTGACCTCAACTAC-3′ Antisense: 5′-GGAAGGCCATGCCAGTGAGC-3′

Statistical Analysis

Statistical analyses were performed using GraphPad Prism 5 software for Windows (GraphPad Software Inc., La Jolla, CA, USA), while comparison between multiple groups were made using single factor analysis of variance (ANOVA), and the differences between groups were evaluated using the Bonferroni *post-hoc* test.

DATA AVAILABILITY STATEMENT

The datasets generated for this study are available on request to the corresponding author.

ETHICS STATEMENT

The animal study was reviewed and approved by animal care and use committee of shanghai ninth people's hospital affiliated to shanghai jiaotong university school of medicine.

AUTHOR CONTRIBUTIONS

SW designed the study and performed the experiments, analyzed the data and wrote the manuscript. YX performed the experiments and analyzed the data. AG wrote and reviewed the manuscript. YW and JC performed animal experiments. BS printed the bilayer membrane scaffold and characterized the properties of bilayer membrane scaffold. JY designed the study, discussed the data, and wrote and reviewed the manuscript.

FUNDING

This work was supported by grants 81871576 from the National Natural Science Foundation of China (No. 81871576), National Natural Science Foundation of China (No. 81802131), and China Postdoctoral Science Foundation (No. 2019T120347).

REFERENCES

Anisha, B. S., Sankar, D., Mohandas, A., Chennazhi, K. P., Nair, S. V., and Jayakumar, R. (2013). Chitosan-hyaluronan/nano chondroitin sulfate ternary composite sponges for medical use. *Carbohydr. Polym.* 92, 1470–1476. doi: 10.1016/j.carbpol.2012.10.058

Boateng, J., and Catanzano, O. (2015). Advanced therapeutic dressings for effective wound healing–a review. *J. Pharm. Sci.* 104, 3653–3680. doi: 10.1002/jps.24610

Boateng, J. S., Matthews, K. H., Stevens, H. N., and Eccleston, G. M. (2014). Wound healing dressings and drug delivery systems: a review. *J. Pharm. Sci.* 97, 2892–2923. doi: 10.1002/jps.21210

Catanzano, O., D'Esposito, V., Acierno, S., Ambrosio, M. R., De Caro, C., Avagliano, C., et al. (2015). Alginate-hyaluronan composite hydrogels accelerate wound healing process. *Carbohydr. Polym.* 131, 407–414. doi: 10.1016/j.carbpol.2015.05.081

Danhier, F., Ansorena, E., Silva, J. M., Coco, R., Le Breton, A., and Preat, V. (2012). PLGA-based nanoparticles: an overview of biomedical applications. *J. Control. Release* 161, 505–522. doi: 10.1016/j.jconrel.2012.01.043

Dong, Y., Hassan, W. U., Kennedy, R., Greiser, U., Pandit, A., Garcia, Y., et al. (2014). Performance of an *in situ* formed bioactive hydrogel dressing from a PEG-based hyperbranched multifunctional copolymer. *Acta Biomater.* 10, 2076–2085. doi: 10.1016/j.actbio.2013.12.045

Eming, S. A., Martin, P., and Tomic-Canic, M. (2014). Wound repair and regeneration: mechanisms, signaling, and translation. *Sci. Transl. Med.* 6:265. doi: 10.1126/scitranslmed.3009337

Ganeshkumar, M., Ponrasu, T., Krithika, R., Iyappan, K., Gayathri, V. S., and Suguna, L. (2012). Topical application of acalypha indica accelerates rat cutaneous wound healing by up-regulating the expression of type i and iii collagen. *J. Ethnopharmacol.* 142,14–22. doi: 10.1016/j.jep.2012.04.005

Gilmartin, D. J., Soon, A., Thrasivoulou, C., Phillips, A. R., Jayasinghe, S. N., and Becker, D. L. (2016). Sustained release of Cx43 Antisense Oligodeoxynucleotides from coated collagen scaffolds promotes wound healing. *Adv. Healthc. Mater.* 14, 1786–1799. doi: 10.1002/adhm.201600175

Goh, C. H., Heng, P. W. S., and Chan, L. W. (2012). Cross-linker and non-gelling Na+ effects on multi-functional alginate dressings. *Carbohyd Polym.* 87, 1796–1802. doi: 10.1016/j.carbpol.2011.09.097

Gu, Q., Hao, J., Lu, Y., Wang, L., Wallace, G. G., and Zhou, Q. (2015). Three-dimensional bio-printing. *Sci. China Life Sci.* 58, 411–419. doi: 10.1007/s11427-015-4850-3

Hudson, D., and Margaritis, A. (2014). Biopolymer nanoparticle production for controlled release of biopharmaceuticals. *Crit. Rev. Biotechnol.* 34, 161–179. doi: 10.3109/07388551.2012.743503

Iii, J. T. S., Tompkins, R. G., and Burke, J. F. (2000). Artificial skin. *Annu. Rev. Med.* 51, 231. doi: 10.1146/annurev.med.51.1.231

Jahangir, S., Hosseini, S., Mostafaei, F., Sayahpour, F. A., and Baghaban Eslaminejad, M. (2018). 3D-porous beta-tricalcium phosphate-alginate-gelatin scaffold with DMOG delivery promotes angiogenesis and bone formation in rat calvarial defects. *J. Mater. Sci. Mater. Med.* 30:1. doi: 10.1007/s10856-018-6202-x

Koch, L., Deiwick, A., Schlie, S., Michael, S., Gruene, M., Coger, V., et al. (2015). Skin tissue generation by laser cell printing. *Biotechnol. Bioeng.* 109, 1855–1863. doi: 10.1002/bit.24455

Lee, K. Y., and Mooney, D. J. (2012). Alginate: properties and biomedical applications. *Prog. Polym. Sci.* 37, 106–126. doi: 10.1016/j.progpolymsci.2011.06.003

Lee, V., Singh, G., Trasatti, J. P., Bjornsson, C., Xu, X., Tran, T. N., et al. (2014). Design and fabrication of human skin by three-dimensional bioprinting. *Tissue Eng. Part C Methods.* 20, 473–484. doi: 10.1089/ten.tec.2013.0335

Lee, W., Debasitis, J. C., Lee, V. K., Lee, J. H., Fischer, K., Edminster, K., et al. (2009). Multi-layered culture of human skin fibroblasts and keratinocytes through three-dimensional freeform fabrication. *Biomaterials* 30, 1587–1595. doi: 10.1016/j.biomaterials.2008.12.009

Murphy, S. V., and Atala, A. (2014). 3D bioprinting of tissues and organs. *Nat. Biotechnol.* 32, 773–785. doi: 10.1038/nbt.2958

Sabine, W., and Richard, G. (2003). Regulation of wound healing by growth factors and cytokines. *Physiol. Rev.* 83, 835–870. doi: 10.1152/physrev.2003.83.3.835

Senapati, A. K., Giri, R. K., Panda, D. S., and Satyanarayan, S. (2011). Wound healing potential of pterospermum acerifolium wild. with induction of tumor necrosis factor-α. *J Basic Clin Pharm.* 2, 203–206.

Seo, S. Y., Lee, G. H., Lee, S. G., Jung, S. Y., Lim, J. O., and Choi, J. H. (2012). Alginate-based composite sponge containing silver nanoparticles synthesized *in situ*. *Carbohydr. Polym*. 90, 109–115. doi: 10.1016/j.carbpol.2012.05.002

Seol, Y. J., Kang, H. W., Lee, S. J., Atala, A., and Yoo, J. J. (2014). Bioprinting technology and its applications. *Eur. J. Cardiothorac. Surg.* 46, 342–348. doi: 10.1093/ejcts/ezu148

Skardal, A., Mack, D., Kapetanovic, E., Atala, A., Jackson, J. D., Yoo, J., et al. (2012). Bioprinted amniotic fluid-derived stem cells accelerate healing of large skin wounds. *Stem Cells Transl. Med.* 1, 792–802. doi: 10.5966/sctm.2012-0088

Song, Y., Yu, Z., Song, B., Guo, S., Lei, L., Ma, X., et al. (2018). Usnic acid inhibits hypertrophic scarring in a rabbit ear model by suppressing scar tissue angiogenesis. *Biomed. Pharmacother.* 108, 524–530. doi: 10.1016/j.biopha.2018.06.176

Sorg, H., Tilkorn, D. J., Hager, S., Hauser, J., and Mirastschijski, U. (2017). Skin wound healing: an update on the current knowledge and concepts. *Eur. Surg. Res.* 58, 81–94. doi: 10.1159/000454919

Stefanie, M., Heiko, S., Claas-Tido, P., Lothar, K., Andrea, D., Boris, C., et al. (2013). Tissue engineered skin substitutes created by laser-assisted bioprinting form skin-like structures in the dorsal skin fold chamber in mice. *PLoS ONE* 8:e57741. doi: 10.1371/journal.pone.0057741

Sun, G., and Mao, J. J. (2012). Engineering dextran-based scaffolds for drug delivery and tissue repair. *Nanomedicine* 7, 1771–1784. doi: 10.2217/nnm.12.149

Sun, X., Zhang, H., He, J., Cheng, R., Cao, Y., Che, K., et al. (2018). Adjustable hardness of hydrogel for promoting vascularization and maintaining stemness of stem cells in skin flap regeneration. *Appl. Mater. Tdy.* 13, 54–63. doi: 10.1016/j.apmt.2018.08.007

Tran, V., and Wen, X. (2014). Rapid prototyping technologies for tissue regeneration. *Rap Proto Biomater*. 4, 97–155. doi: 10.1533/9780857097217.97

Ueno, H., Mori, T., and Fujinaga, T. (2001). Topical formulations and wound healing applications of chitosan. *Adv. Drug Deliv. Rev.* 52, 105–115. doi: 10.1016/S0169-409X(01)00189-2

Zhao, X., Sun, X., Yildirimer, L., Lang, Q., Lin, Z. Y. W., Zheng, R., et al. (2017). Cell infiltrative hydrogel fibrous scaffolds for accelerated wound healing. *Acta Biomater.* 49, 66–77. doi: 10.1016/j.actbio.2016.11.017

Conflict of Interest: The authors declare that the research was conducted in the absence of any commercial or financial relationships that could be construed as a potential conflict of interest.

frontiers
in Bioengineering and Biotechnology

ORIGINAL RESEARCH
published: 21 January 2020
doi: 10.3389/fbioe.2019.00478

Direct-Write Bioprinting Approach to Construct Multilayer Cellular Tissues

Elahe Masaeli [1,2]* *and Christophe Marquette* [2]*

[1] Department of Cellular Biotechnology, Cell Science Research Center, Royan Institute for Biotechnology, ACECR, Isfahan, Iran, [2] 3d.FAB, Univ Lyon, Université Lyon1, CNRS, INSA, CPE-Lyon, ICBMS, UMR 5246, Bat. Lederer, Villeurbanne, France

As a cellular-assembly technique, bioprinting has been extensively used in tissue engineering and regenerative medicine to construct hydrogel-based three-dimensional (3D) tissue-like models with prescribed geometry. Here, we introduced a unique direct-write bioprinting strategy to fabricate a bilayer flat tissue in a hydrogel-free approach. A printed retina pigmented epithelium layer (RPE) was applied as living biopaper for positioning a fibroblast layer without using any hydrogel in bioink. We adjusted the number of cells in the inkjet droplets in order to obtain a uniform printed cell layer and demonstrated the formation of a bilayer construct through confocal imaging. Since our printing system introduced low levels of shear stress to the cells, it did not have a negative effect on cell survival, although cell viability was generally lower than that of control group over 1 week post-printing. In conclusion, our novel direct-write bioprinting approach to spatiotemporally position different cellular layers may represent an efficient tool to develop living constructs especially for regeneration of complex flat tissues.

Keywords: tissue regeneration, cell layer, inkjet bioprinting, living biopaper, tissue complexity

OPEN ACCESS

Edited by:
Tim B. F. Woodfield,
University of Otago, New Zealand

Reviewed by:
Aleksander Skardal,
The Ohio State University,
United States
Jianxun Ding,
Changchun Institute of Applied
Chemistry (CAS), China

Correspondence:
Elahe Masaeli
elahe.masaeli@royaninstitute.org
Christophe Marquette
christophe.marquette@univ-lyon1.fr

Specialty section:
This article was submitted to
Biomaterials,
a section of the journal
Frontiers in Bioengineering and
Biotechnology

Received: *16 September 2019*
Accepted: *23 December 2019*
Published: *21 January 2020*

Citation:
Masaeli E and Marquette C (2020)
Direct-Write Bioprinting Approach to
Construct Multilayer Cellular Tissues.
Front. Bioeng. Biotechnol. 7:478.
doi: 10.3389/fbioe.2019.00478

INTRODUCTION

Current regenerative medicine systems aim to develop three dimensional (3D) engineered constructs mimicking, as much as possible, the natural tissues found in human body. In this regard, different biofabrication approaches, based on lithography, liquid extrusion and mechanical deposition, were developed to precisely create 3D tissue scaffolds with controlled composition, microarchitecture and geometry (Mota et al., 2015; Moroni et al., 2018).

Most of the aforementioned techniques rely on the active role of biomaterials as structural units and do not incorporate cells during the manufacturing process. Consequently, following the fabrication process, a subsequent cell seeding procedure on/within scaffolds is required. In particular, due to the high complexity of living tissues, multiple cells shall be seeded in the same scaffold, using various complicated seeding methods (perfusion, diffusion, rotational seeding) (Van Den Dolder et al., 2003; Nieponice et al., 2008). In some complex layered structures, such as skin, cornea, retina, and trachea, achieving an effective cellular seeding of the architecture is a considerable challenge. Another challenging group of tissue is the osteochondral joint, where the seeding is even more difficult because of the complexity of the interfaces between cellular layers (Atala et al., 2012). To address these challenges, several methods, such as microencapsulation (Orive et al., 2015), loading cells into microfibers/beads (Matsunaga et al., 2011; Onoe and Takeuchi, 2015) and preparation of cell-laden hydrogels are currently under study to incorporate cells into the structure and use these materials as building blocks in top-down tissue engineering approaches.

Bioprinting, as a well-known additive manufacturing process, aimed at the direct construction of cell-laden tissues by utilizing one of the above-mentioned biofabrication approaches. Bioprinting is capable of either patterning materials in a well-defined design and localizing biological components, such as living cells with a controlled geometry to meet clinical needs (Gao et al., 2016; Mandrycky et al., 2016). In doing so, one of the main limitations of typical tissue engineering methods, i.e., control of the cells seeding within scaffold for mimicking complex tissues, can be overcame.

There are two major bioprinting approaches in literatures: hydrogel-based and hydrogel-free bioprinting. In the first approach, cells are printed within a hydrogel network as a supportive matrix for cell proliferation and maturation, while in the second one, cell suspensions are directly used as bioink. This hydrogel-free approach allows cells to aggregate and secrete their own extracellular matrix (ECM) to hold them together (Jakab et al., 2008; Ozbolat, 2015). Nevertheless, since proliferation is low in these scaffold-free systems, starting with a high cell population is mandatory to reduce time of tissue maturation (Ozbolat, 2015).

Usually, in hydrogel-free systems, cell aggregates or tissue spheroids are accurately positioned through one of most common bioprinting approaches, such as inkjet (Daly and Kelly, 2019), laser guidance (Barron et al., 2004), and extrusion bioprinting (Norotte et al., 2009; Jakab et al., 2010; Pourchet et al., 2017). In the meantime, there is some efforts to directly deposit cell suspension into pre-define patterns (Xu et al., 2005; Calvert, 2007), but to the best of our knowledge, controlling layer by layer the position as well as density and uniformity of seeded cells into 3D structures was not yet optimized. The purpose of this study is to facilitate and control the transfer of two different cell types in a layered structure. An inkjet bioprinting system was applied to directly print cells without carrier material in a pre-defined design. Gelatin methacryloyl (GelMa) hydrogel coated cover glass slides were used as cell-adhesive culture substrate, also called "biopaper" on which cells were bioprinted. Using this method we were able to produce complex multilayer cellular models especially useful for soft tissue engineering.

MATERIALS AND METHODS

Printing System

The inkjet bioprinting system has been applied in our earlier study and is briefly summarized here (Masaeli et al., 2019). This is a piezoelectric inkjet dispenser S3 sciFLEXARRAYER (Scienion AG, Germany) composed of two key subsystems: a 3D stage movement system controlled by a stage controller (accuracy 5 μm) and a droplet deposition system controlled by a pulse generator and equipped with an 80 μm diameter glass nozzle, used here as a non-contact print head. The cell droplet generation system is employed to generate building blocks (i.e., cells in culture media with volume of 300 pL), guided by a computer-aided design software. A stroboscopic camera allows visual monitoring to adjust piezo voltages and pulse durations for reliable droplet ejection. This system provides precise spatial control over droplet deposition. The obtained accuracy of the droplet positioning is 5 μm.

Since, the height of printer glass nozzle is less than depth of tissue culture plates, we designed and 3D printed a silicon cylinder part, insert in each well in order to reduce the distance between the printing head and the cover glass (drop distance) to an optimum of 1 mm (**Figure 2A**). This leads the drops to be accurately deposited and not sprayed over the cover glass surface.

Preparation of GelMa Coated Slides

A thin layer of GelMa was coated on circular glass coverslips (0.5 mm thick, 17 mm diameter, T&Q, China), and subsequently used as biopaper substrate for bioprinting. To prepare this GelMa layer, the following protocol was implemented. Irgacure D-2959 (Sigma, France), used as a photoinitiator, was dissolved in dimethyl sulfoxide (DMSO) at a concentration of 1.5% (w/v). Then, coating solution was prepared by dissolving GelMa powder (Sigma, France) at a concentration of 0.2% w/v in the previously prepared Irgacure solution, degassing under vacuum for 10 min to eliminate bubbles and finally heating for 30 min at 55°C. After setting the glass substrate on the spin coater vacuum holder, 200 μL of GelMa coating solution was dropped and spin-coated at 3,000 rev. min^{-1} for 30 s using a WS-650MZ spin coater (Laurell, USA). Finally, in order to obtain fully cross-linked coating, the spin coated slides were exposed to 32 W UV radiation (254 nm) at a distance of 14 cm for 30 min (BLX-E254, Bio-Link, Fisher Biotec, Australia).

Cells' Printing

Green fluorescent protein (GFP)-expressing fibroblasts (NIH3T3/GFP, AKR-214, Cell Biolabs Inc., US) were expanded and suspended in D-MEM (high glucose) (Gibco, France) supplemented with 10% (v/v) fetal bovine serum (FBS, Gibco, France), 0.1 mM MEM non-essential amino acids (NEAA, Invitrogen, France), 2 mM L-glutamine (Gibco, France) and 1% (w/v) penicillin/streptomycin (10,000 U/mL) (Gibco, France).

Retina pigmented epithelium (RPE) cells (ARPE-19, ATCC, France) were expanded and suspended in DMEM-F12 medium (ATCC, France) supplemented with 10% (v/v) fetal bovine serum (FBS, Gibco, France), and 1% (v/v) penicillin/streptomycin (10,000 U/mL) (Gibco, France).

All cells were culture in a 37°C incubator in the presence of 5% CO_2.

Just before bioprinting, cells were trypsinized [0.25% (v/v) trypsin-EDTA (ThermoFisher, France)], and counted. Cell suspensions (2.3×10^7 and 6.4×10^7 cells/mL for NIH3T3 and RPE, respectively) were directly used as bioink within the inkjet process using a direct-write bioprinting strategy. RPE cells were bioprinted first (18 × 18 spots array, 800 μm spot-to-spot distance, 15 nL per spot) on GelMa coated slide, adhered and cultured for 1 week. Then, NIH3T3 cells were bioprinted onto mature RPE layer following a predefined pattern. In this step, a dot pattern of 160 deposition locations of 15 nL drops were dispensed within an array of 18*18 spots (800 μm spot-to-spot distance) (**Figure 2B**). Images of the printed dots were recorded with an Olympus IX51 microscope.

Cell Viability

The post-printing cellular viability was assessed using the TOX8 Resazurin-based *in vitro* Toxicology Assay Kit (Sigma, France), on media collected 1, 3, and 5 days after bioprinting, according to the manufacturer's instructions. In Brief, kit mix, 10% (v/v) of the final volume, was added to each sample and incubated during 2 h at 37°C. Resazurin (non-fluorescent) to resorufin (fluorescent) conversion was measured fluorometrically (Ex/Em = 600/690 nm) using an Infinite M200 Microplate reader (TECAN, France). Manually seeded cells with similar density were used as control group. The assays were performed three times in all experiments to assess variability.

Actin Cytoskeleton Staining

In order to visualize F-actin structures within cells after bioprinting, constructs were fixed with 3.7% (v/v) paraformaldehyde diluted in phosphate buffer saline (PBS, Invitrogen, France) for 30 min at room temperature, permeabilized with 0.1% (v/v) TritonX-100 for 10 min, and finally stained with 5 units of Alexa Fluor 546 phalloidin (Molecular Probes, France) for 40 min at room temperature. Samples were counterstained with the nuclear stain, 4′,6-diamidino-2-phenylindole (DAPI, Invitrogen, France) (0.1 mg/mL) and imaged by confocal microscopy. Images were taken at the Center Technologique des microstructures (University of Lyon, France) using a Zeiss LSM800 confocal microscope.

Statistical Analysis

Statistical analysis was carried out using one-way analysis of variance (ANOVA) and independent sample *t*-test to compare the viability of bioprinted cell and control group. A value of $p \leq 0.05$ was considered statistically significant.

RESULTS AND DISCUSSION

The classical bioprinting strategy to create multicellular tissue models is based on designed deposition of different cell sources within a hydrogel (i.e., cell-laden hydrogel). These models normally lack uniformity of printed cells and thereupon cannot completely mimic tissue structure. Furthermore, depending on the carrier hydrogel viscosity, cells might experience high amounts of shear stress that may unfavorably affects viability, signaling and generate phenotype drifting (Blaeser et al., 2016; Chimene et al., 2016). Direct printing of living cells without hydrogel inks has then here a number of obvious advantages, such as high cell viability but also the fact that in the absence of carrier, cells will freely produce their own extracellular matrix (ECM) and form 3D structures recapitulating physiological tissues' organization (Ozbolat, 2015).

Based on this idea, we applied a direct-write bioprinting setup to reproduce a bilayer construct in a hydrogel-free manner (**Figure 1**). The technique is based on a programmable non-contact piezoelectric inkjet bioprinter with a resolution of 5 µm and a minimum deposition volume of 300 pL. Such a system has been frequently applied in researches, especially for ultra-low volume liquid handling of nanoparticles (Scherbahn et al., 2016), drugs (Tronser et al., 2018), and biomolecules, such as proteins (Kilb et al., 2019) and antibodies (Marquette et al., 2012; Schulz et al., 2019).

In this bioprinting process, a crucial components, named biopaper, acts as a biomimetic tissue fusion-permissive substrate with appropriate biocompatibility and mechanical stability. In different studies, gelatin-derived hydrogels (Imani et al., 2011; Pirlo et al., 2012; Colosi et al., 2016) as well as cell-laden

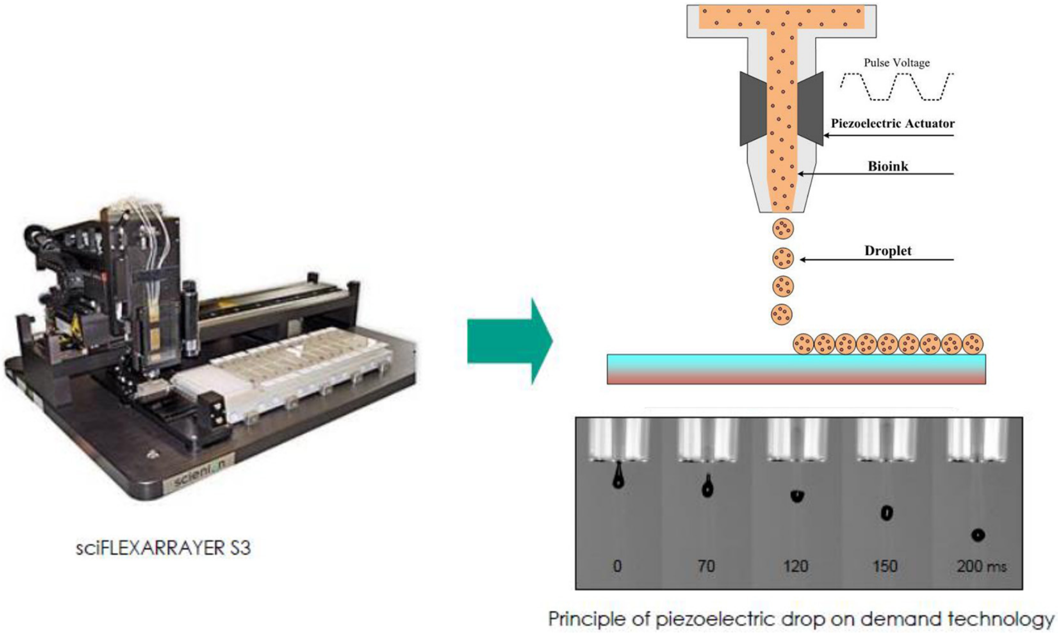

FIGURE 1 | A schematic illustration of direct-write bioprinter setup (www.scienion.de).

bioinks (Nichol et al., 2010; Bertassoni et al., 2014) have been applied as biopaper. In the present study, a 5–20 µm thick GelMa layer [measured using confocal 3D optical profilometer (NanoJura, France)] was coated on glass slide and used as biopaper to enhance the adhesion of the first layer of printed cells. GelMa is a photopolymerizable material composed of modified natural ECM components, containing then significant amount of matrix metalloproteinase and focal adhesion sequences, beneficial to promote cellular functions (Yue et al., 2015). We also previously showed that printed cells were viable and proliferate on GelMa layer over 1-week culture time, and that GelMa coating probably guides cells to form tight junction monolayer sheet (Masaeli et al., 2019).

The cell-printing system was first characterized with NIH3T3 cell suspension using the GelMa coated glass slide as printing support. **Figures 2A,B** depict the dot pattern design which was used to experimentally evaluate size and distance between printed dots (i.e., printing resolution). For sake of comparison, a low viscosity alginate solution was used in addition to the cell suspension. Analysis of captured images showed that average dot diameters were 426 ± 15 and 629 ± 10 µm for alginate and cell solutions, respectively (**Figures 2C,D**). Average drop-to-drop distances were found to be 376 ± 34 and 210 ± 12 µm for alginate and printed solutions, respectively. These measurements helped us determine the final resolution of our inkjet bioprinting system. Indeed, it is well-known that the final resolution of an inkjet printing process can be quite different from the theoretical resolution since the surface chemistry and the ink composition both lead to droplet spreading variations (Binder et al., 2011). As a consequence here, even if the printer should be able to reliably print with resolution of 5 µm, the obtained depositions expanded by 47% between alginate and cell solution and their distance therefore decreased by 44%.

Although some researchers believe that low cell density of inkjet bioprinting is one of its main disadvantages (Holzl et al., 2016; Derakhshanfar et al., 2018), here we were able to use high cell population in each drop (2.3×10^7 cells/mL), probably thanks to the low viscosity ($1.00E^{-03}$ Pa·s) of the bioink cell suspension. Especially for creation of some tissues, such as endothelium, printing with high initial cell densities is essential because cells should be in physical contact with each other. Also, high density of cells is required for tissue engineering when cells with limited to no proliferative potential (such as photoreceptors and chondrocytes…) are introduced into bioprinter (Guillotin et al., 2010).

Another concern related to bioink rheological behavior is that inkjet nozzle could be clogged or generating too much shear stress during cell deposition (Zhang and Zhang, 2015;

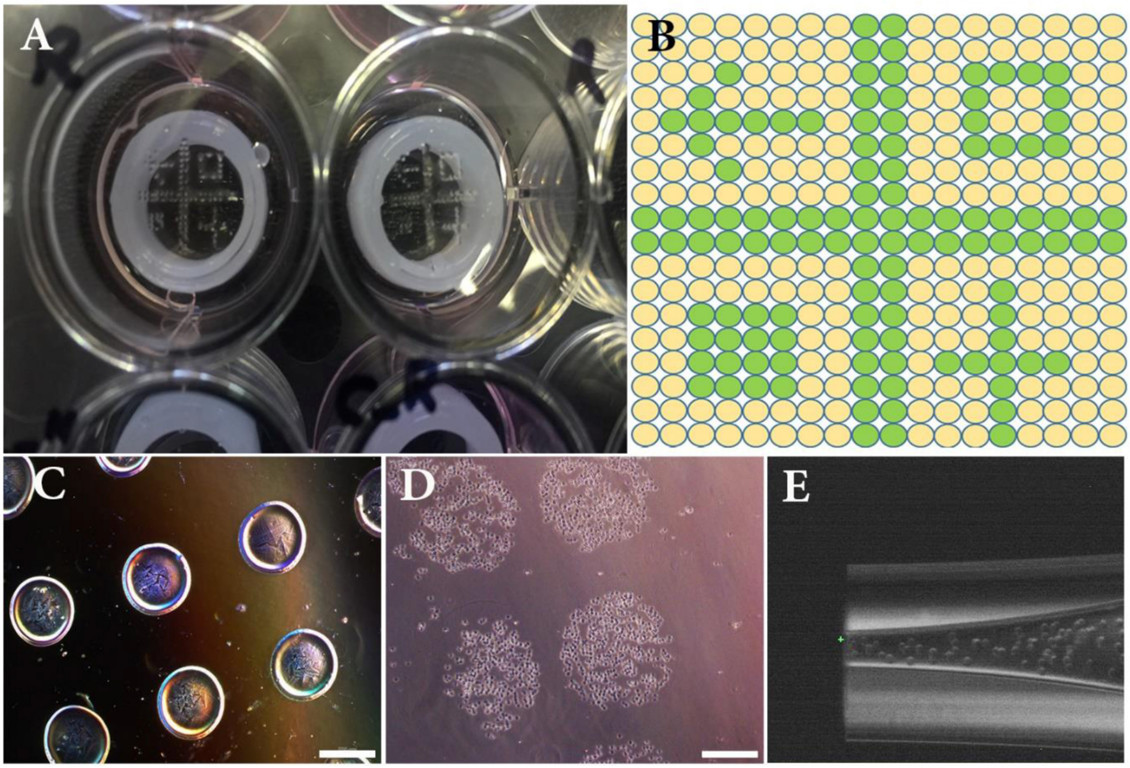

FIGURE 2 | (A) Overview of the experimental set-up composed of a 12-well plate, 3D printed silicone positioning systems, GelMa coated circular glass slides and printed patterns of NIH3T3 cells. **(B)** Overview of the theoretical printing patterns in printer software. **(C)** Printed drops (15 nL) of alginate hydrogel used to setup size and distance between droplets. **(D)** Printed drops (15 nL) of NIH3T3 immediately after bioprinting. **(E)** Close-up image of the bioprinted nozzle filled with NIH3T3 cells. Scale bars: 500 µm.

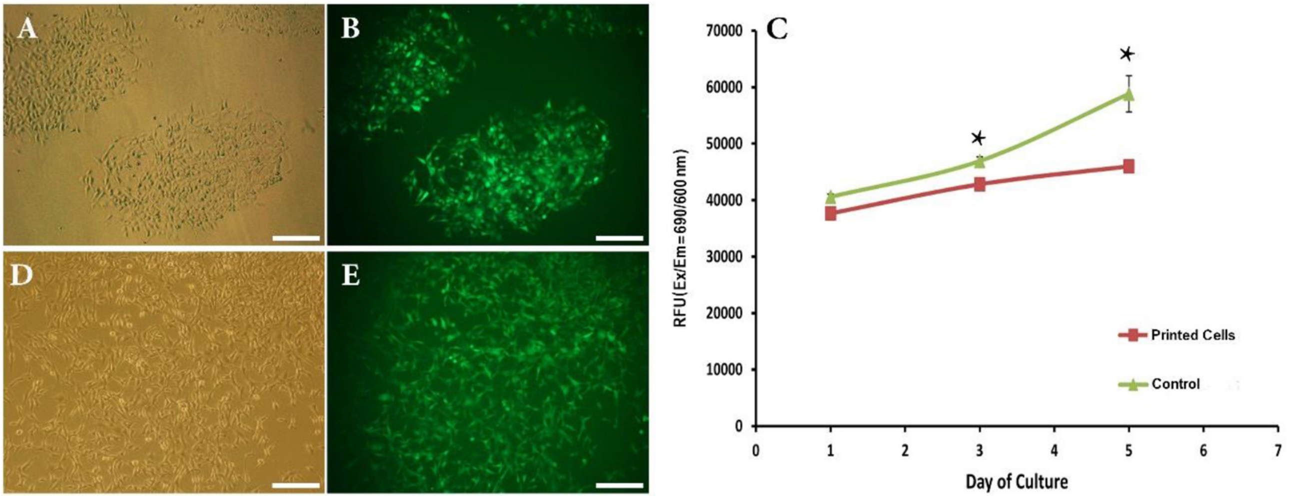

FIGURE 3 | (A,B) Phase contrast and fluorescent images showing attachment of bioprinted NIH3T3 cells 1 day after printing. **(C)** Viability of bioprinted NIH3T3 cells during 5 days after printing. **(D,E)** Phase contrast and fluorescent images showing growth of bioprinted NIH3T3 cells 5 days after printing. Asterisks represent significant difference at $p \leq 0.05$. Scale bars: 200 µm.

Chimene et al., 2016; Bishop et al., 2017). Attempts have been made to overcome these issues by using low viscosity bioinks. For example, Desimone et al. (2015) reduced shear stress inside nozzle by using low viscosity solutions of recombinant spider silk instead of native silk. Colosi et al. prepared a blend of GelMa and alginate as low viscosity (0.08 Pa/s) ink and used it for printing heterogeneous 3D tissue constructs. They believed that printing with low viscosity bioinks shall enhance biological properties and resulting in tissue functions recapitulation (Colosi et al., 2016).

In the present work, not only no clogging was evidenced within the capillary nozzle (**Figure 2E**), but also, the calculated maximum shear stress [calculated using the nozzle geometry and a viscosity of $1.00E^{-03}$ Pa·s: Wall Shear rate: $1.31E^{+08}$ s^{-1}; Wall Shear stress: $1.31E^{+05}$ Pa (3d.FAB, 2018)] was much lower than the previously reported acceptable stress limit (Malda et al., 2013).

We have thus successfully replaced bioprinting ink with cell suspension and set size and distances between inkjet droplets. The next crucial step toward the introduction of this direct-write bioprinting approach is the demonstration of attachment and growth of bioprinted cells over time. This was performed by following cell behavior for 5 days post-bioprinting. **Figures 3A,B** depict images of two adjacent depositions using contrast phase and fluorescent microscopy, respectively. As a matter of fact, bioprinted cells had survived the inkjet process (GFP production is here a clear indicator 1 day after printing).

This qualitative analysis was reinforced by a quantitative study of the cell viability using the TOX8 Resazurin-based *in vitro* assay. **Figure 3C** depicts the obtained results. As can be seen, although the present inkjet bioprinting process induced significant long-term alterations in the proliferation potential of cells (days 3 and 5) when compared to control cells, our hydrogel-free system does not significantly affect cell viability immediately after printing (day 1). In similar way, Blaeser et al. (2016) have stated that printing-induced shear stress does not only have an immediate impact on cell viability but also on their long term fate. Moreover, as shown in **Figures 3D,E**, a clear cell proliferation can be observed, 5 days after bioprinting, evidenced by a colonization of the inter-deposition space by the growing cells, leading to a quasi-confluent cell layer.

In order to fully demonstrate the potential of the developed technique, a 2-layer cell assembly was studied. Here, we applied our hydrogel-free bioprinting approach to directly and uniformly write two cellular layers on top of each other. The final goal being to overcome, through the use of inkjet deposition, the cell seeding variability issues usually experienced using traditional co-culture strategies for layer-by-layer deposition, particularly for population of sensitive cells (Reynolds et al., 2018).

To do so, we have first bioprinted a homogeneous layer of retina pigmented epithelium (RPE) on a GelMa biopaper and cultured them for 7 days (229 ± 19 µm spot distance, 15 nL per spot). Then, once the RPE layer dense enough to cover all the biopaper surface, a second layer of NIH3T3 was printed following a tight deposition pattern (210 ± 12 µm spot distance, 15 nL per spot), chosen to lead to a homogeneous second layer.

RPE cells were selected due to their ability to form cellular monolayer sheet (epithelium layer), a very good substrate for subsequent orientated cell attachment. Numerous studies have been heretofore carried out to model complex flat tissues by layer-by-layer assembly techniques (Tang et al., 2006). For example, Matsusaki et al. (2007) fabricated a multilayer fibroblast construct by preparing fibronectin–gelatin nanofilms. In a similar way, Kawecki et al. (2018) applied human osseous cell sheet as living biopaper to support laser-assisted bioprinting of human endothelial cells.

RPE cells were printed with density of 110 ± 15 RPE cells per deposition, calculated according to their concentration as

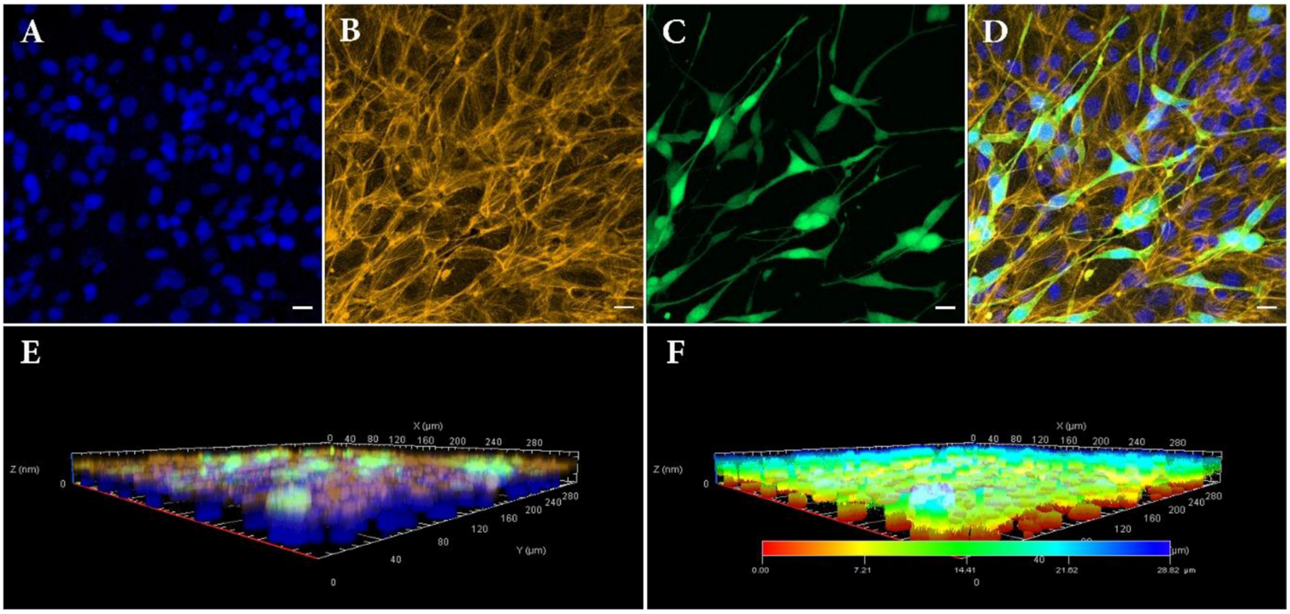

FIGURE 4 | Confocal fluorescence images of bilayer bioprinted construct. **(A)** Counterstained nuclei with DAPI (blue). **(B)** Actin filament staining with phalloidin (Yellow). **(C)** GFP positive NIH3T3 cells (Green). **(D)** Merged image. **(E)** 3D view and **(F)** depth coding of bilayer bioprinted construct. All images were captured on day 3 after printing of NIH3T3 or day 10 after printing RPE cells. Scale bars: 100 µm.

well as their size. One week after bioprinting, RPE cells formed a monolayer sheet, ready to be used as living biopaper for bioprinting NIH3T3 cells. **Figures 4A–D** depict the distribution of the two cell types 3 days after printing the second layer (i.e., 10 days after printing the first layer). As NIH3T3 cells are constitutively producing GFP, they are easily distinguished from RPE cells, especially in merged images (**Figure 4D**).

As a matter of fact, RPE cells were homogeneously distributed as a dense layer over the GelMa surface whereas NIH3T3 cells randomly positioned themselves in a second and less dense layer (160 depositions against 324 depositions for RPE). Separate layers organization of printed cells was also confirmed with 3D confocal imaging (**Figures 4E,F**). Indeed, these images bring evidences that the RPE unlabeled cells (and their nuclei) have been localized in the lowest part of the construct, while GFP positive NIH3T3 cells can be found only on its upper layer. Moreover, depth coding of samples revealed that the full thickness of the construct is around 28.82 µm, consistent with cells' size (**Figure 4F**). Although size, shape and structure of RPE cells depend on age and location, average thickness of a RPE sheet in human is about 14 µm (Forrester et al., 2016). Similarly, NIH3T3 cells size is estimated to be around 15 µm, leading to a theoretical 2-layer construct of 29 µm.

Overall, the capability to direct-write cell using a bioprinting strategy is not only a first step toward successful multilayer printing of dense cells but also a critical indicator of the feasibility of the envisioned organ printing technology. In the absence of a hydrogel ink, we can list the following impacts for the direct-write bioprinting method particularly from the viewpoint of cellular function and tissue remodeling.

First, as the most important point, cell-cell crosstalk is well-established, and the activation of notch signaling for regulating communication between neighboring cells can be guaranteed.

Second, bioprinting is performed with a high density of cells, which is particularly important for generating cell-rich tissue models. This breakthrough is directly dependent on the cell density within bioprinted construct. Indeed, different cells population behaviors, such as development capability and expression of differentiation factors are inefficient when only a small number of cells are present (Payne and You, 2014).

Finally, the ability to create heterogeneous layered models from different cell sources is another advantage of using cell suspensions as printing ink. Obviously, in hydrogel-based bioprinting systems, bioink properties, such as material type, surface tension and viscosity, shall be set according to the cell sources. Furthermore, shear tensions originated from high viscous hydrogels, may adversely affect cell viability.

Here we selected RPE and NIH3T3 cells just for proof-of-concept study, and it is important that in the future, cells' type are being chosen according to the ultimate goal in a more physiologically relevant arrangement. In such case cell-cell communications can assure the transmission of vital molecular signals and trigger cell differentiation and remodeling. Future work by this approach may also look into successive printing of more than two cell layers.

CONCLUSION

It is now clear that bioprinting is a powerful technique with many potential applications for localizing biological components into 3D-engineered structures. Considerable progresses have been made and described in literatures to design and synthesize various hydrogel-based bioinks, compatible with living cells and their microenvironment. These models usually lack uniformity of printed cells and thereupon cannot completely establish immediate vital cellular communications for survival and remodeling of multicellular complex tissues. Another challenge related to application of hydrogels as bioink is that high viscosity of applied materials may generate high shear stress during cell deposition. Therefore, in the current study, we successfully replaced hydrogel ink with cell suspension and set size and distances between inkjet depositions. In this regards, not only no clogging occurred within the capillary nozzle, but also, the calculated maximum shear stress was relatively low. Moreover, thanks to the low viscosity of the cell suspension, we were able to print cells at high density (e.g., 110 ± 15 RPE cells per deposition). After adjusting density and uniformity of printed cells, current hydrogel-free bioprinting approach was extended to directly write two cellular layers on top of each other. To do so, we had first bioprinted a homogeneous epithelium layer, and once the cells covered all the surface, a second layer of cells was printed following first deposition pattern. Here we just applied two different cell sources (NIH3T3 and RPE cells) as models, but for clinical applications, cells must be targeted according to the ultimate goal. To sum up, such direct-write bioprinting strategy is a considerable step forward to the successful printing of complex multicellular tissues, where high density cell layers communicate with each other through direct contact.

DATA AVAILABILITY STATEMENT

All datasets generated for this study are included in the article/supplementary material.

AUTHOR CONTRIBUTIONS

EM and CM conceived and designed the experiments, performed the experiments, analyzed the data, and wrote the paper.

ACKNOWLEDGMENTS

Confocal Microscopy imaging were performed at the Center Technologique des Microstructures (University of Lyon, France) under the supervision of Christelle Fabrer-Boulé and Veronica La Padula.

REFERENCES

3d.FAB (2018). *FLOWTIPS®*. Available online at: http://fabric-advanced-biology.univ-lyon1.fr/flowtips/ (accessed July, 2019).

Atala, A., Kasper, F. K., and Mikos, A. G. (2012). Engineering complex tissues. *Sci. Transl. Med.* 4:160rv112. doi: 10.1126/scitranslmed.3004890

Barron, J. A., Ringeisen, B. R., Kim, H., Spargo, B. J., and Chrisey, D. B. (2004). Application of laser printing to mammalian cells. *Thin Solid Films* 453, 383–387. doi: 10.1016/j.tsf.2003.11.161

Bertassoni, L. E., Cardoso, J. C., Manoharan, V., Cristino, A. L., Bhise, N. S., Araujo, W. A., et al. (2014). Direct-write bioprinting of cell-laden methacrylated gelatin hydrogels. *Biofabrication* 6:024105. doi: 10.1088/1758-5082/6/2/024105

Binder, K. W., Allen, A. J., Yoo, J. J., and Atala, A. (2011). Drop-on-demand inkjet bioprinting: a primer. *Gene Ther. Regul.* 6, 33–49. doi: 10.1142/S1568558611000258

Bishop, E. S., Mostafa, S., Pakvasa, M., Luu, H. H., Lee, M. J., Wolf, J. M., et al. (2017). 3-D bioprinting technologies in tissue engineering and regenerative medicine: current and future trends. *Genes Dis.* 4, 185–195. doi: 10.1016/j.gendis.2017.10.002

Blaeser, A., Duarte Campos, D. F., Puster, U., Richtering, W., Stevens, M. M., and Fischer, H. (2016). Controlling shear stress in 3D bioprinting is a key factor to balance printing resolution and stem cell integrity. *Adv. Healthc. Mater.* 5, 326–333. doi: 10.1002/adhm.201500677

Calvert, P. (2007). Printing cells. *Science* 318, 208–209. doi: 10.1126/science.1144212

Chimene, D., Lennox, K. K., Kaunas, R. R., and Gaharwar, A. K. (2016). Advanced bioinks for 3D printing: a materials science perspective. *Ann. Biomed. Eng.* 44, 2090–2102. doi: 10.1007/s10439-016-1638-y

Colosi, C., Shin, S. R., Manoharan, V., Massa, S., Costantini, M., Barbetta, A., et al. (2016). Microfluidic bioprinting of heterogeneous 3D tissue constructs using low-viscosity bioink. *Adv. Mater.* 28, 677–684. doi: 10.1002/adma.201503310

Daly, A. C., and Kelly, D. J. (2019). Biofabrication of spatially organised tissues by directing the growth of cellular spheroids within 3D printed polymeric microchambers. *Biomaterials* 197, 194–206. doi: 10.1016/j.biomaterials.2018.12.028

Derakhshanfar, S., Mbeleck, R., Xu, K., Zhang, X., Zhong, W., and Xing, M. (2018). 3D bioprinting for biomedical devices and tissue engineering: a review of recent trends and advances. *Bioact. Mater.* 3, 144–156. doi: 10.1016/j.bioactmat.2017.11.008

Desimone, E., Schacht, K., Jungst, T., Groll, J., and Scheibel, T. (2015). Biofabrication of 3D constructs: fabrication technologies and spider silk proteins as bioinks. *Pure Appl. Chem.* 87, 737–749. doi: 10.1515/pac-2015-0106

Forrester, J. V., Dick, A. D., Mcmenamin, P. G., Roberts, F., and Pearlman, E. (2016). "Chapter 1–anatomy of the eye and orbit," in *The Eye (Fourth Edition),* eds. J. V. Forrester, A. D. Dick, P. G. Mcmenamin, F. Roberts and E. Pearlman (W. B. Saunders), 1–102.e102.

Gao, B., Yang, Q., Zhao, X., Jin, G., Ma, Y., and Xu, F. (2016). 4D bioprinting for biomedical applications. *Trends Biotechnol.* 34, 746–756. doi: 10.1016/j.tibtech.2016.03.004

Guillotin, B., Souquet, A., Catros, S., Duocastella, M., Pippenger, B., Bellance, S., et al. (2010). Laser assisted bioprinting of engineered tissue with high cell density and microscale organization. *Biomaterials* 31, 7250–7256. doi: 10.1016/j.biomaterials.2010.05.055

Holzl, K., Lin, S., Tytgat, L., Van Vlierberghe, S., Gu, L., and Ovsianikov, A. (2016). Bioink properties before, during and after 3D bioprinting. *Biofabrication* 8:032002. doi: 10.1088/1758-5090/8/3/032002

Imani, R., Sh, H. E., Sharifi, A.-M., Baheiraei, N., and Fakhrzadeh, F. (2011). Evaluation of novel "biopaper" for cell and organ printing application: an *in vitro* study. *J. Diabetes Metab. Disord.* 10, 1–13. Available online at: http://jdmd.tums.ac.ir/index.php/jdmd/article/view/290

Jakab, K., Norotte, C., Damon, B., Marga, F., Neagu, A., Besch-Williford, C. L., et al. (2008). Tissue engineering by self-assembly of cells printed into topologically defined structures. *Tissue Eng. Part A* 14, 413–421. doi: 10.1089/tea.2007.0173

Jakab, K., Norotte, C., Marga, F., Murphy, K., Vunjak-Novakovic, G., and Forgacs, G. (2010). Tissue engineering by self-assembly and bio-printing of living cells. *Biofabrication* 2:022001. doi: 10.1088/1758-5082/2/2/022001

Kawecki, F., Clafshenkel, W. P., Auger, F. A., Bourget, J.-M., Fradette, J., and Devillard, R. (2018). Self-assembled human osseous cell sheets as living biopapers for the laser-assisted bioprinting of human endothelial cells. *Biofabrication* 10:035006. doi: 10.1088/1758-5090/aabd5b

Kilb, N., Herz, T., Burger, J., Woehrle, J., Meyer, P. A., and Roth, G. (2019). Protein Microarray Copying–Easy on-demand protein microarray generation compatible with fluorescence as well as label-free real-time analysis. *ChemBioChem* 20, 1554–1562. doi: 10.1002/cbic.201800699

Malda, J., Visser, J., Melchels, F. P., Jüngst, T., Hennink, W. E., Dhert, W. J., et al. (2013). 25th anniversary article: engineering hydrogels for biofabrication. *Adv. Mater.* 25, 5011–5028. doi: 10.1002/adma.201302042

Mandrycky, C., Wang, Z., Kim, K., and Kim, D.-H. (2016). 3D bioprinting for engineering complex tissues. *Biotechnol. Adv.* 34, 422–434. doi: 10.1016/j.biotechadv.2015.12.011

Marquette, C. A., Corgier, B. P., and Blum, L. J. (2012). Recent advances in multiplex immunoassays. *Bioanalysis* 4, 927–936. doi: 10.4155/bio.12.56

Masaeli, E., Forster, V., Picaud, S., Karamali, F., Nasr-Esfahani, M.-H., and Marquette, C. A. (2019). Tissue engineering of retina through high resolution 3-dimentional inkjet bioprinting. *Biofabrication*. doi: 10.1088/1758-5090/ab4a20. [Epub ahead of print].

Matsunaga, Y. T., Morimoto, Y., and Takeuchi, S. (2011). Molding cell beads for rapid construction of macroscopic 3D tissue architecture. *Adv. Mater.* 23, H90–H94. doi: 10.1002/adma.201004375

Matsusaki, M., Kadowaki, K., Nakahara, Y., and Akashi, M. (2007). Fabrication of cellular multilayers with nanometer-sized extracellular matrix films. *Angew. Chem. Int. Ed.* 46, 4689–4692. doi: 10.1002/anie.200701089

Moroni, L., Boland, T., Burdick, J. A., De Maria, C., Derby, B., Forgacs, G., et al. (2018). Biofabrication: a guide to technology and terminology. *Trends Biotechnol.* 36, 384–402. doi: 10.1016/j.tibtech.2017.10.015

Mota, C., Puppi, D., Chiellini, F., and Chiellini, E. (2015). Additive manufacturing techniques for the production of tissue engineering constructs. *J. Tissue Eng. Regen. Med.* 9, 174–190. doi: 10.1002/term.1635

Nichol, J. W., Koshy, S. T., Bae, H., Hwang, C. M., Yamanlar, S., and Khademhosseini, A. (2010). Cell-laden microengineered gelatin methacrylate hydrogels. *Biomaterials* 31, 5536–5544. doi: 10.1016/j.biomaterials.2010.03.064

Nieponice, A., Soletti, L., Guan, J., Deasy, B. M., Huard, J., Wagner, W. R., et al. (2008). Development of a tissue-engineered vascular graft combining a biodegradable scaffold, muscle-derived stem cells and a rotational vacuum seeding technique. *Biomaterials* 29, 825–833. doi: 10.1016/j.biomaterials.2007.10.044

Norotte, C., Marga, F. S., Niklason, L. E., and Forgacs, G. (2009). Scaffold-free vascular tissue engineering using bioprinting. *Biomaterials* 30, 5910–5917. doi: 10.1016/j.biomaterials.2009.06.034

Onoe, H., and Takeuchi, S. (2015). Cell-laden microfibers for bottom-up tissue engineering. *Drug Discov. Today* 20, 236–246. doi: 10.1016/j.drudis.2014.10.018

Orive, G., Santos, E., Poncelet, D., Hernández, R. M., Pedraz, J. L., Wahlberg, L. U., et al. (2015). Cell encapsulation: technical and clinical advances. *Trends Pharmacol. Sci.* 36, 537–546. doi: 10.1016/j.tips.2015.05.003

Ozbolat, I. T. (2015). Scaffold-based or scaffold-free bioprinting: competing or complementing approaches? *J. Nanotechnol. Eng. Med.* 6:024701. doi: 10.1115/1.4030414

Payne, S., and You, L. (2014). Engineered cell-cell communication and its applications. *Adv. Biochem. Eng. Biotechnol.* 146, 97–121. doi: 10.1007/10_2013_249

Pirlo, R. K., Wu, P., Liu, J., and Ringeisen, B. (2012). PLGA/hydrogel biopapers as a stackable substrate for printing HUVEC networks via BioLP^{TM}. *Biotechnol. Bioeng.* 109, 262–273. doi: 10.1002/bit.23295

Pourchet, L. J., Thepot, A., Albouy, M., Courtial, E. J., Boher, A., Blum, L. J., et al. (2017). Human Skin 3D Bioprinting Using Scaffold-Free Approach. *Adv. Healthc. Mater.* 6:1601101. doi: 10.1002/adhm.201601101

Reynolds, P. M., Holzmann Rasmussen, C., Hansson, M., Dufva, M., Riehle, M. O., and Gadegaard, N. (2018). Controlling fluid flow to improve cell seeding uniformity. *PLoS ONE* 13:e0207211. doi: 10.1371/journal.pone.0207211

Scherbahn, V., Nizamov, S., and Mirsky, V. M. (2016). Plasmonic detection and visualization of directed adsorption of charged single nanoparticles to patterned surfaces. *Microchimica Acta* 183, 2837–2845. doi: 10.1007/s00604-016-1956-7

Schulz, K., Pöhlmann, C., Dietrich, R., Märtlbauer, E., and Elßner, T. (2019). Electrochemical biochip assays based on anti-idiotypic antibodies for rapid and automated on-site detection of low molecular weight toxins. *Front. Chem.* 7:31. doi: 10.3389/fchem.2019.00031

Tang, Z., Wang, Y., Podsiadlo, P., and Kotov, N. A. (2006). Biomedical applications of layer-by-layer assembly: from biomimetics to tissue engineering. *Adv. Mater.* 18, 3203–3224. doi: 10.1002/adma.200600113

Tronser, T., Demir, K., Reischl, M., Bastmeyer, M., and Levkin, P. A. (2018). Droplet microarray: miniaturized platform for rapid formation and high-throughput screening of embryoid bodies. *Lab Chip* 18, 2257–2269. doi: 10.1039/C8LC00450A

Van Den Dolder, J., Spauwen, P. H., and Jansen, J. A. (2003). Evaluation of various seeding techniques for culturing osteogenic cells on titanium fiber mesh. *Tissue Eng.* 9, 315–325. doi: 10.1089/107632703764664783

Xu, T., Jin, J., Gregory, C., Hickman, J. J., and Boland, T. (2005). Inkjet printing of viable mammalian cells. *Biomaterials* 26, 93–99. doi: 10.1016/j.biomaterials.2004.04.011

Yue, K., Trujillo-De Santiago, G., Alvarez, M. M., Tamayol, A., Annabi, N., and Khademhosseini, A. (2015). Synthesis, properties, and biomedical applications of gelatin methacryloyl (GelMA) hydrogels. *Biomaterials* 73, 254–271. doi: 10.1016/j.biomaterials.2015.08.045

Zhang, X., and Zhang, Y. (2015). Tissue engineering applications of three-dimensional bioprinting. *Cell Biochem. Biophys.* 72, 777–782. doi: 10.1007/s12013-015-0531-x

Conflict of Interest: The authors declare that the research was conducted in the absence of any commercial or financial relationships that could be construed as a potential conflict of interest.

frontiers
in Bioengineering and Biotechnology

ORIGINAL RESEARCH
published: 11 February 2020
doi: 10.3389/fbioe.2020.00057

3D Bioprinting Pluripotent Stem Cell Derived Neural Tissues Using a Novel Fibrin Bioink Containing Drug Releasing Microspheres

Ruchi Sharma*[1], *Imke P. M. Smits*[2], *Laura De La Vega*[1], *Christopher Lee*[3] and *Stephanie M. Willerth*[1,2,4]*

[1] Department of Mechanical Engineering, University of Victoria, Victoria, BC, Canada, [2] Department of Biomedical Engineering, Eindhoven University of Technology, Eindhoven, Netherlands, [3] Djavad Mowafaghian Centre for Brain Health, The University of British Columbia, Vancouver, BC, Canada, [4] Division of Medical Sciences, University of Victoria, Victoria, BC, Canada

3D bioprinting combines cells with a supportive bioink to fabricate multiscale, multicellular structures that imitate native tissues. Here, we demonstrate how our novel fibrin-based bioink formulation combined with drug releasing microspheres can serve as a tool for bioprinting tissues using human induced pluripotent stem cell (hiPSC)-derived neural progenitor cells (NPCs). Microspheres, small spherical particles that generate controlled drug release, promote hiPSC differentiation into dopaminergic neurons when used to deliver small molecules like guggulsterone. We used the microfluidics based RX1 bioprinter to generate domes with a 1 cm diameter consisting of our novel fibrin-based bioink containing guggulsterone microspheres and hiPSC-derived NPCs. The resulting tissues exhibited over 90% cellular viability 1 day post printing that then increased to 95% 7 days post printing. The bioprinted tissues expressed the early neuronal marker, TUJ1 and the early midbrain marker, Forkhead Box A2 (FOXA2) after 15 days of culture. These bioprinted neural tissues expressed TUJ1 (15 ± 1.3%), the dopamine marker, tyrosine hydroxylase (TH) (8 ± 1%) and other glial markers such as glial fibrillary acidic protein (GFAP) (15 ± 4%) and oligodendrocyte progenitor marker (O4) (4 ± 1%) after 30 days. Also, quantitative polymerase chain reaction (qPCR) analysis showed these bioprinted tissues expressed *TUJ1, NURR1* (gene expressed in midbrain dopaminergic neurons), *LMX1B*, *TH*, and *PAX6* after 30 days. In conclusion, we have demonstrated that using a microsphere-laden bioink to bioprint hiPSC-derived NPCs can promote the differentiation of neural tissue.

Keywords: tissue engineering, regenerative medicine, small molecules, drug delivery, guggulsterone, stems cells

Edited by:
Julien Georges Didier Barthès,
Protip Medical, France

Reviewed by:
Jennifer Patterson,
KU Leuven, Belgium
Jose Mauro Granjeiro,
National Institute of Metrology, Quality and Technology, Brazil

****Correspondence:***
Stephanie M. Willerth
willerth@uvic.ca

Specialty section:
This article was submitted to Biomaterials, a section of the journal Frontiers in Bioengineering and Biotechnology

Received: *05 October 2019*
Accepted: *22 January 2020*
Published: *11 February 2020*

Citation:
Sharma R, Smits IPM, De La Vega L, Lee C and Willerth SM (2020) 3D Bioprinting Pluripotent Stem Cell Derived Neural Tissues Using a Novel Fibrin Bioink Containing Drug Releasing Microspheres. Front. Bioeng. Biotechnol. 8:57. doi: 10.3389/fbioe.2020.00057

INTRODUCTION

3D bioprinting has become an increasingly popular strategy for engineering tissues as shown in recent reviews (Gu et al., 2018; Tasnim et al., 2018; De La Vega et al., 2019; Salaris and Rosa, 2019). This process combines cells with bioinks, which are optimized to encourage the formation of target tissues, and deposits them into 3D structures based on specifications given in a digital design file. The properties of the bioink will also determine how well the bioprinted tissue replicates the physiology of the target tissue or organ being printed (Panwar and Tan, 2016; Gungor-Ozkerim et al., 2018; Gopinathan and Noh, 2018). Bioinks should possess a number of characteristics, including high biocompatibility, printability, and the ability to deliver factors to promote the desired behavior from the cells seeded inside. The properties of these bioinks can be tuned for printing specific tissue types as well as to support specific cell populations. In particular, hydrogels often possess the desired characteristics necessary for bioprinting tissues, in terms of viscosity and dealing with the shear stress generated during printing (Gao et al., 2019).

Human induced pluripotent stem cells (hiPSCs) were discovered in 2007 when scientists determined that overexpression of certain transcription factors could revert adult human fibroblasts back into stem cells possessing the property of pluripotency (Takahashi et al., 2007). This discovery has enabled the study of many diseases as these stem cell lines can be derived from patients suffering from different diseases and disorders. Using patient derived hiPSCs lines and differentiating them into a target tissue type is a powerful way to study diseases, including those affecting the nervous system – like Alzheimer's and Parkinson's (Playne and Connor, 2017; Cheng et al., 2018, 2019; Penney et al., 2019). Often, research on hiPSC models of these diseases is conducted in 2D, despite brain tissue possessing a complex 3D structure. Recent work has examined the necessary conditions for 3D printing neural tissues derived from stem cells using hydrogel-based bioinks. For example, Lozano et al. (2015) successfully bioprinted brain-like structures utilizing a bioink composed of gellan gum modified with the RGD peptide containing primary cortical neurons. More recent work from the McAlpine group demonstrated that multiple neural cell types, including neural stem cells derived from hiPSCs, could be printed with relatively high levels of viability into structures that resemble the spinal cord (Joung et al., 2018). However, most of these bioprinting studies have not attempted to generate structures that resemble the brain.

Neural tissues can be generated using many different types of bioprinting technology, including extrusion-based methods, laser assisted printing, inkjet printing, and drop on demand method (Lee et al., 2018). Our lab uses the Aspect Biosystems RX1 printer with its novel microfluidic Lab-on-a-Printer technology due to its ability to protect the cells within the bioink from shear stress during printing – enabling us to maximize cell viability (Beyer et al., 2016; Bsoul et al., 2016). Our own group developed a novel fibrin-based bioink for printing hiPSC-derived neural aggregates that both maintained their viability and differentiated into mature neural tissues after 46 days of culture (Abelseth et al., 2018). This same formulation was also used to print dissociated hiPSC-derived neural progenitor cells (NPCs) that could be matured into spinal cord-resembling tissues upon treatment with specific small molecules (De La Vega et al., 2018a). This bioink formulation supported the generation of ring shaped constructs containing the human glioblastoma cell line where the tissues exhibited high levels of viability and expressed cancer associated protein markers (Lee et al., 2019). We also showed that effects of a potential glioblastoma cancer treatment were different in our 3D bioprinted model compared to 2D culture, illustrating the need for such bioprinted models of neural diseases.

One of the challenges when working with hiPSCs is ensuring their differentiation into the desired, mature phenotypes. Neural differentiation of hiPSCs can take months and require a significant amount of labor and resources (Riemens et al., 2018). One promising strategy for promoting such differentiation requires treating these hiPSCs with small molecule morphogens (Zhang et al., 2012). Our lab has extensively explored the use of small molecule morphogens encapsulated in microspheres, which degrade over time to slowly release the drug in a controlled manner, as a means to direct neural differentiation in an autonomous fashion (Gomez et al., 2015; Agbay et al., 2018; De La Vega et al., 2018b). Guggulsterone, an anti-cancer drug, is a potent agent for differentiating both human embryonic stem cells and hiPSCs into dopaminergic neurons, the cellular population affected by Parkinson's disease (Gonzalez et al., 2013; Robinson et al., 2015). Our recent study demonstrated that we could deliver guggulsterone in a controlled fashion from microspheres as a way to engineer mature neural tissues from hiPSCs (Agbay et al., 2018).

This work now incorporates these novel guggulsterone-releasing microspheres into our fibrin-based bioink as a tool for 3D bioprinting tissues similar to that found in the brain. The goal was to generate neural tissues containing dopaminergic neurons from hiPSCs derived NPCs to model healthy brain tissue in a dish as well as to validate the bioactive properties of our microsphere-containing bioink. In this study, we bioprinted dome shaped constructs containing hiPSC-derived NPCs encapsulated inside of our bioink containing guggulsterone microspheres and characterized their properties. We printed dome shaped structures that were 1 cm in diameter in a layer-by-layer fashion, consisting of six layers. We printed two additional sets of control tissues – (1) tissues containing NPCs and treated with guggulsterone in the media, and (2) tissues containing unloaded microspheres and NPCs. All three sets of constructs were analyzed for cell viability and their expression of markers associated with neural differentiation, in particular dopaminergic neurons.

MATERIALS AND METHODS

Expanding Neural Progenitor Cells From hiPSCs for Bioprinting

Experiments using hiPSC-derived NPCs were conducted with the approval of the University of Victoria's Human Ethics Committee – Protocol No. 12-187. NPCs were derived from undifferentiated hiPSCs (1-DL-01 line – male, WiCell Research Institute) as described previously (Robinson et al., 2015). NPCs were cultured in STEMdiff^{TM} Neural Progenitor Medium (NPM), (STEMCELL^{TM} Technologies, Vancouver, BC, Canada), on cell culture plates coated with poly-L-ornithine (PLO, Sigma, St. Louis, MO, United States) and laminin (Sigma, St. Louis, MO, United States). The NPCs were cultured under standard conditions consisting of 5% CO_2 at 37°C with daily media changes. Cells were cryopreserved in STEMdiff^{TM} Neural Progenitor Freezing Medium (STEMCELL^{TM} Technologies Vancouver, BC, Canada) liquid nitrogen upon reaching 80% confluence.

Preparation of Unloaded and Guggulsterone Microspheres

Microspheres were prepared using an oil-in-water (o/w) emulsion process as previously described (Agbay et al., 2018). 2% poly (vinyl alcohol) (PVA) (Mw ∼ 13,000–23,000, 87%–89% hydrolyzed) (Sigma-Aldrich, St. Louis, MO, United States) solution was prepared by diluting PVA in de-ionized water for an hour at 85°C with 850 rpm on a magnetic mixer (Corning Life Sciences, Tewksbury, MA 01876, United States) for the water phase. Subsequently, 100 ml of 0.3% (w/v) PVA solution was prepared by dissolving 2% PVA with de-ionized water and kept at 35°C. 500 mg of poly- ε-caprolactone (PCL) (Mn ∼ 45,000), was dissolved in 3 ml of dichloromethane (DCM, Fisher Scientific, Ottawa, ON, Canada) on a magnetic mixer for 15 min at 900 rpm for making the oil phase. Later, 0.3 mg of guggulsterone (Sigma-Aldrich, St. Louis, MO, United States) was dissolved in 100% ethanol then added to the oil phase to make microspheres at a concentration of 0.6 μg/mg (w/w, guggulsterone/PCL) microspheres. Unloaded microspheres were prepared by adding an equal volume of ethanol without the drug to the oil phase. 3 ml of 2% PVA was slowly added to the oil solution to prevent disruption of the boundary layer after removal from the magnetic mixer. Afterward, an emulsion (w/o) was then achieved by vortex mixing (Fisher Scientific) at 3000 rpm for 15 s. This (w/o) emulsion was mixed into the 0.5% PVA water phase and held at 35°C at a mixing speed of 500 rpm for 4 h to evaporate of the organic solvent. Then after mixing, the microspheres were isolated by centrifugation at 4,000 rpm (Eppendorf 5810 R model with swinging bucket rotors) and washed with deionized water. The microspheres were lyophilized for 24 h and stored at −20°C. The microspheres were sterilized by low power air-plasma treatment (Harrick Plasma, Ithaca, NY, United States) for 30 s before being added to our bioink.

Bioprinting of Neural Tissues Consisting of hiPSC-Derived NPCs and Microspheres

Bioink was prepared prior to printing as previously described (Abelseth et al., 2018). NPCs at a concentration of 1 million cells/mL were thawed and resuspended in the bioink composed of 20 mg/mL of fibrinogen (Sigma, St. Louis, MO, United States), 0.5% w/v of alginate (120,000–190,000 g/mol, M/G ratio 1.56) (Sigma, St. Louis, MO, United States), and 0.3 mg/mL of genipin (Sigma, St. Louis, MO, United States) dissolved in dimethyl sulfoxide (DMSO) (Sigma, St. Louis, MO, United States), along with 0.5 mg of microspheres in tris-buffered saline (TBS) with phenol red (Sigma, St. Louis, MO, United States) when appropriate. A 15 mL conical tube containing NPCs, bioink and when appropriate microspheres was connected to the "Material 1" channel of the Lab-On-The-Printer (LOP^{TM}) printhead (Aspect Biosystems, Vancouver, BC, Canada) shown in **Figure 1A**. The crosslinker was comprised of 20 mg/mL of calcium chloride (Sigma, St. Louis, MO, United States), 0.075% w/v of chitosan (Sigma, St. Louis, MO, United States), and 1.7 U/mL of thrombin (Sigma, St. Louis, MO, United States) in a conical connected to the crosslinker channel. Cross-linking occurs at the junction of the bioink and crosslinker channels in the printhead (**Figure 1A**). Genipin was included in the bioink solution to avoid cross-linking of the chitosan present in the cross-linker solution before printing. Dome shaped constructs shown in **Figures 1D,E** were bioprinted based on the specifications detailed in the relevant CAD file (**Figure 1B**) generated using Aspect's studio software (V1.2.59.0, Aspect Biosystems, Vancouver, BC, Canada) using a rectilinear infill pattern in a repeated layer by layer fashion. The resulting constructs consisted of 6 deposited layers of cell laden bioink. Specific pressures are applied to each channel to monitor the flow rate to provide sufficient time for the crosslinking reaction to occur. The printing speed used was 25 mm/s and pressure for bioink, crosslinker and buffer channels were 50 mbar, 60 mbar, and 100 mbar, respectively. The bioprinted groups included constructs containing guggulsterone microspheres constructs containing unloaded microspheres, and control constructs soluble guggulsterone (SG). The bioprinted constructs were transferred to 12 well cell culture plates (Greiner Bio-One GmbH, Kremsmünster, Austria) coated with PLO and laminin and incubated at 37°C in 5% CO_2.

Culture of Bioprinted Constructs

The bioprinted constructs were initially cultured in STEMdiff^{TM} Neural Progenitor Media (NPM) (STEMCELL^{TM} Technologies, Vancouver, BC, Canada), on cell culture plates coated with poly-L-ornithine (PLO, Sigma, St. Louis, MO, United States), and laminin (Sigma, St. Louis, MO, United States). with 1% Antibiotic Antimitotic Solution (AAS) (Sigma-Aldrich, St. Louis, Missouri, United States) for the first 10 days after printing. This media contains both epidermal growth factor and basic fibroblast growth factor to promote proliferation of hiPSC-derived NPCs. On day 10, the NPM was replaced by STEMdiff^{TM} Neural Induction Medium (NIM) (STEMCELL^{TM} Technologies, Vancouver, BC, Canada) with 1% AAS to promote maturation of the hiPSC-derived NPCs toward mature neurons as it contains the small molecules SB431542, LDN193189, and rock inhibitor Y-27632. On day 20, the NIM was replaced by Brain Phys Neuronal Medium (STEMCELL^{TM} Technologies, Vancouver, BC, Canada) for all groups to promote further maturation of these bioprinted tissues. The media changes were performed after every 2 days by replacing 50% of media for the first 30 days of culture. Phase contrast imaging was performed with a Leica DMI3000B (Leica Biosystems, Wetzlar, Germany) microscope a QImaging RETIGA 2000R camera (QImaging, Surrey, BC, Canada) at 10X magnification. Imaging of whole bioprinted construct was performed using the Cytation 5^{TM} Gen5 imager and its associated software version 3.05 (BioTek instruments, Winooski, VT, United States).

Assessment of Cell Viability Post Printing

The bioprinted constructs were degraded using the Neural Tissue Dissociation Kit- Postnatal Neurons (Miltenyi Biotec

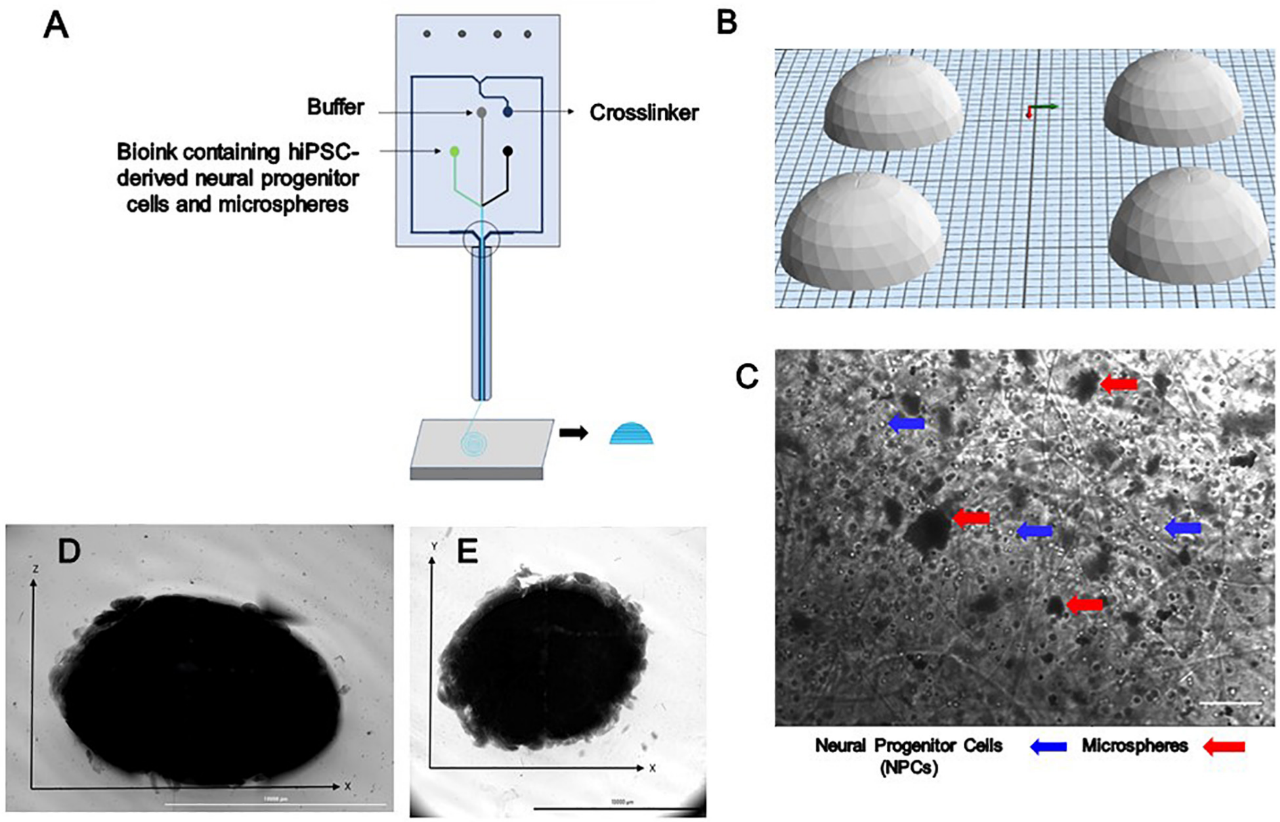

FIGURE 1 | The design and printing of a dome-shaped 3D neural tissue structure. **(A)** Schematic representation of Aspect Biosystems' microfluidic printhead. **(B)** The Computer Aided Design (CAD) file representing dome structures. **(C)** Phase contrast images of day 0 printed construct showing NPCs and microspheres are dispersed throughout the fibers within the constructs (100 μm). Top-down light microscopy image of bioprinted dome shaped construct consisting of neural progenitor cells (NPCs) with bioink containing encapsulated guggulsterone microspheres. **(D)** Image showing the side view of a bioprinted dome and **(E)** showing bottom view of the construct Scale bar for **(D,E)** represents 10,000 μm.

GmbH, Bergisch Gladbach, Germany) in combination with gentleMACS^{TM} Dissociator (Miltenyi, Biotec GmbH, Bergisch Gladbach, Germany) on day 1 and 7 to obtain single cell suspensions for analysis. This process utilizes an optimized combination of enzymatic and mechanical degradation to obtain single cell suspensions. The bioprinted constructs were transferred from each group in to gentleMACS C-tube (Miltenyi Biotec GmbH, Bergisch Gladbach, Germany), from 12 well plate and later, wells of plate were washed with 1960 μL of Enzyme Mix 1 and then that enzyme added into the gentleMACS C-tube. Later, a tightly closed C tube was attached upside down on to the sleeve of gentleMACS Dissociator. Subsequently, the optimized, pre-set gentleMACS program m_brain_01 was run twice on Dissociator for 30 sec each and then constructs incubated for 20 min at 37°C. 45 μL of Enzyme Mix 2 was added to C-tubes and the pre-set gentleMACS program m_brain_02 was run twice for 30 sec each and incubated for 20 min at 37°C then finally, pre-set gentleMACS program m_brain_03 was run twice for 1 min each. Lastly, 2 mL of Fetal Bovine Serum (FBS) (Gibco^{TM}, Thermo Fisher Scientific, Waltham, MA, United States) was added to the mixture to quench the enzymatic reaction and then the cell suspension was run through a 37 μm strainer (STEMCELL^{TM} Technologies, Vancouver, BC, Canada) and centrifuged at 300 × *g* to pellet the cells. The supernatant was removed, and the pellet was resuspended in 1 mL of phosphate buffered solution (PBS) (Thermo Fisher, Waltham, MA, United States). 20 μL of the cell suspension was mixed with 380 μL of Guava ViaCount reagent® (Millipore, Burlington, MA, United States). 100 μL of this mixture was added to the individual wells of the 96-well plate and cell viability was determined using the Guava EasyCyte HT flow cytometer (Millipore, Burlington, MA, United States).

Characterization of Bioprinted Constructs by Immunocytochemistry

Immunofluorescent staining was performed to assess the cell markers expressed by the bioprinted constructs on day 15 and 30. The constructs were fixed with 10% formalin at 4°C for 2 h then permeabilized with 0.1% Triton X (Sigma, St. Louis, MO, United States) at 4°C for 45 min and blocked with 5% Normal Goat Serum (Sigma, St. Louis, MO, United States) and incubated at 4°C for 2 h at 2 rpm on the shaker (The Belly Dancer® orbital shaker) (Sigma-Aldrich Canada Co., Oakville, ON, Canada). The constructs then were incubated with the primary antibody FOXA2 (1:400, AbCam, Eugene, OR, United States) and anti-β-tubulin III (TUJ1) (1:400, Sigma-Aldrich Canada Co., Oakville, ON, Canada) after 15 days of culture. For day 30 constructs, the primary antibodies used were tyrosine hydroxylase (TH) (1:400, Pelfreeze, Arkansas, United States) and TUJ1 (1:400, Sigma-Aldrich Canada Co., Oakville, ON, Canada). The constructs were incubated at 4°C overnight at 100 rpm following three washes with PBS for 15 min at 4°C. Secondary antibodies Alexa Fluor 568 Donkey Anti-Mouse (1:500, AbCam, Eugene, OR, United States), and Alexa Fluor 488 Donkey Anti-Rabbit (1:400, Abam, Eugene, OR, United States) diluted in PBS were added to the constructs. Later, those incubated for an 1 h at room temperature and 3 h at 4°C on the shaker. After incubation with the secondary antibody, cells were washed in PBS three times for 15 min at 2 rpm on the shaker. The cells were counterstained with DAPI (4′,6-diamidino-2-phenylindole) nucleic acid stain (Thermo Fisher Scientific, Waltham, MA, United States). 300 μL of 300-nM DAPI solution in PBS was added to the cultures after the final wash and incubated for 3 min, followed by rinsing with PBS. The bioprinted constructs were then visualized with FIPS – Zeiss Confocal Laser Scanning Microscope ("Objective: 0," Immersion = "Air," Model = "EC Plan-Neofluar 20 × /0.30 M27"; Carl Zeiss Microscopy GmbH, Jena, Germany). The excitation and emission wavelengths used for detecting Alexa Fluor 488 were 479 nm and 519 nm and for detecting Alexa Fluor 588 were 580 nm and 602 nm. The pixel size for 10 × were 1040 × 1040 and 20 × was 710 × 532. The interval used is 10 microns with 20–30 slices in the z stack.

Characterization of Bioprinted Constructs by Flow Cytometry

Bioprinted constructs were analyzed at day 30 using flow cytometry for the following markers: β-tubulin III (βT-III) (TUJ1) (R&D systems, Minneapolis, MN, United States). O4 (oligodendrocytes progenitor marker) (R&D systems, Minneapolis, MN, United States), Anti-Tyrosine Hydroxylase (TH) antibody (AbCam, Eugene, OR, United States), and GFAP (glial fibrillary acidic protein) (AbCam, Eugene, OR, United States) (a mature marker for astrocytes). The bioprinted constructs were degraded and the resulting cell suspension was processed as previously reported in see section "Assessment of Cell Viability Post Printing." Briefly, the cell suspension was washed three times with PBS by centrifuging at 300 *g* for 5 min. The cell suspension was then fixed and stained per the manufacturer's instructions (R&D Systems, Minneapolis, MN, United States). Isotype controls consisted of mouse IgG2A PerCP-conjugated Isotype control (R&D systems, Minneapolis, MN, United States), normal mouse IgM PE-conjugated Control (R&D systems, Minneapolis, MN, United States) and mouse IgG2b, kappa monoclonal [7e10g10] – Isotype control (AbCam, Eugene, OR, United States). The analysis was performed using the Guava EasyCyte HT flow cytometer (Millipore, Burlington, MA, United States).

Characterization of Bioprinted Constructs by Quantitative Reverse Transcriptase Polymerase Chain Reaction (qPCR) Analysis

Total RNA was isolated from the bioprinted constructs using an RNeasy Plus Mini kit according to manufacturer's instructions (Qiagen, Hilden, Germany). RNA content and quality as indicated by the A260/A280 ratio was measured using a NanoVue Plus (GE Healthcare, Chicago, IL, United States). Only samples with an A260/A280 ratio over 1.8 were used. One step PCR was performed on the isolated RNA as per manufacturer's instructions for the QuantiTect SYBR Green Master Mix (204243, Qiagen, Hilden, Germany). RNA isolated from the bioprinted tissues was added to the individual wells of 96 well plates containing reaction mix. This procedure included a reverse transcriptase step followed by the PCR reaction. PCR reactions were performed in triplicates using the relevant QuantiTect Primer Assay or primers in combination with QuantiTect SYBR Green master mix to determine the levels of gene expression. mRNA levels were quantified using the primers for the following genes: Glyceraldehyde-3-phosphate dehydrogenase (*GAPDH* – served as our housekeeping gene, Eurofins Genomics, Luxembourg City, Luxembourg). β-tubulin III (*Tubb3* – plays important roles in axon guidance and maintenance, Qiagen, Hilden, Germany), tyrosine hydroxylase (*TH* – encodes the enzyme tyrosine hydroxylase, Qiagen, Hilden, Germany), nuclear receptor subfamily 4, group A, member 2 (*Nr4a2* also known as *Nurr1,* – plays a role in the differentiation and maintenance of meso-diencephalic dopaminergic neurons, Qiagen, Hilden, Germany), Paired box protein 6 (*PAX6* – promotes neural stem cell proliferation, Qiagen, Hilden, Germany), *LMX1B* (Qiagen, Hilden, Germany) using an Applied Biosystems StepOnePlus Real-Time PCR System (Foster City, CA, United States). Information on the primer assays used can be founded in **Supplementary Table S1**.

Statistical Analysis

Results are presented as the mean values ± standard deviation. Statistical analysis was performed on viability, flow cytometry and qPCR using the one-way ANOVA followed by Tukey's *post hoc* analysis using GraphPad prism 5 statistics software with $p < 0.05$ (95% confidence level) indicating minimal significance.

RESULTS

Generation of Bioprinted Constructs Containing NPCs and Microspheres

Three different types of dome shaped bioprinted constructs containing healthy hiPSC-derived NPCs were printed from the corresponding computer aided design (CAD) file: NPCs only treated with guggulsterone in the media as a positive control referred to as SG, NPCs along with blank microspheres as a negative control referred to as UM, and NPCs along with guggulsterone releasing microspheres referred to as GM. The constructs showed a homogenous distribution of both NPCs and

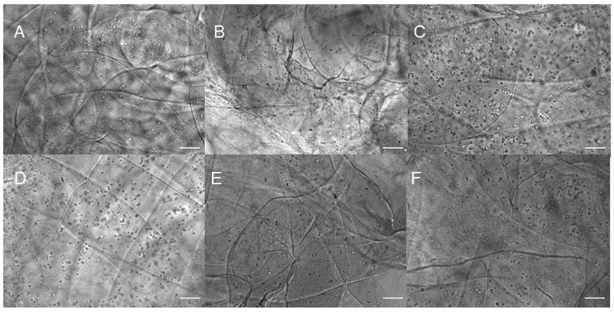

FIGURE 2 | Phase contrast imaging of bioprinted constructs treated with soluble guggulsterone (SG) at **(A)** Day One and **(D)** Day 7, bioprinted constructs containing unloaded microspheres (UM) at **(B)** Day One and **(E)** Day Seven, and bioprinted constructs containing guggulsterone microspheres (GM) at **(C)** Day One and **(F)** Day Seven. Scale bars represent 50 μm.

microspheres after printing (**Figure 1C**). Phase microscopy of the whole constructs showed maintenance of the dome shape post-printing. The structure comprised of 1 cm diameter – dome shape with six layers of fibers with an average width of ∼1.1 cm and height ∼ 0.7 cm (**Figures 1D,E**). Further phase microscopy imaging of the construct on day 1 revealed that the cells and microspheres were spread consistently throughout the construct for all culture conditions (**Figure 2**). While these images only represent the dispersity throughout the whole construct in the *x-y*-direction, but we observed similar distributions at various layers using phase microscopy, suggesting an even distribution throughout the construct.

Cell Viability Analysis of the Bioprinted Tissues

Cell viability of post-printed NPCs was quantified after days 1 and 7 of culture *in vitro* (**Figure 3**). Constructs from all groups showed high viability 1-day post-printing: GM (92 ± 3%), UM (78 ± 11%), SG (89 ± 2%), with no statistical significance between groups observed. The GM group exhibited the highest level of viability on day 7 (98 ± 1%) in comparison with the other two groups (UM – 94 ± 2% and SG – 91 ± 2%). Overall, all groups exhibited high levels of viability post printing. The data is reported as the mean ± S.D ($^{**}p < 0.01$ by one-way ANOVA and Tukey *post hoc* test for significance between samples).

Immunocytochemistry Analysis of the Bioprinted Tissues

ICC was performed on constructs for all three groups for the cellular markers TUJ1 (an immature neuronal maker) and FOXA2 (a midbrain-type dopamine neuron marker) at day 15 (**Figure 4**) and on day 30 for TUJ1 and TH (an enzyme expressed by dopaminergic neurons) (**Figures 5**, **6**). All constructs stained positive for varying levels of TUJ1 and FOXA2 on day 15. Similarly, all constructs expressed TUJ1 on day 30 with the GM and SG tissues expressing TH as well.

Flow Cytometry Analysis of the Bioprinted Tissues

Flow cytometry was performed to quantify the percentage of cells expressing the following markers: TUJ1, TH, glial fibrillary acidic protein (GFAP, marker expressed by astrocytes), and O4 (an oligodendrocyte marker) on day 30 (**Figure 7**). Expression of TUJ1 was significantly higher for the GM tissues (15 ± 1%), followed UM (4 ± 1%), SG (3 ± 1%). Accordingly, expression of TH was the highest for the GM tissues (8 ± 1%), followed by the SG group (7 ± 1.0%) and then UM group has the lowest expression level (4 ± 1%). GFAP expression was the highest for the GM group (15 ± 4%) followed by the UM group (6 ± 1%), with the SG group having the lowest expression levels (3 ± 1%). Finally, both the GM and UM groups had similar levels of O4 expression (5 ± 1%) compared to SG (3 ± 1%). Overall, the guggulsterone microspheres promoted more mature differentiation of the bioprinted NPCs seeded inside of our engineered tissues. The data is reported as the mean ± SD ($n = 3$; $^{*}p < 0.05$, $^{**}p < 0.01$, $^{***}p < 0.001$ by one-way ANOVA and Tukey *post hoc* test for significance between samples for all groups.

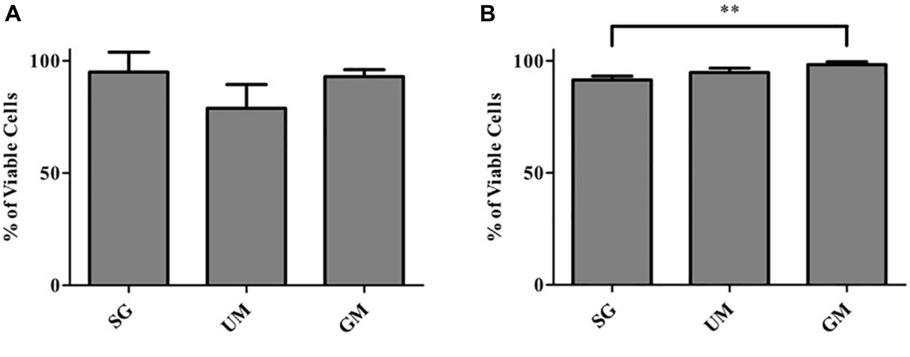

FIGURE 3 | Cell viability analysis for all groups, including the bioprinted constructs treated with soluble guggulsterone (SG), constructs containing unloaded microspheres (UM) and constructs containing guggulsterone microspheres (GM) determined at **(A)** Day 1 and **(B)** Day 7 after being bioprinted. Data is reported as the mean ± S.D ($n = 3$. $^{**}p < 0.01$ by one-way ANOVA and Tukey *post hoc* test for significance between samples).

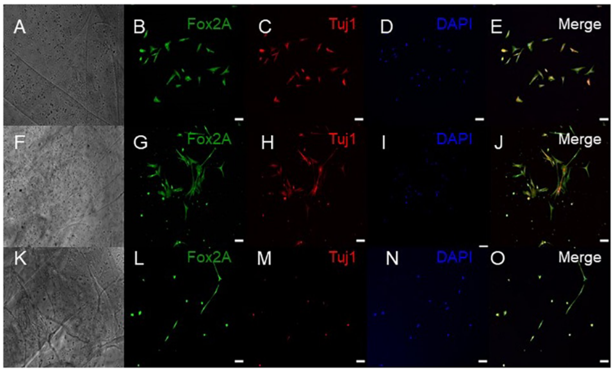

FIGURE 4 | Immunocytochemistry was performed after 15 days of culture for the following markers: FoxA2 (a marker expressed by midbrain-type dopamine neurons shown in green), TUJ1 (an early marker for neurons shown in red), and the nuclear stain DAPI, (4',6-diamidino-2-phenylindole shown in blue). **(A–E)** shows bioprinted tissues treated with soluble guggulsterone (SG), **(F–J)** shows bioprinted tissues containing unloaded microspheres (UM), and **(K–O)** shows bioprinted tissues containing guggulsterone microspheres (GM). The scale bar is 100 μm.

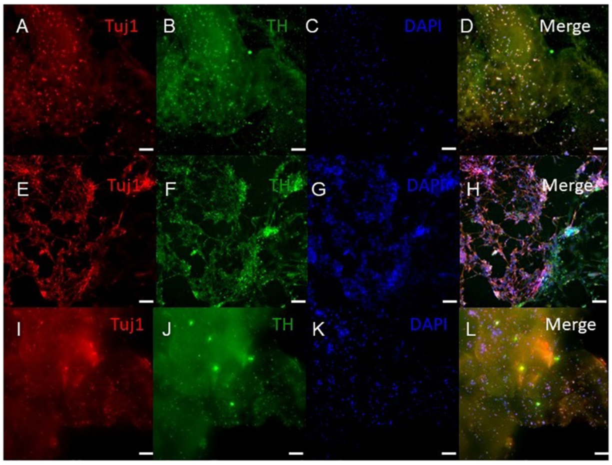

FIGURE 5 | Immunocytochemistry was performed after 30 days of culture on cell that migrated out of the bioprinted constructs for the following markers: TUJ1 (an early marker for neurons shown in red), TH (a dopaminergic neuron marker shown in green), and the nuclear stain DAPI shown in blue. **(A–D)** shows bioprinted tissues treated with soluble guggulsterone (SG), **(E–H)** shows bioprinted tissues containing unloaded microspheres (UM), and **(I–L)** shows bioprinted tissues containing guggulsterone microspheres (GM). The scale bar is 100 μm.

QPCR Analysis of the Bioprinted Tissues

Quantitative polymerase chain reaction was performed to analyze the gene expression levels present in our three different groups of bioprinted tissues on day 30 and the gene expression levels were normalized to the positive control – soluble guggulsterone in the media (**Figure 8**). Both sets of tissues containing microspheres showed increased levels of *TUBB3* (gene encoding for *TUJ1*) in comparison to the tissues treated with soluble guggulsterone as well reduced levels of *NR4A2* (Nurr1) (dopaminergic neurotransmitter phenotype gene). Interestingly, both the SG and GM groups showed higher levels of TH RNA in comparison to the UM group. The tissues showed decreased *LMX1B* expression in comparison to the tissues treated with soluble guggulsterone. Finally, the GM group also exhibited the highest levels of *PAX6* RNA (a neural progenitor marker).

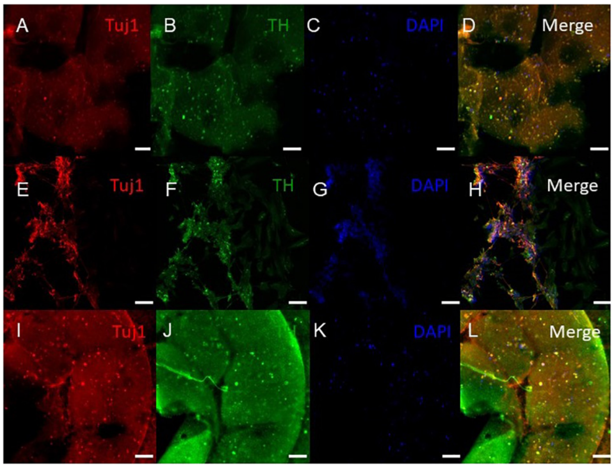

FIGURE 6 | Immunocytochemistry was performed after 30 days of culture on the cells embedded in different layers of bioprinted constructs for the following markers: TUJ1 (an early marker for neurons shown in red), TH (a dopaminergic neuron marker shown in green), and the nuclear stain DAPI shown in blue. **(A–D)** shows bioprinted tissues treated with soluble guggulsterone (SG), **(E–H)** shows bioprinted tissues containing unloaded microspheres (UM), and **(I–L)** shows bioprinted tissues containing guggulsterone microspheres (GM). The scale bar is 100 μm.

DISCUSSION

3D bioprinting combines cells with biocompatible materials to create 3D structures with defined micro and macro architectures (Hsieh and Hsu, 2015). In comparison to traditional 2D cultures, 3D bioprinted tissues provide an improved platform for mimicking tissues *in vitro*. In particular, 3D structures can replicate the influence of the microenvironment on cell growth as well as cell-cell and cell-matrix interactions (Lee et al., 2010). Such bioprinted microenvironments can promote the differentiation of hiPSC-derived NPCs into mature, electrophysiologically active neurons. Our group has engineered 3D bioprinted hiPSC-derived neural tissue that mimics spinal cord tissue by treating these tissues with a variety of small molecules (De La Vega et al., 2018a). While these 3D bioprinted constructs show promise as an *in vitro* neural tissue models, there is still significant room for improvement. Traditional neural differentiation methods require supplementing media with small molecules and growth factors is the conventional technique for inducing neural differentiation. Incorporating drug releasing microspheres in our bioinks can improve the differentiation efficiency of the cells inside while minimizing the number of media changes. As such, our 3D bioprinted constructs could be improved by increasing distribution of differentiation

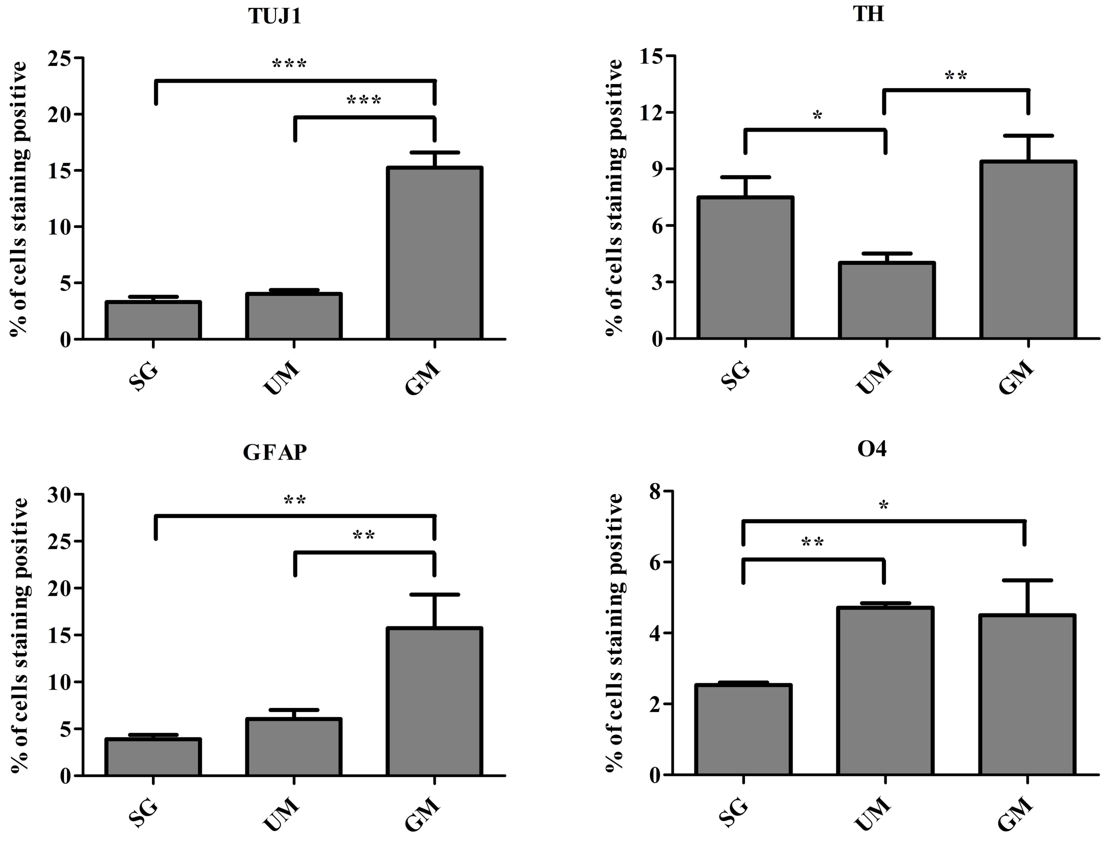

FIGURE 7 | Quantitative flow cytometry assessment of the cell types present on day 30 in the bioprinted constructs treated with soluble guggulsterone (SG), bioprinted constructs containing unloaded microspheres (UM), and bioprinted constructs containing guggulsterone microspheres (GM) for the following markers: TUJ1 (an early marker for neurons), tyrosine hydroxylase (TH, a dopaminergic neuronal marker), glial fibrillary acidic protein (GFAP, a protein expressed by astrocytes), O4 (a marker expressed by oligodendrocytes). Data is reported as the mean ± SD ($n = 3$; $^{*}p < 0.05$, $^{**}p < 0.01$, $^{***}p < 0.001$ by one-way ANOVA and Tukey *post hoc* test for significance between samples for all groups.

factors within the bioinks. 3D bioprinted constructs containing microspheres and compared their properties to pure bioprinted hydrogels and found incorporation of microspheres enhanced cell viability in the 3D constructs (Tan et al., 2016). The goal of this study was to improve functional maturation of 3D printed neural tissue models by incorporating drug releasing microspheres in our bioink. In particular, the incorporation of guggulsterone releasing microspheres in our bioink was evaluated as a method to induce cells to differentiate toward a dopaminergic neuronal fate. 3D printing enables the generation of objects with geometric structures that would be difficult to produce using traditional tissues engineering methods. In the present study, we have focused on bioprinting of dome-shaped constructs containing NPCs to produce a functional tissue with a homogeneous distribution of cells throughout the construct so they can interact in three dimensions. Additionally, this shape more accurately replicates the microenvironment in the brain compared to cross-hatched structures printed in previous studies (Gu et al., 2016). Finally, our dome-shaped constructs possessed a porous structure that enabled transfer of nutrients and oxygen, allowing the long-term culture of cells *in vitro*.

First, we successfully bioprinted NPCs in combination with drug releasing microspheres containing guggulsterone to create a complex tissue model the using Aspect Biosystems RX1 bioprinter. Phase contrast microscopy revealed that post printing cells are homogenously placed with microspheres throughout the fibers in different layers (**Figure 1C**). Most of the researchers focused on bioprinting neural stem cells (NSCs) with different biocompatible materials and differentiating them with several factors in to mature neurons and glial cells (Hsieh and Hsu, 2015; Gu et al., 2016; Huang et al., 2017; Zhou et al., 2018). While previous research using our bioink showed high cell viability post printing (De La Vega et al., 2018a; Lee et al., 2019), the effect of the addition of microspheres had not been studied. Here we investigated bioprinting NPCs along with guggulsterone releasing microspheres for generating tissues containing mature neurons. The bioprinted tissues containing NPCs showed high levels of viability on both day 1- and 7-day post printing. Cell viability for GM and SG was 92% and 94%, respectively, 1 day post printing while the UM group had 78% cell viability. These percentages are higher than those reported by Gu et al. (2016) where immediately after printing using a bioink made up of alginate, carboxymethyl chitosan and agarose 25% of frontal

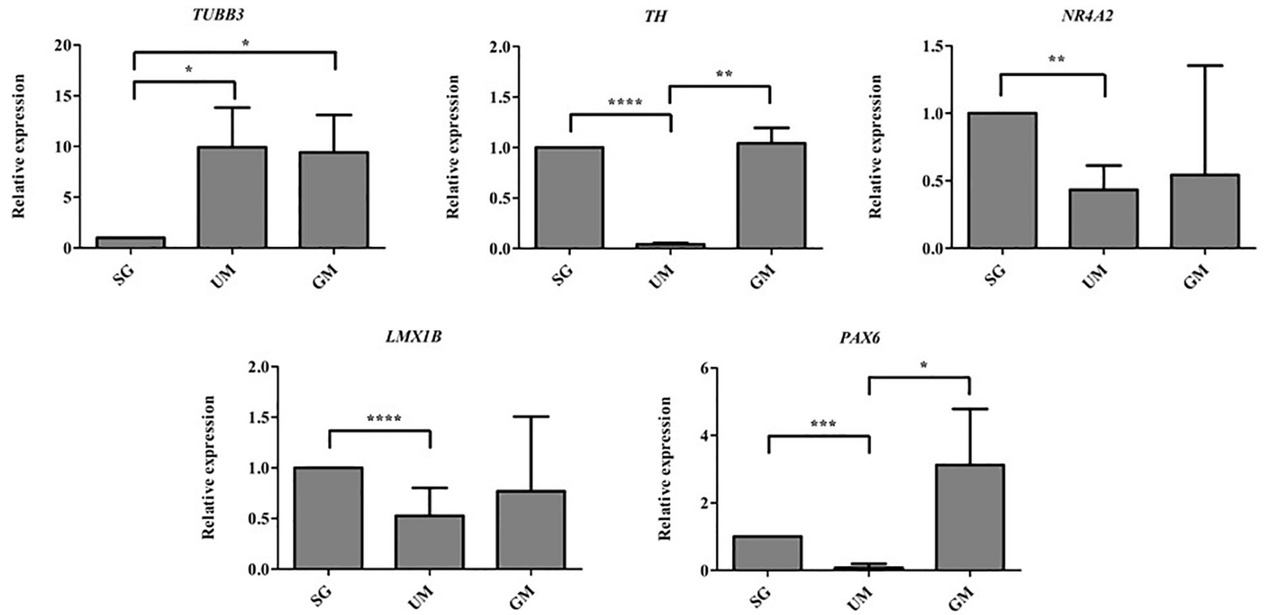

FIGURE 8 | qPCR was performed on Day 30 to determine the relative gene expression levels of the following neurodevelopmental genes: β-tubulin III (*Tubb3*), tyrosine hydroxylase (*TH*), nuclear receptor subfamily 4, group A, member 2 (*Nr4a2* also known as *Nurr1*), LIM homeobox transcription factor 1β (*LMX1B*), Paired box protein 6 (*PAX6*). Gene expression levels were normalized to *GAPDH* and then to levels expressed the bioprinted constructs treated with soluble guggulsterone (SG). Data is reported as the mean ± SD ($n = 3$; $*p < 0.05$, $**p < 0.01$, $***p < 0.001$, $****p < 0.0001$ by one-way ANOVA and Tukey *post hoc* test for significance between samples).

cortical human NSCs died. Additionally, Joung et al. (2018) reported the cell viability of spinal NPCs printed in hydrogel matrices consisting of gelatin methacrylate (GelMa) and gelatin mixed with fibrin ranged from 75 to 88% after 3 h and later decreased to 50% after 1 day. Later, bioprinted iPSC-derived spinal NPCs and oligodendrocyte progenitor cells (OPCs) after 4 days remained 75% viable in a 50% Matrigel bioink. Thus, our bioprinting process preserves cell viability at higher levels than previously reported by other groups.

Cell viability was above 90% for all groups, where GM and UM showed the highest levels of cell viability at 98% and 94%, respectively, and SG showed 91% cell viability on day 7. These percentages are higher than those reported by Salaris et al. (2019) where cell viability of NPCs were 71% after 7 days of culture in a bioink comprised of a Matrigel/alginate solution (Salaris et al., 2019). De La Vega et al. (2018a) reported the cell viability of hiPSC-derived NPCs as >81%. Additionally, Tan et al. (2016) reported the post printing viability of bioprinted mouse fibroblasts L929 cells with poly (D,L-lactic-co-glycolic acid) (PLGA) microspheres was greater than 90% after 2, 7, and 14 days. They reported that microspheres provide a cushion around the cells for preventing shear stress produced during printing process and post printing. This study has demonstrated that these bioprinted constructs containing microspheres provide a suitable 3D environment for different types of cells to grow. Importantly, our work here corroborates that the addition of microspheres does not negatively affect cell viability within the printed constructs. Furthermore, the increased viability on day 7 suggests that cells adapted to the scaffold microenvironment in the presence of microspheres, which enabled the cells to positively proliferate. The microspheres also became less prominent over time, suggesting that they were being degraded by the presence of cells.

Our 3D bioprinted tissues were cultured for 15 and 30 days *in vitro* for analysis of the tissue composition which longer than done in previous studies where ICC staining was performed after 12 days post printing (Zhou et al., 2018). 3D bioprinted constructs showed positive staining for the TUJ1 and FOXA2 at day 15 and expression of TH at day 30. FOXA2 was positively expressed in SG, GM, and UM. Several studies have suggested that FOXA2 plays an important role in directing NPCs to differentiate into dopaminergic neurons and its expression is critical for phenotype maintenance, function and survival in this neuronal subtype (Stott et al., 2013; Kim et al., 2017). Its upregulation in all groups indicates that 3D bioprinted environment enabling NPCs toward the dopaminergic neuron fate (**Figure 4**). Zhou et al. (2018) cultured their bioprinted constructs for 12 days to assess the potential of 3D (GelMA)-functionalized dopamine (DA) scaffolds to induce neuronal differentiation and demonstrated significant TUJ1 staining was noted on GelMA and GelMA–DA scaffolds over time. In present study, at day 30, TUJ1 was positively expressed by GM and SG in similar way when compared to UM. Upregulation of TUJ1 in all of our bioprinted tissue conditions suggests cells are adopting moving further toward a neuronal fate. In comparison with UM; SG and GM expressed comparatively more of the TH enzyme that synthesizes dopamine (Zhou et al., 2018), and its upregulation in SG and GM imply the adoption of a dopaminergic fate due to the presence of guggulsterone. Interestingly, in Gu et al. (2017), their bioprinted constructs had expressed mature neuronal markers, such as microtubule associated protein 2 (MAP2), gamma-aminobutyric acid (GABA), and Synaptophysin at day 40 though we did not examine these markers in our current study.

Flow cytometry was performed to quantify observed changes in neural marker expression. Previously, Gu et al. (2016) reported low levels expression of TUJ1 (2%) after 21 days of differentiation for bioprinted hiPSC-derived NPCs. These levels of TUJ1 expression are significantly higher in our studies at day 30. The expression was observed to be higher in GM tissues when compared to UM and SG tissues, implying the delivery of guggulsterone through microspheres provided the best environment for neuronal differentiation. Interestingly, SG tissues had the lowest expression of TUJ1. It may be that soluble drug did not influence differentiation of cells embedded in the bioink to same extent as the delivery of guggulsterone by microspheres. Previous work from our group has shown how such drug releasing microspheres can promote differentiation of hiPSC-derived NPCs into mature neural tissues (Agbay et al., 2018). Additionally, the UM group expressing higher levels of TUJ1 than SG implies that the presence of the physical presence of the microspheres can influence differentiation. Previous studies also observed similar expression of TUJ1 in tissues treated with GM and SG. The same study showed that TUJ1 expression was the lowest in conditions lacking both guggulsterone and microspheres (Agbay et al., 2018). Here, we also observed that TH expression was higher in GM and SG groups than in tissues containing UM. This result was expected, as guggulsterone works as an effective inducer of pluripotent stem cell-derived neural stem cells into dopaminergic neurons (Gonzalez et al., 2013; Robinson et al., 2015). Interestingly it was observed that the percentage of cells expressing GFAP – a marker for astrocytes – was highest in the GM group. Previous studies have determined guggulsterone to be a potent inhibitor of the signal transducer and activator of transcription 3 (STAT3) pathway, an intracellular pathway responsible for directing neural progenitors toward an astroglial fate (Gonzalez et al., 2013).

The results of current studies suggest that NPCs react differently to guggulsterone when grown in a 3D environment. Consequently, this microenvironment assists NPCs to differentiate into glial fate along with TH positive neurons. Additionally, it was found that UM showed the highest percentage of cells expressing O4, suggesting that PCL microspheres preferably assisted in differentiation toward oligodendrocytes rather than neurons and astrocytes. The tissues containing GM also expressed O4, indicating that these tissues possess all three major neural subtypes – neurons, astrocytes, and oligodendrocytes.

We then used qPCR to confirm the transcriptional profile of 3D bioprinted neural tissue after 30 days. Huang et al. (2017) reported expressions of neural-related genes such as nestin, β-tubulin, and GFAP for NSCs in different hydrogel constructs after 3 days by qPCR. Moreover, Salaris et al. (2019) reported bioprinted constructs cultured for 45 days showed expression of neural progenitor markers such as *PAX6, FOXG1*, and *TBR2,* an astrocyte marker GFAP and mature cortical neuron marker TBR1. However, our study demonstrated *TUBB3 (TUJ1)* expression was observed to be higher in GM tissues alongside UM tissues when compared to SG tissues at day 30. It may be that soluble drug did not induce bioprinted NPCs to express this gene while the incorporated microspheres increased expression. A study by Gu et al. (2017) reported gene expression analysis by qRT-PCR supported by flow cytometry and immunofluorescence post printing 3 weeks showing upregulation of *TUJ1, OLIGO2*, and *GFAP*. TUJ1 was upregulated in previous studies when hiPSCs were differentiated with guggulsterone for deriving dopaminergic neurons (Gonzalez et al., 2013). Similar to the results observed using flow cytometry, the UM groups demonstrated a high expression of *TUBB3* suggests that the microspheres strongly influencing differentiation. Previous studies also confirmed PCL microspheres induced the differentiation of hiPSC-derived NPCs into neurons (Agbay et al., 2018). Thus, it is possible that the particles present in the bioink influence growth and differentiation of cells. Increased *TH* expression indicated by GM and SG group suggests that guggulsterone is an effective inducer of neural precursors into dopaminergic neurons. Previous studies indicated the importance of *NR4A2 (Nurr1) and LMX1B* in generation of dopaminergic neurons (Chinta and Andersen, 2005; Niu et al., 2018). Two transcription factors that regulate dopaminergic differentiation *NR4A2 (Nurr1)* and *LMX1B* were also more highly expressed in GM and SG groups than UM. These results indicate that guggulsterone is potentially differentiating NPCs into dopaminergic neurons. The UM group expressed lower levels of *NR4A2 (Nurr1)* and *LMX1B,* which indicates the pivotal role of guggulsterone in inducing the dopaminergic fate in these bioprinted tissues.

The transcription factor *PAX6* is known as a neurogenic determinant in adult NPCs during development, is expressed in selectively populated dopaminergic neurons, and plays a significant role in Parkinson's disease (Sebastián-Serrano et al., 2012; Chandrasekaran et al., 2017). Higher levels of *PAX6* were observed in GM and SG when compared with the UM group. The GM and SG groups expressed *PAX6,* which implies an increased proliferation of NPCs.

TH, *NURR1,* and *LMX1B* mRNAs were upregulated in the guggulsterone containing group, which suggests that bioprinted NPCs possess dopaminergic fate. 3D bioprinted NPCs with GM and SG positively expressed dopaminergic neuron-enriched transcription regulators *NURR1*, *LMX1B*, FOXA2, and TH. These results were similar to other studies that used guggulsterone to derive dopaminergic neurons from hiPSCs (Gonzalez et al., 2013; Robinson et al., 2015). These results also suggest that the bioprinted tissues containing guggulsterone releasing microspheres possess gene and protein expression profiles similar to those for dopaminergic neurons.

Our results suggested that microsphere incorporated scaffolds could potentially generate dopaminergic neurons and a number of committed differentiated neurons. Once optimized, these 3D bioprinted neural tissues could be used to model neurodegenerative diseases using patient-specific hiPSC lines, as currently done in 2D (Poon et al., 2017; Fantini et al., 2019). This study provides an approach to generate 3D neural tissues containing dopaminergic neurons as a clinically relevant model for drug discovery as well as a potential way to generate tissue to replace the lost neurons that die off during Parkinson's disease.

Our work validates that 3D-printed customizable microsphere-based bioinks can play a positive role in promoting neural differentiation into specific neuronal subtypes while maintaining high levels of cell viability. This work suggests that this technique is promising for enhancing tissue corroborated regeneration in the future. Since a major challenge in transplantation is low cell viability, our bioprinted 3D structures could provide an attractive avenue for the regeneration of cell-specific tissues. The results reported here demonstrate how the controlled release of the bioactive small molecule guggulsterone from microspheres can be used for neuronal differentiation toward dopaminergic neurons when used in combination with hiPSC-derived NPCs. Accordingly, further research could focus on increasing the efficiency of dopaminergic neurons in bioprinted neural tissues, as in previously described protocols, For example, additional microspheres delivering retinoic acid and purmorphamine along with these guggulsterone releasing microspheres could further encourage the growth and maturation of tissues (De La Vega et al., 2018b). Additionally, the controlled delivery of other signaling factors could be explored to increase the neuronal efficiency and maturation of 3D bioprinted neural tissues.

CONCLUSION

Adding drug releasing microspheres to a novel bioink improves cell survival and differentiation, particularly when engineering tissue from stem cells, to indicate their value as a tool for engineering tissues. Here, we show how the controlled release of guggulsterone from microspheres can enhance the survival of NPCs present in bioprinted tissues as well as their differentiation into mature neural tissues. This work lays the groundwork for producing engineered neural tissues from pluripotent stem cells to serve as a potential tool for high-throughput drug screening.

DATA AVAILABILITY STATEMENT

The raw data supporting the conclusions of this article will be made available by the authors, without undue reservation, to any qualified researcher.

AUTHOR CONTRIBUTIONS

RS designed, performed, supervised the experimental procedures and data analysis, and contributed to writing, reviewing, and editing the manuscript. IS assisted on experimental set-up and data analysis. LD assisted on experimental set-up and helped with data analysis. CL helped in editing the manuscript and figures. SW provided the input into experimental design, provided the feedback and supervision on the experimental analysis, as well as writing and editing the manuscript and responding to reviewers.

FUNDING

This work was funded by the NSERC Discovery Grant Program, NSERC Idea to Innovation Program, Innovate BC's Ignite Program, the Alzheimer's Association, and the Michael Smith Foundation for Health Research and Pacific Parkinson's Research Institute's Innovation to Commercialization Grant. This work was also funded by the Canada Research Chairs Program.

ACKNOWLEDGMENTS

We thank Aspect Biosystems for their technical support of this research project.

SUPPLEMENTARY MATERIAL

The Supplementary Material for this article can be found online at: https://www.frontiersin.org/articles/10.3389/fbioe.2020.00057/full#supplementary-material

REFERENCES

Abelseth, E., Abelseth, L., De La Vega, L., Beyer, S. T., Wadsworth, S. J., and Willerth, S. M. (2018). 3D printing of neural tissues derived from human induced pluripotent stem cells using a fibrin-based bioink. *ACS Biomater. Sci. Eng.* 5, 234–243. doi: 10.1021/acsbiomaterials.8b01235

Agbay, A., De La Vega, L., Nixon, G., and Willerth, S. (2018). Guggulsterone-releasing microspheres direct the differentiation of human induced pluripotent stem cells into neural phenotypes. *Biomed. Mater.* 13:034104. doi: 10.1088/1748-605X/aaaa77

Beyer, S. T., Walus, K., Mohamed, T., and Bsoul, A. A. M. (2016). *System For Additive Manufacturing Of Three-Dimensional Structures And Method For Same*. Us Patent 20,160,136,895. Vancouver: Aspect Biosystems Ltd., doi: 10.1007/s10544-017-0247-3

Bsoul, A., Pan, S., Cretu, E., Stoeber, B., and Walus, K. (2016). Design, microfabrication, and characterization of a moulded Pdms/Su-8 inkjet dispenser for a Lab-on-a-Printer platform technology with disposable microfluidic chip. *Lab. Chip* 16, 3351–3361. doi: 10.1039/c6lc00636a

Chandrasekaran, A., Avci, H. X., Ochalek, A., Rösingh, L. N., Molnár, K., László, L., et al. (2017). Comparison of 2D and 3D neural induction methods for the generation of neural progenitor cells from human induced pluripotent stem cells. *Stem Cell Res.* 25, 139–151. doi: 10.1016/j.scr.2017.10.010

Cheng, Y. C., Huang, C. Y., Ho, M. C., Hsu, Y. H., Syu, S. H., Lu, H. E., et al. (2018). Generation of 2 induced pluripotent stem cell lines derived from patients with Parkinson's disease carrying Lrrk2 G2385R variant. *Stem Cell Res.* 28, 1–5. doi: 10.1016/j.scr.2018.01.034

Cheng, Y. C., Lin, H. I., Syu, S. H., Lu, H. E., Huang, C. Y., Lin, C. H., et al. (2019). Reprogramming of a human induced pluripotent stem cell (ipsc) line (Ibmsi012-A) from an early-onset Parkinson's disease patient harboring a homozygous p.D331Y mutation in the Pla2G6 gene. *Stem Cell Res.* 37:101432. doi: 10.1016/j.scr.2019.101432

Chinta, S. J., and Andersen, J. K. (2005). Dopaminergic neurons. *Int. J. Biochem. Cell Biol.* 37, 942–946.

De La Vega, L., Lee, C., Sharma, R., Amereh, M., and Willerth, S. M. (2019). 3D bioprinting models of neural tissues: the current state of the field and future directions. *Brain Res. Bull.* 150, 240–249. doi: 10.1016/j.brainresbull.2019.06.007

De La Vega, L., Karmirian, K., and Willerth, S. M. (2018b). Engineering neural tissue from human pluripotent stem cells using novel small molecule releasing microspheres. *Adv. Biosyst.* 2:1800133. doi: 10.1002/adbi.201800133

De La Vega, L., Rosas Gómez, D. A., Abelseth, E., Abelseth, L., Allisson Da Silva, V., and Willerth, S. (2018a). 3D bioprinting human induced pluripotent stem cell-derived neural tissues using a novel lab-on-a-printer technology. *Appl. Sci.* 8:2414. doi: 10.3390/app8122414

Fantini, V., Bordoni, M., Scocozza, F., Conti, M., Scarian, E., Carelli, S., et al. (2019). Bioink composition and printing parameters for 3D modeling neural tissue. *Cells* 8:830. doi: 10.3390/cells8080830

Gao, F., Ruan, C., and Liu, W. (2019). High-strength hydrogel-based bioinks. *Mater. Chem. Front.* 1736–1746.

Gomez, J. C., Edgar, J. M., Agbay, A. M., Bibault, E., Montgomery, A., Mohtaram, N. K., et al. (2015). Incorporation of retinoic acid releasing microspheres into pluripotent stem cell aggregates for inducing neuronal differentiation. *Cell. Mol. Bioeng.* 8, 307–319. doi: 10.1007/s12195-015-0401-z

Gonzalez, R., Garitaonandia, I., Abramihina, T., Wambua, G. K., Ostrowska, A., Brock, M., et al. (2013). Deriving dopaminergic neurons for clinical use. A practical approach. *Sci. Rep.* 3:1463. doi: 10.1038/srep01463

Gopinathan, J., and Noh, I. (2018). Recent trends in bioinks for 3D printing. *Biomater. Res.* 22:11. doi: 10.1186/s40824-018-0122-1

Gu, Q., Tomaskovic-Crook, E., Lozano, R., Chen, Y., Kapsa, R. M., Zhou, Q., et al. (2016). Functional 3D neural mini-tissues from printed gel-based bioink and human neural stem cells. *Adv. Healthc. Mater.* 5, 1429–1438. doi: 10.1002/adhm.201600095

Gu, Q., Tomaskovic-Crook, E., Wallace, G. G., and Crook, J. M. (2017). 3D Bioprinting human induced pluripotent stem cell constructs for in situ cell proliferation and successive multilineage differentiation. *Adv. Healthc. Mater.* 6, 1–11.

Gu, Q., Tomaskovic-Crook, E., Wallace, G. G., and Crook, J. M. (2018). Engineering Human Neural Tissue by 3D Bioprinting. *Methods Mol. Biol.* 1758, 129–138. doi: 10.1007/978-1-4939-7741-3_10

Gungor-Ozkerim, P. S., Inci, I., Zhang, Y. S., Khademhosseini, A., and Dokmeci, M. R. (2018). Bioinks for 3D bioprinting: an overview. *Biomater. Sci.* 6, 915–946. doi: 10.1039/c7bm00765e

Hsieh, F. Y., and Hsu, S. H. (2015). 3D bioprinting: a new insight into the therapeutic strategy of neural tissue regeneration. *Organogenesis* 11, 153–158. doi: 10.1080/15476278.2015.1123360

Huang, C.-T., Kumar Shrestha, L., Ariga, K., and Hsu, S.-H. (2017). A graphene–polyurethane composite hydrogel as a potential bioink for 3D bioprinting and differentiation of neural stem cells. *J. Mater. Chem. B* 5, 8854–8864. doi: 10.1039/c7tb01594a

Joung, D., Truong, V., Neitzke, C. C., Guo, S.-Z., Walsh, P. J., Monat, J. R., et al. (2018). 3D printed stem-cell derived neural progenitors generate spinal cord scaffolds. *Adv. Funct. Mater.* 28:1801850. doi: 10.1002/adfm.201801850

Kim, T., Song, J. J., Puspita, L., Valiulahi, P., Shim, J. W., and Lee, S. H. (2017). *In vitro* generation of mature midbrain-type dopamine neurons by adjusting exogenous Nurr1 and Foxa2 expressions to their physiologic patterns. *Exp. Mol. Med.* 49:e300. doi: 10.1038/emm.2016.163

Lee, C., Abelseth, E., De La Vega, L., and Willerth, S. M. (2019). Bioprinting a novel glioblastoma tumor model using a fibrin-based bioink for drug screening. *Mater. Today Chem.* 12, 78–84. doi: 10.1016/j.mtchem.2018.12.005

Lee, S.-J., Esworthy, T., Stake, S., Miao, S., Zuo, Y. Y., Harris, B. T., et al. (2018). Advances in 3D bioprinting for neural tissue engineering. *Adv. Biosyst.* 2:1700213. doi: 10.1002/adbi.201700213

Lee, Y. B., Polio, S., Lee, W., Dai, G., Menon, L., Carroll, R. S., et al. (2010). Bio-printing of collagen and Vegf-releasing fibrin gel scaffolds for neural stem cell culture. *Exp. Neurol.* 223, 645–652. doi: 10.1016/j.expneurol.2010.02.014

Lozano, R., Stevens, L., Thompson, B. C., Gilmore, K. J., Gorkin, R. III, Stewart, E. M., et al. (2015). 3D printing of layered brain-like structures using peptide modified gellan gum substrates. *Biomaterials* 67, 264–273. doi: 10.1016/j.biomaterials.2015.07.022

Niu, W., Zang, T., Wang, L. L., Zou, Y., and Zhang, C. L. (2018). Phenotypic reprogramming of striatal neurons into dopaminergic neuron-like cells in the adult mouse brain. *Stem Cell Rep.* 11, 1156–1170. doi: 10.1016/j.stemcr.2018.09.004

Panwar, A., and Tan, L. P. (2016). Current status of bioinks for micro-extrusion-based 3D bioprinting. *Molecules* 21:E685.

Penney, J., Ralvenius, W. T., and Tsai, L. H. (2019). Modeling Alzheimer's disease with ipsc-derived brain cells. *Mol. Psychiatry* 5, 1057–1081.

Playne, R., and Connor, B. (2017). Understanding Parkinson's disease through the use of cell reprogramming. *Stem Cell Rev. Rep.* 13, 151–169. doi: 10.1007/s12015-017-9717-5

Poon, A., Zhang, Y., Chandrasekaran, A., Phanthong, P., Schmid, B., Nielsen, T. T., et al. (2017). Modeling neurodegenerative diseases with patient-derived induced pluripotent cells: possibilities and challenges. *N. Biotechnol.* 39, 190–198. doi: 10.1016/j.nbt.2017.05.009

Riemens, R. J., Van Den Hove, D., Esteller, M., and Delgado-Morales, R. (2018). Directing neuronal cell fate in vitro: achievements and challenges. *Prog. Neurobiol.* 168, 42–68. doi: 10.1016/j.pneurobio.2018.04.003

Robinson, M., Yau, S.-Y., Sun, L., Gabers, N., Bibault, E., Christie, B. R., et al. (2015). Optimizing differentiation protocols for producing dopaminergic neurons from human induced pluripotent stem cells for tissue engineering applications. *Biomark. Insights* 61–70.

Salaris, F., Brighi, C., Soloperto, A., De Turris, V., Benedetti, M. C., Ghirga, S., et al. (2019). 3D bioprinted human cortical neural constructs derived from induced pluripotent stem cells. *J. Clin. Med.* 8:1595. doi: 10.3390/jcm8101595

Salaris, F., and Rosa, A. (2019). Construction of 3D in vitro models by bioprinting human pluripotent stem cells: challenges and opportunities. *Brain Res.* 1723:146393. doi: 10.1016/j.brainres.2019.146393

Sebastián-Serrano, A., Sandonis, A., Cardozo, M., Rodríguez-Tornos, F. M., Bovolenta, P., and Nieto, M. (2012). Pαx6 expression in postmitotic neurons mediates the growth of axons in response to SFRP1. *PLoS One* 7:e31590. doi: 10.1371/journal.pone.0031590

Stott, S. R., Metzakopian, E., Lin, W., Kaestner, K. H., Hen, R., and Ang, S. L. (2013). Foxa1 and Foxa2 are required for the maintenance of dopaminergic properties in ventral midbrain neurons at late embryonic stages. *J. Neurosci.* 33, 8022–8034. doi: 10.1523/JNEUROSCI.4774-12.2013

Takahashi, K., Tanabe, K., Ohnuki, M., Narita, M., Ichisaka, T., Tomoda, K., et al. (2007). Induction of pluripotent stem cells from adult human fibroblasts by defined factors. *Cell* 131, 861–872. doi: 10.1016/j.cell.2007.11.019

Tan, Y. J., Tan, X., Yeong, W. Y., and Tor, S. B. (2016). Hybrid microscaffold-based 3D bioprinting of multi-cellular constructs with high compressive strength: a new biofabrication strategy. *Sci. Rep.* 6:39140. doi: 10.1038/srep39140

Tasnim, N., De La Vega, L., Anil Kumar, S., Abelseth, L., Alonzo, M., Amereh, M., et al. (2018). 3D bioprinting stem cell derived tissues. *Cell. Mol. Bioeng.* 11, 219–240. doi: 10.1007/s12195-018-0530-2

Zhang, Y., Li, W., Laurent, T., and Ding, S. (2012). Small molecules, big roles–the chemical manipulation of stem cell fate and somatic cell reprogramming. *J. Cell Sci.* 125, 5609–5620. doi: 10.1242/jcs.096032

Zhou, X., Cui, H., Nowicki, M., Miao, S., Lee, S. J., Masood, F., et al. (2018). Three-dimensional-bioprinted dopamine-based matrix for promoting neural regeneration. *ACS Appl. Mater. Interf.* 10, 8993–9001. doi: 10.1021/acsami.7b18197

Conflict of Interest: SW has a collaborative research agreement with Aspect Biosystems to commercialize the results of their 3D printed tissues and related reagents.

The remaining authors declare that the research was conducted in the absence of any commercial or financial relationships that could be construed as a potential conflict of interest.

frontiers
in Bioengineering and Biotechnology

REVIEW
published: 12 February 2020
doi: 10.3389/fbioe.2020.00061

Reconstruction of Large Skeletal Defects: Current Clinical Therapeutic Strategies and Future Directions Using 3D Printing

*Luciano Vidal[1]†, Carina Kampleitner[2]†, Meadhbh Á. Brennan[1,3], Alain Hoornaert[1,4] and Pierre Layrolle[1]**

[1] INSERM, UMR 1238, PHY-OS, Bone Sarcomas and Remodeling of Calcified Tissues, Faculty of Medicine, University of Nantes, Nantes, France, [2] Department of Pharmacology and Toxicology, University of Vienna, Vienna, Austria, [3] Harvard School of Engineering and Applied Sciences, Harvard University, Cambridge, MA, United States, [4] CHU Nantes, Department of Implantology, Faculty of Dental Surgery, University of Nantes, Nantes, France

OPEN ACCESS

Edited by:
Hasan Uludag,
University of Alberta, Canada

Reviewed by:
Nathalie Chevallier,
Université Paris-Est Créteil, France
Agnes Dupret-Bories,
Institut Claudius Regaud, France

Correspondence:
Pierre Layrolle
pierre.layrolle@inserm.fr

†These authors have contributed equally to this work

Specialty section:
This article was submitted to Biomaterials,
a section of the journal Frontiers in Bioengineering and Biotechnology

Received: *14 November 2019*
Accepted: *24 January 2020*
Published: *12 February 2020*

Citation:
Vidal L, Kampleitner C, Brennan MÁ, Hoornaert A and Layrolle P (2020) Reconstruction of Large Skeletal Defects: Current Clinical Therapeutic Strategies and Future Directions Using 3D Printing.
Front. Bioeng. Biotechnol. 8:61.
doi: 10.3389/fbioe.2020.00061

The healing of bone fractures is a well-orchestrated physiological process involving multiple cell types and signaling molecules interacting at the fracture site to replace and repair bone tissue without scar formation. However, when the lesion is too large, normal healing is compromised. These so-called non-union bone fractures, mostly arising due to trauma, tumor resection or disease, represent a major therapeutic challenge for orthopedic and reconstructive surgeons. In this review, we firstly present the current commonly employed surgical strategies comprising auto-, allo-, and xenograft transplantations, as well as synthetic biomaterials. Further to this, we discuss the multiple factors influencing the effectiveness of the reconstructive therapy. One essential parameter is adequate vascularization that ensures the vitality of the bone grafts thereby supporting the regeneration process, however deficient vascularization presents a frequently encountered problem in current management strategies. To address this challenge, vascularized bone grafts, including free or pedicled fibula flaps, or *in situ* approaches using the Masquelet induced membrane, or the patient's body as a bioreactor, comprise feasible alternatives. Finally, we highlight future directions and novel strategies such as 3D printing and bioprinting which could overcome some of the current challenges in the field of bone defect reconstruction, with the benefit of fabricating personalized and vascularized scaffolds.

Keywords: large bone defects, bone regeneration, tissue engineering, vascularization, three-dimensional printing

INTRODUCTION

The reconstruction of large bone defects caused by trauma, disease or tumor resection is a fundamental challenge for orthopedic and plastic surgeons. Their critical size exceeds the intrinsic capacity of self-regeneration and consequently bone repair is delayed and impaired. This type of lesion is termed non-union bone fracture and requires additional treatment with bone graft materials in order to restore pre-existing function (Dimitriou et al., 2011). Successful bone augmentation procedures should include an osteoconductive scaffold with sufficient mechanical stability, an osteoinductive stimulus to induce osteogenesis, and should enable osseointegration and vascularity (Albrektsson and Johansson, 2001; Giannoudis et al., 2008). The currently available treatment strategies of bone loss are based on autologous, allogeneic or xenogeneic bone transplantation, as well as synthetic biomaterials. Although autologous bone grafting still represents the gold standard technique for large bone reconstruction, several factors limit its application. A major restricting parameter is the volume of bone needed to treat this type of injury, as well as the associated pain and possible donor site complications due to the additional surgical intervention at the bone harvest site. Similar disadvantages may be observed for allogenic bone grafts including immunogenic reactions and transfer of diseases (Aro and Aho, 1993). Furthermore, many of these standard clinical grafting approaches fail due to the lack of adequate vascularization. Insufficient vascularity of the fracture site reduces the exchange of gas, nutrients and waste between the tissue and the blood system, as well as the delivery of cells to the site of injury, leading to inner graft necrosis (Mercado-Pagan et al., 2015; Fernandez de Grado et al., 2018). To circumvent this problem, vascularized bone transfers represent an excellent option that ensures bone vitality and avoids graft resorption. Nevertheless, complex fractures and their reconstructions require modeling of the transferred bone to adapt to the anatomical shape and extensive microsurgical techniques to connect the graft to the blood system. Some patient bioreactor attempts have also been made whereby a customized bone graft is implanted ectopically in the patient for several weeks before transferring it into the bone defect. Innovative fabrication approaches in the field of bone tissue engineering include three-dimensional (3D) printing and bioprinting to enable *ex vivo* personalized bone grafts based on anatomical medical imaging. They are generally composed of calcium phosphate/polymer composites or porous titanium. To enhance the material healing properties, 3D printed scaffolds can potentially include cells, growth factors, and vasculature. In this review, we present the current techniques clinically available for the reconstruction of critical-sized bone defects and point out future challenges and possibilities of new treatment modalities using customized and vascularized bone grafts with a focus on 3D printing and bioprinting fabrication methods.

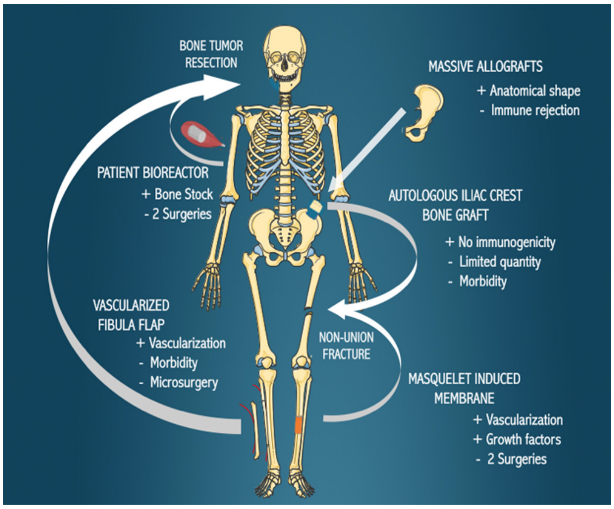

FIGURE 1 | Current biological bone reconstruction techniques. Bone defects arising due to the resection of tumors or non-union fractures can be treated with the various methods indicated, with the benefits (+) and disadvantages (–) of each technique outlined.

PRESENT MANAGEMENT STRATEGIES FOR LARGE BONE LESIONS

The current reconstructive options for large bone defects, including autologous iliac grafting, autologous vascularized fibula transplantation, Masquelet's induced membrane, massive allografts and *in vivo* patient bioreactor strategies are presented in **Figure 1** and discussed in this section.

Bone Grafts

The leading treatment for bone defect reconstruction remains bone grafting. The purpose of a bone graft is to support the repair process through osteoinduction, osteoconduction, and osteogenesis (Albrektsson and Johansson, 2001; Oryan et al., 2014). They can be categorized into different types based on the tissue source: autologous, allogeneic and xenogeneic bone grafts, as well as synthetic and biological biomaterials (Brydone et al., 2010). The selection of the ideal bone graft depends on several factors including the geometry, size and tissue viability of the bone defect, the biological and biomechanically characteristics of the bone graft, and the known advantages and associated complications of each graft option (Laurencin et al., 2014).

Autografts

Autologous bone grafting, still the clinical standard reconstruction technique, entails harvesting bone tissue from an anatomical donor site and transplanting it to the recipient defect site (Sanan and Haines, 1997). The iliac crest is the preferred harvesting site for this type of transplant, whereby approximately 20 cm^3 of cancellous bone is collected and used as a bone block or morselized into bone chips in order to fill a bone defect (Athanasiou et al., 2010). Autologous bone contains the patient's own osteogenic cells and osteoinductive proteins, such as bone morphogenetic protein 2 (BMP2), BMP7, and platelet-derived growth factor (PDGF), providing optimal osteogenic, osteoinductive, and osteoconductive properties without risk of viral transmissions, while pain, hematoma, possible visceral injuries at the donor site and extended surgery time because of the two surgical sites are the main drawbacks (Albrektsson and Johansson, 2001; Parikh, 2002). Another disadvantage of cancellous bone grafting is that large amounts of bone graft cannot be obtained for critical-sized defect reconstruction (Oryan et al., 2013). Successful repair depends on osteogenic cell survival and tissue viability after transplantation to the recipient site, while neovascularization plays a determinant role. To overcome the disadvantage of limited vascularization, free vascularized bone flaps have been employed. Taylor et al. reported the first successful large bone defect reconstruction using a free vascularized bone transfer (Taylor et al., 1975).

Vascularized bone grafts, such as an autologous vascularized fibula flap, iliac crest flap, rib flap, and radius flap, allow the reconstruction of large bone defects and are often used as a last resort to avoid limb amputation for patients. Fibula and iliac crest flaps have been used for the pelvis, head of long bones, and maxillofacial reconstruction. Free vascularized bone flaps are particularly suitable for mandible reconstructions after ballistic trauma or tumor resections. An optimal option for large bone defect reconstruction using autografts is a vascularized cortical autograft (Rizzo and Moran, 2008). Mandible reconstruction is predominantly performed by a fibula flap. Another option described in the literature for a hemimandible reconstruction is the iliac crest flap that has an adequate bone height to ensure osseointegration (Taylor, 1982, 1983, 1985) and allows optimal shape reconstruction of the mandible ramus. The fibula is dissected, harvested with a vascular pedicle, shaped and transplanted into the bone defect where it is reconnected to the local vasculature (**Figure 2**). This vascularized bone graft contains the patient's own cells, growth factors and a vascularization bed thereby reducing graft resorption, enhancing healing and permitting better diffusion of antibiotics. Hidalgo et al. evaluated the fibula flap for mandible reconstruction and reported long-term outstanding functional and aesthetic results without bone resorption in non-irradiated and irradiated patients (Hidalgo and Pusic, 2002). Free fibula flap transfers for mandibular and maxillary reconstruction achieved 98.7% graft survival in some studies (Peng et al., 2005; Taylor et al., 2016). Further to this, pelvic ring reconstruction employing a double-barreled free vascularized autologous patient fibula graft after resection of malignant pelvic bone tumors was reported (Ogura et al., 2015). Additionally, lumbosacral spinal defects reconstruction was also achieved with the use of a fibula flap (Moran et al., 2009). The major complications of free vascularized bone flaps are post-operative vascular thrombosis and hence failure and free flap loss. The fibula flap requires laborious microsurgery to reconnect to the vasculature, and the need for sculpting of the graft to fit the anatomy of the bone defect. Furthermore, this technique requires extended anesthesia, specialized technical surgical skills and the sacrifice of blood vessels.

Allografts

Bone allografts are harvested from living donors during joint replacement (e.g., femoral heads) or from cadavers, and stored frozen and processed and transplanted into another patient (Keating and McQueen, 2001). Given the limitations of autografts, allografts became an alternative to large bone defect reconstruction. Allografts are used as powders, chips or complete bone structural forms, so called massive allografts and can be provided as a fresh graft, fresh-frozen, freeze-dried, demineralized, de-lipidized by solvents or supercritical carbon dioxide, and sterilized by irradiation (Bostrom and Seigerman, 2005; Zimmermann and Moghaddam, 2011). The primary advantage of allografts is their immediate availability in different sizes and shapes (Muscolo et al., 2004). They are composed of the extracellular bone matrix containing growth factors that stimulate regeneration, do not present complications associated with donor site harvesting, and present favorable mechanical strength (Mankin et al., 1996). For these reasons, allografts are particularly interesting for complex skeletal reconstruction after resection of bone tumors in pelvic bones of young patients. However, allografts present variable osteoinductive and osteoconductive properties and have lower osteogenic potential compared to autografts (Coquelin et al., 2012). Other disadvantages are the possibility of immune rejection and disease transmission (Aro and Aho, 1993). To overcome the latter disadvantage, Capanna et al. (1993) described a technique for the reconstruction of large metadiaphyseal bone defects, combining a massive allograft to support a centrally located autologous fibula flap with the aim of improving allograft incorporation and decreasing the risk of mechanical instability. This technique has proven efficacy for large bone defect reconstruction (Bakri et al., 2008). Other clinical studies described the use of allografts alone or associated with other therapies such as autologous concentrated bone marrow-derived cells (Putzier et al., 2009; Faldini et al., 2011; Scaglione et al., 2014).

Xenografts

Xenografts are harvested from different species and transplanted for patient bone defect repair, and the most commonly used are of bovine, porcine, or coral origin. The primary advantages are the high availability, favorable porosity for bone tissue ingrowth and comparable mechanical strength to native bone. However, similar to allografts, xenografts, when treated for clinical use, may lose part of their osteoinductive and osteoconductive abilities (Dimitriou et al., 2011). Moreover, a significant disadvantage of xenografts is the possible transmission of zoonotic diseases and immune rejection. Finally, xenografts have ethical and religious concerns. Karalashvili et al. (2017) described the use of a decellularized bovine bone graft in a zygomatic large bone defect reconstruction and reported long-term retention of graft shape without resorption and bone integration. Bovine cancellous xenografts have also been used in the treatment of tibial fractures in elderly patients and showed favorable healing outcomes (Bansal et al., 2009). However, the number of published studies using xenografts in large bone defect reconstruction is still limited and indeed clinical trials using bovine bone have shown poor results, describing graft rejection and failure in host tissue integration (Elliot and Richards, 2011; Patil et al., 2011; Shibuya et al., 2012; Ledford et al., 2013).

Synthetic Biomaterials

Langer and Vacanti described tissue engineering by the use of biocompatible materials associated with cells and/or biological factors, in order to replace or repair tissues or organs. Various biomaterials have been employed in the treatment of bone defects. Calcium phosphate ceramics (CaP ceramics) are synthetic materials composed of calcium hydroxyapatites (HA), therefore possessing a composition similar to the native bone matrix. CaP ceramics are primarily produced by sintering at high temperatures and are available with variable porosity and in construct or granules format, with their main advantage being their osteoconductivity (Albrektsson and Johansson, 2001; Lee et al., 2006; Samavedi et al., 2013). CaP ceramics most commonly

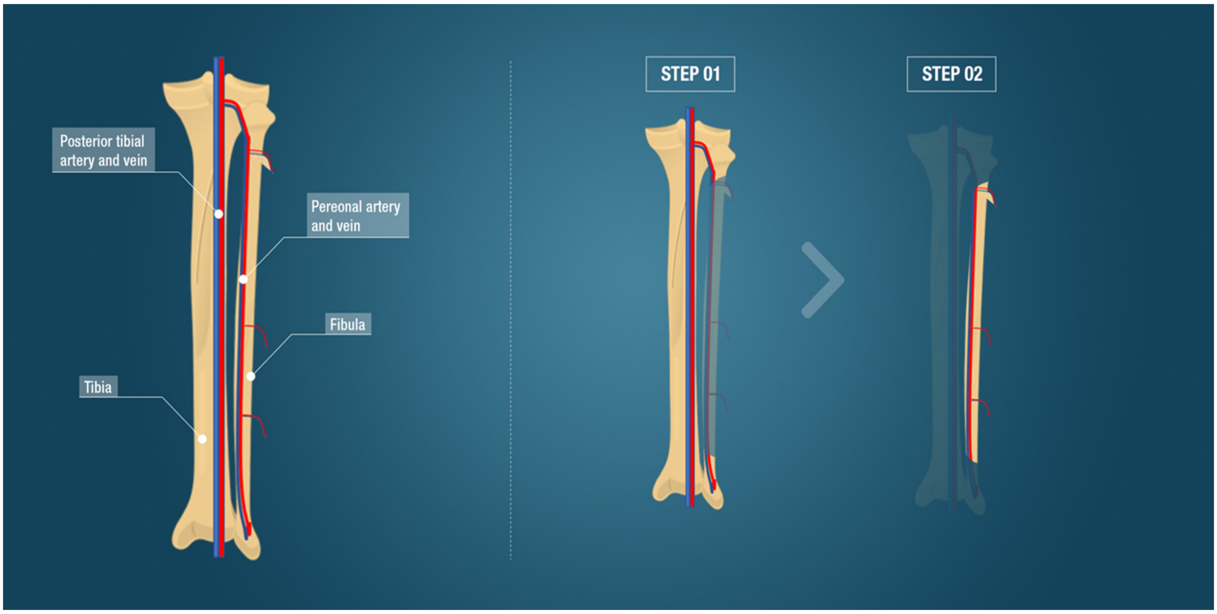

FIGURE 2 | Fibula free vascularized flap. The anatomy including the tibia, fibula and major vessels is indicated. The surgical steps comprising the fibula flap, the gold standard clinical technique for large bone defect reconstruction, is demonstrated. Step 1 illustrates the flap dissection to obtain the bone flap with its vascular pedicle. Step 2 represents the bone flap with its vascular pedicle ready to be transplanted to the bone defect.

employed in bone reconstruction are biphasic calcium phosphate (BCP), tricalcium phosphate (TCP), and HA. HA presents excellent osteoconductive and osseointegration properties and their macroporosity and pore interconnectivity allow excellent cell adhesion and proliferation, leading to osteoconduction and osteoinduction after transplantation *in vivo*, as well as revascularization of the implant (Bucholz et al., 1987; Eggli et al., 1988). TCP has higher pore interconnectivity than HA which is crucial for neovascularization and osteoconduction (Ogose et al., 2006), however, this higher interconnectivity gives TCP lower mechanical properties compared to HA and TCP is reabsorbed faster than HA after implantation (Torres et al., 2011). BCP is the combination of TCP and HA. BCP exploits the main advantages of both TCP and HA as they can be combined in various ratios (Daculsi et al., 1989). Calcium phosphate cement (CPC) differs from calcium phosphate ceramics because they are made at ambient temperatures from hydrolysis and are regarded as biomimetic. CPC can be used as filler by injection and for creating 3D printing constructs (Brown and Chow, 1983; Brown, 1987; Bertol et al., 2016), however, their slow degradation may delay bone formation (Lodoso-Torrecilla et al., 2018). Bioactive glass or bioglass is a synthetic silicate-based ceramic. It is rapidly resorbed in the first 2 weeks after implantation allowing a rapid new bone and vascularized implant ingrowth (Gerhardt and Boccaccini, 2010; Kurien et al., 2013). Synthetic bone substitutes are an excellent alternative to biological grafts in small bone defect reconstruction. However, due to the insufficient strength to sustain the body load and insufficient neovascularization ingrowth, bone substitutes are not the best option for large bone defect reconstruction (Stanovici et al., 2016). Their association with recombinant human growth factors and/or stem cell therapies could be a solution for this main disadvantage (Gomez-Barrena et al., 2011, 2019). Orthounion is an ongoing clinical trial studying the use of bone marrow mesenchymal stem cells combined with a bone substitute to fill the non-union in a surgical procedure (Verboket et al., 2018). Another ongoing clinical trial, Maxibone[1], is studying the safety and efficacy of autologous cultured stem cells and calcium phosphate biomaterials in alveolar bone augmentation (Gjerde et al., 2018).

Megaprothesis

After trauma or resection of a malignant or benign aggressive tumor, the reconstruction of large bone defects is necessary to prevent amputation. The use of metal megaprotheses began in the 70s, and in the 90s, it became popular. Megaprotheses replace the affected bone tissue instead of regenerating bone tissue and there has been a significant evolution of their components since inception in order to ensure corrosion resistance, to avoid fractures of the material, for better fixation, and to guarantee osseointegration. Modular megaprostheses today allow the association of different components to customize large bone defect reconstruction (Hattori et al., 2011). Prostheses may have a coating of hydroxyapatite and silver for osseointegration and to prevent infection and various studies have shown excellent limb survival after surgery with a follow up of up at 20 years (Mittermayer et al., 2001; Gosheger et al., 2006; Jeys and Grimer, 2009; Shehadeh et al., 2010). There are two significant complications after reconstruction with megaprosthesis, mechanical and

---

[1] www.maxibone.eu

non-mechanical complications. Implant design may cause inherent mechanical complications and those reported in the literature include aseptic loosening, failure of soft tissue attachments, and prosthesis stem fractures. These complication rates are between 5 and 48%, as described in the literature (Ahlmann et al., 2006; Gosheger et al., 2006; Holl et al., 2012) and robust modular megaprostheses have helped to reduce this mechanical complication (Choong et al., 1996; Jawad and Brien, 2014). Non-mechanical complications include infection, tumor relapse, and wound healing disorders. Infection and wound necrosis are common complications in oncological cases due to malnutrition, immunosuppression, lack of local tissue vascularization, and extensive implant reconstruction (Jeys et al., 2005; Jeys and Grimer, 2009; Pala et al., 2015). Silver coated prosthesis, antibiotics therapy, and meticulous surgery techniques may reduce these complications; however, non-mechanical complications are the primary threat in large bone defect reconstruction using megaprosthesis.

Masquelet Induced Membrane Technique

The induced membrane method known as the Masquelet technique consists of a two-stage operative procedure. The first stage includes a debridement of the defect site, soft-tissue repair and the insertion of a cement spacer composed of polymethyl methacrlyate (PMMA) that allows the maintenance of the bone height and stability, and the formation of a pseudosynovial membrane due to a foreign-body reaction. In the second step, performed 6–8 weeks later, the cement spacer is removed and the cavity is refilled with an autologous cancellous bone graft (e.g., from the iliac crests), while preserving the induced membrane. This membrane has various functions, in particular it prevents the resorption of the cancellous bone graft, supports vascularization and corticalization, and functions as a delivery system for osteomodulatory and angiogenic growth factors like transforming growth factor (TGFβ), bone morphogenetic protein 2 (BMP2) and vascular endothelial derived growth factor (VEGF) (Masquelet, 2003; Pelissier et al., 2004; Masquelet and Begue, 2010). This innovative technique is indicated in acute and chronic infected or non-infected massive bone defects of any size (4–25 cm) and shape, at different anatomical sites in children and adults (Masquelet et al., 2000; Azi et al., 2019). Its consolidation rate varies from 82 to 100% with delays ranging from 4 months to 1 year. The main complications include infection, failure of a step in the surgical procedure (persisting infection or non-union), re-fracture and severe bone graft resorption (Morelli et al., 2016; Han et al., 2017). Different studies reported the Masquelet's approach as effective, for instance Sivakumar et al. (2016) and Mathieu et al. (2019) described the use of the induced membrane technique in the management of large bone defect reconstruction in open fractures of the femur, tibia, and fibula bones. A recently published review reported the application of the induced membrane technique in patients with osteomyelitis, suggesting this technique is an excellent alternative to solve long bone infected defects by controlling the local infection (Careri et al., 2019).

Ilizarov Method

The Ilizarov method is a convenient tool for the treatment of patients suffering from poly—trauma conditions, with multiple fractures, osteomyelitis, and infected non-unions. The principle of the Ilizarov's technique is to stimulate bone growth by bone distraction that produces neovascularization, and stimulates new bone formation (Aronson et al., 1989; Ilizarov, 1990). The surgical procedure consists of the use of an external circular fixator and a corticotomy. The external fixator stabilizes the bone and allows early weight-bearing. A distraction of 0.25 mm, four times per day, commencing after a delay of 5 to 10 days post-surgery is performed and an osteogenesis activity occurs in the bone gap (Spiegelberg et al., 2010). The length of bone that can be produced by this technique is up to 20 cm per limb segment. Barbarossa et al. conducted a study of 30 patients with osteomyelitis and infected non-union of the femur treated with the Ilirazov technique and reported efficacy in saving the limbs with osteomyelitis (Barbarossa et al., 2001). Large blood vessels expressing smooth muscle α-actin were shown to co-express BMP2 which was involved in enhancing osteogenic activity at the site (Matsubara et al., 2012). The Ilizarov's bone distraction technique also offers the possibility of correcting a defect of axis, and allows a lengthening of the limb, however, it has associated drawbacks such as several weeks lag time required to heal large segmental defects, with extended hospital recovery and discomfort for patients, as well as risks of osteomyelitis along the transcutaneous pins.

FUTURE DIRECTIONS IN LARGE BONE DEFECT RECONSTRUCTION

In-Patient Bioreactor

The principle of this approach is to use the patient as their own bioreactor, and entail the fabrication of a customized bone graft utilizing medical imaging and 3D printing, and the implantation of these osteoinductive materials in ectopic sites such as under the skin or in muscles. After several weeks, the pre-fabricated bone graft is used for large skeletal reconstruction. The possibility of producing substitute organs or body parts inside human bodies, therefore using the body as a living bioreactor was introduced (Cao et al., 1997; Vacanti and Langer, 1999) and Orringer et al. (1999) first treated an angle to angle mandible and total lower-lip reconstruction with a prefabricated osteocutaneous flap. A dacron-polyurethane tray was packed with autologous cancellous bone graft and with BMP7. This tray was implanted in the fascia above the scapula for generating a composite pre-fabricated flap (Orringer et al., 1999). Warnke et al. (2004) developed the bone-muscle-flap prefabrication technique for maxillofacial reconstruction. They grew a subtotal mandible composed of a titanium mesh cage filled with bone bovine mineral blocks, bone mineral granules associated with BMP7, and autologous bone marrow concentrated cells inside the latissimus muscle and vascularization was provided by the thoracodorsal pedicle. Seven weeks postoperatively, the

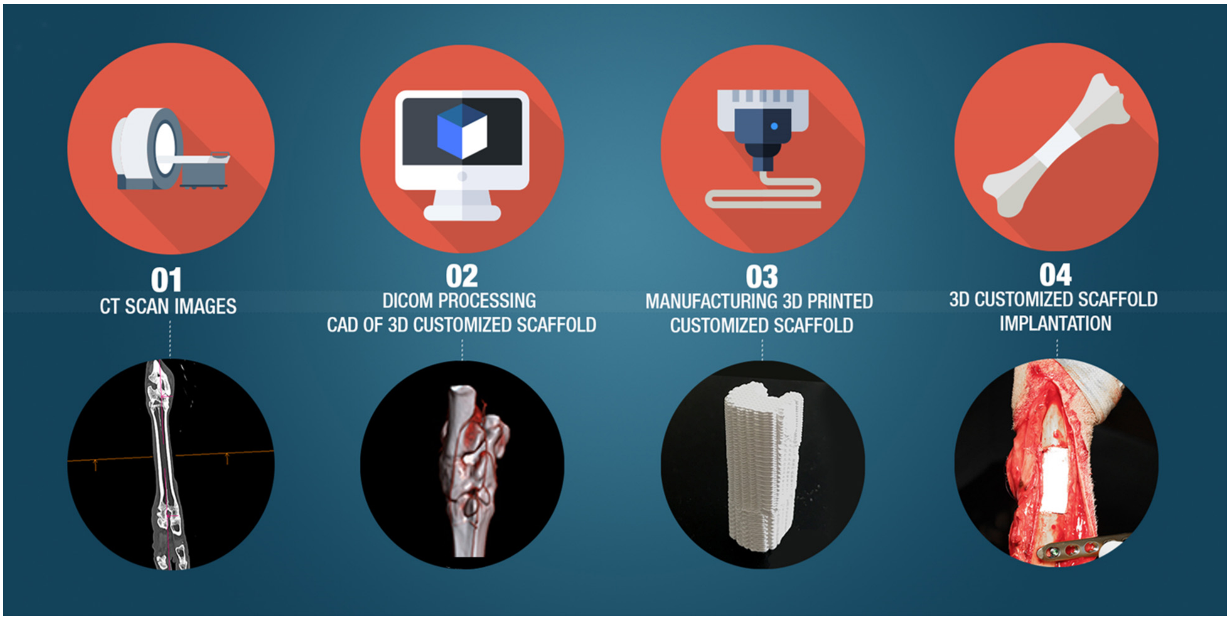

FIGURE 3 | Workflow involved in customizable bone construct fabrication. (1) CT scans of the patient's bone are acquired. (2) Computer aided software enables the processing of CT images in order to (3) 3D print personalized scaffolds for (4) bone defect reconstruction. The lower panel illustrates a real large bone defect reconstruction in a sheep metatarsal bone model.

prefabricated bone muscle flap was microsurgically transplanted with its vascular pedicle in the mandible. Vascular supply of the flap was successfully maintained. A favorable aesthetic and functional outcome was obtained (Warnke et al., 2004). Mesimaki et al. (2009) then described a 3 step surgery method to reconstruct a large bone maxillary defect by forming a prevascularized construct by filling a titanium mesh cage with autologous adipose-derived stem cells (ASCs), BMP2 and beta-tricalcium phosphate (β-TCP) granules and inserting it in the patient's left rectus abdominis muscle, with vascularization provided by the inferior epigastric artery, and subsequent transplantation for maxillary bone reconstruction. Other studies described the use of the pectoralis major – hydroxyapatite blocks flap, pedicled using the thoracoacromial artery, for mandible reconstruction (Heliotis et al., 2006; Tatara et al., 2014). A further alternative comprised a polymethylmethacrylate chamber filled with autograft implanted against the periosteum of the iliac crest which was transplanted to the mandibular site after 8 weeks, with the donor periosteum sutured with the local periosteum to reestablish the vascularization (Cheng et al., 2006). Kokemueller et al. (2010) reported hemimandible reconstruction by utilizing cylinders of β-TCP loaded with cells and morcellized autologous bone graft that were implanted in the latissimus dorsi muscle with a central vascular bundle and transplanted after 6 months. The main advantage of the patient bioreactor method compared to the alternative surgical treatments proposed for large bone defects reconstructions (e.g., autologous vascularized fibula, iliac crest) is that it avoids the process of harvesting native bone and creating further skeletal defects. However, this method does not apply to emergency cases and requires at least two surgical sites.

3D Printing Techniques and Production of Personalized Surgical Guides and Scaffolds

3D printing is an emerging technology that permits the manufacture of complex-shaped structures with high precision using layer-by-layer printing of different materials. As illustrated in **Figure 3**, the structures of the defects to be reconstructed in patients are identified based on digital images obtained from a computed tomography (CT) scan or magnetic resonance imaging (MRI), and by using computer-aided design (CAD) software, 3D printing technology and bioprinting 3D medical models can be developed (Colin and Boire, 1997; Winder and Bibb, 2005). The 3D printing technologies used for polymer scaffold construction are: (1) fused deposition modeling (FDM), (2) selective laser sintering (SLS), and (3) stereolithography (SLA). The FDM method is the most popular technique developed in the 1980s and based on construction by melting deposition. The material commonly used is a thermoplastic polymer, in powder or filament format, which feeds an extruder tip that melts the plastic and at its exit is deposited on a surface at a much lower temperature so that it solidifies rapidly. The extruder tip moves in the x and y planes to print layer by layer the pattern of the scaffold (Xu et al., 2014). The resolution of the printed construct is defined by multiple factors: nozzle diameter, print speed, and number and height of the layers (Yang et al., 2018). This technique is simple, rapid, and cost-effective, however, there are limited choices of biocompatible, medical-grade thermoplastic polymers available. SLS uses a CO_2 laser that sinters, layer by layer, the material in a powder state, forming the final piece. The final piece needs to be cleaned to withdraw the powder excess and to provide smoothness to the construct surface. SLS allows the fabrication of large and sophisticated structures (Deckard, 1989; Mazzoli, 2013). SLA produces 3D models by tracing a beam of UV light or a laser on a base of a photosensitive resin that polymerizes (Mondschein et al., 2017). The main benefit of this 3D printing technology is the high level of detail and the excellent surface resolution (Ji et al., 2018).

3D Printing in Bone Tissue Engineering Applications

3D printing prototype models can significantly assist with pre-operative evaluation and intraoperative procedures, for example for the use of surgical guides in mandibular reconstruction with osteocutaneous flaps (Bosc et al., 2017; Dupret-Bories et al., 2018). These studies showed the advantages of using 3D printed preoperative models and surgical guides including a reduction in operating time, flap ischemia, morbidity and associated complications such as infections. Many studies describe the use of 3D printing scaffolds for bone tissue engineering (Kao et al., 2015; Petrochenko et al., 2015; Saito et al., 2015; Wang et al., 2015). Various types of ceramics, like HA, β-TCP, alpha-tricalcium phosphate (α-TCP), BCP, bioactive glasses, and more, have been used in recent years for the development of 3D printed scaffolds (Vorndran et al., 2008; Suwanprateeb et al., 2009; Klammert et al., 2010b), however, these materials are often brittle and do not match the mechanical properties of bone. To obtain similar mechanical strength to bone, bioceramics can be blended with polymers, such as cellulose, poly(D,L-lactic acid-co-glycolic acid) or polycaprolactone (PCL), before being printed (Liao et al., 2011). PCL is a polymer, with FDA approval that is widely used in 3D printing. It has a low melting temperature (60°C) (Wang et al., 2015), favorable viscoelasticity, and is biodegradable. Its slow degradation and high stiffness make PCL one of the preferred polymers for the manufacture of a 3D printing scaffold for bone tissue engineering (Brunello et al., 2016). The use of CT to create anatomically accurate scaffolds of calcium phosphate for cranial defects and alpha-TCP for maxillofacial deformities reconstruction have been described (Saijo et al., 2009; Klammert et al., 2010a). Direct ink writing (DIW), also called robocasting, has been one of the most studied and commonly used techniques for the development of 3D bioceramic scaffolds. DIW is an extrusion-based additive manufacturing method, in which a liquid-phase ink containing a high volume content of ceramic powder is dispensed through a nozzle, following a digitally defined pattern to create a 3D construct in a layer-by-layer manner (Lewis, 2006; Feilden et al., 2016). The chief advantages of DIW is that it applies to a wide range of bioceramics and it is possible to control pore size, pore orientation, and lattice design of the printed scaffold. Moreover, it is a high speed, simple and economic technique (Michna et al., 2005; Miranda et al., 2006) and has been used to create a hydroxyapatite scaffold for possible use in maxillofacial reconstruction (Cesarano Iii et al., 2005).

The main advantage of 3D printing is direct control over both the microarchitecture and complex anatomical structure. These 3D printed models allow the manufacture of customized scaffolds that mimics the patient's anatomy (Wubneh et al., 2018). However, there are different challenges in the translation of 3D printing bioceramics to clinical application. Firstly, 3D printed bioceramics are brittle and not suitable for load-bearing clinical applications. Secondly, the fabrication of a large-size scaffold for large bone defect reconstruction is time-consuming and expensive. Moreover, for producing these 3D printed bioceramics, toxic solvents, and high-temperatures are used in the printing procedures which may compromise cell viability (Rodríguez-Lorenzo et al., 2001; Lewis et al., 2006; Trombetta et al., 2017; Wen et al., 2017; Chen et al., 2019). There have been multiple *in vivo* animal studies conducted with 3D printed customized scaffolds for bone regeneration (Park et al., 2018; Choi et al., 2019), however, these techniques are still in a developmental stage for clinical application and not capable of fabricating large-sized bioceramic scaffolds.

3D Bioprinting a Custom Living and Vascularized Bone Graft

Bioprinting is another 3D printing technique that uses cell-laden hydrogels to print structures that after a period of maturation, will develop complex tissues, such as skin, cartilage, and bone. Vascularization can be aided by the incorporation of angiogenic growing factors or endothelial cells into bio-inks (Kolesky et al., 2014; Fahimipour et al., 2017; Benning et al., 2018). Three major procedures are the most used in bioprinting: inkjet, extrusion, and laser-assisted bioprinting. For tissue engineering applications, thermal and piezoelectric inkjet bioprinters are commonly used. In the piezoelectric inkjet bioprinter system, a piezoelectric crystal is used to create different potentials which generates pressure that allows the bioink ejection in the form of droplets. In thermal inkjet bioprinting, the printhead is heated up to 300°C that generates small air bubbles that produce pressure pulses to eject bioink droplets. The size of droplets depends on multiple factors, such as ink viscosity, the frequency of the current pulse and the gradient of the temperature (Hock et al., 1996; Hudson et al., 2000; Cui et al., 2012). The significant advantage of inkjet bioprinting is its rapid fabrication (Murphy and Atala, 2014). In extrusion bioprinting, a bioink is dispensed using pneumatic air pressure or mechanical systems composed of a screw or a piston. The flow of the bioink is more controlled in the mechanical system due to the action of the screw. With the pneumatic air, an interrupted filament is ejected, allowing high precision in the printed construct. Cells are exposed to high mechanical stress during this procedure, which may affect cell viability (Mandrycky et al., 2016). Extrusion bioprinting allows printing of different types of inks with different viscosities (Ozbolat and Hospodiuk, 2016; Paxton et al., 2017). The main disadvantage of this technique is that the high viscosity of the bioink or cell aggregation can clog the printer tip. Laser bioprinting consists of the interaction of a pulsed laser source with a ribbon. This ribbon contains an energy-absorbing layer, and below it, the bioink is located. A collector-slide receives the droplets of hydrogel created by the dynamic jet facilitated by the energy deposition that is created by the laser effect in the ribbon. In this procedure cells are not submitted to a mechanical stress (Gruene et al., 2011; Unger et al., 2011) and it is a nozzle-free cell printing technique with high resolution. Although 3D bioprinting brings the potential of producing a customized and vacsularized living bone transplant, this biofabrication technique has not yet been tested in clinical cases. Numerous remaining challenges such as obtaining optimal cell numbers, adequate cell viability and spatial cell differentiation of the 3D construct, as well as reconnection to the local vasculature are yet to be resolved.

CONCLUSION

In this review, the current bone reconstructive options for large skeletal defects such as autologous, allogeneic, biological and synthetic bone grafts are presented, as well as the future directions in bone tissue engineering that take advantage of 3D printing. The current gold standard technique for large bone defect reconstruction is autologous free vascularized bone flap transplantation that contains the patient's cells, growth factors, and a vascularization bed. However, its main disadvantages are donor site morbidity, laborious microsurgery, and the need to sculpt the construct to the anatomy of the bone defect. Alternatively, allogeneic bone is also used to reconstruct large bone defects, but it is less osteogenic than autologous bone and may induce immunogenic rejection and transfer of disease. 3D printing technologies permit the fabrication of personalized bone grafts and the improvements in the incorporation of cells, growth factors, and vasculature may revolutionize bone tissue regeneration.

AUTHOR CONTRIBUTIONS

LV, CK, and MB wrote the main manuscript text and prepared the figures. AH edited the manuscript. PL edited the manuscript and prepared the figures. All authors have read and approved the final version of the manuscript.

FUNDING

This work was supported by the European Commission through the H2020 projects ORTHOUNION "Orthopedic randomized clinical trial with expanded bone marrow MSC and bioceramics versus autograft in long bone non-unions" under grant agreement #733288 and MAXIBONE "Personalized maxillofacial bone regeneration" under grant agreement #779322. MB is funded through a Marie Skłodowska Curie Individual Fellowship PARAGEN H2020-MSCA-IF-2015-708711.

ACKNOWLEDGMENTS

LV was financially supported for his Ph.D. thesis by the patient's charity "Ligue Française contre la neurofibromatose" that is greatly acknowledged.

REFERENCES

Ahlmann, E. R., Menendez, L. R., Kermani, C., and Gotha, H. (2006). Survivorship and clinical outcome of modular endoprosthetic reconstruction for neoplastic disease of the lower limb. *J. Bone Joint Surg. Br.* 88, 790–795. doi: 10.1302/0301-620X.88B6.17519

Albrektsson, T., and Johansson, C. (2001). Osteoinduction, osteoconduction and osseointegration. *Eur. Spine J.* 10(Suppl. 2), 96–101. doi: 10.1007/s005860100282

Aro, H. T., and Aho, A. J. (1993). Clinical use of bone allografts. *Ann. Med.* 25, 403–412. doi: 10.3109/07853899309147303

Aronson, J., Harrison, B. H., Stewart, C. L., and Harp, J. H. (1989). The histology of distraction osteogenesis using different external fixators. *Clin. Orthop. Relat. Res.* 241, 106–116.

Athanasiou, V. T., Papachristou, D. J., Panagopoulos, A., Saridis, A., Scopa, C. D., and Megas, P. (2010). Histological comparison of autograft, allograft-DBM, xenograft, and synthetic grafts in a trabecular bone defect: an experimental study in rabbits. *Med. Sci. Monit.* 16, BR24–BR31.

Azi, M. L., Teixeira, A. A. A., Cotias, R. B., Joeris, A., and Kfuri, M. (2019). Induced-membrane technique in the management of posttraumatic bone defects. *JBJS Essent. Surg. Tech.* 9:e22. doi: 10.2106/JBJS.ST.18.00099

Bakri, K., Stans, A. A., Mardini, S., and Moran, S. L. (2008). Combined massive allograft and intramedullary vascularized fibula transfer: the capanna technique for lower-limb reconstruction. *Semin. Plast. Surg.* 22, 234–241. doi: 10.1055/s-2008-1081406

Bansal, M. R., Bhagat, S. B., and Shukla, D. D. (2009). Bovine cancellous xenograft in the treatment of tibial plateau fractures in elderly patients. *Int. Orthop.* 33, 779–784. doi: 10.1007/s00264-008-0526-y

Barbarossa, V., Matković, B. R., Vucić, N., Bielen, M., and Gluhinić, M. (2001). Treatment of osteomyelitis and infected non-union of the femur by a modified Ilizarov technique: follow-up study. *Croat. Med. J.* 42, 634–641.

Benning, L., Gutzweiler, L., Trondle, K., Riba, J., Zengerle, R., Koltay, P., et al. (2018). Assessment of hydrogels for bioprinting of endothelial cells. *J. Biomed. Mater. Res. A* 106, 935–947. doi: 10.1002/jbm.a.36291

Bertol, L. S., Schabbach, R., and dos Santos, L. A. L. (2016). Dimensional evaluation of patient-specific 3D printing using calcium phosphate cement for craniofacial bone reconstruction. *J. Biomater. Appl.* 31, 799–806. doi: 10.1177/0885328216682672

Bosc, R., Hersant, B., Carloni, R., Niddam, J., Bouhassira, J., De Kermadec, H., et al. (2017). Mandibular reconstruction after cancer: an in-house approach to manufacturing cutting guides. *Int. J. Oral Maxillofac. Surg.* 46, 24–31. doi: 10.1016/j.ijom.2016.10.004

Bostrom, M. P. G., and Seigerman, D. A. (2005). The clinical use of allografts, demineralized bone matrices, synthetic bone graft substitutes and osteoinductive growth factors: a survey study. *HSS J.* 1, 9–18. doi: 10.1007/s11420-005-0111-115

Brown, W., and Chow, L. (1983). A new calcium-phosphate setting cement. *J. Dent. Res.* 62, 672–672.

Brown, W. E. (1987). "A new calcium phosphate, water-setting cement," in *Cements Research Progress*, ed. P. W. Brown (Westerville, OH: American Ceramic Society), 351–379.

Brunello, G., Sivolella, S., Meneghello, R., Ferroni, L., Gardin, C., Piattelli, A., et al. (2016). Powder-based 3D printing for bone tissue engineering. *Biotechnol. Adv.* 34, 740–753. doi: 10.1016/j.biotechadv.2016.03.009

Brydone, A. S., Meek, D., and Maclaine, S. (2010). Bone grafting, orthopaedic biomaterials, and the clinical need for bone engineering. *Proc. Inst. Mech. Eng.* 224, 1329–1343. doi: 10.1243/09544119JEIM770

Bucholz, R. W., Carlton, A., and Holmes, R. E. (1987). Hydroxyapatite and tricalcium phosphate bone graft substitutes. *Orthop. Clin. North Am.* 18, 323–334.

Cao, Y., Vacanti, J. P., Paige, K. T., Upton, J., and Vacanti, C. A. (1997). Transplantation of chondrocytes utilizing a polymer-cell construct to produce tissue-engineered cartilage in the shape of a human ear. *Plast. Reconstr. Surg.* 100, 297–302. doi: 10.1097/00006534-199708000-199708001

Capanna, R., Bufalini, C., and Campanacci, M. (1993). A new technique for reconstructions of large metadiaphyseal bone defects. *Orthop. Traumatol.* 2, 159–177. doi: 10.1007/BF02620523

Careri, S., Vitiello, R., Oliva, M. S., Ziranu, A., Maccauro, G., and Perisano, C. (2019). Masquelet technique and osteomyelitis: innovations and literature review. *Eur. Rev. Med. Pharmacol. Sci.* 23(2 Suppl.), 210–216. doi: 10.26355/eurrev_201904_17495

Cesarano Iii, J., Dellinger, J. G., Saavedra, M. P., Gill, D. D., Jamison, R. D., Grosser, B. A., et al. (2005). Customization of load-bearing hydroxyapatite lattice scaffolds. *Int. J. Appl. Ceram. Technol.* 2, 212–220. doi: 10.1111/j.1744-7402.2005.02026.x

Chen, Z., Li, Z., Li, J., Liu, C., Lao, C., Fu, Y., et al. (2019). 3D printing of ceramics: a review. *J. Eur. Ceram. Soc.* 39, 661–687. doi: 10.1016/j.jeurceramsoc.2018.11.013

Cheng, M.-H., Brey, E. M., Ulusal, B. G., and Wei, F.-C. (2006). Mandible augmentation for osseointegrated implants using tissue engineering strategies. *Plast. Reconstr. Surg.* 118, 1e–4e. doi: 10.1097/01.prs.0000221120.11128.1a

Choi, S., Oh, Y.-I., Park, K.-H., Lee, J.-S., Shim, J.-H., and Kang, B.-J. (2019). New clinical application of three-dimensional-printed polycaprolactone/β-tricalcium phosphate scaffold as an alternative to allograft bone for limb-sparing surgery in a dog with distal radial osteosarcoma. *J. Vet. Med. Sci.* 81, 434–439. doi: 10.1292/jvms.18-0158

Choong, P. F., Sim, F. H., Pritchard, D. J., Rock, M. G., and Chao, E. Y. (1996). Megaprostheses after resection of distal femoral tumors. A rotating hinge design in 30 patients followed for 2-7 years. *Acta Orthop. Scand.* 67, 345–351. doi: 10.3109/17453679609002328

Colin, A., and Boire, J.-Y. (1997). A novel tool for rapid prototyping and development of simple 3D medical image processing applications on PCs. *Comput. Methods Programs Biomed.* 53, 87–92. doi: 10.1016/S0169-2607(97)01807-1805

Coquelin, L., Fialaire-Legendre, A., Roux, S., Poignard, A., Bierling, P., Hernigou, P., et al. (2012). In vivo and in vitro comparison of three different allografts vitalized with human mesenchymal stromal cells. *Tissue Eng. Part A* 18, 1921–1931. doi: 10.1089/ten.TEA.2011.0645

Cui, X., Boland, T., D'Lima, D. D., and Lotz, M. K. (2012). Thermal inkjet printing in tissue engineering and regenerative medicine. *Recent Pat. Drug Deliv. Formul.* 6, 149–155. doi: 10.2174/187221112800672949

Daculsi, G., LeGeros, R. Z., Nery, E., Lynch, K., and Kerebel, B. (1989). Transformation of biphasic calcium phosphate ceramics in vivo: ultrastructural and physicochemical characterization. *J. Biomed. Mater. Res.* 23, 883–894. doi: 10.1002/jbm.820230806

Deckard, C. R. (1989). *Method and Apparatus for Producing Parts by Selective Sintering*. U.S. Patent No. 4,863,538. Washington, DC: U.S. Patent and Trademark Office.

Dimitriou, R., Jones, E., McGonagle, D., and Giannoudis, P. V. (2011). Bone regeneration: current concepts and future directions. *BMC Med.* 9:66. doi: 10.1186/1741-7015-9-66

Dupret-Bories, A., Vergez, S., Meresse, T., Brouillet, F., and Bertrand, G. (2018). Contribution of 3D printing to mandibular reconstruction after cancer. *Eur. Ann. Otorhinolaryngol. Head Neck Dis.* 135, 133–136. doi: 10.1016/j.anorl.2017.09.007

Eggli, P. S., Muller, W., and Schenk, R. K. (1988). Porous hydroxyapatite and tricalcium phosphate cylinders with two different pore size ranges implanted in the cancellous bone of rabbits. A comparative histomorphometric and histologic study of bony ingrowth and implant substitution. *Clin. Orthop. Relat. Res.* 232, 127–138.

Elliot, R. R., and Richards, R. H. (2011). Failed operative treatment in two cases of pseudarthrosis of the clavicle using internal fixation and bovine cancellous xenograft (Tutobone). *J. Pediatr. Orthop.* 20, 349–353. doi: 10.1097/BPB.0b013e328346c010

Fahimipour, F., Rasoulianboroujeni, M., Dashtimoghadam, E., Khoshroo, K., Tahriri, M., Bastami, F., et al. (2017). 3D printed TCP-based scaffold incorporating VEGF-loaded PLGA microspheres for craniofacial tissue engineering. *Dent. Mater.* 33, 1205–1216. doi: 10.1016/j.dental.2017.06.016

Faldini, C., Miscione, M. T., Acri, F., Chehrassan, M., Bonomo, M., and Giannini, S. (2011). Use of homologous bone graft in the treatment of aseptic forearm nonunion. *Musculoskelet. Surg.* 95, 31–35. doi: 10.1007/s12306-011-0117-118

Feilden, E., Blanca, E. G.-T., Giuliani, F., Saiz, E., and Vandeperre, L. (2016). Robocasting of structural ceramic parts with hydrogel inks. *J. Eur. Ceram. Soc.* 36, 2525–2533. doi: 10.1016/j.jeurceramsoc.2016.03.001

Fernandez de Grado, G., Keller, L., Idoux-Gillet, Y., Wagner, Q., Musset, A.-M., Benkirane-Jessel, N., et al. (2018). Bone substitutes: a review of their characteristics, clinical use, and perspectives for large bone defects management. *J. Tissue Eng.* 9, 1–18. doi: 10.1177/2041731418776819

Gerhardt, L. C., and Boccaccini, A. R. (2010). Bioactive glass and glass-ceramic scaffolds for bone tissue engineering. *Materials* 3, 3867–3910. doi: 10.3390/ma3073867

Giannoudis, P. V., Einhorn, T. A., Schmidmaier, G., and Marsh, D. (2008). The diamond concept - open questions. *Injury* 39, S5–S8. doi: 10.1016/S0020-1383(08)70010-X

Gjerde, C., Mustafa, K., Hellem, S., Rojewski, M., Gjengedal, H., Yassin, M. A., et al. (2018). Cell therapy induced regeneration of severely atrophied mandibular bone in a clinical trial. *Stem Cell Res. Ther.* 9:213. doi: 10.1186/s13287-018-0951-959

Gomez-Barrena, E., Rosset, P., Gebhard, F., Hernigou, P., Baldini, N., Rouard, H., et al. (2019). Feasibility and safety of treating non-unions in tibia, femur and humerus with autologous, expanded, bone marrow-derived mesenchymal stromal cells associated with biphasic calcium phosphate biomaterials in a multicentric, non-comparative trial. *Biomaterials* 196, 100–108. doi: 10.1016/j.biomaterials.2018.03.033

Gomez-Barrena, E., Rosset, P., Muller, I., Giordano, R., Bunu, C., Layrolle, P., et al. (2011). Bone regeneration: stem cell therapies and clinical studies in orthopaedics and traumatology. *J. Cell. Mol. Med.* 15, 1266–1286. doi: 10.1111/j.1582-4934.2011.01265.x

Gosheger, G., Gebert, C., Ahrens, H., Streitbuerger, A., Winkelmann, W., and Hardes, J. (2006). Endoprosthetic reconstruction in 250 patients with sarcoma. *Clin. Orthop. Relat. Res.* 450, 164–171. doi: 10.1097/01.blo.0000223978.36831.39

Gruene, M., Unger, C., Koch, L., Deiwick, A., and Chichkov, B. (2011). Dispensing pico to nanolitre of a natural hydrogel by laser-assisted bioprinting. *Biomed. Eng. Online* 10:19. doi: 10.1186/1475-925X-10-19

Han, W., Shen, J., Wu, H., Yu, S., Fu, J., and Xie, Z. (2017). Induced membrane technique: advances in the management of bone defects. *Int. J. Surg.* 42, 110–116. doi: 10.1016/j.ijsu.2017.04.064

Hattori, H., Mibe, J., and Yamamoto, K. (2011). Modular megaprosthesis in metastatic bone disease of the femur. *Orthopedics* 34, e871–e876. doi: 10.3928/01477447-20111021-20111013

Heliotis, M., Lavery, K. M., Ripamonti, U., Tsiridis, E., and di Silvio, L. (2006). Transformation of a prefabricated hydroxyapatite/osteogenic protein-1 implant into a vascularised pedicled bone flap in the human chest. *Int. J. Oral Maxillofac. Surg.* 35, 265–269. doi: 10.1016/j.ijom.2005.07.013

Hidalgo, D. A., and Pusic, A. L. (2002). Free-flap mandibular reconstruction: a 10-year follow-up study. *Plast. Reconstr. Surg.* 110, 438–451.

Hock, S. W., Johnson, D. A., and Van Veen, M. A. (1996). *Print Quality Optimization for a Color Ink Jet Printer by Using a Larger Nozzle for the Black Ink Only*. Palo Alto, CA: Hewlett Packard.

Holl, S., Schlomberg, A., Gosheger, G., Dieckmann, R., Streitbuerger, A., Schulz, D., et al. (2012). Distal femur and proximal tibia replacement with megaprosthesis in revision knee arthroplasty: a limb-saving procedure. *Knee Surg. Sports Traumatol. Arthrosc.* 20, 2513–2518. doi: 10.1007/s00167-012-1945-1942

Hudson, K. R., Cowan, P. B., and Gondek, J. S. (2000). *Ink Drop Volume Variance Compensation for Inkjet Printing*. Palo Alto, CA: Hewlett Packard.

Ilizarov, G. A. (1990). Clinical application of the tension-stress effect for limb lengthening. *Clin. Orthop. Relat. Res.* 250, 8–26.

Jawad, M. U., and Brien, E. W. (2014). Proximal femoral reconstruction with a constrained acetabulum in oncologic patients. *Orthopedics* 37, e187–e193. doi: 10.3928/01477447-20140124-20140124

Jeys, L., and Grimer, R. (2009). "The long-term risks of infection and amputation with limb salvage surgery using endoprostheses," in *Treatment of Bone and Soft Tissue Sarcomas*, ed. P.-U. Tunn (Berlin: Springer), 75–84. doi: 10.1007/978-3-540-77960-5_7

Jeys, L. M., Grimer, R. J., Carter, S. R., and Tillman, R. M. (2005). Periprosthetic infection in patients treated for an orthopaedic oncological condition. *J. Bone Joint Surg. Am.* 87, 842–849. doi: 10.2106/JBJS.C.01222

Ji, K., Wang, Y., Wei, Q., Zhang, K., Jiang, A., Rao, Y., et al. (2018). Application of 3D printing technology in bone tissue engineering. *Biodes. Manuf.* 1, 203–210. doi: 10.1007/s42242-018-0021-22

Kao, C. T., Lin, C. C., Chen, Y. W., Yeh, C. H., Fang, H. Y., and Shie, M. Y. (2015). Poly(dopamine) coating of 3D printed poly(lactic acid) scaffolds for bone tissue engineering. *Mater. Sci. Eng. C Mater. Biol. Appl.* 56, 165–173. doi: 10.1016/j.msec.2015.06.028

Karalashvili, L., Chichua, N., Menabde, G., Atskvereli, L., and Grdzelidze, T. (2017). Decellularized bovine bone graft for zygomatic bone reconstruction. *Med. Case Rep.* 4:52. doi: 10.21767/2471-8041.100087

Keating, J. F., and McQueen, M. M. (2001). Substitutes for autologous bone graft in orthopaedic trauma. *J. Bone Joint Surg. Br.* 83, 3–8. doi: 10.1302/0301-620x.83b1.11952

Klammert, U., Gbureck, U., Vorndran, E., Rodiger, J., Meyer-Marcotty, P., and Kubler, A. C. (2010a). 3D powder printed calcium phosphate implants for reconstruction of cranial and maxillofacial defects. *J. Craniomaxillofac. Surg.* 38, 565–570. doi: 10.1016/j.jcms.2010.01.009

Klammert, U., Vorndran, E., Reuther, T., Muller, F. A., Zorn, K., and Gbureck, U. (2010b). Low temperature fabrication of magnesium phosphate cement scaffolds by 3D powder printing. *J. Mater. Sci. Mater. Med.* 21, 2947–2953. doi: 10.1007/s10856-010-4148-4148

Kokemueller, H., Spalthoff, S., Nolff, M., Tavassol, F., Essig, H., Stuehmer, C., et al. (2010). Prefabrication of vascularized bioartificial bone grafts in vivo for segmental mandibular reconstruction: experimental pilot study in sheep and first clinical application. *Int. J. Oral Maxillofac. Surg.* 39, 379–387. doi: 10.1016/j.ijom.2010.01.010

Kolesky, D. B., Truby, R. L., Gladman, A. S., Busbee, T. A., Homan, K. A., and Lewis, J. A. (2014). 3D bioprinting of vascularized, heterogeneous cell-laden tissue constructs. *Adv. Mater.* 26, 3124–3130. doi: 10.1002/adma.201305506

Kurien, T., Pearson, R. G., and Scammell, B. E. (2013). Bone graft substitutes currently available in orthopaedic practice. *Bone Joint J.* 95, 583–597. doi: 10.1302/0301-620X.95B5.30286

Laurencin, C., Khan, Y., and Veronick, J. (2014). "Bone graft substitutes: past, present and future," in *Bone Graft Substitutes and Bone Regenerative Engineering*, eds C. T. Laurencin, and T. Jiang (West Conshohocken, PA: ASTM International), 1–9. doi: 10.1520/mono62013002501

Ledford, C. K., Nunley, J. A. II, Viens, N. A., and Lark, R. K. (2013). Bovine xenograft failures in pediatric foot reconstructive surgery. *J. Pediatr. Orthop.* 33, 458–463. doi: 10.1097/BPO.0b013e318287010d

Lee, K. Y., Park, M., Kim, H. M., Lim, Y. J., Chun, H. J., Kim, H., et al. (2006). Ceramic bioactivity: progresses, challenges and perspectives. *Biomed. Mater.* 1, R31–R37. doi: 10.1088/1748-6041/1/2/r01

Lewis, J. A. (2006). Direct ink writing of 3D functional materials. *Adv. Funct. Mater.* 16, 2193–2204. doi: 10.1002/adfm.200600434

Lewis, J. A., Smay, J. E., Stuecker, J., and Cesarano, J. (2006). Direct ink writing of three-dimensional ceramic structures. *J. Am. Ceram. Soc.* 89, 3599–3609. doi: 10.1111/j.1551-2916.2006.01382.x

Liao, H.-T., Chang, K.-H., Jiang, Y., Chen, J.-P., and Lee, M.-Y. (2011). Fabrication of tissue engineered PCL scaffold by selective laser-sintered machine for osteogeneisis of adipose-derived stem cells. *Virtual Phys. Protoyp.* 6, 57–60. doi: 10.1080/17452759.2011.559742

Lodoso-Torrecilla, I., van Gestel, N. A. P., Diaz-Gomez, L., Grosfeld, E. C., Laperre, K., Wolke, J. G. C., et al. (2018). Multimodal pore formation in calcium phosphate cements. *J. Biomed. Mater. Res. A* 106, 500–509. doi: 10.1002/jbm.a.36245

Mandrycky, C., Wang, Z., Kim, K., and Kim, D.-H. (2016). 3D bioprinting for engineering complex tissues. *Biotechnol. Adv.* 34, 422–434. doi: 10.1016/j.biotechadv.2015.12.011

Mankin, H. J., Gebhardt, M. C., Jennings, L. C., Springfield, D. S., and Tomford, W. W. (1996). Long-term results of allograft replacement in the management of bone tumors. *Clin. Orthop. Relat. Res.* 324, 86–97. doi: 10.1097/00003086-199603000-199603011

Masquelet, A. C. (2003). Muscle reconstruction in reconstructive surgery: soft tissue repair and long bone reconstruction. *Langenbecks Arch. Surg.* 388, 344–346. doi: 10.1007/s00423-003-0379-371

Masquelet, A. C., and Begue, T. (2010). The concept of induced membrane for reconstruction of long bone defects. *Orthop. Clin. North Am.* 41, 27–37. doi: 10.1016/j.ocl.2009.07.011

Masquelet, A. C., Fitoussi, F., Begue, T., and Muller, G. P. (2000). Reconstruction of the long bones by the induced membrane and spongy autograft. *Ann. Chir. Plast. Esthet.* 45, 346–353.

Mathieu, L., Bilichtin, E., Durand, M., de l'Escalopier, N., Murison, J. C., Collombet, J. M., et al. (2019). Masquelet technique for open tibia fractures in a military setting. *Eur. J. Trauma Emerg. Surg.* 24, 1–7. doi: 10.1007/s00068-019-01217-y

Matsubara, H., Hogan, D. E., Morgan, E. F., Mortlock, D. P., Einhorn, T. A., and Gerstenfeld, L. C. (2012). Vascular tissues are a primary source of BMP2 expression during bone formation induced by distraction osteogenesis. *Bone* 51, 168–180. doi: 10.1016/j.bone.2012.02.017

Mazzoli, A. (2013). Selective laser sintering in biomedical engineering. *Med. Biol. Eng. Comput.* 51, 245–256. doi: 10.1007/s11517-012-1001-x

Mercado-Pagan, A. E., Stahl, A. M., Shanjani, Y., and Yang, Y. (2015). Vascularization in bone tissue engineering constructs. *Ann. Biomed. Eng.* 43, 718–729. doi: 10.1007/s10439-015-1253-1253

Mesimaki, K., Lindroos, B., Tornwall, J., Mauno, J., Lindqvist, C., Kontio, R., et al. (2009). Novel maxillary reconstruction with ectopic bone formation by GMP adipose stem cells. *Int. J. Oral Maxillofac. Surg.* 38, 201–209. doi: 10.1016/j.ijom.2009.01.001

Michna, S., Wu, W., and Lewis, J. A. (2005). Concentrated hydroxyapatite inks for direct-write assembly of 3D periodic scaffolds. *Biomaterials* 26, 5632–5639. doi: 10.1016/j.biomaterials.2005.02.040

Miranda, P., Saiz, E., Gryn, K., and Tomsia, A. P. (2006). Sintering and robocasting of β-tricalcium phosphate scaffolds for orthopaedic applications. *Acta Biomater.* 2, 457–466. doi: 10.1016/j.actbio.2006.02.004

Mittermayer, F., Krepler, P., Dominkus, M., Schwameis, E., Sluga, M., Heinzl, H., et al. (2001). Long-term followup of uncemented tumor endoprostheses for the lower extremity. *Clin. Orthop. Relat. Res.* 388, 167–177. doi: 10.1097/00003086-200107000-200107024

Mondschein, R. J., Kanitkar, A., Williams, C. B., Verbridge, S. S., and Long, T. E. (2017). Polymer structure-property requirements for stereolithographic 3D printing of soft tissue engineering scaffolds. *Biomaterials* 140, 170–188. doi: 10.1016/j.biomaterials.2017.06.005

Moran, S. L., Bakri, K., Mardini, S., Shin, A. Y., and Bishop, A. T. (2009). The use of vascularized fibular grafts for the reconstruction of spinal and sacral defects. *Microsurgery* 29, 393–400. doi: 10.1002/micr.20655

Morelli, I., Drago, L., George, D. A., Gallazzi, E., Scarponi, S., and Romano, C. L. (2016). Masquelet technique: myth or reality? A systematic review and meta-analysis. *Injury* 47(Suppl. 6), S68–S76. doi: 10.1016/S0020-1383(16)30842-30847

Murphy, S. V., and Atala, A. (2014). 3D bioprinting of tissues and organs. *Nat. Biotechnol.* 32:773. doi: 10.1038/nbt.2958

Muscolo, D. L., Ayerza, M. A., Aponte-Tinao, L., Ranalletta, M., and Abalo, E. (2004). Intercalary femur and tibia segmental allografts provide an acceptable alternative in reconstructing tumor resections. *Clin. Orthop. Relat. Res.* 426, 97–102. doi: 10.1097/01.blo.0000141652.93178.10

Ogose, A., Kondo, N., Umezu, H., Hotta, T., Kawashima, H., Tokunaga, K., et al. (2006). Histological assessment in grafts of highly purified beta-tricalcium phosphate (OSferion®) in human bones. *Biomaterials* 27, 1542–1549. doi: 10.1016/j.biomaterials.2005.08.034

Ogura, K., Sakuraba, M., Miyamoto, S., Fujiwara, T., Chuman, H., and Kawai, A. (2015). Pelvic ring reconstruction with a double-barreled free vascularized fibula graft after resection of malignant pelvic bone tumor. *Arch. Orthop. Trauma Surg.* 135, 619–625. doi: 10.1007/s00402-015-2197-2197

Orringer, J. S., Shaw, W. W., Borud, L. J., Freymiller, E. G., Wang, S. A., and Markowitz, B. L. (1999). Total mandibular and lower lip reconstruction with a prefabricated osteocutaneous free flap. *Plast. Reconstr. Surg.* 104, 793–797. doi: 10.1097/00006534-199909030-199909028

Oryan, A., Alidadi, S., and Moshiri, A. (2013). Current concerns regarding healing of bone defects. *Hard Tissue* 2:13.

Oryan, A., Alidadi, S., Moshiri, A., and Maffulli, N. (2014). Bone regenerative medicine: classic options, novel strategies, and future directions. *J. Orthop. Surg. Res.* 9:18. doi: 10.1186/1749-799X-9-18

Ozbolat, I. T., and Hospodiuk, M. (2016). Current advances and future perspectives in extrusion-based bioprinting. *Biomaterials* 76, 321–343. doi: 10.1016/j.biomaterials.2015.10.076

Pala, E., Trovarelli, G., Calabro, T., Angelini, A., Abati, C. N., and Ruggieri, P. (2015). Survival of modern knee tumor megaprostheses: failures, functional results, and a comparative statistical analysis. *Clin. Orthop. Relat. Res.* 473, 891–899. doi: 10.1007/s11999-014-3699-3692

Parikh, S. N. (2002). Bone graft substitutes: past, present, future. *J. Postgrad. Med.* 48, 142–148.

Park, S. A., Lee, H. J., Kim, K. S., Lee, S. J., Lee, J. T., Kim, S. Y., et al. (2018). In vivo evaluation of 3D-printed polycaprolactone scaffold implantation combined with beta-TCP powder for alveolar bone augmentation in a beagle defect model. *Materials* 11:238. doi: 10.3390/ma11020238

Patil, S., Auyeung, J., and Gower, A. (2011). Outcome of subtalar fusion using bovine cancellous bone graft: a retrospective case series. *J. Foot Ankle Surg.* 50, 388–390. doi: 10.1053/j.jfas.2011.04.019

Paxton, N., Smolan, W., Böck, T., Melchels, F., Groll, J., and Jungst, T. (2017). Proposal to assess printability of bioinks for extrusion-based bioprinting and evaluation of rheological properties governing bioprintability. *Biofabrication* 9:044107. doi: 10.1088/1758-5090/aa8dd8

Pelissier, P. H., Masquelet, A. C., Bareille, R., Pelissier, S. M., and Amedee, J. (2004). Induced membranes secrete growth factors including vascular and osteoinductive factors and could stimulate bone regeneration. *J. Orthop. Res.* 22, 73–79. doi: 10.1016/S0736-0266(03)00165-167

Peng, X., Mao, C., Yu, G. Y., Guo, C. B., Huang, M. X., and Zhang, Y. (2005). Maxillary reconstruction with the free fibula flap. *Plast. Reconstr. Surg.* 115, 1562–1569. doi: 10.1097/01.prs.0000160691.63029.74

Petrochenko, P. E., Torgersen, J., Gruber, P., Hicks, L. A., Zheng, J., Kumar, G., et al. (2015). Laser 3D printing with sub-microscale resolution of porous elastomeric scaffolds for supporting human bone stem cells. *Adv. Healthc. Mater.* 4, 739–747. doi: 10.1002/adhm.201400442

Putzier, M., Strube, P., Funk, J. F., Gross, C., Monig, H. J., Perka, C., et al. (2009). Allogenic versus autologous cancellous bone in lumbar segmental spondylodesis: a randomized prospective study. *Eur. Spine J.* 18, 687–695. doi: 10.1007/s00586-008-0875-877

Rizzo, M., and Moran, S. L. (2008). Vascularized bone grafts and their applications in the treatment of carpal pathology. *Semin. Plast. Surg.* 22, 213–227. doi: 10.1055/s-2008-1081404

Rodríguez-Lorenzo, L. M., Vallet-Regí, M., and Ferreira, J. M. F. (2001). Colloidal processing of hydroxyapatite. *Biomaterials* 22, 1847–1852. doi: 10.1016/S0142-9612(00)00366-365

Saijo, H., Igawa, K., Kanno, Y., Mori, Y., Kondo, K., Shimizu, K., et al. (2009). Maxillofacial reconstruction using custom-made artificial bones fabricated by inkjet printing technology. *J. Artif. Organs* 12, 200–205. doi: 10.1007/s10047-009-0462-467

Saito, E., Suarez-Gonzalez, D., Murphy, W. L., and Hollister, S. J. (2015). Biomineral coating increases bone formation by ex vivo BMP-7 gene therapy in rapid prototyped poly(L-lactic acid) (PLLA) and poly(epsilon-caprolactone) (PCL) porous scaffolds. *Adv. Healthc. Mater.* 4, 621–632. doi: 10.1002/adhm.201400424

Samavedi, S., Whittington, A. R., and Goldstein, A. S. (2013). Calcium phosphate ceramics in bone tissue engineering: a review of properties and their influence on cell behavior. *Acta Biomater.* 9, 8037–8045. doi: 10.1016/j.actbio.2013.06.014

Sanan, A., and Haines, S. J. (1997). Repairing holes in the head: a history of cranioplasty. *Neurosurgery* 40, 588–603. doi: 10.1097/00006123-199703000-199703033

Scaglione, M., Fabbri, L., Dell'Omo, D., Gambini, F., and Guido, G. (2014). Long bone nonunions treated with autologous concentrated bone marrow-derived cells combined with dried bone allograft. *Musculoskelet. Surg.* 98, 101–106. doi: 10.1007/s12306-013-0271-272

Shehadeh, A., Noveau, J., Malawer, M., and Henshaw, R. (2010). Late complications and survival of endoprosthetic reconstruction after resection of bone tumors. *Clin. Orthop. Relat. Res.* 468, 2885–2895. doi: 10.1007/s11999-010-1454-x

Shibuya, N., Jupiter, D. C., Clawson, L. D., and La Fontaine, J. (2012). Incorporation of bovine-based structural bone grafts used in reconstructive foot surgery. *J. Foot Ankle Surg.* 51, 30–33. doi: 10.1053/j.jfas.2011.09.008

Sivakumar, R., Mohideen, M. G., Chidambaram, M., Vinoth, T., Singhi, P. K., and Somashekar, V. (2016). Management of large bone defects in diaphyseal fractures by induced membrane formation by Masquelet's technique. *J. Orthop. Case Rep.* 6, 59–62. doi: 10.13107/jocr.2250-0685.508

Spiegelberg, B., Parratt, T., Dheerendra, S. K., Khan, W. S., Jennings, R., and Marsh, D. R. (2010). Ilizarov principles of deformity correction. *Ann. R. Coll. Surg. Engl.* 92, 101–105. doi: 10.1308/003588410X12518836439326

Stanovici, J., Le Nail, L. R., Brennan, M. A., Vidal, L., Trichet, V., Rosset, P., et al. (2016). Bone regeneration strategies with bone marrow stromal cells in orthopaedic surgery. *Curr. Res. Transl. Med.* 64, 83–90. doi: 10.1016/j.retram.2016.04.006

Suwanprateeb, J., Sanngam, R., Suvannapruk, W., and Panyathanmaporn, T. (2009). Mechanical and in vitro performance of apatite-wollastonite glass ceramic reinforced hydroxyapatite composite fabricated by 3D-printing. *J. Mater. Sci. Mater. Med.* 20, 1281–1289. doi: 10.1007/s10856-009-3697-3691

Tatara, A. M., Wong, M. E., and Mikos, A. G. (2014). In vivo bioreactors for mandibular reconstruction. *J. Dent. Res.* 93, 1196–1202. doi: 10.1177/0022034514547763

Taylor, G. I. (1982). Reconstruction of the mandible with free composite iliac bone grafts. *Ann. Plast. Surg.* 9, 361–376. doi: 10.1097/00000637-198211000-198211003

Taylor, G. I. (1983). The current status of free vascularized bone grafts. *Clin. Plast. Surg.* 10, 185–209.

Taylor, G. I. (1985). Composite tissue transfer to the lower limb. *Recent Adv. Plast. Surg.* 3, 83–109.

Taylor, G. I., Corlett, R. J., and Ashton, M. W. (2016). The evolution of free vascularized bone transfer: a 40-year experience. *Plast. Reconstr. Surg.* 137, 1292–1305. doi: 10.1097/PRS.0000000000002040

Taylor, G. I., Miller, G. D., and Ham, F. J. (1975). The free vascularized bone graft. A clinical extension of microvascular techniques. *Plast. Reconstr. Surg.* 55, 533–544. doi: 10.1097/00006534-197505000-197505002

Torres, J., Tamimi, F., Alkhraisat, M., Prados-Frutos, J. C., and Lopez-Cabarcos, E. (2011). "Bone substitutes," in *Implant Dentistry - The Most Promising Discipline of Dentistry*, ed. I. Turkyilmaz (London: Intech), 4–105.

Trombetta, R., Inzana, J. A., Schwarz, E. M., Kates, S. L., and Awad, H. A. (2017). 3D printing of calcium phosphate ceramics for bone tissue engineering and drug delivery. *Ann. Biomed. Eng.* 45, 23–44. doi: 10.1007/s10439-016-1678-1673

Unger, C., Gruene, M., Koch, L., Koch, J., and Chichkov, B. N. (2011). Time-resolved imaging of hydrogel printing via laser-induced forward transfer. *Appl. Phys. A* 103, 271–277. doi: 10.1007/s00339-010-6030-6034

Vacanti, J. P., and Langer, R. (1999). Tissue engineering: the design and fabrication of living replacement devices for surgical reconstruction and transplantation. *Lancet* 354, S32–S34. doi: 10.1016/S0140-6736(99)90247-90247

Verboket, R., Leiblein, M., Seebach, C., Nau, C., Janko, M., Bellen, M., et al. (2018). Autologous cell-based therapy for treatment of large bone defects: from bench to bedside. *Eur. J. Trauma Emerg. Surg.* 44, 649–665. doi: 10.1007/s00068-018-0906-y

Vorndran, E., Klarner, M., Klammert, U., Grover, L. M., Patel, S., Barralet, J. E., et al. (2008). 3D Powder printing of β-tricalcium phosphate ceramics using different strategies. *Adv. Eng. Mater.* 10, B67–B71. doi: 10.1002/adem.200800179

Wang, M. O., Vorwald, C. E., Dreher, M. L., Mott, E. J., Cheng, M.-H., Cinar, A., et al. (2015). Evaluating 3D-printed biomaterials as scaffolds for vascularized bone tissue engineering. *Adv. Mater.* 27, 138–144. doi: 10.1002/adma.201403943

Warnke, P. H., Springer, I. N., Wiltfang, J., Acil, Y., Eufinger, H., Wehmoller, M., et al. (2004). Growth and transplantation of a custom vascularised bone graft in a man. *Lancet* 364, 766–770. doi: 10.1016/S0140-6736(04)16935-16933

Wen, Y., Xun, S., Haoye, M., Baichuan, S., Peng, C., Xuejian, L., et al. (2017). 3D printed porous ceramic scaffolds for bone tissue engineering: a review. *Biomater. Sci.* 5, 1690–1698. doi: 10.1039/c7bm00315c

Winder, J., and Bibb, R. (2005). Medical rapid prototyping technologies: state of the art and current limitations for application in oral and maxillofacial surgery. *J. Oral Maxillofac. Surg.* 63, 1006–1015. doi: 10.1016/j.joms.2005.03.016

Wubneh, A., Tsekoura, E. K., Ayranci, C., and Uludag, H. (2018). Current state of fabrication technologies and materials for bone tissue engineering. *Acta Biomater.* 80, 1–30. doi: 10.1016/j.actbio.2018.09.031

Xu, N., Ye, X., Wei, D., Zhong, J., Chen, Y., Xu, G., et al. (2014). 3D artificial bones for bone repair prepared by computed tomography-guided fused deposition modeling for bone repair. *ACS Appl. Mater. Interfaces* 6, 14952–14963. doi: 10.1021/am502716t

Yang, X., Lu, Z., Wu, H., Li, W., Zheng, L., and Zhao, J. (2018). Collagen-alginate as bioink for three-dimensional (3D) cell printing based cartilage tissue engineering. *Mater. Sci. Eng. C* 83, 195–201. doi: 10.1016/j.msec.2017.09.002

Zimmermann, G., and Moghaddam, A. (2011). Allograft bone matrix versus synthetic bone graft substitutes. *Injury* 42(Suppl. 2), S16–S21. doi: 10.1016/j.injury.2011.06.199

Conflict of Interest: The authors declare that the research was conducted in the absence of any commercial or financial relationships that could be construed as a potential conflict of interest.

frontiers
in Bioengineering and Biotechnology

ORIGINAL RESEARCH
published: 25 March 2020
doi: 10.3389/fbioe.2020.00217

3D Printing of Bone Grafts for Cleft Alveolar Osteoplasty – *In vivo* Evaluation in a Preclinical Model

Paula Korn[1]*, Tilman Ahlfeld[2], Franziska Lahmeyer[3], David Kilian[2], Philipp Sembdner[4], Ralph Stelzer[4], Winnie Pradel[3], Adrian Franke[3], Martina Rauner[5], Ursula Range[6], Bernd Stadlinger[7], Anja Lode[2], Günter Lauer[3] and Michael Gelinsky[2]

[1] Department of Oral and Maxillofacial Surgery, Charité – Universitätsmedizin Berlin, Corporate Member of Freie Universität Berlin, Humboldt-Universität zu Berlin, and Berlin Institute of Health, Berlin, Germany, [2] Centre for Translational Bone, Joint and Soft Tissue Research, University Hospital "Carl Gustav Carus", Faculty of Medicine, Technische Universität Dresden, Dresden, Germany, [3] Department of Oral and Maxillofacial Surgery, Faculty of Medicine "Carl Gustav Carus", Technische Universität Dresden, Dresden, Germany, [4] Institute of Machine Elements and Machine Design, Technische Universität Dresden, Dresden, Germany, [5] Division of Endocrinology, Diabetes, and Bone Diseases, Department of Medicine III and Center for Healthy Aging, Faculty of Medicine "Carl Gustav Carus", Technische Universität Dresden, Dresden, Germany, [6] Institute for Medical Informatics and Biometry, Faculty of Medicine "Carl Gustav Carus", Technische Universität Dresden, Dresden, Germany, [7] Clinic of Cranio-Maxillofacial and Oral Surgery, University Hospital Zurich, University of Zurich, Zurich, Switzerland

Edited by:
*Luciano Vidal,
Institut National de la Santé et de la Recherche Médicale (INSERM), France*

Reviewed by:
*Agnes Dupret-Bories,
Institut Claudius Regaud, France
Derek Rosenzweig,
McGill University, Canada*

***Correspondence:**
*Paula Korn
paula.korn@charite.de*

Specialty section:
This article was submitted to Biomaterials, a section of the journal Frontiers in Bioengineering and Biotechnology

Received: 04 November 2019
Accepted: 04 March 2020
Published: 25 March 2020

Citation:
Korn P, Ahlfeld T, Lahmeyer F, Kilian D, Sembdner P, Stelzer R, Pradel W, Franke A, Rauner M, Range U, Stadlinger B, Lode A, Lauer G and Gelinsky M (2020) 3D Printing of Bone Grafts for Cleft Alveolar Osteoplasty – In vivo Evaluation in a Preclinical Model. Front. Bioeng. Biotechnol. 8:217. doi: 10.3389/fbioe.2020.00217

One of the most common hereditary craniofacial anomalies in humans are cleft lip and cleft alveolar bone with or without cleft palate. Current clinical practice, the augmentation of the persisting alveolar bone defect by using autologous bone grafts, has considerable disadvantages motivating to an intensive search for alternatives. We developed a novel therapy concept based on 3D printing of biodegradable calcium phosphate-based materials and integration of osteogenic cells allowing fabrication of patient-specific, tissue-engineered bone grafts. Objective of the present study was the *in vivo* evaluation of implants in a rat alveolar cleft model. Scaffolds were designed according to the defect's geometry with two different pore designs (60° and 30° rotated layer orientation) and produced by extrusion-based 3D plotting of a pasty calcium phosphate cement. The scaffolds filled into the artificial bone defect in the palate of adult Lewis rats, showing a good support. Half of the scaffolds were colonized with rat mesenchymal stromal cells (rMSC) prior to implantation. After 6 and 12 weeks, remaining defect width and bone formation were quantified histologically and by microCT. The results revealed excellent osteoconductive properties of the scaffolds, a significant influence of the pore geometry (60° > 30°), but no enhanced defect healing by pre-colonization with rMSC.

Keywords: 3D printing, bone graft, bone tissue engineering, alveolar cleft model, calcium phosphate cement

INTRODUCTION

During embryologic development of the craniomaxillofacial anatomy, tissue fusion is essential. In cases of non- or incomplete fusion, soft and/or hard tissue defects will remain after birth. The most common examples for congenital craniofacial anomalies caused by an incomplete tissue fusion are cleft lip and cleft alveolus with or without a cleft palate. The prevalence in humans varies between different ethnical groups and averaged for Caucasians at one per 700 live births (Dixon et al., 2011). Three of four cleft lip and palate patients expose an alveolar osseous defect (Guo et al., 2011). Children suffering from a complete cleft palate, alveolus and lip require an extensive treatment from their first months until adolescence. One aspect of the surgical therapy is the augmentation of the persisting alveolar bone defect, called alveolar cleft osteoplasty, by autologous bone grafts. This has to be performed at the age of 9–11 years in order to create sufficient bone volume, allowing the eruption of the permanent canine. Additionally, bone grafting of this defect normalizes facial and dental function. Failure to reconstruct this osseous deformity may result in oronasal fistula, fluid reflux, speech pathology, anteroposterior deficiency of the maxilla, transverse deficiency of the maxilla, lack of bone support for the teeth, dental crowding, and facial asymmetry (Waite and Waite, 1996).

Up to now, the alveolar cleft osteoplasty uses mainly autologous bone grafts from the iliac crest, providing osteogenic, osteoinductive and osteoconductive properties (Lopez et al., 2018). A disadvantage of these bone grafts is the need of harvesting with associated donor site morbidity. In cases of maxillofacial and cleft reconstructions, the following rates of complications in the donor site region are summarized by a review of Boehm et al. (2018): acute (45.7%) and chronic (1.5%) gait disturbance, acute (17.8%) and chronic nerve changes (1.4%), hypertrophic/painful scar (9.1%), chronic pain (3.1%), hematoma (2.2%), seroma (2.0%), infection (1.0%) and iliac crest fracture (1.2%). Against this background, it is of great clinical interest to evaluate biomaterials regarding their potential to be an alternative for the autologous bone grafts. For small oral bone defects alloplastic and xenogenic materials are well established, but for congenital and critical size defects the clinical results of these materials are currently not sufficient (Feinberg et al., 1989). Hence, there are great efforts to develop bone grafts, which can be used for the reconstruction of critical size defects like alveolar clefts (Silva Gomes Ferreira et al., 2018). The bone grafts should have the following characteristics: osteoconductivity, mechanical stability, promotion of vascular ingrowth and stem cell recruitment, and progressive resorption during the replacement by native tissue (Hutmacher et al., 2007; Kim et al., 2017).

Ideally, the bone graft is patient-specific and fits exactly into the defect area. This can be achieved by additive manufacturing of an implant based on a 3D model that is designed by using computer tomography (CT) or magnet resonance tomography (MRT) data of the defect region (Pfister et al., 2004). In the last two decades, various methods of additive manufacturing have been adapted to the fabrication of medical implants and tissue engineering constructs, amongst them extrusion-based fabrication methods (Landers et al., 2002; Malda et al., 2013). Extrusion printing in mild conditions, for example by avoidance of unphysiological temperatures, pH or energy-intensive post-printing treatment, is called 3D plotting (Moroni et al., 2018). The mild processing conditions allow the combined processing of materials and biological substances like proteins/growth factors and cells (called bioplotting) (Fedorovich et al., 2008; Poldervaart et al., 2013).

The regeneration of tissue defects is accomplished by cells; the biomaterial just fills the defect volume and provides a supporting substrate by mimicking the extracellular matrix. The cells invade into the defect region from the surrounding tissue or the biomaterial scaffold is pre-colonized with regenerative cells according to the tissue engineering concept; growth factors and other signaling molecules can be integrated in the material to stimulate cellular reactions necessary for tissue regeneration such as migration, proliferation and differentiation (Hutmacher et al., 2007). Previous preclinical studies investigated tissue engineering approaches in the context of alveolar cleft osteoplasty by testing calcium phosphate-based biomaterials which were pre-colonized with rat mesenchymal stromal cells (rMSC) (Korn et al., 2014, 2017) or coated with bone morphogenetic protein 2 (BMP-2) (Nguyen et al., 2009) in rat alveolar cleft models. The mentioned material combinations showed local bone formation within the artificial defect, but no complete osseous defect healing. First trials of clinical application of tissue engineered bone grafts led to promising results. An example is the study of Pradel and Lauer (2012), who found comparable rates of bone formation for pure autologous (from iliac crest) and mixed alloplastic (autologous osteoblasts obtained from maxilla bone biopsies and cultured on demineralized bone matrix Osteovit bone grafts). Guo et al. (2011) reported for collagen bone graft substitutes impregnated with BMP-2 (InFuse bone graft, Sofamor-Danek, United States) comparable results. However, most studies have in common, that the small number of patients might led to a high bias of the results and up to now no real alternative bone graft is clinically established (Liang et al., 2018).

We aim to develop a novel concept for the treatment of alveolar cleft patients by the combination of 3D plotting of patient-specific bone implants and tissue engineering approaches; due to their resemblance of the natural bone mineral, we focus on calcium phosphate-based materials. Herein, we utilized a plottable, clinically approved calcium phosphate cement paste (CPC), which is composed of calcium phosphate precursors (mainly α-tricalcium phosphate) and a biocompatible, but hydrophobic (oil-based) carrier liquid (Heinemann et al., 2013; Lode et al., 2018). This composition allows long storage and unlimited extrusion in mild conditions (Lode et al., 2014). Macroporous CPC scaffolds can be plotted with high accuracy, afterward the scaffolds need to be hardened in an aqueous environment (Akkineni et al., 2015; Ahlfeld et al., 2017). During this setting procedure, the carrier liquid vanishes from the scaffold structure without residues and the precursors set to nanocrystalline calcium-deficient, carbonated hydroxyapatite, which can be resorbed by osteoclasts (Bernhardt et al., 2014; Reitmaier et al., 2018). The mechanical properties of bulk and plotted CPC samples were characterized thoroughly in the past (Ahlfeld et al., 2017; Lode et al., 2018). Patient-specific scaffold structures can be fabricated by 3D plotting of CPC (Ahlfeld et al., 2018b).

In the present study, we analyzed custom-made bone grafts consisting of 3D plotted CPC scaffolds and rMSC in a small animal model of cleft alveolar osteoplasty. The hypothesis of the study was "The application of a 3D plotted bone graft into an artificial maxillary bone defect leads to a significant reduction of the defect width after 12 weeks." To better understand the performance of 3D plotted implants, we investigated the influence of the fabricated pore geometry on bone formation in the defect area, as well as the effect of rMSC seeded onto the scaffold prior to implantation.

MATERIALS AND METHODS

3D Plotting of CPC Scaffolds

The plottable CPC paste (INNOTERE Paste-CPC), manufactured by INNOTERE GmbH (Radebeul, Germany), was sterilized by γ-irradiation (25 kGy) and transferred into cartridges (Nordson EFD, Oberhaching, Germany) which were placed into a three-axis robotic dispensing system (Bioscaffolder 3.1, GeSiM mbH, Radeberg, Germany). For the *in vitro* and *in vivo* study, scaffolds with a diameter of 3.0 and 3.2 mm and a height of 0.48 mm (four layers) were plotted utilizing a 230 μm needle (Globaco GmbH, Rödermark, Germany) with a plotting speed of 10 mm·s^{-1} and an air pressure of 150 kPa. Inner geometry of the scaffolds was adjusted as follows: strand-to-strand distance 0.5 mm, layer-to-layer orientation 60° (Scaffold A) or 30° (Scaffold B). After plotting, scaffolds were incubated for 3 days in water-saturated atmosphere (humidity $> 95\%$, temperature 37.4°C) (Akkineni et al., 2015), followed by three intensive washing steps in acetone to remove residual oil of the CPC paste. The whole fabrication process was conducted under sterile conditions. Scaffolds were immersed in cell culture medium consisting of alpha-MEM (Gibco, Thermo Fisher Scientific GmbH, Germany) with 10% fetal calf serum (FCS), 100 Uml^{-1} penicillin and 100 mgml^{-1} streptomycin (Pen/Strep, all from Biochrom, Berlin, Germany) 24 h prior to subsequent cell seeding. The anatomical model was virtually segmented, modified and constructed with the softwares Dornheim segmenter (Dornheim Medical Images GmbH, Magdeburg, Germany), Geomagic Studio (RSI 3D-Systems, Oberursel, Germany) and Geomagic Freeform (RSI 3D-Systems, Oberursel, Germany). As sacrificial ink a 10% methylcellulose (mc, M0512, Sigma, United States, molecular weight ≈88000 Da, 4000 cP) paste was prepared in water as described before (Ahlfeld et al., 2018b). The sacrificial ink was plotted utilizing a 410 μm needle with a speed of 10 mm·s^{-1}; after post-processing, it was washed away in the fridge overnight.

Seeding of the Scaffolds With rMSC for *in vitro* and *in vivo* Experiments

rMSC were isolated from the bone marrow of adult Lewis rats as described previously (Korn et al., 2017). In brief, bone marrow was aspirated from the femur, centrifuged for 10 min at 1200 rpm and the pellet was resuspended in cell culture medium consisting of alpha-MEM with 10% fetal calf serum, Pen/Strep, 1% Amphotericin and 1 M HEPES buffer solution (all from Gibco, Thermo Fisher). The cell suspension was transferred into culture flasks; the medium was changed every 3–4 days and the cells were expanded until the second passage. For cell seeding, the immersed scaffolds were placed into 0.2 ml PP multiply-pro cups (Sarstedt; one scaffold per tube) and 280 μl cell suspension containing either 1×10^5 cells (for the *in vitro* experiments) or 2×10^5 cells (for the *in vivo* experiments) were added. The scaffold colonization was performed by a rotation method: during a period of 6 h, the tubes were rotated every 30 min one and a half turn while they were stored in the incubator at 37°C and 5% CO_2. Finally, the scaffolds were placed in 96-well plates which were filled with cell culture medium. For the *in vivo* experiments, the bone grafts stayed in the incubator at 37°C, 5% CO_2 and 95% humidity for 3 days until implantation. The scaffolds which were not colonized with cells were treated with the same procedure to ensure same conditions for the material prior to implantation.

In vitro Experiment

Seeded scaffolds were cultivated in cell culture medium at 37°C, 5% CO_2 and 95% humidity for 28 days; for half of the samples osteogenic supplements (10^{-7} M dexamethasone, 0.05 mM ascorbic acid 2-phosphate, 10 mM beta-glycerophosphate; all from Sigma-Aldrich) were added to the medium starting 1 day after seeding. For fluorescence microscopic analyses, cell-colonized scaffolds were fixed using 4% formaldehyde and actin cytoskeletons and cell nuclei were stained with AlexaFluor 488® phalloidin (Invitrogen) and DAPI (Sigma-Aldrich); imaging was performed with a Keyence BZ9000E. For biochemical analysis of LDH and ALP activity, the samples, frozen at different time points of cell culture, were thawed and incubated with lysis buffer (1% Triton X-100 in PBS) for 50 min on ice; cell lysis was supported by sonication for 10 min. LDH activity in the lysates was determined with the CytoTox 96 Non-radioactive Cytotoxicity Assay (Promega) according to the manufacturer's instruction and correlated with the cell number using a calibration line. Measurement of ALP activity was done as described previously (Lode et al., 2014). In brief, an aliquot of the lysate was incubated with 1 mg ml^{-1} *p*-nitrophenylphosphate (Sigma-Aldrich) in ALP substrate buffer (0.1 M diethanolamine, 1% Triton X-100, 1 mM $MgCl_2$, pH 9.8) at 37°C for 30 min. The enzymatic reaction was stopped by addition of 1 M NaOH and the *p*-nitrophenolate (pNp) formation was quantified by measurement of the absorbance at 405 nm. Using a *p*-nitrophenol calibration line, the amount of pNp produced by the cell lysate was calculated and related to the cell number in each sample (calculated from the LDH activity).

In vivo Application in a Rat Alveolar Cleft Model

The animal study was approved by the Commission for Animal Studies at the District Government Dresden, Germany (DD24-5131/354/26). For the study, 80 adult male Lewis rats (Janvier Labs, Le Genest-Saint-Isle, France) with an average body weight of 450 g and an age of 6 months at the beginning were used. All animals were housed according to the current regulations in a light- and temperature-controlled environment. They had access to water *ad libitum* and were fed with pellets (ssniff-Spezialdiäten GmbH, Soest, Germany). After statistical calculation of the required number of animals per group all rats were randomly divided into the 5 experimental groups (see **Table 1**). The rats were anesthetized by intraperitoneal injection of ketamine (100 mg/kg body weight) and xylazine (10 mg/kg body weight) and fixed in a dorsal position. An artificial alveolar cleft was created surgically in the anterior maxilla of each animal. First, a sagittal incision was made following the mid-palatal suture. After elevation of a mucosal flap and removal of the periosteum, a localized bone defect with 3.3 mm in diameter was created using a diamond-coated cylindrical shaped drill (DiT Dental-Instrumente GmbH, Oberlungwitz, Germany). According to the randomized distribution, each rat received one bone graft (**Table 1**). After insertion of the bone graft, the flap was repositioned and wound closure was performed using 5-0 Ethilon suture (Ethicon, Norderstedt, Germany). Postoperatively, the animals received amoxicillin trihydrate (Fort Dodge Veterinär GmbH, Würselen, Germany) 15 mg/kg body weight once and 4 mg/kg body weight carprofen (Rimadyl;Pfizer Deutschland GmbH) every 24 h for 4 days. All drugs were injected subcutaneously. The animals were fed with a soft diet for the first 3 days and, subsequently, received a regular diet. Postoperatively, the animals and their behavior were monitored and the body weight was measured every 2 weeks. For the *ex vivo* assessment of the dynamic bone formation, all rats received intraperitoneal injections of the fluorochrome dyes alizarine (20 mg/kg body weight) and calcein (30 mg/kg body weight) 7 and 3 days prior to sacrifice.

Evaluation Methods

After sacrifice, the cranium of each rat was dissected and fixed in 4% formaldehyde. MicroCT and preparation of the histological samples followed.

MicroCT

One 2D-microCT per rat was performed *ex vivo* using a VivaCT (SCANCO Medical AG, Brüttisellen, Switzerland) with the following adjustments: x-ray energy 70kVp and 114 mA, integration time 200 ms, voxel size 30 μm and conebeam continuous rotation. A 3D reconstruction of the defect area by Software Script (SCANCO) followed. The fitting accuracy of the scaffolds were characterized descriptively.

TABLE 1 | Experimental groups investigated *in vivo*.

Number of animals	Bone graft	Description	Healing time [weeks]
8	Scaffold A	60° layer rotation	6
8	Scaffold A		12
8	Scaffold A + rMSC		6
8	Scaffold A + rMSC		12
8	Scaffold B	30° layer rotation	6
8	Scaffold B		12
8	Scaffold B + rMSC		6
8	Scaffold B + rMSC		12
8	Control	Empty defect	6
8	Control		12

Histology

After dehydration in a graded series of ethanol, all samples were embedded in methylmethacrylate (Technovit 9100, HeraeusKulzer, Wehrheim, Germany) as described previously (Korn et al., 2014). Coronal sections were produced according to Donath's sawing and grinding technique (Donath and Breuner, 1982). Thus, the four central sections of each specimen could be achieved for evaluation. Subsequently, the sections measuring 60 μm in thickness were polished. After analysis of the fluorochrome marker uptake, Masson-Goldner trichrome staining followed.

Histological Analysis

All samples were imaged by fluorescence microscopy and, after staining, by light microscopy (Olympus BX 61, Olympus Deutschland GmbH, Hamburg, Germany) using cellˆF Imaging Software for Life Science (Olympus). Multiple image alignment was performed using an automatic scanning table (Märzhäuser, Wetzlar, Germany). Thus, 8 images per sample were scanned with a 10 × 10-fold magnification and manually fused to one image. Fluorochrome marker uptake was analyzed to assess the dynamics of bone formation at the defect margins. Focus were the direction and distribution of the bone formation marked by the red fluorescent alizarin and the green fluorescent calcein. Thereafter, all specimens were stained according to Masson-Goldner trichrome staining. A descriptive analysis evaluated the position of the scaffold, it's surface, the interactions between host bone and bone graft and the bone formation on the defect margins. Again, a 10 × 10-fold magnification was chosen. For quantification of the osseous healing the following parameter were measured: remaining defect width (Equation 1), bone formation in the defect area, and percentage of the new formed bone relating to the particular initial defect area (Equation 2). All measurements were realized by one examiner who was masked regarding to the experimental groups.

$$\textit{remaining defect width} = \frac{\textit{distance}_{\textit{defect margins cranial}} + \textit{distance}_{\textit{defect margins caudal}}}{2} \qquad (1)$$

$$\textit{newly formed bone} = \frac{\textit{new formed bone area}}{\textit{initial osseous defect area}} \times 100 \qquad (2)$$

Statistics

Results obtained *in vitro* were checked for statistical significance by one-way ANOVA coupled with Tukey's multiple comparison test utilizing GraphPad Prism version 8 software (GraphPad Software, La Jolla, CA, United States).

Statistical analysis of the *in vivo* results were performed with SPSS 25 software (IBM Germany, Ehningen, Germany) and mean as well standard deviations were calculated for all groups. The impact of scaffold and healing time were tested by a two-way-ANOVA. The interactions between healing time, scaffold and rMSC colonization could be studied by t-tests with Bonferroni-adjustment. For all analysis the level of significance was set at 95% ($p = 0.05$).

RESULTS

Tissue Engineered, Bioresorbable Bone Grafts for Artificial Cleft Palates in Lewis Rats

Tissue Engineering Concept

The tissue engineering concept investigated in this study is shown in **Figure 1**. Allogenic mesenchymal stromal cells (rMSC) were isolated from bone marrow of Lewis rats and expanded until passage 2. The transfer of allogenic cells causes no immunological problems, as Lewis rats are an inbreeding breed of genetically identical animals. Nevertheless, during the later clinical application, we favored the usage of autologous cells. Miniaturized, precisely fitting scaffolds consisting of CPC were plotted in 60° (scaffold A) and 30° (scaffold B) layer-to-layer orientation and post-processed by setting in water-saturated atmosphere (**Figures 1**, **2A,B**). After setting, the strand widths of the scaffolds A and B were determined as 199.8 ± 9 μm and 195.6 ± 9 μm, respectively. Next, scaffolds were colonized with the isolated rMSC according to the classical tissue engineering approach; actin/nuclei stainings of the scaffolds A and B seeded with rMSC are shown in **Figures 2A,B**. After a cultivation time of 3 days, scaffolds were implanted into the Lewis rats. To investigate the influence of rMSC on healing, cell-free samples were used as controls. All scaffold types, no matter on layer orientation or cell population, fitted precisely into the artificial alveolar cleft (**Figure 2C**).

In vitro Evaluation

Scaffolds of type A and B were seeded with 1×10^5 rMSC and cultivated over 28 days in cell culture medium with and without osteogenic supplements (OS), respectively. At various time points, cell distribution and density on the scaffolds were visualized by fluorescence microscopy after staining cell nuclei and actin cytoskeletons (**Figure 3A**); the number of cells grown on the scaffolds was determined by measurement of lactate dehydrogenase (LDH) activity and osteogenic differentiation was evaluated by measurement of alkaline phosphatase (ALP) activity (**Figure 3B**).

Both, the microscopic analysis and the analysis of LDH activity as a measure for the number of viable cells indicated a significant higher initial cell number (day 1) for scaffold A compared to scaffold B. However, in both cases, a uniform cell distribution on the scaffolds was achieved by the rotation seeding method (see Materials and Methods). The seeding efficiency was approx. 20% in case of scaffold B and nearly 45% in case of scaffold A. After day 1, the number of cells decreased first but increased after day 7 when cultured without osteogenic supplements (OS−); in the presence of osteogenic supplements (OS+), the decrease of cell number was even stronger, staying constant during further cultivation (**Figure 3B**). Nevertheless, microscopic analyses revealed a complete and uniform coverage of the CPC strands in all cases (**Figure 3A**). An increase of the ALP activity was detected for cells cultivated with osteogenic supplements (OS+), but not without (OS−), indicating their differentiation toward the osteoblastic lineage after stimulation; no significant effect of the pore geometry (scaffold A vs. B) has been observed (**Figure 3B**).

In vivo Evaluation

Design of the *in vivo* Study and Post-operative Evaluation

Table 1 lists all groups investigated in this study. Scaffolds of type A and B were implanted either with or w/o cells (seeding cell number 2×10^5). Healing times were either 6 or 12 weeks. An empty defect was chosen as control. The study was completed by 78 of 80 rats, which represents a survival rate of 97.5%. Two rats died 3 days after surgery due to unknown reason. They were replaced and finally in all groups 8 rats has been analyzed. Unfortunately, 2 bone defects of the group Scaffold B + rMSC after 6 weeks of healing time were prepared too flat, as visible in the histological sections, and hence were excluded from the evaluation 74 of 80 scaffolds did not show signs of ruptures due to mechanical load caused by chewing. Five of the six fractured scaffolds belong to the group B with the 30° strand rotation. Nevertheless the fractured fragments were not dislocated into the area outside of the defect. The rats' body weight at the end of the study was comparable to the initial weight and all rats

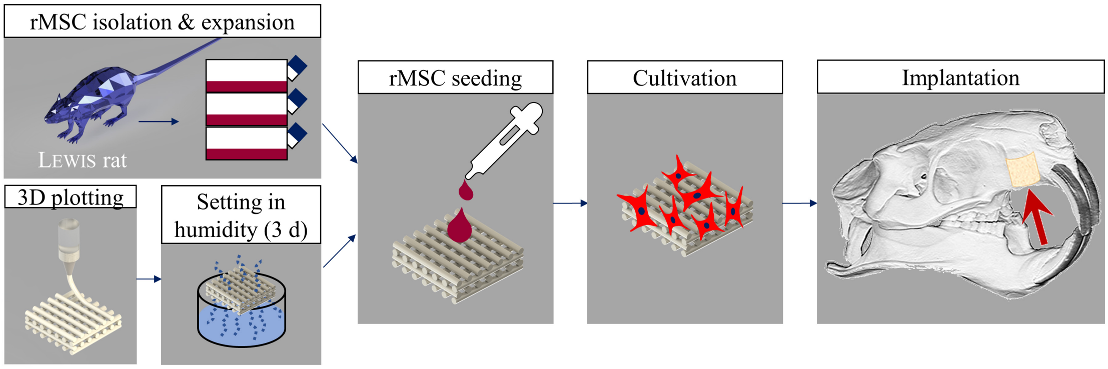

FIGURE 1 | Tissue engineering approach carried out in this study. Rat MSC were isolated from bone marrow of Lewis rats, expanded and seeded onto 3D plotted CPC scaffolds. After 3 days of cultivation, the tissue engineered bone grafts were implanted. Cell-free scaffolds were used as control.

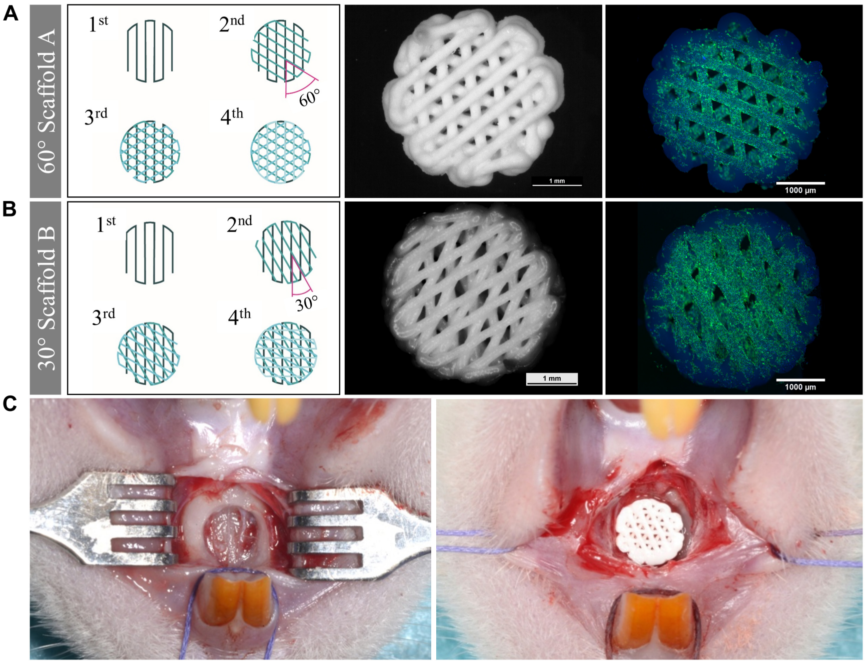

FIGURE 2 | Morphology of scaffolds of type A and B, cell colonization and implantation. **(A,B)** Scheme of the scaffolds, stereomicroscopical images of the scaffolds after plotting and fluorescence-microscopical images of the scaffolds seeded with rMSC (green: actin cytoskeletons, blue: nuclei, CPC exhibits blue autofluorescence). Scaffolds of type A were fabricated with 60° layer-to-layer orientation and scaffolds of type B with 30° layer-to-layer orientation. **(C)** Empty defect of the cleft (left) and filled defect with a precisely fitting scaffold (right).

showed an undisturbed behavior. No clinical wound healing complications were observed.

Microcomputed Tomography Analysis

In µCT images, lamellar and cancellous bone as well as the scaffolds were isodense. Nevertheless discrimination between bone and scaffold was possible due to morphological characteristics. Rarely a fusion of bone and scaffold margin was visible. The descriptive analysis of the scaffold position, being performed in axial and coronal sections, showed no differences between the groups (**Figure 4**). In some cases, the scaffold was inserted too far in cranial or caudal direction. Further an angular scaffold position occurred as well as six scaffolds (5x scaffold B, 1x scaffold A) were fractured at the measurement time point.

Histomorphology: Polyfluorochrome Labeling

For the *ex vivo* assessment of the dynamic bone formation, all rats received intraperitoneal injections of the fluorochrome dyes alizarine and calcein 7 and 3 days prior to sacrifice. All specimens exposed distinctive green fluorescent calcein labels at both time points, whereas the red alizarin dye was more pronounced after 6 compared to 12 weeks healing time. In general, two directions of bone formation occurred: starting from defect margin and from the nasal septum. The control group showed a homogenous ossification, which led to cone-like shaped areas of cancellous bone, beginning on the former defect margin (**Figures 5A,B**). After 12 weeks maturation into lamellar bone was observable. In cases of scaffold insertion, a green auto-fluorescence of the biomaterial, as well as bone formation toward the scaffold were visible. After 6 weeks, a bone-to-scaffold contact was detected in some cases of scaffold A (**Figures 5C,D**). In this situation, the labeling was interrupted in the area of contact. Scaffold A + rMSC exposed a comparably smaller fluorescence labeling, indicating a reduced rate of bone formation at the time point of marker application. The insertion of scaffold B also led to an osteogenesis starting at the defect margins. Compared to scaffold A the bone-to-scaffold-contact was rarely visible in scaffold B. Between 6 and 12 weeks, both groups of scaffold B (with and w/o rMSC) increased bone formation, but to a smaller extent compared to scaffold A. In cases of suboptimal scaffold position, e.g., angular position, the bone formation was more pronounced on the defect site, which was closer to the biomaterial. If the scaffold was inserted too far into a cranial position, the bone grew underneath.

Histomorphology: Masson-Goldner Trichrome Staining

All animals showed a healed defect site and no oronasal fistulae were detected. The discrimination between host bone, which was dense lamellar bone, and newly formed bone was easily detectable due to morphological characteristics. Irrespective of the experimental group, after 6 weeks cone-like shaped cancellous bone grew into direction of the defect center and also osteoid structures were detectable at the tip of the cone. With ongoing healing time, bone maturation occurred, resulting in a more or less pronounced osseous bridging of the defect. In the control group the defect was filled with soft tissue and no osseous

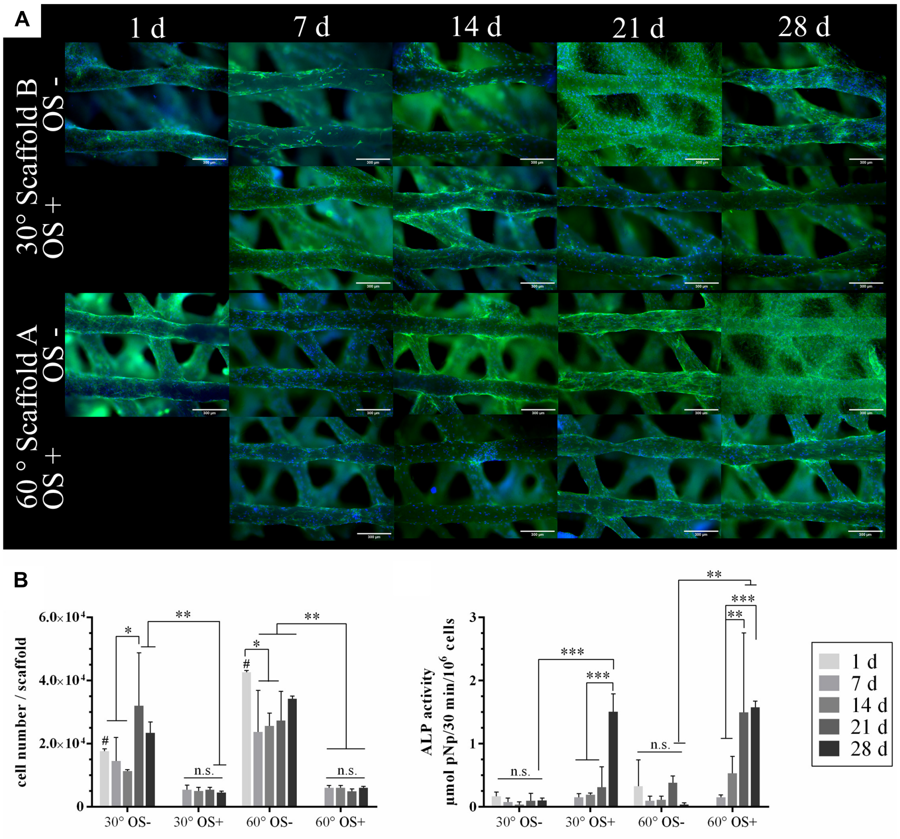

FIGURE 3 | Colonization of the plotted CPC scaffolds with rMSC and osteogenic differentiation *in vitro*. **(A)** Stainings of actin cytoskeletons (green) and nuclei (blue) of rMSC on the scaffold types A and B. CPC revealed a blue autofluorescence. Scale bars represent 300 µm. **(B)** Cell number analyzed by LDH activity and specific ALP activity of the rMSC cultured with (OS+) and w/o (OS–) osteogenic supplements ($n = 4$, mean ± SD, $^{*}p < 0.05$, $^{**}p < 0.01$, $^{***}p < 0.001$, # marks the difference between 30° and 60° with $p < 0.05$, n.s., no significance).

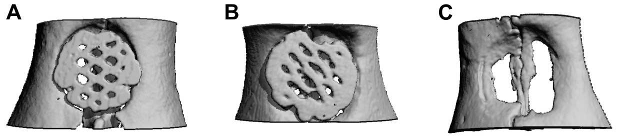

FIGURE 4 | Micro-CT after 12 weeks. Exemplary axial sections are shown for **(A)** Scaffold A, **(B)** Scaffold B, and **(C)** control group.

bridging took place. Groups with the scaffold types A and B primarily showed a fibrous integration of the defect, however, on the scaffold surface itself cancellous bone grew toward the defect center and the biomaterial acted as a guiding structure (**Figure 6A**). The shape of the newly formed bone was determined by the scaffold geometry. During the healing period, cancellous bone matured into lamellar bone (**Figure 6B**). In comparison to cell-free scaffolds of type A, rMSC-colonized scaffolds showed only negligible differences in bone formation. A bone-to-scaffold-contact occurred more frequently for the non-enriched scaffold compared to the scaffold + rMSC. Defects augmented with scaffold B exposed a smaller amount of newly formed bone compared to scaffold A, irrespective of rMSC colonization. In all groups, no resorption of the biomaterial was visible and no complete osseous healing of the defect was detected. Bone formation was especially impeded, in case scaffolds and their pores were covered by a thick layer of fibrous tissue.

Histomorphometry

Remaining defect width [mm]

The remaining defect width decreased in all experimental groups in comparison to the initial defect's width and with ongoing healing time. The reduction of the defect width from 6 to 12 weeks was statistically significant for control and scaffold A groups (**Figure 7A**). This parameter showed no statistically significant differences, comparing all experimental groups.

Bone formation in the defect area [mm^2]

Osseous defect healing was detectable in all groups, but the extent differed (**Figure 7B**). After 6 weeks, the highest values were measured for scaffold B + rMSC, followed by the control group, scaffold A + rMSC, scaffold A and scaffold B; however, these differences were not significant. After 12 weeks, the results changed as the control and scaffold A exposed the largest areas of bone formation – only for this two groups the increase from

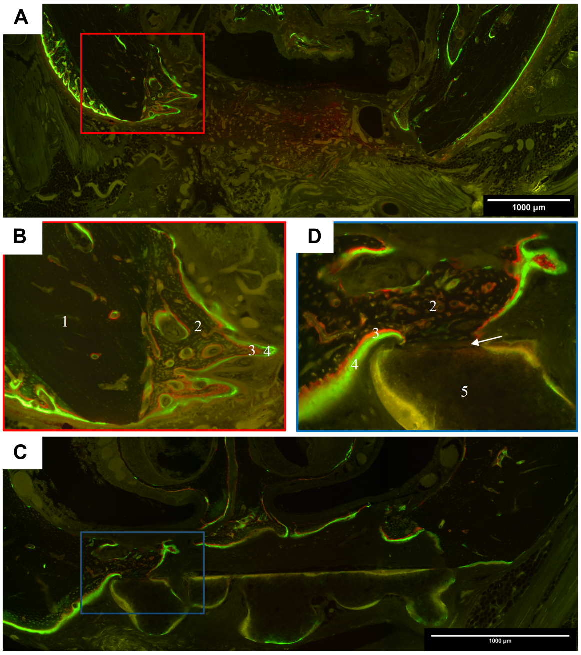

FIGURE 5 | Representative images of polyfluorchrome labeling with alizarin and calcein in coronal histological sections. **(A)** Control group after 6 weeks healing time; 10 × 10 magnification; cone-like shaped bone formation started from the former defect margins, which led to a partial ossification of the defect area, but no complete osseous healing. **(B)** Detail of the defect margin of image A, 20 × 10 magnification; green calcein labels were followed by red alizarin labels, showing that cancellous bone grew from the former defect margin toward the center. **(C)** Scaffold A group after 6 weeks healing time; 10 × 10 magnification; the scaffold is located in the defect center and cancellous bone grew on the cranial site of its surface. **(D)** Detail of the defect margin of image C, 20 × 10 magnification, newly formed bone with dense contact to the scaffold. In the contact zone, the labeling is interrupted. *(1 lamellar host bone, 2 new formed cancellous bone, 3 alizarin label, 4 calcein label, 5 scaffold, arrow represents the contact zone between scaffold and bone).*

6 to 12 weeks was statistically significant (control: $p = 0.002$; scaffold A $p = 0.001$). Comparing all groups among each other after 12 weeks, the following result was found: the control group showed significantly more bone formation compared to scaffold A + rMSC ($p = 0.028$), scaffold B ($p = 0.021$) and scaffold B + rMSC ($p = 0.031$); bone formation in the scaffold A group was in the same range as those in the control group. Also scaffold A led to more osseous healing within the defect area compared to scaffold A + rMSC after 12 weeks ($p = 0.048$); in case of scaffold B, no significant differences between the groups with and without rMSC were observed. These findings were supported by measurements of the closest distance between scaffold and ingrowing bone, which was decreasing with ongoing healing time (**Supplementary Figure S1** and **Supplementary Table S2**).

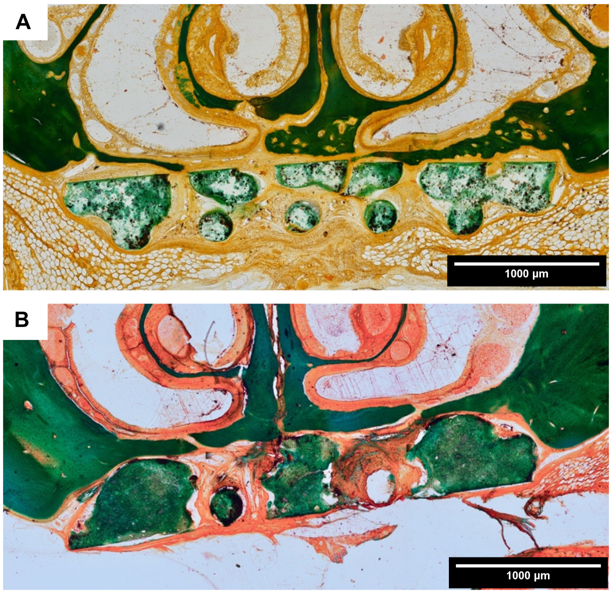

FIGURE 6 | Histomorphology: representative images of Masson-Goldner trichrome staining in coronal sections. **(A)** Scaffold A after 6 weeks healing time; **(B)** scaffold A after 12 weeks healing time (both 10 × 10 magnification). There is an ongoing bone formation detectable, whereby the scaffold acts as a guiding structure for the cancellous bone. The scaffold did not show signs of resorption at the end of the healing period.

Percentage of the newly formed bone related to the initial defect area [%]

If the area of bone formation was calculated against the particular initial defect area, the values were in accordance to the results of the bone area (**Figure 7C**). After 6 weeks, the control group exposed an osseous defect healing of 13.2% (mean) with a significant increase to 22.5% at the end of the study. Also scaffold A showed a significantly increasing bone formation from 8.2 to 19.0%. The other groups had a smaller percentage of bone formation and no significant differences occurred between 6 and 12 weeks within the groups (**Figure 7C**). After 12 weeks, the control group showed significantly higher values of bone formation compared to scaffold A + rMSC, scaffold B, and scaffold B + rMSC (all $p < 0.001$). Also 19.0% of scaffold A was significantly more than 10.2% of scaffold B ($p = 0.02$), 10.8 of scaffold A + rMSC ($p = 0.035$) or 8.75% of scaffold A + rMSC ($p = 0.002$).

Fabrication of Patient-Specific, CPC-Based Bone Grafts for Alveolar Cleft Osteoplasty: Proof of Concept

For the application in patients, the fabrication process has to be scaled up and the shape of the implant has to be tailored to the patient-individual cleft geometry. In a recent study, we showed that multichannel 3D plotting of CPC and a methylcellulose sacrificial ink enables the fabrication of complex shaped constructs exhibiting anatomical relevant features including convex and concave curvature at surfaces (Ahlfeld et al., 2018b). Herein, we successfully transferred that principle to the full additive manufacturing process chain from clinical three-dimensional imaging to the fabrication of a perfectly fitting patient-specific implant (**Figure 8**). In the

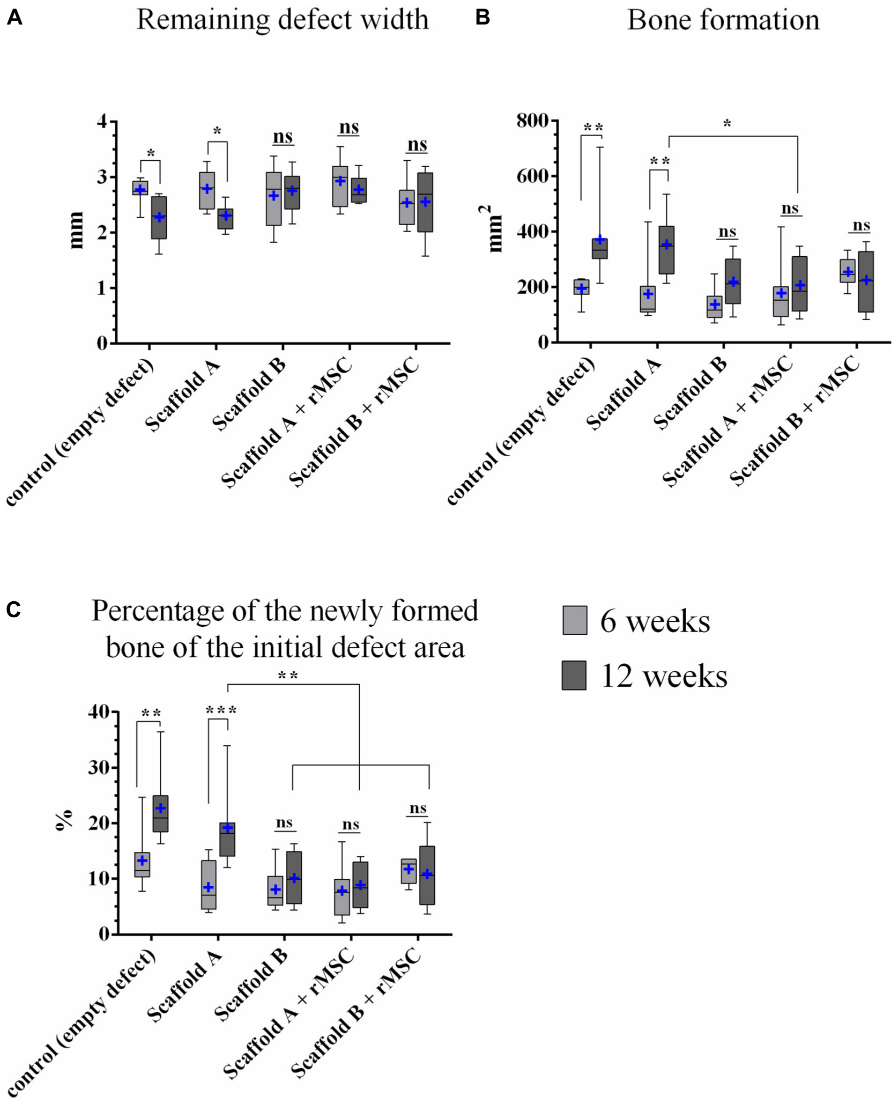

FIGURE 7 | Histomorphometric analysis. **(A)** Remaining defect width, **(B)** bone formation, and **(C)** percentage of the newly formed bone related to the initial defect area ($n = 8$; median and minimum/maximum values; mean is marked by +; $^*p < 0.05$, $^{**}p < 0.01$, $^{***}p < 0.001$). All mean values and standard deviations are shown in **Supplementary Table S1**.

first step, anonymized CT data of patients with an alveolar cleft were reconstructed using the software Dornheim segmenter achieving a 3D rendered model of the damaged maxilla of the patient (**Figure 8A**). The 3D model was then further processed (i.e., closing holes or smoothing of the polygonal mesh) with the software tool Geomagic Studio. Finally, the exact defect area was identified in order to enable the design of a patient-specific implant. In this case, the modeling of the patient specific shaped implant was performed utilizing Geomagic Freeform. This software offers the possibility of haptic interaction. This enabled us to fit the implant model into the given geometry of the upper jaw in the best possible way (**Figure 8A**). The implant was designed according to the internal and external geometry of the contralateral orofacial anatomy represented by the CT data. The dimension of the outer barrier was chosen to entirely cover the defect's side edge-to-edge with the surrounding jaw bone.

The support structure, being required for the production of real three-dimensional shapes with overhanging structures, was designed as a negative form of the partially convex shape of the implant. The resulting *3mf* file, capable to distinguish the two materials (methylcellulose as sacrificial ink and CPC as biomaterial ink for the implant) was transferred to the multichannel plotter software being used for the production of the *in vivo* scaffolds. Both inks could be fabricated in layer-wise structure achieving the desired geometry. The angle between deposited layers was chosen at 60° according to the obtained results for ideal tissue integration.

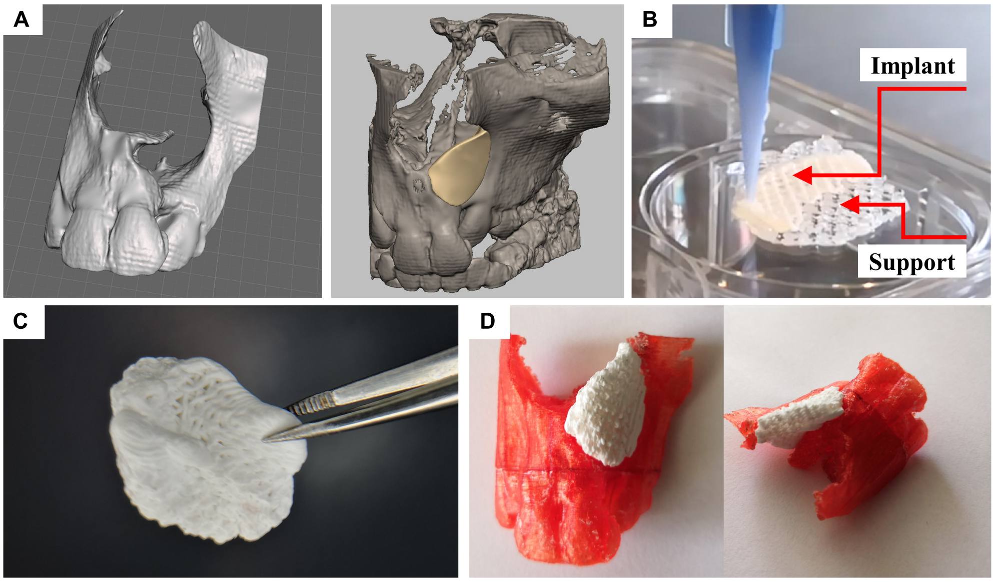

FIGURE 8 | Design and fabrication process of a patient-specific implant consisting of a calcium phosphate cement. **(A)** Three-dimensional reconstruction of a CT scan of a patient and designed model of a perfectly fitting implant. **(B)** Fabrication process by multichannel 3D plotting of a sacrificial ink and the CPC. **(C)** Photograph of the implant, after the sacrificial ink was washed away. **(D)** The hardened implant fits perfectly into the defect of the patient. Red: Plastic model of the maxilla with incisors, white: 3D plotted CPC implant.

After hardening of the CPC, the methylcellulose could easily be dissolved without affecting the implants' integrity and geometry (**Figures 8B,C**). During the mild post-processing of the CPC (setting in water-saturated atmosphere), no swelling or shrinking of the plotted scaffolds occurred. This allowed perfect fitting of the CPC implant into the defect site, as demonstrated in a partial thermoplastic model of the maxilla, fabricated based on the reconstructed CT data by fused filament fabrication (**Figure 8D**).

DISCUSSION

3D Plotting – Impact of Geometry

The study hypothesis was, that "The application of a 3D plotted bone graft into an artificial maxillary bone defect leads to a significant reduction of the defect width after 12 weeks." This could be confirmed for the scaffold A group. Crucially, in this experimental group, a significant ongoing bone formation was measurable, which led to a reduction of the defect width (significant between 6 and 12 weeks healing time), confirming that 3D plotting of bone grafts is a promising approach for application in maxillofacial surgery and especially for the treatment of alveolar clefts. To evaluate the defect model itself, an empty defect was compared and significant bone formation was also shown. However, it must be stressed, that only the scaffold groups have clinical relevance for the application in patients, because clinically there is a strong recommendation for defect augmentation. Alveolar cleft osteoplasty is performed to build up a sufficient bone volume into the former cleft area, which is filled by fibrous tissue and doesn't enable an eruption of e.g., the permanent canine. Besides the positive effect on the tooth eruption the surgery closes oronasal fistulas, which can lead to oronasal fluid reflux during drinking or eating. If the alveolar osteoplasty is not performed a disadvantage in maxillary growing occurs and the deficiency in transversal and anterior-posterior jaw development causes facial asymmetries and interferences in dental occlusion. After 12 weeks, scaffold A led to a significant higher percentage of bone tissue within the defect area compared to scaffold B. The hypothesis has to be rebutted for the experimental group of scaffold B, as the bone formation and reduction of the defect width did not reach statistical significance after 12 weeks. Thus, it can be concluded, that the pore geometry of an applied bone graft has a considerable impact on the treatment of artificial alveolar clefts.

Extrusion-based additive manufacturing techniques (3D plotting and fused deposition modeling) allow high control over the internal pore geometry of scaffolds which was demonstrated to influence both, mechanical and biological properties (Hutmacher et al., 2001; Obregon et al., 2015; Kelly et al., 2018). For example, pore gradients in an osteochondral tissue model consisting of printed poly-ε-caprolactone scaffolds showed enhanced osteogenic differentiation of hMSC and expression of bone markers for a 15° layer orientation compared to 90° layer orientation, but enhanced chondrogenic differentiation of hMSC in the reverse case (Luca et al., 2016). In addition, Ostrowska et al. (2016) investigated the differentiation of hMSC on printed PCL scaffolds *in vitro* and observed differences in the ALP expression depending on the layer orientation. Confirming our findings, also in this study the layer orientations of 30° and 60° did not influence the ALP activity significantly (Ostrowska et al., 2016). Almeida et al. (2014) compared 3D printed chitosan scaffolds with 90° and 45° layer orientation, and thus different pore geometries, and evidenced an influence of these pores on the immune response by measuring different levels of TNF-α and Interleukin 12/23 expression. Likewise, ceramic scaffolds can be produced by extrusion printing and pore geometry was demonstrated to play a crucial role on both, mechanics and bone formation *in vivo* (Roohani-Esfahani et al., 2016; Entezari et al., 2019). For plotted CPC constructs, scaffolds with 90° (Moussa et al., 2015; Barba et al., 2017; Baranowski et al., 2018; Reitmaier et al., 2018) and 60° (Ahlfeld et al., 2019) lay-down patterns were investigated *in vivo* and bone formation could be evidenced in every study. However, to the best knowledge of the authors, a comparative study with CPC scaffolds was not performed so far and the influence of pore geometry is still not answered satisfactorily.

In our approach, the layer orientation of 60° was superior compared to the layer orientation of 30°. Crucially, the layer orientation did not just influence the inner pore structure, but also the pores at the outer periphery of the CPC scaffolds (caused by the meanders between the strands, see **Figure 2**) which are in direct contact with the host bone. These outer pores are crucial for ingrowing bone, which utilizes the scaffold's surface as guiding structure, and therefore, their size and shape might influence this process.

Another aspect of geometry has to be considered for comprehension of the *in vivo* results: the contact between scaffold and osseous defect margin was found to depend on the scaffold orientation. During surgery, it was easy to place the scaffolds A or B in the bone defect and clinically the fitting was acceptable in both groups; no unwanted movement of the scaffold or gaps occurred. Retrospectively we observed a relevance of the placement of the bone grafts with the "right site" into the defect: the scaffolds exhibited a smooth, flattened site due to a layer deformation which occurred in the first layer due to the contact with the plotting stage. In layer 2–4, the CPC strands stayed in round shape and the upper site of the scaffold displayed convex and concave surfaces. As it did not clinically matter which site was turned into nasal or oral direction, the position of the scaffold was randomly chosen. However, analysis of the micro-CT and histological images revealed that the fitting was better, showing a minimal distance between bone and scaffold, if the smooth (bottom) site was placed into oral direction. In this case, the scaffold represented a guiding structure for newly formed bone and the closure of a critical size defect became probable. Thus, both, inner and outer geometry of the 3D plotted bone scaffolds played a crucial role on the osseous healing.

Compared to our previous studies conducted in the same defect model (Korn et al., 2014, 2017), the 3D plotted CPC scaffolds were superior to granular materials with respect to fitting into the defect. In both studies, the initial clinical fitting of the bone grafts, hydroxyapatite-beta-tricalcium phosphate with a granular structure (BONIT matrix®) (Korn et al., 2014) and hydroxyapatite granules embedded in a fast resorbing collagen matrix (BioOss® Collagen) (Korn et al., 2017), were good and there was clinically no distance between defect margin and scaffold. However, in case of BioOss® Collagen, the initial compact structure of the biomaterial was dispersed into smaller granula and in both studies, fibrous encapsulation of the particles was observed, probably because of their instable position within the defect; accordingly, no osseous integration or complete defect ossification occurred. If the granulae were located adjacent to the host bone osseous integration took place leading to the conclusion, that a more stable, defined structure of the scaffold is required for further studies. Therefore, plotted CPC scaffolds were chosen and it can be concluded from the current results that after 12 weeks the scaffold position was more predictable compared to the previously tested materials. Although the problem of dislocation did not occur anymore, there is still improvement required: a partial degradation of the scaffold is necessary as the newly formed bone should replace the bone graft after a defined period of time leading to a complete defect ossification.

One essential aspect of future research on geometrical issues could be the realization of anisotropic artificial scaffold structures as they appear in native bone. Today, this can be achieved via variation of the strand-to-strand distance and porosity. Our future aim will be the generation of density gradients in spatial definition within the fabrication process without the need of changing the total number of strands by implementing alternative printing path patterns, which replace the usual printing paths of straight lines between two points.

Tissue Engineering – Impact of Cell Pre-colonization

Considering the great potential of the tissue engineering approach (as alternative to autologous bone graft), we investigated whether a pre-colonization of the plotted CPC scaffolds with rMSC enhances bone formation. Compared to our previous studies, which were conducted with the same defect model using commercially available and clinically established materials, the findings presented in the present study showed distinctly different insights into scaffold-bone interactions (Korn et al., 2014, 2017). In the first study, resorbable bone grafts consisting of a synthetic nanocrystalline hydroxyapatite-beta-tricalcium phosphate mixture (BONIT matrix®), which had a granular structure, were colonized with undifferentiated as well as osteogenically differentiated rMSC prior to implantation. The smallest defect, and therefore strongest new bone formation, was observed in the group using bone grafts with undifferentiated rMSC (remaining defect width after 6 weeks: 2.39 mm ± 0.23 mm). Compared to the non-enriched scaffolds, which exposed a remaining defect width of 2.70 mm after 6 weeks, the pre-colonized scaffold was superior, but this was not statistically significant (Korn et al., 2014). Also in combination with a bovine hydroxyapatite granule-collagen graft (BioOss® Collagen), the undifferentiated rMSC were more effective compared to the colonization with osteogenic differentiated rMSC. Nevertheless, the non-enriched scaffold without rMSC pre-colonization finally exposed the significantly smallest remaining defect width after 12 weeks (Korn et al., 2017). Based on the previous results, only undifferentiated rMSC were chosen for this experimental study. It was surprising, that in the current study both, cells on scaffold A or B, did not show this positive effect. Considering these diverse and partly contradictory results of preclinical studies, the impact of rMSC onto the healing in the alveolar cleft remains unclear. Also in a clinical trial with 20 patients, Hermund et al. (2012) observed no significant difference of bone formation in the maxilla between bone scaffolds with or without cells. Ricci et al. (2012) demonstrated that in cases of vital bone adjacent to the defect, it may not require a cell-seeded scaffold for complete defect ossification. They accentuated the inherent problems with cell-seeding strategies and recommended in case of bone repair osteoconductive materials like CPC or ceramics in shape of highly organized 3D scaffolds, that guide the newly formed bone across the bone defect also without additional cell colonization (Ricci et al., 2012). In contrast, cell-seeded bone grafts were shown to induce better bone formation than cell-free equivalents in other studies (Eniwumide et al., 2007; Korn et al., 2014). Although our *in vitro* characterization clearly demonstrated that rMSC were able to proliferate and differentiate, no significantly increased bone formation was observed *in vivo*. In the light of these observations and the fact that especially after seeding of scaffolds with clinically relevant dimensions the cells often suffer from an insufficient supply after implantation due to the lack of vascularization (Jaklenec et al., 2012), the classical tissue engineering approach is questionable. A promising alternative for further studies might be the concept of *in situ* tissue engineering which envisages the recruitment of host stem and progenitor cells to the defect site by chemoattractive factors released from the scaffold (Ko et al., 2013).

3D Plotted CPC Scaffolds as Potential Material for Alveolar Cleft Osteoplasty

Classical fabrication methods of bone grafts are limited in their clinical application with respect to patient-individual treatment, however, additive manufacturing seems to be a promising technique to produce implants for alveolar defects. In contrast to other bone defects, it is mandatory to use biodegradable materials for the treatment of alveolar clefts, as the patients are children in growth and non-degradable materials would possibly influence local growth. This might be the reason, why, up to now, only a few materials were tested for the treatment of such defects and most studies concentrate on secondary bone grafting (Seifeldin, 2016). These materials include hydroxyapatite granules (Korn et al., 2014, 2017), bio-ceramics coated with bovine collagen and dipyridamole (Lopez et al., 2018), tricalcium phosphates (TCP) (Janssen et al., 2014; Berger et al., 2015), demineralized bone matrix (Francis et al., 2013), thermoplastic poly-ε-caprolactone (PCL) (Ahn et al., 2018; Puwanun et al., 2018) or a β-TCP/PCL composite (Raúl et al., 2019). In a recent review, Martín-del-Campo et al. (2019) suggested several biomaterial-based strategies which have high potential for cleft repair. Herein, we introduced a self-setting CPC for the three-dimensional fabrication of cleft alveolar osteoplasties offering several advantages. CPC can be plotted into complex shaped scaffolds revealing high shape fidelity and accuracy and plotted structures do not change dimensions while post-processing (Lode et al., 2014; Ahlfeld et al., 2018b). Plotted CPC scaffolds are highly biocompatible (Lode et al., 2014; Raymond et al., 2018; Ahlfeld et al., 2019) and can be biofunctionalized to enhance their biological performance, for example by growth factor loading (Akkineni et al., 2015; Ahlfeld et al., 2017, 2019; Baranowski et al., 2018) or even by integration of CPC into bioprinting with spatially defined cells (Ahlfeld et al., 2018a). For this first approach, we utilized pure CPC, which is clinically approved and answers general questions of this approach. CPC plotting can be miniaturized achieving filigree structures (Ahlfeld et al., 2017) as used in the scaffolds of this study. Furthermore, we could show in this work, that CPC scaffolds can be fabricated in clinically relevant geometries to fill real alveolar defects. As the CPC formulation transforms into nanocrystalline, bioresorbable hydroxyapatite (Heinemann et al., 2013), the scaffolds can be resorbed by osteoclasts (Bernhardt et al., 2014) and are integrated into the natural bone remodeling process [lasting about 200 days until 2 years in the human body (Eriksen, 2010)], which we consider as advantageous for the healing process. However, our investigations did not confirm visible resorptions of the scaffolds, which is related to the general slow degradation of HA forming cements (Thormann et al., 2013). This might be overcome by composites consisting of CPC and fast degrading biomaterials such as mesoporous bioactive glass, which were shown to enhance the degradation of such constructs distinctly and even to promote osteogenesis (Schumacher et al., 2017; Richter et al., 2019) or by a novel oil-based calcium doped magnesium phosphate cement which demonstrated enhanced degradation (Ewald et al., 2019).

First clinical studies evaluated the effects of printed bone grafts on osseous healing in alveolar cleft patients. Ahn et al. (2018) fabricated cleft osteoplasties consisting of PCL by fused filament fabrication. In an initial case study with a 10-years-old patient, the scaffold promoted bone formation; after 6 months 45% of the defect was filled by ingrowing bone (Ahn et al., 2018). A similar approach utilizing a PCL-β-tricalcium phosphate composite evidenced the potential of bioresorbable bone grafts for cleft palates (Raúl et al., 2019). In the light of these results, the approach investigated in this study utilizing 3D plotted CPC scaffolds demonstrates very high potential for further research and clinical application (approximately 20% bone formation after 3 months). Nevertheless, more studies are needed to ascertain the long-term clinical results of alveolar cleft reconstruction using tissue engineered and additively manufactured bone grafts (Wu et al., 2018).

Limitations of the Study

The complexity of a congenital human alveolar cleft or palate cannot be fully displayed by any pre-clinical model. Therefore, experimental studies are limited to artificial bone defects in different models. An established small animal model is the rat. This is due to the fact that a cleft-like defect can be prepared surgically in its maxillary bone (Mehrara et al., 2000; Mostafa et al., 2014). If cells should be transferred inter-individually, the selection of an inbreeding breed, like Lewis rats, avoid immunological problems. Advantage of the chosen animal model, is the possibility to insert bone grafts intraorally. However, physiological interactions with the oral microorganism as well as chewing forces can occur. One disadvantage of the oral defect in a small animal model is the inability of a complete wound rest. For this reason, rats were fed a soft diet to reduce micromovements. In a clinical setting, patients can be nourished by a nasal gastral tube to enable a proper initial wound rest. A limitation of this study may be the fact, that the results after 6 and 12 weeks are not gained for the same animal by e.g., intravital micro-CT imaging. The reason was, that the imaging properties of CPC did not enable an accurate quantification of the bone formation and therefore *ex vivo* histology was essential to evaluate the defect healing. Also the number of specimens per defect was limited due to the sawing- and grinding method, but average 3.2 samples are acceptable to quantify bone formation *in vivo* (Bernhardt et al., 2012). After identifying a promising bone graft in a small animal model the evaluation in a larger model would be necessary. Suitable models are dogs (Zhang et al., 2011), primate (Boyne, 2001), and pigs (Caballero et al., 2015). From a clinical point of view, the tissue engineered bone grafts should be compared with autologous bone graft and not only with an empty control defect. This however is only feasible in large animal models (Pourebrahim et al., 2013). Assuming application of autologous bone grafts in the rat model, e.g., from the femur, the fixation into the defect would be challenging. Reasons are the low height of the defect (less than 0.5 mm) and the open connection into the nasal cavity, which would lead to an initial dislocation of the bone granules.

CONCLUSION

3D plotting of CPC is suitable for the fabrication of scaffolds, which are fitting exactly in an artificial alveolar defect. We could show that the fabrication of such scaffolds can also be translated toward clinical indications and real defect geometries of patients. The pore geometry influences bone formation significantly; a 60° strand rotation leading to triangular-shaped pores performed significantly better than a 30° strand rotation. In this study, an additional colonization with undifferentiated rMSC did not result in an increased bone formation. Furthermore, no signs of scaffold degradation occurred, pointing out the necessity of further material development like modification of the cement matrix with porogens or adapting the composition toward more soluble phases. The creation of a sufficient 3D printed and tissue-engineered bone graft for alveolar cleft osteoplasty could preserve patients from donor site morbidity. Further studies will focus on improving the degradation properties of the 3D plotted bone grafts by using CPC modifications as well as on the stable fixation in the defect area which might increase the local bone formation. With regard to clinical application, the behavior of a new bone graft should also be tested in alveolar defects of large animal models.

DATA AVAILABILITY STATEMENT

The datasets generated for this study are available on request to the corresponding author.

ETHICS STATEMENT

The animal study was reviewed and approved by Commission for Animal Studies at the District Government Dresden, Germany (DD24-5131/354/26).

AUTHOR CONTRIBUTIONS

PK: study design, surgery, histology, evaluation micro-CT, and manuscript editing. TA: design and preparation of the 3D printed scaffolds, *in vitro* evaluation, and manuscript editing. FL: histomorphology and histomorphometry, evaluation of micro-CT images, statistics, and manuscript editing. DK: design and preparation of the patient specific implant, and manuscript editing. PS: design and preparation of the patient specific implant. RS: design of the patient specific implant. WP: surgery and manuscript editing. AF: surgery. MR: planning and realization micro-CT evaluation. UR: statistics. BS: study design and manuscript editing. AL: study design, *in vitro* evaluation, and manuscript editing. GL: study design. MG: study design and manuscript editing.

FUNDING

The study was financially supported by an internal research grant "MeDDriveStart" of the Faculty of Medicine "Carl Gustav Carus," Technische Universität Dresden (Germany) and by the European Social Fund (ESF) and the Free State of Saxony (young researchers group "IndivImp"). We acknowledge support from the German Research Foundation (DFG) and the Open Access Publication Fund of Charité – Universitätsmedizin Berlin.

ACKNOWLEDGMENTS

We thank Diana Jünger and Anna-Maria Placht for excellent technical assistance, Dr. Roland Jung and the team at the Experimental Centre of the Faculty of Medicine "Carl Gustav Carus", Technische Universität Dresden for the care of the animals and for assistance with the animal experiments and the microscopy facility CFCI of the Technische Universität Dresden for providing equipment and support in cell imaging. We also thank Dr. Cindy Elschner for providing the rat skull scheme of **Figure 2**.

SUPPLEMENTARY MATERIAL

The Supplementary Material for this article can be found online at: https://www.frontiersin.org/articles/10.3389/fbioe.2020.00217/full#supplementary-material

FIGURE S1 | Histomorphometric analysis. Closest distance between scaffold and defect margin. **(A)** Initial distance at time point of implant placement. **(B)** Final distance at the end of the study after 6 or 12 weeks (median and minimum/maximum values, mean is marked by +, $^{*}p < 0.05$, $^{**}p < 0.01$).

TABLE S1 | Measurements in the histomorphological images (mean ± standard deviation) for the remaining defect width, bone formation and percentage of the newly formed bone related to the initial defect area after 6 and 12 weeks.

TABLE S2 | Measurements in the histomorphological images (mean ± standard deviation) for the initial and final distance between bony defect margin and scaffold margin after 6 and 12 weeks.

REFERENCES

Ahlfeld, T., Akkineni, A. R., Förster, Y., Köhler, T., Knaack, S., Gelinsky, M., et al. (2017). Design and fabrication of complex scaffolds for bone defect healing: combined 3D plotting of a calcium phosphate cement and a growth factor-loaded hydrogel. *Ann. Biomed. Eng.* 45, 224–236. doi: 10.1007/s10439-016-1685-4

Ahlfeld, T., Doberenz, F., Kilian, D., Vater, C., Korn, P., Lauer, G., et al. (2018a). Bioprinting of mineralized constructs utilizing multichannel plotting of a self-setting calcium phosphate cement and a cell-laden bioink. *Biofabrication* 10:045002. doi: 10.1088/1758-5090/aad36d

Ahlfeld, T., Köhler, T., Czichy, C., Lode, A., and Gelinsky, M. (2018b). A methylcellulose hydrogel as support for 3D plotting of complex shaped calcium phosphate scaffolds. *Gels* 4:68. doi: 10.3390/gels4030068

Ahlfeld, T., Schuster, F. P., Förster, Y., Quade, M., Akkineni, A. R., Rentsch, C., et al. (2019). 3D plotted biphasic bone scaffolds for growth factor delivery: biological characterization in vitro and in vivo. *Adv. Healthc. Mater.* 8:1801512. doi: 10.1002/adhm.201801512

Ahn, G., Lee, J.-S., Yun, W.-S., Shim, J.-H., and Lee, U.-L. (2018). Cleft alveolus reconstruction using a three-dimensional printed bioresorbable scaffold with human bone marrow cells. *J. Craniofac. Surg.* 29, 1880–1883. doi: 10.1097/SCS.0000000000004747

Akkineni, A. R., Luo, Y., Schumacher, M., Nies, B., Lode, A., and Gelinsky, M. (2015). 3D plotting of growth factor loaded calcium phosphate cement scaffolds. *Acta Biomater.* 27, 264–274. doi: 10.1016/j.actbio.2015.08.036

Almeida, C. R., Serra, T., Oliveira, M. I., Planell, J. A., Barbosa, M. A., and Navarro, M. (2014). Impact of 3-D printed PLA- and chitosan-based scaffolds on human monocyte/macrophage responses: unraveling the effect of 3-D structures on inflammation. *Acta Biomater.* 10, 613–622. doi: 10.1016/j.actbio.2013.10.035

Baranowski, A., Klein, A., Ritz, U., Götz, H., Mattyasovszky, S. G., Rommens, P. M., et al. (2018). Evaluation of bone sialoprotein coating of three-dimensional printed calcium phosphate scaffolds in a calvarial defect model in mice. *Materials* 11:2336. doi: 10.3390/ma11112336

Barba, A., Diez-Escudero, A., Maazouz, Y., Rappe, K., Espanol, M., Montufar, E. B., et al. (2017). Osteoinduction by foamed and 3D-printed calcium phosphate scaffolds: effect of nanostructure and pore architecture. *ACS Appl. Mater. Interfaces* 9, 41722–41736. doi: 10.1021/acsami.7b14175

Berger, M., Probst, F., Schwartz, C., Cornelsen, M., Seitz, H., Ehrenfeld, M., et al. (2015). A concept for scaffold-based tissue engineering in alveolar cleft osteoplasty. *J. Craniomaxillofac. Surg.* 43, 830–836. doi: 10.1016/j.jcms.2015.04.023

Bernhardt, A., Schumacher, M., and Gelinsky, M. (2014). Formation of osteoclasts on calcium phosphate bone cements and polystyrene depends on monocyte isolation conditions. *Tissue Eng. C. Met.* 21, 160–170. doi: 10.1089/ten.tec.2014.0187

Bernhardt, R., Kuhlisch, E., Schulz, M. C., Eckelt, U., and Stadlinger, B. (2012). Comparison of bone-implant contact and bone-implant volume between. *Eur. Cell Mater.* 23, 237–247. discussion 247–248,

Boehm, K. S., Al-Taha, M., Morzycki, A., Samargandi, O. A., Al-Youha, S., and LeBlanc, M. R. (2018). Donor site morbidities of iliac crest bone graft in craniofacial surgery: a systematic review. *Ann. Plast. Surg.* 83, 352–358. doi: 10.1097/SAP.0000000000001682

Boyne, P. J. (2001). Application of bone morphogenetic proteins in the treatment of clinical oral and maxillofacial osseous defects. *J. Bone Joint Surg. Am.* 83-A (Suppl. 1) (Pt 2), 146–150.

Caballero, M., Morse, J. C., Halevi, A. E., Emodi, O., Pharaon, M. R., Wood, J. S., et al. (2015). Juvenile swine surgical alveolar cleft model to test novel autologous stem cell therapies. *Tissue Eng. Part C Methods* 21, 898—-908. doi: 10.1089/ten.TEC.2014.0646

Dixon, M. J., Marazita, M. L., Beaty, T. H., and Murray, J. C. (2011). Cleft lip and palate: understanding genetic and environmental influences. *Nat. Rev. Genet.* 12, 167–178. doi: 10.1038/nrg2933

Donath, K., and Breuner, G. (1982). A method for the study of undecalcified bones and teeth with attached soft tissues. The Sage-Schliff (sawing and grinding) technique. *J. Oral Pathol.* 11, 318–326. doi: 10.1111/j.1600-0714.1982.tb00172.x

Eniwumide, J. O., Yuan, H., Cartmell, S. H., Meijer, G. J., and de Bruijn, J. D. (2007). Ectopic bone formation in bone marrow stem cell seeded calcium phosphate scaffolds as compared to autograft and (cell seeded) allograft. *Eur. Cell Mater.* 14, 30–38. doi: 10.22203/eCM.v014a03

Entezari, A., Roohani, I., Li, G., Dunstan, C. R., Rognon, P., Li, Q., et al. (2019). Architectural design of 3D printed scaffolds controls the volume and functionality of newly formed bone. *Adv. Healthc. Mater.* 8:1801353. doi: 10.1002/adhm.201801353

Eriksen, E. F. (2010). Cellular mechanisms of bone remodeling. *Rev. Endocr. Metab. Disord.* 11, 219–227. doi: 10.1007/s11154-010-9153-1

Ewald, A., Kreczy, D., Brückner, T., Gbureck, U., Bengel, M., Hoess, A., et al. (2019). Development and bone regeneration capacity of premixed magnesium phosphate cement pastes. *Materials* 12:2119. doi: 10.3390/ma12132119

Fedorovich, N. E., De Wijn, J. R., Verbout, A. J., Alblas, J., and Dhert, W. J. A. (2008). Three-dimensional fiber deposition of cell-laden, viable, patterned constructs for bone tissue printing. *Tissue Eng. Part A* 14, 127–133. doi: 10.1089/ten.a.2007.0158

Feinberg, S. E., Weisbrode, S. E., and Heintschel, G. (1989). Radiographic and histological analysis of tooth eruption through calcium phosphate ceramics in the cat. *Arch. Oral Biol.* 34, 975–984. doi: 10.1016/0003-9969(89)90055-1

Francis, C., Mobin, S. S., Lypka, M., Rommer, E., Yen, S., Urata, M., et al. (2013). rhBMP-2 with a demineralized bone matrix scaffold versus autologous iliac crest bone graft for alveolar cleft reconstruction. *Plast. Reconstr. Surg.* 131, 1107–1115. doi: 10.1097/PRS.0b013e3182865dfb

Guo, J., Li, C., Zhang, Q., Wu, G., Deacon, S. A., Chen, J., et al. (2011). Secondary bone grafting for alveolar cleft in children with cleft lip or cleft lip and palate. *Cochrane Database Syst. Rev.* 6:CD008050. doi: 10.1002/14651858.CD008050.pub2

Heinemann, S., Rössler, S., Lemm, M., Ruhnow, M., and Nies, B. (2013). Properties of injectable ready-to-use calcium phosphate cement based on water-immiscible liquid. *Acta Biomater.* 9, 6199–6207. doi: 10.1016/j.actbio.2012.12.017

Hermund, N. U., Stavropoulos, A., Donatsky, O., Nielsen, H., Clausen, C., Reibel, J., et al. (2012). Reimplantation of cultivated human bone cells from the posterior maxilla for sinus floor augmentation. Histological results from a randomized controlled clinical trial. *Clin. Oral Implants Res.* 23, 1031–1037. doi: 10.1111/j.1600-0501.2011.02251.x

Hutmacher, D. W., Schantz, J. T., Lam, C. X. F., Tan, K. C., and Lim, T. C. (2007). State of the art and future directions of scaffold-based bone engineering from a biomaterials perspective. *J. Tissue Eng. Regen. Med.* 1, 245–260. doi: 10.1002/term.24

Hutmacher, D. W., Schantz, T., Zein, I., Ng, K. W., Teoh, S. H., and Tan, K. C. (2001). Mechanical properties and cell cultural response of polycaprolactone scaffolds designed and fabricated via fused deposition modeling. *J. Biomed. Mater. Res.* 55, 203–216. doi: 10.1002/1097-4636(200105)55:2<203::AID-JBM1007>3.0.CO;2-7

Jaklenec, A., Stamp, A., Deweerd, E., Sherwin, A., and Langer, R. (2012). Progress in the tissue engineering and stem cell industry "are we there yet?". *Tissue Eng. Part B Rev.* 18, 155–166. doi: 10.1089/ten.teb.2011.0553

Janssen, N. G., Weijs, W. L. J., Koole, R., Rosenberg, A. J. W. P., and Meijer, G. J. (2014). Tissue engineering strategies for alveolar cleft reconstruction: a systematic review of the literature. *Clin. Oral Investig.* 18, 219–226. doi: 10.1007/s00784-013-0947-x

Kelly, C. N., Miller, A. T., Hollister, S. J., Guldberg, R. E., and Gall, K. (2018). Design and structure-function characterization of 3D printed synthetic porous biomaterials for tissue engineering. *Adv. Healthc. Mater.* 7:1701095. doi: 10.1002/adhm.201701095

Kim, H. D., Amirthalingam, S., Kim, S. L., Lee, S. S., Rangasamy, J., and Hwang, N. S. (2017). Biomimetic materials and fabrication approaches for bone tissue engineering. *Adv. Healthc. Mater.* 6:1700612. doi: 10.1002/adhm.201700612

Ko, I. K., Lee, S. J., Atala, A., and Yoo, J. J. (2013). In situ tissue regeneration through host stem cell recruitment. *Exp. Mol. Med.* 45:e57. doi: 10.1038/emm.2013.118

Korn, P., Hauptstock, M., Range, U., Kunert-Keil, C., Pradel, W., Lauer, G., et al. (2017). Application of tissue-engineered bone grafts for alveolar cleft osteoplasty in a rodent model. *Clin. Oral Investig.* 21, 2521–2534. doi: 10.1007/s00784-017-2050-1

Korn, P., Schulz, M. C., Range, U., Lauer, G., and Pradel, W. (2014). Efficacy of tissue engineered bone grafts containing mesenchymal stromal cells for cleft alveolar osteoplasty in a rat model. *J. Craniomaxillofac. Surg.* 42, 1277–1285. doi: 10.1016/j.jcms.2014.03.010

Landers, R., Pfister, A., Hübner, U., John, H., Schmelzeisen, R., and Mülhaupt, R. (2002). Fabrication of soft tissue engineering scaffolds by means of rapid prototyping techniques. *J. Mater. Sci.* 37, 3107–3116. doi: 10.1023/A:1016189724389

Liang, F., Leland, H., Jedrzejewski, B., Auslander, A., Maniskas, S., Swanson, J., et al. (2018). Alternatives to autologous bone graft in alveolar cleft reconstruction: the state of alveolar tissue engineering. *J. Craniofac. Surg.* 29, 584–593. doi: 10.1097/SCS.0000000000004300

Lode, A., Heiss, C., Knapp, G., Thomas, J., Nies, B., Gelinsky, M., et al. (2018). Strontium-modified premixed calcium phosphate cements for the therapy of osteoporotic bone defects. *Acta Biomater.* 65, 475–485. doi: 10.1016/j.actbio.2017.10.036

Lode, A., Meissner, K., Luo, Y., Sonntag, F., Glorius, S., Nies, B., et al. (2014). Fabrication of porous scaffolds by three-dimensional plotting of a pasty calcium phosphate bone cement under mild conditions. *J. Tissue Eng. Regen. Med.* 8, 682–693. doi: 10.1002/term.1563

Lopez, C. D., Witek, L., Torroni, A., Flores, R. L., Demissie, D. B., Young, S., et al. (2018). The role of 3D printing in treating craniomaxillofacial congenital anomalies. *Birth Defects Res.* 110, 1055–1064. doi: 10.1002/bdr2.1345

Luca, A. D., Lorenzo-Moldero, I., Mota, C., Lepedda, A., Auhl, D., Blitterswijk, C. V., et al. (2016). Tuning cell differentiation into a 3D scaffold presenting a pore shape gradient for osteochondral regeneration. *Adv. Healthc. Mater.* 5, 1753–1763. doi: 10.1002/adhm.201600083

Malda, J., Visser, J., Melchels, F. P., Jüngst, T., Hennink, W. E., Dhert, W. J. A., et al. (2013). 25th anniversary article: engineering hydrogels for biofabrication. *Adv. Mater.* 25, 5011–5028. doi: 10.1002/adma.201302042

Martín-del-Campo, M., Rosales-Ibañez, R., and Rojo, L. (2019). Biomaterials for cleft lip and palate regeneration. *Int. J. Mol. Sci.* 20:2176. doi: 10.3390/ijms20092176

Mehrara, B. J., Saadeh, P. B., Steinbrech, D. S., Dudziak, M., Grayson, B. H., Cutting, C. B., et al. (2000). A rat model of gingivoperiosteoplasty. *J. Craniofac. Surg.* 11, 54–58. doi: 10.1097/00001665-200011010-00010

Moroni, L., Boland, T., Burdick, J. A., Maria, C. D., Derby, B., Forgacs, G., et al. (2018). Biofabrication: a guide to technology and terminology. *Trends Biotechnol.* 36, 384–402. doi: 10.1016/j.tibtech.2017.10.015

Mostafa, N. Z., Doschak, M. R., Major, P. W., and Talwar, R. (2014). Reliable critical sized defect rodent model for cleft palate research. *J. Craniomaxillofac. Surg.* 42, 1840–1846. doi: 10.1016/j.jcms.2014.07.001

Moussa, M., Carrel, J.-P., Scherrer, S., Cattani-Lorente, M., Wiskott, A., and Durual, S. (2015). Medium-term function of a 3D printed TCP/HA structure as a new osteoconductive scaffold for vertical bone augmentation: a simulation by BMP-2 activation. *Materials* 8, 2174–2190. doi: 10.3390/ma8052174

Nguyen, P. D., Lin, C. D., Allori, A. C., Schachar, J. S., Ricci, J. L., Saadeh, P. B., et al. (2009). Scaffold-based rhBMP-2 therapy in a rat alveolar defect model: implications for human gingivoperiosteoplasty. *Plast. Reconstr. Surg.* 124, 1829–1839. doi: 10.1097/PRS.0b013e3181bf8024

Obregon, F., Vaquette, C., Ivanovski, S., Hutmacher, D. W., and Bertassoni, L. E. (2015). Three-dimensional bioprinting for regenerative dentistry and craniofacial tissue engineering. *J. Dent. Res.* 94, 143S–152S. doi: 10.1177/0022034515588885

Ostrowska, B., Di Luca, A., Moroni, L., and Swieszkowski, W. (2016). Influence of internal pore architecture on biological and mechanical properties of three-dimensional fiber deposited scaffolds for bone regeneration. *J. Biomed. Mater. Res.* 104, 991–1001. doi: 10.1002/jbm.a.35637

Pfister, A., Landers, R., Laib, A., Hübner, U., Schmelzeisen, R., and Mülhaupt, R. (2004). Biofunctional rapid prototyping for tissue-engineering applications: 3D bioplotting versus 3D printing. *J. Polym. Sci. A Polym. Chem.* 42, 624–638. doi: 10.1002/pola.10807

Poldervaart, M. T., Wang, H., van der Stok, J., Weinans, H., Leeuwenburgh, S. C. G., Öner, F. C., et al. (2013). Sustained release of BMP-2 in bioprinted alginate for osteogenicity in mice and rats. *PLoS One* 8:e72610. doi: 10.1371/journal.pone.0072610

Pourebrahim, N., Hashemibeni, B., Shahnaseri, S., Torabinia, N., Mousavi, B., Adibi, S., et al. (2013). A comparison of tissue-engineered bone from adipose-derived stem cell with autogenous bone repair in maxillary alveolar cleft model in dogs. *Int. J. Oral Maxillofac. Surg.* 42, 562–568. doi: 10.1016/j.ijom.2012.10.012

Pradel, W., and Lauer, G. (2012). Tissue-engineered bone grafts for osteoplasty in patients with cleft alveolus. *Ann. Anat.* 194, 545–548. doi: 10.1016/j.aanat.2012.06.002

Puwanun, S., Delaine-Smith, R. M., Colley, H. E., Yates, J. M., MacNeil, S., and Reilly, G. C. (2018). A simple rocker−induced mechanical stimulus upregulates mineralization by human osteoprogenitor cells in fibrous scaffolds. *J. Tissue Eng. Regen. Med.* 12, 370–381. doi: 10.1002/term.2462

Raúl, R. I., Nieves, C. M., María, R. L. L., Navarrete Amairany, R., and Olga, F. S. M. L. (2019). Potential benefits from 3D printing and dental pulp stem cells in cleft palate treatments: an in vivo model study. *BJSTR* 16, 11950–11953. doi: 10.26717/BJSTR.2019.16.002831

Raymond, S., Maazouz, Y., Montufar, E. B., Perez, R. A., González, B., Konka, J., et al. (2018). Accelerated hardening of nanotextured 3D-plotted self-setting calcium phosphate inks. *Acta Biomater.* 75, 451–462. doi: 10.1016/j.actbio.2018.05.042

Reitmaier, S., Kovtun, A., Schuelke, J., Kanter, B., Lemm, M., Hoess, A., et al. (2018). Strontium(II) and mechanical loading additively augment bone formation in calcium phosphate scaffolds. *J. Orthop. Res.* 36, 106–117. doi: 10.1002/jor.23623

Ricci, J. L., Clark, E. A., Murriky, A., and Smay, J. E. (2012). Three-dimensional printing of bone repair and replacement materials: impact on craniofacial surgery. *J. Craniofac. Surg.* 23, 304–308. doi: 10.1097/SCS.0b013e318241dc6e

Richter, R. F., Ahlfeld, T., Gelinsky, M., and Lode, A. (2019). Development and characterization of composites consisting of calcium phosphate cements and mesoporous bioactive glass for extrusion-based fabrication. *Materials* 12:2022. doi: 10.3390/ma12122022

Roohani-Esfahani, S.-I., Newman, P., and Zreiqat, H. (2016). Design and fabrication of 3D printed scaffolds with a mechanical strength comparable to cortical bone to repair large bone defects. *Sci. Rep.* 6:19468. doi: 10.1038/srep19468

Schumacher, M., Reither, L., Thomas, J., Kampschulte, M., Gbureck, U., Lode, A., et al. (2017). Calcium phosphate bone cement/mesoporous bioactive glass composites for controlled growth factor delivery. *Biomater. Sci.* 5, 578–588. doi: 10.1039/c6bm00903d

Seifeldin, S. A. (2016). Is alveolar cleft reconstruction still controversial? (Review of literature). *Saudi Dent. J.* 28, 3–11. doi: 10.1016/j.sdentj.2015.01.006

Silva Gomes Ferreira, P. H., De Oliveira, D., Duailibe De Deus, C. B., and Okamoto, R. (2018). Evaluation of the different biomaterials used in alveolar cleft defects in children. *Ann. Maxillofac. Surg.* 8, 315–319. doi: 10.4103/ams.ams_140_17

Thormann, U., Ray, S., Sommer, U., ElKhassawna, T., Rehling, T., Hundgeburth, M., et al. (2013). Bone formation induced by strontium modified calcium phosphate cement in critical-size metaphyseal fracture defects in ovariectomized rats. *Biomaterials* 34, 8589–8598. doi: 10.1016/j.biomaterials.2013.07.036

Waite, P. D., and Waite, D. E. (1996). Bone grafting for the alveolar cleft defect. *Semin. Orthod.* 2, 192–196. doi: 10.1016/s1073-8746(96)80014-4

Wu, C., Pan, W., Feng, C., Su, Z., Duan, Z., Zheng, Q., et al. (2018). Grafting materials for alveolar cleft reconstruction: a systematic review and best-evidence synthesis. *Int. J. Oral Maxillofac. Surg.* 47, 345–356. doi: 10.1016/j.ijom.2017.08.003

Zhang, D., Chu, F., Yang, Y., Xia, L., Zeng, D., Uludag, H., et al. (2011). Orthodontic tooth movement in alveolar cleft repaired with a tissue engineering bone: an experimental study in dogs. *Tissue Eng. Part A* 17, 1313–1325. doi: 10.1089/ten.TEA.2010.0490

Conflict of Interest: The authors declare that the research was conducted in the absence of any commercial or financial relationships that could be construed as a potential conflict of interest.

frontiers
in Bioengineering and Biotechnology

BRIEF RESEARCH REPORT
published: 31 March 2020
doi: 10.3389/fbioe.2020.00230

A Developmental Engineering-Based Approach to Bone Repair: Endochondral Priming Enhances Vascularization and New Bone Formation in a Critical Size Defect

Fiona E. Freeman[1,2,3], Meadhbh Á. Brennan[4], David C. Browe[1,2], Audrey Renaud[4], Julien De Lima[4], Daniel J. Kelly[1,2,5,6], Laoise M. McNamara[3] and Pierre Layrolle[4]*

[1] Trinity Centre for Biomedical Engineering, Trinity Biomedical Sciences Institute, Trinity College Dublin, Dublin, Ireland, [2] Department of Mechanical and Manufacturing Engineering, School of Engineering, Trinity College Dublin, Dublin, Ireland, [3] Biomechanics Research Centre (BMEC), Biomedical Engineering, National University of Ireland Galway, Galway, Ireland, [4] INSERM, UMR 1238, PHY-OS, Laboratory of Bone Sarcomas and Remodelling of Calcified Tissues, Faculty of Medicine, University of Nantes, Nantes, France, [5] Department of Anatomy, Royal College of Surgeons in Ireland, Dublin, Ireland, [6] Advanced Materials and Bioengineering Research Centre (AMBER), Royal College of Surgeons in Ireland and Trinity College Dublin, Dublin, Ireland

Edited by:
Julien Georges Didier Barthès,
Protip Medical, France

Reviewed by:
Magali Cucchiarini,
Saarland University Medical Center,
Germany
Waldemar Hoffmann,
Nobel Biocare, Switzerland

***Correspondence:**
Pierre Layrolle
pierre.layrolle@inserm.fr

Specialty section:
This article was submitted to
Biomaterials,
a section of the journal
Frontiers in Bioengineering and
Biotechnology

Received: 20 December 2019
Accepted: 05 March 2020
Published: 31 March 2020

Citation:
Freeman FE, Brennan MÁ,
Browe DC, Renaud A, De Lima J,
Kelly DJ, McNamara LM and
Layrolle P (2020) A Developmental
Engineering-Based Approach to Bone
Repair: Endochondral Priming
Enhances Vascularization and New
Bone Formation in a Critical Size
Defect.
Front. Bioeng. Biotechnol. 8:230.
doi: 10.3389/fbioe.2020.00230

There is a distinct clinical need for new therapies that provide an effective treatment for large bone defect repair. Herein we describe a developmental approach, whereby constructs are primed to mimic certain aspects of bone formation that occur during embryogenesis. Specifically, we directly compared the bone healing potential of unprimed, intramembranous, and endochondral primed MSC-laden polycaprolactone (PCL) scaffolds. To generate intramembranous constructs, MSC-seeded PCL scaffolds were exposed to osteogenic growth factors, while endochondral constructs were exposed to chondrogenic growth factors to generate a cartilage template. Eight weeks after implantation into a cranial critical sized defect in mice, there were significantly more vessels present throughout defects treated with endochondral constructs compared to intramembranous constructs. Furthermore, 33 and 50% of the animals treated with the intramembranous and endochondral constructs respectively, had full bone union along the sagittal suture line, with significantly higher levels of bone healing than the unprimed group. Having demonstrated the potential of endochondral priming but recognizing that only 50% of animals completely healed after 8 weeks, we next sought to examine if we could further accelerate the bone healing capacity of the constructs by pre-vascularizing them *in vitro* prior to implantation. The addition of endothelial cells alone significantly reduced the healing capacity of the constructs. The addition of a co-culture of endothelial cells and MSCs had no benefit to either the vascularization or mineralization potential of the scaffolds. Together, these results demonstrate that endochondral priming alone is enough to induce vascularization and subsequent mineralization in a critical-size defect.

Keywords: endochondral ossification, intramembranous ossification, bone tissue engineering, pre-vascularization, mesenchymal stem cells

INTRODUCTION

Successful reconstruction of large bone defects remains an important challenge for reconstructive surgeons. Autologous bone grafting, using bone harvested from the patient's own body, remains the gold standard for healing large bone defects, albeit that significant donor site morbidity has been reported and the quantity of bone available for grafting is limited (Reid, 1968; Coventry and Tapper, 1972; Younger and Chapman, 1989; Ahlmann et al., 2002; Finkemeier, 2002; St John et al., 2003; Brydone et al., 2010; Dimitriou et al., 2011). Recent studies have proposed that *in vitro* tissue engineering approaches should strive to simulate *in vivo* developmental processes and thereby imitate natural factors governing cell differentiation and matrix production, following the paradigm defined as "developmental engineering" (Lenas et al., 2009). During early fetal development, bone is formed via two specific mechanisms: intramembranous ossification and endochondral ossification. Both mechanisms begin with a two-step process whereby an organic matrix (osteoid/cartilage template) is initially laid down by osteoblasts/chondrocytes and then mineral crystals are produced and grow slowly over time to produce bone tissue (McNamara, 2011). These processes are distinguished from each other by the fact that the intramembranous process does not rely on the production of a cartilage template but the mesenchymal stromal cells (MSCs) form bone directly, whereas endochondral ossification involves the formation and remodeling of a cartilaginous template together with its vascularization.

Tissue engineering approaches have typically focused on the direct osteogenic differentiation of MSCs seeded on 3D scaffolds in a process resembling intramembranous ossification (Meijer et al., 2007; Sheehy et al., 2019). However, these strategies have been found to have their own limitations, primarily core degradation, due to a lack of a functional vascular supply upon implantation (Ko et al., 2007; Phelps and Garcia, 2009; O'Brien, 2011; Amini et al., 2012), whereby the formation of a calcified matrix during *in vitro* culture can inhibit *in vivo* vascularization of the graft by sealing up the pores of a scaffold (Lyons et al., 2010; Sheehy et al., 2019). Recent tissue engineering strategies have sought to replicate certain aspects of the endochondral ossification process as it may overcome some of the limitations associated with the traditional intramembranous approach (Jukes et al., 2008; Farrell et al., 2009, 2011; Scotti et al., 2010, 2013; Miot et al., 2012; Freeman et al., 2013, 2015a,b; Harada et al., 2014; Martin, 2014; Gawlitta et al., 2015; Sheehy et al., 2015; Visser et al., 2015; Thompson et al., 2016; Daly et al., 2018). The results thus far have been promising as bone marrow–derived MSCs cultured chondrogenically *in vitro* have an inherent tendency to become hypertrophic, which is the next step in the endochondral ossification pathway that plays a critical role in promoting the conversion of avascular tissue to vascularized tissue, a process that is imperative for the survival of the tissue engineered construct (Farrell et al., 2011; Sheehy et al., 2015, 2019). However, although it has been shown that cartilage templates can become vascularized *in vivo* (Scotti et al., 2013; Daly et al., 2016; Thompson et al., 2016), vascularization and subsequent mineralization occur predominately in the peripheral regions of large tissue engineering constructs whereas avascular cartilage persists at the core (Mesallati et al., 2015; Sheehy et al., 2015; Daly et al., 2018). Previously, we have shown the benefits of both endochondral priming and pre-vascularization of MSC aggregates *in vitro* (Freeman et al., 2015b), as it led to enhanced vessel infiltration into the center of the cellular aggregate when implanted subcutaneously *in vivo* (Freeman et al., 2015a). However, whether this strategy can accelerate and direct vascularization in a scaled-up critical sized defect has yet to be established.

The aim of this study was to directly compare intramembranous and endochondral priming in a critical sized defect by employing a biomaterial delivery construct that supports cell attachment and colonization, and has a highly interconnected porous network to permit tissue in-growth and vascularization when implanted *in vivo* (Navarro et al., 2008; Brennan et al., 2015). Once the optimal priming condition was established, it was then advanced to include endothelialisation prior to implantation, to evaluate the capacity of such tissue engineered implants to accelerate the repair of critically-sized calvaria defects *in vivo*.

MATERIALS AND METHODS

Fabrication of Micro-Fiber PCL Scaffolds

Polycaprolactone (PCL) micro-fiber constructs were supplied by Biomedical Tissues (Nantes, France) and produced as previously described (Abdal-hay et al., 2013; Sohier et al., 2014; Brennan et al., 2015). Briefly, PCL (Sigma Aldrich, molecular weight 80,000 g mol^{-1}), was dissolved in chloroform (VWR, Fontenay-sous-Bois, France) to a concentration of 0.1 g mL^{-1} by stirring at 400 rpm at ambient temperature. PCL solution was sprayed using compressed air (8 bars), as the chloroform evaporated a polymer jet was produced, and the micro-fibers were collected on a grid at a distance of 40–50 cm from the spray nozzle. PCL non-woven membranes with a thickness of 400 μm were fabricated and sterilized by gamma irradiation.

Cell Culture

Bone marrow was collected from the iliac crest as described previously (Brennan et al., 2014), by standard puncture and aspiration into heparinized syringes, from three young, healthy human donors after receiving informed consent according to the Declaration of Helsinki and approval by the Ethical Committee of Ulm University. Human bone marrow stem cells (MSCs) were isolated *ex vivo* by plastic adherence and expanded *in vitro* in triple layered cell stack flasks in standard basal media [αMEM supplemented with 100 U/mL penicillin and 100 μg/mL streptomycin, 10% foetal bovine serum (FBS)]. Human umbilical vein endothelial cells (HUVECs) from one donor were purchased from PromoCell, Heidelberg Germany and cultured in endothelial growth media (EGM-2) (C-22216 basal media with the addition of C-39211 growth medium 2 supplement pack, Promocell). Media were replaced every 3 days and, upon reaching 80–90% confluency, cells were passaged using trypsin-EDTA solution. HUVECs were further cultured to passage 4. For all cell culture performed in this study, cell culture media was changed twice weekly.

In vitro Human Bone Marrow MSC Culture in PCL Micro-Fiber 3D Scaffolds

Mesenchymal stromal cells were seeded onto micro-fiber PCL jet-sprayed scaffolds at a density of 2.7 × 10^4/cm^2 and cultured in basal media for up to 21 days. Samples were fixed in 4% paraformaldehyde and rinsed in Phosphate Buffered Saline (PBS). Scanning Electroscope Microscopy (SEM) was used to analyze cell attachment and morphology of MSCs 1.5 h after initial cell seeding. Fixed samples were dehydrated in graded series of ethanol and were mounted on aluminum stubs, sputter coated with gold, and observed with a scanning electron microscope (SEM, Hitachi TM3000, Tokyo, Japan) operating at an acceleration voltage of 5 kV. Cytoskeleton morphology was assessed by fluorescent staining 24 h and 4 days post-seeding. After fixing cells, they were permeabilized with 0.1% Triton X-100 and 0.2% Tween in PBS for 15 min at 4°C followed by incubation with 1% BSA and 5% goat serum at 37°C to reduce non-specific staining. The actin cytoskeleton of MSCs was stained with rhodamine phalloidin (Alexa Fluor 488 Phalloidin, Invitrogen by Life Technologies, Saint Aubin, France) at a dilution of 1/40 with 1% BSA in PBS. Cell nuclei were stained with 4′,6-Diamidino-2-Phenylindole, Dihydrochloride (DAPI, Molecular Probes by Life Technologies) at a concentration of 1/40 000. Images were captured using a Nikon A1R confocal laser-scanning microscope (Nikon, Amstelveen, Netherlands). After 21 days of culture samples were embedded in cryomatrix (Neg 50, Thermoscientific) and submerged in isopentane that was cooled in liquid nitrogen. Cryosections (10 μm thick) were prepared using a cryostat (Micron HM560, Micron Microtech, France). To assess cellular infiltration, frozen sections were air-dried, and fixed in 70% ethanol. Cryosections were processed either by nuclear staining with DAPI and analyzed using fluorescent microscopy (Leica DFC 300 FX), Hematoxylin and Eosin (H&E) staining, or picro-sirus red (All Sigma Aldrich) staining for collagen.

MSCs Priming in PCL Micro-Fiber Scaffolds Prior to *in vivo* Implantation

A total of 1.25 × 10^5 MSCs in passages 3–5 were seeded onto the top of PCL scaffolds (8 mm diameter disks) in 20 μL in basal media and incubated for 1 h to allow for cellular attachment, while 10 μL of basal media was added at constant intervals to avoid the scaffold from drying out. After 1 h of incubation the cell seeding procedure was repeated on the opposite side, such that the overall seeding density of the scaffolds was 2.5 × 10^5 cells/scaffold, comparable to those used previously (Freeman et al., 2015a,b). The seeded scaffolds were cultured for 24 h in basal media, after which they were cultured under the following culture conditions in normoxia: *Unprimed* - cultured in basal media for 21 days; *Endochondral Priming* – cultured in chondrogenic media (chemically defined media which consisted of high-glucose DMEM GlutaMAXTM (Gibco, Life Sciences), 10 ng/ml TGF-β3 (ProSpec-Tany TechnoGene Ltd., Ness-Ziona, Israel), 50 μg/ml ascorbic acid (Sigma-Aldrich), 4.7 μg/ml linoleic acid (Sigma-Aldrich), 100 nM dexamethasone (Sigma-Aldrich) and 1 × insulin–transferrin–selenium (ITS; BD Biosciences, Bedford, MA, United States) for 21 days; *Intramembranous Priming* – cultured in osteogenic media (basal media supplemented with 250 μM ascorbic acid, 10 mM β-glycerolphosphate, and 100 nM dexamethasone) for 21 days. To establish if pre-vascularizing the scaffold prior to implantation would accelerate the *in vivo* angiogenesis and bone healing potential of the endochondrally primed scaffolds the following culture conditions were also performed: *Endochondral Priming + HUVECs* – MSC-seeded scaffolds were cultured in chondrogenic media for 21 days after which HUVECs were then seeded on to the scaffolds (125,000 HUVECs/scaffold), using the same process as described above, and cultured for a further 21 days in endothelial growth media prior to implantation; *Endochondral Priming + Co-culture* – MSC seeded scaffolds were cultured in chondrogenic media for 21 days after which a 1:1 co-culture of MSCs:HUVECs were then seeded on to the scaffolds (125,000 cells/scaffold), further cultured for another 21 days in endothelial growth media prior to implantation. MSCs from three different human donors were used, with two scaffolds of each priming group were prepared per donor (n = 6 scaffolds per priming group).

Implantation of Micro-Fiber PCL Scaffolds in Calvaria Defects

All animal experiments were performed according to Directive 2010/63/UE and after approval of protocols from the local ethical committee (CEEA, Pays-de-la-Loire, France). Immunocompromised female mice (RjOrl: NMRIFoxn1nu/Foxn1nu) were sourced from a professional breeder (Janvier Labs, Saint-Berthevin, France) at 4 weeks of age. Mice were placed in HEPA filtered cages with water and food *ad libitum* and were quarantined for a minimum of 10 days before surgery. For calvaria implants, the mouse was maintained on a stereostatic frame and a skin incision of 1 cm was made to expose the skull. A 4 mm diameter critical-sized defect was created in the calvaria bone using a trephine and a dental micromotor (Nouvag NM3000; NOUVAG, Goldach, Switzerland). Constant saline irrigation was used during drilling. The cell-laden scaffolds were placed on top of the calvaria defect. Blank scaffolds for each priming condition were incubated for 21 days prior to implantation to serve as controls. Skin incisions were closed with sutures (Filapeau; Peters Surgical, Bobigny, Ile-de-France, France) and analgesic (20 μg/kg; Buprenorphine, Axience, France) was injected intramuscularly before surgery and every 8 h for 3 days after surgery. Animals were observed daily and body weights were determined weekly. After 8 weeks, the mice were euthanized by inhalation of an overdose of carbon dioxide gas. Sample sizes for calvaria implantations were as follows: *blank scaffolds* (basal media, chondrogenic media, osteogenic media, n = 2/group);

Unprimed (Donor 1, n = 1, Donor 2, n = 2 Donor 3, n = 2); *Endochondral Priming* (Donor 1, n = 2, Donor 2, n = 2 Donor 3, n = 2); *Intramembranous Priming* (Donor 1, n = 2, Donor 2, n = 2 Donor 3, n = 2); *Endochondral Priming + HUVECs* (Donor 1, n = 2, Donor 2, n = 2 Donor 3, n = 1); *Endochondral Priming + Co-culture* (Donor 1, n = 2, Donor 2, n = 2 Donor 3, n = 2).

X-Ray, Histological, and Immunohistochemical Analysis

Explants were observed for signs of tissue necrosis, inflammation or infection, dissected and fixed in 10 volumes of buffered 4% formaldehyde for 72 h. Using the scoring system previously established (Patel et al., 2008), blind scoring for each planar radiograph (Faxitron MD20, Hologic, United States) was conducted by six impartial people (n = 6 scores) to establish the extent of bony bridging and union of the experimental groups.

The skulls were further dissected using a diamond saw. Explants were decalcified in 4.13% ethylenediamine tetraacetic acid (EDTA)/0.2% paraformaldehyde in phosphate-buffered saline, pH 7.4 for 96 h at 50°C using an automated microwave decalcifying apparatus (KOS Histostation; Milestone Medical, Kalamazoo, Michigan, United States). Samples were then dehydrated in ascending series of ethanol baths (80, 95, and 100%) and finally in butanol in an automated dehydration station (Microm Microtech, Lyon, France), and then embedded in paraffin (Histowax; Histolab, Gottenburg, Sweden). Blocks were cut using a standard microtome (Leica RM2255; Leica Biosystems, Nanterre, Ile-de-France, France) and histology sections (5–8 μm thick) in the middle of calvaria defects were made. Sections were stained by Masson trichrome technique using an automated coloration station (Microm Microtech). Histomorphometry of images were processed on the whole implant sections using Image J software (National Institute of Health, Bethesda, MA, United States) and the percentage areas of bone tissue per total area of the calvaria defect was measured. Sections were also stained with Hematoxylin and Eosin (H&E, Sigma Aldrich) and Goldner's Trichrome (Hematoxyline de Groat, Fuchsine Ponceau, 0.1% Orange G molybdique, 2% Fast Green, All Sigma Aldrich) and quantified for vessel infiltration, whereby vessels (positive staining for endothelium and erythrocytes present within the lumen), were counted on separate sections (n = 3 slices per defect) and a taken throughout each construct.

To identify the specific collagen types, immunohistochemistry was performed for collagen type I and II, as previously described (Buckley et al., 2010; Browe et al., 2019). Briefly, after dewaxing and rehydrating the sections antigen retrieval was performed by incubation with Chondrotinase ABC for collagen types I and II. After blocking for non-specific binding, sections were incubated with primary antibody (anti collagen type I (1:400), Abcam, United Kingdom; anti collagen type II (1:400), Santa-Cruz) overnight at 4°C. Endogenous peroxidase activity was blocked with hydrogen peroxide (Sigma) prior to incubation with the anti-mouse IgG secondary antibody (Sigma). Sections were then incubated with 3,30 -diaminobenzidine peroxidase substrate (Vector Labs, United Kingdom) to visualize positive staining. All Stained slices were scanned (NanoZoomer; Hamamatsu, Photonics, Hamamatsu City, Shizuoka Prefecture, Japan) and observed on a virtual microscope (NDP view; Hamamatsu).

Statistical Analysis

Results were expressed as mean ± standard deviation. Statistical analysis was performed using one-way analyses of variance (ANOVA) with the addition of Tukey's correction for multiple comparisons testing. All analyses were performed using GraphPad (GraphPad Software, La Jolla, CA, United States)[1]. For all comparisons, the level of significance was $p \leq 0.05$.

RESULTS

PCL Micro-Fiber Scaffold Permitted MSC Spreading, Infiltration and Matrix Formation

The morphology of MSCs following attachment to PCL scaffolds was visualized using SEM and confocal imaging of fluorescently stained cells (**Figures 1A,B**). As early as 1.5 h after seeding, MSCs were well attached to the scaffold along the lengths of the scaffold micro-fibers and exhibit an elongated morphology (**Figure 1B**). Confocal imaging after 1 and 4 days shows that MSCs assumed a spread morphology and were orientated in different directions along the struts of the scaffolds, with intense cytoskeleton staining. Cell ingress into the scaffolds was observed by DAPI stained cell nuclei and H&E staining of scaffold cross sections. As demonstrated in **Figure 1C**, by day 21 MSCs penetrated through the entire depth of the scaffolds and exhibited significant collagen matrix deposition as shown by the pink staining (pico sirus red).

Endochondral Priming of the Scaffolds Enhanced Vessel Infiltration and Lead to Increased Bone Union

To assess the osteoconductive nature of the scaffolds 8 weeks-post implantation, we looked at areas within the defect where the scaffold was laid upon undamaged calvaria bone (**Figure 2A**). Goldner's Trichrome staining revealed abundant bone formation within the scaffolds and that there did not seem to be any differences in the osteoconductive nature of the scaffolds between all three groups, elucidating that the osteoconductivity was due to the designed PCL scaffold and not the culture conditions. When examined in the center of the defects, all defects treated with the controlled blank scaffolds were filled with fibrous tissue, as seen in the positive red staining (see **Supplementary Figure S1A**). They also all showed limited vessel infiltration, new bone formation and bone union (see **Supplementary Figures S1B–E**). Masson's Trichrome staining revealed predominantly fibrous tissue formation, similar to what was seen in the blank scaffolds, in the *Unprimed* group (**Figure 2B**). On the other hand, in the defects of the

---

[1] www.graphpad.com

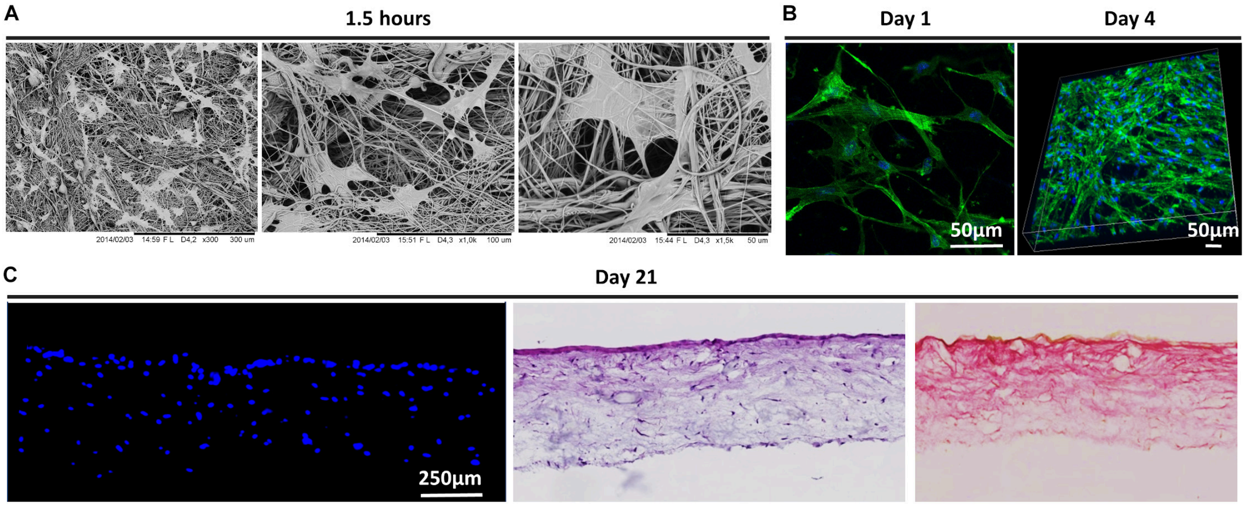

FIGURE 1 | (A) Morphology of human bone marrow MSCs attached to scaffolds 1.5 h after cell seeding as observed by SEM. Black scale bars represent 300 and 100 μm on the left and right, respectively. **(B)** Confocal microscopy of MSCs on scaffolds 24 h and 4 days after seeding cells. Actin cytoskeleton arrangement is shown in green by fluorescent staining with rhodamine phalloidin and nuclei are depicted in blue by DAPI staining. White scale bars represent 50 μm. **(C)** MSCs infiltration into scaffolds after 21 days post-culture as shown by fluorescent DAPI staining of cell nuclei in scaffold cryo-sections and H&E staining. Collagen matrix formation is observed in pink by pico-sirus red staining. Scale bars represents 250 μm.

Endochondral and *Intramembranous Primed* groups there was little to no fibrous tissue present. Histological analysis of H&E and Goldner's Trichrome stained samples revealed the presence of vessels in all three experimental groups (denoted by red arrow heads). These vessels appeared mature with endothelium and perfused with erythrocytes (see **Supplementary Figure S2**). The *Unprimed* and *Intramembranous Primed* groups had vessels predominantly located in the periphery of the scaffold, with little to none present within the center of the scaffold (denoted by the white dashed lines). In contrast, vessels were present both in the periphery and in the center of the *Endochondral Primed* group. When quantified there was significantly more vessels ($p < 0.01$) present in the *Endochondral Primed* group compared to both the *Intramembranous* and *Unprimed* groups (**Figure 2D**). Next, we sought to assess bone regeneration capability of the scaffolds under the different priming conditions. First, Masson's Trichrome and H&E staining revealed there was positive staining for new bone, complete with marrow cavities, in both the *Intramembranous* and *Endochondral Primed* groups 8 weeks post-implantation (see **Figure 2B**). When quantified, there was significantly more new bone ($p < 0.01$) found in the *Intramembranous Primed* group compared to the *Unprimed* group (see **Figure 2E**). This was further verified using immunohistochemistry where the *Intramembranous Primed* group had the highest amount of positive Collagen Type I staining whereas the *Endochondral Primed* group had the highest amount of positive Collagen Type II staining (**Figure 4A**). There was no significant difference in percentage new bone formed between the *Intramembranous* and the *Endochondral Primed* groups. Although the X-ray analysis revealed limited bone healing in all three groups, the *Unprimed* group had the poorest healing potential, with no bone unions present in any of the animals within this group (see **Figure 2C**). Interestingly, in the other two treatment groups there was clear healing along the sagittal suture line of the mice craniums (denoted by red arrows). In fact, 33 and 50% of the animals had full bone union in the *Intramembranous* and *Endochondral Primed* groups respectively. When scored blind, the *Endochondral* and *Intramembranous Primed* groups had significantly higher ($p < 0.05$) bone union score than the *Unprimed* group (**Figure 2F**).

Pre-vascularization of the Cartilage Template did Not Further Enhance the Bone Healing Potential of the Scaffolds

Having demonstrated the potential of endochondral priming but recognizing that only limited healing was achieved after 8 weeks, we next sought to examine if we could further accelerate the bone healing capacity of the constructs by pre-vascularizing them *in vitro* prior to implantation. There was no sign of fibrous tissue formation in any of the defects treated with all three experimental groups (**Figure 3A**). All three groups had vessels present throughout the defects, and when quantified there was no significant difference in vessel number between any of the groups (**Figure 3C**). We next sought to assess the nature of new bone tissue being formed using histological staining. All three experimental groups had positive staining for new bone and when quantified there was no increase in new bone formed due to the pre-vascularization process (**Figure 3D**). This was further verified as all three groups had positive staining for Collagen Type I (**Figure 4B**). Interestingly, the X-rays reveal a difference in where the bone was formed. In both the *Endochondral Primed* and the *Endochondral Primed + Co-culture* groups, similar to what was seen previously, bone healed along the sagittal suture line (**Figure 3B**). However, in the *Endochondral Primed + HUVECs* group bone was formed sporadically with a

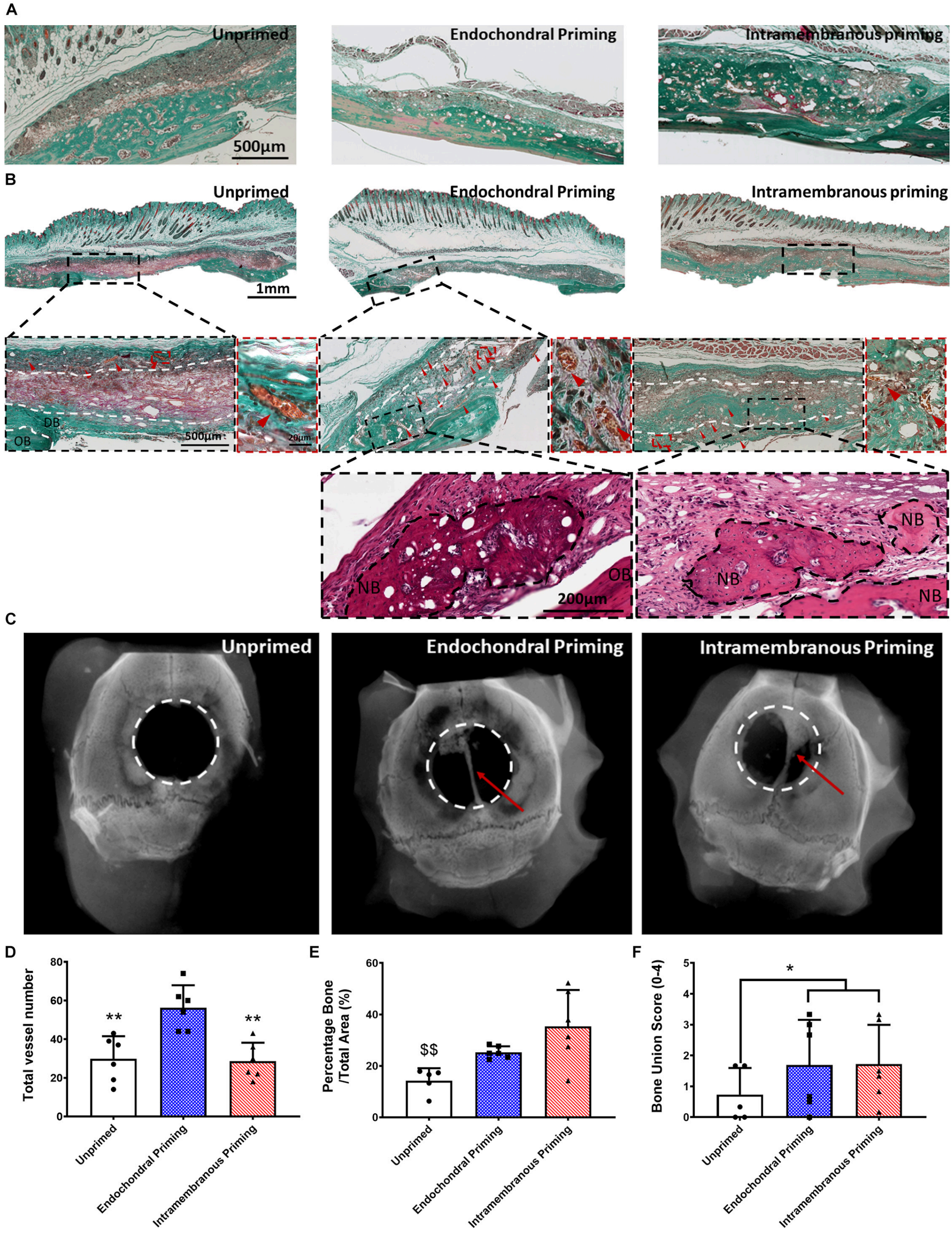

FIGURE 2 | (A) Masson's Trichrome stained sections of all groups after 8 weeks *in vivo,* showing the osteoconductive nature of the scaffolds. **(B)** Masson's Trichrome and H&E stained sections of all groups taken in the middle of the defect after 8 weeks *in vivo.* All Images taken at 20X. White dashed lines denoting periphery and center, OB denoted original bone, and NB denotes new bone. Red arrow heads denote vessels. **(C)** Representative X-ray images of the three experimental groups 8 weeks after implantation. Quantification of the amount of panel **(D)** total number of vessels, **(E)** percentage new bone, and **(F)** bone union score for all three experimental groups 8 weeks post implantation. Error bars denote standard deviation, $^{**}p < 0.01$ vs. Endochondral Priming group, $^{\$\$}p < 0.01$ vs. Intramembranous Priming group, $n = 6$ animals.

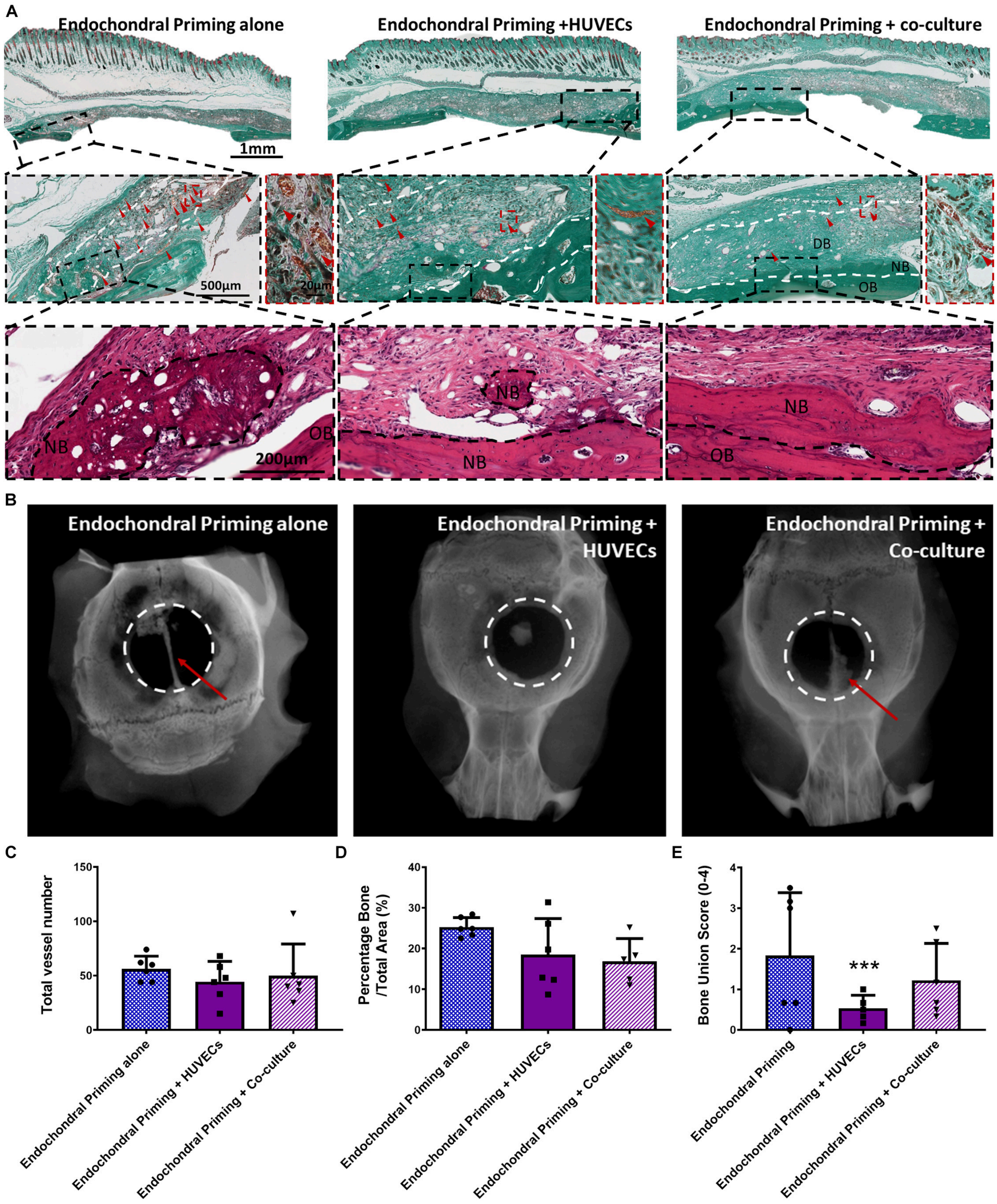

FIGURE 3 | (A) Masson's Trichrome and H&E stained sections of all groups taken in the middle of the defect after 8 weeks *in vivo.* All Images taken at 20X. White dashed lines denoting periphery and centre, OB denoted original bone, and NB denotes new bone. Red arrow heads denote vessels. **(B)** Representative X-ray images of the three experimental groups 8 weeks after implantation. Quantification of the amount of panel **(C)** total number of vessels, **(D)** percentage new bone, and **(E)** bone union score for all three experimental groups 8 weeks post implantation. Error bars denote standard deviation, ***$p < 0.01$ vs. Endochondral Priming alone group, $n = 6$ animals.

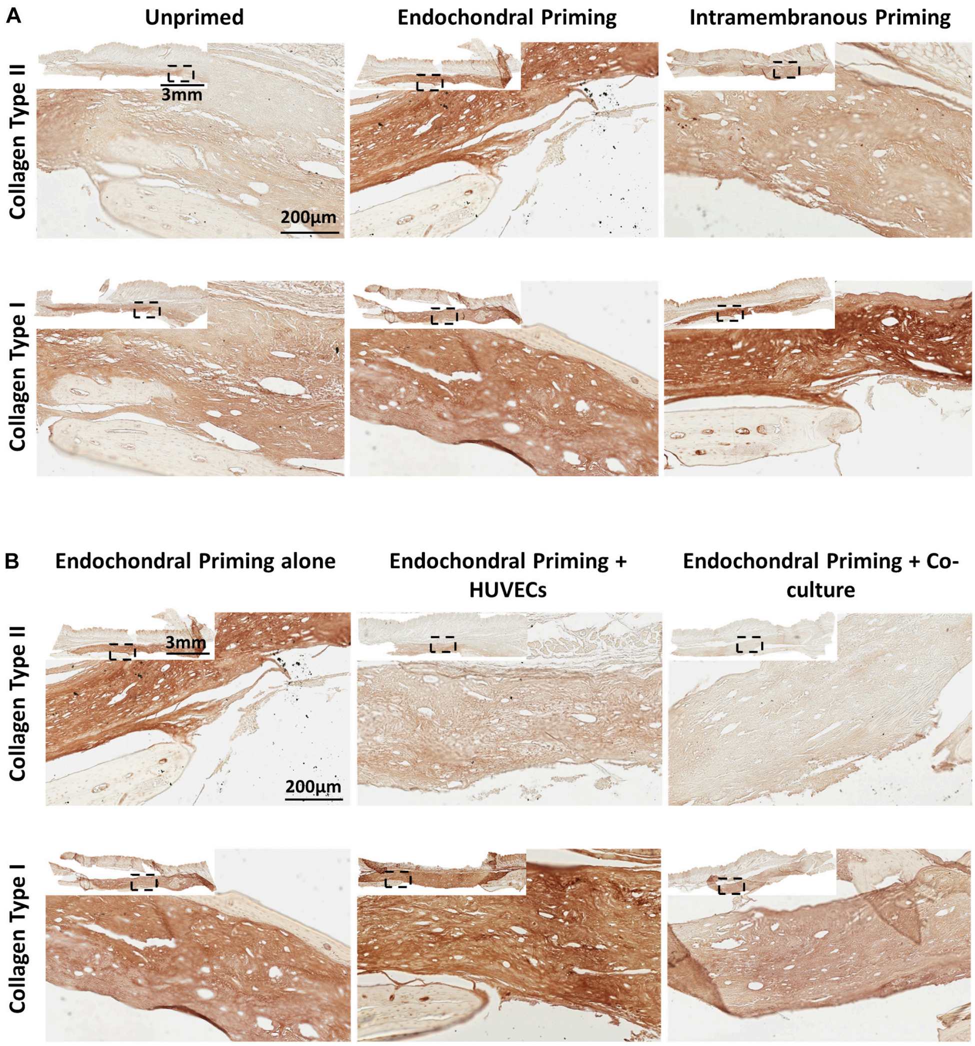

FIGURE 4 | (A) Immunohistochemistry (Collage Type I and Collagen Type II) stained sections of *Unprimed, Endochondral and Intramembranous primed* groups taken in the middle of the defect after 8 weeks *in vivo.* All Images taken at 20X. **(B)** Immunohistochemistry (Collage Type I and Collagen Type II) stained sections of *Endochondral priming alone, Endochondral priming + HUVECs and Endochondral priming + Co-culture* groups taken in the middle of the defect after 8 weeks *in vivo.* All Images taken at 20X.

few bony spicules dispersed throughout the defect. In fact, all the *Endochondral Primed + HUVECs* group were non-union defects after 8 weeks. Whereas, 50 and 17% of the animals had full bone bridging in the *Endochondral Primed* and the *Endochondral Primed + Co-culture* groups, respectively. When scored blind the *Endochondral Primed* group had a significantly higher ($p < 0.001$) bone union score than the *Endochondral Primed + HUVECs* group (**Figure 3E**). There was no significant difference between the *Endochondral Primed* group and the *Endochondral Primed + Co-culture* group.

DISCUSSION

To date most bone tissue engineering strategies that have reached the clinic have tried to produce a construct that mimics the function or mechanical properties of native bone tissue, and although this strategy has produced extensive amount of research, *in vitro* tissue regeneration constructs for the clinical treatment of bone defects has not reached its full potential (Frohlich et al., 2008; Ma et al., 2014). In this vein, recent tissue engineering strategies have sought to replicate features that occur during embryogenesis or "developmental engineering" (Jukes et al., 2008; Farrell et al., 2009, 2011; Lenas et al., 2009; Scotti et al., 2010, 2013; Miot et al., 2012; Freeman et al., 2013, 2015a,b; Harada et al., 2014; Martin, 2014; Gawlitta et al., 2015; Sheehy et al., 2015; Visser et al., 2015; Thompson et al., 2016; Daly et al., 2018). The results from this study further demonstrate the tremendous potential of "developmental engineering," as both intramembranous and endochondral priming showing a significant increase in new bone formation over scaffolds with

MSCs that were not developmentally primed. Furthermore, endochondral priming alone was sufficient to increase bone healing, but further endothelialisation provided no benefit or acceleration in vessel infiltration or bone healing in a critical-sized defect.

Essential features of biomaterials for bone reconstruction include; a structure that supports osteogenic cell responses, appropriate biodegradability and biocompatibility, and a highly interconnected porous network to permit tissue in-growth and vascularization (Navarro et al., 2008). There are currently several commercial products which utilize collagen to direct bone repair. However, in order to avoid rapid degradation, collagen is usually cross-linked, and the use of chemical cross-linkers such as glutaraldehyde can cause long-term cytotoxicity (van Wachem et al., 1994; Marinucci et al., 2003). Cross-linking also reduced scaffold pore sizes which have been shown to inhibit vascularization (Shields et al., 2004). In this study, instead of recapitulating the native collagen ECM, a biomimetic polymer biomaterial was developed to mimic the nanofibrous structure of the ECM. This scaffold not only allowed for cell infiltration but also promoted spread morphology with intense actin cytoskeleton staining. It has previously been shown that MSCs with a large spreading area showed a higher degree of osteogenic differentiation (Yang et al., 2019) and indeed, we previously showed that this micro-fiber scaffold with highly interconnected porous network promoted osteogenic cell responses *in vitro* (Brennan et al., 2015). Here we show that the microfiber PCL scaffold permits tissue in-growth, vascularization and also supports osteogenesis *in vivo*.

We next sought to investigate the bone healing potential of MSC-laden PCL scaffolds that were first primed for either intramembranous or endochondral prior to implantation. During early fotal development the cranium is formed via the intramembranous ossification process and in this study, we investigated the optimum priming condition to enhance the regeneration potential of a calvaria critical sized defect model. The bone healing potential was significantly increased if the scaffolds where loaded with MSCs that were first primed along either an intramembranous or endochondral pathway. Intramembranous bone growth is achieved through bone formation within a periosteum or by bone formation at suture lines (Opperman, 2000). Interestingly, the bone healing pattern seen in this study was characterized by new bone predominately laid down along the sagittal suture line of the cranium. Interestingly, endochondral priming of the cells prior to implantation does not change this bone formation pattern, with 50% of the animals (vs. 33% for intermembranous) having full bone bridging along the sagittal suture line, there was a trend toward increased bone regeneration potential. Directly comparing the bone formation of the two priming conditions, there was no significant difference in the bone healing capacity between either group. Similar to previous studies (Thompson et al., 2016), histomorphological analysis showed an increase in percentage new bone in the intramembranous group over the endochondral ossification group, however the trend was not significant. Furthermore, similar to previous studies (Thompson et al., 2016), there was significantly more vessels present in the endochondral primed constructs over the intramembranous primed constructs. Unlike previous studies (Mesallati et al., 2015; Sheehy et al., 2015; Thompson et al., 2016; Daly et al., 2018), the vascularization was throughout the defect and not predominately in the peripheral regions of large tissue engineering constructs. It was due to this significant increase in vessel infiltration that endochondral priming was chosen as the optimum priming condition and was taken forward to be endothelialised prior to implantation. Exogenous osteogenic and chondrogenic growth factors (ascorbic acid, dexamethasone, β-glycerol, and TGF-β3) were introduced into the culture media of MSCs to encourage MSC differentiation down to specific pathways. Therefore, in order to clearly distinguish whether any of these factors contributed to the differences seen between the groups we includeed control PCL scaffold groups that were exposed to the same osteogenic or chondrogenic factors, but with no cells, and observed no increase in bone healing or vascularization, leading us to believe that the therapeutic effect in the experimental groups is due to the priming of the MSCs and not due to the presence of the exogenous growth factors.

One potential limitation to the study was that we did not investigate the cell viability of the human MSCs post-implantation. Previously, we have shown that following subcutaneous implantation of endochondrally primed and prevascularised human MSC cellular aggregates, the human MSCs survived up to 21 days (Freeman et al., 2015a). This correlated with other studies which have investigated the cell viability of human MSCs following implantation (Vilalta et al., 2008; Brennan et al., 2014; Manassero et al., 2016). With this in mind, even though the primed human MSCs may not survive the entire implantation their presence starts a cascade of events *in vivo* toward increased bone regeneration. Future work should delve further into understanding the cell viability and the exact role the primed MSCs have on the bone regeneration capacity of the implants.

The addition of endothelial cells prior to implantation did not increase the bone healing or vascularization potential of the endochondral primed constructs. In fact, when endothelial cells alone were added to the endochondral primed construct, it hindered the bone healing capacity of the construct. This was a complete contradiction to our previous work (Freeman et al., 2015a,b), where the mineralization of cellular aggregates was improved through the pre-vascularization process. This could may be explained by the fact that during endochondral ossification, hypertrophic chondrocyte secretes VEGF, which is a potent chemoattractant for the recruitment of endothelial cells and osteoclasts and promotes cartilage resorption. The addition of endothelial cells to hypertrophic chondrocytes present in the endochondral primed construct, may suppress the hypertrophic chondrocytes from secreting VEGF, as endothelial cells are already present, thereby, hindering the bone healing process (Hans-Peter et al., 1999; Gerber and Ferrara, 2000). Interestingly, the healing capacity is restored when both MSCs and endothelial cells are added in a co-culture. This further cooperates with our hypothesis because in this approach half the number of endothelial cells was added to the scaffold, which may have minimized communication between hypertrophic chondrocytes and endothelial cells and healing capacity was restored. However, future studies should look further into the direct communication between the hypertrophic cartilage template and endothelial cells to elucidate this finding further and determine an appropriate methodology for pre-vascularizing an endochondral primed construct. Taken together, the results presented in this study demonstrate that endochondral priming alone is enough to induce vascularization and subsequent bone healing in a critically sized defect.

DATA AVAILABILITY STATEMENT

The datasets generated for this study are available on request to the corresponding author.

ETHICS STATEMENT

All animal experiments were performed according to Directive 2010/63/UE and after approval of protocols from the local ethical committee (CEEA, Pays-de-la-Loire, France).

AUTHOR CONTRIBUTIONS

FF and MB performed the experiments, data analysis and interpretation, and wrote the manuscript. DB performed all the immunohistochemistry. AR performed all the animal surgeries. JD sliced and performed some of the Masson's Trichrome Histology. DK, LM, and PL oversaw the collection of results and data interpretation and finalized the manuscript.

FUNDING

This project was supported by the European Research Council Grant 258992 (BONEMECHBIO), European Regional Development Fund through the Science Foundation Ireland (SFI) Investigators Programme Grant 258992, European Research Council (ERC) under Grant Number 647004 and the Irish Research Council (GOIPD/2016/324), the Ulysses Irish Research Council Grant, and the 7th Framework programme through the project REBORNE Grant number HEALTH—2009—1.4.2—241879.

ACKNOWLEDGMENTS

The authors would like to thank Markus Rojewski and Hubert Schrezenmeier of the Institute for Clinical Transfusion Medicine and Immunogenetics Ulm, German Red Cross Blood Donor Service, University of Ulm, for supplying the bone marrow stromal cells. The authors would also like to thank Kian Eichholz, Simon Carroll, Dan Ahern, Grainne Cunniffe, and Mathieu Riffault for being the blind scorers for this study.

SUPPLEMENTARY MATERIAL

The Supplementary Material for this article can be found online at: https://www.frontiersin.org/articles/10.3389/fbioe.2020.00230/full#supplementary-material

FIGURE S1 | (A) Masson's Trichrome stained sections of control scaffolds after 8 weeks *in vivo*. Images taken at 20X. **(B)** Representative X-ray images of the three control groups 8 weeks after implantation. Quantification of the amount of panel **(C)** total number of vessels, **(D)** percentage new bone, and **(E)** bone union score for all three control groups 8 weeks post implantation. Error bars denote standard deviation, $n = 2$ animals.

FIGURE S2 | Goldner's Trichrome stained sections of control scaffolds after 8 weeks *in vivo*. Red arrow heads denote mature vessels perfused with erythrocytes. Images taken at 20X.

REFERENCES

Abdal-hay, A., Sheikh, F. A., and Lim, J. K. (2013). Air jet spinning of hydroxyapatite/poly(lactic acid) hybrid nanocomposite membrane mats for bone tissue engineering. *Colloids Surf. B Biointerfaces* 102, 635–643. doi: 10.1016/j.colsurfb.2012.09.017

Ahlmann, E., Patzakis, M., Roidis, N., Shepherd, L., and Holtom, P. (2002). Comparison of anterior and posterior iliac crest bone grafts in terms of harvest-site morbidity and functional outcomes. *J. Bone Joint Surg.* 84, 716–720. doi: 10.2106/00004623-200205000-00003

Amini, A. R., Laurencin, C. T., and Nukavarapu, S. P. (2012). Bone tissue engineering: recent advances and challenges. *Crit. Rev. Biomed. Eng.* 40, 363–408. doi: 10.1615/critrevbiomedeng.v40.i5.10

Brennan, M. A., Renaud, A., Amiaud, J., Rojewski, M. T., Schrezenmeier, H., Heymann, D., et al. (2014). Pre-clinical studies of bone regeneration with human bone marrow stromal cells and biphasic calcium phosphate. *Stem Cell Res. Ther.* 5:114. doi: 10.1186/scrt504

Brennan, M. A., Renaud, A., Gamblin, A. L., D'Arros, C., Nedellec, S., Trichet, V., et al. (2015). 3D cell culture and osteogenic differentiation of human bone marrow stromal cells plated onto jet-sprayed or electrospun micro-fiber scaffolds. *Biomed. Mater.* 10:045019. doi: 10.1088/1748-6041/10/4/045019

Browe, D. C., Mahon, O. R., Diaz-Payno, P. J., Cassidy, N., Dudurych, I., Dunne, A., et al. (2019). Glyoxal cross-linking of solubilized extracellular matrix to produce highly porous, elastic, and chondro-permissive scaffolds for orthopedic tissue engineering. *J. Biomed. Mater. Res. A* 107, 2222–2234. doi: 10.1002/jbm.a.36731

Brydone, A. S., Meek, D., and Maclaine, S. (2010). Bone grafting, orthopaedic biomaterials, and the clinical need for bone engineering. proceedings of the Institution of mechanical engineers, Part H. *J. Eng. Med.* 224, 1329–1343. doi: 10.1243/09544119jeim770

Buckley, C. T., Vinardell, T., Thorpe, S. D., Haugh, M. G., Jones, E., McGonagle, D., et al. (2010). Functional properties of cartilaginous tissues engineered from infrapatellar fat pad-derived mesenchymal stem cells. *J. Biomech.* 43, 920–926. doi: 10.1016/j.jbiomech.2009.11.005

Coventry, M. B., and Tapper, E. M. (1972). Pelvic instability: a consequence of removing iliac bone for grafting. *J. Bone Joint* 54, 83–101. doi: 10.2106/00004623-197254010-00008

Daly, A. C., Cunniffe, G. M., Sathy, B. N., Jeon, O., Alsberg, E., and Kelly, D. J. (2016). 3D bioprinting of developmentally inspired templates for whole bone organ engineering. *Adv. Healthc. Mater.* 5, 2353–2362. doi: 10.1002/adhm.201600182

Daly, A. C., Pitacco, P., Nulty, J., Cunniffe, G. M., and Kelly, D. J. (2018). 3D printed microchannel networks to direct vascularisation during endochondral bone repair. *Biomaterials* 162, 34–46. doi: 10.1016/j.biomaterials.2018.01.057

Dimitriou, R., Jones, E., McGonagle, D., and Giannoudis, P. V. (2011). Bone regeneration: current concepts and future directions. *BMC Med.* 9:66. doi: 10.1186/1741-7015-9-66

Farrell, E., Both, S. K., Odorfer, K. I., Koevoet, W., Kops, N., O'Brien, F. J., et al. (2011). In-vivo generation of bone via endochondral ossification by in-vitro chondrogenic priming of adult human and rat mesenchymal stem cells. *BMC Musculoskelet. Disord.* 12:31. doi: 10.1186/1471-2474-12-31

Farrell, E., van der Jagt, O. P., Koevoet, W., Kops, N., van Manen, C. J., Hellingman, C. A., et al. (2009). Chondrogenic priming of human bone marrow stromal cells: a better route to bone repair? *Tissue Eng. Part C* 15, 285–295. doi: 10.1089/ten.tec.2008.0297

Finkemeier, C. G. (2002). Bone-grafting and bone-graft substitutes. *J. Bone Joint* 84-A, 454–464. doi: 10.2106/00004623-200203000-00020

Freeman, F. E., Allen, A. B., Stevens, H. Y., Guldberg, R. E., and McNamara, L. M. (2015a). Effects of in vitro endochondral priming and pre-vascularisation of human MSC cellular aggregates in vivo. *Stem Cell Res. Ther.* 6:218. doi: 10.1186/s13287-015-0210-212

Freeman, F. E., Haugh, M. G., and McNamara, L. (2015b). An in vitro bone tissue regeneration strategy combining chondrogenic and vascular priming enhances the mineralisation potential of MSCs in vitro whilst also allowing for vessel formation. *Tissue Eng. Part A* 21, 1320–1332. doi: 10.1089/ten.tea.2014.0249

Freeman, F. E., Haugh, M., and McNamara, L. (2013). Investigation of the optimal timing for chondrogenic priming of MSCs to enhance osteogenic differentiation in vitro as a bone tissue engineering strategy. *J. Tissue Eng. Regen. Med.* 10, E250–E262. doi: 10.1002/term.1793

Frohlich, M., Grayson, W. L., Wan, L. Q., Marolt, D., Drobnic, M., and Vunjak-Novakovic, G. (2008). Tissue engineered bone grafts: biological requirements. tissue culture and clinical relevance. *Curr. Stem Cell Res. Ther.* 3, 254–264. doi: 10.2174/157488808786733962

Gawlitta, D., Benders, K. E. M., Visser, J., van der Sar, A. S., Kempen, D. H. R., Theyse, L. F. H., et al. (2015). Decellularized cartilage-derived matrix as substrate for endochondral bone regeneration. *Tissue Eng. Part A* 21, 694–703. doi: 10.1089/ten.tea.2014.0117

Gerber, H. P., and Ferrara, N. (2000). Angiogenesis and bone growth. *Trends Cardiovas. Med.* 10, 223–228. doi: 10.1016/S1050-1738(00)00074-78

Hans-Peter, G., Thiennu, H. V., Anne, M. R., Joe, K., Zena, W., and Napoleone, F. (1999). VEGF couples hypertrophic cartilage remodeling, ossification and angiogenesis during endochondral bone formation. *Nat. Med.* 5, 623–628. doi: 10.1038/9467

Harada, N., Watanabe, Y., Sato, K., Abe, S., Yamanaka, K., Sakai, Y., et al. (2014). Bone regeneration in a massive rat femur defect through endochondral ossification achieved with chondrogenically differentiated MSCs in a degradable scaffold. *Biomaterials* 35, 7800–7810. doi: 10.1016/j.biomaterials.2014.05.052

Jukes, J. M., Both, S. K., Leusink, A., Sterk, L. M. T., van Blitterswijk, C. A., and de Boer, J. (2008). Endochondral bone tissue engineering using embryonic stem cells. *Proc. Natl. Acad. Sci. U.S.A.* 105, 6840–6845. doi: 10.1073/pnas.0711662105

Ko, H. C., Milthorpe, B. K., and McFarland, C. D. (2007). Engineering thick tissues–the vascularisation problem. *Eur. Cells Mat.* 14, 18–19.

Lenas, P., Moos, M., and Luyten, F. P. (2009). Developmental engineering: a new paradigm for the design and manufacturing of cell-based products. Part I: from three-dimensional cell growth to biomimetics of *in vivo* development. *Tissue Eng. Part B* 15, 381–394. doi: 10.1089/ten.TEB.2008.0575

Lyons, F. G., Al-Munajjed, A. A., Kieran, S. M., Toner, M. E., Murphy, C. M., Duffy, G. P., et al. (2010). The healing of bony defects by cell-free collagen-based scaffolds compared to stem cell-seeded tissue engineered constructs. *Biomaterials* 31, 9232–9243. doi: 10.1016/j.biomaterials.2010.08.056

Ma, J. L., Both, S. K., Yang, F., Cui, F. Z., Pan, J. L., Meijer, G., et al. (2014). Concise review: cell-based strategies in bone tissue engineering and regenerative medicine. *Stem Cells Trans. Med.* 3, 98–107. doi: 10.5966/sctm.2013-2126

Manassero, M., Paquet, J., Deschepper, M., Viateau, V., Retortillo, J., Bensidhoum, M., et al. (2016). Comparison of survival and osteogenic ability of human mesenchymal stem cells in orthotopic and ectopic sites in mice. *Tissue Eng. Part A* 22, 534–544. doi: 10.1089/ten.TEA.2015.0346

Marinucci, L., Lilli, C., Guerra, M., Belcastro, S., Becchetti, E., Stabellini, G., et al. (2003). Biocompatibility of collagen membranes crosslinked with glutaraldehyde or diphenylphosphoryl azide: an in vitro study. *J. Biomed. Mater. Res. A* 67, 504–509. doi: 10.1002/jbm.a.10082

Martin, I. (2014). Engineered tissues as customized organ germs. *Tissue Eng. Part A* 20, 1132–1133. doi: 10.1089/ten.tea.2013.0772

McNamara, L. M. (2011). "Bone as a material," in *Comprehensive Biomaterials*, ed. P. Ducheyne (Amsterdam: Elsevier Ltd), 169–186.

Meijer, G. J., de Bruijn, J. D., Koole, R., and van Blitterswijk, C. A. (2007). Cell-based bone tissue engineering. *PLoS Med.* 4:e9. doi: 10.1371/journal.pmed.0040009

Mesallati, T., Sheehy, E. J., Vinardell, T., Buckley, C. T., and Kelly, D. J. (2015). Tissue engineering scaled-up, anatomically shaped osteochondral constructs for joint resurfacing. *Eur. Cell Mater.* 30, 163–186. doi: 10.22203/ecm.v030a12

Miot, S., Brehm, W., Dickinson, S., Sims, T., Wixmerten, A., Longinotti, C., et al. (2012). Influence of in vitro maturation of engineered cartilage on the outcome of osteochondral repair in a goat model. *Eur. Cells Mat.* 23, 222–236.

Navarro, M., Michiardi, A., Castano, O., and Planell, J. A. (2008). Biomaterials in orthopaedics. *J. R Soc. Interface* 5, 1137–1158. doi: 10.1098/rsif.2008.0151

O'Brien, F. J. (2011). Biomaterials & scaffolds for tissue engineering. *Mat. Today* 14, 88–95. doi: 10.1016/S1369-7021(11)70058-X

Opperman, L. A. (2000). Cranial sutures as intramembranous bone growth sites. *Dev. Dyn.* 219, 472–485 doi: 10.1002/1097-0177(2000)9999:9999<::aid-dvdy1073>3.0.co;2-f

Patel, Z. S., Young, S., Tabata, Y., Jansen, J. A., Wong, M. E., and Mikos, A. G. (2008). Dual delivery of an angiogenic and an osteogenic growth factor for bone regeneration in a critical size defect model. *Bone* 43, 931–940. doi: 10.1016/j.bone.2008.06.019

Phelps, E. A., and Garcia, A. J. (2009). Update on therapeutic vascularization strategies. *Regener. Med. Res.* 4, 65–80. doi: 10.2217/17460751.4.1.65

Reid, R. L. (1968). Hernia through an iliac bone-graft donor site. *J. Bone Joint* 50, 757–760. doi: 10.2106/00004623-196850040-00012

Scotti, C., Piccinini, E., Takizawa, H., Todorov, A., Bourgine, P., Papadimitropoulos, A., et al. (2013). Engineering of a functional bone organ through endochondral ossification. *Proc. Natl. Acad. Sci. U.S.A.* 110, 3997–4002. doi: 10.1073/pnas.1220108110

Scotti, C., Tonnarelli, B., Papadimitropoulos, A., Scherberich, A., Schaeren, S., Schauerte, A., et al. (2010). Recapitulation of endochondral bone formation using human adult mesenchymal stem cells as a paradigm for developmental engineering. *Proc. Natl. Acad. Sci. U.S.A.* 107, 7251–7256. doi: 10.1073/pnas.1000302107

Sheehy, E. J., Kelly, D. J., and O'Brien, F. J. (2019). Biomaterial-based endochondral bone regeneration: a shift from traditional tissue engineering paradigms to developmentally inspired strategies. *Mat. Today Bio.* 3:100009. doi: 10.1016/j.mtbio.2019.100009

Sheehy, E. J., Mesallati, T., Kelly, L., Vinardell, T., Buckley, C. T., and Kelly, D. J. (2015). Tissue engineering whole bones through endochondral ossification: regenerating the distal phalanx. *Biores. Open Access* 4, 229–241. doi: 10.1089/biores.2015.0014

Shields, K. J., Beckman, M. J., Bowlin, G. L., and Wayne, J. S. (2004). Mechanical properties and cellular proliferation of electrospun collagen type II. *Tissue Eng.* 10, 1510–1517. doi: 10.1089/ten.2004.10.1510

Sohier, J., Corre, P., Perret, C., Pilet, P., and Weiss, P. (2014). Novel and simple alternative to create nanofibrillar matrices of interest for tissue engineering. *Tissue Eng. Part C Met.* 20, 285–296. doi: 10.1089/ten.TEC.2013.0147

St John, T. A., Vaccaro, A. R., Sah, A. P., Schaefer, M., Berta, S. C., Albert, T., et al. (2003). Physical and monetary costs associated with autogenous bone graft harvesting. *Am. J. Ortho.* 32, 18–23.

Thompson, E. M., Matsiko, A., Kelly, D. J., Gleeson, J. P., and O'Brien, F. J. (2016). An endochondral ossification-based approach to bone repair: chondrogenically primed mesenchymal stem cell-laden scaffolds support greater repair of critical-sized cranial defects than osteogenically stimulated constructs *in vivo*. *Tissue Eng. Part A* 22, 556–567. doi: 10.1089/ten.tea.2015.0457

van Wachem, P. B., van Luyn, M. J., Olde Damink, L. H., Dijkstra, P. J., Feijen, J., and Nieuwenhuis, P. (1994). Biocompatibility and tissue regenerating capacity of crosslinked dermal sheep collagen. *J. Biomed. Mater. Res.* 28, 353–363. doi: 10.1002/jbm.820280310

Vilalta, M., Degano, I. R., Bago, J., Gould, D., Santos, M., Garcia-Arranz, M., et al. (2008). Biodistribution, long-term survival, and safety of human adipose tissue-derived mesenchymal stem cells transplanted in nude mice by high sensitivity non-invasive bioluminescence imaging. *Stem Cells Dev.* 17, 993–1003. doi: 10.1089/scd.2007.0201

Visser, J., Gawlitta, D., Benders, K. E. M., Toma, S. M. H., Pouran, B., van Weeren, P. R., et al. (2015). Endochondral bone formation in gelatin methacrylamide hydrogel with embedded cartilage-derived matrix particles. *Biomaterials* 37, 174–182. doi: 10.1016/j.biomaterials.2014.10.020

Yang, Y., Wang, X., Wang, Y., Hu, X., Kawazoe, N., Yang, Y., et al. (2019). Influence of cell spreading area on the osteogenic commitment and phenotype maintenance of mesenchymal stem cells. *Sci. Rep.* 9:6891. doi: 10.1038/s41598-019-43362-43369

Younger, E. M., and Chapman, M. W. (1989). Morbidity at bone graft donor sites. *J. Ortho. Trauma* 3, 192–195. doi: 10.1097/00005131-198909000-00002

Conflict of Interest: Research undertaken in DK's laboratory at Trinity College Dublin is part-funded by Johnson & Johnson. The funder was not involved in the study design, collection, analysis, interpretation of data, the writing of this article or the decision to submit it for publication.

The remaining authors declare that the research was conducted in the absence of any commercial or financial relationships that could be construed as a potential conflict of interest.

frontiers
in Bioengineering and Biotechnology

REVIEW
published: 31 March 2020
doi: 10.3389/fbioe.2020.00121

Advancements in Soft-Tissue Prosthetics Part A: The Art of Imitating Life

Rena L. J. Cruz, Maureen T. Ross, Sean K. Powell* and Maria A. Woodruff

Institute of Health and Biomedical Innovation, Queensland University of Technology, Brisbane, QLD, Australia

Physical disfigurement due to congenital defects, trauma, or cancer causes considerable distress and physical impairment for millions of people worldwide; impacting their economic, psychological and social wellbeing. Since 3000 B.C., prosthetic devices have been used to address these issues by restoring both aesthetics and utility to those with disfigurement. Internationally, academic and industry researchers are constantly developing new materials and manufacturing techniques to provide higher quality and lower cost prostheses to those people who need them. New advanced technologies including 3D imaging, modeling, and printing are revolutionizing the way prostheses are now made. These new approaches are disrupting the traditional and manual art form of prosthetic production which are laborious and costly and are being replaced by more precise and quantitative processes which enable the rapid, low cost production of patient-specific prostheses. In this two part review, we provide a comprehensive report of past, present and emerging soft-tissue prosthetic materials and manufacturing techniques. In this review, part A, we examine, historically, the ideal properts of a polymeric material when applied in soft-tissue prosthetics. We also detail new research approaches to target specific tissues which commonly require aesthetic restoration (e.g. ear, nose and eyes) and discuss both traditional and advanced fabrication methods, from hand-crafted impression based approaches to advanced manufactured prosthetics. We discuss the chemistry and related details of most significant synthetic polymers used in soft-tissue prosthetics in Part B. As advanced manufacturing transitions from research into practice, the five millennia history of prosthetics enters a new age of economic, personalized, advanced soft tissue prosthetics and with this comes significantly improved quality of life for the people affected by tissue loss.

Keywords: prosthetic, prosthesis, polymer, silicone, additive manufacturing, maxillofacial

Edited by:
Julien Georges Didier Barthès, PROTiP Medical, France

Reviewed by:
Nihal Engin Vrana, Sparta Medical, France
Henrique de Amorim Almeida, Polytechnic Institute of Leiria, Portugal

***Correspondence:**
Sean K. Powell
sean.powell@qut.edu.au

Specialty section:
This article was submitted to Biomaterials, a section of the journal Frontiers in Bioengineering and Biotechnology

Received: *04 November 2019*
Accepted: *07 February 2020*
Published: *31 March 2020*

Citation:
Cruz RLJ, Ross MT, Powell SK and Woodruff MA (2020) Advancements in Soft-Tissue Prosthetics Part A: The Art of Imitating Life. Front. Bioeng. Biotechnol. 8:121. doi: 10.3389/fbioe.2020.00121

INTRODUCTION

Physical disfigurement due to congenital defects, trauma, or cancer causes considerable distress and physical impairment for millions of people worldwide. It impacts their economic, psychological and social wellbeing, often with devastating effects (Tagkalakis and Demiri, 2009). Significantly, physical disfigurement leads to a disruption of body image; an individual's mental perception of their physical self (Galpin, 1996; Tagkalakis and Demiri, 2009). This fundamental and critical factor of identity affects emotions and influences their decision making. In addition to body image, deformities can lead to bullying, discrimination, and reduced social and economic opportunities.

Since as early as 3000 B.C., prosthetic devices have been used to address these issues and restore both aesthetics and utility to those with disfigurement (Ring, 1991). A prosthetic device is referred to technically as a prosthesis, though it is commonly referred to as a prosthetic. For the purposes of this paper, prosthetic will be used solely as an adjective and prosthetics to refer to the prosthetic field. For optimal prosthetic performance, many factors must be considered such as fabrication methods, aesthetics, function, attachment, robustness, and cost. Fundamental to all of these is the choice of materials.

From basic carved wood in the middle of the last century (Ring, 1991) to current composite 3D printable polymers, materials and fabrication methods in prosthetics have become more sophisticated over time. Improvements in materials science and fabrication engineering, such as 3D printing, will further improve key aspects of prostheses leading to better outcomes. This article is a thorough review of the literature surrounding the applications, chemistry, fabrication processes and physical properties of the most significant polymers used in soft tissue prosthetics, both today and moving into the future.

History of Prosthetics

Early prostheses were hand formed out of the most basic natural materials. As materials knowledge improved, more sophisticated material choices became available and led to improvements in quality, durability, biocompatibility, aesthetics, and fabrication approaches. A summary of some key innovations in prosthetics over time is illustrated in **Figure 1**. In the 16th century prosthetic noses, eyes and palates were crafted from wax, parchment, wood, gold, silver, copper and hard rubber (Ring, 1991). For example, Ring et al. (Ring, 1991) describes a silver prosthetic ear, a nose and eyes made by Ambroise Paré during the 16th century. Metals were a key prosthetic material through to the 19th century with the ability to be shaped and moulded as required (Andres et al., 1992b; Lai and Hodges, 1999). Significant historical events were often a driver in materials innovation. In the 20th century, World War I and II created a large demand for prostheses and reconstruction but there was a limited supply of glass. A substitute came in the way of polymer acrylic resin which quickly became the most common prosthetic material (Artopoulou et al., 2006; Patil et al., 2008). The use of polymers as the main material in the fabrication of prostheses has continued ever since. It wasn't until the 1960's that silicones were first used by Barnhart (1960) and became the materials of choice in external soft tissue prosthetics in the 1970s (Gearhart, 1970). Silicones offer many benefits in addition to their ability to mimic soft tissue, such as their ease of manipulation, chemical inertness, durability and strength (Andres et al., 1992b). Today, researchers are making advancements with new prosthetic technology through 3D scanning, 3D modeling and 3D printing, along with modern synthesis of advanced polymeric materials. This generates novel prosthetic solutions that cannot be produced using traditional approaches, and leads to real-world clinical outcomes with a focus on higher patient satisfaction from increased customization and increased accessibility.

The Impact of Disfigurement

The psychological adjustment to an acquired disfigurement is challenging for many people, but there are very few studies that provide empirical evidence showing its impact on people's lives. One limitation of many studies conducted on congenital conditions, is that most have been retrospective, and in many cases, they consist of clinically insignificant participant numbers (Horlock et al., 2005; Steffen et al., 2008, 2010; Tam et al., 2014; Johns et al., 2016). However, the few published studies are informative. A prospective study by Li et al. (2010), which included 170 participants with a congenital malformation of the external ear (termed microtia), observed the psychological effect of this condition as well as the effects of surgical correction. The most significant findings were that psychosocial problems begin at approximately 8 years of age and significantly improve after successful surgical correction. However, a poor reconstructive result was found to result in a negative impact on body image. A study by Noor and Musa (2007) suggested that, in children born with cleft lip and/or palate, between 62 and 75% of participants report experiencing teasing (Hunt et al., 2006). Similarly, in the case of tumor surgery such as mastectomy, the negative impact on body image, sexuality and psychological health is well documented (Maguire et al., 1978; Wolberg et al., 1989; Ganz et al., 1996). However, in these cases it is often hard to distinguish whether these difficulties are due to the surgery or the cancer diagnosis itself (Metcalfe et al., 2004). Given the importance of mental health on the life experience of those with disfigurement, it is not surprising that achieving the highest level of prosthetic realism and function is of great significance.

Although prostheses have wide use in cases of both aesthetic and functional disability, from missing limbs to soft tissue damage, this paper focuses on the application of polymers to restore aesthetics.

Desirable Properties of Polymeric Prosthetic Materials

The desire for both functional and aesthetic prostheses places many unique and often conflicting demands on material selection. To explore this, five core considerations have been found that are discussed in much of the relevant literature, as illustrated in **Figure 2**; aesthetics, attachment, fabrication, robustness, and patient wellbeing. Achievement of all of these desirable properties is not yet realizable in a single material, however, several existing polymers satisfy many of these requirements. The reader is directed to Part B of this review for details of commonly used materials and their properties.

Aesthetics

The visual and tactile properties of a prosthesis are important to ensure it is of the highest realism and is as aesthetically pleasing as possible. This requires the material to be translucent, similar to natural human skin (Bulbulian, 1941;

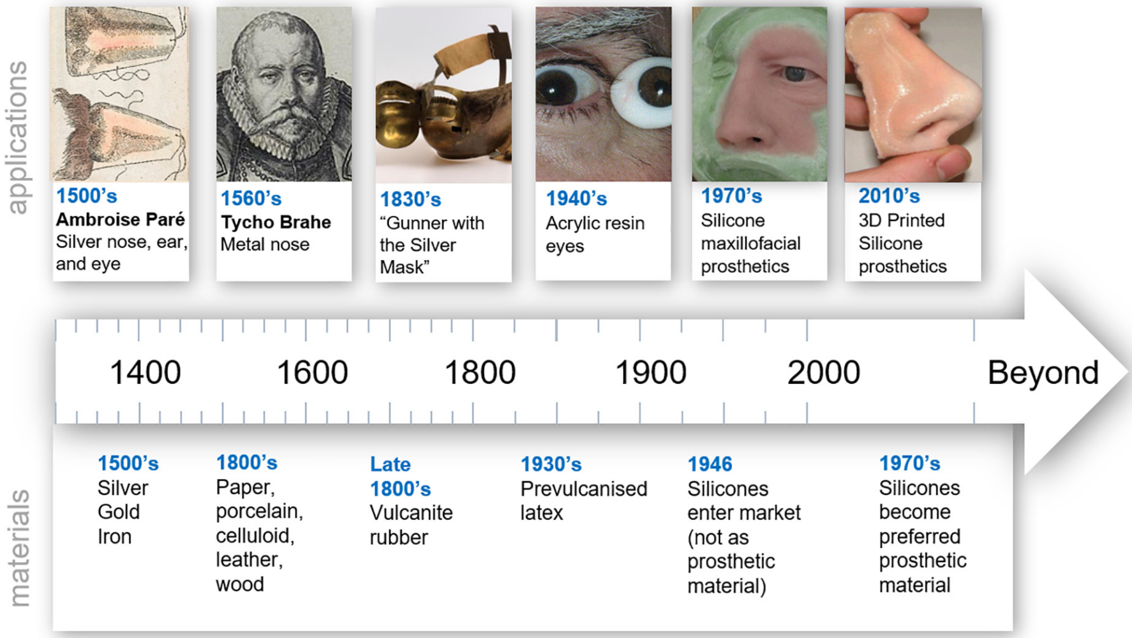

FIGURE 1 | Timeline of trends in prosthetic materials. "Hand colored illustration of a prosthetic nose. 1561 By: Ambroise Paré." Reproduced under a Creative Commons Attribution 2.0., Tycho Brahe image. Reproduced with permission from "Tycho Brahe Museum," Gunner with the silver mask. Reproduced with permission from University of Edinburgh, Ocular prosthetic image. Reproduced with permission from Oculuar Prosthethic Inc., Nose prosthesis. Reproduced with permission from JM Yates.

Lewis and Castleberry, 1980; Andres et al., 1992a), and be capable of intrinsic staining to ensure overall color and textures matches the patient's skin (Lewis and Castleberry, 1980; Andres et al., 1992a). To assist with the homogenous mixing of the colorants, the material must be sufficiently viscous during polymerization (Lewis and Castleberry, 1980). Furthermore, tints must be soluble in the material so as not to clump, and the native color of the material should be neutral to enable effective colorization (Lewis and Castleberry, 1980). Extrinsically, the material must be able to be custom colored to add realistic detailing, preferably without any further modification to the material's surface (Andres et al., 1992a).

The tactile properties of the prosthesis should also mimic those of skin and flesh to achieve a realistic feel. Skin has a particular softness and pliability when touched, so the material must be soft and with suitable surface elasticity (Bulbulian, 1941; Lewis and Castleberry, 1980; Andres et al., 1992a; Aziz et al., 2003). Lewis and Castleberry (1980) defined the ideal hardness as 25 to 35 Shore A and the ideal tensile strength as 1000 to 2000 psi (6.9 to 13.8 MPa). Surface friction is also important in maintaining a realistic feel, a coefficient of friction of 0.4 to 0.8 is ideal (Lewis and Castleberry, 1980). It is also important to ensure optimal surface tension so the material accommodates oil-based cosmetics for blending (sufficiently low critical surface tension) while still facilitating the removal of the cosmetics with soap and water for cleaning (sufficiently high critical surface tension), defined as 30 to 45 dynes/cm (Lewis and Castleberry, 1980).

Attachment

In addition to visual and tactile realism, a successful prosthesis must remain attached to the patient throughout the course of the day as they undergo their usual activities, either by direct adhesion to skin or by mechanical means (e.g. clips or magnets) (Lewis and Castleberry, 1980; Andres et al., 1992a; Polyzois et al., 2000). Direct adhesion to skin requires the chosen adhesive to be compatible with the prosthetic material; achieving adherence without causing material deterioration. The prosthesis, and therefore materials, must also be able to be used and removed without harming the patient or damaging the prosthesis (Lewis and Castleberry, 1980; Andres et al., 1992a; Polyzois et al., 2000). Often mechanical attachment methods require the prosthesis to have an integrated stiff framework. This can be achieved using internal integration of the framework within the prosthetic material and/or by bonding of the framework to the prosthetic material (Lewis and Castleberry, 1980; Andres et al., 1992a). Approaches to reduce the stresses of attachment include limiting the weight of the prosthesis (Bulbulian, 1941; Lewis and Castleberry, 1980; Andres et al., 1992a; Liu et al., 2013), limiting heat conduction to prevent contraction (Bulbulian, 1941), and ensuring sufficient elasticity to enable facial motions and other external forces, depending on the specific requirements (Bulbulian, 1941).

Fabrication

The fabrication process of a prosthesis dictates the cost of the prosthesis, repeatability, accuracy and level of detail that can be

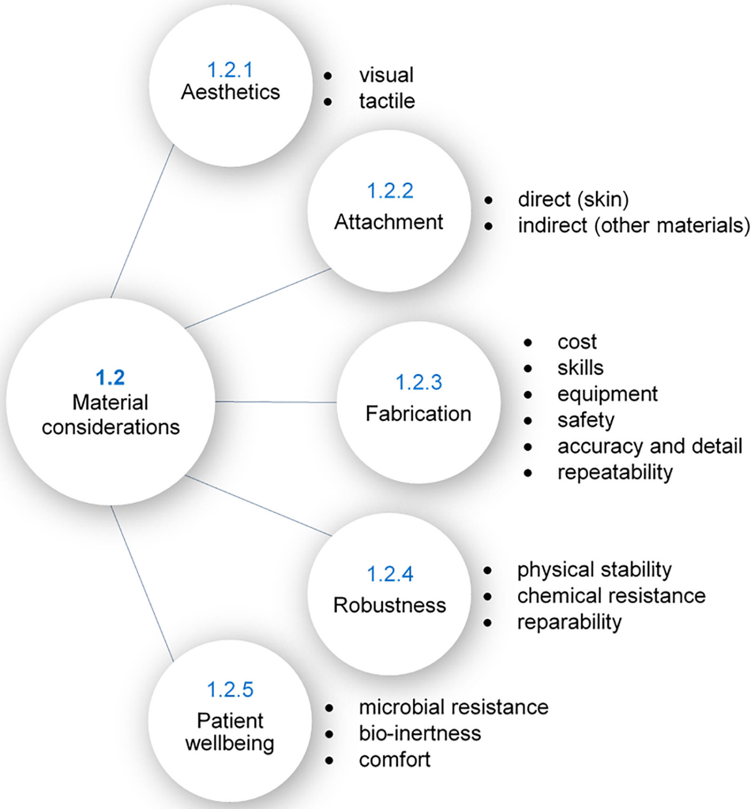

FIGURE 2 | Material specifications in prosthetics.

achieved, as well as fabrication time. Considerations regarding fabrication involve the cost of purchasing and running the required machinery, complexity of methods, cost of materials (prosthetic and otherwise), the safe processing and handling of the materials, storage requirements, shelf life, and the amount of waste produced (Bulbulian, 1941; Lewis and Castleberry, 1980; Andres et al., 1992a; Lai and Hodges, 1999). For example, one consideration is the processing temperature of the material. Some prosthetic materials can be processed at room temperature using low cost dental stone, acrylic or epoxy molds (Lewis and Castleberry, 1980; Andres et al., 1992a; Lai and Hodges, 1999), while others set in higher temperatures, requiring the use of more expensive metal molds with more complex fabrication techniques (Andres et al., 1992a; Lai and Hodges, 1999).

The level of technical skill required to process a given material, as well as the complexity of the required machinery, directly impacts the processing time and cost of the prosthesis. Many polymerization processes, for example, are highly sensitive to both technique and the processing environment (e.g. presence of moisture) (Goldberg et al., 1978; Craig et al., 1980; Aggarwal et al., 2016). This often requires highly skilled technicians so as to avoid failed attempts and waste. It is also important that technicians have sufficient time to work with (i.e. mix, pigment, degas, mold, etc.) the material during polymerization (working time). In addition, the material should be safe to work with and have no toxic by-products or other components that could harm the technician (Andres et al., 1992a).

Fabrication processes directly impact the repeatability and level of detail of the final prosthesis. In the case of molding approaches, the viscosity of the fluid during the working time should be sufficiently low to allow polymer to flow into the narrow parts of the mold (Bulbulian, 1941; Lewis and Castleberry, 1980; Andres et al., 1992a) and achieve that desired detail, while at the same time being sufficiently high to keep any added colorants homogenously suspended in the mixture for consistent coloration (10 000 to 75 000 centipoise or millipascal seconds) (Lewis and Castleberry, 1980). Other considerations include the ease of prosthesis removal from the mold and material shrinkage during processing to preserve detail and ensure the best patient fit (Bulbulian, 1941; Lewis and Castleberry, 1980; Andres et al., 1992a). Shrinking can occur both due to material properties and due to the presence of air in the mixture (Lewis and Castleberry, 1980). Most importantly, the methods should be repeatable to produce consistent high quality prostheses

(Bulbulian, 1941; Lewis and Castleberry, 1980; Andres et al., 1992a; Polyzois et al., 2000).

Robustness

It is desirable that the properties of a prosthetic material are maintained throughout its service life. Its chemical and physical stability must survive exposure to various environmental conditions [e.g. sunlight (UV), hot or cold temperatures, humid or dry conditions, etc.] (Bulbulian, 1941; Lewis and Castleberry, 1980; Polyzois et al., 2000). Materials can be sensitive to these environmental factors and undergo changes to both appearance and mechanical properties. For example, stiffening of a material can occur at 10 to 20°C above its glass transition temperature (Lewis and Castleberry, 1980). This means the chosen material should have a glass transition temperature sufficiently low to maintain flexibility in cold environments. Furthermore, the heat distortion temperature should be sufficiently high (~121°C) to prevent distortion during sterilization with boiling water or steam (Lewis and Castleberry, 1980).

It is also preferable for the material to be non-porous, resistant to staining, and therefore washable (Bulbulian, 1941; Polyzois et al., 2000; Aziz et al., 2003). This is important as during washing and regular use, prosthetic materials may be exposed to water, saliva, sweat, and other fluids (Polyzois et al., 2000; Aziz et al., 2003). If absorbed, these fluids might affect physical properties, cause color changes, and cause degeneration of the polymeric structure (Polyzois et al., 2000; Aziz et al., 2003). Furthermore, exposure to fluids is an avenue by which plasticizers and additives may leach out of materials, causing further changes to their physical properties and appearance (Lewis and Castleberry, 1980).

These issues are particularly important with the thin margins at the edges of prostheses which are made to blend with the skin, as they are susceptible to tearing. To prevent this damage, the material requires high tear strength, high tensile strength and high elongation at break (Lewis and Castleberry, 1980; Andres et al., 1992a; Aziz et al., 2003; Liu et al., 2013).

Although primary material robustness is important, it is possible with some materials that adjustment, repair or relining can be performed to extend the service life of the prosthesis (Lewis and Castleberry, 1980; Andres et al., 1992a).

Patient Wellbeing

Prostheses are often worn by patients for many hours each day, such that there are several important comfort and tissue compatibility issues that must be considered when selecting a material (Bulbulian, 1941; Lewis and Castleberry, 1980; Andres et al., 1992a). These requirements demand that the prosthetic material should be light weight, not conduct excessive heat, and have sufficient elasticity for tissue material compliance (Bulbulian, 1941; Lewis and Castleberry, 1980; Andres et al., 1992a; Aziz et al., 2003; Liu et al., 2013) so as to reduce stresses on the patient's tissues. Additionally, the material should be breathable to prevent skin irritation and odorless (Andres et al., 1992b).

The prosthetic material must also have sufficient surface wettability (Andres et al., 1992a; Aziz et al., 2003; Liu et al., 2013) as poor surface wettability leads to poor lubrication of the prosthetic surface. This leads to friction on the skin and thus skin irritation and even infection (Waters et al., 1999; Aziz et al., 2003; Preoteasa et al., 2011; Liu et al., 2013). Poor surface wettability is also correlated with the attachment of microorganisms such as Candida albicans (Park et al., 2003; Frade and Arthington-Skaggs, 2011; Ariani et al., 2012; Li et al., 2012). This commensal microorganism is found in the oral cavity and known to adhere to one another to form biofilms, thereby resisting disinfection (Ariani et al., 2012; Shinde et al., 2012; Atay et al., 2013). The effects of this can be seen in **Figure 3a**. The formation of a biofilm is not only a nuisance for those trying to keep their prostheses clean, but the microorganisms can also penetrate into the prosthetic material itself leading to bag-like defects (Ariani et al., 2012). This is particularly an issue with prostheses due to the humidity and temperature at the skin-prosthetic interface, a perfect environment for the proliferation of opportunistic bacteria and fungi (Goiato et al., 2010; Ariani et al., 2012).

A study by Ariani et al. (2012) found that skin occluded by silicone prostheses showed ten times more culturable microflora than corresponding unaffected skin. Porosity and roughness have also been shown to play important roles in microbial colonization as they provide pathways into the material and facilitate the

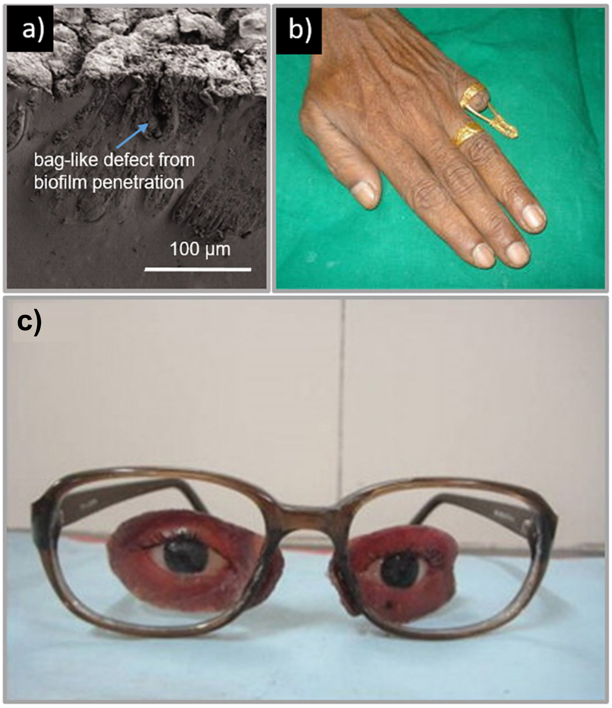

FIGURE 3 | (a) Example of a facial prosthesis with sampling side cut made at the margin that is in contact with the skin. The prosthesis shows a tear on the periphery and brownish decoloration where the material is in contact with the skin. Reproduced with permission from Taylor & Francis (Ariani et al., 2012), **(b)** Prosthetic finger; (left) brass rod connected to a ring for attachment of hollow silicone prosthesis. Reproduced with permission from *Springer* (Saxena et al., 2014). **(c)** Facial prosthesis retained by attachment to spectacles. Reproduced with permission from *Elsevier* (Pruthi and Jain, 2013).

spread of unwanted microorganisms (Fernandes et al., 2010; Li et al., 2012; Atay et al., 2013). Fernandes et al. (2010) found that the critical surface roughness is 0.2 μm, below which there is not significant reduction in microbial settling. This presents an issue, as many prostheses are processed using dental stone molds which produce rough surfaces for the colonization of microflora (Hulterström et al., 2008; Atay et al., 2013). One way to control microbial colonization is to ensure that prosthetic materials are able to be easily and thoroughly cleaned (Bulbulian, 1941; Lewis and Castleberry, 1980; Polyzois et al., 2000; Aziz et al., 2003). However, while mechanical methods of cleaning are sufficient in removing biofilms on prosthetic surfaces, they are not able to remove microbes buried within the material (Goiato et al., 2010; Ariani et al., 2012); requiring chemical soaking for sufficient disinfection (Goiato et al., 2010). Therefore the material must also be compatible with these chemical agents; including hypochlorites, peroxides, neutral peroxides with enzymes, acid enzymes, and disinfectants (Goiato et al., 2010).

Given today's materials and surgical procedures, infections are uncommon (Mohan et al., 2016). However, serious complications can lead to significant consequences for the patient, although there exist only a few studies in literature that discuss the management and treatment of infections related to soft tissue prostheses. Often, in the case of prosthetics, complications are related to the attachment method rather than the prosthetic itself. For example, a study by Hamming et al. (2009) found that in the case of osseointegrated titanium screws used to attach prosthetic ears, no implants failed, 1/3 of the ears developed abutment site skin complications and 1/9 needed soft tissue revision surgery (Hamming et al., 2009). Another more recent study by Al Kadah et al. (2018) found that 71.4% of patients who received osseointegrated silicone prosthetic ears presented with reactions of the skin surrounding the titanium implant site (Al Kadah et al., 2018). Similarly with facial prostheses, issues surrounding the attachment method have been observed. A retrospective study by Karakoca et al. (2010) evaluated 25 orbital and 13 nasal prostheses and found an estimated mean survival time of 14.5 months for the first of the patient's prosthesis, with common complications involving clip activation, bar screw and abutment loosening and detaching of the silicone from the acrylic substructure (Karakoca et al., 2010). A larger retrospective study involving 99 patients with custom facial prostheses was carried out by Papaspyrou et al. in 2018 (Papaspyrou et al., 2018). This included 53 patients with ear prostheses, 27 with eye prostheses and 19 with nasal prostheses with 82.8% or the prostheses designed to be magnetically attached via osseointegrated implants. The study found no serious complications and no osteoradionecrosis, but found 32% of the patients had skin redness, 17% with itching and 8% suffering burning sensation. In the case of breast implants, the rate of complications is relatively low. A retrospective analysis undertaken in the United Kingdom of 3002 women who received aesthetic breast prosthetics found infections were experienced by 33 patients (1.1%) (Araco et al., 2007). Pittet et al. (2005) found in their global survey of 10914 patients, a similar rate of 1.7% reported acute post-operative infection.

It is also vital that the chosen prosthetic material is bioinert and biocompatible for its intended application and is therefore non-toxic, non-allergenic, and non-carcinogenic (Lewis and Castleberry, 1980; Andres et al., 1992a; Liu et al., 2013).

APPLICATIONS OF POLYMERS IN EXTERNAL PROSTHETICS

Polymers have found extensive use in modern prosthetics. Here we briefly summarize some important research in the production of prostheses for tissue that commonly requires aesthetic restoration, as illustrated in **Figure 4**; the ear, face, eye, breast, and hand.

Prosthetic Ears

Microtia and Treacher Collins syndrome are examples of congenital disorders that result in malformations of the external ear (auricle). The ear may also be lost through trauma or cancer. Although traditional hand-made approaches comprise the majority of prosthetic ears that are fabricated today (Butler et al., 2000; Singh et al., 2013), current research seeks to leverage automated 3D scanning, modeling and 3D printing to create customized, patient specific ear prostheses.

As with prostheses for other regions of the body, traditional fabrication approaches involve taking an impression of existing

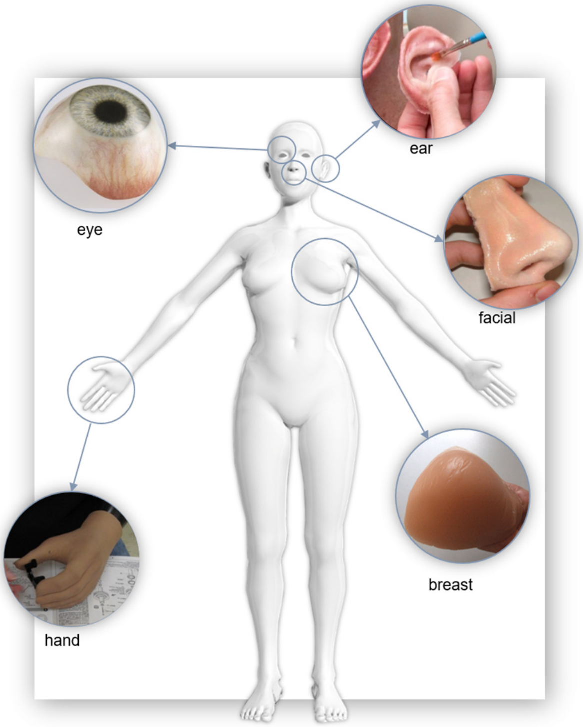

FIGURE 4 | Examples of polymer soft tissue prostheses. "Eye" Reproduced with permissions from *Erickson Labs Northwest* (Northwest_Eye_Design, 2019), "Ear" by United States Air Force photo/Staff Sgt. Kevin Iinuma, "Nose" reproduced with permission from JM Yates (Zardawi et al., 2015a), "Breast" reproduced with permission from the Cancer Australia 2019, "Hand" United States Defense Dept. photo by Fred W. Baker III.

structures (areas of attachment and anatomy to be replicated such as bilateral structures), casting the existing structures and sculpting the prosthesis, creating the mold for the prosthesis and casting the final prosthesis. For ears, this is often followed up by hand-painting fine details to provide even greater realism. A detailed discussion of traditional fabrication methodology can be found in section "Traditional Approaches."

One significant advantage of 3D digital approaches over traditional means is that patient anatomy can be obtained without the need for taking uncomforable alginated gel or plaster impressions of the ear. Subburaj et al. (2007) presented methodology for using CT images with CAD/CAM technology to create a prototype prosthesis which was then 3D printed. This work was followed up by Karatas et al. (2011) (Karatas et al., 2011), who used similar methods but included two clinical patient cases. A different approach was taken by Ciocca et al. (2007, 2010a) where a laser scanner was used to capture the patient's microtia affected ear, with the unaffected ear scanned for use as a model. Using these computer models, they manufactured prosthetic ears by 3D printing an inverse mold of the ear model, which was directly filled with silicone. Liacouras et al. (2011) have adopted a similar approach, utilizing 3D photography systems (3dMD LLC). Section "Impression" further expands on these 3D digital approaches.

Facial Prostheses

Facial prostheses can include the nose, jaw, and/or surrounding tissue areas. The highly visible and personalized nature of the face makes creating accurate and life-like prostheses both extremely important and challenging. Polymers used in this region must closely match the patient's skin tone and texture in order to blend in, and contain excellent mechanical properties to ensure robustness and flexibility; particularly in mobile regions around the mouth and jaw. Facial prostheses also often require complex substrates and supporting structures for successful attachment (Kurunmäki et al., 2008). The majority of facial prostheses use medical grade silicone for the bulk of the prosthesis, although direct 3D printed starch infiltrated with silicone has also been explored (Xiao et al., 2013, 2014; Zardawi et al., 2015a,b). Aside from matching patient surface color and texture, a central challenge of fabricating facial prostheses is long-term adherence.

In many cases, osseointegrated implants (Fantini et al., 2013) and surgical adhesives have be employed to attach the facial prosthesis to the patient. Other approaches involve attaching facial prostheses to spectacle frames which are then be worn by the patient (Ciocca et al., 2009, 2010b,c, 2016; Bhandari et al., 2014; Neto et al., 2015). In another study involving a larger facial and jaw prosthesis, prostheses were retained using magnets and an acrylic conformer (hollow cylinder) (Venugopalan et al., 2014).

Studies comparing 3D printing of facial prostheses to traditional methods have highlighted a reduced cost and time from using these technologies over more manual and traditional processes (Sansoni et al., 2009; Eggbeer et al., 2012; Sun et al., 2013; Ciocca et al., 2016). In many cases, a digital database was used to pick a nose to best match the aesthetic of the patient's face (Wu et al., 2008; Ciocca et al., 2010b,c; Qiu et al., 2011; Sun et al., 2013). This model was then smoothed onto the patient's scan to create a prosthetic design.

In recent studies, Sansoni et al. (2009) and Sun et al. (2011) both 3D printed positive models of the patients face and their prosthetic 3D design. These models were then used to mold wax patterns, and conventional fabrication was used to create the final prosthesis. Substructures were also designed and fabricated using 3D modeling and printers to give the prosthesis stability and provide attachment points. These substructures were put inside the molds before they were packed with either silicone or resin and then polymerized. Ciocca et al. (2009, 2010a) used silicone adhesive to seal the extrinsic colors of the prosthesis which was then finished with a matting dispersion liquid to reduce the gloss of the final facial prosthesis. The most recent clinical report by Ciocca et al. (2016), building on their earlier work using 3D scanning and printing for fabricating a prosthetic nose, described that reducing the minimum thickness of peripheral facial regions to 1.7 mm reduced its weight and created a more skin like appearance and feel. This allowed it to more accurately follow facial movements when speaking and smiling.

A study by Eggbeer et al. (2012) compared two different 3D printing techniques for fabricating prosthetic noses; a direct and an indirect approach. The direct approach printed the "body" of the prosthesis in a transparent, acrylate-base material (TangoPlus) using the Objet Connex 500 (Stratasys, Ltd., Eden Prairie, MN, United States) 3D printer. The "TangoPlus" material was chosen because of its similarity to silicone rubber. To complete the prosthesis, a high consistency HC20 silicone (Technovent Ltd., Newport, United Kingdom) was mill rolled to ∼0.4 mm and then wrapped around the base of the prosthesis where a primer was coated to create adhesion between the two materials. A second, viscous layer of HC20 silicone was then wrapped around the prosthesis to create a deeper and more natural color. The indirect approach for fabricating the prosthetic nose used a 3D printer to produce an inverse mold which was then filled with intrinsically stained silicone. The study compared the tensile, elongation and tear strengthen properties of the two prostheses. Despite the promise of direct 3D printing facial prostheses, the results highlighted the limitation of the TangoPlus material for this application. Despite its similar flexibility to conventional silicone, the study found its tensile strength and tear strength limits would result in early failure from daily wear and tear.

Facial Prostheses of the Eye

Prosthetic eyes can be broadly separated into two types; those for patients with a functioning eye socket and those for patients without. For those with intact eye sockets, only an eyeball prosthesis is required. Otherwise, a customized prosthesis encompassing surrounding soft tissue regions is needed to fully restore the aesthetics of the area. Due to the different mechanical and aesthetic properties between the eye and surrounding tissue, prostheses are often made from multiple materials including acrylic resin, polyurethane and silicone. Attachment of the prosthetic eye depends on the patient case and include the use of the native eye socket, medical adhesive, spectacle frames or osseointegrated implants.

Patients who require only a prosthesis of the eyeball often have the option of stock prostheses. These are mass-produced and are available in a very limited number of sizes and a small range of colors. Whilst cheaper and more accessible, they have the potential to cause irritation due to imperfect size matching. These prostheses also produce voids between the prosthesis and the tissue which collect mucous and debris, potentially leading to infection. These issues are mitigated for customized prostheses that fit well against the tissue bed of the eye socket (Sarin et al., 2015). For example, a case study for the fabrication of a custom prosthetic eye to fit into a functioning eye socket was performed by Gunaseelaraj et al. (2012). In this case, a patient was using a stock prosthesis but had been experiencing irritation due to poor fit. An impression of the eye socket was first obtained using the external tray technique; involving the injection of the ophthalmic alginate impression material through the hollow stem of the impression device (tray) which is held up against the eye socket. Although alginate was used in this study, other impression materials are also available including irreversible hydrocolloid (Sarin et al., 2015), light viscosity polyvinyl siloxane (Shankaran et al., 2016) or silicone based impression materials (Cevik et al., 2012). After the impression was cast, a wax pattern of the prosthesis was made, tried on the patient, and further sculpted to fit the socket. The wax pattern was then used to make a mold which was then filled with scleral resin. Aesthetic details (irises, pupils, fine red threads added to mimic blood vessels) were then painted on. A thin layer of clear acrylic syrup was coated onto the sclera to keep the painting and blood vessels in place. Clear acrylic was then processed onto the sclera and, before final insertion, the prosthesis was disinfected. A similar study by Sarin et al. (2015) described the use of a printed photograph of the contralateral eye in place of hand-painting the blank.

In cases where the eye socket is not functional, the prosthesis is more complex, involving composite materials each having different functions and material properties (Padmanabhan et al., 2012; Veerareddy et al., 2012; Pruthi and Jain, 2013; Shetty et al., 2016). An example of a traditional fabrication approach, described by Shetty et al. (2016), a custom prosthesis made for a patient with facial disfigurement, including the loss of the left eye. This patient did not have any bony or soft tissue underlay to aid attachment of the prosthesis and a two way silicone adhesive was chosen to attach the prosthesis to the skin. The patient chose to use a common attachment approach where the prosthesis is attached to spectacles, similar to other studies (Padmanabhan et al., 2012; Veerareddy et al., 2012; Pruthi and Jain, 2013). These other methods, however, use a heat cured acrylic resin for the soft tissue substitute, which is a more robust material for attaching to spectacles (Padmanabhan et al., 2012; Veerareddy et al., 2012; Pruthi and Jain, 2013), as depicted in **Figure 3c**. Regardless of the attachment approach, many studies suggest that wearing spectacles can improve the overall cosmetic appearance of the prosthesis (Pruthi and Jain, 2013; Shetty et al., 2016).

As an alternative to traditional approaches, Ruiters et al. (2016) described a fabrication method that used advanced manufacturing. Using CT scans of the patient's orbital cavity, a prototype prosthetic eye was designed on computer software and 3D printed in resin using the Objet Connex350 3D printer (Stratasys, 2019). This prototype was then trialed in the patient before a final prosthesis was made from acrylic resin in the traditional manner. Another advanced manufacturing approach by Ciocca and Scotti (2014) aimed to restore the aesthetic of the eye and face. Using MRI scans and 3D laser scans of the patient, the patient anatomy was obtained. CAD software was then used to design the final prosthesis. The facial prosthesis required an underlying substructure (polyamide material) which connected the nose piece to the middle of the glasses arm, and to retain the ocular shell. The inverse mold for fabricating the silicone substitute for soft tissue was 3D printed using laser sintering of polyamide powder. The mold was then filled with intrinsically colored silicone followed by post-processing with extrinsic colors, sealants and matting agents. This approach was similar to that used in other clinical case studies by the same author (Ciocca et al., 2007, 2009, 2010a,b,c, 2016; Fantini et al., 2013).

Prosthetic Hands and Fingers

Prostheses for the hand and finger include both non-functional aesthetic prostheses and, more recently, functional prostheses incorporating robotic or bionic electronic components surrounded by a life-like aesthetic outer shell; a cosmetic glove. External materials for these prostheses include both PVC and silicone, which may encase the electronics, being functionally robust and aesthetically pleasing. Investigations have been made into the effect of these cosmetic gloves on the power required from articulating prosthetic hands (Tolou et al., 2012; Smit and Plettenburg, 2013; Kuret et al., 2016), one such study termed this effect as "stiffness compensation" (Tolou et al., 2012).

The majority of case reports describing purely aesthetic prostheses involve the restoration of one or two fingers. The typical fabrication methodology used irreversible hydrocolloid to take an impression of the defect, followed by the creation of a positive cast using dental stone. The final wax patterns were then sculpted using either an impression of the contralateral finger (Shanmuganathan et al., 2011; Jacob et al., 2012; Aydin et al., 2013; Raghu et al., 2013; Saxena et al., 2014) or a donor finger (Arora et al., 2011; Kaira and Dabral, 2014) for their shape. Attachment strategies for non-functional prosthetic fingers include a glove fit over the stump of the remaining finger (Arora et al., 2011; Shanmuganathan et al., 2011; Jacob et al., 2012; Kaira and Dabral, 2014), implants (Aydin et al., 2013), or by a ring (Arora et al., 2011; Raghu et al., 2013). In the case of the glove fit approach, the diameter of the wax pattern was reduced by 0.5–1 mm so the final silicone prosthesis would have to be stretched over the stump, creating a tight fit (Arora et al., 2011; Shanmuganathan et al., 2011; Jacob et al., 2012; Kaira and Dabral, 2014). For the final prosthetic finger, the most commonly used material was RTV silicone. In some cases a thickener was added to the silicone base to give the prostheses a more natural appearance and feel (Jacob et al., 2012; Raghu et al., 2013). Prosthetic fingernails typically employ a heat cured clear acrylic material further secured with RTV silicone or a cyanoacrylate adhesive (Arora et al., 2011; Kaira and Dabral, 2014).

Saxena et al. (2014) developed a separate prosthetic finger fabrication and attachment approach as depicted in **Figure 3b**. In this case, the wax pattern of the finger was designed to be hollow to allow for the insertion of a conically shaped brass rod (5 mm thick) to be inside the prosthesis for stability. The top of this rod was then interlocked with the silicone prosthesis using a wire mesh welded to the top of the rod. The final prosthetic finger was then attached to the stump of the patient's finger by connecting the brass rod with a ring at the base of the prosthesis. This was connected to another ring worn by the patient on their intact ring finger to ensure attachment and stability (Saxena et al., 2014).

Prosthetic Breasts

For women who have undergone mastectomy, restoration of the breast tissue can be vital to their quality of life. In cases where the patient cannot or does not want reconstructive surgery, externally worn prosthetic breasts, typically an off the shelf product, can be used (Glaus and Carlson, 2009; Jetha et al., 2017). Important factors that need to be considered in the design of these prostheses are: how they feel and act comparatively to natural breasts, weight, interaction with scar tissue, and how they will be retained. The weight of prosthetic breasts is also important because of their effect on balance and posture, and the damage they cause to the shoulders and back (Rostkowska et al., 2006; Gallagher et al., 2009).

The most common material used in external prosthetic breasts is silicone gel due to its ability to mimic the feel of a natural breast (Gallagher et al., 2009). These prostheses are usually retained in a brassiere, although self-supporting prostheses are also available. One of the disadvantages of using silicone gel for prosthetic breasts, however, is their weight (Gallagher et al., 2009). Because of this, there is some research around alternative designs for light-weight prostheses, with several patented. In some cases, polyurethane film was chosen as the material for the outer skin layer (Huang, 2009; Laghi and Vint, 2012). For example, Huang (2009) designed a prosthetic breast with a two chamber design underneath the outer polyurethane layer. One chamber contained silicone gel to ensure the prosthesis maintained the ideal feel, and the second chamber contained a lighter substance such as air, liquid or a foamed material to reduce the overall weight of the prosthesis. Another approach taken by Laghi and Vint (2012) replaced the use of silicone gel with a co-polymer gel filler comprising mineral oil, thermoplastic and glass microspheres. This enabled the clinician to heat the prosthesis and remold it for patient customization, unlike silicone prosthetic breasts which have a permanent shape determined by the mold used for manufacturing (Laghi and Vint, 2012).

The use of CAD/CAM technology for the fabrication of personalized prosthetic breasts is described in Eggbeer and Evans (2011). Similar to their approach used for the production of a personalized prosthetic nose (Eggbeer et al., 2012), the authors used a 3DMD 3D scanning system (3dMD LLC) to capture the torso of the patient post-mastectomy. To produce the computer model of the final prosthesis, a scan of the contralateral breast was mirrored. From this model, a two-part mold was designed with two holes – one for injection and the second as a vent. This mold was then 3D printed in clear resin using stereolithography. The advantages of using stereolithography for the mold was the ability to print the mold in a translucent material so they could ensure the mold was filled. To reduce the weight of the prosthesis from that of a silicone-gel-only prosthesis, a low-density, open-cell foam polyurethane was molded for the center of the prosthesis which was then surrounded by silicone.

Given the range of available sizes, shapes, weights and colors, the use of off-the-shelf prosthetic breasts provide many options for women post-mastectomy (Gallagher et al., 2009; Glaus and Carlson, 2009). With the rise in 3D printing for fabricating prostheses, the ability to produce personalized prosthetic breasts matching the patients' natural breasts will become widely available.

FABRICATION METHODS FOR EXTERNAL PROSTHETICS

Traditional Approaches

Many different prostheses are traditionally fashioned by highly skilled prosthetic technicians, also known as anaplastologists or prosthetists (Larson, 2014). The technicians build up the prostheses over several steps, beginning with taking an impression of the relevant anatomy, followed by sculpting and molding, with the prosthesis cast in the mold before detail is added (Larson, 2014).

Impression

The traditional method for fabricating a prosthesis often requires taking impressions of the existing tissue structures on the patient (Castillo and Ruiz, 2012). These structures include anatomical features and, in the case of prostheses with mechanical attachments, the location of the abutments. These abutments are connected to osseointegrated implants and are used to attach a prosthesis to the wearer through the use of a bar onto which the prosthesis may be clipped [as shown in **Figure 5a** or by the use of magnets (Karakoca et al., 2008)]. The impression is fundamental in ensuring passive fit of the finished prosthesis; defined as "the absence of strain development following framework fixation," or as a 10–150 μm gap between framework and abutments (Pozzi et al., 2013). The bending moments and loading stresses of a misfit may result in damage to the prosthesis or to the patient's bone; including loss of attachment, fracture of veneering material, screw loosening, framework fracture, screw fracture, implant fracture, bone remodeling, micro-damage, and/or loss of osseointegration (Lee et al., 2008; Pozzi et al., 2013).

The most common impression materials are polyvinyl siloxane and polyether; studies comparing these two materials have found no difference in resulting accuracy of the impression (**Figure 6b**; Kubon and Anderson, 2003; Lee et al., 2008; Baig, 2014). Irreversible hydrocolloid (known more commonly as dental alginate) and silicone also appear commonly as impression materials in prosthetic and dental literature (Coleman et al., 1995; Mathews et al., 2000; Kubon and Anderson, 2003; Baig, 2014). Impression material can be supported by a rigid material such as impression plaster, acrylic tray resin (**Figure 6c**), or wire mesh (Hutcheson and Udagama, 1980; Coleman et al., 1995;

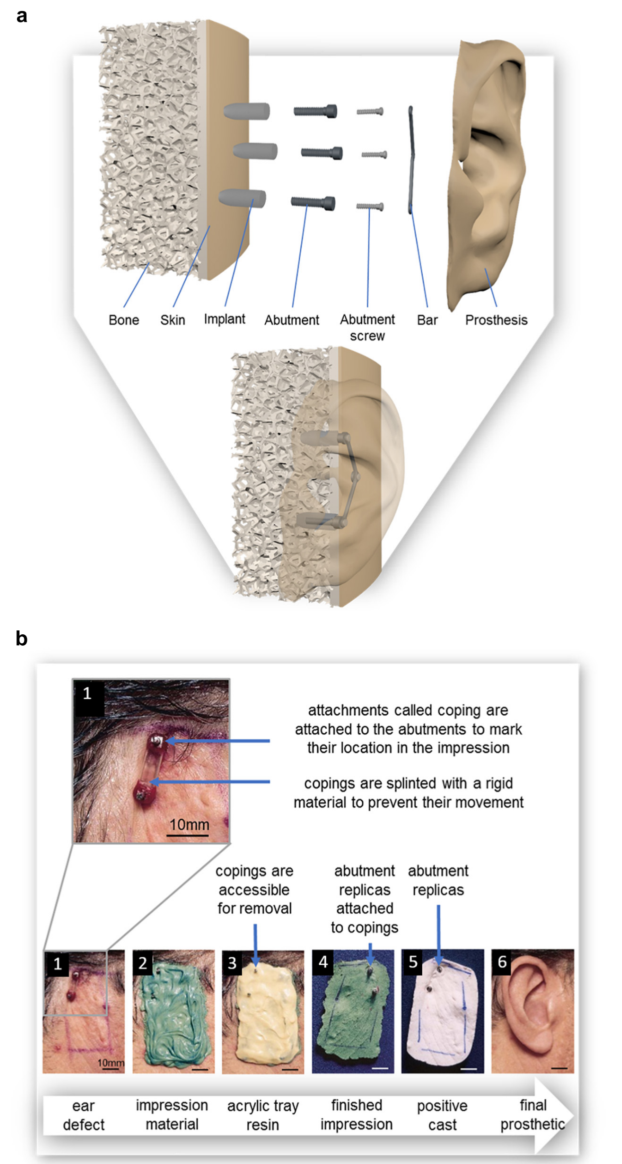

FIGURE 5 | (a) Diagram of osseointegrated implants for the use of a bar and clip prosthetic attachment system; exploded view and assembled view, **(b)** The pick-up method for taking an impression of (1) the defect site, in this case the location of a missing ear; where attachments called impression copings are attached to the abutments prior to the (2) application of the polyvinyl siloxane impression material and are removed with (3) the custom-made impression tray; (4) Abutment replicas are attached to the impression copings after the impression is set so that they can be incorporated into (5) a positive cast of the defect on which 6) the final prosthesis is sculpted. Reproduced with permission from *Elsevier* (Kubon and Anderson, 2003).

Wolfaardt and Coss, 1996; Kubon and Anderson, 2003; Karakoca et al., 2008). The use of impression plaster as a support material requires the application of a thick layer, the weight of which is known to cause distortion of the soft tissues during impression, but with minimal expansion during setting which would have caused further distortion of the impression (Coleman et al., 1995; Kubon and Anderson, 2003). Although acrylic tray resin is known to contract during polymerization distorting the impression, this is minimized by the addition of fillers (Kubon and Anderson, 2003). Acrylic support can also be relatively thin, resulting in a lightweight impression. The greatest disadvantage is the exothermic setting of acrylic which may cause discomfort and even burn the patient's skin (Kubon and Anderson, 2003; Karakoca et al., 2008).

Impressions are preferably taken with the patient in a physiological rest position (i.e. sitting upright) to maintain accuracy, as lying down may cause distortion of the soft tissues (Kubon, 2001; Kubon and Anderson, 2003). Taking an impression may require the patient to remain still for several minutes, during which time the patient may experience discomfort or irritation from the impression material (Castillo and Ruiz, 2012).

To include the location of the abutments in the impression, temporary attachments called impression copings are placed onto the abutments, these copings may be splinted with a rigid material to prevent their individual movement while taking the impression (**Figure 6a**; Kubon and Anderson, 2003; Lee et al., 2008; Pozzi et al., 2013), a practice supported by most recent studies (Lee et al., 2008; Pozzi et al., 2013; Baig, 2014). Low shrinking autopolymerising acrylic resin is the most common material used for splinting (Lee et al., 2008; Pozzi et al., 2013). Alternatively, impression plaster can be used. While impression plaster sets quickly, is easy to handle, is less time consuming and less expensive than acrylic resin, it is also susceptible to fracture (Pozzi et al., 2013).

Impressions of the copings are either taken with transfer (i.e. closed tray) or pick up (i.e. open tray) methods (Kubon, 2001; Chee and Jivraj, 2006; Lee et al., 2008; Ahmed et al., 2010; Pozzi et al., 2013). In transfer methods, impressions are taken of copings and the surrounding structures with closed impression trays. The copings remain connected to the abutments as the impression is removed. In pick up methods such as that depicted in **Figure 5b**, impressions are taken of copings and the surrounding structures with custom made trays with openings to access the copings (**Figure 5b-3**). The copings can then be unscrewed and removed with the impression. Studies have indicated that pick up methods produce more accurate results with regards to the location of abutments (Chee and Jivraj, 2006; Baig, 2014).

Cast and Sculpture

Casts are produced by pouring plaster or dental stone into the impressions (Kubon and Anderson, 2003; Castillo and Ruiz, 2012). From these casts the prosthesis can then be sculpted by hand in dental wax using carving tools, bristle brushes and an alcohol torch (Guttal et al., 2009; Castillo and Ruiz, 2012), though sometimes clay is used. This is the most time consuming step in fabrication and the final result is highly dependent on the skills of the technician (Castillo and Ruiz, 2012). The model is sculpted from descriptions of a pre-existing structure (Castillo and Ruiz, 2012) or, in the cases where bilateral structures are present (e.g. an existing ear), by repetitive comparison with a cast of those bilateral structures, as shown in **Figure 6b**.

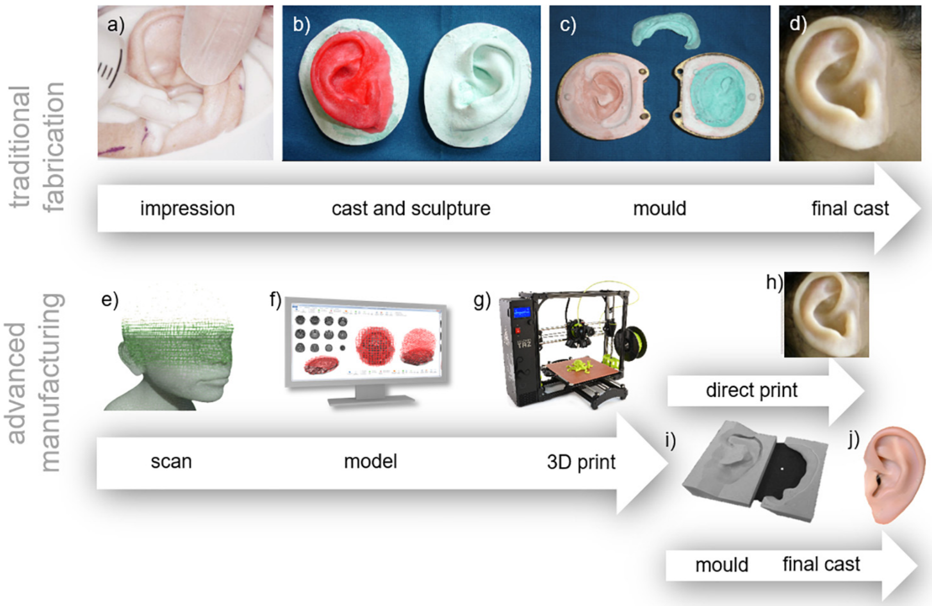

FIGURE 6 | Comparison of traditional and advanced techniques. Traditional techniques follow the workflow of **(a)** impression taking - Reproduced with permission from John Wiley and Sons (Mathews et al., 2000), **(b)** casting existing structures and sculpture of the prosthesis, **(c)** creating the mould, and **(d)** final cast – Reproduced with permission from Elsevier (Subburaj et al., 2007), **(e)** 3D scanning, **(f)** 3D modeling, **(g)** 3D printing, reproduced under CC BY-SA 4.0 International by Fargo Additive Manufacturing Equipment 3D **(h)** the final prosthesis or **(i)** the mold for panel **(j)** the final cast.

Mold

Molds, like those shown in **Figure 6c**, are then made using the wax model described above. Previously, when prostheses were made with polymers that required high temperatures to cure, metal molds were used (Guerra and Canada, 1976; May and Guerra, 1978; Oral and Zini, 1978; Choy et al., 1981; Chambers et al., 1996; Lund, 1996; Lai and Hodges, 1999; Mekayarajjananonth et al., 2003). The fabrication of these molds was difficult, expensive, and time consuming (Zini et al., 1975; Lund, 1996; Lai and Hodges, 1999); resulting in highly expensive prostheses for those with disfigurements. They were produced by first creating investment models; replicas of the wax model made with a material able to withstand high temperatures (e.g. dental stone). Then linotype metal melted to 260°C was poured onto the investment models which had been heated to 150°C (Zini et al., 1975; Guerra and Canada, 1976).

Today, plaster and dental stone (gypsum) molds are produced using the "lost wax method," where plaster or dental stone is poured over the wax model and then the wax is simply removed with hot water (Chambers et al., 1996; Lund, 1996; Mekayarajjananonth et al., 2003; Guttal et al., 2009; Castillo and Ruiz, 2012). These molds are easy to construct and are inexpensive, while maintaining accuracy. They are, however, quite fragile and susceptible to fracture, even when reinforced (Chambers et al., 1996; Lund, 1996; Lai and Hodges, 1999; Mekayarajjananonth et al., 2003). Sometimes damage can be corrected, but often the entire mold (and wax model) must be replaced.

Final Cast

The inner surface of the mold can be painted and prosthetic material, often tinted silicone, is poured into the mold. After the material cures, the addition of more details such as painted skin defects and facial hair can be added to produce the final prosthesis (Karakoca et al., 2008; Guttal et al., 2009; Castillo and Ruiz, 2012).

3D Printing and Advanced Manufacturing

Traditional hand-crafted approaches for manufacturing prostheses are being increasingly replaced by 3D printing and advanced manufacturing approaches which are revolutionizing the way in which we can make medical devices, proving faster, cheaper and more customized solutions. Regardless of the particular prosthesis being made, 3D printing approaches utilize the same general techniques: 3D scanning of the patient's anatomy, 3D computer modeling of the prosthesis, and either direct 3D printing of the prosthesis or printing of a mold. A visual comparison between traditional and 3D printing approaches is shown in **Figure 6**.

3D Scanning

Scanning of anatomical structures depicted in **Figure 6e** can be broadly separated into clinical medical scans and 3D surface scans. Clinical scans include computed tomography (CT) (Penkner et al., 1999; Subburaj et al., 2007; Zeng et al., 2008; Liacouras et al., 2011; Qiu et al., 2011; Sun et al., 2013; Kang et al., 2016) and magnetic resonance imaging (MRI) (Kang et al., 2016). These approaches use x-rays and nuclear magnetic effects to produce 3D images of tissue structures within the body.

Although capable of generating 3D models of patient specific anatomy, clinical scans are expensive, have typically low imaging resolution (several millimeters per voxel), and require the patient to lie down (causing distortion of the soft tissue surface) (Sun et al., 2013). Furthermore, use of these techniques has limited use due to radiation exposure in the case of CT scans, or dangerous interaction with the magnetic field for patients with metallic implants. However, by penetrating the tissue surface, they are able to detect the surfaces of concavities that cannot be accessed by surface scanners (Sun et al., 2013).

Another approach for obtaining 3D models of patient anatomy is 3D surface scanning. One technique, laser scanning, directs a laser onto the patient and the reflected light is used to determine 3D geometry. During scanning, the patient must not move and, in some cases, may be required to lie down (causing soft tissue deformation) to prevent any movement (Ciocca et al., 2010b). Alternatively, a physical cast (alginate or plaster) may be scanned in place of the patient (Ciocca and Scotti, 2004; Chandra et al., 2005; Watson and Hatamleh, 2014). These scans can either be taken from a stationary scanner (Coward et al., 1997, 2000; Ciocca and Scotti, 2004; Ciocca et al., 2007, 2010a,b,c; De Crescenzio et al., 2011; Reiffel et al., 2013; Watson and Hatamleh, 2014), or a hand held scanning device (Chandra et al., 2005). Complete patient scans from stationary scanners have been achieved where several scans must be taken from different angles and then aligned in post-processing (Ciocca and Scotti, 2004; Ciocca et al., 2007, 2010b,c; De Crescenzio et al., 2011). Handheld laser scanning approaches have also been developed, some with real time assembly of scans into larger 3D models. The motion of the scanners during scanning can be tracked with electromagnetic motion tracking (Chandra et al., 2005), a measurement arm (Reichinger et al., 2013), or preplaced visual markers (Reichinger et al., 2013). The use of lasers for scanning also introduces relatively high costs and eye safety hazards (Ciocca et al., 2010b,c).

Another approach is structured light scanning, where a light pattern is projected onto the patient and the reflected pattern is observed from several cameras (Wu et al., 2008; Feng et al., 2010; Sun et al., 2011, 2013; Rennesson, 2012). Here, the computer uses information about the distortion of the structured light pattern to determine distance to the surface and compute resultant 3D geometries. These scanners produce comparable resolution to laser scanners but without eye-safety concerns.

Lastly, 3D photography has been applied in producing 3D surface models of patient anatomy (Zardawi et al., 2015b). The 3dMD systems (3dMD LLC, Atlanta, GA, United States) use images taken simultaneously from cameras of known distances and angles to produce accurate 3D models (Liacouras et al., 2011; Sabol et al., 2011). The patient is only required to remain still for a short time and their eyes may be kept open. A similar approach, called photogrammetry, uses many photographs of the patient's anatomy taken from different locations to reconstruct a 3D point cloud of significant features which are then stitched together to produce a 3D model. One advantage of photogrammetry over other scanning techniques is the ability to use accessible cameras such as those found in smart-phones (Ross et al., 2018a).

Computer-Aided Design

Regardless of the scanning technique used, post-processing is required; such as model alignment if there are multiple scans, elimination of abnormalities by deleting/editing mesh geometry, smoothing of bumps, scaling the scan to the correct dimensions, hole filling, and remeshing (Ciocca and Scotti, 2004; Ciocca et al., 2010b; Sun et al., 2011).

Computer-aided design (CAD), also referred to as computer modeling or 3D modeling is performed using a wide variety of existing CAD programs and software suites. After scans are obtained and converted into a polygon mesh, the software is used to produce a 3D model of the required prosthesis. In some cases, scanned patient anatomy is mirrored and forms the basis for the prosthetic computer model (Ciocca et al., 2010c; De Crescenzio et al., 2011) and in other cases, a library of anatomical models are available to be used (Wu et al., 2008; Ciocca et al., 2010a,b,c; Qiu et al., 2011; Fantini et al., 2013; Sun et al., 2013). A study by Ciocca et al. (2010c) produced a partial facial prosthesis including nose using a combination of patient and library geometry.

Rapid Prototyping

Advanced manufacturing technologies of external prosthetics can be broadly divided into subtractive manufacturing and additive manufacturing. Subtractive manufacturing involves the use of a computer numerical controlled (CNC) mill to carve a prosthesis from a block of polymer material, such as polyurethane (Penkner et al., 1999). This process has recently given way to additive manufacturing, also referred to as 3D printing; a layer by layer manufacturing technique to produce 3D physical models from a CAD file (Rengier et al., 2010; Hofmann, 2014). **Figure 7** shows several common additive manufacturing approaches that are capable of fabricating complex objects out of a large range of materials including rigid polymer models, wax models, molds, and even full prostheses.

Stereolithography

In the 1980s, the first 3D printing process was developed by Charles Hull, who called it stereolithography (SLA). It became commercially available in 1988 as the SLA-250 (3D Systems, Rock Hill, SC, United States) (Ventola, 2014). As illustrated in **Figure 7e**, SLA uses a liquid photopolymer, a combination of monomer and oligomer components contained within a vat, which is selectively cured in a layer-by-layer manner via ultraviolet (UV) crosslinking (Rengier et al., 2010; Sabol et al., 2011; Hofmann, 2014). The most common approach is to write the layer patterns using a UV laser beam, although 2D image projection methods also exist. The printing bed descends by one layer height after the cure of each layer in preparation of the next layer (Hofmann, 2014).

The advantage of SLA over other techniques is that the polymers are highly cross-linked and therefore have a strong polymer network. The use of a laser to control the patterns leads to very high printing resolution. The SLA 7000, used to produce a prosthetic model (Sabol et al., 2011), printed with a minimum layer thickness of 0.0254 mm (3D_Systems, 2019). SLA can also produce polymeric materials of varying properties including biocompatible and flexible materials (Hofmann, 2014). The

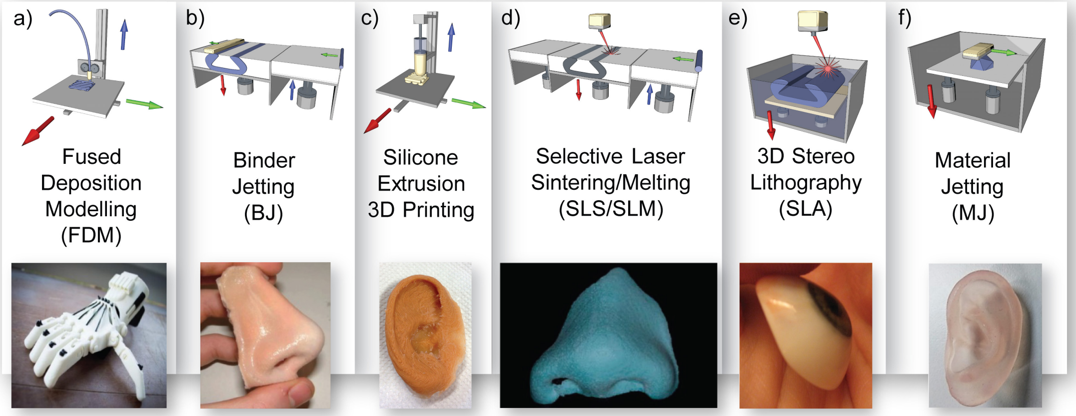

FIGURE 7 | 3D printing processes in prosthetics; **(a)** fused deposition modeling diagram with prosthetic hand example reproduced with permission from *Inpressco* (Mounika et al., 2017), **(b)** 3D powder printing diagram with prosthetic nose example reproduced with permission from JM Yates (Zardawi et al., 2015a), **(c)** silicone extrusion printing diagram with prosthetic ear example reproduced with permission from Fripp Design, **(d)** selective laser sintering diagram and wax nose reproduced with permission from Elsevier (Wu et al., 2008), **(e)** 3D stereolithography diagram with eye model, Creative Commons Attribution-ShareAlike by Topaz, and **(f)** material jetting diagram with ear model example reused with permission from Mohammed et al. of Deakin University.

materials costs are also relatively low and the process leaves little material wastage. The greatest disadvantage of SLA is potential curling and warping of the polymer. This deformation is due to the internal stresses within the structure from fast polymerization and cure shrinkage. However, by tuning the cure rate, this curling and warping can be reduced (Hofmann, 2014). The application of SLA in the fabrication of prostheses is additionally limited by the availability of photocuring materials. Currently, groups have used SLA to produce prosthetic prototypes (Sabol et al., 2011; Sun et al., 2011) and prosthetic molds (**Figures 8a–c**; Qiu et al., 2011) fabricated with acrylic resin.

Selective laser sintering

Selective laser sintering (SLS), as depicted in **Figure 7d**, uses thermal energy to fuse layers of powdered material. A roller first deposits a thin layer of powdered material and a laser then selectively sinters the powder into the desired pattern. With each layer of the printed object, the print bed descends and a layer of fine powder is spread over the print bed. The layer of powder is then selectively fused by a high powered infrared laser beam, sintering the powder into a solid material (Hofmann, 2014). The process of SLS requires the powdered material to be able to be sintered at high temperatures; such as thermoplastic materials, certain metal alloys, or ceramic materials (Rengier et al., 2010; Hofmann, 2014; Ventola, 2014).

SLA requires a great amount of energy to power the laser beam which serves as the energy source to fuse the material particles together, rather than a trigger for polymerization (as in SLA). Comparatively, one study (Sabol et al., 2011) employed the use of a 0.8 W SLA machine (3D_Systems, 2019) to produce a polymer prosthetic model, while another study (Feng et al., 2010) used a 30–50 W SLS machine (Yuan et al., 2016) to produce a wax prosthetic model with a minimum later thickness of 0.08 mm (Yuan et al., 2016). Consequently, SLS printers are more expensive to operate. SLS can be used to produce prostheses out of polystyrene resin (Wu et al., 2008) and PBS (polybutylene succinate) prototypes as well as wax prototypes (Wu et al., 2008; Feng et al., 2010).

Fused deposition modeling

Fused deposition modeling (FDM), as illustrated in **Figure 7a**, is a 3D printing method developed by Scott Crump in 1989 (Crump, 1992). The process melts and extrudes a thermoplastic polymer filament, the most popular materials being acrylonitrile butadiene styrene (ABS) and polylactic acid (PLA), through a heated nozzle and onto a printing bed to produce a 3D object in a layer-by-layer manner (Rengier et al., 2010; Hofmann, 2014). One of the complexities inherent to FDM printing is the need to print support structures for parts of the object that contain overhangs. Following printing, this support material must be removed and connection points to the object smoothed. Recently, the ability to print in multiple materials using multiple print heads has been commercialized. This has enabled the use of a water soluble support material which can then easily be removed with hot soapy water (Ciocca et al., 2010a,b,c; De Crescenzio et al., 2011; Sun et al., 2013). Due to the simplicity of the approach, FDM is an inexpensive and common method of 3D printing.

For 3D printing of prostheses, FDM has been used for the fabrication of low-cost prototypes (Subburaj et al., 2007; Sun et al., 2013) and molds (Ciocca et al., 2010a,b,c; De Crescenzio et al., 2011; He et al., 2014). A limitation of the extrusion method is the minimum physical thickness of each layer which can lead to a "staircase" effect due to the layer-by-layer process by which they are made; layer thickness is typically in the range of 0.3mm for low-cost (US$570) options (He et al., 2014) to 0.05 mm for more advanced printers (US$5000) (Aleph Objects, 2019). When used to produce molds for silicone casting, the staircase effect affects the surface quality and roughness of the resultant silicone prosthesis. He et al. (2014) published a method of polishing an FDM printed mold with an acetone vapor to reduce the "staircase" effect described, however this only works when an acetone-soluble material, such as ABS, is used as the mold material (He et al., 2014).

Material jetting

Material jetting uses inkjet (piezo electric) technology to selectively deposit liquid material in a layer by layer fashion as illustrated in **Figure 7f**. Following deposition, the material is solidified by a UV lamp in the case of a photocurable polymer or sets as it cools in the case of a thermoset material (e.g. wax).

One example is the Polyjet technology printer (Stratasys, Ltd., Eden Prairie, MN, United States) which deposits tiny droplets of polymer in a layer-by-layer fashion to produce the desired 3D object. With each layer, an ultraviolet lamp photocures the deposited polymer in preparation for the next layer.

One advantage of material jetting is that this method can produce 3D objects made of multiple materials with a high layer resolution of 0.1 mm (Stratasys, 2019). Multi-head MJ printers can produce complex multi-material objects and can tailor the material properties on a microscopic scale by selectively mixing materials during deposition (e.g. mixing rigid materials with flexible materials at chosen ratios to produce the desired properties). Like FDM, however, there is a need to print support structures for overhangs.

Mohammed et al. (2016, 2017) employed PolyJet technology to produce a multimaterial prosthetic ear (**Figures 8d,e**) and nose prototypes using the Stratasys' Connex 3 500 3D printer. This proprietary technology is designed to only print with Stratasys' materials; in this case, "Tango Plus," a clear rubber like material and "Vero," a rigid colored material. While "Tango Plus" was found to provide a soft tactile feel desirable in a prosthetic material, it was colorless. For the prosthetic ear, "Vero" was used to provide the color and rigidity to mimic cartilage tissue. The Connex printer used in this study was only capable of printing with three materials simultaneously, which prevented accurately coloring the prosthetic ear as shown in **Figure 8e**. Furthermore, it was found that printing thicknesses less than

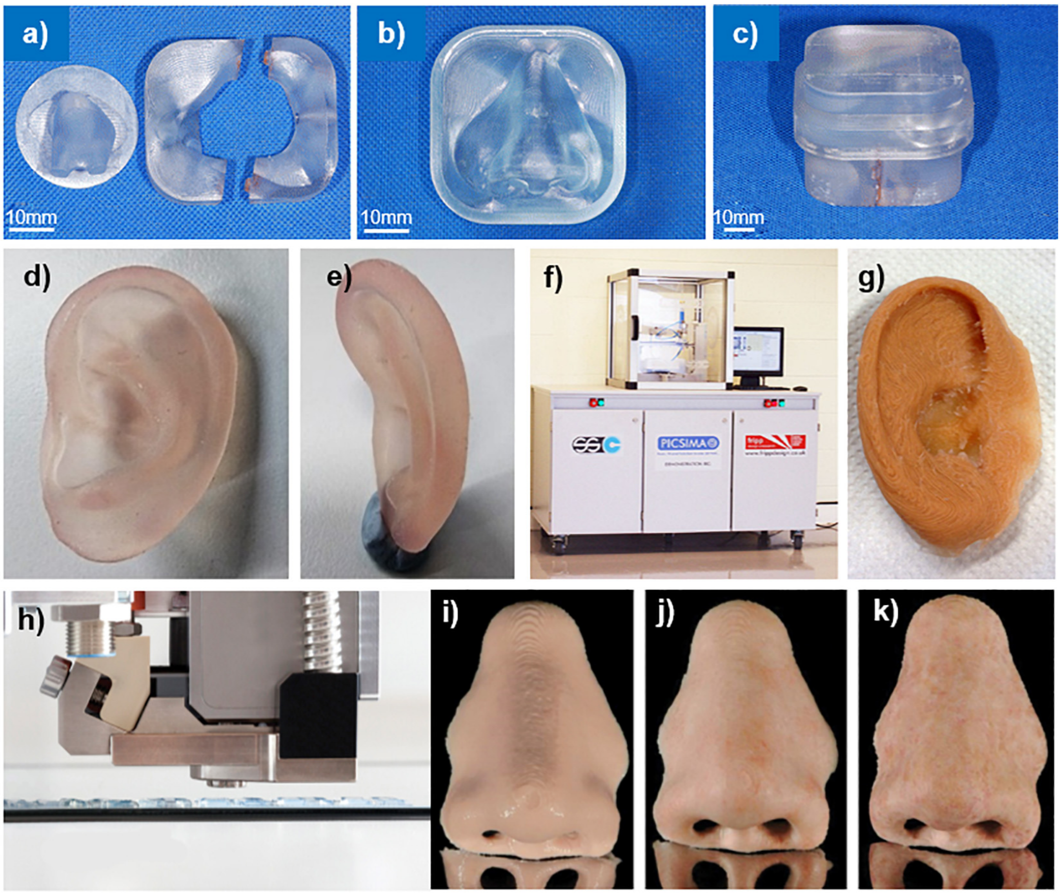

FIGURE 8 | 3D printed prosthetics; **(a)** parts 1, 2, and 3, **(b)** part 4, **(c)** complete prosthetic mold. Reproduced with permission from *Springer* (Qiu et al., 2011); PolyJet 3D printed ear model from panel **(d)** side, and **(e)** behind. Reproduced with permission from Dr. Mazher Iqbal Mohammed, Deakin University (Mohammed et al., 2016); **(f)** The Picsima silicone printer with **(g)** a 3D printed silicone ear. Reproduced with permission from Fripp Design. and **(h)** the Drop-on-Demand ACEO system with a 3D printed nose **(i)** without post-processing, **(j)** sealed with silicone coating and colored, and **(k)** polished with fine milling cutter, sealed with silicone coating, and colored. Reproduced with permission from *Elsevier* (Unkovskiy et al., 2018).

1mm lead to rupture of the prosthesis during removal of the support material. To mitigate this, the model was modified to increase the thickness of or remove areas with thicknesses below 1 mm (Mohammed et al., 2016, 2017).

Alam et al. (2017) similarly, used PolyJet technology to print hollow prosthetic eyes with medical-grade acrylic resin. These were then hand-painted to match the patient's unaffected eye. They found that the use of advanced manufacturing techniques reduced time to fabricate the prosthetic eyes from 10 to 2.5 h and resulted in superior comfort when compared with traditional methods.

A wax Thermojet Printer (3D Systems) has also been used to produce wax prosthetic prototypes (Chandra et al., 2005). These prototypes were then able to be further processed using traditional methods to produce a final prosthesis.

Powder printing

Powder printing (also known as binder jetting) uses inkjet technology from 2D printers to fuse layers of powdered material (e.g. plaster or starch) with a liquid resin (Rengier et al., 2010; Hofmann, 2014; Ventola, 2014; Fereshtenejad and Song, 2016). A schematic of this technique is shown in **Figure 7b**. With each layer of the printed object, the print bed descends and a layer of fine powder is spread over the print bed. A 2D pattern of bound powder is then produced by controlling the deposition of the liquid resin over the layer. The 3D object is then built up layer-by-layer by repeating this process (Hofmann, 2014; Fereshtenejad and Song, 2016). This solid is initially fragile (Zardawi et al., 2015b) but can be infiltrated with material such as acrylic resin (cyanoacrylate) for strength (Ciocca and Scotti, 2004; Liacouras et al., 2011; Sabol et al., 2011). One advantage of the approach is that multiple print heads can be used, each jetting a different color, enabling full color 3D printed object to be fabricated (Hofmann, 2014). Though relatively expensive compared to FDM printers, binder jetting printers such as the ZPrinters (3D_Systems, 2010) which retailed at US$ 14,900 at their least expensive (3D Systems), have been employed in the different stages of prosthetic fabrication; such as models (Ciocca and Scotti, 2004; Watson and Hatamleh, 2014) and molds (Ciocca et al., 2007; Liacouras et al., 2011; Sabol et al., 2011) with layer thicknesses as low as 0.1 mm (Liacouras et al., 2011; Sabol et al., 2011).

Due to the difficulties in directly 3D printing silicone for use in soft tissue prostheses, most studies to date have concentrated on 3D printing molds. Fripp Design (Sheffield, United Kingdom) and the University of Sheffield have bypassed the molding process and have directly 3D printed prostheses. Their initial system involved color printing onto a starch powder with a binder jetting Zprinter (3D Systems) and then infiltrating the print with medical grade silicone (Xiao et al., 2013, 2014; Zardawi et al., 2015a,b). Zardawi et al. (2015a,b) compared these 3D printed prostheses with handmade silicone polymer prostheses and found the infiltrated starch specimens had lower tensile strength, percentage elongation and tear strength. They concluded that the final 3D printed prostheses were significantly harder and had lower mechanical properties.

Silicone 3D printing

More recently, efforts have been made to directly print silicone prostheses. These printers have the potential to revolutionize prosthetic production, allowing the direct fabrication of realistic and customized silicone prostheses from 3D models.

In 2016, Fripp obtained a patent for a new 3D silicone printer technology, the Picsima (**Figures 8f,g**; Grunewald, 2016). Their patent employs room temperature vulcanizing (RTV) platinum catalyzed silicone. By selectively injecting a catalyst into a vat of the uncured silicone, a 3D silicone object can be produced.

Another attempt at direct 3D printing of silicone, described in Jindal et al. (2016, 2017), involves the development of an extrusion-based silicone 3D printer. This printer uses a two-part RTV silicone; the composition (percentage of crosslinking, filler, and catalyst as well as blend of silicone chain lengths) of which was tailored to achieve optimal mechanical properties (Jindal et al., 2016). The two silicone components are loaded into separate controlled syringe pumps mounted onto the head of the vertical axis of the printer. The components are then extruded together into a mixing device prior to being deposited onto the x-y stage. As the RTV silicone used in the printer normally cures in under one minute, a moderator was incorporated into both components to extend the working time to 30 min (Jindal et al., 2017). A thixotropic agent (a time-dependent shear thinning agent) was also added to both components to increase the viscosity of the printed silicone, thereby enabling a more rigid and stable printed structure (Jindal et al., 2017).

A recent clinical report by Unkovskiy et al. (2018) described their directly printed silicone prosthesis for a nasal defect in comparison with a traditionally fabricated prosthesis. This prosthesis was printed using the Drop-on-Demand ACEO system (Wacker Chemie AG, Munich, Germany), in which droplets of material are selectively deposited and cured with a UV lamp (**Figure 8h**). They found that the fit of the directly printed silicone prosthesis was clinically acceptable owing to the precision of the digital process. However, they noted that the marginal adaptation was not as smooth as with traditionally fabricated prostheses due to the layer thickness (0.4 mm) of the direct 3D printed prosthesis, requiring post-processing (**Figures 8i–k**).

Overcoming some of these limitations is critical for direct 3D printed silicone prosthetics. A recent rheological study by Courtial et al. (2019) found that standard silicone formulations do not provide sufficient yield stress for liquid deposition modeling 3D printing of silicone, thereby limiting their applicability (Courtial et al., 2019). To overcome this, different lengths of polyethylene glycol were added to the silicone as yield stress agents. They found this approach lead to drastic improvements without negatively impacting the final mechanical properties. Research addressing the rheological limitations of silicone were also addressed by Zhou et al. (2019), who added, nanosilica to improve their direct ink writing 3D printing (Zhou et al., 2019). This work produced a highly stretchable silicone (elongation to break of 2000%), which could be printed in high speed leading to the potential application in the direct 3D printing of robust silicone prosthetics.

Zhao et al. (2019) recently introduced photo curable approach for direct 3D printing silicone using a digital light projector (DLP) ceramic 3D printer and novel formulations of photosensitive silicone resins (Zhao et al., 2019). In this work, they produced a series of photoresins using different content of reinforcing filler silica particles and photoinitiators, resulting in DLP 3D printable silicone elastomers that have tunable mechanical properties and hardness. These silicone based elastomers, along with the other methods for direct 3D printing silicone such as extrusion-based approaches, will profoundly impact prosthetic fabrication and potentially enable directly printed prosthetics that have customizable materials properties to more precisely meet the needs of each patient.

CONCLUSION

The impact of synthetic polymers on the lives of millions of people worldwide cannot be understated, with significantly improved function and aesthetics over natural materials. The challenge for materials scientists, prosthetists and technologists is to develop synthetic materials and manufacturing capabilities to enable highly personalized and life-like prosthetics that mimic the unique properties of tissue. In addition, prosthetics are worn daily over many years and need to withstand environmental conditions such as salt water, UV light, cleaning solutions, skin secretions, biological contamination and physical wear and tear. As such, it is important to understand the chemical, physical, and biological changes of polymers over their useful lifetime to ensure the soft tissue prosthetic provides optimal performance for the patient to improve their quality of life.

Although no ideal synthetic polymer yet exists, the progression of materials science has produced many impressive advancements, with better aesthetics, attachment options, fabrication techniques, material robustness and patient wellbeing. Also important is the materials choice and design for various regions of the body.

In this part A of this two part review, we discussed the history of prosthetics, desirable properties of polymeric prosthetic materials, applications of polymers in external prosthetics and fabrication methods for external prosthetics, including traditional and advanced manufacturing approaches. In part B of this review, we will detail the chemistry of commonly used, and some historical, synthetic polymers used in soft tissue prosthetics, including the polymer fundamental chemistry and synthesis, fabrication approaches, materials properties and degradation.

Modern prosthetic materials have impressive characteristics. New and upcoming advanced manufacturing and 3D printing technologies and materials will replace traditional hand-crafting approaches and revolutionize the achievable levels of realism and function of prostheses, with the goal of improving the lives of millions of people worldwide. For many conditions, tissue engineered and biofabrication approaches promise to offer an alternative to prosthetics, restoring aesthetics and function using the patient's own tissue (Paxton et al., 2016). For example, recent studies have shown the fabrication of 3D porous ear cartilage scaffolds based on the patient's morphology and containing the patient's cartilage cells which were surgically implanted under the patient's skin (Ross et al., 2018b; Zhou et al., 2018). Although there has been much recent progress in the field, significant challenges remain before biofabrication and tissue engineering is available for routine clinical use. The potential availability of tissue engineered solutions, however, may not always be suitable or desired by the patient. Future advances in soft-tissue prosthetics will emerge from close collaboration between researchers, industry, clinicians and healthcare teams, and patients, leading to better, lower cost and more robust prosthetics.

AUTHOR CONTRIBUTIONS

MW and SP contributed to the conception of the manuscript, structured, reviewed, and revised the manuscript. RC and MR researched and wrote the first draft and revised the manuscript. All authors contributed to manuscript revision, and have read and approved the submitted version.

FUNDING

This work was supported by the Australian Government Research Training Program (2016); Advance Queensland (PhD Top Up Scholarship, 2016 and Knowledge Transfer Partnership, 2016); and MTP Connect (Grant Number PRJ2016-38).

ACKNOWLEDGMENTS

Thank you to the Australian Government, Advance Queensland, and MTP connect for the funding to conduct this research.

This two part manuscript provides an extensive review of past, present and upcoming materials and methods for the fabrication of soft-tissue prosthetics, particularly for the ears, face, eyes, breasts and hands. In Part A, it discusses literature around the desirable properties of prosthetic materials, traditional materials and methods, and reviews the latest polymer research and advanced manufacturing approaches. In Part B, this paper comprehensively reviews the chemistry of polymers used in external prostheses, including their history, chemical properties including manufacture, reinforcement approaches and material degradation. This two part review article is a key resource for those interested in the fabrication of soft tissue prostheses, and is particularly relevant given the impact of 3D printing and advanced manufacturing on the field.

REFERENCES

3D_Systems, (2019). *SLA 7000*. Available online at: https://au.3dsystems.com/3d-printers/projet-7000-hd (accessed September 13, 2019).

3D_Systems (2010). *Two Value-Priced 3D Printers Starting at Just $14,900*. Available online at: https://www.3dsystems.com/press-releases/z-corp-introduces-two-value-priced-3d-printers-starting-just-14900 (accessed September 13, 2019).

Aggarwal, H., Kumar, P., and Singh, S. V. (2016). Modified technique to improve fabrication and outcome of definitive orbital prosthesis. *Orbit* 35, 66–68. doi: 10.3109/01676830.2015.1078379

Ahmed, B., Butt, A. M., Hussain, M., Amin, M., and Yazdanie, N. (2010). Rehabilitation of nose using silicone based maxillofacial prosthesis. *J. Coll. Physicians Surg. Pak.* 20, 65–67.

Al Kadah, B., Naumann, A., Schneider, M., Schick, B., Linxweiler, M., and Papaspyrou, G. (2018). Auricular reconstruction with polyethylene implants or silicone prosthesis: a single institution experience. *J. Cranio Maxillofac. Surg.* 46, 2150–2156. doi: 10.1016/j.jcms.2018.10.005

Alam, M. S., Sugavaneswaran, M., Arumaikkannu, G., and Mukherjee, B. (2017). An innovative method of ocular prosthesis fabrication by bio-CAD and rapid 3-D printing technology: a pilot study. *Orbit* 36, 223–227. doi: 10.1080/01676830.2017.1287741

Aleph Objects (2019). *Aleph Objects Announces LulzBot Industrial-Grade Desktop 3D Printer*. Available online at: https://www.lulzbot.com/learn/announcements/aleph-objects-announces-lulzbot-industrial-grade-desktop-3d-printer (accessed September 13, 2019).

Andres, C. J., Haug, S. P., Brown, D. T., and Bernal, G. (1992a). Effects of environmental factors on maxillofacial elastomers: part II—report of survey. *J. Prosthet. Dent.* 68, 519–522. doi: 10.1016/0022-3913(92)90422-7

Andres, C. J., Haug, S. P., Munoz, C. A., and Bernal, G. (1992b). Effects of environmental factors on maxillofacial elastomers: part I—literature review. *J. Prosthet. Dent.* 68, 327–330. doi: 10.1016/0022-3913(92)90339-c

Araco, A., Gravante, G., Araco, F., Delogu, D., Cervelli, V., and Walgenbach, K. (2007). Infections of breast implants in aesthetic breast augmentations: a single-center review of 3,002 patients. *Aesth. Plast. Surg.* 31, 325–329. doi: 10.1007/s00266-006-0156-y

Ariani, N., Vissink, A., van Oort, R. P., Kusdhany, L., Djais, A., Rahardjo, T. B. W., et al. (2012). Microbial biofilms on facial prostheses. *Biofouling* 28, 583–591. doi: 10.1080/08927014.2012.698614

Arora, D., Singh, S., Shakila, R., Jagdish, S. K., Anand, S., Kumar, V. R. A., et al. (2011). Finger prostheses - overcoming a social stigma: clinical case reports. *Indian J. Multidiscip. Dent.* 2, 407–410.

Artopoulou, I.-I., Montgomery, P. C., Wesley, P. J., and Lemon, J. C. (2006). Digital imaging in the fabrication of ocular prostheses. *J. Prosthet. Dent.* 95, 327–330. doi: 10.1016/j.prosdent.2006.01.018

Atay, A., Piskin, B., Akin, H., Sipahi, C., Karakas, A., and Saracli, M. A. (2013). Evaluation of *Candida albicans* adherence on the surface of various maxillofacial silicone materials. *J. Mycol. Med.* 23, 27–32. doi: 10.1016/j.mycmed.2012.12.005

Aydin, C., Nemli, S. K., and Yilmaz, H. (2013). Esthetic, functional, and prosthetic outcomes with implant-retained finger prostheses. *Prosthet. Orthot. Int.* 37, 168–174. doi: 10.1177/0309364612449850

Aziz, T., Waters, M., and Jagger, R. (2003). Analysis of the properties of silicone rubber maxillofacial prosthetic materials. *J. Dent.* 31, 67–74. doi: 10.1016/s0300-5712(02)00084-2

Baig, M. R. (2014). Accuracy of impressions of multiple implants in the edentulous arch: a systematic review. *Int. J. Oral Maxillofac. Implants* 29, 869–880. doi: 10.11607/jomi.3233

Barnhart, G. W. (1960). A new material and technic in the art of somato-prosthesis. *J. Dent. Res.* 39, 836–844. doi: 10.1177/00220345600390041001

Bhandari, A., Manvi, P., Mehrotra, A., and Rao, Y. (2014). A simplified and easy approach for the fabrication of nasal prosthesis: a clinical report. *J. Indian Prosthodont. Soc* 14, 313–318. doi: 10.1007/s13191-014-0371-1

Bulbulian, A. H. (1941). Repair of facial defects with prosthesis using a latex compound. *Am. J. Orthod. Oral Surg.* 27, A323–A327.

Butler, D. F., Gion, G. G., and Rapini, R. P. (2000). Silicone auricular prosthesis. *J. Am. Acad. Dermatol.* 43, 687–690. doi: 10.1067/mjd.2000.107503

Castillo, H. I. M., and Ruiz, V. M. (2012). "Design and rapid fabrication of customised ear prosthesis: a case study in biomedical engineering," in *Proceedings of the ASME 2012 International Mechanical Engineering Congress and Exposition* (New York, NY: American Society of Mechanical Engineers), 351–358.

Cevik, P., Dilber, E., and Eraslan, O. (2012). Different techniques in fabrication of ocular prosthesis. *J. Craniofac. Surg.* 23, 1779–1781. doi: 10.1097/SCS.0b013e31826701bb

Chambers, M. S., Lemon, J. C., Martin, J. W., and Wesley, P. J. (1996). A hybrid-mold technique for fabricating facial prostheses. *J. Prosthet. Dent.* 75, 53–55. doi: 10.1016/s0022-3913(96)90417-5

Chandra, A., Watson, J., Rowson, J. E., Holland, J., Harris, R. A., and Williams, D. J. (2005). Application of rapid manufacturing techniques in support of maxillofacial treatment: evidence of the requirements of clinical applications. *Proc. Inst. Mech. Eng. Part B J. Eng. Manuf.* 219, 469–475. doi: 10.1243/095440505x32300

Chee, W., and Jivraj, S. (2006). Impression techniques for implant dentistry. *Br. Dent. J.* 201, 429–432.

Choy, E., Hutton, J. E., and Lemons, J. E. (1981). A comparison of three techniques for fabricating metal molds. *J. Prosthet. Dent.* 46, 430–436. doi: 10.1016/0022-3913(81)90453-4

Ciocca, L., Bacci, G., Mingucci, R., and Scotti, R. (2009). CAD-CAM construction of a provisional nasal prosthesis after ablative tumour surgery of the nose: a pilot case report. *Eur. J. Cancer Care* 18, 97–101. doi: 10.1111/j.1365-2354.2008.01013.x

Ciocca, L., De Crescenzio, F., Fantini, M., and Scotti, R. (2010a). CAD/CAM bilateral ear prostheses construction for Treacher Collins syndrome patients using laser scanning and rapid prototyping. *Comput. Methods Biomech. Biomed. Eng.* 13, 379–386. doi: 10.1080/10255840903251304

Ciocca, L., Fantini, M., De Crescenzio, F., Persiani, F., and Scotti, R. (2010b). New protocol for construction of eyeglasses-supported provisional nasal prosthesis using CAD/CAM techniques. *J. Rehabil. Res. Dev.* 47, 595–604.

Ciocca, L., Fantini, M., Marchetti, C., Scotti, R., and Monaco, C. (2010c). Immediate facial rehabilitation in cancer patients using CAD–CAM and rapid prototyping technology: a pilot study. *Support. Care Cancer* 18, 723–728. doi: 10.1007/s00520-009-0676-5

Ciocca, L., Mingucci, R., Gassino, G., and Scotti, R. (2007). CAD/CAM ear model and virtual construction of the mold. *J. Prosthet. Dent.* 98, 339–343. doi: 10.1016/S0022-3913(07)60116-4

Ciocca, L., and Scotti, R. (2004). CAD-CAM generated ear cast by means of a laser scanner and rapid prototyping machine. *J. Prosthet. Dent.* 92, 591–595. doi: 10.1016/j.prosdent.2004.08.021

Ciocca, L., and Scotti, R. (2014). Oculo-facial rehabilitation after facial cancer removal: updated CAD/CAM procedures. A pilot study. *Prosthet. Orthot. Int.* 38, 505–509. doi: 10.1177/0309364613512368

Ciocca, L., Tarsitano, A., Marchetti, C., and Scotti, R. (2016). Updates on the construction of an eyeglass-supported nasal prosthesis using computer-aided design and rapid prototyping technology. *J. Prosthodont.* 25, 61–65. doi: 10.1111/jopr.12332

Coleman, A. J., Schweiger, J. W., Urquiola, J., and Tompkins, K. A. (1995). A two-stage impression technique for custom facial prostheses. *J. Prosthet. Dent.* 73, 370–372. doi: 10.1016/s0022-3913(05)80333-6

Courtial, E.-J., Perrinet, C., Colly, A., Mariot, D., Frances, J.-M., Fulchiron, R., et al. (2019). Silicone rheological behavior modification for 3D printing: evaluation of yield stress impact on printed object properties. *Addit. Manuf.* 28, 50–57. doi: 10.1016/j.addma.2019.04.006

Coward, T. J., Scott, B. J. J., Watson, R. M., and Richards, R. (2000). Laser scanning of the ear identifying the shape and position in subjects with normal facial symmetry. *Int. J. Oral Maxillofac. Surg.* 29, 18–23. doi: 10.1034/j.1399-0020.2000.290104.x

Coward, T. J., Watson, R. M., and Scott, B. J. J. (1997). Laser scanning for the identification of repeatable landmarks of the ears and face. *Br. J. Plast. Surg.* 50, 308–314. doi: 10.1016/s0007-1226(97)90538-5

Craig, R. G., Koran, A., and Yu, R. (1980). Elastomers for maxillofacial applications. *Biomaterials* 1, 112–117. doi: 10.1016/0142-9612(80)90010-1

Crump, S. S. (1992). Apparatus and method for creating three-dimensional objects. U.S. Patent No 5,121,329. Washington, DC: U.S. Patent and Trademark Office.

De Crescenzio, F., Fantini, M., Ciocca, L., Persiani, F., and Scotti, R. (2011). Design and manufacturing of ear prosthesis by means of rapid prototyping technology. *Proc. Inst. Mech. Eng. Part H J. Eng. Med.* 225, 296–302. doi: 10.1243/09544119JEIM856

Eggbeer, D., Bibb, R., Evans, P., and Ji, L. (2012). Evaluation of direct and indirect additive manufacture of maxillofacial prostheses. *Proc. Inst. Mech. Eng. Part H J. Eng. Med.* 226, 718–728. doi: 10.1177/0954411912451826

Eggbeer, D., and Evans, P. (2011). Computer-aided methods in bespoke breast prosthesis design and fabrication. *Proc. Inst. Mech. Eng. Part H J. Eng. Med.* 225, 94–99. doi: 10.1243/09544119jeim755

Fantini, M., De Crescenzio, F., and Ciocca, L. (2013). Design and Rapid Manufacturing of anatomical prosthesis for facial rehabilitation. *Int. J. Interact. Des. Manuf.* 7, 51–62. doi: 10.1007/s12008-012-0159-7

Feng, Z., Dong, Y., Zhao, Y., Bai, S., Zhou, B., Bi, Y., et al. (2010). Computer-assisted technique for the design and manufacture of realistic facial prostheses. *Br. J. Oral Maxillofac. Surg.* 48, 105–109. doi: 10.1016/j.bjoms.2009.05.009

Fereshtenejad, S., and Song, J.-J. (2016). Fundamental study on applicability of powder-based 3D printer for physical modeling in rock mechanics. *Rock Mech. Rock Eng.* 49, 2065–2074. doi: 10.1007/s00603-015-0904-x

Fernandes, A. ÙR., Goiato, M. C., and dos Santos, D. M. (2010). Effect of weathering and thickness on roughness of acrylic resin and ocular button. *Contact Lens Anterior Eye* 33, 124–127. doi: 10.1016/j.clae.2009.12.008

Frade, J. P., and Arthington-Skaggs, B. A. (2011). Effect of serum and surface characteristics on *Candida albicans* biofilm formation. *Mycoses* 54, e154–e162. doi: 10.1111/j.1439-0507.2010.01862.x

Gallagher, P., Buckmaster, A., O'Carroll, S., Kiernan, G., and Geraghty, J. (2009). Experiences in the provision, fitting and supply of external breast prostheses: findings from a national survey. *Eur. J. Cancer Care* 18, 556–568. doi: 10.1111/j.1365-2354.2007.00898.x

Galpin, C. (1996). Body image changes associated with surgery. *Br. J. Theatre Nurs.* 6, 22–23.

Ganz, P. A., Coscarelli, A., Fred, C., Kahn, B., Polinsky, M. L., and Petersen, L. (1996). Breast cancer survivors: psychosocial concerns and quality of life. *Breast Cancer Res. Treat.* 38, 183–199. doi: 10.1007/bf01806673

Gearhart, D. F. (1970). Polyvinyl Chloride (Cordo) facial and body prostheses. *Bull. Prosthet. Res* .10, 214–218.

Glaus, S. W., and Carlson, G. W. (2009). Long-term role of external breast prostheses after total mastectomy. *Breast J.* 15, 385–393. doi: 10.1111/j.1524-4741.2009.00742.x

Goiato, M. C., Rossatti Zucolotti, B. C., Mancuso, D. N., dos Santos, D. M., Pellizzer, E. P., and Ramos Verri, F. (2010). Care and cleaning of maxillofacial prostheses. *J. Craniofac. Surg.* 21, 1270–1273. doi: 10.1097/SCS.0b013e3181e1b431

Goldberg, A. J., Craig, R. G., and Filisko, F. E. (1978). Polyurethane elastomers as maxillofacial prosthetic materials. *J. Dent. Res.* 57, 563–569. doi: 10.1177/00220345780570040501

Grunewald, S. J. (2016). *Fripp Design Finally Gains Patent for 3D Printed Silicone Picsima Process and is Now Seeking Partners.* Available online at: 3dprint.com [accessed March 16, 2016].

Guerra, O. N., and Canada, K. (1976). Open-cast technique for metal molds used in constructing facial prostheses. *J. Prosthet. Dent.* 36, 421–425. doi: 10.1016/0022-3913(76)90166-9

Gunaseelaraj, R., Karthikeyan, S., Kumar, M. N., Balamurugan, T., and Jagadeeshwaran, A. R. (2012). Custom-made ocular prosthesis. *J. Pharm. Bioallied Sci.* 4, S177–S179. doi: 10.4103/0975-7406.100264

Guttal, S. S., Patil, N. P., Thakur, S., Kumar, S., and Kulkarni, S. S. (2009). Implant-retained nasal prosthesis for a patient following partial rhinectomy: a clinical report. *J. Prosthodont.* 18, 353–358. doi: 10.1111/j.1532-849X.2008.00422.x

Hamming, K. K., Lund, T. W., Lander, T. A., and Sidman, J. D. (2009). Complications and satisfaction with pediatric osseointegrated external ear prostheses. *Laryngoscope* 119, 1270–1273. doi: 10.1002/lary.20305

He, Y., Xue, G., and Fu, J. (2014). Fabrication of low cost soft tissue prostheses with the desktop 3D printer. *Sci. Rep.* 4:6973. doi: 10.1038/srep06973

Hofmann, M. (2014). 3D printing gets a boost and opportunities with polymer materials. *ACS Macro Lett.* 3, 382–386. doi: 10.1021/mz4006556

Horlock, N., Vögelin, E., Bradbury, E. T., Grobbelaar, A. O., and Gault, D. T. (2005). Psychosocial outcome of patients after ear reconstruction: a retrospective study of 62 patients. *Ann. Plast. Surg.* 54, 517–524. doi: 10.1097/01.sap.0000155284.96308.32

Huang, C. K. (2009). Lightweight breast prosthesis. U.S. Patent No 20090299472. Washington, DC: U.S. Patent and Trademark Office.

Hulterström, A. K., Berglund, A., and Ruyter, I. E. (2008). Wettability, water sorption and water solubility of seven silicone elastomers used for maxillofacial prostheses. *J. Mater. Sci. Mater. Med.* 19, 225–231. doi: 10.1007/s10856-006-0027-8

Hunt, O., Burden, D., Hepper, P., Stevenson, M., and Johnston, C. (2006). Self-reports of psychosocial functioning among children and young adults with cleft lip and palate. *Cleft Palate Craniofac. J.* 43, 598–605. doi: 10.1597/05-080

Hutcheson, P. E., and Udagama, A. (1980). Surgical nasal prosthesis. *J. Prosthet. Dent.* 43, 78–81. doi: 10.1016/0022-3913(80)90357-1

Jacob, P. C., Shetty, K. H. M., Garg, A., and Pal, B. (2012). Silicone finger prosthesis, a clinical report. *J. Prosthodont.* 21, 631–633. doi: 10.1111/j.1532-849X.2012.00886.x

Jetha, Z. A., Gul, R. B., and Lalani, S. (2017). Women experiences of using external breast prosthesis after mastectomy. *Asia Pac. J. Oncol. Nurs.* 4, 250–258. doi: 10.4103/apjon.apjon_25_17

Jindal, S. K., Sherriff, M., Waters, M. G., and Coward, T. J. (2016). Development of a 3D printable maxillofacial silicone: part I: optimization of polydimethylsiloxane chains and cross-linker concentration. *J. Prosthet. Dent.* 116, 617–622. doi: 10.1016/j.prosdent.2016.02.020

Jindal, S. K., Sherriff, M., Waters, M. G., Smay, J. E., and Coward, T. J. (2017). Development of a 3D printable maxillofacial silicone: part II: optimization of moderator and thixotropic agent. *J. Prosthet. Dent.* 116, 617–622. doi: 10.1016/j.prosdent.2017.04.028

Johns, A. L., Lewin, S. L., and Im, D. D. (2016). Teasing in younger and older children with microtia before and after ear reconstruction. *J. Plast. Surg. Hand Surg.* 51, 205–209. doi: 10.1080/2000656X.2016.1222294

Kaira, L., and Dabral, E. (2014). Improving esthetics of finger prosthesis by glove silicone. *J. Orofac. Sci.* 6, 114–117. doi: 10.4103/0975-8844.143054

Kang, H.-W., Lee, S. J., Ko, I. K., Kengla, C., Yoo, J. J., and Atala, A. (2016). A 3D bioprinting system to produce human-scale tissue constructs with structural integrity. *Nat. Biotechnol.* 34, 312–319. doi: 10.1038/nbt.3413

Karakoca, S., Aydin, C., Yilmaz, H., and Bal, B. T. (2010). Retrospective study of treatment outcomes with implant-retained extraoral prostheses: survival rates and prosthetic complications. *J. Prosthet. Dent.* 103, 118–126. doi: 10.1016/s0022-3913(10)60015-7

Karakoca, S., Aydin, C., Yilmaz, H., and Korkmaz, T. (2008). An impression technique for implant-retained orbital prostheses. *J. Prosthet. Dent.* 100, 52–55. doi: 10.1016/S0022-3913(08)60137-7

Karatas, M. O., Cifter, E. D., Ozenen, D. O., Balik, A., and Tuncer, E. B. (2011). Manufacturing implant supported auricular prostheses by rapid prototyping techniques. *Eur. J. Dent.* 5, 472–477. doi: 10.1055/s-0039-1698921

Kubon, T. M. (2001). Creating an adaptable anterior margin for an implant-retained auricular prosthesis. *J. Prosthet. Dent.* 86, 233–240. doi: 10.1067/mpr.2001.118019

Kubon, T. M., and Anderson, J. D. (2003). An implant-retained auricular impression technique to minimize soft tissue distortion. *J. Prosthet. Dent.* 89, 97–101. doi: 10.1067/mpr.2003.16

Kuret, Z., Burger, H., Vidmar, G., and Maver, T. (2016). Impact of silicone prosthesis on hand function, grip power and grip-force tracking ability after finger amputation. *Prosthet. Orthot. Int.* 40, 744–750. doi: 10.1177/0309364615596064

Kurunmäki, H., Kantola, R., Hatamleh, M. M., Watts, D. C., and Vallittu, P. K. (2008). A fiber-reinforced composite prosthesis restoring a lateral midfacial defect: a clinical report. *J. Prosthet. Dent.* 100, 348–352. doi: 10.1016/S0022-3913(08)60235-8

Laghi, A. A., and Vint, N. (2012). Light-weight external breast prosthesis. U.S. Patent No US20120010705A1. Washington, DC: U.S. Patent and Trademark Office.

Lai, J. H., and Hodges, J. S. (1999). Effects of processing parameters on physical properties of the silicone maxillofacial prosthetic materials. *Dent. Mater.* 15, 450–455. doi: 10.1016/s0109-5641(99)00074-3

Larson, J. (2014). "Prosthetics," in *Applied Science: Science and Medicine*, ed. D. R. Franceschetti, (Pasadena, CA: Salem Press), 578–583.

Lee, H., So, J. S., Hochstedler, J. L., and Ercoli, C. (2008). The accuracy of implant impressions: a systematic review. *J. Prosthet. Dent.* 100, 285–291. doi: 10.1016/S0022-3913(08)60208-5

Lewis, D. H., and Castleberry, D. J. (1980). An assessment of recent advances in external maxillofacial materials. *J. Prosthet. Dent.* 43, 426–432. doi: 10.1016/0022-3913(80)90215-2

Li, D., Chin, W., Wu, J., Zhang, Q., Xu, F., Xu, Z., et al. (2010). Psychosocial outcomes among microtia patients of different ages and genders before ear reconstruction. *Aesth. Plast. Surg* 34, 570–576. doi: 10.1007/s00266-010-9502-1

Li, J., Hirota, K., Goto, T., Yumoto, H., Miyake, Y., and Ichikawa, T. (2012). Biofilm formation of *Candida albicans* on implant overdenture materials and its removal. *J. Dent.* 40, 686–692. doi: 10.1016/j.jdent.2012.04.026

Liacouras, P., Garnes, J., Roman, N., Petrich, A., and Grant, G. T. (2011). Designing and manufacturing an auricular prosthesis using computed tomography, 3-dimensional photographic imaging, and additive manufacturing: a clinical report. *J. Prosthet. Dent.* 105, 78–82. doi: 10.1016/S0022-3913(11)60002-4

Liu, Q., Shao, L. Q. Q., Xiang, H. F. F., Zhen, D., Zhao, N., Yang, S. G. G., et al. (2013). Biomechanical characterization of a low density silicone elastomer filled with hollow microspheres for maxillofacial prostheses. *J. Biomater. Sci. Polym. Ed.* 24, 1378–1390. doi: 10.1080/09205063.2012.762292

Lund, T. (1996). Comparison of techniques for reinforcing stone molds used to construct facial prostheses. *J. Prosthet. Dent.* 76, 297–301. doi: 10.1016/s0022-3913(96)90175-4

Maguire, G. P., Lee, E. G., Bevington, D. J., Küchemann, C. S., Crabtree, R. J., and Cornell, C. E. (1978). Psychiatric problems in the first year after mastectomy. *Br. Med. J.* 1, 963–965. doi: 10.1136/bmj.1.6118.963

Mathews, M. F., Sutton, A. J., and Smith, R. M. (2000). The auricular impression: an alternate technique. *J. Prosthodont.* 9, 106–109. doi: 10.1111/j.1532-849x.2000.00106.x

May, P. D., and Guerra, L. R. (1978). Maxillofacial prostheses of chlorinated polyethylene. *J. Biomed. Mater. Res. Part A* 12, 421–431. doi: 10.1002/jbm.820120313

Mekayarajjananonth, T., Salinas, T. J., Chambers, M. S., and Lemon, J. C. (2003). A mold-making procedure for multiple orbital prostheses fabrication. *J. Prosthet. Dent.* 90, 97–100. doi: 10.1016/s0022-3913(03)00216-6

Metcalfe, K. A., Esplen, M. J., Goel, V., and Narod, S. A. (2004). Psychosocial functioning in women who have undergone bilateral prophylactic mastectomy. *Psychooncology* 13, 14–25. doi: 10.1002/pon.726

Mohammed, M. I., Tatineni, J., Cadd, B., Peart, G., and Gibson, I. (2017). "Advanced auricular prosthesis development by 3D modelling and multi-material printing," in *Proceedings of the International Conference on Design and Technology*, Dubai, 37–43.

Mohammed, M. I., Tatineni, J., Cadd, B., Peart, P., and Gibson, I. (2016). "Applications of 3D topography scanning and multi-material additive manufacturing for facial prosthesis development and production," in *Proceedings of the 27th Annual International Solid Freeform Fabrication Symposium* (Texas, USA: Verlag nicht ermittelbar), 1695–1707.

Mohan, K., Cox, J. A., Dickey, R. M., Gravina, P., Echo, A., Izaddoost, S. A., et al. (2016). Treatment of infected facial implants. *Semin. Plast. Surg.* 30, 78–82.

Mounika, M. P., Phanisankar, S. S., and Manoj, M. (2017). Design & analysis of prosthetic hand with EMG technology in 3-D printing machine. *Int. J. Curr. Eng. Technol.* 77, 2277–4106.

Neto, R., Costa-Ferreira, A., Leal, N., Machado, M., and Reis, A. (2015). An engineering-based approach for design and fabrication of a customized nasal prosthesis. *Prosthet. Orthot. Int.* 39, 422–428. doi: 10.1177/0309364614535232

Noor, S. N., and Musa, S. (2007). Assessment of patients' level of satisfaction with cleft treatment using the Cleft Evaluation Profile. *Cleft Palate Craniofac. J.* 44, 292–303. doi: 10.1597/05-151

Northwest_Eye_Design, (2019). *Prosthetic Eyes*. Available online at: https://nweyedesign.com/eyes/ [accessed March 1, 2019].

Oral, K., and Zini, I. (1978). Direct wax method for fabrication of three-piece metal molds. *J. Prosthet. Dent.* 40, 558–562. doi: 10.1016/0022-3913(78)90093-8

Padmanabhan, T. V., Mohamed, K., Parameswari, D., and Nitin, S. K. (2012). Prosthetic rehabilitation of an orbital and facial defect: a clinical report. *J. Prosthodont.* 21, 200–204. doi: 10.1111/j.1532-849X.2011.00817.x

Papaspyrou, G., Yildiz, C., Bozzato, V., Bohr, C., Schneider, M., Hecker, D., et al. (2018). Prosthetic supply of facial defects: long-term experience and retrospective analysis on 99 patients. *Eur. Arch. Otorhinolaryngol.* 275, 607–613. doi: 10.1007/s00405-017-4835-x

Park, S. E., Periathamby, A. R., and Loza, J. C. (2003). Effect of surface-charged poly(methyl methacrylate) on the adhesion of *Candida albicans*1. *J. Prosthodont.* 12, 249–254. doi: 10.1016/S1059-941X(03)00107-4

Patil, S. B., Meshramkar, R., Naveen, B. H., and Patil, N. P. (2008). Ocular prosthesis: a brief review and fabrication of an ocular prosthesis for a geriatric patient. *Gerodontology* 25, 57–62. doi: 10.1111/j.1741-2358.2007.00171.x

Paxton, N. C., Powell, S. K., and Woodruff, M. A. (2016). Biofabrication: the future of regenerative medicine. *Tech. Orthop.* 31, 190–203. doi: 10.1097/BTO.0000000000000184

Penkner, K., Santler, G., Mayer, W., Pierer, G., and Lorenzoni, M. (1999). Fabricating auricular prostheses using three-dimensional soft tissue models. *J. Prosthet. Dent.* 82, 482–484. doi: 10.1016/S0022-3913(99)70038-7

Pittet, B., Montandon, D., and Pittet, D. (2005). Infection in breast implants. *Lancet Infect. Dis.* 5, 94–106. doi: 10.1016/S1473-3099(05)70084-0

Polyzois, G. L., Tarantili, P. A., Frangou, M. J., and Andreopoulos, A. G. (2000). Physical properties of a silicone prosthetic elastomer stored in simulated skin secretions. *J. Prosthet. Dent.* 83, 572–577. doi: 10.1016/S0022-3913(00)70017-5

Pozzi, A., Tallarico, M., Mangani, F., and Barlattani, A. (2013). Different implant impression techniques for edentulous patients treated with CAD/CAM complete-arch prostheses: a randomised controlled trial reporting data at 3 year post-loading. *Eur. J. Oral Implantol.* 6, 325–340.

Preoteasa, C. T., Nabil, S. A., Popa, L., Ghica, M. V., Ionescu, E., Maria, A., et al. (2011). Studies regarding the wettability of acrylic and silicone dental materials. *Farmacia* 59, 871–878.

Pruthi, G., and Jain, V. (2013). Light weight prosthesis for a patient with bilateral orbital exenteration-A clinical report. *J. Prosthodont. Res.* 57, 135–139. doi: 10.1016/j.jpor.2013.01.001

Qiu, J., Gu, X., Xiong, Y., and Zhang, F. (2011). Nasal prosthesis rehabilitation using CAD-CAM technology after total rhinectomy: a pilot study. *Support. Care Cancer* 19, 1055–1059. doi: 10.1007/s00520-011-1157-1

Raghu, K. M., Gururaju, C. R., Sundaresh, K. J., and Mallikarjuna, R. (2013). Aesthetic finger prosthesis with silicone biomaterial. *BMJ Case Rep.* 2013:bcr2013010385. doi: 10.1136/bcr-2013-85

Reichinger, A., Majdak, P., Sablatnig, R., and Maierhofer, S. (2013). "Evaluation of methods for optical 3-D scanning of human Pinnas," in *Proceedings of the 2013 International Conference on 3D Vision-3DV 2013* (Seattle: IEEE), 390–397.

Reiffel, A. J., Kafka, C., Hernandez, K. A., Popa, S., Perez, J. L., Zhou, S., et al. (2013). High-fidelity tissue engineering of patient-specific auricles for reconstruction of pediatric microtia and other auricular deformities. *PLoS One* 8:e56506. doi: 10.1371/journal.pone.0056506

Rengier, F., Mehndiratta, A., von Tengg-Kobligk, H., Zechmann, C. M., Unterhinninghofen, R., Kauczor, H.-U., et al. (2010). 3D printing based on imaging data: review of medical applications. *Int. J. Comput. Assist. Radiol. Surg.* 5, 335–341. doi: 10.1007/s11548-010-0476-x

Rennesson, J.-L. (2012). "A full-range of 3D body scanning solutions," in *Proceedings of the 3rd International Conference on 3D Body Scanning Technology*, Lugano, 16–17.

Ring, M. E. (1991). The history of maxillofacial prosthetics. *Plast. Reconstr. Surg.* 87, 174–184. doi: 10.1097/00006534-199101000-00031

Ross, M. T., Cruz, R., Brooks-Richards, T., Hafner, L. M., Powell, S. K., and Woodruff, M. A. (2018a). Smartphones for frugal three-dimensional scanning of the external ear with application to microtia. *J. Plast. Reconstr. Aesthet. Surg.* 71, 1362–1380. doi: 10.1016/j.bjps.2018.05.037

Ross, M. T., Cruz, R., Hutchinson, C., Arnott, W. L., Woodruff, M. A., and Powell, S. K. (2018b). Aesthetic reconstruction of microtia: a review of current techniques and new 3D printing approaches. *Virtual Phys. Prototyp.* 13, 117–130. doi: 10.1080/17452759.2018.1430246

Rostkowska, E., Bak, M., and Samborski, W. (2006). Body posture in women after mastectomy and its changes as a result of rehabilitation. *Adv. Med. Sci.* 51, 287–297.

Ruiters, S., Sun, Y., De Jong, S., Politis, C., and Mombaerts, I. (2016). Computer-aided design and three-dimensional printing in the manufacturing of an ocular prosthesis. *Br. J. Ophthalmol.* 100, 879–881. doi: 10.1136/bjophthalmol-2016-308399

Sabol, J. V., Grant, G. T., Liacouras, P., and Rouse, S. (2011). Digital image capture and rapid prototyping of the maxillofacial defect. *J. Prosthodont.* 20, 310–314. doi: 10.1111/j.1532-849X.2011.00701.x

Sansoni, G., Cavagnini, G., Docchio, F., and Gastaldi, G. (2009). Virtual and physical prototyping by means of a 3D optical digitizer: application to facial prosthetic reconstruction. *Virtual Phys. Prototyp.* 4, 217–226. doi: 10.1080/17452750903236658

Sarin, S., Gupta, R., Luthra, R. P., Sharma, V., and Ahirrao, R. (2015). Fabrication of a custom resin artificial eye for rehabilitation of a bear mauled patient - a case report. *J. Adv. Med. Dent. Sci. Res.* 3, 160–164.

Saxena, K., Sharma, A., Hussain, M. A. Z., Thombare, R. U., and Bhasin, S. S. (2014). A hollow silicone finger prosthesis with modified metal-mesh conformer. *J. Indian Prosthodont. Soc.* 14, 301–304. doi: 10.1007/s13191-012-0204-z

Shankaran, G., Deogade, S. C., and Dhirawani, R. (2016). Fabrication of a cranial prosthesis combined with an ocular prosthesis using rapid prototyping: a case report. *J. Dent.* 13, 68–72.

Shanmuganathan, N., Maheswari, M. U., Anandkumar, V., Padmanabhan, T. V., Swarup, S., and Jibran, A. H. (2011). Aesthetic finger prosthesis. *J. Indian Prosthodont. Soc.* 11, 232–237. doi: 10.1007/s13191-011-0074-9

Shetty, S., Mohammad, F., Shetty, R., and Shenoy, K. (2016). Prosthetic rehabilitation of an orbital defect for a patient with hemifacial atrophy. *J. Indian Prosthodont. Soc.* 16, 91–95. doi: 10.4103/0972-4052.175716

Shinde, R. B., Raut, J. S., and Karuppayil, M. S. (2012). Biofilm formation by *Candida albicans* on various prosthetic materials and its fluconazole sensitivity: a kinetic study. *Mycoscience* 53, 220–226. doi: 10.1007/S10267-011-0155-Y

Singh, A., Ghosh, S., Kar, S., and Ahmed, I. (2013). Silicone prosthesis for a patient with unilateral ear defect: a clinical case report. *Eur. J. Gen. Dent.* 2, 315–319. doi: 10.4103/2278-9626.115997

Smit, G., and Plettenburg, D. H. (2013). Comparison of mechanical properties of silicone and PVC (polyvinylchloride) cosmetic gloves for articulating hand prostheses. *J. Rehabil. Res. Dev.* 50, 723–732. doi: 10.1682/JRRD.2011.12.0238

Steffen, A., Klaiber, S., Katzbach, R., Nitsch, S., König, I. R., and Frenzel, H. (2008). The psychosocial consequences of reconstruction of severe ear defects or third-degree microtia with Rib cartilage. *Aesthet. Surg. J.* 28, 404–411. doi: 10.1016/j.asj.2008.06.003

Steffen, A., Wollenberg, B., König, I. R., and Frenzel, H. (2010). A prospective evaluation of psychosocial outcomes following ear reconstruction with rib cartilage in microtia. *J. Plast. Reconstr. Aesthet. Surg.* 63, 1466–1473. doi: 10.1016/j.bjps.2009.09.005

Stratasys (2019). Stratasys PolyJet Technology for 3D Printing. Available online at: https://www.objective3d.com.au/technologies/polyjet-technology/ (accessed September 13, 2019).

Subburaj, K., Nair, C., Rajesh, S., Meshram, S. M., and Ravi, B. (2007). Rapid development of auricular prosthesis using CAD and rapid prototyping technologies. *Int. J. Oral Maxillofac. Surg.* 36, 938–943. doi: 10.1016/j.ijom.2007.07.013

Sun, J., Chen, X., Liao, H., and Xi, J. (2013). Template-based framework for nasal prosthesis fabrication. *Rapid Prototyp. J.* 19, 68–76. doi: 10.1108/13552541311302914

Sun, J., Xi, J., Chen, X., and Xiong, Y. (2011). A CAD/CAM system for fabrication of facial prostheses. *Rapid Prototyp. J.* 17, 253–261. doi: 10.1108/13552541111138379

Tagkalakis, P., and Demiri, E. (2009). A fear avoidance model in facial burn body image disturbance. *Ann. Burns Fire Disasters* 22, 203–207.

Tam, C. K., McGrath, C. P., Ho, S. M. Y., Pow, E. H. N., Luk, H. W. K., and Cheung, L. K. (2014). Psychosocial and quality of life outcomes of prosthetic auricular rehabilitation with CAD/CAM technology. *Int. J. Dent.* 2014:393571. doi: 10.1155/2014/393571

Tolou, N., Smit, G., Nikooyan, A. A., Plettenburg, D. H., and Herder, J. L. (2012). Stiffness compensation mechanism for body powered hand prostheses with cosmetic covering. *J. Med. Devices* 6:011004. doi: 10.1115/1.4005781

Unkovskiy, A., Spintzyk, S., Brom, J., Huettig, F., and Keutel, C. (2018). Direct 3D printing of silicone facial prostheses: a preliminary experience in digital workflow. *J. Prosthet. Dent.* 120, 303–308. doi: 10.1016/j.prosdent.2017.11.007

Veerareddy, C., Nair, K. C., and Reddy, G. R. (2012). Simplified technique for orbital prosthesis fabrication: a clinical report. *J. Prosthodont.* 21, 561–568. doi: 10.1111/j.1532-849X.2012.00869.x

Ventola, C. L. (2014). Medical applications for 3D printing: current and projected uses. *Pharm. Ther.* 39, 704–711.

Venugopalan, S., Ariga, P., Aggarwal, P., and Viswanath, A. (2014). Magnetically retained silicone facial prosthesis. *Niger. J. Clin. Pract.* 17, 260–264. doi: 10.4103/1119-3077.127575

Waters, M. G. J., Jagger, R. G., and Polyzois, G. L. (1999). Wettability of silicone rubber maxillofacial prosthetic materials. *J. Prosthet. Dent.* 81, 439–443. doi: 10.1016/s0022-3913(99)80011-0

Watson, J., and Hatamleh, M. M. (2014). Complete integration of technology for improved reproduction of auricular prostheses. *J. Prosthet. Dent.* 111, 430–436. doi: 10.1016/j.prosdent.2013.07.018

Wolberg, W. H., Romsaas, E. P., Tanner, M. A., and Malec, J. F. (1989). Psychosexual adaptation to breast cancer surgery. *Cancer* 63, 1645–1655. doi: 10.1002/1097-0142(19890415)63:8<1645::aid-cncr2820630835>3.0.co;2-8

Wolfaardt, J. F., and Coss, P. (1996). An impression and cast construction technique for implant-retained auricular prostheses. *J. Prosthet. Dent.* 75, 45–49. doi: 10.1016/s0022-3913(96)90415-1

Wu, G., Zhou, B., Bi, Y., and Zhao, Y. (2008). Selective laser sintering technology for customized fabrication of facial prostheses. *J. Prosthet. Dent.* 100, 56–60. doi: 10.1016/S0022-3913(08)60138-9

Xiao, K., Zardawi, F., van Noort, R., and Yates, J. M. (2013). Color reproduction for advanced manufacture of soft tissue prostheses. *J. Dent.* 41, e15–e23. doi: 10.1016/j.jdent.2013.04.008

Xiao, K., Zardawi, F., van Noort, R., and Yates, J. M. (2014). Developing a 3D colour image reproduction system for additive manufacturing of facial prostheses. *Int. J. Adv. Manuf. Technol.* 70, 2043–2049. doi: 10.1007/s00170-013-5448-1

Yuan, F., Lv, P., Wang, P., Wang, Y., Wang, Y., and Sun, Y. (2016). Custom fabrication of try-in wax complete denture. *Rapid Prototyp. J.* 22, 539–543. doi: 10.1108/RPJ-09-2014-0129

Zardawi, F. M., Xiao, K., van Noort, R., and Yates, J. M. (2015a). Investigation of elastomer infiltration into 3D printed facial soft tissue prostheses. *Anaplastology* 4, 2161–1173.

Zardawi, F. M., Xiao, K., van Noort, R., and Yates, J. M. (2015b). Mechanical properties of 3D printed facial prostheses compared to handmade silicone polymer prostheses. *Eur. Sci. J.* 11:12.

Zeng, W., Lin, F., Shi, T., Zhang, R., Nian, Y., Ruan, J., et al. (2008). Fused deposition modelling of an auricle framework for microtia reconstruction based on CT images. *Rapid Prototyp. J.* 14, 280–284. doi: 10.1108/13552540810907947

Zhao, T., Yu, R., Li, S., Li, X., Zhang, Y., Yang, X., et al. (2019). Superstretchable and processable silicone elastomers by digital light processing 3D printing. *ACS Appl. Mater. Interfaces* 11, 14391–14398. doi: 10.1021/acsami.9b03156

Zhou, G., Jiang, H., Yin, Z., Liu, Y., Zhang, Q., Zhang, C., et al. (2018). *In vitro* regeneration of patient-specific ear-shaped cartilage and its first clinical application for auricular reconstruction. *EBioMedicine* 28, 287–302. doi: 10.1016/j.ebiom.2018.01.011

Zhou, L., Gao, Q., Fu, J., Chen, Q., Zhu, J., Sun, Y., et al. (2019). Multimaterial 3D printing of highly stretchable silicone elastomers. *ACS Appl. Mater. Interfaces* 11, 23573–23583. doi: 10.1021/acsami.9b04873

Zini, I., Krill, R. L., and Aramany, M. A. (1975). Direct wax method for fabrication of metallic facial molds. *J. Prosthet. Dent.* 33, 85–88. doi: 10.1016/s0022-3913(75)80151-x

Conflict of Interest: The authors declare that the research was conducted in the absence of any commercial or financial relationships that could be construed as a potential conflict of interest.

frontiers
in Bioengineering and Biotechnology

REVIEW
published: 23 April 2020
doi: 10.3389/fbioe.2020.00147

Advancements in Soft-Tissue Prosthetics Part B: The Chemistry of Imitating Life

Rena L. J. Cruz, Maureen T. Ross, Sean K. Powell* and Maria A. Woodruff

Institute of Health and Biomedical Innovation, Queensland University of Technology, Brisbane, QLD, Australia

Each year, congenital defects, trauma or cancer often results in considerable physical disfigurement for many people worldwide. This adversely impacts their psychological, social and economic outlook, leading to poor life experiences and negative health outcomes. In many cases of soft tissue disfigurement, highly personalized prostheses are available to restore both aesthetics and function. As discussed in part A of this review, key to the success of any soft tissue prosthetic is the fundamental properties of the materials. This determines the maximum attainable level of aesthetics, attachment mechanisms, fabrication complexity, cost, and robustness. Since the early-mid 20th century, polymers have completely replaced natural materials in prosthetics, with advances in both material properties and fabrication techniques leading to significantly improved capabilities. In part A, we discussed the history of polymers in prosthetics, their ideal properties, and the application of polymers in prostheses for the ear, nose, eye, breast and finger. We also reviewed the latest developments in advanced manufacturing and 3D printing, including different fabrication technologies and new and upcoming materials. In this review, Part B, we detail the chemistry of the most commonly used synthetic polymers in soft tissue prosthetics; silicone, acrylic resin, vinyl polymer, and polyurethane elastomer. For each polymer, we briefly discuss their history before detailing their chemistry and fabrication processes. We also discuss degradation of the polymer in the context of their application in prosthetics, including time and weathering, the impact of skin secretions, microbial growth and cleaning and disinfecting. Although advanced manufacturing promises new fabrication capabilities using exotic synthetic polymers with programmable material properties, silicones and acrylics remain the most commonly used materials in prosthetics today. As research in this field progresses, development of new variations and fabrication techniques based on these synthetic polymers will lead to even better and more robust soft tissue prosthetics, with improved life-like aesthetics and lower cost manufacturing.

Keywords: prosthetic, prosthesis, polymer, silicone, additive manufacturing, maxillofacial

Edited by:
Julien Georges Didier Barthès,
PROTiP Medical, France

Reviewed by:
Jianxun Ding,
Changchun Institute of Applied Chemistry (CAS), China
Ajay Devidas Padsalgikar,
DSM (United States), United States

****Correspondence:***
Sean K. Powell
sean.powell@qut.edu.au

Specialty section:
This article was submitted to Biomaterials, a section of the journal Frontiers in Bioengineering and Biotechnology

Received: *04 November 2019*
Accepted: *12 February 2020*
Published: *23 April 2020*

Citation:
Cruz RLJ, Ross MT, Powell SK and Woodruff MA (2020) Advancements in Soft-Tissue Prosthetics Part B: The Chemistry of Imitating Life. Front. Bioeng. Biotechnol. 8:147. doi: 10.3389/fbioe.2020.00147

INTRODUCTION

Congenital defects, trauma, or cancer often causes loss or disfigurement of tissue leading to distress and impairment for millions worldwide, significantly affecting their social, economic and psychological health (Tagkalakis and Demiri, 2009). The impact of physical disfigurement extends to the individuals' body image, their perception of their physical self (Galpin, 1996; Tagkalakis and Demiri, 2009). In addition, disfigurement often leads to discrimination, bullying and less opportunities for the affected individual to participate fully in their society. Prosthetic devices have long been used to restore aesthetics and function to individuals with soft tissue disfigurement. Advances in materials and fabrication techniques over the centuries has enabled improvements in the capabilities of prostheses, particularly with respect to their aesthetics, attachment, function, cost and robustness.

Polymers are now used extensively in modern external prosthetics, having replaced many of the primary and natural materials that were available prior to their advent. The advantages of polymers extend to their ability to more realistically mimic native tissue both esthetically and functionally, as well as providing excellent safety, effectiveness, robustness and accessibility. Their application in prosthetics has also been extensively studied and the discovery of new prostheses and processing methods has led to radical shifts in many areas of prosthetic design. In some cases, this has led to significant advances in the realism and capability of prostheses with positive impacts on the lives of millions of people worldwide. **Table 1** summarizes the mechanical and manufacturing properties of the polymers used in soft tissue prosthetics in modern times; some of which have been discontinued, many still in common use, and others still emerging.

In this part of this two-part review, part B, we detailed the chemistry of common synthetic polymers in prosthetics, particularly their fundamental chemistry, synthesis, materials properties, fabrication and material degradation. In part A of this review, we discussed literature around the history of prosthetic materials, their desirable properties, some example applications to different tissues, and traditional and advanced manufacturing approaches to producing personalized soft tissue prosthetics. As stated in Section 1.2 of Part A, to mimic soft tissue a material should have a hardness between 25 and 35 Shore A (Shore hardness index), have a tensile strength of 6.9 to 13.8 MPa, be colorless and be easily intrinsically and extrinsically colored (Lewis and Castleberry, 1980). Simple processing methods are desired, such as simple casting methods with low cost molds or 3D printing.

We begin with a highly detailed description of the use and chemistry of silicone (polydimethylsiloxane), the most widely used polymer for mimicing soft tissues; including the usage and properties of the different types of silicones applied to prosthetics over its long history in this industry as well as current developments being made to lengthen the lifespan of silicone prostheses (Aziz et al., 2003a,b; Goiato et al., 2010a; Hatamleh and Watts, 2010c; Montgomery and Kiat-Amnuay, 2010). While silicone has predominantly replaced the more rigid acrylic resin in prosthetics, this important polymer was a forerunner in the domination of polymers in the prosthetic industry and still finds use in the fabrication of occular prostheses and as a substructure for weaker silicone prostheses (Chalian and Phillips, 1974; Craig et al., 1980; Artopoulou et al., 2006; Callaghan et al., 2006; Raizada and Rani, 2007; Goiato et al., 2014). Silicones have also nearly completely replaced the use of vinyl polymers in the fabrication of prostheses due to the improved color integrity and realistic feel. We also discuss literature around the degredation of silicone, particularly in the context of soft tissue prosthetics. However, before the development of stronger silicones, vinyls were the most favored prosthetic material for their high tear strength and softer feel when compared with rigid materials such as acrylic resin (Gearhart, 1970; Kenworthy and Small, 1974; Yu et al., 1983; Carroll and Fyfe, 2004; Smit et al., 2014). Polyurethanes have also been used as a prosthetic material, both as a bulk material and as a foam. However, they have not seen as wide spread use as silicone due to the difficulties of fabrication inherent with working with polyurethanes and tendancy toward yellow discoloration with aging (Chalian and Phillips, 1974; Goldberg et al., 1978; Craig et al., 1980). Chlorinated polyethylene, a newer prosthetic material has struggled to enter into common use since its introduction by the National Institute of Dental Research. Despite the potential of new 3D printable elastomeric materials (Çötert, 2015), silicone remains the material of choice for soft-tissue prostheses either due to ease of use or personal biases (Kiat-amnuay et al., 2010). The structure and properties of these polymers are summarized in **Table 1**.

In modern soft-tissue prosthetics polymers are widely used to restore aesthetics for conditions involving the ear (Ross et al., 2018), face (Fantini et al., 2013), eye (Alam et al., 2017), breast (Cancer Australia, 2019) and hand (Kaira and Dabral, 2014). These prosthetics are often hand-crafted by skilled prosthetists and tailored to the individual anatomy of each patient. Typically, physical casts are taken of the patient's anatomy which are then used to produce molds into which the polymer is added for curing. More recent approaches involve the use of 3D scanning of the patient followed by computer modeling of the desired mold or prosthetic. Often, given the complexity of some prosthetics, reinforcement is required and included into the prosthetic. The following sections detail the chemistry of polymers used in prosthetics of the ear, face, eye, breast and hand. In part A of this review, the desired properties of polymeric materials used in soft-tissue prosthetics are discussed. We also discuss different approaches that have been used to address the need for realistic and robust prostheses.

SILICONE

Silicone, or silicone elastomer, typically refers to polydimethylsiloxane (PDMS). This popular polymer now

TABLE 1 | Properties of polymers historically used in soft tissue prostheses.

Polymer	Polymer repeat structure	Processing methods	Hardness (shore A)/ tensile strength (MPa)	Pigmentation	Examples used in prosthetics
Silicone: room temperature vulcanizing					
One-part condensation		Painted onto surface as sealants, adhesives, and external colorants	28 – 35/ 2.0 – 3.3	Intrinsic colorants incorporated for application	Medical Adhesive Type A
Two-part condensation	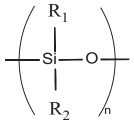 $\left(-\overset{R_1}{\underset{R_2}{Si}}-O- \right)_n$	Simple casting	38 – 43/ 2.7 – 4.2	Intrinsic colorants incorporated prior to cure and extrinsic details added.	Discontinued usage
Two-part addition		Simple casting, 3D printing in development	25 – 32/ 4.8 – 5.0	Intrinsic colorants incorporated prior to cure and extrinsic details	A-2186, A-2186F, MDX4-4120
Silicone: High temperature vulcanizing					
Peroxide curing		Injection molding	25 – 75/ 5.9 – 6.9	Milling required for intrinsic colorants and extrinsic details added	Discontinued usage
Addition curing	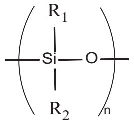 $\left(-\overset{R_1}{\underset{R_2}{Si}}-O- \right)_n$	Press and injection molding	20 – 80/ 9.3	Milling required for intrinsic colorants and extrinsic details added	Q7-4720, Q7-4735, Q7-4750, Q7-4765, and Q7-4780
Liquid silicone rubber		Injection molding	24/ 8.4	Intrinsic colorants incorporated prior to cure and extrinsic details added	MED-4920 (NuSil)
Poly(methyl methacrylate)/PMMA/acrylic resin	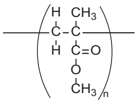 $\left(-\overset{H}{\underset{H}{C}}-\overset{CH_3}{\underset{\substack{C=O\\O\\CH_3}}{C}}-\right)_n$	Simple casting with flexible molds, 3D printable	96 (Shore D)/ 68.3	Intrinsic colorants incorporated prior to cure and extrinsic details added.	Scleral acrylic resin (Factor II Inc.)
Polyvinyl chloride	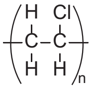 $\left(-\overset{H}{\underset{H}{C}}-\overset{Cl}{\underset{H}{C}}-\right)_n$	Simple casting with metal molds	53/4.0	Intrinsic colorants incorporated prior to cure and extrinsic details added.	RSL Steeper
Polyurethane	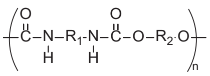 $\left(-\overset{O}{\overset{\|}{C}}-\underset{H}{N}-R_1-\underset{H}{N}-\overset{O}{\overset{\|}{C}}-O-R_2-O-\right)_n$	Simple casting as solid or foam, 3D printable	45/ 4.14 – 7.52	Intrinsic colorants incorporated prior to cure and extrinsic details added.	
Chlorinated polyethylene	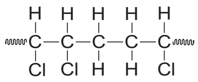 $\sim\overset{H}{\underset{Cl}{C}}-\overset{H}{\underset{Cl}{C}}-\overset{H}{\underset{H}{C}}-\overset{H}{\underset{H}{C}}-\overset{H}{\underset{Cl}{C}}\sim$	Thermoplastic material that is cast in layers, 3D printable	29/ 1.28	Milling required for intrinsic colorants and extrinsic details added	Tyrin CM0136

has vast uses in a wide variety of industries from personal care to the automotive industry (Aziz et al., 2003b; Bellamy et al., 2003; Curtis and Colas, 2004; Hatamleh and Watts, 2010c). The first silicones were introduced in 1946 (Chalian and Phillips, 1974) and began being used in maxillofacial prosthetics in the 1960s (Barnhart, 1960). Today, it is the most widely used material in maxillofacial prosthetics, favored for its flexibility, heat resistance, transparency, and biocompatibility despite its inability to be modified or repaired (Aziz et al., 2003a,b; Goiato et al., 2010a; Hatamleh and Watts, 2010c; Montgomery and Kiat-Amnuay, 2010).

Chemistry of Silicone and Prosthetic Fabrication

Silicone is produced when water is added to dimethyldichlorosilane, a compound formed by the reaction of silicon and methyl chloride. The resulting fluid polymer can then be cross-linked to form a solid. As shown in **Table 1**, the unique properties of silicone are a result of its chemical structure which is composed of an inorganic backbone of alternating silicon and oxygen atoms (siloxane structure) to which organic side groups, typically methyl (CH_3), propyl ((C_3H_7) or phenyl (C_6H_{11}) groups, are bonded (Chalian and Phillips, 1974; Curtis and Colas, 2004; Lorenz and Kandelbauer, 2014). Comparison of the siloxane (Si-O) structure (Curtis and Colas, 2004; Lorenz and Kandelbauer, 2014) with the carbon backbone of organic polymers illustrates why silicones have such unique physical properties. The siloxane structure is strengthened by being composed solely of single bonds (saturation) as well as the high covalent bond energy between silicon and oxygen atoms (Curtis and Colas, 2004; Lorenz and Kandelbauer, 2014). The element silicon is also less electromagnetic and larger than carbon, allowing for greater flexibility (Curtis and Colas, 2004; Lorenz and Kandelbauer, 2014). This unique chemical structure gives silicone the advantages that make it a popular prosthetic material.

The three chemical processes with which liquid silicone can be cross-linked are: free radical polymerization (peroxide curing), condensation polymerization, and addition polymerization (**Figure 1**; Colas, 2005; Andriot et al., 2009). Cross-linking processes can be broadly separated into room temperature approaches (room temperature vulcanizing systems or RTV) or elevated temperature approaches (high temperature vulcanizing systems or HTV) (**Figure 1**). While numerous silicone cross-linking approaches have been commonly used in prosthetic fabrication throughout the years, addition polymerization at room temperature has become the most common method due to its simplicity (Montgomery and Kiat-Amnuay, 2010).

Room Temperature Vulcanizing Silicone

Room temperature vulcanising (RTV) systems involve crosslinking by either condensation or addition polymerization using a catalyst and crosslinking agent. As the reaction occurs at room temperature, low-cost plaster and gypsum (dental stone) (Chalian and Phillips, 1974) can be used in the fabrication of the mold into which the silicone can be cured. The condensation polymerization systems are available as either a one-part (classified as RTV-1) or two-part (classified as RTV-2) system (Jerschow, 2001). Addition polymerization systems occur only as RTV-2 systems (Jerschow, 2001).

Condensation polymerization only occurs as room temperature vulcanizing systems with an organotin catalyst (e.g., stannous octoate) and crosslinker (e.g., methyl triacetoxy silane) (Jerschow, 2001; Lai et al., 2002; Aziz et al., 2003b; Curtis and Colas, 2004; Colas, 2005; Lorenz and Kandelbauer, 2014). Crosslinking begins as functional groups on the crosslinker become hydrolyzed to create silanols which trigger condensation and the release of a by-product (Jerschow, 2001; Lai et al., 2002; Curtis and Colas, 2004; Colas, 2005; Lorenz and Kandelbauer, 2014); the more common functional groups are acetoxy and alkyloxy groups, which polymerize to release acetic acid and methyl alcohol, respectively (Curtis and Colas, 2004; Lorenz and Kandelbauer, 2014). This reaction, if incomplete, can be reversed at temperatures exceeding 90°C (Jerschow, 2001; Curtis and Colas, 2004). Some of the disadvantages of the use of silicones cured through condensation polymerization in prosthetics include: long curing time, susceptibility of the material to degradation, low tear strength, low edge strength, and the formation of by-products which can lead to a porous structure, promoting sorption of liquids (Lai et al., 2002; Hulterström et al., 2008).

Room temperature vulcanising-1 condensation systems are commercially used as sealants and adhesives (Jerschow, 2001). As crosslinking begins immediately on contact with moisture in the air, they need to be stored in sealed cartridges. As moisture is required during its polymerization process, the practical cross-sectional thickness of the object being produced is limited, limiting their use in prosthetics (Lai et al., 2002; Curtis and Colas, 2004; Colas, 2005; Lorenz and Kandelbauer, 2014). Despite this, RTV-1 condensation systems have found use in prosthetics. An example of one such product is Medical Adhesive Type A (also called Silastic 891) (Dow Corning Company, Midland, MI, United States), which is solely used in external colorants on the surface of the prosthesis where it can be used in a thin layer to allow the passage of moisture throughout its cross-sectional thickness for complete polymerization (Lai et al., 2002). In a 1992 survey of American prosthetists (Andres et al., 1992), 35.2% of 88 respondents used Medical Adhesive Type A. In a more recent 2010 survey (Montgomery and Kiat-Amnuay, 2010), 39.5% of 43 respondents were still employing it for external detailing. RTV-1 condensation systems also have poor performance on a range of measures such as long time to complete polymerization, poor mechanical properties, and importantly, the creation of acetic acid (an irritant to skin) during production (Lai et al., 2002).

Crosslinking in RTV-2 condensation polymerization systems is initiated when the two components, a base and curing agent (catalyst), are combined without requiring the presence of moisture (Jerschow, 2001; Curtis and Colas, 2004; Colas, 2005; Lorenz and Kandelbauer, 2014). Commonly used silicone products using this curing process have been marketed in the past as Silastic 382 and Silastic 399 (Dow Corning Company). Silastic 382 was a viscous opaque white fluid base which was polymerized by a stannous octoate catalyst (Chalian and Phillips, 1974; Craig et al., 1980). Silastic 399 was viscous and non-flowing and required the addition of two different catalysts for polymerization (Craig et al., 1980). Up until the late 1980s, these materials were commonly used in the fabrication of implants and maxillofacial prostheses (Chalian and Phillips, 1974). However, concerns regarding their safety emerged in the 1980s (Lam and Hurry, 1992; Reisch, 1993; Cook et al., 1994; Wise, 2000; Curtis and Colas, 2004; Segal et al., 2012) and they were discontinued (Wise, 2000; Segal et al., 2012).

In room temperature vulcanizing addition polymerization systems (i.e., RTV platinum catalyzed silicones), unsaturated vinyl (–CH = CH2) terminated poly (siloxanes) are triggered by a platinum catalyst to react with silyl hydride (–SiH) groups and undergo polymerization (Lai and Hodges, 1999; Jerschow, 2001; Aziz et al., 2003b; Curtis and Colas, 2004; Colas, 2005). Though these are RTV systems, these silicones may be heat cured at temperatures up to 100°C to decrease curing time. One significant advantage to this polymerization approach is that

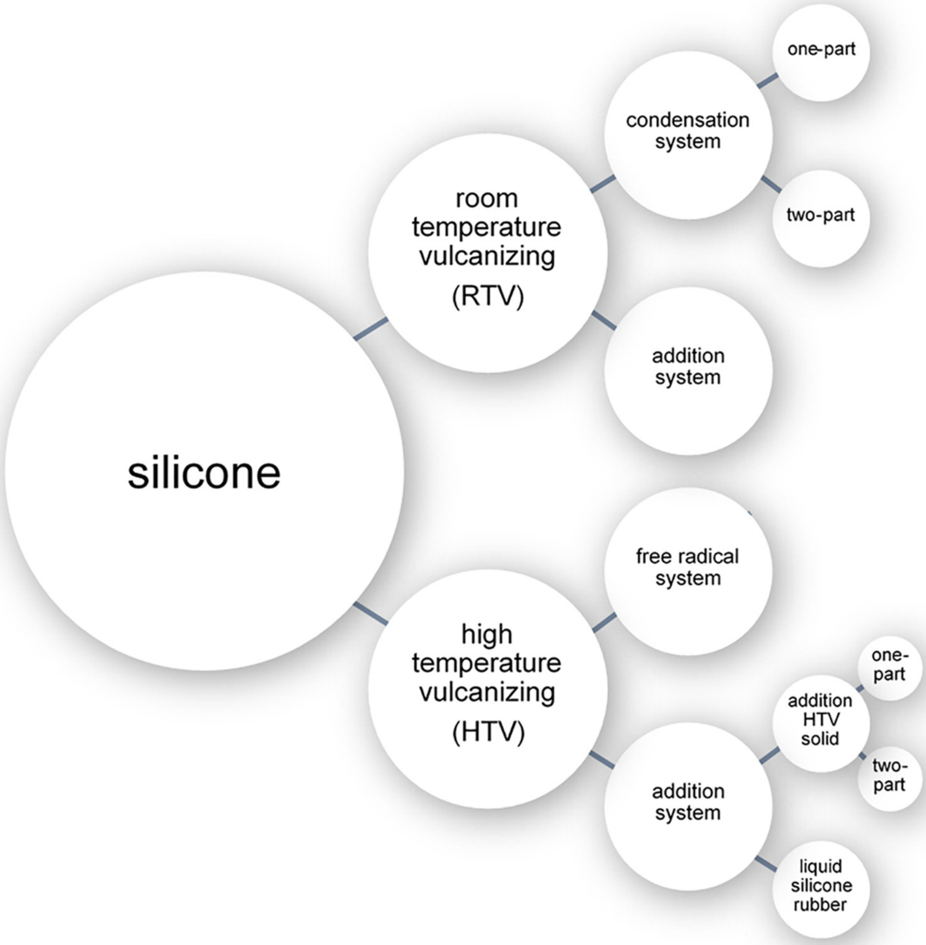

FIGURE 1 | Diagram of the different classes of silicone.

shrinking does not occur as no by-product is created in this reaction (Jerschow, 2001; Curtis and Colas, 2004; Colas, 2005; Lorenz and Kandelbauer, 2014). The base component typically consists of dimethylsiloxane polymer, reinforced silica, and a platinum or rhodium catalyst (Lai and Hodges, 1999; Lai et al., 2002; Curtis and Colas, 2004). The curing agent consists of dimethylsiloxane polymer, an inhibitor, and a siloxane crosslinker (Lai and Hodges, 1999; Lai et al., 2002). In the context of their use in prosthetics, the disadvantages of addition polymerization include material hydrophobicity, selective adhesion, inability to be extrinsically stained, short working time and inhibition of curing by impurities (e.g., amines, sulfurous or other catalyst poisons) (Jerschow, 2001; Lai et al., 2002; Curtis and Colas, 2004; Lorenz and Kandelbauer, 2014).

Despite these limitations, the majority of maxillofacial prostheses are manufactured using RTV platinum catalyzed silicones (Montgomery and Kiat-Amnuay, 2010). The most popular being A-2186 (Factor II, Inc., Lakeside, AZ, United States), a clear two-part (10:1, base: catalyst) pourable silicone that was first introduced in 1986 (Montgomery and Kiat-Amnuay, 2010). A fast polymerization rate version was introduced in 1987 as A-2186F (Factor II, Inc.). A 1992 survey of 88 American prosthetists (Andres et al., 1992) found that 6.8% of respondents used A-2186 and a 2010 survey (Montgomery and Kiat-Amnuay, 2010) found that this had increased to 32.6% of 43 respondents. A-2186F, the faster polymerization rate version, did not appear in the 1992 survey, but was used by 20.9% of 2010 respondents. In the year 2000, A-2000 (Factor II, Inc.) was introduced as the first generation of 1:1 mixture platinum silicone, followed by A-2006 in 2006 (Factor II, Inc.) (Montgomery and Kiat-Amnuay, 2010); the 2010 survey found that these were used by 20.9 and 11.6% of respondents, respectively. MDX4-4210 (Dow Corning Company), another clear two-part (10:1, base: catalyst) pourable silicone, was first introduced to the maxillofacial industry in the 1970s and was most popular in the 1990s (Montgomery and Kiat-Amnuay, 2010). In the 1992 survey, MDX4-4210 was used by the majority (59.1%) of respondents, and was still used in the

2010 survey by 18.6% together with catalyst A-103 (Factor II, Inc.) and 16.3% together with Medical Adhesive Type A (Dow Corning Company).

High Temperature Vulcanizing Silicones

High temperature vulcanising (HTV) systems involve crosslinking by either free radical or addition polymerization. One of the advantages of high temperature vulcanizing silicones (between 100°C and 200°C) is the longer working time of approximately 30 min prior to polymerization. This, however, comes at a significantly increased cost over room temperature polymerization (Lorenz and Kandelbauer, 2014), and requires intense milling prior to polymerization for the incorporation of intrinsic pigments (Anusavice, 2013).

Free radical polymerization reactions (also known as peroxide-initiated reaction) are useful for producing high-consistency silicones (Curtis and Colas, 2004). By incorporating an organic peroxide to the silicone prior to heating, radicals involved in crosslinking are produced at high temperatures (Chalian and Phillips, 1974; Curtis and Colas, 2004; Colas, 2005; Lorenz and Kandelbauer, 2014). Typically, these silicones are catalyzed by dichlorobenzoyl peroxide (Craig et al., 1980) which is stable at room temperature and is activated at elevated temperatures (104–132°C); activating methylene groups that form ethylene crosslinks between chains of uncured polymer (Lorenz and Kandelbauer, 2014). The efficiency of this reaction is increased with the presence of vinyl groups in the polymer (Curtis and Colas, 2004; Colas, 2005). These silicones have high tear resistance and have excellent thermal stability and therefore ideal for prostheses where these properties are important. However, silicones cross-linked with radicals have low elasticity and therefore cannot be used in mobile regions, such as areas affected by jaw movement. Other disadvantages include opacity, yellowing after cure, odor during- and post-production, taste in the case of intra-oral prostheses, high friction (tacky) surface, release of peroxide split products, and possibility of peroxide residues which can create voids in the finished product as well as act as a catalyst for depolymerization at elevated temperatures (Jerschow, 2001; Curtis and Colas, 2004; Colas, 2005). Following high temperature polymerization, further processing may be applied to remove volatile peroxide residues (Jerschow, 2001; Curtis and Colas, 2004; Colas, 2005). Despite their tear resistance and thermal properties, the use of radical cross-linked silicones in prosthetics has been discontinued due to the availability of superior products, such as silicones produced by addition cure systems.

High temperature vulcanization through addition polymerization works similarly to RTV addition polymerization systems leading to silicones that are highly transparent with no yellowing, no odors, that are easy to demould, do not require post cure processing, and have high tear and tensile strength (Jerschow, 2001; Aziz et al., 2003b). These are available as either one-part systems (1K) with a shelf-life of 3–6 months or two-part (2K) systems with a shelf-life of 18 months when separated or 1–7 days once mixed (Jerschow, 2001; Dow Corning, 2006). Another feature of two-part systems is that flexibility can be tailored by altering the proportions of the two components.

Liquid silicone rubbers (LSR) are two-part addition curing compounds with consistency that can be tailored from pourable to pasty (Jerschow, 2001; Lorenz and Kandelbauer, 2014). The curing rate is also adjustable and occurs relatively slowly at room temperature due to the presence of both catalyst and inhibitor, and more rapidly at temperatures of 170°C to 200°C (Jerschow, 2001; Lorenz and Kandelbauer, 2014). The chemical structure of the cured material is similar to HTVs cross-linked with radicals, but the polymer chains are shorter (Lorenz and Kandelbauer, 2014). One example, MED-4920 (NuSil^{TM} Technology LLC, Carpinteria, CA, United States), is a 1:1 LSR that is used for prostheses; however, it is more commonly used in medical devices such as balloon catheters and tubing. It is translucent, moderately strong and can mimic soft tissue. Prior to curing, it is too viscous for pouring into a mold, but is suitable for injection molding (Aziz et al., 2003a,b; NuSil).

Properties of Silicone in Prosthetics

Mechanical properties of silicone depend on three main factors; molecular weight, degree of crosslinking, and incorporation of fillers and pigments (Aziz et al., 2003b; Bellamy et al., 2003; Hatamleh and Watts, 2010c).

Molecular weight distribution has a direct effect on the strength and flexibility of the polymer. By blending long and short chains of the same polymer, a bimodal molecular weight distribution can be created (Aziz et al., 2003b). Shorter polymer chains (lower molecular weight) result in higher crosslinking which, in the case of silicone, results in a brittle inelastic material that does not mimic soft tissue. On the other hand, a low degree of crosslinking results in a highly elastic but weak material. It is therefore important to adjust the crosslinking density to balance between these two extremes to achieve a soft tissue prosthesis that also has a long service life (Aziz et al., 2003b; Bellamy et al., 2003).

Another approach to strengthen the mechanical properties of silicone and reduce its susceptibility to tearing is to incorporate filler. This is often referred to as extending, as it can lower the cost of the elastomer (Jerschow, 2001), thereby lowering the cost of the prosthesis. The filler works by dissipating energy during material deformation, allowing molecular chains to easily move past each other (Santawisuk et al., 2010; Zayed et al., 2014). It should be noted that, often the particles present in intrinsic coloring pigments can have a similar effect. The most common filler in silicone production is hydrophobic surface treated silica (SiO_2 in the form of diatomaceous earth or ground quartz). This has been found to increase material hydrophobicity, increase strength, increase storage modulus, increase loss modulus, increase damping factor and decrease elasticity (Chalian and Phillips, 1974; Jerschow, 2001; Aziz et al., 2003b; Bellamy et al., 2003; Curtis and Colas, 2004; Santawisuk et al., 2010). Although these changes can increase the service life of the prosthesis, too much filler impacts tissue-like characteristics; leading to hardening and reduced comfort through reduced elasticity and decreased wettability.

In addition to silica, other materials have been explored for use as fillers. The incorporation of titanium, zinc, and cerium nano-oxides on strengthening silicone was investigated by Han et al. (2008). It was found that the addition of these nanoparticles in concentrations of 2.0 to 2.5%wt. increased the hardness, tear strength, tensile strength, and elongation of silicone at break. However, at higher concentrations of 3.0%wt., the nanoparticles were observed to have a tendency to agglomerate and thereby act as stress concentrating centers. This reduced the tear strength, tensile strength, and elongation of the silicone, effectively shortening the material's service life. However, Zayed et al. (2014) found that silica (the most common filler) showed reduced agglomeration when incorporated as nano-sized particles (i.e., hydrophobic nano-SiO_2 coated with silane coupling agent) instead of as typical macroparticles (Zayed et al., 2014), achieving significant increases in tear strength and elongation with a lower increase in hardness.

Other tested reinforcement materials include microspheres (Liu et al., 2013, 2015). These microspheres were fully enclosed, containing a light gas, thereby decreasing their overall weight (Liu et al., 2013). In one comprehensive study, Liu et al. (2013, 2015) tested microspheres of two materials for use as a reinforcement material: polymer microspheres 461 DET 40 d25 (acrylonitrile-vinylidene chloride methyl-methacrylate copolymer) and silica microspheres Permata MS 380E (SiO_2). The polymer microspheres could be incorporated into the silicone without agglomeration at relatively low concentrations of 5 and 15%vol., however, at 30%vol., the microspheres tended to agglomerate creating locations for stress concentration and material failure (Liu et al., 2013). The polymer microsphere reinforced silicone demonstrated a similar wettability to normal silicone but had lower density, decreased thermal conductivity, improved shock absorption and increased tensile strength at concentrations of 5%vol., and increased elongation at break and increased hardness at concentrations of 5, 15, and 30% vol. (Liu et al., 2013). It was found, however, that the tear strength of the silicone decreased with increasing concentration of polymer microspheres, likely due to microsphere agglomeration (Liu et al., 2013). The study found that the silica microspheres, on the other hand, did not reportedly agglomerate but instead imbedded into the silicone matrix (Liu et al., 2013). The silica microsphere reinforced silicone showed improved shock absorption, increased tensile strength, increased elongation at break, and increased hardness with increasing concentration of silica microspheres. The overall results indicate that silicone containing silica microspheres had higher density and greater tensile strength and shock absorption, and similar tear strength compared with silicone containing polymer microspheres (Liu et al., 2015). This suggests that the inclusion of silica microspheres could potentially improve silicone prosthesis strength without compromising comfort and a realistic feel.

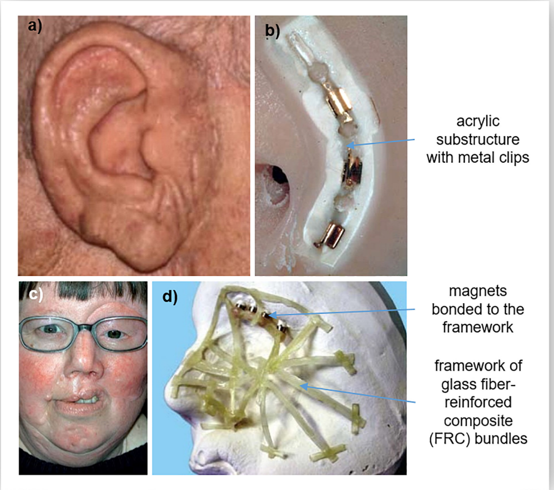

FIGURE 2 | Acrylic substructures for silicone prostheses: **(a)** a prosthetic ear and its **(b)** substructure for clip attachment, and **(c)** a large facial prosthesis and its **(d)** glass fiber-reinforced composite (FCR) substructure for reinforcement. Reproduced with permission from Elsevier (Ciocca et al., 2007; Kurunmäki et al., 2008).

Acrylic Substructures for Silicone in Prosthetics

An important consideration for the use of silicones in prosthetics is the need to attach the prosthesis to the patient. Often, silicone prostheses are attached using osseointegrated implants along with a retentive structure that uses either bar clips (**Figures 2a,b**) or magnets (**Figure 2c**; Hatamleh and Watts, 2010a,c; Haddad et al., 2012; Yerci Kosor et al., 2015). The use of clips or magnets simplifies the routine of attachment of the prosthesis by providing guides. In many cases, these retentive structures are fabricated using acrylic resin (Hatamleh and Watts, 2010a,c; Haddad et al., 2012; Yerci Kosor et al., 2015). A few of examples are depicted in **Figure 2**, which shows the acrylic substructure on the attachment face of a silicone nose and ear and the substructure for a partial face prosthesis with magnetic attachment parts. To ensure adequate attachment of the prosthesis to the patient, it is therefore important that the silicone is suitably attached to the acrylic substructure.

Direct bonding between silicone and acrylic is difficult, as molecular adhesion also does not occur due to their different chemical structures (Hatamleh and Watts, 2010a; Haddad et al., 2012; Yerci Kosor et al., 2015). Adhesives have also been found to insufficient (Haddad et al., 2012). This challenge of enhancing the bond strength between silicone and acrylic resin has been shown to be overcome using primers that contain both an organic solvent and an adhesive agent (Hatamleh and Watts, 2010a,c; Haddad et al., 2012; Yerci Kosor et al., 2015). The primer acts as a chemical intermediate, reacting with both materials (Hatamleh and Watts, 2010a; Haddad et al., 2012); etching into the resin to enable the silicone to impregnate the surface of the resin by activating hydrogen bonds and covalent coupling. This causes swelling of the surface to increase wettability (Hatamleh and Watts, 2010a,c; Haddad et al., 2012; Yerci Kosor et al., 2015). While the adhesive acts on the silicone; the hydrophilic and hydrophobic groups react and bond with the functional groups of the silicone (Hatamleh and Watts, 2010a,c; Haddad et al., 2012; Yerci Kosor et al., 2015).

Degradation of Silicone

Over time, all prostheses will undergo mechanical and chemical changes that limit their service life. Despite excellent durability, silicone eventually begins to look and feel unrealistic through color degradation, staining, weathering, changes to elasticity, and premature tearing. In addition, contact with the chemical environment of the skin secretions further degrades the polymer and also encourages microbial growth, leading to potential irritation and infection for the patient and microbial induced polymer degradation. Investigating ways to reduce this material degradation is important given the cost and complexities of producing many prostheses.

Time and Weathering

The greatest factor in the degradation of silicone's mechanical properties is photo-oxidation. Photo-oxidation is usually attributed to environmental causes, particularly ultraviolet radiation; but also pollution, variations in temperature, and variations in humidity (Goiato et al., 2012b). Generally, this degradation mechanism can be described in three steps: initiation, propagation, and termination. Initiation occurs with the formation of free radicals (Eleni et al., 2009a,b,d, 2011b,c; Rabek, 2012). For silicone, the inorganic backbone is highly resistive to irradiation due to the very high energy needed to cleave S-O bonds (Stathi et al., 2010). Therefore, the silyl radicals are often formed through cleaving of the methyl side groups (Rabek, 2012). During propagation, silyl radicals react with oxygen to produce polymer oxy radicals, peroxy radicals, and secondary polymer radicals, resulting in chain scissions (Eleni et al., 2009a,b,d, 2011b,c; Rabek, 2012; Al-Harbi et al., 2015). Termination occurs when radicals react with each other, often creating crosslinks between the chains (Eleni et al., 2009a,b,d, 2011b,c; Rabek, 2012; Al-Harbi et al., 2015). Initiation, propagation, and termination all occur simultaneously; with chain scission and crosslinking continuously occurring.

Another degradation mechanism for silicone is continual crosslinking that occurs over time. This has been seen in several nuclear magnetic resonance and infrared spectroscopy studies (Eleni et al., 2009d, 2011b,c; Stathi et al., 2010; Hatamleh et al., 2011; Al-Harbi et al., 2015) and results in an increase in hardness, glass transition temperature, elastic modulus, and viscoelasticity; and a decrease in tear strength, maximum stress, and maximum strain. These changes, which significantly affect the feel of the prosthesis and lead to tearing, result from increases in the density of the structural network of the silicone as bonds continue to form between chains (Eleni et al., 2009b,d, 2011b,c; Stathi et al., 2010; Hatamleh et al., 2011; Goiato et al., 2012b; Al-Harbi et al., 2015). This continued polymerization also occurs in the absence of environmental factors such as ultraviolet radiation. Silicone specimens stored in a dark room change their mechanical properties over time (at a rate lower than specimens exposed to weathering) due, in part, to continued polymerization well beyond the recommended time of curing (Guiotti et al., 2010; Polyzois et al., 2011).

In addition to mechanical changes, continued polymerization and photo-oxidation leads to unwanted color changes (Mancuso et al., 2009; dos Santos et al., 2010, 2011; Hatamleh and Watts, 2010b; Stathi et al., 2010). Both unpigmented and pigmented silicone undergoes accelerated color changes due to weathering, owing to enhanced crosslinking in the presence of UV radiation, air pollutants, temperature changes, and moisture (Hatamleh and Watts, 2010b; Stathi et al., 2010). However, the use of pigments has been shown to increase the rate of discoloration (Mancuso et al., 2009; dos Santos et al., 2010; Hatamleh and Watts, 2010b; Stathi et al., 2010; Al-Harbi et al., 2015); with organic pigments more susceptible than inorganic pigments to color changes (Mancuso et al., 2009; dos Santos et al., 2010). This color change is due to the migration of pigment particles within the polymer matrix (Mancuso et al., 2009; dos Santos et al., 2010); organic pigments are assumed to be larger than inorganic pigments, able to separate from the matrix more readily (Mancuso et al., 2009; dos Santos et al., 2010).

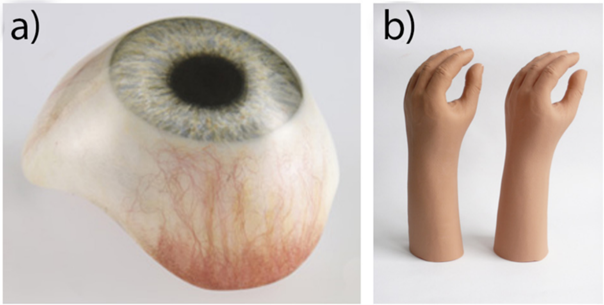

FIGURE 3 | (a) Acrylic prosthetic eye. Reproduced with permission from Erickson Labs Northwest (Northwest_Eye_Design, 2019). **(b)** PVC glove (left) and silicone glove (right), illustrating an equivalent aesthetic appearance. Reproduced with permission from Sage (Smit et al., 2014).

Another complication in the color degradation of silicone prostheses is that pigments of the same type (and manufacturer), but of different colors vary in their susceptibility to color change (Eleni et al., 2007, 2009a; Han et al., 2010; Stathi et al., 2010). This means that different prostheses made to match the skin of two different individuals may discolor at different rates.

In an attempt to maintain the aesthetic appearance of prostheses and lengthen their service lives, methods for reducing and preventing color change have been investigated (Han et al., 2010, 2013; dos Santos et al., 2011). One approach is through the incorporation of additives to decrease the translucency of the silicone. dos Santos et al. (2011), for example, found that barium sulfate (0.2wt%) prevented color change in unpigmented silicone, silicone pigmented with inorganic pigments, and silicone pigmented with functional pigments. This additive also has the advantage of strongly associating within the silicone matrix, thereby staying within the silicone and not greatly effecting the material hardness (Goiato et al., 2010a).

Han et al. (2010) tested titanium dioxide nanoparticles for inhibiting color change, finding that the addition of titanium dioxide nanoparticles can inhibit color change in silicone specimens with organic pigments. Furthermore, Wang et al. (2014) found that the addition of titanium dioxide has the added benefit of increasing tensile strength, increasing elongation at break, improving tear strength, and improving anti-thermal aging properties; with the disadvantage of increased hardness. This hardening effect of opacifiers, however, has been found to decrease following disinfection with neutral soap or effervescent (Goiato et al., 2010a). Both the addition of barium sulfate and titanium dioxide to silicone cause significantly higher dimensional changes during disinfection (Goiato et al., 2010a; Haddad et al., 2011). Furthermore, Han et al. (2013) found that commonly used opacifiers inhibited color changes in silicone in accelerated aging tests, but increased changes to the silicone's mechanical properties.

Skin Secretions

During regular wear, prostheses are not only exposed to natural environmental conditions, but also the skin of the wearer. Polyzois et al. (2000); Eleni et al. (2011a), Hatamleh et al. (2011), and Al-Dharrab et al. (2013) performed comprehensive studies on the effects of simulated skin secretions such as acidic perspiration, alkaline perspiration, and sebum on the mechanical behavior of different commercial prosthetic silicones; Elastomer 42 (Technovent Ltd.), Techsil S25 (Technovent Ltd.), Cosmesil M511 (Technovent Ltd.), and Episil (Dreve-Dentamid GmbH). The results of these studies are summarized in **Table 2**. In short; acidic and alkaline perspiration is generally absorbed which weakens silicone while increasing elasticity and increasing hardness, and sebum interacts with the silicone surface with highly variable results depending on the type of silicone.

These silicone property changes have been generally attributed to structural modifications in the distribution of the polymer chains (Hatamleh et al., 2011). In the case of silicone in simulated sebum; mechanical changes are attributed to interactions between fatty acids and the surface of the specimens (Polyzois et al., 2000; Eleni et al., 2011a; Hatamleh et al., 2011), breaking chain bonds (Hatamleh et al., 2011), increasing crosslinking density (Eleni et al., 2011a), and absorption of or secretion from silicone (Polyzois et al., 2000; Eleni et al., 2011a). Changes to silicone in simulated perspiration are attributed to the propagation of crosslinking reactions, creating a denser polymer network to increase elastic modulus and hardness (Polyzois et al., 2000; Eleni et al., 2011a; Hatamleh et al., 2011). Other changes include water absorption which leads to an increase in weight (Polyzois et al., 2000; Eleni et al., 2011a). However, the hydrophobic nature of silica fillers and vinyl functional silanes of some intrinsic pigments may prevent water absorption (Al-Dharrab et al., 2013). In particular, simulated acidic perspiration was found to have a possible catalytic effect on crosslinking, known as reversion; defined as the decomposition of junctions in the polymer network (Hatamleh et al., 2011).

Although silicone color changes due to simulated skin secretions were found to vary between different commercial silicones, they all showed a greater color change when placed in simulated sebum than in simulated perspiration except for Episil, which showed less color change in simulated sebum (Polyzois et al., 2000; Hatamleh and Watts, 2010b; Eleni et al., 2011a).

Microbial Growth

In addition to affecting polymer degradation, contact with skin promotes microbial growth. This is known to adversely affect the mechanical properties and appearance of the prosthesis reducing its service life, as well as cause irritation and possibly infection on the skin of the patient. While silicone itself does not chemically promote the growth of microorganisms, the porosity and surface roughness of silicone allows the material to be colonized by a variety of commensal microorganisms which form biofilms and resist removal. This can be seen in the SEM images of **Figure 4a** (Goiato et al., 2010c; Rodger et al., 2010; Ariani et al., 2012). Additionally, the hydrophobic nature of silicone aids in microbial colonization and the tendency of silicone to accurately reproduce the surface of the molding material can lead to a rough surface environment ideal for microbial growth (Hulterström et al., 2008; Preoteasa et al., 2011; Ariani et al., 2012).

When biofilms form on silicone, microorganisms are able to penetrate into the silicone matrix and create bag-like defects and reduce the service life of the prosthesis (Rodger et al., 2010; Ariani et al., 2012). The two mechanisms behind this degradation of silicone are believed to be: mechanical degradation due to turgor pressure of blastospores and hyphae in the pores of the material, and chemical degradation due to the release of extracellular enzymes or free radicals (Rodger et al., 2010). Interestingly, a study by Rodger et al. (2010) found that an increase in filler content may aide to hinder the colonization of C. albicans, one of the more common commensal microorganisms.

Disinfection

The service life and quality of a prosthesis can generally be extended by regularly cleaning and disinfecting to remove skin secretions and microorganisms. However, the cleaning products and disinfectants themselves can also degrade the silicone. Several studies have investigated the degradative effects of different disinfection methods. These include studies on microwave disinfection, the use of effervescent tablets, 4% chlorhexidine gluconate solution, 1% sodium hypochlorite solution, neutral soap, and commercial disinfectants (Goiato et al., 2008, 2009, 2010a,b, 2012b; Guiotti et al., 2010; Haddad et al., 2011; Hatamleh et al., 2011; Eleni et al., 2013a,b; Kotha et al., 2016).

The effect of storing silicone in sodium hypochlorite solution, neutral soap, and a commercial disinfectant on material hardness have been tested by Hatamleh et al. (2011) and Eleni et al. (2013a; 2013b). When measuring hardness with a durometer, they found that all three disinfection methods led to an overall decrease in material hardness (Eleni et al., 2013a). However, microindentation tests performed by the same group in a second study found that both neutral soap and the commercial disinfectant caused an increase in material hardness and elastic modulus (Eleni et al., 2013b). This apparent conflict between results was thought to be due to an overall absorption of solution into the silicone generally decreasing its bulk hardness, but extraction of surface compounds by neutral soap and the commercial disinfectant increasing hardness. In addition to changing the hardness of the silicone, storage in commercial disinfectant has also shown to significantly decrease tear strength (Hatamleh et al., 2011).

TABLE 2 | Effect of skin secretions on different silicone products.

Material	Study	Types of testing	Acidic perspiration	Alkaline perspiration	Simulated sebum
Elastomer 42	Eleni et al., 2011a	Compression Hardness Absorption	↓ Maximum stress ↓ Maximum strain ↑ Elastic modulus ↓ Viscoelasticity parameter ↑ Hardness ↑↑ Weight	↓ Maximum stress ↓ Maximum strain ↑ Elastic modulus ↓ Viscoelasticity parameter ↑ Hardness ↑ Weight	↓ Maximum stress ↑ Maximum strain ↓ Elastic modulus ↑ Viscoelasticity parameter ↑ Hardness ↑↑ Weight
Techsil S25	Eleni et al., 2011a	Compression Hardness Absorption	↓ Maximum stress ↓ Maximum strain ↑ Elastic modulus ↑ Viscoelasticity parameter ↑ Hardness ↑↑ Weight	↓ Maximum stress ↓ Maximum strain ↑ Elastic modulus ↑ Viscoelasticity parameter ↑ Hardness ↑ Weight	↓ Maximum stress ↑ Maximum strain ↑ Elastic modulus ↓ Viscoelasticity parameter ↑ Hardness ↑↑ Weight
	Hatamleh et al., 2011	Tensile Tear Hardness	↓ Maximum stress ↓ Maximum strain ↑ Elastic modulus ↓ Tear strength ↑ Hardness	N/A	↓ Maximum stress ↓ Maximum strain = Elastic modulus ↓ Tear strength ↓ Hardness
Cosmesil M511	Eleni et al., 2011a	Compression Hardness Absorption	↓ Maximum stress ↓ Maximum strain ↑ Elastic modulus ↓ Viscoelasticity parameter ↑ Hardness ↑↑ Weight	↓ Maximum stress ↓ Maximum strain ↑ Elastic modulus ↓ Viscoelasticity parameter ↑ Hardness ↑ Weight	↓ Maximum stress ↑ Maximum strain ↑ Elastic modulus ↓ Viscoelasticity parameter ↑ Hardness ↓ Weight
	Al-Dharrab et al., 2013	Absorption	= Weight	= Weight	= Weight
Episil	Polyzois et al., 2000	Tensile Hardness Absorption	↑Maximum stress ↓ Maximum strain ↑↑ Elastic modulus ↑Tear strength ↑ Hardness ↑↑Weight	↑Maximum stress ↓ Maximum strain ↑ Elastic modulus ↓ Tear strength ↑ Hardness ↑ Weight	↑Maximum stress ↓ Maximum strain ↑ Elastic modulus ↑Tear strength ↓ Hardness ↓ Weight

The effect of other disinfection techniques on the properties of silicone have also been investigated. Eleni et al. (2013a; 2013b), as previously discussed, investigated microwave disinfection by immersing silicone samples in water and microwaving for 3 min, 365 times, to simulate daily disinfection for 1 year. While the hardness appears to decrease by a small amount when measuring with a durometer (Eleni et al., 2013a), microindentation tests showed an increase in hardness (Eleni et al., 2013b). Additionally, Kotha et al. (2016) demonstrated that longer duration microwave disinfection at 8 min damaged the surface of silicone and reduced tensile strength.

Less frequent disinfecting appears to reduce the negative effects of disinfectants. Several studies using the disinfectants chlorhexidine, effervescent method, and neutral soap, did not see any significant change in mechanical properties or dimension of silicone without additives (Goiato et al., 2008, 2009, 2010a,b, 2012b; Haddad et al., 2011). However, specimens with additives including ceramic pigments, make-up, or titanium dioxide opacifiers (used to match the appearance of patient's tissue); showed changes in mechanical properties even with the reduced disinfection regime. Additionally, the effect of different methods of prosthetic silicone disinfection vary between different additives, such as pigments and opacifiers (Goiato et al., 2010a; Guiotti et al., 2010).

ACRYLIC RESIN

Acrylic resin typically refers to the polymer poly (methyl methacrylate; PMMA). It is a clear rigid polymer mostly used as a dental base material, but also used in the fabrication of prostheses. It also has important application in prosthetic substructures for softer materials like silicone (Chalian and Phillips, 1974; Craig et al., 1980; Callaghan et al., 2006; Goiato et al., 2014). In 1944, during World War II when there was a shortage of glass, the United States Naval Dental and Medical School developed a technique to fabricate prosthetic eyes using acrylic resin (Artopoulou et al., 2006; Patil et al., 2008). The acrylic prosthetic eyes were found superior to glass; being lightweight, easy to fit and adjust, stronger than glass, translucent, easily fabricated, able to be intrinsically and extrinsically colored, and inert to socket secretions (Artopoulou et al., 2006; Raizada and Rani, 2007). As a result, acrylic resin replaced glass as the preferred material in the fabrication of prosthetic eyes like the one shown in **Figure 3a**. Unlike with silicone, there is no widely preferred products among acrylic resins, with most studies preferring the use of locally available dental resins with both (Bindhoo and Aruna, 2011; Cevik et al., 2012; Goiato et al., 2012a; Goyal et al., 2012; Ruiters et al., 2016; Shrivastava et al., 2013; Tomar et al., 2018), though many studies in India prefer dental acrylic resin from Dental Products of India (Mumbai, India) (Gupta and Padmanabhan, 2012; Veerareddy et al., 2012; Pruthi and Jain, 2013; Thirunavukkarasu et al., 2014; Tripuraneni et al., 2015; Shankaran et al., 2016; Shetty et al., 2016).

Chemistry of Acrylic Resin and Fabrication in Prosthetics

Acrylic resin is composed of units of methyl methacrylate (MMA), an ester of methacrylic acid (Callaghan et al., 2006). MMA consists of a backbone of two carbon atoms connected by a double bond; one of which is covalently bonded to two hydrogen atoms and the other is covalently bonded to a methyl and an acrylic group (Callaghan et al., 2006).

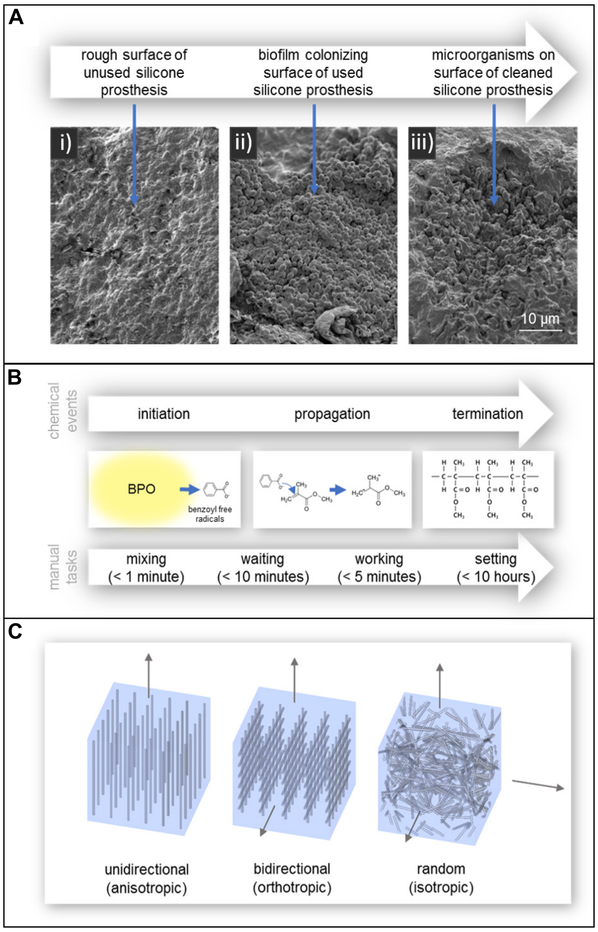

FIGURE 4 | (A) SEM images of (i) the rough surface of an unused silicone prosthesis, (ii) a biofilm colonizing the surface of a used silicone prosthesis, and (iii) microorganism remaining embedded in the defects of the prosthesis after cleaning. Reproduced from *Taylor and Francis* (Ariani et al., 2012). **(B)** Polymerization of acrylic resin and the manual tasks associated with working with autopolymerising acrylic resin. Times are according to manufacturer Factor II, Incorporated (Product Information - Heat Cured Acrylics, 2010). **(C)** Fiber reinforcement of acrylic resin; (left) unidirectional, (center) bidirectional, and (right) randomly oriented.

As the polymerization process of pure MMA monomer is quite slow, taking hours to days to cure, a more efficient method of polymerization was needed for many applications, including prosthetics. In 1936, Walter Bauer developed a solution that efficiently fabricates acrylic resin. His technique is still in use today in a variety of industries including prosthetics and dentistry (Ratner et al., 2004; Callaghan et al., 2006; Pan et al., 2013). The method works by way of a two-component system; a powder component consisting of pre-polymerized solid acrylic resin beads 10 to 150 µm in diameter, and a liquid component consisting of MMA monomer. These two components are then combined to form a dough-like material (Dumitriu, 2001; Ratner et al., 2004; Callaghan et al., 2006; Goiato et al., 2014). One of the major advantages of the two-component system in prosthetic fabrication is the ease of manipulation due to the doughy consistency of the mixed material, minimization of the heat produced (as MMA polymerization is a highly exothermic reaction), and minimization of volumetric shrinkage that occurs during MMA polymerization (therefore maintaining shape and accuracy) (Ratner et al., 2004; Callaghan et al., 2006).

The mixing of these two components can be achieved in three ways; by hand mixing alone, hand mixing followed by centrifugation, and mixing in an evacuated device (vacuum mixing) (Callaghan et al., 2006). Hand mixing is performed by combining the components in an open bowl and mixing with a spatula, creating pores in the mixture. As the mixing continues, this porosity increases. One of the drawbacks with this method is that the pores can create sites of stress concentration and also microbial growth. Centrifugation after hand mixing attempts to remove these pores by removing air from the mixture (Callaghan et al., 2006), during which MMA is often chilled to decrease the rate of polymerization, reduce mixture viscosity, and allow trapped air to evacuate (Callaghan et al., 2006). Mixing in a vacuum, while most effective at decreasing porosity and preventing MMA monomer residue, can lead to excessive shrinkage and the formation of cracks, causing inaccuracies and leaving the material prone to failure (Callaghan et al., 2006).

One of the challenges with the two component mixing approach is that pure MMA polymerizes readily if exposed to light or heat (Dumitriu, 2001), such that the liquid component requires a stabilizer (e.g., hydroquinone) to absorb any free radicals that may appear (Dumitriu, 2001; Callaghan et al., 2006).

As shown in **Figure 4b**, the polymerization process occurs in three chemical stages; initiation, propagation, and termination (Callaghan et al., 2006). In the initiation stage, benzoyl peroxide (BPO), incorporated into the powder component, is activated and decomposes into benzoyl free radicals (Ratner et al., 2004; Callaghan et al., 2006). This can occur in several ways; heat by water bath, heat by microwave radiation, incorporation of an activator (autopolymerisation/self-curing), or light (Goiato et al., 2014). The benzoyl free radicals then react with MMA monomer in the propagation stage, breaking the double bond between two carbon atoms. The MMA monomer then becomes a free radical which continues to react with another MMA monomer or attach to prepolymerised resin and the process repeats (Callaghan et al., 2006). This process ends in the termination stage, where propagation stops by chain coupling. However, not all the MMA monomers become polymerized as the curing of the polymer makes monomer diffusion more difficult. As a result, some residual monomer remains in the final polymer (Callaghan et al., 2006).

One polymerization approach, heat polymerization, involves heating the uncured resin to just above 60°C, at which BPO is activated. The advantage of this approach in prosthetics is that cheaper dental stone (gypsum) molds can be used, lowering the overall cost of the prosthesis (Chalian and Phillips, 1974; Craig et al., 1980; Ratner et al., 2004). The application of heat is achieved using a heated water bath or microwave. Of these, microwave curing has been shown to lead to a more uniform distribution of polymerization throughout the matrix and therefore, less shape distortion (Fernandes et al., 2009b).

Autopolymerisation or self-curing relies on the incorporation of chemical agents, as activators, to initiate polymerization. For BPO, this is typically an amine activator (N, N-dimethyl-p-toluidine or DMPT) (Dumitriu, 2001). Acrylic resin cured via the autopolymerisation approach releases more residual monomer than heat-polymerized resin. This leads to a greater color instability, reducing the aesthetic appearance of the final prosthesis. Another drawback is the possibility of higher cytotoxicity levels which is highly undesirable for a prosthesis regularly in contact with a person's skin or mucosal cavities such as the mouth and eye socket (de Andrade Lima Chaves et al., 2012; Goiato et al., 2014).

In the context of prosthetic production, polymerization of acrylic resin can alternatively be divided into four stages according to the associated manual tasks; mixing, waiting, working, and hardening/setting periods, as shown in **Figure 4b** (Callaghan et al., 2006).

The mixing stage involves dissolving the acrylic resin powder into the MMA monomer (Callaghan et al., 2006). The mixture becomes viscous, resulting in a tacky and paste-like consistency (Ratner et al., 2004; Callaghan et al., 2006). During the waiting period, viscosity increases until the mixture becomes doughy (Ratner et al., 2004; Callaghan et al., 2006). The working period begins when the dough is no longer tacky and can be worked and molded (Callaghan et al., 2006). In the final hardening/setting stage for autopolymerising resin, polymerization will continue with increasing viscosity and the production of heat (Callaghan et al., 2006). The final hardening stage for heat-cured resin requires them to be placed in an oven to cure. Following polymerization, prosthetic finishing includes polishing and heat treatment to smooth any rough surfaces and remove any residual monomer.

Properties of Acrylic Resin

Acrylic resin is a hard rigid material suitable as a prosthesis for rigid areas of the body such as the eye, and is also used as a reinforcing material in composite prostheses (dos Santos et al., 2012). Although highly suited to these applications, limitations include the formation of pores (or voids), volumetric shrinkage, incomplete polymerization, and tendency to fracture (Pan et al., 2013).

The mechanism behind shrinkage relates to the differing densities of MMA monomer (0.943 g/ml) and polymerized acrylic resin (120 g/ml). This shrinkage is minimized by the incorporation of acrylic resin powder; the typical mixing ratio being 1:3 (vol./vol.) MMA liquid to acrylic resin powder, respectively. This change in volume during polymerization leads to incomplete polymerization and pores may be introduced into the final product. Although this shrinkage is usually below 7%, it is still problematic in prosthetic applications that require high accuracy (e.g., connecting osseointegrated implants) (Callaghan et al., 2006).

Pores can be introduced through air dissolved in powder particles, aeration during mixing, incomplete fusion of acrylic resin beads with MMA monomer, and evaporation of MMA monomer at temperatures greater than 100°C (Callaghan et al., 2006). Pores lead to incomplete polymerization; adversely affecting the mechanical properties of acrylic resin, including mechanical strength, surface roughness and hardness (Callaghan et al., 2006; Fernandes et al., 2009a, 2010). Pores which exceed the critical size of 70 μm also act as sites for stress concentration (Callaghan et al., 2006). They also provide locations for microbial growth which can alter the material color, degrade the mechanical properties of the acrylic resin and potentially infect the patient (Fernandes et al., 2010).

Another issue with incomplete polymerization is the presence of toxic chemical residues which are undesirable when used in contact with skin and mucosal cavities, such as the mouth and eye socket (Fernandes et al., 2009a; Goiato et al., 2014). These include formaldehyde, methacrylic acid, benzoic acid, dibutyl phthalate, phenyl benzoate, phenyl salicylate, and MMA monomer (Goiato et al., 2014). For intra-oral applications, polishing is required to reduce gingival (gum) inflammation. Acrylic resin can be exposed to heat treatments or water immersion for at least 24 h to reduce the quantity of residues (Siqueira Gonçalves et al., 2008; Ata and Yavuzyılmaz, 2009; Bural et al., 2011; Saravi et al., 2012; Goiato et al., 2014). Additionally, the replacement of 10wt% of MMA monomer with dimethyl itaconate (DMI) and di-n-butyl itaconate (DBI) can reduce water sorption and residual monomer content (Spasojevic et al., 2015). In the context of intra-oral applications, this replacement would reduce gingival inflammation but decrease storage modulus, ultimate tensile strength, and impact fracture resistance; resulting in a prosthetic material more susceptible to fracture.

Degradation of Acrylic Resin

Like other materials used in prosthetics, the aesthetic and mechanical characteristics of acrylic resin degrades during use. This can occur from exposure to liquids, mechanical forces, thermal changes, and exposure to ultraviolet radiation. These changes negatively affect the aesthetic appearance of the prosthesis by changing the material color, and can degrade the material's mechanical properties leading to a greater tendency to deform or to fracture.

Acrylic resin is known to absorb water due to its polar nature (Bettencourt et al., 2010) in a process known as imbibition; the absorbed water separates the polymer chains, causing expansion of the resin and reduces flexural strength which, again, results in a greater tendency to fracture (Ekstrand et al., 1987; Fernandes et al., 2009b; Goiato et al., 2012a). Water sorption in an acrylic prosthesis also causes the diffusion of unbound/uncured monomers and/or additives from the polymer matrix (Bettencourt et al., 2010); wet artificial weathering and exposure to saliva have been found to increase microhardness due to the elimination of unpolymerized monomer on the resin surface (Fernandes et al., 2009a; Bettencourt et al., 2010). If in contact with saliva as in intra-oral prostheses, the esterases present in saliva encourage the esterification of methacrylates in the resin (Bettencourt et al., 2010). As such, contact with water or saliva may have a plasticizing effect by creating more distance between polymer chains (Ekstrand et al., 1987; Fernandes et al., 2009b; Bettencourt et al., 2010; Goiato et al., 2012a) (susceptible to deformation) or make the resin more rigid (susceptible to fracture), depending on the plasticizing effect of the additives that are leached out (Bettencourt et al., 2010).

Another source of acrylic polymer degradation in prosthetics is through applied mechanical forces, particularly weak repetitive loads such as facial movements, leading to material fatigue in the polymer matrix (Bettencourt et al., 2010). These loads, combined with voids and residual stresses already present in the matrix, encourage the initiation and propagation of cracks leading to increased water absorption, and in turn, fracture (Bettencourt et al., 2010). Internal and surface stresses can also be created by thermal changes combined with differences in linear coefficients of thermal expansion between the acrylic resin and any materials adhered within or outside of the acrylic resin (Bettencourt et al., 2010).

Color change in pigmented acrylic resin is primarily due to degradation of the pigments themselves. However, colorless acrylic resin still discolors (yellow) with age (dos Santos et al., 2010), reducing the aesthetic appearance of the prosthesis. One of these sources of color degradation is ultraviolet degradation, which can be mitigated though the incorporation of inorganic nanoparticles to absorb and dissipate much of the ultraviolet light. Unfortunately, these particles can also negatively affect flexural strength of the material (Andreotti et al., 2014).

Reinforcement of Acrylic Resin

In many prosthetic applications, the strength of some components must be enough to withstand high loads. To strengthen acrylic resin and lengthen the service life of prostheses, fibers of inorganic material (e.g., glass, carbon/graphite, and Kevlar) or high modulus polyethylene fibers may be added for reinforcement (Ekstrand et al., 1987; Vallittu, 1998, 1999; Uzun et al., 1999; Kanie et al., 2000, 2004; Chen et al., 2001; Kim and Watts, 2004; Narva et al., 2005; Pan et al., 2013). These fibers have been shown to increase properties such as impact strength and modulus of elasticity (Ekstrand et al., 1987; Uzun et al., 1999; Vallittu, 1999; Narva et al., 2005). There are several factors affecting the strength of such composites; including fiber orientation, fiber concentration, adhesion between the fibers and resin, and the fibers and resin themselves (Meriç and Ruyter, 2008). Limitations still exist in the ability to successfully reinforce acrylic, such as achieving fiber homogeneity and the desired fiber orientations, limited ability to sufficiently saturate the fibers in resin (leading to voids), and methods to avoid defects (Vallittu, 1999; Pan et al., 2013).

Unidirectional fiber reinforcement provides anisotropic mechanical properties (Meriç and Ruyter, 2008); strengthening and stiffening the material under load only along the direction of the fibers can be seen in **Figure 4c** (Uzun et al., 1999; Meriç and Ruyter, 2008). Bidirectional fiber reinforcement, such as woven glass fibers, provide enhanced orthotropic mechanical strengthening only along the surface of the fiber mesh, but much lower than with unidirectional fibers. Randomly oriented fibers provide isotropic (in all directions) material strengthening (Meriç and Ruyter, 2008).

Fiber density within the acrylic resin matrix significantly impacts the resulting composite material properties. A higher concentration of fibers within the matrix improves flexural characteristics (Chen et al., 2001; Meriç and Ruyter, 2008). Chen et al. (2001) found that impact strength increases with increased fiber concentration, however, a practical concentration limit of 3wt% was found, beyond which it became difficult to manipulate the material into the desired form. Another advantage of increasing fiber concentration is that it decreases the material's ability to absorb water, thereby maintaining mechanical properties in wet environments of mucosal cavities such as the mouth and eye socket (Meriç and Ruyter, 2008). Chen et al. also found that longer fibers resulted in higher impact strength and that none of the fibers tested (polyester, Kevlar, and glass) significantly affected bending strength or surface hardness of the final reinforced acrylic (Chen et al., 2001).

Issues that must be considered when reinforcing acrylic with fibers are voids that may arise due to the insufficient saturation of fibers. These act as oxygen reserves which inhibit polymerization and increase the percentage of residual monomer in the final prosthesis (Vallittu, 1999). Further defects can also arise following fabrication of the prosthesis during everyday use from insufficient adhesion between the fiber reinforcer and resin, making the prosthesis more prone to failure. Considering this, glass has shown superior adhesion to acrylic resin when compared with polyethylene fibers (Vallittu, 1999; Meriç and Ruyter, 2008). Further improvements in glass/polymer adhesion can be gained by using techniques such as salinization or pre-treating these glass fibers with monomer, improving the wettability of the fibers during impregnation (Meriç and Ruyter, 2008; Meriç et al., 2008).

Achieving homogenous distribution of reinforcing fibers throughout the acrylic resin is mechanically challenging. Efforts to overcome this have been attempted by using pre-impregnation of reinforcing glass fibers with resin. The products Stick and StickNET (GC EUROPE, Leuven, Belgium) pre-impregnate continuous unidirectional glass fibers or woven glass fiber with porous resin, respectively (Vallittu, 1999). The voids in the porous resin allow monomers to penetrate into the existing resin matrix when combined with powder and liquid resin (Vallittu, 1999).

Failure to achieve optimal fiber reinforcement can result in stress concentration in the material, leading to fracture and to a reduction of tensile strength below suggested theoretical values (Ekstrand et al., 1987; Vallittu, 1998). Furthermore, the use of inorganic materials as reinforcements have shown to cause mucosal irritation and damage in areas such as the mouth and eye socket (Pan et al., 2013). Voids may also be produced due to poorly saturated fibers, encouraging microbial growth (Vallittu, 1999). Other issues extend to difficulties in achieving an aesthetic natural appearance when incorporating dark-colored fibers (i.e., carbon/graphite and Kevlar). This is not an issue, however, with glass fibers and polyethylene fibers which are almost invisible when incorporated into acrylic resin (Uzun et al., 1999).

VINYL POLYMERS

Plasticized polyvinyl chloride (PVC) was once the most widely used material in soft tissue prosthetics, and is still used today in the production of gloves for prosthetic hands like the one depicted in **Figure 3b** (Gearhart, 1970; Kenworthy and Small, 1974; Carroll and Fyfe, 2004; Smit et al., 2014). It was once favored over silicones due to its lower costs, higher tear strength and lighter weight (Yu et al., 1983; Carroll and Fyfe, 2004). However, in the 1970s, its use began to dwindle as new stronger RTV silicones were developed with a higher tear strength. The increased production of these newer silicones continued over the decade, reducing their cost (Gearhart, 1970). By the time of the 1992 survey of American prosthetists, only one in 88 respondents used PVC (Andres et al., 1992). Compared to PVC, prostheses made using RTV silicone are now easier to manufacture, contain better color integrity, and have more human skin-like characteristics in both appearance and feel.

Chemistry of Vinyl Polymers and Fabrication in Prosthetics

An ideal PVC molecule would only contain single bonds of C-C, C-H, and C-Cl. However, defects as shown in **Figure 5a** tend to be present; such as unsaturated bonds (allylic chlorine), chain end groups, and branch points (i.e., tertiary-bonded chloride atoms and oxidized structures) (Shi et al., 2008; Singh and Sharma, 2008; Rabek, 2012). Unsaturated bonds (i.e., multiple bonds) enhance material degradation, discoloration and changes in mechanical properties. The degree of polymerization (i.e., number of monomeric units in a macromolecule) also impacts the number of defects present, producing locations susceptible to degradation. Shi et al. (2008) found that while PVC with a degree of polymerization of 800, 1000, or 1300 had small numbers of defects, PVC with a degree of polymerization of 3000 contained a larger number of pendant double bonds due to copolymerization with a crosslinking agent, hence a larger number of defects.

For many prosthetic applications, PVC plastisol resin is available for use. This PVC resin comprises a moderately viscous to putty-like suspension of solid polymer within a liquid plasticizer (Craig et al., 1980; Yu et al., 1983). The use of the plasticizer allows time for molding the prosthesis before PVC polymerization, but also results in shrinkage upon polymerization. When the resin is heated to 200°C using high temperature molds (Craig et al., 1980; Hutcheson and Udagama, 1980), the solid polymer swells and dissolves in the plasticizer. The mixture then becomes a gel as the temperature is lowered (Yu et al., 1983).

Plasticizers used for PVC production are usually from a group of chemicals called phthalates, particularly di-2-ethyl hexyl phthalate (DEHP). This plasticizer is usually incorporated with concentrations of at least 30wt% of PVC plastisols (Vedanarayanan and Fernandez, 1987; Heudorf et al., 2007). Phthalate plasticizers are commonly used and can be found in a range of everyday items such as building materials, household furnishings, clothing, cosmetics, pharmaceuticals, nutritional supplements, medical devices, dentures, toys, glow sticks, modeling clay, food packaging, automobiles, lubricants, waxes, cleaning materials and insecticides (Schettler, 2006; Heudorf et al., 2007).

Properties of Vinyl Polymers

Pure PVC is a clear, hard and rigid plastic (Chalian and Phillips, 1974; Craig et al., 1980). It is tasteless, odorless, darkens and yellows when exposed to UV, can be intrinsically and extrinsically stained, is insoluble in inorganic solvents and soluble in aqueous solutions. Furthermore, it can be degraded by microorganisms found in septic systems, landfills, compost and soil by enzymatic processes (Chalian and Phillips, 1974; Craig et al., 1980). To enhance the softness and elasticity of PVC, plasticizers (phthalates) are added to produce PVC plastisol (Craig et al., 1980). This compound, however, is still stiffer in comparison with typical RTV silicones.

In general, prostheses made from plasticized PVC have a natural appearance with a texture similar in feel and pliability to skin. They also have a basic translucency similar to natural flesh and are relatively easily processed, easily colored intrinsically and extrinsically, easily cleaned, retain shape, and are fairly durable (Gearhart, 1970). One of the drawbacks of plasticized PVC for use in prosthetics is their limited tear resistance which is too low to allow for molding extremely thin edges, required to integrate esthetically with native tissue. Another disadvantage is that they are environmentally unstable; being susceptible to drying and cracking, tackiness, and color changes (Gearhart, 1970; May and Guerra, 1978).

The use of phthalates as plasticizers for PVC, which enable PVC to have human skin-like properties, has important potential biocompatibility implications. As there is almost no chemical bonding between phthalates and PVC, phthalates in prostheses can leach from PVC by saline, anticoagulant citrate dextrose (ACD) solution, plasma and blood (Vedanarayanan and Fernandez, 1987; Heudorf et al., 2007). Exposure to phthalates is achieved through ingestion, inhalation, and dermal exposure. This is, in part, due to their lipophilic nature which allows them to pass through the human bi-lipid cell membrane (Schettler, 2006). Phthalates have also been extensively investigated for many possible and significant toxic effects. These include carcinogenicity, disruption of the reticulo-endocrine systems (encouraging platelet aggregation), reduction of birth weight for fetuses exposed through their mother's blood, shortening of anogenital distance in males, reduction of serum testosterone levels, and decrease of spermatocyte numbers (Vedanarayanan and Fernandez, 1987; Schettler, 2006; Heudorf et al., 2007). While DEHP, in particular, has been found to cause hepatocellular carcinoma and other

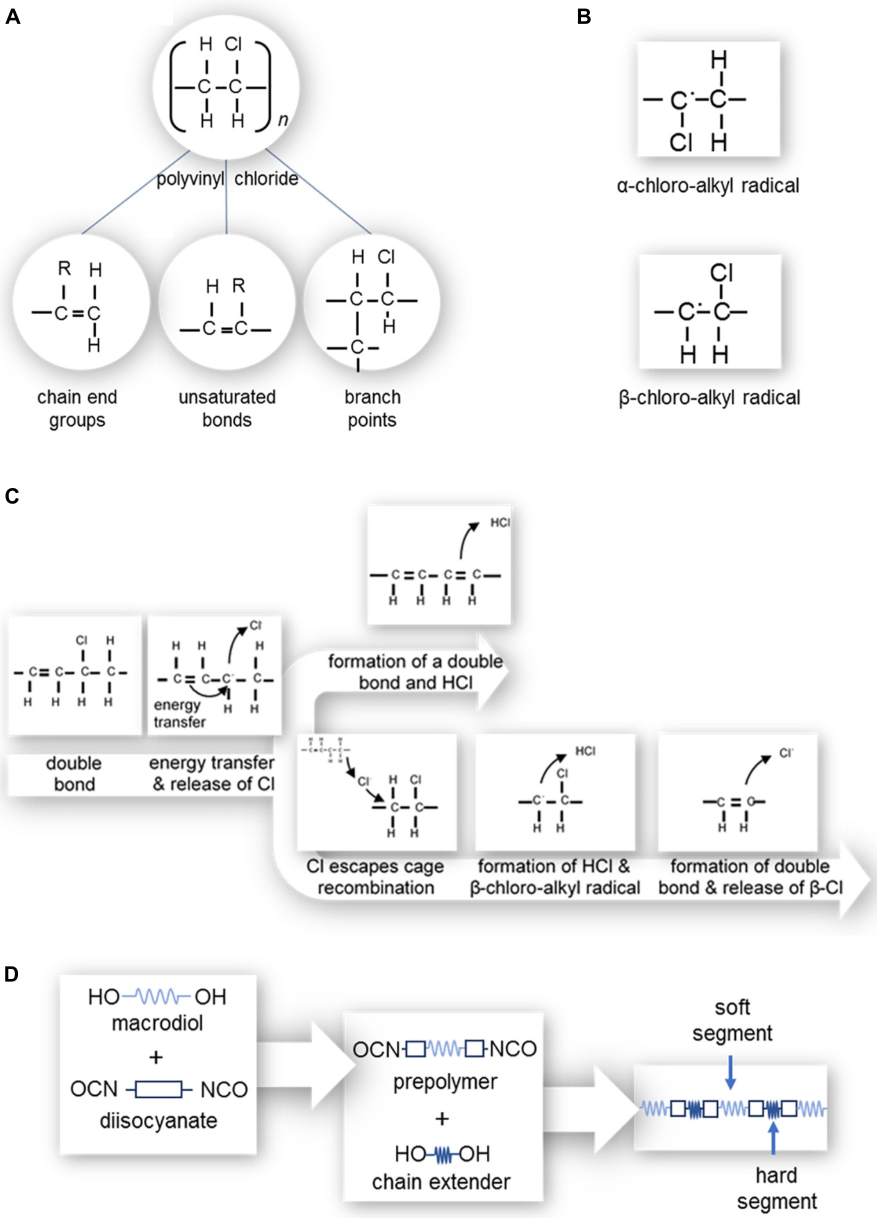

FIGURE 5 | (A) Polyvinyl chloride structure and possible defects, where the R can be either a hydrogen or chlorine atom; (left) chain end groups with an unsaturated bond, (center) branch points, and (right) unsaturated bonds along the length of the polymer chain. **(B)** α-chloro-alkyl and β-chloro-alkyl free radicals. **(C)** Zip dehydrochlorination of PVC. **(D)** Polymerization of polyurethane.

hepatocellular effects in rodents, there is no evidence that there are carcinogenic effects within the human population (Heudorf et al., 2007). There is, however, evidence to suggest that DEHP may cause disruption of the reticulo-endocrine system (Heudorf et al., 2007).

In addition to plasticizer, the vinyl chloride monomer itself possesses toxic effects and is a known human carcinogen affecting the liver (angiosarcoma), brain, lungs, and hematopoietic and lymphopoietic systems. Despite this potential, the low levels of residual monomer in clinical and commercial PVC use have not been shown to cause cancer (Vedanarayanan and Fernandez, 1987).

Degradation of Vinyl Polymers

There are two main processes involved in the degradation of PVC: 'zip' dehydrochlorination and oxidation.

Zip Dehydrochlorination of PVC

'Zip' dehydrochlorination, depicted in **Figure 5c**, leads to the progression of double bonds along the length of the polymer chain (Shi et al., 2008; Singh and Sharma, 2008; Rabek, 2012) and occurs where there is already at least one double bond present in the length of the chain (Singh and Sharma, 2008; Rabek, 2012). As such, PVC with a high degree of polymerization which has more defects, is more susceptible to 'zip' dehydrochlorination (Shi et al., 2008). Polymeric C=C bonds readily absorb energy, which can transfer to a neighboring allylic (C-Cl or C-H) bond, causing the release of a chlorine free radical or hydrogen free radical. During the release of a chlorine free radical, the neighboring hydrogen atom may be released to from a double bond (-CH = CH-) and HCl molecule, or the chlorine free radical may escape cage recombination. In the case of the release of a hydrogen free radical, a β-chloro-alkyl radical (**Figure 5b**) is formed. This radical has a short lifespan as it readily releases a β-chlorine free radical to form a double bond (–CH = CH–).

This chlorine free radical, or those which have escaped cage recombination, is able to attack other allylic bonds, forming α-chloro-alkyl or β-chloro-alkyl free radicals (**Figure 5b**) and subsequent double bonds (Rabek, 2012). In the context of prosthetics, the formation of double bonds progressively degrades the color of PVC to a yellow and then dark red-brown, creating an obvious mismatch with native tissues (Shi et al., 2008; Rabek, 2012).

Oxidation of PVC

Oxidation of PVC occurs with the removal of hydrogen from PVC by a free radical, resulting in α-chloro-alkyl and β-chloro-alkyl free radicals (**Figure 5b**). These polymer alkyl radicals react with molecular oxygen, resulting in polymer peroxy radicals which subsequently remove hydrogen from neighboring allylic bonds or allylic bonds of other molecules (Rabek, 2012). As for zip' dehydrochlorination, PVC oxidation also causes the PVC's color to degrade to yellow before turning a dark red-brown. Additionally, the peroxy radicals become hydroperoxides which decompose to form ketones, aldehydes, acids, etc., which can lead to skin irritation of the person wearing the prosthesis (Shi et al., 2008; Rabek, 2012).

Reinforcement of Vinyl Polymers

Polyvinyl chloride can be reinforced with a copolymer, polyvinyl acetate, to produce polyvinyl chloride acetate (PVCA). This copolymer is usually composed of 5–20% vinyl acetate polymers and copolymers. The advantages of reinforcing in this manner are improved stability to light and heat as well as lower temperature softening point. Other advantages over non-reinforced PVC are improved flexibility, chemical resistance, and heat and UV stability (Chalian and Phillips, 1974).

POLYURETHANE ELASTOMER

In 1937, Otto Bayer discovered that diisocyanates and aliphatic diols (glycols) reacted to produce a material useful as a plastic or as a fiber (Covolan et al., 2004; Sharmin and Zafar, 2012). This material, called polyurethane (PU), is named such due to the urethane bond joining their monomers. As a prosthetic material, polyurethanes are useful as a bulk elastic polymer, as a liner, and as a foam.

Chemistry of Polyurethane and Fabrication in Prosthetics

Since Bayer's discovery, the synthesis of polyurethanes has expanded to include the reactions of many more isocyanates and diols (two hydroxyl groups)/polyols (multiple hydroxyl groups) to produce a large range of different physical properties through the combination of hard and soft segments (Chalian and Phillips, 1974; Goldberg et al., 1978; Craig et al., 1980; Affrossman et al., 1991; Covolan et al., 2004).

In the synthesis of polyurethanes, polyols can include aliphatic diols, hydroxyl terminated polyethers or polyesters. Longer chain polyethers and polyesters form the soft segments of the polymer chain. These are important in prosthetics to produce a soft skin-like feeling. Polyether polyols are preferable in the fabrication of soft tissue prosthetics; as they add flexibility, elasticity, softness, hydrophobicity, and resistance to hydrolytic degradation (Touchet and Cosgriff-Hernandez, 2016) while polyesters are susceptible to hydrolytic degradation with strong mechanical properties (Sharmin and Zafar, 2012; Touchet and Cosgriff-Hernandez, 2016).

The isocyanate groups, which compose the hard segments of the polymer chain, can be di or poly functional (Craig et al., 1980). They can also be aliphatic or an aromatic, with the aliphatic groups being more resistant against degradation due to UV exposure and hydrolysis, important for improved prosthetic service life (Chalian and Phillips, 1974; Craig et al., 1980). Aromatic groups, however, have stronger mechanical properties which may be given preference over UV stability (Touchet and Cosgriff-Hernandez, 2016).

Chain propagation (polymerization) occurs through the reaction between the polyol and isocyanate groups to result in a chain of hard and soft segments (Chalian and Phillips, 1974; Goldberg et al., 1978; Craig et al., 1980). Crosslinking between chains then occurs by trifunctional chain extenders, allophanate linkage, biuret linkage, and physical crosslinks on paracrystalline domains (Goldberg et al., 1978). It is possible to achieve this process of crosslinking at 100°C, allowing the use of dental stone molds and thereby lowering the cost of prosthetic production (Craig et al., 1980).

Often, diisocyanate-terminated pre-polymers are prepared in an initial stage, as shown in **Figure 5d** (Covolan et al., 2004). These pre-polymers are then joined through the use of a highly reactive diol chain extender/crosslinker (Goldberg et al., 1978; Covolan et al., 2004). This joins two isocyanate groups with a short diol producing a hard segment (Goldberg et al., 1978). The process allows for improved control over the chain sequence with longer soft segments produced as prepolymers before being connected by hard segments. The ability to tailor the segment lengths allows high degrees of control over the softness of the final prosthesis.

Polyurethane synthesis is stoichiometric, where the mass of the products equals the mass of the reactants, and therefore is a very sensitive technique (Goldberg et al., 1978; Craig et al., 1980; Aggarwal et al., 2016). Furthermore, the presence of moisture during this reaction will cause voids due to the release of carbon dioxide. These voids produce many unwanted effects such as altering the overall appearance and feeling of the prosthesis, reducing the reactivity of isocyanate groups which leads to incomplete polymerization, and producing polyureas which can irritate the skin of the wearer of the prosthesis (Chalian and Phillips, 1974; Goldberg et al., 1978; Craig et al., 1980; Affrossman et al., 1991). Organotin catalysts are another chemical used during synthesis to increase the rate of chain propagation (Goldberg et al., 1978; Craig et al., 1980). However, their effect can be neutralized by moisture which causes oxidation of catalysts. This, in turn, lowers the crosslink density and molecular weight of the final prosthesis (Goldberg et al., 1978).

When fabricating polyurethane foam, used in prosthetics where cushioning is needed (Rothman, 1962), the presence of moisture is not an error, but a necessity. The addition of both water and an emulsifier to the polyol-isocyanate reaction allows polymerization and the formation of gas to occur simultaneously. This results in desired voids within a gel structure (Rothman, 1962). The stiffness of the foam depends in part on the molecular structure of the chosen polyols. It is of note, that the stiffness of foam is not a constant as it undergoes multi-phase load-deformation (Todd et al., 1998).

Thermoplastic polyurethane elastomers can also be fabricated based on polycarbonates or polysiloxanes (Špírková et al., 2011; Liu et al., 2019). These additions can significantly change the mechanical and thermal properties of the polyurethane, in many cases improving their tensile strength and modulus and lowering the elasticity of the material. Polycarbonate based polyurethanes also generally possess improved resistance to organic solvents and are less sensitive to biodegradation (Eceiza et al., 2008). For example, the addition of polycarbonate nanoparticles into the polyurethane shows a distinctly segmented structure with strong changes seen in the tensile properties and large effects on dynamic mechanical thermal properties (Špírková et al., 2011). It is also possible to tailor the mechanical properties of the material by varying the molecular weights of the hard and soft segments. For example, synthesizing for a greater content of hard segments has been shown to increase the tensile modulus and decrease elongation at break (Eceiza et al., 2008). The properties of polycarbonate based polyurethanes lend themselves to orthopedic implant and cardiovascular prosthetics applications, however, they have found limited use in soft-tissue external prosthetics (Gostev et al., 2018). Polysiloxane based polyurethanes also have important biomedical engineering applications such as prosthetic dentistry, tissue engineering, breast prostheses and prosthetic linings, with good biocompatibility and material flexibility (González Calderón et al., 2019). Polyurethanes can have important application in prosthetics as a liner to interface between silicone prostheses and the patient's skin. Silicones, as previously described, have many disadvantages including poor tear resistance at thin edges, vulnerability to microbial colonization, and absorption of facial oils (Grant et al., 2001; Deng et al., 2004; Chang et al., 2009). In 1987, Udagama (Udagama, 1987) studied the use of an aromatic polyether polyurethane film (Factor II, Inc.)[1] to line silicone facial prostheses by preparing the silicone with Medical Adhesive Type A (Dow Corning Company) and the polyurethane sheet with S-2260 primer (Dow Corning Company) (Udagama, 1987; Deng et al., 2004; Kiat-amnuay et al., 2008; Chang et al., 2009; Patil et al., 2010; Shrivastava et al., 2015). The addition of the polyurethane liner improves the tear resistance of the thin regions of the silicone prosthesis, seals the silicone from absorbing oil, allows the use of water-based skin adhesives, increases surface smoothness thereby increasing comfort and ease of cleaning, and limiting microbial growth (Grant et al., 2001; Deng et al., 2004; Kiat-amnuay et al., 2008; Chang et al., 2009; Abd El-Fattah et al., 2013; Aggarwal et al., 2016). However, the methods of lining a silicone prosthesis with polyurethane methods have been described as lengthy and sophisticated (Abd El-Fattah et al., 2013) and Medical Adhesive Type A (Dow Corning Company) is known to produce acetic acid (an irritant) as it cures (Chang et al., 2009). In 1992, 8.0% of 88 respondents to a survey of American prosthetists (Andres et al., 1992) used this technique to line prostheses. A 2010 survey of 43 respondents found that 20.9% of respondents still used polyurethane lining for silicone prostheses with 41.9% of respondents having used it in the past (Montgomery and Kiat-Amnuay, 2010). The respondents of the 2010 survey used 0.05 mm polyurethane sheeting from Factor II, Inc. with PR-1205 (Dow Corning Company), Sofreliner (Tokuyama Dental America Inc., Encinitas, CA, United States), and A-330-G (Factor II Inc.) primers.

Properties of Polyurethane

Polyurethane used in prosthetics is pigmentable, relatively environmentally stable, does not require plasticizers to achieve a low modulus of elasticity, has a high tensile strength, and has high tear resistance. However the reactions to produce polyurethane are stoichiometric, therefore difficult to work with, furthermore the material shows a yellow discoloration after aging (Chalian and Phillips, 1974; Goldberg et al., 1978; Craig et al., 1980). As discovered in a study by Leonhard et al. (2013), polyurethanes are also more susceptible to biofilm formation than silicone, potentially due to crack formation that occurs if the polyurethane becomes saturated with water.

The use of polyurethane as a liner for silicone prostheses is made more challenging due to difficulties adhering polyurethane with silicone layers. Although adherence can be improved through the use of a primer, it is still limited and prone to failure (Grant et al., 2001; Deng et al., 2004; Chang et al., 2009). This delamination has been shown to be repairable by Wu and Gerngross (2009), who reapplied polyurethane liner onto a silicone prosthesis.

---

[1] https://solutions.covestro.com/en/brands/dureflex

Degradation of Polyurethane

The use of polyurethane as a liner in silicone prostheses has been shown to improve the preservation of tear resistance, elasticity and tensile strength of silicone prostheses (Abd El-Fattah et al., 2013). The advantages of this polymer as a liner, however, are mitigated due to a heightened vulnerability of unwanted biofilm formation on polyurethane over silicone as shown in a study by Leonhard et al. (2013). The reason for this has been investigated by Boubakri et al. (2010) who found that, when immersed in water, micro-cracks appear in the surface. This is because polyurethane first follows a Fickian domain, such that the rate of absorption is proportional to the square root of time of immersion. During this time there is an initial plasticization effect; the water molecules increase flexibility and tensile properties of polyurethane as they diffuse between the molecular chains (Boubakri et al., 2010). However, as the level of absorption exceeds saturation, micro-cracks appear (Boubakri et al., 2010), forming ideal environments for the formation of biofilms.

CHLORINATED POLYETHYLENE

In 1973, at a conference on the state of maxillofacial prosthetic materials held by the National Institute of Dental Research, the Gulf South Research Institute proposed that research be conducted into a variety of industrial rubber materials as potential maxillofacial prosthetic materials (Lemon et al., 2005). The institute received a grant to fund their research from 1976 to 1979 (May and Guerra, 1978; Lemon et al., 2005). During this time, a new prosthetic material made from thermoplastic chlorinated polyethylene (CPE) was formulated. This material appeared to have similar material properties to silicones, but was low cost and possessed thermoplastic properties such as the ability to be easily repaired, relined, reconditioned and reprocessed (May and Guerra, 1978; Kiat-amnuay et al., 2010). CPE is also more easily bonded than silicone and possesses a greater tear strength and surface wettability (May and Guerra, 1978; Kiat-amnuay et al., 2008). Further funding was obtained from 1983 to 1987 which enabled the formula to be refined and a small clinical trial at the Charity Hospital of New Orleans commenced (Lemon et al., 2005). In 2010, Kiat-amnuay et al. (2010) published a prospective, randomized, controlled, double-blind, single-crossover, multicentre, phase III clinical trial comparing maxillofacial prostheses made of CPE and medical-grade silicone. Amongst other findings, it was shown that while patients who were familiar with silicone prostheses found silicone to be superior in comfort and appearance, patients who were unfamiliar with silicone prostheses showed no preference between the two materials.

Chemistry of Chlorinated Polyethylene and Fabrication in Prosthetics

Chlorinated polyethylene is produced by the controlled chlorination of high-density polyethylene in an aqueous slurry, such that the chlorination of the polymer chain occurs randomly. CPEs vary in chlorine content (approximately 25 to 42%), molecular weight and crystallinity (Manaila et al., 2012).

In order to use CPE as a material in prosthetic fabrication, it must be processed on heated mills into large sheets. During this process, intrinsic colorants may be added as needed to match the pigment color of the patient (Kiat-amnuay et al., 2008, 2010). To further improve the aesthetics of the final prosthesis, the sheets can also be processed with red rayon flocking to appear as capillaries on the surface (Kiat-amnuay et al., 2010). The CPE and mold are then heated to 110–115° (Kiat-amnuay et al., 2008, 2010; Eleni et al., 2009c, 2011c) or placed in a pressure cooker at approximately 60kPa (equivalent to 115°C) (Kiat-amnuay et al., 2008, 2010) for 10 min. This necessitates that the mold must be placed into a metal flask to prevent fracture (Kiat-amnuay et al., 2008, 2010). After this, more CPE is added and the process repeated until the mold is sufficiently filled (Kiat-amnuay et al., 2010). Kiat-amnuay et al. (2010), in their clinical trial, found that prosthetic technicians criticized CPE prostheses as more complex, harder to manipulate, having more flaws, and more likely to break during fabrication when compared with conventional silicone prostheses. These criticisms were formed even though the overall time to fabricate CPE prostheses was reported to be shorter than that for silicone (Kiat-amnuay et al., 2010).

Properties of Chlorinated Polyethylene

Chlorinated polyethylene is a thermoplastic with applications as a maxillofacial prosthetic material as an alternative to silicones, partly due to its low cost and thermoplastic properties (May and Guerra, 1978; Kiat-amnuay et al., 2010). As a thermoplastic, CPE can be repaired, relined, reconditioned, and reprocessed in a short time for small corrections. CPE can also be used with a wider variety of adhesives than silicone, and has much greater tear strength, and surface wettability comparable to skin (May and Guerra, 1978; Kiat-amnuay et al., 2008). In addition, CPE is very low in toxicity, non-carcinogenic, less irritating to the mucosa than silicone, and does not support fungus growth (Kiat-amnuay et al., 2010). The drawbacks of CPE in soft tissue prosthetics, however, is that prostheses of CPE tend to have thicker borders and are more difficultly matched to the skin color and texture of the patient (Kiat-amnuay et al., 2010).

Degradation of Chlorinated Polyethylene

Like other polymers used in prosthetics, CPE is also susceptible to degradation over time. Outdoor weathering has been found to affect CPE by increasing maximum stress and strain while decreasing the elastic modulus (compression and tensile), yield stress and strain, hardness, and glass transition temperature (Eleni et al., 2009b,d, 2011c). Unlike silicone, which undergoes crosslinking over time (becoming harder), nuclear magnetic resonance and infrared spectroscopy studies have found that CPE mainly undergoes chain scission reactions during photo-oxidative degradation, leading to softening of the polymer (Eleni et al., 2009b,d, 2011c).

The relative newness of this polymer means there are few studies on the effect of skin secretions on its aesthetic and mechanical properties. While simulated perspiration has been found to increase the elastic modulus, hardness, and the weight of CPE to make it less skin like; simulated sebum decreases the elastic modulus, hardness, and weight (Eleni et al., 2009c). It is theorized that while simulated perspiration (an aqueous solution) causes water absorption and the propagation of crosslinking reactions, simulated sebum (a fatty solution) interacts with the surface of the polymer to extract compounds (Eleni et al., 2009c). Maximum stress and strain, however, are not significantly affected by either solution. Color, on the other hand, is significantly changed by both simulated perspiration and sebum, more greatly by simulated sebum. This is not ideal for a prosthesis that must blend in with native tissues. Glass transition temperature was increased by simulated perspiration; and melting temperature was increased in both solutions (Eleni et al., 2009c).

The effect of different disinfection methods is more unclear. Eleni et al. published two papers in 2013 (Eleni et al., 2013a,b), investigating the effects of microwave disinfection, sodium hypochlorite solution, neutral soap, and commercial disinfectant on CPE. The two papers found contrasting results on whether sodium hypochlorite solution caused an increase (Eleni et al., 2013b) or a decrease (Eleni et al., 2013a) in hardness, suggesting that more work is needed to understand the material.

CONCLUSION

Polymers in soft tissue prosthetics are life-changing for most people affected by disfigurement by restoring function and aesthetics. The key challenge is to replicate all unique properties of natural living tissue using these synthetic polymer materials. Furthermore, with the prosthetic polymers' exposure to UV light, salt water, make up and skin secretions, it is vital to understand and control physical, chemical, biological and aesthetic changes in the polymers over time to ensure patients are provided with the best possible improvement in their quality of life.

From simple woods and metals used as prosthetics thousands of years ago to composite polymers, the progression of materials science has seen impressive advancements. Although there is no perfect material available for all applications, consideration must be given to the aesthetics, attachment, fabrication, robustness and the wellbeing of the patient. Prostheses for various regions of the body also require unique considerations, mimicking as closely as possible their unique anatomies and environments.

Commonly used prosthetic materials possess an impressive array of characteristics. Today represents the crossroad in materials development and fabrication techniques as new 3D healthcare technologies begin to replace traditional hand-crafting techniques. This will revolutionize the aesthetics and function of prostheses themselves, and lead to new innovations that provide even greater realism and lower costs. These 3D manufacturing technologies and new techniques will drive down healthcare costs to bring the goal of universal access to better polymer prostheses closer to the patient. Though developments in tissue-engineered solutions are posed to replace the use of these temporary external prostheses, there will always be a role for external prostheses, either as a temporary or more affordable solution to restoring facial aesthetic. These tissue-engineered implants will employ a different range of biopolymers; such as polycaprolactone, polylactic acid, and polyglycolic acid; to meet a different set of requirements in the fabrication of 3D printed tissues (Ding et al., 2019; Zhang et al., 2019). The future of prosthetics, developed through the close collaboration between researchers, industry, healthcare workers and patients, will continue to provide better solutions and ensure improved quality of life for millions of people around the world.

AUTHOR CONTRIBUTIONS

MW and SP contributed to the conception of the manuscript. RC and MR researched and wrote the first draft and revised the manuscript. MW and SP structured, reviewed, and revised the manuscript. All authors contributed to manuscript revision, and have read and approved the submitted version.

FUNDING

This work was supported by the Australian Government Research Training Program (2016); Advance Queensland (Ph.D. Top Up Scholarship, 2016, Knowledge Transfer Partnership, 2016); and MTP Connect: (Grant Number PRJ2016-38).

ACKNOWLEDGMENTS

Thank you to the Australian Government, Advance Queensland, and MTP connect for the funding to conduct this research.

REFERENCES

Abd El-Fattah, M. Y., Rashad, H. M., Kashef, N. A., and El Ebiary, M. A. (2013). Evaluation of two different reinforcing materials used with silicone auricular prostheses. *Tanta Dent. J.* 10, 31–38. doi: 10.1016/j.tdj.2013.08.001

Affrossman, S., Barbenel, J. C., Forbes, C. D., MacAllister, J. M. R., Meng, J., Pethrick, R. A., et al. (1991). Surfasce structure and biocompatibility of polyurethanes. *Clin. Mater.* 8, 25–31. doi: 10.1016/0267-6605(91)90006-2

Aggarwal, H., Kumar, P., and Singh, S. V. (2016). Modified technique to improve fabrication and outcome of definitive orbital prosthesis. *Orbit* 35, 66–68. doi: 10.3109/01676830.2015.1078379

Alam, M. S., Sugavaneswaran, M., Arumaikkannu, G., and Mukherjee, B. (2017). An innovative method of ocular prosthesis fabrication by bio-CAD and rapid 3-D printing technology: a pilot study. *Orbit* 36, 223–227. doi: 10.1080/01676830.2017.1287741

Al-Dharrab, A. A., Tayel, S. B., and Abodaya, M. H. (2013). The effect of different storage conditions on the physical properties of pigmented medical grade I silicone maxillofacial material. *ISRN Dent.* 2013:582051. doi: 10.1155/2013/582051

Al-Harbi, F. A., Ayad, N. M., Saber, M. A., ArRejaie, A. S., and Morgano, S. M. (2015). Mechanical behavior and color change of facial prosthetic elastomers after outdoor weathering in a hot and humid climate. *J. Prosthet. Dent.* 113, 146–151. doi: 10.1016/j.prosdent.2014.09.008

Andreotti, A. M., Goiato, M. C., Moreno, A., Nobrega, A. S., Pesqueira, A. A., and dos Santos, D. M. (2014). Influence of nanoparticles on color stability, microhardness, and flexural strength of acrylic resins specific for ocular prosthesis. *Int. J. Nanomed.* 9, 5779–5787. doi: 10.2147/IJN.S71533

Andres, C. J., Haug, S. P., Brown, D. T., and Bernal, G. (1992). Effects of environmental factors on maxillofacial elastomers: part II—report of survey. *J. Prosthet. Dent.* 68, 519–522. doi: 10.1016/0022-3913(92)90422-7

Andriot, M., Chao, S. H., Colas, A. R., Cray, S. E., DeBuyl, F., DeGroot, J. V., et al. (2009). Silicones in industrial applications. *Silicon-Based Inorg. Polym.* 84, 1–160.

Anusavice, K. J. (2013). *Phillips' Science of Dental Materials - E-Book*, 12th Edn. Philadelphia, PA: Saunders.

Ariani, N., Vissink, A., van Oort, R. P., Kusdhany, L., Djais, A., Rahardjo, T. B. W., et al. (2012). Microbial biofilms on facial prostheses. *Biofouling* 28, 583–591. doi: 10.1080/08927014.2012.698614

Artopoulou, I.-I., Montgomery, P. C., Wesley, P. J., and Lemon, J. C. (2006). Digital imaging in the fabrication of ocular prostheses. *J. Prosthet. Dent.* 95, 327–330. doi: 10.1016/j.prosdent.2006.01.018

Ata, S. O., and Yavuzyılmaz, H. (2009). *In vitro* comparison of the cytotoxicity of acetal resin, heat-polymerized resin, and auto-polymerized resin as denture base materials. *J. Biomed. Mater. Res. Part B Appl. Biomater.* 91B, 905–909. doi: 10.1002/jbm.b.31473

Aziz, T., Waters, M., and Jagger, R. (2003a). Analysis of the properties of silicone rubber maxillofacial prosthetic materials. *J. Dent.* 31, 67–74. doi: 10.1016/s0300-5712(02)00084-2

Aziz, T., Walters, M., and Jagger, R. (2003b). Development of a new poly(dimethylsiloxane) maxillofacial prosthetic material. *J. Biomed. Mater. Res.* 65B, 252–261. doi: 10.1002/jbm.b.10559

Barnhart, G. W. (1960). A new material and technic in the art of somato-prosthesis. *J. Dent. Res.* 39, 836–844. doi: 10.1177/00220345600390041001

Bellamy, K., Limbert, G., Waters, M. G., and Middleton, J. (2003). An elastomeric material for facial prostheses: synthesis, experimental and numerical testing aspects. *Biomaterials* 24, 5061–5066. doi: 10.1016/s0142-9612(03)00412-5

Bettencourt, A. F., Neves, C. B., de Almeida, M. S., Pinheiro, L. M., Oliveira, S. A. E., Lopes, L. P., et al. (2010). Biodegradation of acrylic based resins: a review. *Dent. Mater* 26, e171–e180. doi: 10.1016/j.dental.2010.01.006

Bindhoo, Y. A., and Aruna, U. (2011). Prosthetic rehabilitation of an orbital defect: a case report. *J. Indian Prosthodont. Soc.* 11, 258–264. doi: 10.1007/s13191-011-0093-6

Boubakri, A., Haddar, N., Elleuch, K., and Bienvenu, Y. (2010). Impact of aging conditions on mechanical properties of thermoplastic polyurethane. *Mater. Des.* 31, 4194–4201. doi: 10.1016/j.matdes.2010.04.023

Bural, C., Aktaş, E., Deniz, G., Ünlüçerçi, Y., and Bayraktar, G. (2011). Effect of leaching residual methyl methacrylate concentrations on in vitro cytotoxicity of heat polymerized denture base acrylic resin processed with different polymerization cycles. *J. Appl. Oral Sci.* 19, 306–312. doi: 10.1590/S1678-77572011005000002

Callaghan, J. J., Rosenberg, A. G., and Rubash, H. E. (2006). *The adult hip*. Lippincott: Willliams & Wilkins.

Cancer Australia, (2019). *External Breast Prostheses*. Available online at: https://breast-cancer.canceraustralia.gov.au/treatment/surgery/breast-reconstruction/external-breast-prostheses (Accessed February 25, 2019).

Carroll, ÁM., and Fyfe, N. (2004). A comparison of the effect of the aesthetics of digital cosmetic prostheses on body image and well-being. *JPO J. Prosthetics Orthot* 16, 66–68. doi: 10.1097/00008526-200404000-00007

Cevik, P., Dilber, E., and Eraslan, O. (2012). Different techniques in fabrication of ocular prosthesis. *J. Craniofac. Surg.* 23, 1779–1781. doi: 10.1097/SCS.0b013e31826701bb

Chalian, V. A., and Phillips, R. W. (1974). Materials in maxillofacial prosthetics. *J. Biomed. Mater. Res. Part A* 8, 349–363. doi: 10.1002/jbm.820080415

Chang, P. P., Hansen, N. A., Phoenix, R. D., and Schneid, T. R. (2009). The effects of primers and surface bonding characteristics on the adhesion of polyurethane to two commonly used silicone elastomers. *J. Prosthodont.* 18, 23–31. doi: 10.1111/j.1532-849X.2008.00371.x

Chen, S., Liang, W., and Yen, P. (2001). Reinforcement of acrylic denture base resin by incorporation of various fibers. *J. Biomed. Mater. Res.* 58, 203–208. doi: 10.1002/1097-4636(2001)58:2<203::aid-jbm1008>3.0.co;2-g

Ciocca, L., Mingucci, R., Gassino, G., and Scotti, R. (2007). CAD/CAM ear model and virtual construction of the mold. *J. Prosthet. Dent.* 98, 339–343. doi: 10.1016/S0022-3913(07)60116-4

Colas, A. (2005). *Silicones: Preparation, Properties and Performance*. Amsterdam: Elsevier.

Cook, R. R., Harrison, M. C., and Levier, R. R. (1994). The breast implant controversy. *Arthritis Rheum.* 37, 153–157. doi: 10.1002/art.1780370202

Çötert, H. S. (2015). Stereolithographic rapid prototyping of ear prostheses. *Int. J. Appl. Dent. Sci.* 1, 64–67.

Covestro-Films-Dureflex® . Thermoplastic Polyurethane (TPU).

Covolan, V. L., Di Ponzio, R., Chiellini, F., Grillo Fernandes, E., Solaro, R., and Chiellini, E. (2004). *Polyurethane Based Materials for the Production of Biomedical Materials. in Macromolecular Symposia*. Hoboken, NJ: Wiley Online Library, 273–282.

Craig, R. G., Koran, A., and Yu, R. (1980). Elastomers for maxillofacial applications. *Biomaterials* 1, 112–117. doi: 10.1016/0142-9612(80)90010-1

Curtis, J. M., and Colas, A. (2004). Dow Corning® silicone biomaterials: history, chemistry & medical applications of silicones. *Biomater. Sci* 2,

de Andrade Lima Chaves, C., Machado, A. L., Vergani, C. E., de Souza, R. F., and Giampaolo, E. T. (2012). Cytotoxicity of denture base and hard chairside reline materials: a systematic review. *J. Prosthet. Dent.* 107, 114–127. doi: 10.1016/S0022-3913(12)60037-7

Deng, H.-Y., Zwetchkenbaum, S., and Noone, A.-M. (2004). Bond strength of silicone to polyurethane following immersion of silicone in cleaning solutions. *J. Prosthet. Dent.* 91, 582–585. doi: 10.1016/j.prosdent.2003.09.005

Ding, J., Zhang, J., Li, J., Li, D., Xiao, C., Xiao, H., et al. (2019). Electrospun polymer biomaterials. *Prog. Polym. Sci.* 90, 1–34. doi: 10.1016/j.progpolymsci.2019.01.002

dos Santos, D. M., Goiato, M. C., Moreno, A., Pesqueira, A. A., and Haddad, M. F. (2011). Influence of pigments and opacifiers on color stability of an artificially aged facial silicone. *J. Prosthodont.* 20, 205–208. doi: 10.1111/j.1532-849X.2010.00657.x

dos Santos, D. M., Goiato, M. C., Sinhoreti, M. A. C., Fernandes, A. ÚR., Ribeiro, P., do, P., et al. (2010). Color stability of polymers for facial prosthesis. *J. Craniofac. Surg* 21, 54–58. doi: 10.1097/SCS.0b013e3181c3b58e

dos Santos, D. M., Goiato, M. C., Sinhoreti, M. A. C., Moreno, A., Dekon, S. F., de, C., et al. (2012). Influence of natural weathering on colour stability of materials used for facial prosthesis. *J. Med. Eng. Technol.* 36, 267–270. doi: 10.3109/03091902.2012.682113

Dow Corning, (2006). *SILASTIC BioMedical Grade Liquid Silicone Rubbers*. Midland, MI: Dow Corning.

Dumitriu, S. (2001). *Polymeric Biomaterials, Revised and Expanded.* . Boca Raton, FL: CRC Press.

Eceiza, A., Martin, M. D., de la Caba, K., Kortaberria, G., Gabilondo, N., Corcuera, M. A., et al. (2008). Thermoplastic polyurethane elastomers based on polycarbonate diols with different soft segment molecular weight and chemical structure: mechanical and thermal properties. *Polym. Eng. Sci* 48, 297–306. doi: 10.1002/pen.20905

Ekstrand, K., Ruyter, I., and Wellendorf, H. (1987). Carbon/graphite fiber reinforced poly (methyl methacrylate): properties under dry and wet conditions. *J. Biomed. Mater. Res. Part A* 21, 1065–1080. doi: 10.1002/jbm.820210902

Eleni, P. N., Katsavou, I., Krokida, M. K., and Polyzois, G. L. (2009a). Color stability of facial silicone prosthetic elastomers after artificial weathering. *Dent. Res. J.* 5, 71–79.

Eleni, P. N., Krokida, M., Polyzois, G., Gettleman, L., and Bisharat, G. I. (2011c). Effects of outdoor weathering on facial prosthetic elastomers. *Odontology* 99, 68–76. doi: 10.1007/s10266-010-0145-0

Eleni, P. N., Krokida, M. K., Frangou, M. J., Polyzois, G. L., Maroulis, Z. B., and Marinos-Kouris, D. (2007). Structural damages of maxillofacial biopolymers under solar aging. *J. Mater. Sci. Mater. Med.* 18, 1675–1681. doi: 10.1007/s10856-007-3027-4

Eleni, P. N., Krokida, M. K., and Polyzois, G. L. (2011a). Effects of storage in simulated skin secretions on mechanical behavior and color of polydimethylsiloxanes elastomers. *J. Craniofac. Surg.* 22, 830–836. doi: 10.1097/SCS.0b013e31820f36e0

Eleni, P. N., Krokida, M. K., Polyzois, G. L., Charitidis, C. A., Koumoulos, E. P., Tsikourkitoudi, V. P., et al. (2011b). Mechanical behaviour of a poydimethylsiloxane elastomer after outdoor weathering in two different weathering locations. *Polym. Degrad. Stab.* 96, 470–476. doi: 10.1016/j.polymdegradstab.2011.01.017

Eleni, P. N., Krokida, M. K., Polyzois, G. L., and Gettleman, L. (2013a). Effect of different disinfecting procedures on the hardness and color stability of two maxillofacial elastomers over time. *J. Appl. Oral Sci.* 21, 278–283. doi: 10.1590/1679-775720130112

Eleni, P. N., Perivoliotis, D., Dragatogiannis, D. A., Krokida, M. K., Polyzois, G. L., Charitidis, C. A., et al. (2013b). Tensile and microindentation properties of maxillofacial elastomers after different disinfecting procedures. *J. Mech. Behav. Biomed. Mater.* 28, 147–155. doi: 10.1016/j.jmbbm.2013.07.013

Eleni, P. N. N., Katsavou, I., Krokida, M. K. K., Polyzois, G. L. L., and Gettleman, L. (2009b). Mechanical behavior of facial prosthetic elastomers after outdoor weathering. *Dent. Mater.* 25, 1493–1502. doi: 10.1016/j.dental.2009.06.018

Eleni, P. N., Krokida, M. K., Polyzois, G. L., and Gettleman, L. (2009c). Material properties of a maxillofacial chlorinated polyethylene elastomer stored in simulated skin secretions. *J. Biomed. Mater. Res. Part B Appl. Biomater.* 91B, 964–974. doi: 10.1002/jbm.b.31482

Eleni, P. N., Krokida, M. K., and Polyzois, G. L. (2009d). The effect of artificial accelerated weathering on the mechanical properties of maxillofacial polymers PDMS and CPE. *Biomed. Mater.* 4:035001. doi: 10.1088/1748-6041/4/3/035001

Fantini, M., De Crescenzio, F., and Ciocca, L. (2013). Design and rapid manufacturing of anatomical prosthesis for facial rehabilitation. *Int. J. Interact. Des. Manuf.* 7, 51–62. doi: 10.1007/s12008-012-0159-7

Fernandes, A. Ù. R., Goiato, M. C., and dos Santos, D. M. (2009a). Effect of weathering and thickness on the superficial microhardness of acrylic resin and ocular button. *Contact Lens Anterior Eye* 32, 283–287. doi: 10.1016/j.clae.2009.09.001

Fernandes, A. Ú. R., Portugal, A., Veloso, L. R., Goiato, M. C., and dos Santos, D. M. (2009b). Assessment of the flexural strength of two heat-curing acrylic resins for artificial eyes. *Braz. Oral Res* 23, 263–267. doi: 10.1590/S1806-83242009000300007

Fernandes, A. ÙR., Goiato, M. C., and dos Santos, D. M. (2010). Effect of weathering and thickness on roughness of acrylic resin and ocular button. *Contact Lens Anterior Eye* 33, 124–127. doi: 10.1016/j.clae.2009.12.008

Galpin, C. (1996). Body image changes associated with surgery. *Br. J. Theatr. Nurs. NATNews Off. J. Natl. Assoc. Theatr. Nurses* 6, 22–23.

Gearhart, D. F. (1970). Polyvinyl chloride (Cordo) facial and body prostheses. *Bull Prosthet Res* 10, 214–218.

Goiato, M. C., dos Santos, D. M., Moreno, A., Iyda, M. G., Rezende, M. C. R. A., and Haddad, M. F. (2012a). Effect of disinfection and storage on the flexural strength of ocular prosthetic acrylic resins. *Gerodontology* 29, 838–844. doi: 10.1111/j.1741-2358.2011.00570.x

Goiato, M. C., Pesqueira, A. A., Moreno, A., dos Santos, D. M., Haddad, M. F., and Bannwart, L. C. (2012b). Effects of pigment, disinfection, and accelerated aging on the hardness and deterioration of a facial silicone elastomer. *Polym. Degrad. Stab.* 97, 1577–1580. doi: 10.1016/j.polymdegradstab.2012.06.033

Goiato, M. C., Freitas, E., dos Santos, D., de Medeiros, R., and Sonego, M. (2014). Acrylic resin cytotoxicity for denture base–literature review. *Adv. Clin. Exp. Med. Off. organ Wrocław Med. Univ.* 24, 679–686. doi: 10.17219/acem/33009

Goiato, M. C., Haddad, M. F., Santos, D. M., dos Pesqueira, A. A., and Moreno, A. (2010a). Hardness evaluation of prosthetic silicones containing opacifiers following chemical disinfection and accelerated aging. *Braz. Oral Res.* 24, 303–308. doi: 10.1590/S1806-83242010000300008

Goiato, M. C., Haddad, M. F. C., Sinhoreti, M. A., dos Santos, D. M., Pesqueira, A. A., and Moreno, A. (2010b). Influence of opacifiers on dimensional stability and detail reproduction of maxillofacial silicone elastomer. *Biomed. Eng* 9, 85. doi: 10.1186/1475-925X-9-85

Goiato, M. C., Rossatti Zucolotti, B. C., Mancuso, D. N., dos Santos, D. M., Pellizzer, E. P., and Ramos Verri, F. (2010c). Care and cleaning of maxillofacial prostheses. *J. Craniofac. Surg.* 21, 1270–1273. doi: 10.1097/SCS.0b013e3181e1b431

Goiato, M. C., Pesqueira, A. A., dos Santos, D. M., Falcón Antenucci, R. M., do Prado Ribeiro, P., Antenucci, R. M., et al. (2008). Evaluation of dimensional change and detail reproduction in silicones for facial prostheses. *Acta Odontol Latinoam* 21, 85–88.

Goiato, M. C., Pesqueira, A. A., Santos, D. M., dos, and Dekon, C. (2009). Evaluation of hardness and surface roughness of two maxillofacial silicones following disinfection. *Braz. Oral Res.* 23, 49–53. doi: 10.1590/S1806-83242009000100009

Goldberg, A. J., Craig, R. G., and Filisko, F. E. (1978). Polyurethane elastomers as maxillofacial prosthetic materials. *J. Dent. Res.* 57, 563–569. doi: 10.1177/00220345780570040501

González Calderón, J. A., Contreras López, D., Pérez, E., and Vallejo Montesinos, J. (2019). Polysiloxanes as polymer matrices in biomedical engineering: their interesting properties as the reason for the use in medical sciences. *Polym. Bull* 1–69. doi: 10.1007/s00289-019-02869-x

Gostev, A. A., Karpenko, A. A., and Laktionov, P. P. (2018). Polyurethanes in cardiovascular prosthetics. *Polym. Bull.* 75, 4311–4325. doi: 10.1007/s00289-017-2266-x

Goyal, A., Hingrajia, D., Chawla, N., and Shah, R. J. (2012). Prosthetic rehabilitation of a patient with an orbital defect: a simplified approach. *J. Indian Prosthodont. Soc.* 12, 187–190. doi: 10.1007/s13191-012-0128-7

Grant, G. T., Taft, R. M., and Wheeler, S. T. (2001). Practical application of polyurethane and Velcro in maxillofacial prosthetics. *J. Prosthet. Dent.* 85, 281–283.

Guiotti, A. M., Goiato, M. C., and dos Santos, D. M. (2010). Evaluation of the Shore A Hardness of Silicone for Facial Prosthesis as to the Effect of Storage Period and Chemical Disinfection. *J. Craniofac. Surg.* 21, 323–327. doi: 10.1097/SCS.0b013e3181cf5fa4

Gupta, R. K., and Padmanabhan, T. V. (2012). Prosthetic rehabilitation of a post evisceration patient with custom made ocular prosthesis: a case report. *J. Indian Prosthodont. Soc.* 12, 108–112. doi: 10.1007/s13191-012-0115-z

Haddad, M. F., Goiato, M. C., dos Santos, D. M., Pesqueira, A. A., Moreno, A., and Pellizzer, E. P. (2011). Influence of pigment and opacifier on dimensional stability and detail reproduction of maxillofacial silicone elastomer. *J. Craniofac. Surg.* 22, 1612–1616. doi: 10.1097/SCS.0b013e31822e5ef2

Haddad, M. F., Goiato, M. C., Santos, D. M., dos Crepaldi, N., de, M., Pesqueira, A. A., et al. (2012). Bond strength between acrylic resin and maxillofacial silicone. *J. Appl. Oral Sci.* 20, 649–654. doi: 10.1590/S1678-77572012000600010

Han, Y., Kiat-amnuay, S., Powers, J. M., and Zhao, Y. (2008). Effect of nano-oxide concentration on the mechanical properties of a maxillofacial silicone elastomer. *J. Prosthet. Dent.* 100, 465–473. doi: 10.1016/S0022-3913(08)60266-8

Han, Y., Powers, J. M., and Kiat-amnuay, S. (2013). Effect of opacifiers and UV absorbers on pigmented maxillofacial silicone elastomer, part 1: color stability after artificial aging. *J. Prosthet. Dent.* 109, 397–401. doi: 10.1016/S0022-3913(13)60327-3

Han, Y., Zhao, Y., Xie, C., Powers, J. M., and Kiat-amnuay, S. (2010). Color stability of pigmented maxillofacial silicone elastomer: effects of nano-oxides as opacifiers. *J. Dent.* 38, e100–e105. doi: 10.1016/j.jdent.2010.05.009

Hatamleh, M. M., Polyzois, G. L., Silikas, N., and Watts, D. C. (2011). Effect of extraoral aging conditions on mechanical properties of maxillofacial silicone elastomer. *J. Prosthodont.* 20, 439–446. doi: 10.1111/j.1532-849X.2011.00736.x

Hatamleh, M. M., and Watts, D. C. (2010a). Bonding of maxillofacial silicone elastomers to an acrylic substrate. *Dent. Mater.* 26, 387–395. doi: 10.1016/j.dental.2010.01.001

Hatamleh, M. M., and Watts, D. C. (2010b). Effect of extraoral aging conditions on color stability of maxillofacial silicone elastomer. *J. Prosthodont.* 19, 536–543. doi: 10.1111/j.1532-849X.2010.00627.x

Hatamleh, M. M., and Watts, D. C. (2010c). Mechanical properties and bonding of maxillofacial silicone elastomers. *Dent. Mater.* 26, 185–191.

Heudorf, U., Mersch-Sundermann, V., and Angerer, J. (2007). Phthalates: toxicology and exposure. *Int. J. Hyg. Environ. Health* 210, 623–634.

Hulterström, A. K., Berglund, A., and Ruyter, I. E. (2008). Wettability, water sorption and water solubility of seven silicone elastomers used for maxillofacial prostheses. *J. Mater. Sci. Mater. Med.* 19, 225–231.

Hutcheson, P. E., and Udagama, A. (1980). Surgical nasal prosthesis. *J. Prosthet. Dent.* 43, 78–81.

Jerschow, P. (2001). *Silicone Elastomers.* Akron, OH: Rapra Technology Limited.

Kaira, L., and Dabral, E. (2014). Improving esthetics of finger prosthesis by glove silicone. *J. Orofac. Sci.* 6, 114–117. doi: 10.4103/0975-8844.143054

Kanie, T., Arikawa, H., Fujii, K., and Ban, S. (2004). Flexural properties of denture base polymers reinforced with a glass cloth–urethane polymer composite. *Dent. Mater.* 20, 709–716.

Kanie, T., Fujii, K., Arikawa, H., and Inoue, K. (2000). Flexural properties and impact strength of denture base polymer reinforced with woven glass fibers. *Dent. Mater.* 16, 150–158.

Kenworthy, G., and Small, A. D. S. (1974). New techniques used in the production of cosmetic gloves. *Med. Biol. Eng. Comput.* 12, 120–123.

Kiat-amnuay, S., Jacob, R. F., Chambers, M. S., Anderson, J. D., Sheppard, R. A., Johnston, D. A., et al. (2010). Clinical trial of chlorinated polyethylene for facial prosthetics. *Int. J. Prosthodont.* 23, 263–270.

Kiat-amnuay, S., Waters, P. J., Roberts, D., and Gettleman, L. (2008). Adhesive retention of silicone and chlorinated polyethylene for maxillofacial prostheses. *J. Prosthet. Dent.* 99, 483–488. doi: 10.1016/S0022-3913(08)60113-4

Kim, S.-H., and Watts, D. C. (2004). The effect of reinforcement with woven E-glass fibers on the impact strength of complete dentures fabricated with high-impact acrylic resin. *J. Prosthet. Dent.* 91, 274–280.

Kotha, S. B., Ramakrishnaiah, R., Devang Divakar, D., Celur, S. L., Qasim, S., and Matinlinna, J. P. (2016). Effect of disinfection and sterilization on the tensile strength, surface roughness, and wettability of elastomers. *J. Investig. Clin. Dent* 8:e12244. doi: 10.1111/jicd.12244

Kurunmäki, H., Kantola, R., Hatamleh, M. M., Watts, D. C., and Vallittu, P. K. (2008). A fiber-reinforced composite prosthesis restoring a lateral midfacial defect: a clinical report. *J. Prosthet. Dent.* 100, 348–352. doi: 10.1016/S0022-3913(08)60235-8

Lai, J. H., and Hodges, J. S. (1999). Effects of processing parameters on physical properties of the silicone maxillofacial prosthetic materials. *Dent. Mater.* 15, 450–455.

Lai, J. H., Wang, L. L., Ko, C. C., DeLong, R. L., and Hodges, J. S. (2002). New organosilicon maxillofacial prosthetic materials. *Dent. Mater.* 18, 281–286.

Lam, Z. S. F., and Hurry, D. (1992). *Dow Corning and the Silicone Implant Controversy*. Dallas, TX: Southern Methodist University.

Lemon, J. C., Kiat-amnuay, S., Gettleman, L., Martin, J. W., and Chambers, M. S. (2005). Facial prosthetic rehabilitation: preprosthetic surgical techniques and biomaterials. *Curr. Opin. Otolaryngol. Head Neck Surg.* 13, 255–262.

Leonhard, M., Tobudic, S., Moser, D., Zatorska, B., Bigenzahn, W., and Schneider-Stickler, B. (2013). Growth kinetics of candida biofilm on medical polymers: A long-term in vitro study. *Laryngoscope* 123, 732–737. doi: 10.1002/lary.23662

Lewis, D. H., and Castleberry, D. J. (1980). An assessment of recent advances in external maxillofacial materials. *J. Prosthet. Dent.* 43, 426–432.

Liu, Q., Shao, L., Fan, H., Long, Y., Zhao, N., Yang, S., et al. (2015). Characterization of maxillofacial silicone elastomer reinforced with different hollow microspheres. *J. Mater. Sci.* 50, 3976–3983. doi: 10.1007/s10853-015-8953-9

Liu, Q., Shao, L. Q. Q., Xiang, H. F. F., Zhen, D., Zhao, N., Yang, S. G. G., et al. (2013). Biomechanical characterization of a low density silicone elastomer filled with hollow microspheres for maxillofacial prostheses. *J. Biomater. Sci. Polym. Ed.* 24, 1378–1390. doi: 10.1080/09205063.2012.762292

Liu, S. H., Shen, M. Y., Kuan, C. F., Kuan, H. C., Ke, C. Y., and Chiang, C. L. (2019). Improving thermal stability of polyurethane through the addition of hyperbranched polysiloxane. *Polymers* 11, 1–16. doi: 10.3390/polym11040697

Lorenz, G., and Kandelbauer, A. (2014). "14 - Silicones," in, 3rd Edn, Vol. 14 - Silicones, eds H. Dodiuk, and S. H. Goodman, (Boston: William Andrew Publishing), 555–575.

Manaila, E., Daniela, M., Craciu, G., and Boczkowska, A. (2012). "Aspects regarding radiation crosslinking of elastomers," in *Advanced Elastomers - Technology, Properties and Applications*, (London: InTech).

Mancuso, D. N., Goiato, M. C., and Santos, D. M. (2009). Color stability after accelerated aging of two silicones, pigmented or not, for use in facial prostheses. *Braz. Oral Res.* 23, 144–148. doi: 10.1590/S1806-83242009000200009

May, P. D., and Guerra, L. R. (1978). Maxillofacial prostheses of chlorinated polyethylene. *J. Biomed. Mater. Res. Part A* 12, 421–431.

Meriç, G., Dahl, J. E., and Ruyter, I. E. (2008). Cytotoxicity of silica–glass fiber reinforced composites. *Dent. Mater.* 24, 1201–1206. doi: 10.1016/j.dental.2008.01.010

Meriç, G., and Ruyter, I. E. (2008). Influence of thermal cycling on flexural properties of composites reinforced with unidirectional silica-glass fibers. *Dent. Mater.* 24, 1050–1057. doi: 10.1016/j.dental.2007.12.003

Montgomery, P. C., and Kiat-Amnuay, S. (2010). Survey of currently used materials for fabrication of extraoral maxillofacial prostheses in North America, Europe, Asia, and Australia. *J. Prosthodont* 19, 482–490. doi: 10.1111/j.1532-849X.2009.00538.x

Narva, K. K., Lassila, L. V., and Vallittu, P. K. (2005). The static strength and modulus of fiber reinforced denture base polymer. *Dent. Mater.* 21, 421–428.

Northwest_Eye_Design, (2019). *Prosthetic Eyes*. Available online at: https://nweyedesign.com/eyes/ (Accessed March 1, 2019).

NuSil, (0000). *NuSil MED-4920, Liquid Silicone Rubber*. Available online at: https://nusil.com/product/med-4920_liquid-silicone-rubber (accessed September 13, 2019).

Pan, Y., Liu, F., Xu, D., Jiang, X., Yu, H., and Zhu, M. (2013). Novel acrylic resin denture base with enhanced mechanical properties by the incorporation of PMMA-modified hydroxyapatite. *Prog. Nat. Sci. Mater. Int.* 23, 89–93.

Patil, P. G., Cameron, S., Knudson, R., Runyan, D., Weinlander, M., Lorant, J., et al. (2010). Modified technique to fabricate a hollow light-weight facial prosthesis for lateral midfacial defect: a clinical report. *J. Adv. Prosthodont.* 2, 65. doi: 10.4047/jap.2010.2.3.65

Patil, S. B., Meshramkar, R., Naveen, B. H., and Patil, N. P. (2008). Ocular prosthesis: a brief review and fabrication of an ocular prosthesis for a geriatric patient. *Gerodontology* 25, 57–62. doi: 10.1111/j.1741-2358.2007.00171.x

Polyzois, G. L., Eleni, P. N., and Krokida, M. K. (2011). Effect of time passage on some physical properties of silicone maxillofacial elastomers. *J. Craniofac. Surg.* 22, 1617–1621. doi: 10.1097/SCS.0b013e31822e5e62

Polyzois, G. L., Tarantili, P. A., Frangou, M. J., and Andreopoulos, A. G. (2000). Physical properties of a silicone prosthetic elastomer stored in simulated skin secretions. *J. Prosthet. Dent.* 83, 572–577. doi: 10.1016/S0022-3913(00)70017-5

Preoteasa, C. T., Nabil, S. A., Popa, L., Ghica, M. V., Ionescu, E., Maria, A., et al. (2011). Studies regarding the wettability of acrylic and silicone dental materials. *Farmacia* 59, 871–878.

Product Information - Heat Cured Acrylics, (2010).

Pruthi, G., and Jain, V. (2013). Light weight prosthesis for a patient with bilateral orbital exenteration-A clinical report. *J. Prosthodont. Res.* 57, 135–139. doi: 10.1016/j.jpor.2013.01.001

Rabek, J. F. (2012). *Polymer Photodegradation: Mechanisms and Experimental Methods*. Berlin: Springer Science & Business Media.

Raizada, K., and Rani, D. (2007). Ocular prosthesis. *Contact Lens Anterior Eye* 30, 152–162. doi: 10.1016/j.clae.2007.01.002

Ratner, B. D., Hoffman, A. S., Schoen, F. J., and Lemons, J. E. (2004). *Biomaterials Science: an Introduction to Materials in Medicine*. Cambridge, MA: Academic press.

Reisch, M. S. (1993). Dow Corning moving back on track following breast implant controversy. *Chem. Eng. News* 71, 13–16.

Rodger, G., Taylor, R. L., Pearson, G. J., and Verran, J. (2010). In vitro colonization of an experimental silicone by *Candida albicans*. *J. Biomed. Mater. Res. Part B Appl. Biomater.* 92B, 226–235. doi: 10.1002/jbm.b.31509

Ross, M. T., Cruz, R., Hutchinson, C., Arnott, W. L., Woodruff, M. A., and Powell, S. K. (2018). Aesthetic reconstruction of microtia: a review of current techniques and new 3D printing approaches. *Virtual Phys. Prototyp.* 13, 117–130. doi: 10.1080/17452759.2018.1430246

Rothman, O. (1962). Plastic foams in prosthetics. *Orthot. Prosthetics* 16, 139–143.

Ruiters, S., Sun, Y., De Jong, S., Politis, C., and Mombaerts, I. (2016). Computer-aided design and three-dimensional printing in the manufacturing of an ocular prosthesis. *Br. J. Ophthalmol.* 100, 879–881. doi: 10.1136/bjophthalmol-2016-308399

Santawisuk, W., Kanchanavasita, W., Sirisinha, C., and Harnirattisai, C. (2010). Dynamic viscoelastic properties of experimental silicone soft lining materials. *Dent. Mater. J.* 29, 454–460. doi: 10.4012/dmj.2009-126

Saravi, M. E., Vojdani, M., and Bahrani, F. (2012). Evaluation of cellular toxicity of three denture base acrylic resins. *J. Dent. Tehran Univ. Med. Sci.* 9, 180–188.

Schettler, T. E. D. (2006). Human exposure to phthalates via consumer products. *Int. J. Androl.* 29, 134–139.

Segal, S. J., Tsui, A. O., and Rogers, S. (2012). *Demographic and Programmatic Consequences of Contraceptive Innovations*. Berlin: Springer Science & Business Media.

Shankaran, G., Deogade, S. C., and Dhirawani, R. (2016). Fabrication of a cranial prosthesis combined with an ocular prosthesis using rapid prototyping: a case report. *J. Dent.* 13, 68–72.

Sharmin, E., and Zafar, F. (2012). "Polyurethane: An Introduction," in *Polyurethane*, ed. T. J. Kemp, (London: InTech).

Shetty, S., Mohammad, F., Shetty, R., and Shenoy, K. (2016). Prosthetic rehabilitation of an orbital defect for a patient with hemifacial atrophy. *J. Indian Prosthodont. Soc.* 16, 91–95. doi: 10.4103/0972-4052.175716

Shi, W., Zhang, J., Shi, X.-M., and Jiang, G.-D. (2008). Different photodegradation processes of PVC with different average degrees of polymerization. *J. Appl. Polym. Sci.* 107, 528–540. doi: 10.1002/app.25389

Shrivastava, K. J., Shrivastava, S., Agarwal, S., and Bhoyar, A. (2015). Prosthetic rehabilitation of large mid-facial defect with magnet-retained silicone prosthesis. *J. Indian Prosthodont. Soc.* 15, 276–280. doi: 10.4103/0972-4052.161571

Shrivastava, S., Agarwal, S., Shrivastava, K. J., and Tyagi, P. (2013). Custom-made ocular prosthesis for a pediatric patient with unilateral anopthalmia: a case report. *J. Indian Soc. Pedod. Prev. Dent.* 31, 194. doi: 10.4103/0970-4388.117973

Singh, B., and Sharma, N. (2008). Mechanistic implications of plastic degradation. *Polym. Degrad. Stab.* 93, 561–584. doi: 10.1016/j.polymdegradstab.2007.11.008

Siqueira Gonçalves, T., Minghelli Schmitt, V., Thomas, M., Lopes, de Souza, M. A., and Macedo de Menezes, L. (2008). Cytotoxicity of two autopolymerized acrylic resins used in orthodontics. *Angle Orthod.* 78, 926–930. doi: 10.2319/072407-343.1

Smit, G., Plettenburg, D., and Van der Helm, F. (2014). A mechanism to compensate undesired stiffness in joints of prosthetic hands. *Prosthet. Orthot. Int.* 38, 96–102. doi: 10.1177/0309364613488620

Spasojevic, P., Zrilic, M., Panic, V., Stamenkovic, D., Seslija, S., and Velickovic, S. (2015). The mechanical properties of a Poly(methyl methacrylate) denture base material modified with dimethyl itaconate and Di- *n* -butyl Itaconate. *Int. J. Polym. Sci.* 2015, 1–9. doi: 10.1155/2015/561012

Špírková, M., Pavličević, J., Strachota, A., Poreba, R., Bera, O., Kaprálková, L., et al. (2011). Novel polycarbonate-based polyurethane elastomers: composition-property relationship. *Eur. Polym. J.* 47, 959–972. doi: 10.1016/j.eurpolymj.2011.01.001

Stathi, K., Tarantili, P. A., and Polyzois, G. (2010). The effect of accelerated ageing on performance properties of addition type silicone biomaterials. *J. Mater. Sci. Mater. Med.* 21, 1403–1411. doi: 10.1007/s10856-010-3991-y

Tagkalakis, P., and Demiri, E. (2009). A fear avoidance model in facial burn body image disturbance. *Ann. Burns Fire Disasters* 22, 203–207.

Thirunavukkarasu, I., Rai, R., Prabhu, R., Deshpande, V. A., and Arun Kumar, S. (2014). Rehabilitation of partially eviscerated eye with custom made ocular prosthesis: a case report. *J. Clin. Diagnostic Res.* 8, 285–287. doi: 10.7860/JCDR/2014/7558.3976

Todd, B. A., Smith, S. L., and Vongpaseuth, T. (1998). Polyurethane foams: effects of specimen size when determining cushioning stiffness. *J. Rehabil. Res. Dev.* 35:219.

Tomar, B., Mishra, S., Chandu, G., Chowdhary, R., and Singh, S. (2018). Improving the ocular esthetics of a patient with custom-made ocular prosthesis fabricated using digital photograph. *J. Dent. Allied Sci.* 7:38. doi: 10.4103/jdas.jdas_41_17

Touchet, T. J., and Cosgriff-Hernandez, E. M. (2016). "Hierarchal structure–property relationships of segmented polyurethanes," in *Advances in Polyurethane Biomaterials*, eds S. L. Cooper, and J. Guan, (Amsterdam: Elsevier), 3–22.

Tripuraneni, S., Vadapalli, S., Ravikiran, P., and Nirupama, N. (2015). An innovative impression technique for fabrication of a custom made ocular prosthesis. *Indian J. Ophthalmol.* 63, 545–547. doi: 10.4103/0301-4738.162626

Udagama, A. (1987). Urethane-lined silicone facial prostheses. *J. Prosthet. Dent.* 58, 351–354. doi: 10.1016/0022-3913(87)90056-4

Uzun, G., Hersek, N., and Tincer, T. (1999). Effect of five woven fiber reinforcements on the impact and transverse strength of a denture base resin. *J. Prosthet. Dent.* 81, 616–620.

Vallittu, P. K. (1998). Some aspects of the tensile strength of unidirectional glass fibre–polymethyl methacrylate composite used in dentures. *J. Oral Rehabil.* 25, 100–105.

Vallittu, P. K. (1999). Flexural properties of acrylic resin polymers reinforced with unidirectional and woven glass fibers. *J. Prosthet. Dent.* 81, 318–326.

Vedanarayanan, P. V., and Fernandez, A. C. (1987). Toxicology of Biomedical Polymers. *Def. Sci. J.* 37, 173–183.

Veerareddy, C., Nair, K. C., and Reddy, G. R. (2012). Simplified technique for orbital prosthesis fabrication: a clinical report. *J. Prosthodont.* 21, 561–568. doi: 10.1111/j.1532-849X.2012.00869.x

Wang, L., Liu, Q., Jing, D., Zhou, S., and Shao, L. (2014). Biomechanical properties of nano-TiO2 addition to a medical silicone elastomer: the effect of artificial ageing. *J. Dent.* 42, 475–483. doi: 10.1016/j.jdent.2014.01.002

Wise, D. L. (2000). *Handbook of Pharmaceutical Controlled Release Technology*. CRC Press.

Wu, K. K., and Gerngross, P. (2009). Repair procedure for partially separated polyurethane-lined facial prosthesis. *J. Prosthet. Dent.* 101, 142–143. doi: 10.1016/S0022-3913(09)60011-1

Yerci Kosor, B., Artunç, C., and Şahan, H. (2015). Adhesive retention of experimental fiber-reinforced composite, orthodontic acrylic resin, and aliphatic urethane acrylate to silicone elastomer for maxillofacial prostheses. *J. Prosthet. Dent.* 114, 142–148. doi: 10.1016/j.prosdent.2014.12.018

Yu, R., Koran, A., and Powers, J. M. (1983). Effect of processing temperature on the properties of a polyvinyl chloride maxillofacial elastomer. *J. Dent. Res.* 62, 1098–1100.

Zayed, S. M., Alshimy, A. M., and Fahmy, A. E. (2014). Effect of surface treated silicon dioxide nanoparticles on some mechanical properties of maxillofacial silicone elastomer. *Int. J. Biomater.* 2014:750398. doi: 10.1155/2014/750398

Zhang, Y., Liu, X., Zeng, L., Zhang, J., Zuo, J., Zou, J., et al. (2019). Polymer fiber scaffolds for bone and cartilage tissue engineering. *Adv. Funct. Mater.* 29:1903279. doi: 10.1002/adfm.201903279

Conflict of Interest: The authors declare that the research was conducted in the absence of any commercial or financial relationships that could be construed as a potential conflict of interest.

frontiers
in Bioengineering and Biotechnology

ORIGINAL RESEARCH
published: 28 April 2020
doi: 10.3389/fbioe.2020.00374

Bioprinting Cell- and Spheroid-Laden Protein-Engineered Hydrogels as Tissue-on-Chip Platforms

Daniela F. Duarte Campos[1]*, Christopher D. Lindsay[1], Julien G. Roth[2], Bauer L. LeSavage[3], Alexis J. Seymour[3], Brad A. Krajina[1], Ricardo Ribeiro[4], Pedro F. Costa[4], Andreas Blaeser[5] and Sarah C. Heilshorn[1]*

[1] Department of Materials Science & Engineering, Stanford University, Stanford, CA, United States, [2] Stanford Medical School, Institute for Stem Cell Biology and Regenerative Medicine, Stanford University, Stanford, CA, United States, [3] Department of Bioengineering, Stanford University, Stanford, CA, United States, [4] Biofabics, Porto, Portugal, [5] Institute for BioMedical Printing Technology, Technical University of Darmstadt, Darmstadt, Germany

OPEN ACCESS

Edited by:
Julien Georges Didier Barthès,
Protip Medical, France

Reviewed by:
Stephanie Michelle Willerth,
University of Victoria, Canada
Aleksander Skardal,
The Ohio State University,
United States

****Correspondence:***
Daniela F. Duarte Campos
daniela.campos@rwth-aachen.de;
dcampos@ukaachen.de
Sarah C. Heilshorn
heilshorn@stanford.edu

Specialty section:
This article was submitted to
Biomaterials,
a section of the journal
Frontiers in Bioengineering and
Biotechnology

Received: *25 January 2020*
Accepted: *06 April 2020*
Published: *28 April 2020*

Citation:
Duarte Campos DF, Lindsay CD, Roth JG, LeSavage BL, Seymour AJ, Krajina BA, Ribeiro R, Costa PF, Blaeser A and Heilshorn SC (2020) Bioprinting Cell- and Spheroid-Laden Protein-Engineered Hydrogels as Tissue-on-Chip Platforms. Front. Bioeng. Biotechnol. 8:374. doi: 10.3389/fbioe.2020.00374

Human tissues, both in health and disease, are exquisitely organized into complex three-dimensional architectures that inform tissue function. In biomedical research, specifically in drug discovery and personalized medicine, novel human-based three-dimensional (3D) models are needed to provide information with higher predictive value compared to state-of-the-art two-dimensional (2D) preclinical models. However, current *in vitro* models remain inadequate to recapitulate the complex and heterogenous architectures that underlie biology. Therefore, it would be beneficial to develop novel models that could capture both the 3D heterogeneity of tissue (e.g., through 3D bioprinting) and integrate vascularization that is necessary for tissue viability (e.g., through culture in tissue-on-chips). In this proof-of-concept study, we use elastin-like protein (ELP) engineered hydrogels as bioinks for constructing such tissue models, which can be directly dispensed onto endothelialized on-chip platforms. We show that this bioprinting process is compatible with both single cell suspensions of neural progenitor cells (NPCs) and spheroid aggregates of breast cancer cells. After bioprinting, both cell types remain viable in incubation for up to 14 days. These results demonstrate a first step toward combining ELP engineered hydrogels with 3D bioprinting technologies and on-chip platforms comprising vascular-like channels for establishing functional tissue models.

Keywords: protein engineered hydrogel, bioink, bioprinting, 3D cell culture, tissue model

INTRODUCTION

Three-dimensional (3D) cell culture systems that model the microenvironment of tissues and organs are expected to yield results with higher predictive value in drug discovery, preclinical testing, and personalized medicine (Langhans, 2018). It is well-accepted that 3D culture systems that mimic key factors of native extracellular matrix (ECM) are more representative of the *in vivo* microenvironment than comparative two-dimensional (2D) cultures (Petersen et al., 1992; Ravi et al., 2015). For example, 3D cancer models have shown more physiologically relevant outcomes in migration and invasion assays compared to 2D models (Katt et al., 2016). However, existing 3D models remain inadequate to recapitulate the complex and heterogenous architectures present *in vivo*. In particular, vascularization is typically absent from many 3D tissue models (Zhang et al., 2016). Vascular tissue interfaces are particularly important in *in vitro* models of the neural stem cell niche (Tavazoie et al., 2008), blood-brain-barrier (Brown et al., 2015), and *in vitro* models of cancer metastasis (Carey et al., 2013; Curtin et al., 2018).

Microfluidic and on-chip technologies are experimental models that can include dynamic vascular-like channels (Cochrane et al., 2019). In a recent study, a low permeability microfluidic platform was developed for screening pharmaceuticals that target neurodegenerative diseases (Bang et al., 2017). Although such platforms have shown vascular permeability comparable to reported *in vivo* studies, they fail to recapitulate the 3D architecture of the native tissue, as cells are cultured on 2D polydimethylsiloxane (PDMS) substrates. *In vitro* models of the neural stem cell niche commonly use random co-culture mixtures or transwell inserts that do not mimic the spatial proximity and geometry of the cross-talk between neural progenitor cells (NPCs) and endothelial cells (Shen et al., 2004). Similar culture systems have been reported in cancer research (Sontheimer-Phelps et al., 2019). Here, we hypothesized that conventional microfluidic devices could be combined with 3D bioprinting technology to fabricate *ex vivo* tissue mimics with on-chip vascular-like networks.

3D bioprinting technologies are key biomanufacturing methods used to create 3D constructs by sequential deposition of cell-laden bioink layers (Murphy and Atala, 2014; Leberfinger et al., 2019). Several recent examples have demonstrated the promise of 3D bioprinting to create *in vitro* models of human tissues and disease. For example, microextrusion bioprinting was used to generate expansion lattices for neural research (Gu et al., 2018; Lindsay et al., 2019), whereas microextrusion and laser-based bioprinting were used to construct 3D co-culture models of interacting cancer and endothelial cells (Phamduy et al., 2015; Zhou et al., 2016). Despite these exciting advances, the biomaterials commonly used as bioinks, such as alginate and gelatin methacrylate, poorly capture the biochemical complexity and biodegradability of the native ECM.

Previous studies have identified bioink stiffness as a key element for directing cell morphology and differentiation in 3D cultures after bioprinting (Blaeser et al., 2015; Duarte Campos et al., 2015). Cells encapsulated within polymeric 3D microenvironments also require matrix remodeling to spread, migrate, and proliferate. Unfortunately, a trade-off frequently exists between printability and biological outcome when designing bioinks (Duarte Campos et al., 2016). In general, increasing the bioink stiffness can also improve printing precision, whereas cell spreading and differentiation are often improved by decreasing the bioink stiffness. For this reason, proteolytically degradable hydrogels, such as elastin-like protein (ELP) hydrogels, have been successfully engineered to control encapsulated cell phenotype and stemness (Madl et al., 2017). ELP hydrogels are a family of recombinant engineered-protein materials that contain elastin-like repeat units alternating with modular and customizable bioactive domains (Straley and Heilshorn, 2009). The initial stiffness of ELP hydrogels can be tuned by variation of the final concentration of ELP or variation of the crosslinker concentration. For example, in previous work, ELP hydrogel stiffness was varied between 0.5 and 50 kPa in 3–10 wt% ELP hydrogels (Madl et al., 2017). Cell-laden ELP hydrogels were shown to be stable for at least 2 weeks. These materials are proteolytically degradable by collagenases, elastases, and other proteases, resulting in local remodeling of the matrix and enabling cell proliferation over 2 weeks (Chung et al., 2012a; Madl et al., 2017).

In this study, we explore the feasibility of ELP hydrogels with the fibronectin-derived, cell-adhesive RGD amino acid sequence (ELP-RGD) as bioinks for engineering 3D *in vitro* models with on-chip vascular-like channels (**Figure 1**). Bioink printability, single-cell and cell-spheroid viability after bioprinting, as well as proof-of-concept bioprinting of a neural tissue-on-chip, were assessed using ELP-RGD hydrogels. Analysis of neural progenitor cell and cancer spheroid survival after bioprinting showed encouraging results after 7 days of culture. Prolonged cultures up to 14 days showed that NPCs spread and cancer spheroids continued growing at a comparable rate as non-bioprinted controls. Preliminary analysis of the endothelialized channels demonstrated distribution of endothelial cells along the entire lumen of the channel.

MATERIALS AND METHODS

Synthesis of ELP-RGD Bioinks and Sacrificial Inks

ELP-RGD hydrogels were synthesized as previously described (Madl et al., 2017; LeSavage et al., 2018). Briefly, ELP was cloned into pET15b plasmids and expressed in BL21(DE3)pLysS *Escherichia coli*. Bacterial cultures containing the plasmids grew to an OD600 of 0.8 before inducing ELP expression with 1 mM isopropyl β-D-1-thiogalactopyranoside (IPTG). After culture, bacteria were harvested, resuspended and lysed by repetitive freeze-thaw cycles. ELP was next purified by inverse temperature cycling, dialyzed, and lyophilized to a solid state. ELP-RGD hydrogels were prepared by first dissolving the lyophilized ELP in phosphate-buffered saline (PBS) to a concentration of 3.75, 5.0, or 6.75 wt%. These ELP solutions were then mixed with a diluted solution of the amine-reactive crosslinker, tetrakis(hydroxymethyl)phosphonium chloride (THPC), in a 4:1 volumetric ratio (ELP solution:THPC solution), resulting in final ELP-RGD hydrogel concentrations of 3, 4, or 5 wt%, respectively. For each hydrogel condition, the THPC solution was initially diluted in PBS such that the hydrogels had a final crosslinking ratio of 0.5:1 (THPC reactive sites:primary amines on ELP). For cell experiments, all components used to prepare the ELP-RGD hydrogels and bioinks were sterile-filtered prior to culture using a 0.22 μm syringe filter.

For bioprinting experiments using the chip design with sacrificial gel-made channels, 5 wt% gelatin was used to encapsulate human umbilical vein endothelial cells (HUVECs) that endothelialized the channel. Stocks of 5 wt% gelatin were prepared by dissolving gelatin powder (Sigma) in deionized water at 37°C, sterile filtering with a 0.22 μm syringe filter, aliquoting in 1 ml tubes, and storing at −20°C. Prior to bioprinting experiments, frozen stocks were thawed at 37°C, mixed with HUVECs, and extruded directly inside the chip with a syringe coupled to an 18G needle. Agarose hydrogels were used to

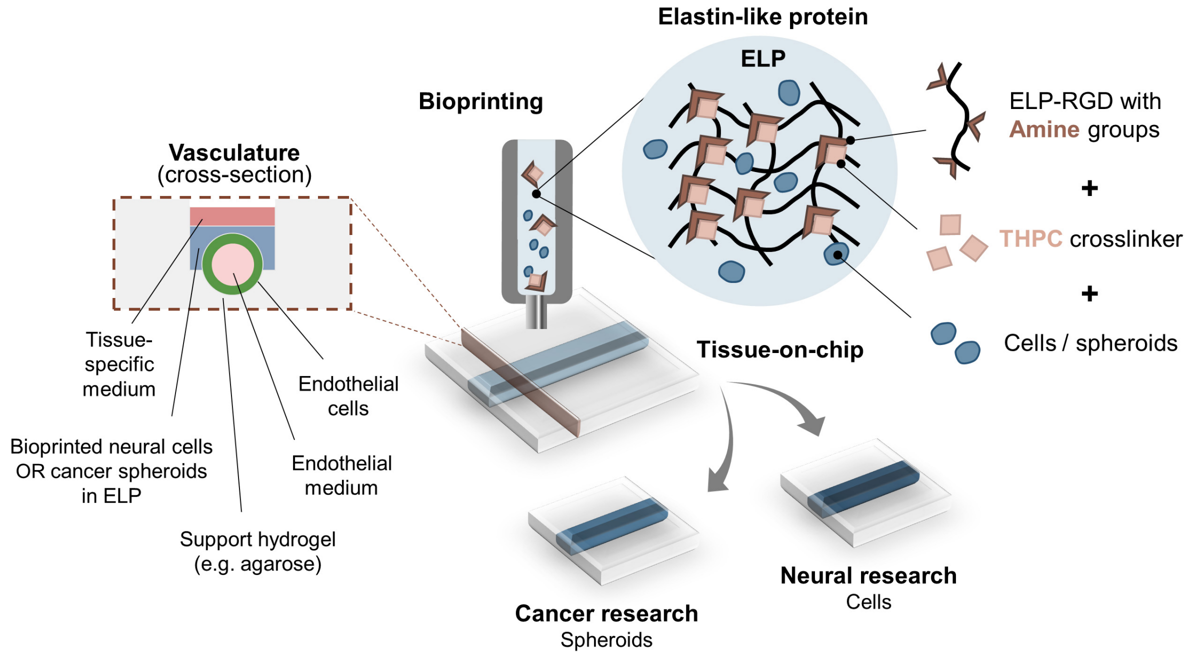

FIGURE 1 | Bioprinting ELP-RGD bioinks with encapsulated cells or spheroids as tissue-on-chip platforms. ELP-RGD bioinks with pendant primary amine groups crosslink in the presence of tetrakis(hydroxymethyl)phosphonium chloride (THPC), which is a tetra-functional, amine-reactive, small molecule crosslinker. Pre-mixed ELP-RGD/THPC bioinks with cells or spheroids are loaded into the bioprinting cartridge and bioprinted directly onto microfluidic chips that enable fabrication of endothelialized vascular-like channels. Two distinct types of culture media are used: endothelial medium is perfused in the lumen of the vascular channel, while neural- or cancer-specific medium is added to the upper culture chamber.

support the formation of gelatin channels. A stock solution of 3 wt% agarose (Bio-Rad) was prepared by dissolving agarose powder in deionized water, followed by autoclave sterilization at 121°C.

For printability experiments using the microextruder, Pluronic F127 (Sigma) was used as a supporting gel in a reservoir. 26 wt% Pluronic gel was prepared by dissolving it in deionized water at 4°C. Molds containing 26 wt% Pluronic were cast prior to ELP-RGD printability testing.

Matrigel was used as non-bioprinted control for encapsulation of cells and spheroids, and for the expansion of cancer spheroids prior to bioprinting experiments. Stocks of Matrigel (#354277, Corning) were stored frozen at −20°C and thawed at 4°C prior to use.

Bioprinting Setup and Printability of ELP-RGD Bioinks

Printability of ELP-RGD bioinks was tested by drop-on-demand (DoD) and microextrusion bioprinting. DoD experiments were performed using a hand-held bioprinter (DropGun, BlackDrop Biodrucker GmbH, Aachen, Germany), consisting of a hand-held bioink reservoir connected to an air compressor, mounted with a 300 μm micro-valve, and regulated by a controller unit (Duarte Campos et al., 2019). Average drop diameter and weight of ELP-RGD bioinks at concentrations of 3, 4, and 5 wt%, and deionized water (as liquid control) were analyzed. First, the hand-held bioprinter, ELP-RGD hydrogel precursors, and THPC solutions were placed on ice for 15 min prior to the printability experiments in order to slow down the crosslinking speed of ELP-RGD bioinks. ELP-RGD hydrogels at concentrations of 3.75, 5.0, and 6.75 wt% were mixed with a diluted THPC solution in 4:1 volumetric ratio using manual pipetting, and immediately transferred to the bioprinter reservoir. Each printing experiment was performed using a single ejection valve or needle, without use of coaxial needles. These formulations have previously reported to have crosslinking times that vary between 5 and 30 min (Chung et al., 2012b). The loaded hand-held bioprinter was fixed at a 1 cm distance from the printing substrate (glass slide). All materials were dispensed with a valve opening time (gating time) of 450 μs, and at defined pressures of 0.25, 0.5, 0.75, 1.0, or 1.5 bar. Images of the printed drops (n = 10 for each material and variable) were recorded immediately after printing, and drop diameter was measured with ImageJ (National Institutes of Health, NIH). For assessing drop weight, 100 drops of each testing material were collected in 500 μl tubes and weighed.

Qualitative printability tests were performed with 3 wt% ELP-RGD bioink by DoD in circular and S shapes (by hand). Additional printability tests by microextrusion were performed using a 3D-bioprinter (Biobot1, Allevi, Philadelphia, PA, United States) mounted with a flat-tip 27G needle. 3 wt% ELP-RGD bioink was pre-mixed with 5 μl green food color, added to one printer head, and extruded in a spiral shape in a Pluronic print bath. Images were taken of both DoD and microextruded specimens.

Chip Design and Fabrication

Two distinct chips were custom-designed using an online platform (Biofabics Toolbox)[1], and manufactured (Biofabics, Porto, Portugal): (1) chip with ready-made channel and (2) chip with sacrificial gel-made channel.

Chip 1 was designed with tool number 4 of the Biofabics Toolbox (**Figure 2A**), consisting of a 96-well plate layout with 6.5 mm well diameter, 3.5 mm well height, 11.5 mm channel length, 1 mm channel diameter, 1 mm base thickness, and a square chamber with 6.5 mm width/length. A column of two device units was selected, and all remaining parameters were kept at zero. Each chamber was perfused with a 0.8 mm diameter molding line, which was removed after bioprinting of ELP bioinks.

Chip 2 was designed with tool number 5 of the Biofabics Toolbox (**Figure 2B**), consisting of a 96-well plate layout with a round chamber with 8 mm chamber height, 5 mm chamber diameter, 2 mm channel diameter, 2 mm channel to chamber bottom distance, and 1 mm base thickness. A column of three device units was selected, and all remaining parameters were kept at zero. The inlet/outlet fittings of each chip were fastened to silicone tubes, which were coupled to syringes as inlets (fresh medium supply, three inlets), or outlets (culture medium waste, three outlets).

Cell Isolation and Culture

Murine NPCs from micro-dissected dentate gyrus of adult female mice (C57Bl/6) were kindly provided by Prof. Theo Palmer (Stanford Neurosurgery) (Babu et al., 2007). All animal work followed protocols reviewed and approved by the Stanford Administrative Panel on Laboratory Animal Care. NPCs were cultured and expanded in 2D, and encapsulated in 3D ELP-RGD hydrogels for bioprinting experiments, following previously established protocols (Madl et al., 2017; LeSavage et al., 2018). After isolation, NPCs were expanded in maintenance medium [Neurobasal-A (Thermo Fisher Scientific), 2% B27 supplement (Gibco), 2 mM GlutaMAX (Life Technologies), 20 ng/ml fibroblast growth factor 2 (FGF-2), and 20 ng/ml epidermal growth factor (EGF) (PeproTech)] on Poly-L-ornithine and laminin coated tissue culture plastic (Madl et al., 2016). For cell passaging and encapsulation in ELP-RGD bioinks, NPCs were trypsinized, pelleted, resuspended, and counted. For expansion, NPCs were plated at 1×10^4 cells/cm^2, and, for encapsulation, cells were mixed with hydrogel components to achieve a final density of 1.5×10^7 cells/ml. For bioprinting experiments, NPCs were encapsulated in 3 wt% ELP-RGD bioinks, pre-mixed with THPC, as described above, and loaded into the printing cartridge. After bioprinting, specimens were incubated at room temperature for 15 min, followed by incubation at 37°C for 30 min prior to adding culture medium. Culture medium was replaced every 2 days during cell expansion and every day after bioprinting.

Human induced pluripotent stem cells (hiPSCs, line: 8343.2) were differentiated into cortical neural progenitors following a previously established protocol (Shi et al., 2012). Briefly, hiPSCs were maintained in Essential 8 (E8) medium (Gibco) on Matrigel-coated tissue culture plastic and differentiated in N3 medium consisting of 50% DMEM/F-12, 50% Neurobasal A, 1% N-2 supplement, 2% B-27 supplement, 2 mM GlutaMAX, 1% MEM Non-Essential Amino Acid Solution (NEAA), and 2.5 μg/ml human recombinant insulin (all Thermo Fisher Scientific). N3 medium was further supplemented with 5 μM transforming growth factor beta (TGF-beta) receptor inhibitor [SB-431542 (Tocris)] and 100 nM activin receptorlike kinase 2 (ALK2) and ALK3 inhibitor [LDN-193189 (Stemgent)] for the first 11 days of culture. At day 12, hiPSCs were dissociated with Cell Dissociation Solution (Sigma) and plated on pre-coated plates with 50 μg/ml Poly-D-Lysine (Sigma) and 5 μg/ml Laminin (Roche). Next, hiPSC-derived NPCs were further cultured in N3 medium without SB-431542 or LDN-193189 until day 16. Prior to bioprinting experiments, hiPSC-NPCs were dissociated and encapsulated in 3 wt% ELP-RGD bioinks pre-mixed with THPC at a density of 1.5×10^7 cells/ml. After bioprinting, specimens were incubated at room temperature for 15 min, followed by incubation at 37°C for 30 min prior to adding culture medium. Culture medium was replaced daily before and after bioprinting.

HUVECs were purchased from PromoCell. HUVECs were expanded in EGM-2 growth medium (Lonza) containing 0.04% hydrocortisone, 0.4% human FGF-2, 0.1% vascular endothelial growth factor (VEGF), 0.1% recombinant analog of insulin-like growth factor (R3-IGF-1), 0.1% ascorbic acid, 0.1% human EGF, 0.1% gentamicin sulfate-amphotericin (GA-1000), 0.1% heparin, and 2% fetal bovine serum (FBS). For cell passaging and encapsulation in gelatin, HUVECs were trypsinized, pelleted, resuspended, and counted. HUVECs were plated at 1×10^4 cells/cm^2 for expansion. For encapsulation, cells were mixed with 5 wt% gelatin to achieve a final density of 1×10^7 cells/ml. Culture medium was replaced every 2 days during cell expansion and every day after bioprinting.

Human premalignant breast epithelial cells (MCF10ATs) were kindly provided by Jan Liphardt (Stanford Bioengineering) and expanded, following a previously published protocol (Leung and Brugge, 2012). Briefly, MCF10ATs were expanded in DMEM/F-12 medium (Gibco) supplemented with 100 μg/ml EGF (Gibco), 1 mg/ml hydrocortisone (Sigma), 1 mg/ml cholera toxin (Sigma), 10 mg/ml insulin (Sigma), and 100x penicillin/streptomycin (Gibco). For cell passaging and encapsulation in Matrigel, MCF10ATs were trypsinized, pelleted, resuspended, and counted. For expansion, MCF10ATs were plated at 1×10^4 cells/cm^2, and for encapsulation, cells were mixed with Matrigel to achieve a final density of 5×10^5 cells/ml. After 7 days culture in Matrigel, MCF10AT spheroids with approximately 50 μm diameter, containing dozens of cells, were harvested for bioprinting experiments. Briefly, MCF10AT-laden Matrigel cultures were incubated in 5 mM EDTA in PBS for 45 min on ice. Dissociated Matrigel, containing MCF10AT spheroids, was pelleted and resuspended in basal medium. MCF10AT spheroids were encapsulated at a density of 1×10^7 spheroids/ml in 3 wt% ELP-RGD bioinks pre-mixed with THPC, as described above, and loaded into the printing cartridge. After bioprinting, specimens were incubated at room temperature for 15 min, followed by incubation at 37°C for 30 min prior to adding culture medium.

---

[1] www.biofabics-toolbox.com

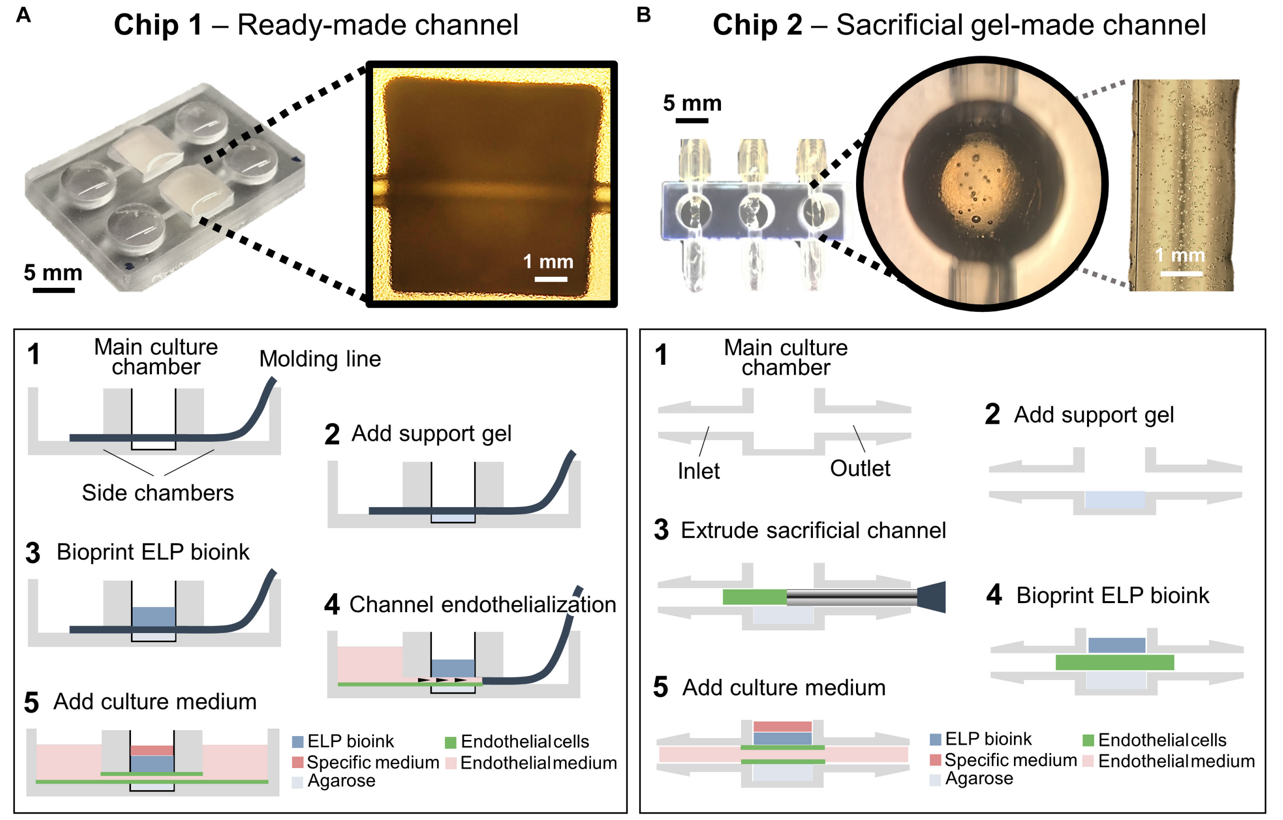

FIGURE 2 | Chip designs used for the biofabrication of printed tissue frameworks with on-chip vascular-like channels. Chips designs with **(A)** ready-made channels, and **(B)** sacrificial gel-made channels were evaluated. Sequence of events (1–5) indicates the necessary working steps to fabricate both types of tissue models. Sacrificial gel-made channels can be used to incorporate endothelial cells that will form monolayers on the channel surface after removing the sacrificial gel. The inset photograph in **(A)** shows the channel formation at step 5. The inset photograph in **(B)** shows the presence of endothelial cells inside the sacrificial gel at step 3.

Culture medium was replaced every 2 days during expansion and daily after bioprinting.

Bioprinting of Cells and Spheroids in Tissue-on-Chips

Before bioprinting experiments, chips were washed thrice in 70% ethanol and sterile PBS. Cell and spheroid-laden 3 wt% ELP-RGD bioinks were prepared as described above and bioprinted by DoD. For chip 1, bioprinting of bioinks was performed prior to channel endothelialization. First, each main culture chamber was filled with 100 µl bioink. After crosslinking, HUVECs suspended in culture medium were added to one of the supporting chambers, and the molding line was carefully removed, allowing the HUVEC suspension to fill the channel by capillary action. Subsequently, chips were flipped and incubated bottom-up at 37°C for 4 h to allow for cell seeding on the upper segment of the channel, followed by upright incubation at 37°C for 5 days. Culture media for both cell types was replaced daily.

Bioprinting into chip 2 was performed after channel formation. First, sterile 18G needles were inserted in the chips through the side tube connectors. Twenty microliter 3 wt% agarose was cast in the bottom of each main culture chamber to support the formation of a HUVEC-laden gelatin channel. HUVEC-laden 5 wt% gelatin was prepared as described above and extruded via syringe inside the culture chamber at room temperature. After gelation of the gelatin channel, 50 µl cell-laden ELP-RGD bioinks were bioprinted by DoD into each chamber and allowed to crosslink for 15 min at room temperature. Next, chips were flipped and incubated bottom up at 37°C for 4 h. At this step, gelatin channels melted and HUVECs sedimented by gravity on the upper segment of the channel. Chips were once again flipped and incubated upright for 5 days. Syringes with fresh EGM-2 medium for HUVEC culture were connected to one side of the chamber, and empty syringes were connected to the opposite side to collect media waste. Cell-specific culture medium was added to the upper part of the main chamber, and both culture media were replaced daily.

Viability Staining

Three, seven, and fourteen days after cell and spheroid encapsulation in hydrogels and bioprinting experiments, specimens were removed from the incubator, washed once with PBS, and stained with Live/Dead viability staining (Thermo Fisher Scientific). Staining conditions were optimized for cells encapsulated in Matrigel and ELP-RGD. For Matrigel samples, stock solutions were diluted to 0.5 µg/ml calcein and 2 µl/ml ethidium homodimer-1 (EthD-1) in PBS, and incubated for 30 min at 37°C. Cells in 3 wt% ELP-RGD were incubated in solutions of 1 μl/ml calcein and 2 μl/ml EthD-1 diluted in PBS for 30 min at 37°C. After incubation, samples were washed once with PBS and imaged using a Leica SPE confocal microscope. Percent (%) viability was calculated based on the number of counted live and dead cells (Equation 1). Three independent biological replicates were used for each time point and variable ($N = 3$).

Percent (%) viability of cells and spheroids.

$$\%Viability = \frac{Live\ Cells}{Live\ Cells + Dead\ Cells} \times 100 \qquad (1)$$

Immunocytochemical Staining

For immunocytochemistry, samples were fixed with 4% paraformaldehyde in PBS for 30 min at 37°C. Samples were permeabilized with 0.25% Triton X-100 in PBS (PBST) for 1 h at room temperature. The samples were then blocked with 5% bovine serum albumin (BSA) and 5% goat serum in PBST for 3 h at room temperature. Primary antibodies against sex determining region Y-box 2 (Sox2) (1:400, rabbit, Cell Signaling Technology, 23064S) and/or cluster of differentiation 31 (CD31) (1:200, mouse, PECAM-1, Sigma, P8590) were diluted in PBST containing 2.5% goat serum, added to samples, and incubated overnight at 4°C. The samples were then washed thrice with PBST, incubated with secondary antibodies [AlexaFluor488 (goat anti-rabbit, 1:500); AlexaFluor647 (goat anti-mouse, 1:500); and/or tetramethylrhodamine (TRITC) phalloidin 532 (F-actin, 1:500)], and counterstained with 4′,6-diamidino-2-phenylindole dihydrochloride (DAPI) overnight at 4°C. Samples were washed thrice with PBST and imaged using a Leica SPE confocal microscope. Three independent biological replicates were used for each time point and variable ($N = 3$).

Analysis of Confocal Images

Confocal images were analyzed with ImageJ (NIH). Images recorded with the same magnification (20× objective) were transformed into 8-bit images. Color channels of each image were split, and the threshold was manually adjusted prior to measuring percent cell area values. Total cell area was calculated as a function of the total image area of 2.9×10^5 μm^2. Three independent biological replicates were used for each time point and variable ($N = 3$).

Statistical Analysis

Comparisons between two experimental groups were made using two-tailed Student's *t*-tests (Prism 8, version 8.3.0, GraphPad Software). Comparisons between three or more experimental groups were made using one-way ANOVA with Tukey's *post hoc* test. Statistical significance was considered as $^{*}p < 0.05$, $^{**}p < 0.005$, and $^{***}p < 0.001$. Independent biological replicates and exact *P*-values are indicated in each Figure including statistical analyses. Experimental data are presented as means ± standard deviation.

RESULTS

ELP-RGD Printability by Drop-on-Demand and Microextrusion Bioprinting

The printability of ELP-RGD bioinks at varying concentrations was tested by DoD (**Figure 3A**) and microextrusion bioprinting (**Figure 3B**). For all tests, the ELP-RGD engineered protein was solubilized in PBS and pre-mixed with the tetra-functional crosslinker THPC at a 0.5:1 stoichiometric ratio between THPC functional groups and primary amines in the protein. DoD printability tests were performed with a hand-held bioprinter connected to an air compressor, which allowed for hand-guided dispensing of single bioink drops in circular and S shapes. Microextrusion printability tests were performed using a 3D-bioprinter, which allowed for continuous extrusion of the bioink in spiral shapes submerged in a Pluronic print-bath. The smallest diameter observed for single drops of ELP-RGD bioinks printed by DoD was 1.4 mm (5 wt% ELP-RGD at 0.25 bar, **Figure 3C**). By increasing the applied pressure during printing, it was possible to increase the drop size without varying bioink concentration or nozzle diameter. Drops larger than 4 mm in diameter were difficult to measure due to impaired droplet integrity wherein large drops tended to splatter into smaller drops. Nevertheless, drop size and weight continued to increase upon increasing the applied pressure, as shown in **Figures 2C**, **3D**. Interestingly, the mass of the printed drops decreased with increasing ELP-RGD concentration and constant pressure. For example, at 0.75 bar, the 3 wt% ELP-RGD formed single drops with an average mass of 342 μg, whereas that of 4 wt% and 5 wt% ELP-RGD inks had average single drops of 311 and 257 μg, respectively.

Chip Design and Visualization of Perfused Channels

Toward the long-term goal of culturing bioprinted 3D tissue models with vascular-like channels, we evaluated two different chip designs and fabrication protocols. In one method, a simple, easy-to-use chip design with ready-made channels was evaluated (**Figure 2A**). This chip comprised two main culture chambers, where the tissue models were bioprinted, and four supporting chambers, where cell culture medium was added. Two plastic molding lines with 0.8 mm diameters were inserted in each chip by traversing the main culture chambers and the two supporting chambers connected to them. After DoD bioprinting of the ELP-RGD layers onto the plastic wire, HUVECs suspended in medium were added to one of the sides of the chip and were subsequently seeded in the inner wall of the channel by removing the plastic line. As a second method, a chip design comprising culture chambers with tubing connectors suitable for dynamic perfusion culture was evaluated (**Figure 2B**). This type of chip design allowed for HUVEC seeding in the vascular-like channel within a sacrificial gelatin hydrogel. The ELP-RGD ink was bioprinted directly on top of the sacrificial gelatin to form an upper layer of printed tissue. After the last bioprinting step, the chips were placed in an incubator at 37°C allowing for further crosslinking

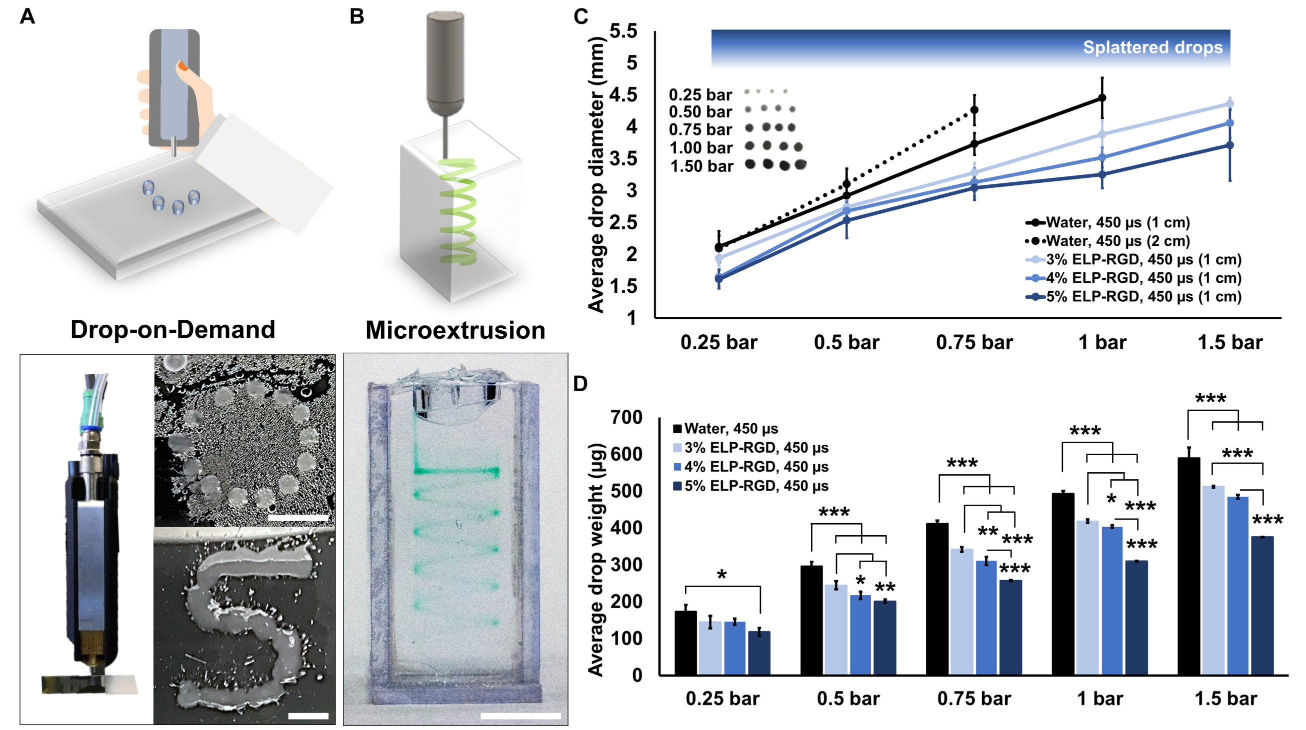

FIGURE 3 | Printability of ELP-RGD bioinks. **(A)** Qualitative drop-on-demand (DoD) printability tests of 3 wt% ELP-RGD printed as single drops into circular and S shapes. Scale bars represent 5 mm. **(B)** Qualitative microextrusion printability test of 3 wt% ELP-RGD in a spiral shape within a Pluronic bath. Scale bar represents 5 mm. **(C)** Average single drop diameter of deionized water, 3, 4, and 5 wt% ELP-RGD printed by DoD at applied pressures ranging from 0.25 to 1.5 bar (*n* = 10). **(D)** Average single drop mass of deionized water, 3, 4, and 5 wt% ELP-RGD printed by DoD at applied pressures ranging from 0.25 to 1.5 bar (*n* = 3, 100 drops each). Valve opening time (gating time) was fixed at 450 µs for all experiments. Statistical significance marked as $^*p < 0.05$, $^{**}p < 0.005$, and $^{***}p < 0.001$ (One-way ANOVA with Tukey's *post hoc* test).

and solidification of the ELP-RGD bioink, and simultaneous fluidization and removal of the sacrificial gelatin channel.

Cell and Spheroid Viability in ELP-RGD Bioinks

Several variables have been reported to impact cell viability during different bioprinting methods, including bioink viscosity, printing nozzle size, and applied printing pressure (Duarte Campos et al., 2015; Dubbin et al., 2017). Therefore, an important step toward developing a bioprinted *in vitro* tissue-on-chip model is to evaluate cell viability. In this study, cell and spheroid viability was analyzed after DoD bioprinting using dissociated NPCs (**Figure 4A**) and MCF10AT spheroids (**Figure 4C**). Cells and spheroids encapsulated in 3 wt% ELP-RGD bioinks and Matrigel without bioprinting were included as controls. NPC survival in 3 wt% ELP-RGD was greater than 88.9% in both experimental groups, including non-bioprinted and bioprinted samples (**Figure 4B**). The lowest NPC survival of about 77.4% was observed in non-bioprinted Matrigel controls after 7 days of culture. The overall MCF10AT spheroid viability rates at day three of culture were lower compared to NPC cultures (**Figure 4D**). The lowest MCF10AT spheroid survival rate observed was about 70.2% 3 days after bioprinting. Interestingly, upon further time in culture, bioprinted MCF10AT viability rates increased to about 88.3% at day seven of culture. This cell viability at 7-days post-printing was not statistically significantly different than the 7-day viability without printing in either ELP-RGD (82.3%) or Matrigel (93.3%).

Endothelialization of the Channels Contained in the Culture Chips

Perfused and endothelialized tissue-on-chips are important components of many *ex vivo* tissue models. In neural research, such models may be used to mimic the neural stem cell niche to study the requirements for stem cell maintenance and activation, or in the future to recapitulate the blood-brain-barrier to study the penetration of new drugs across the barrier. In cancer research, these models may be used to investigate cancer cell migration and metastasis through blood vessels. In this work, we evaluated the endothelialization of chips with a ready-made channel design. After HUVEC seeding, culture, and fixation, entire chips were stained, sectioned, and imaged by confocal microscopy. Cross-section views with different 3D perspectives of endothelialized channels are shown in **Figure 5a**. A HUVEC monolayer was formed along the inner wall of the channel contained in the culture chip. Next, the endothelialized channel was imaged lengthwise to show the presence of HUVECs at different z heights

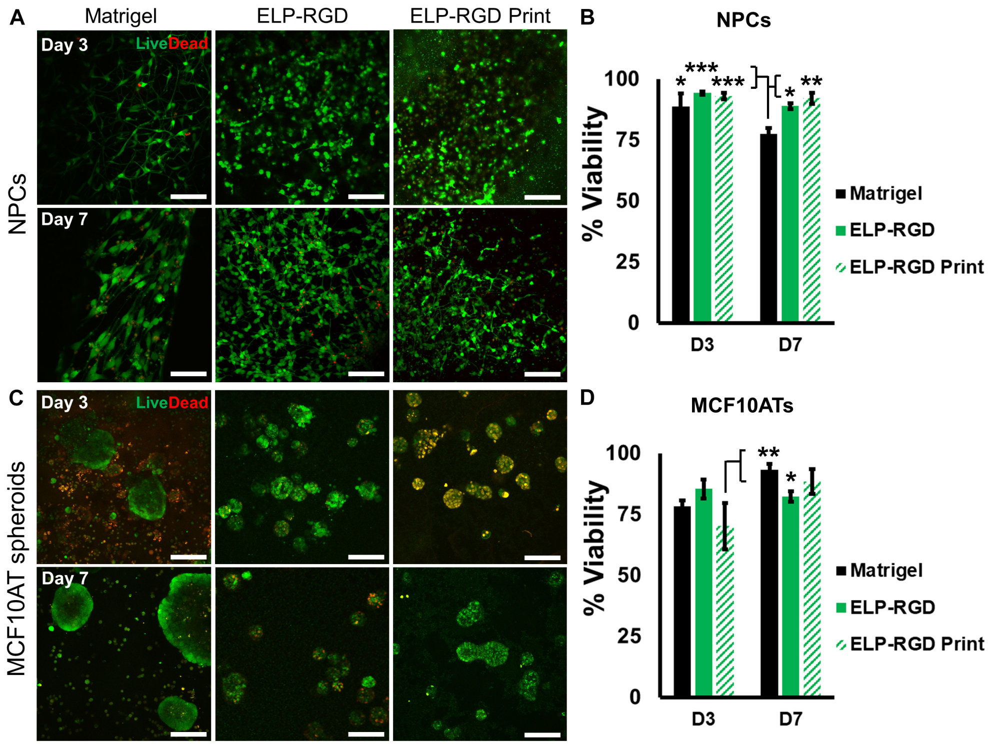

FIGURE 4 | Viability of dissociated cells and spheroids with and without bioprinting. Live cells are stained with calcein (green) and dead cells are stained with ethidium homodimer-1 (red). **(A)** Live/Dead staining of murine neural progenitor cells (NPCs) on days 3 and 7 within Matrigel (not bioprinted), 3 wt% ELP-RGD (not bioprinted), and 3 wt% ELP-RGD after DoD bioprinting. Scale bars represent 100 µm. **(B)** Quantified viability of NPCs at days 3 and 7. Statistical significance marked as $^{*}p < 0.05$, $^{**}p < 0.005$, and $^{***}p < 0.001$ ($N = 3$, One-way ANOVA with Tukey's *post hoc* test). **(C)** Live/Dead staining of human premalignant breast epithelial cell spheroids (MCF10ATs) in Matrigel (not bioprinted), 3 wt% ELP-RGD (not bioprinted), and 3 wt% ELP-RGD after DoD bioprinting at days 3 and 7. Scale bars represent 100 µm. **(D)** Quantified viability of MCF10ATs at days 3 and 7. Statistical significance marked as $^{*}p < 0.05$, and $^{**}p < 0.005$ ($N = 3$, One-way ANOVA with Tukey's *post hoc* test).

(**Figure 5b**) and in 3D perspective (**Figure 5c**). A compiled view of the y-z cross-section of the channel (**Figure 5d**) demonstrates a uniform distribution of HUVECs along the inner wall of the channel.

Morphology of Printed NPCs and Premalignant Breast Epithelial Spheroids

To develop tissue-on-chips suitable for use as *ex vivo* tissue models, it is important to evaluate cell and spheroid morphological changes during culture. NPCs encapsulated in bioprinted and non-bioprinted matrices showed morphological changes from rounded at day 1 to elongated at day 14 (**Figure 6A**). In contrast, MCF10AT spheroids did not show morphological alterations throughout the culture period (**Figure 6B**). F-actin staining of NPCs encapsulated in each matrix, both with or without bioprinting, showed a significant increase ($^{*}p < 0.05$) in total cell area from days 1 to 14, suggesting increased cell spreading and elongation (**Figure 6C**). No statistically significant differences in NPC cell-spreading were observed between the various matrices, with or without bioprinting. Similarly, MCF10AT spheroid size was not significantly different within the different matrices. In addition, total cell area of MCF10AT spheroids encapsulated in bioprinted and non-bioprinted matrices did not significantly change between days 1 and 14 of culture (**Figure 6D**).

Bioprinted on-Chip Co-culture With Vascular-Like Channel

After assessing bioink printability, cell viability after bioprinting, and cell morphological changes during *in vitro* culture, we developed and analyzed a proof-of-concept *ex vivo* model of the neural stem cell niche that included both HUVECs and hiPSC-derived NPCs. For this experiment, the chip with the ready-made channel was used. hiPSC-NPCs were encapsulated in 3 wt% ELP-RGD bioinks and bioprinted by DoD over the main chamber of the chip. After bioprinting of hiPSC-NPCs, HUVECs suspended in medium were added to one side chamber of the chip, and the perfusion line was removed to induce HUVEC seeding within the vascular-like channel. Confocal images of the tissue chips after 5 days of culture showed the presence of hiPSC-NPCs (Sox-2-positive, a marker of neural progenitor cell pluripotency) within the printed ELP-RGD hydrogel and the presence of HUVECs (CD31-positive, also known as platelet endothelial cell adhesion molecule (PECAM-1), a common endothelial marker) within the vascular-like channel (**Figure 7**).

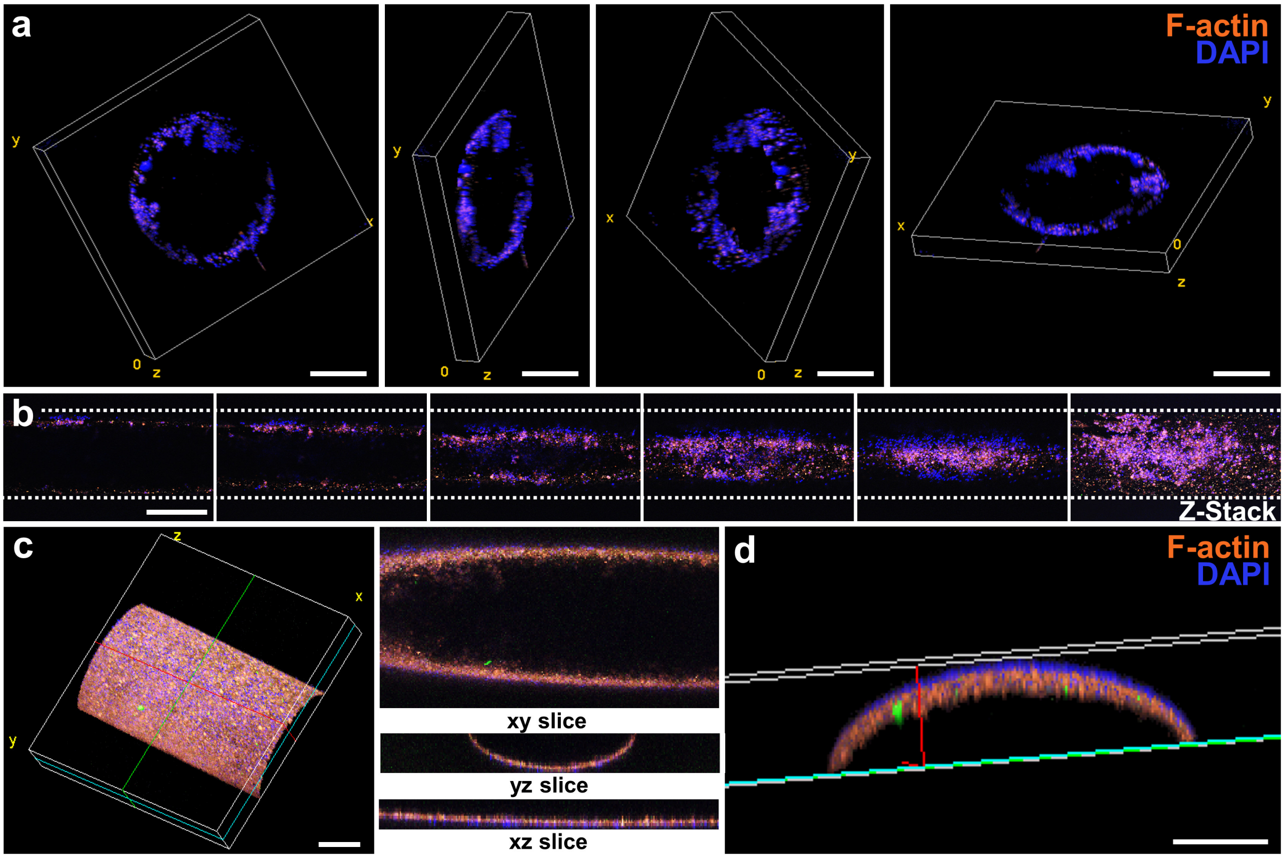

FIGURE 5 | Endothelialization of the luminal wall of the chip. **(a)** Sequence of cross-sectional confocal images showing the position of HUVECs seeded within the channel. Scale bars represent 250 µm. **(b)** Sequence of confocal images taken lengthwise to the channel. The image at the far-right shows a z-stack projection of the sequence of images at varying z heights. Scale bar represents 500 µm. **(c)** 3D projection of an endothelialized channel showing the cross-section views at the xy, yz, and xz planes. Scale bar represents 250 µm. **(d)** Cross-section yz view of **(d)**. Scale bar represents 100 µm.

DISCUSSION

The goal of this study was to explore the feasibility of using ELP-RGD hydrogels as bioinks to fabricate 3D tissue models on microfluidic chips with vascular-like channels. Following a previously established protocol (LeSavage et al., 2018), we synthesized ELP-RGD hydrogels and tested their printability as bioinks. First, the printability by DoD was tested using a hand-held bioprinting device. DoD bioprinting was chosen for this study, because it has been previously reported as a more cell-friendly and freeform method compared to, for example, microextrusion bioprinting (Blaeser et al., 2017). Drop size and weight strongly varied depending on the concentration of ELP-RGD bioink (3, 4, or 5 wt%), applied printing pressure, and distance to the printing substrate. This outcome is in accordance with previous studies, which used other hydrogels with similar rheological properties, such as polysaccharides (Blaeser et al., 2015; Duarte Campos et al., 2019). Comparable ELP-based bioinks were tested in previous works using microextrusion bioprinting (Salinas-Fernández et al., 2019). In this previous work, the geometric printability outcomes highly depended on the concentration and amino acid sequence of the ELP bioink. In our work, qualitative printability experiments by microextrusion showed well-defined 3D shapes with complex and freeform geometry (spirals, **Figure 2B**).

Survival of neural cells and cancer spheroids encapsulated in 3 wt% ELP-RGD was assessed after DoD bioprinting. We found that the average neural cell survival (88.9%) was in accordance with other studies that used the same bioprinting method in combination with other bioinks and cell types (Forget et al., 2017; Kreimendahl et al., 2017; Ng et al., 2017). Contrastingly, average cancer spheroid survival after bioprinting (70.2%) was markedly lower compared to neural cell survival. This result may be due to the larger diameter of cellular MCF10AT spheroids (approximately 50 µm) compared to dissociated, single NPCs (about 10 µm). It is well-known that increased fluid stresses within the printing nozzle can negatively affect cell viability (Aguado et al., 2012; Blaeser et al., 2015; Foster et al., 2017; Lindsay et al., 2019). Nozzle shape, orifice diameter, bioink viscosity, cell density in the bioink, and cell size are parameters that will influence fluid stress, thus making cell aggregates more susceptible to damage (Cidonio et al., 2019). Despite this, cell aggregates with large diameters, including cell clusters like spheroids, may be helpful for the fabrication of

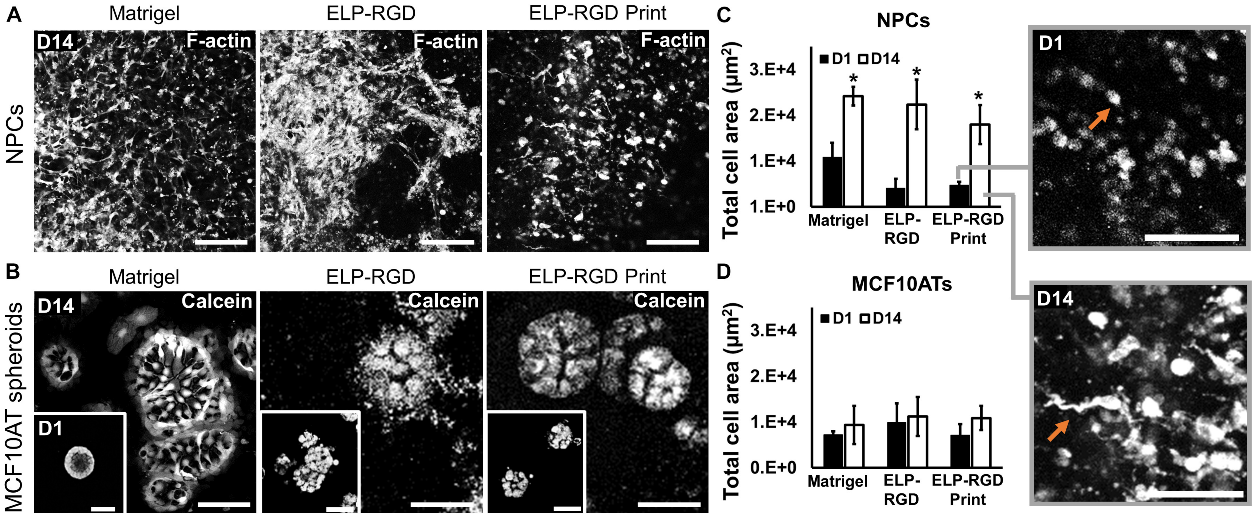

FIGURE 6 | Morphology of dissociated NPCs and MCF10AT spheroids after 14 days of culture within 3D hydrogels. **(A)** Confocal images of NPCs cultured for 14 days in Matrigel, 3 wt% ELP-RGD without bioprinting, and 3 wt% ELP-RGD after DoD bioprinting. Scale bars represent 100 μm. **(B)** Confocal images of MCF10AT spheroids cultured for 14 days in Matrigel, 3 wt% ELP-RGD without bioprinting, and 3 wt% ELP-RGD after DoD bioprinting. Scale bars represent 50 μm. Insets show MCF10AT spheroids at day 1 of culture in the respective material. Scale bars represent 100 μm. **(C)** Total cell area of stained NPCs in confocal images taken at days 1 and 14 of culture. Statistical significance between days 1 and 14 of each material marked as $^*p < 0.05$ ($N = 3$, two-tailed *t*-test, unpaired). Insets are magnified views of NPCs cultured in 3 wt% ELP-RGD after bioprinting, showing round cells at day 1 and spread cells at day 14 (orange arrows). Scale bars represent 100 μm. **(D)** Total cell area of stained MCF10AT spheroids in confocal images taken at days 1 and 14 of culture. One-way ANOVA with Tukey's *post hoc* test did not show statistical significance between groups.

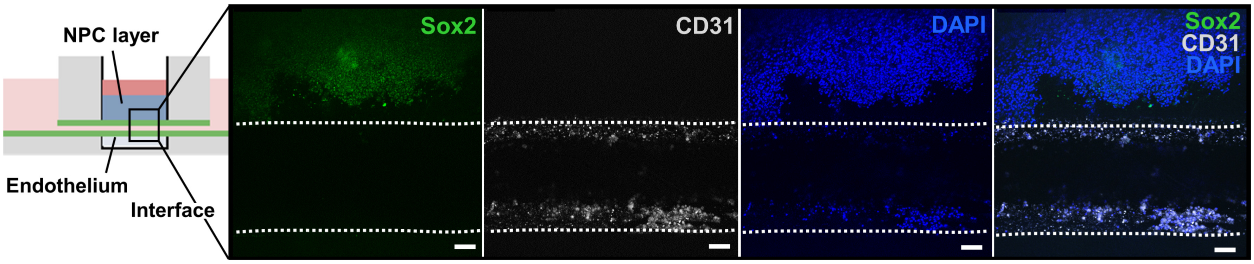

FIGURE 7 | Bioprinted tissue-on-chip with vascular-like channel. Schematic of the tissue-on-chip design. Confocal images of hiPSC-NPCs encapsulated within 3 wt% ELP-RGD bioprinted on top of a channel seeded with HUVECs and cultured for 5 days. hiPSC-NPCs were visualized with Sox2 immunostaining, HUVECs were visualized with CD31 immunostaining, and all cells were visualized by nuclear staining with DAPI. Scale bars represent 50 μm.

ex vivo tissue models (Li and Kumacheva, 2018). Therefore, future work should further evaluate the possible correlation between cell aggregate diameter and low viability post printing. Despite this decrease in cell viability immediately post-printing, by day 7 the printed cultures had recovered and displayed viability and sizes similar to those that had not been exposed to printing. Importantly, day 7 viability and day 14 spheroid size were statistically similar for cultures grown in Matrigel or bioprinted in ELP-RGD. Together, these data suggest that this engineered bioink hydrogel can support the long-term culture of these cancer spheroids after direct bioprinting on a microfluidic chip.

NPCs are a promising cell source for recreating a model of the neural environment. The native neural stem cell niche includes a vascular network that is critical in maintenance of NPC stemness (Tavazoie et al., 2008), with known cross-talk between endothelial cells and NPCs (Schänzer et al., 2006). *In vitro* differentiation toward astrocytes and neurons can be challenging in 3D, and thus, bioinks and the bioprinting process should ideally not restrict NPC differentiation potential. An important aspect of a bioink to support NPC differentiation is to enable cell-cell contact by cell-mediated matrix remodeling (Madl et al., 2019). In this work, we showed that NPCs elongated to spindle-like shapes in 3 wt% ELP-RGD bioinks after bioprinting and kept growing up to 14 days in culture. This morphology suggests that the encapsulated NPCs are able to remodel the printed matrix and make cell-cell contacts that are required for maintenance of stemness. These results are further confirmed by the continued expression of the neural stem cell marker Sox2. The use of ELP-RGD hydrogels as bioinks is an advancement in the fabrication of on-chip tissues to mimic aspects of the neural-vascular interface. Many of these previous studies have used hydrogels that allow little to no cell-driven matrix remodeling, such as agarose (Gasperini et al., 2014; Duarte Campos et al., 2016; Gu et al., 2018).

Vascularization is a frequent goal for the fabrication of engineered tissues *in vitro* (Zhang et al., 2016). For this reason, we used custom-designed on-chip platforms that contained vascular-like channels and that allowed for integrated 3D bioprinting. Microfluidic platforms have been used in previous studies, for example, to investigate cancer metastasis *in vitro* (Sontheimer-Phelps et al., 2019). However, these technologies are difficult to combine with current 3D bioprinting strategies, given that chamber and channel size is in the micrometer range. Therefore, we designed on-chip platforms consisting of culture chambers and channels in the millimeter range, which can be easily accessed with a bioprinter. Two distinct chip designs were considered for their suitability with tissue bioprinting. The first design, which was used for static culture, was simpler and easier to use, as it required fewer preparation steps. HUVECs were successfully seeded onto the inner walls of the channels in these platforms. We showed that HUVECs were distributed along the entire wall of these channels. Microvascular *in vitro* models containing several cell types and layers that resemble native (micro)vessels were previously reported (Jaeger et al., 2013; Cochrane et al., 2019). Although *in vitro* vascular-like structures are typically generated using only endothelial cells, such as HUVECs, more complex 3D models will require triple-layered vascular structures, including fibroblasts, endothelial, and smooth muscle cells (Gao et al., 2019). A limitation of our study was the use of only endothelial cells to cover the inner wall of the channels. Future experiments will consider improving the *in vivo* relevance of the channels by inducing additional cell types. Additionally, functional characteristics of the endothelialized layer, including permeability to nutrients, need to be assessed (Bang et al., 2017).

Finally, as proof-of-concept, a tissue-on-chip was fabricated by bioprinting hiPSC-derived NPCs using protein-engineered-bioinks onto a device with a vascular-like, endothelialized channel. Research studying the cross-talk between endothelial cells and NPCs uses random co-culture mixtures or transwell inserts (Shen et al., 2004), but these do not properly recapitulate the spatial proximity and geometry of these cells in the native stem cell niche, thus resulting in non-physiological concentration gradients of secreted, diffusible factors and inappropriate presentation of cell-surface receptors. In this study, we suggest that a combination of bioprinting and on-chip technologies can be used to realize NPC/HUVEC co-cultures with physiologically relevant geometric patterning. In our previous work, we found that NPCs would lose their Sox2 expression within 2 days in matrices that could not support stemness maintenance (Madl et al., 2017). In this experiment, we showed that both cell types remained viable over 5 days of culture, retained their proper positioning within the co-culture device, and maintained NPC stemness. Although the bioprinter used in this study is hand-held, our results provide a proof-of-concept demonstration that (i) it is feasible to bioprint ELP-RGD bioinks with precision and spatial control, (ii) these bioinks are compatible with the materials commonly used to fabricate microfluidic devices, and (iii) these bioinks are compatible with several cell types of interest. Importantly, this bioprinting technology can be easily mounted onto a stereotactic controller (Blaeser et al., 2015; Duarte Campos et al., 2019). Such automated dispensing of cell-laden hydrogels within microfluidic devices would offer higher spatial precision, greater reproducibility, and more efficient scale-up compared to manual pipetting.

Here we have successfully demonstrated that bioprinted NPCs are able to maintain their stem-like phenotype and hence remain Sox2-positive during co-culture with endothelial cells within a microfluidic device. This platform is well-suited for future cell biology studies investigating the cross-talk between ECs and NPCs that mediate stem cell maintenance and activation.

CONCLUSION

In this work, we used protein-engineered ELP-RGD hydrogels as bioinks for producing *in vitro* tissue-on-chip platforms. We showed that ELP-RGD bioinks are dispensable by DoD and microextrusion, and that 3D constructs can be generated. Assessment of neural progenitor cell and cancer spheroid survival after bioprinting showed encouraging results after 7 days of culture. Prolonged cultures up to 14 days showed that NPCs spread, and cancer spheroids continue growing at a comparable rate as non-bioprinted controls. Preliminary analysis of the endothelialized channels demonstrated distribution of endothelial cells along the entire lumen of the channel. The results presented here represent a first step in combining ELP engineered hydrogels with 3D bioprinting technologies and on-chip platforms for establishing vascularized *in vitro* tissue models. In the future, these platforms may be further developed for *in vitro* studies of interactions between the vascular interface and patterned, three-dimensional tissue mimics.

DATA AVAILABILITY STATEMENT

The datasets generated for this study are available on request to the corresponding author.

AUTHOR CONTRIBUTIONS

DD and SH: conceptualization. DD, CL, JR, BL, AS, and BK: data acquisition. DC: writing-original draft preparation. DD, CL, JR, BL, AS, BK, RR, PC, AB, and SH: writing and editing and final approval of manuscript. DD, SH, PC, and RR: funding acquisition.

FUNDING

This research was supported by the German Research Foundation (DFG-425869082 to DD) and the U.S. National Science Foundation (DMR-1808415 to SH) and the U.S. National

Institutes of Health (R01-HL142718, R01-EB027171, R01-EB027666, R21-HL138042, R21-NS114549 to SH). This project has received funding from the European Union's Horizon 2020 research and innovation programme under the Marie Sklodowska-Curie grant agreement No 798014 (to PC). This project has received funding from the European Union's Horizon 2020 research and innovation programme under grant agreement No 828835 (to RR).

REFERENCES

Aguado, B. A., Mulyasasmita, W., Su, J., Lampe, K. J., and Heilshorn, S. C. (2012). Improving viability of stem cells during syringe needle flow through the design of hydrogel cell carriers. *Tissue Eng. Part A* 18, 806–815. doi: 10.1089/ten.tea.2011.0391

Babu, H., Cheung, G., Kettenmann, H., Palmer, T. D., and Kempermann, G. (2007). Enriched monolayer precursor cell cultures from micro-dissected adult mouse dentate gyrus yield functional granule cell-like neurons. *PLoS One* 2:e388. doi: 10.1371/journal.pone.0000388

Bang, S., Lee, S.-R., Ko, J., Son, K., Tahk, D., Ahn, J., et al. (2017). A Low permeability microfluidic blood-brain barrier platform with direct contact between perfusable vascular network and astrocytes. *Sci. Rep.* 7:8083. doi: 10.1038/s41598-017-07416-7410

Blaeser, A., Duarte Campos, D. F., and Fischer, H. (2017). 3D bioprinting of cell-laden hydrogels for advanced tissue engineering. *Curr. Opin. Biomed. Eng.* 2, 58–66. doi: 10.1016/j.cobme.2017.04.003

Blaeser, A., Duarte Campos, D. F., Puster, U., Richtering, W., Stevens, M. M., and Fischer, H. (2015). Controlling shear stress in 3d bioprinting is a key factor to balance printing resolution and stem cell integrity. *Adv. Healthc. Mater.* 5, 326–333. doi: 10.1002/adhm.201500677

Brown, J. A., Pensabene, V., Markov, D. A., Allwardt, V., Neely, M. D., Shi, M., et al. (2015). Recreating blood-brain barrier physiology and structure on chip: a novel neurovascular microfluidic bioreactor. *Biomicrofluidics* 9:054124. doi: 10.1063/1.4934713

Carey, S. P., Starchenko, A., McGregor, A. L., and Reinhart-King, C. A. (2013). Leading malignant cells initiate collective epithelial cell invasion in a three-dimensional heterotypic tumor spheroid model. *Clin. Exp. Metastasis* 30, 615–630. doi: 10.1007/s10585-013-9565-x

Chung, C., Anderson, E., Pera, R. R., Pruitt, B. L., and Heilshorn, S. C. (2012a). Hydrogel crosslinking density regulates temporal contractility of human embryonic stem cell-derived cardiomyocytes in 3D cultures. *Soft Matter* 8, 10141–10148. doi: 10.1039/C2SM26082D

Chung, C., Lampe, K. J., and Heilshorn, S. C. (2012b). Tetrakis(hydroxymethyl) phosphonium chloride as a covalent cross-linking agent for cell encapsulation within protein-based hydrogels. *Biomacromolecules* 13, 3912–3916. doi: 10.1021/bm3015279

Cidonio, G., Glinka, M., Dawson, J. I., and Oreffo, R. O. C. (2019). The cell in the ink: improving biofabrication by printing stem cells for skeletal regenerative medicine. *Biomaterials* 209, 10–24. doi: 10.1016/j.biomaterials.2019.04.009

Cochrane, A., Albers, H. J., Passier, R., Mummery, C. L., van den Berg, A., Orlova, V. V., et al. (2019). Advanced in vitro models of vascular biology: human induced pluripotent stem cells and organ-on-chip technology. *Adv. Drug Deliv. Rev.* 140, 68–77. doi: 10.1016/j.addr.2018.06.007

Curtin, C., Nolan, J. C., Conlon, R., Deneweth, L., Gallagher, C., Tan, Y. J., et al. (2018). A physiologically relevant 3D collagen-based scaffold–neuroblastoma cell system exhibits chemosensitivity similar to orthotopic xenograft models. *Acta Biomater.* 70, 84–97. doi: 10.1016/J.ACTBIO.2018.02.004

Duarte Campos, D. F., Blaeser, A., Buellesbach, K., Sen, K. S., Xun, W., Tillmann, W., et al. (2016). Bioprinting Organotypic hydrogels with improved mesenchymal stem cell remodeling and mineralization properties for bone tissue engineering. *Adv. Healthc. Mater.* 5, 1336–1245. doi: 10.1002/adhm.201501033

Duarte Campos, D. F., Blaeser, A., Korsten, A., Neuss, S., Jäkel, J., Vogt, M., et al. (2015). The stiffness and structure of three-dimensional printed hydrogels direct the differentiation of mesenchymal stromal cells toward adipogenic and osteogenic lineages. *Tissue Eng. Part A* 21, 740–756. doi: 10.1089/ten.TEA.2014.0231

Duarte Campos, D. F., Zhang, S., Kreimendahl, F., Köpf, M., Fischer, H., Vogt, M., et al. (2019). Hand-held bioprinting for de novo vascular formation applicable to dental pulp regeneration. *Connect. Tissue Res.* 9, 1–11. doi: 10.1080/03008207.2019.1640217

Dubbin, K., Tabet, A., and Heilshorn, S. C. (2017). Quantitative criteria to benchmark new and existing bio-inks for cell compatibility. *Biofabrication* 9:044102. doi: 10.1088/1758-5090/aa869f

Forget, A., Blaeser, A., Miessmer, F., Köpf, M., Duarte Campos, D. F., Voelcker, N. H., et al. (2017). Mechanically tunable bioink for 3d bioprinting of human cells. *Adv. Healthc. Mater.* 6:1700255. doi: 10.1002/adhm.201700255

Foster, A. A., Marquardt, L. M., and Heilshorn, S. C. (2017). The diverse roles of hydrogel mechanics in injectable stem cell transplantation. *Curr. Opin. Chem. Eng.* 15, 15–23. doi: 10.1016/j.coche.2016.11.003

Gao, G., Kim, H., Kim, B. S., Kong, J. S., Lee, J. Y., Park, B. W., et al. (2019). Tissue-engineering of vascular grafts containing endothelium and smooth-muscle using triple-coaxial cell printing. *Appl. Phys. Rev.* 6:041402. doi: 10.1063/1.5099306

Gasperini, L., Mano, J. F., and Reis, R. L. (2014). Natural polymers for the microencapsulation of cells. *J. R. Soc. Interface* 11:20140817. doi: 10.1098/rsif.2014.0817

Gu, Q., Tomaskovic-Crook, E., Wallace, G. G., and Crook, J. M. (2018). "Engineering human neural tissue by 3D bioprinting," in *Methods in Molecular Biology*, Ed. J. M. Walker (Totowa, NJ: Humana Press Inc), 129–138. doi: 10.1007/978-1-4939-7741-3_10

Jaeger, A. A., Das, C. K., Morgan, N. Y., Pursley, R. H., McQueen, P. G., Hall, M. D., et al. (2013). Microfabricated polymeric vessel mimetics for 3-D cancer cell culture. *Biomaterials* 34, 8301–8313. doi: 10.1016/j.biomaterials.2013.07.013

Katt, M. E., Placone, A. L., Wong, A. D., Xu, Z. S., and Searson, P. C. (2016). In vitro tumor models: advantages, disadvantages, variables, and selecting the right platform. *Front. Bioeng. Biotechnol.* 4:12. doi: 10.3389/fbioe.2016.00012

Kreimendahl, F., Köpf, M., Thiebes, A. L., Duarte Campos, D. F., Blaeser, A., Schmitz-Rode, T., et al. (2017). Three-dimensional printing and angiogenesis: tailored Agarose-Type I collagen blends comprise three-dimensional printability and angiogenesis potential for tissue-engineered substitutes. *Tissue Eng. Part C Methods* 23, 604–615. doi: 10.1089/ten.tec.2017.0234

Langhans, S. A. (2018). Three-dimensional in vitro cell culture models in drug discovery and drug repositioning. *Front. Pharmacol.* 9:6. doi: 10.3389/fphar.2018.00006

Leberfinger, A. N., Dinda, S., Wu, Y., Koduru, S. V., Ozbolat, V., Ravnic, D. J., et al. (2019). Bioprinting functional tissues. *Acta Biomater.* 95, 32–49. doi: 10.1016/j.actbio.2019.01.009

LeSavage, B. L., Suhar, N. A., Madl, C. M., and Heilshorn, S. C. (2018). Production of elastin-like protein hydrogels for encapsulation and immunostaining of cells in 3D. *J. Vis. Exp.* 2018:57739. doi: 10.3791/57739

Leung, C. T., and Brugge, J. S. (2012). Outgrowth of single oncogene-expressing cells from suppressive epithelial environments. *Nature* 482, 410–413. doi: 10.1038/nature10826

Li, Y., and Kumacheva, E. (2018). Hydrogel microenvironments for cancer spheroid growth and drug screening. *Sci. Adv.* 4:aas8998. doi: 10.1126/sciadv.aas8998

Lindsay, C. D., Roth, J. G., LeSavage, B. L., and Heilshorn, S. C. (2019). Bioprinting of stem cell expansion lattices. *Acta Biomater.* 95, 225–235. doi: 10.1016/j.actbio.2019.05.014

Madl, C. M., Katz, L. M., and Heilshorn, S. C. (2016). Bio-orthogonally crosslinked, engineered protein hydrogels with tunable mechanics and biochemistry for cell encapsulation. *Adv. Funct. Mater.* 26, 3612–3620. doi: 10.1002/adfm.201505329

Madl, C. M., LeSavage, B. L., Dewi, R. E., Dinh, C. B., Stowers, R. S., Khariton, M., et al. (2017). Maintenance of neural progenitor cell stemness in 3D hydrogels requires matrix remodelling. *Nat. Mater.* 16, 1233–1242. doi: 10.1038/NMAT5020

Madl, C. M., LeSavage, B. L., Dewi, R. E., Lampe, K. J., and Heilshorn, S. C. (2019). Matrix remodeling enhances the differentiation capacity of neural progenitor cells in 3D Hydrogels. *Adv. Sci.* 6:1801716. doi: 10.1002/advs.201801716

Murphy, S. V., and Atala, A. (2014). 3D bioprinting of tissues and organs. *Nat. Biotechnol.* 32, 773–785. doi: 10.1038/nbt.2958

Ng, W. L., Lee, J. M., Yeong, W. Y., and Win Naing, M. (2017). Microvalve-based bioprinting-process, bio-inks and applications. *Biomater. Sci.* 5, 632–647. doi: 10.1039/c6bm00861e

Petersen, O. W., Ronnov-Jessen, L., Howlett, A. R., and Bissell, M. J. (1992). Interaction with basement membrane serves to rapidly distinguish growth and differentiation pattern of normal and malignant human breast epithelial cells. *Proc. Natl. Acad. Sci. U.S.A.* 89, 9064–9068. doi: 10.1073/pnas.89.19.9064

Phamduy, T. B., Sweat, R. S., Azimi, M. S., Burow, M. E., Murfee, W. L., and Chrisey, D. B. (2015). Printing cancer cells into intact microvascular networks: a model for investigating cancer cell dynamics during angiogenesis. *Integr. Biol.* 7, 1068–1078. doi: 10.1039/c5ib00151j

Ravi, M., Paramesh, V., Kaviya, S. R., Anuradha, E., and Paul Solomon, F. D. (2015). 3D cell culture systems: advantages and applications. *J. Cell. Physiol.* 230, 16–26. doi: 10.1002/jcp.24683

Salinas-Fernández, S., Santos, M., Alonso, M., Quintanilla, L., and Rodríguez-Cabello, J. C. (2019). Genetically engineered elastin-like recombinamers with sequence-based molecular stabilization as advanced bioinks for 3D bioprinting. *Appl. Mater. Today* 2019:100500. doi: 10.1016/j.apmt.2019.100500

Schänzer, A., Wachs, F.-P., Wilhelm, D., Acker, T., Cooper-Kuhn, C., Beck, H., et al. (2006). Direct stimulation of adult neural stem cells in vitro and neurogenesis in vivo by vascular endothelial growth factor. *Brain Pathol.* 14, 237–248. doi: 10.1111/j.1750-3639.2004.tb00060.x

Shen, Q., Goderie, S. K., Jin, L., Karanth, N., Sun, Y., Abramova, N., et al. (2004). Endothelial cells stimulate self-renewal and expand neurogenesis of neural stem cells. *Science* 304, 1338–1340. doi: 10.1126/science.1095505

Shi, Y., Kirwan, P., and Livesey, F. J. (2012). Directed differentiation of human pluripotent stem cells to cerebral cortex neurons and neural networks. *Nat. Protoc.* 7, 1836–1846. doi: 10.1038/nprot.2012.116

Sontheimer-Phelps, A., Hassell, B. A., and Ingber, D. E. (2019). Modelling cancer in microfluidic human organs-on-chips. *Nat. Rev. Cancer* 19, 65–81. doi: 10.1038/s41568-018-0104-106

Straley, K. S., and Heilshorn, S. C. (2009). Independent tuning of multiple biomaterial properties using protein engineering. *Soft Matter* 5, 114–124. doi: 10.1039/b808504h

Tavazoie, M., Van der Veken, L., Silva-Vargas, V., Louissaint, M., Colonna, L., Zaidi, B., et al. (2008). A specialized vascular niche for adult neural stem cells. *Cell Stem Cell* 3, 279–288. doi: 10.1016/j.stem.2008.07.025

Zhang, Y. S., Duchamp, M., Oklu, R., Ellisen, L. W., Langer, R., and Khademhosseini, A. (2016). Bioprinting the cancer microenvironment. *ACS Biomater. Sci. Eng.* 2, 1710–1721. doi: 10.1021/acsbiomaterials.6b00246

Zhou, X., Zhu, W., Nowicki, M., Miao, S., Cui, H., Holmes, B., et al. (2016). 3D Bioprinting a Cell-laden bone matrix for breast cancer metastasis study. *ACS Appl. Mater. Interfaces* 8, 30017–30026. doi: 10.1021/acsami.6b10673

Conflict of Interest: PC and RR were employed by the company Biofabics Lda. PC was also shareholder of the company Biofabics Lda.

The remaining authors declare that the research was conducted in the absence of any commercial or financial relationships that could be construed as a potential conflict of interest.

frontiers
in Bioengineering and Biotechnology

ORIGINAL RESEARCH
published: 24 June 2020
doi: 10.3389/fbioe.2020.00552

Polymer-Bioactive Glass Composite Filaments for 3D Scaffold Manufacturing by Fused Deposition Modeling: Fabrication and Characterization

Thomas Distler [1], Niklas Fournier [1], Alina Grünewald [1], Christian Polley [2], Hermann Seitz [2], Rainer Detsch [1] and Aldo R. Boccaccini [1]*

[1] Department of Materials Science and Engineering, Institute of Biomaterials, Friedrich-Alexander-University Erlangen-Nuremberg, Erlangen, Germany, [2] Chair of Microfluidics, Faculty of Mechanical Engineering and Marine Technology, University of Rostock, Rostock, Germany

Critical size bone defects are regularly treated by auto- and allograft transplantation. However, such treatments require to harvest bone from patient donor sites, with often limited tissue availability or risk of donor site morbidity. Not requiring bone donation, three-dimensionally (3D) printed implants and biomaterial-based tissue engineering (TE) strategies promise to be the next generation therapies for bone regeneration. We present here polylactic acid (PLA)-bioactive glass (BG) composite scaffolds manufactured by fused deposition modeling (FDM), involving the fabrication of PLA-BG composite filaments which are used to 3D print controlled open-porous and osteoinductive scaffolds. We demonstrated the printability of PLA-BG filaments as well as the bioactivity and cytocompatibility of PLA-BG scaffolds using pre-osteoblast MC3T3E1 cells. Gene expression analyses indicated the beneficial impact of BG inclusions in FDM scaffolds regarding osteoinduction, as BG inclusions lead to increased osteogenic differentiation of human adipose-derived stem cells in comparison to pristine PLA. Our findings confirm that FDM is a convenient additive manufacturing technology to develop PLA-BG composite scaffolds suitable for bone tissue engineering.

Keywords: 3D printing, fused deposition modeling, 3D printing filaments, bioactive glass, polymer ceramic composites, bone tissue engineering

OPEN ACCESS

Edited by:
Luciano Vidal,
Institut National de la Santé et de la Recherche Médicale (INSERM), France

Reviewed by:
Saeid Kargozar,
Mashhad University of Medical Sciences, Iran
Junchao Wei,
Nanchang University, China

***Correspondence:**
Aldo R. Boccaccini
aldo.boccaccini@ww.uni-erlangen.de

Specialty section:
This article was submitted to Biomaterials, a section of the journal Frontiers in Bioengineering and Biotechnology

Received: 20 January 2020
Accepted: 07 May 2020
Published: 24 June 2020

Citation:
Distler T, Fournier N, Grünewald A, Polley C, Seitz H, Detsch R and Boccaccini AR (2020) Polymer-Bioactive Glass Composite Filaments for 3D Scaffold Manufacturing by Fused Deposition Modeling: Fabrication and Characterization. Front. Bioeng. Biotechnol. 8:552. doi: 10.3389/fbioe.2020.00552

INTRODUCTION

Bone is known for its self-healing abilities (Bose et al., 2013). The healing of bone fractures is a remarkable repairing process, resulting in the complete reconstruction of the tissue achieving its original form and functionality (Kumar and Narayan, 2014). Bone healing is a well-orchestrated process and for most minor fractures a mechanical fixation of the damaged bone region is sufficient for successful convalescence. However, if a defect reaches a critical size ($\sim\geq 2.5$ cm (Schemitsch, 2017; Nauth et al., 2018), depending on the surgical case), the endogenous regenerative capacity of bone tissue is insufficient for self-repair (Mothersill et al., 1991). Critical size bone defects caused by diseases such as osteogenesis imperfecta, osteoarthritis, osteomyelitis, osteoporosis, or conditions related to infection or induced by wear, still remain key challenges to be addressed in clinical practice (Porter et al., 2009; Nauth et al., 2018). Besides illnesses, trauma and tumors can lead to a critical size bone defect (Porter et al., 2009). The gold standard treatment involves autografts (bone taken from the patient's own body) and allografts (bone tissue taken from a donor) (Bose et al., 2013). Even if successful, challenges like the limited supply of autografts, transmission of diseases, rejection of grafts, donor site pain and morbidity, limitation in volume of donor tissue that can be safely harvested, and the possibility of harmful immune responses to allografts, drive surgeons and engineers to seek for alternative methods and materials to repair bone defects (Crane et al., 1995; Hill et al., 1999; Linero Palacios et al., 2002; Palmer et al., 2008; Garg et al., 2012). With the availability of novel manufacturing technologies like additive manufacturing (AM) (e.g., 3D-printing), new approaches to design and create engineered biomaterial alternatives to autografts and allografts have started to be developed (Bose et al., 2013; Ibrahim, 2017). Combining 3D printed scaffolds with cells, biotechnological platforms arise in which cells may proliferate, grow, and remodel to potentially develop 3D bone tissue analogs in a tissue engineering approach (Langer and Vacanti, 1993; Mantalaris et al., 2004; Salgado et al., 2004). Through AM and computer aided design (CAD), the fabrication of scaffolds with complex internal pores and shapes (architecture) as well as scaffolds catering to patient-specific needs are possible (Bose et al., 1999, 2003, 2013; Hutmacher et al., 2004). The AM of polymer-based scaffolds for bone engineering has been demonstrated utilizing various techniques (Hutmacher, 2000; Simon et al., 2006; Bose et al., 2013; Ibrahim, 2017; Tappa and Jammalamadaka, 2018). Among others, fused deposition modeling promises to be a solvent-free 3D printing approach with the potential to create patient-specific polymer-based biomaterial scaffolds (Hutmacher, 2000; Bose et al., 2013). FDM is based on the 3D printing of prior fabricated thermoplastic filaments which are subsequently processed in a second step using a hot extrusion nozzle to fabricate 3D structures without the use of a solvent (Hutmacher, 2000; Bose et al., 2013). Hutmacher (2000) demonstrated the 3D printing of polycaprolactone (PCL)-hydroxyapatite composites via FDM. Besides hydroxyapatite, bioactive glass is a well-known osteoinductive and osteoconductive material (Hench et al., 1971; Xynos et al., 2000; Hench, 2006). Combined with biopolymers, BG has been used to develop composite scaffolds for bone engineering (Hench, 2006; Chen et al., 2008; Gerhard and Boccaccini, 2010; Fu et al., 2011; Hench and Jones, 2015; Barbeck et al., 2017). Direct solvent-assisted printing has been demonstrated to successfully process polymer-BG composites (Russias et al., 2007; Bose et al., 2013; Murphy et al., 2016; Ibrahim, 2017). Exemplarily, Russias et al. (2007) showed solvent-based robocasting of PLA-BG and PCL-BG composites. Murphy et al. (2016) processed PCL-borate BG composites by mixing BG particles with PCL dissolved in chloroform to form a printable paste. Kolan et al. (2017) printed PCL-borate BG composites alternating with a Pluronic F127 support to produce 3D scaffolds through pressure-based extrusion. Barbeck et al. (2017) printed PLA/polyethyleneglycol (PEG)/calcium-phosphate-glass using PEG as a plasticizer to allow better rheological properties for direct extrusion. Eqtesadi et al. (2016b) robo-casted BG scaffolds followed by infiltration of PLA to improve the mechanical properties of the 3D printed BG scaffolds. One advantage of FDM over direct extrusion methods is the intermediate filament production step, allowing to achieve potentially storable filament materials for high throughput fabrication of reproducible scaffolds using FDM 3D printers. The FDM of PLA-BG has been demonstrated by Estrada et al. (2017), showing that the scaffolds were bioactive. However, the characterization of PLA-BG composite filaments for 3D printing, the reproducible fabrication of porous scaffolds and the assessment of the scaffold mechanical properties, cytocompatibility and osteoinductivity remain to be addressed to prove PLA-BG scaffold applicability for bone engineering. Among highly proliferative and available osteoblastic cell lines, murine pre-osteoblast cells (MC3T3E1) have been frequently used to study the cytocompatibility of biomaterials for bone engineering *in vitro* (López-Álvarez et al., 2013; Fu et al., 2017; Liu et al., 2018). Their main advantage is their potential for osteogenic differentiation in comparison to e.g., MG-63 cells which are arrested in pre-osteoblastic state (Czekanska et al., 2012). The potential of adipose-derived stem cells (ASC) for bone engineering has been recently highlighted (Vishnubalaji et al., 2012; Bhattacharya et al., 2016; Iaquinta et al., 2019; Storti et al., 2019) and ASC have been applied on biomaterial scaffolds as a potential critical size defect treatment strategy (Du et al., 2018). The high availability of ASC from body lipoaspirates (Yang et al., 2019) combined with the potential for osteogenic differentiation (Zhang et al., 2015) and defect reconstruction (Mesimäki et al., 2009; Yoshida et al., 2019; Zang et al., 2019) *in vivo* renders ASC excellent candidates to study the osteoinductive properties of biomaterials, with promising implications towards clinical translation (Barba et al., 2017). The aim of this study was to fabricate filaments for high throughput FDM of polymer-BG composite scaffolds with bioactive, cytocompatible, and osteoinductive properties. Composite filaments made from PLA and 45S5 BG were produced. The composite filaments were used for the FDM of porous scaffolds with bioactive and osteoinductive properties. 3D printed scaffolds were studied regarding their physicochemical properties as well as cytocompatibility and osteoinductivity using MC 3T3-E1 cells and human ASC.

MATERIALS AND METHODS

Fabrication of PLA-Bioactive Glass (BG) Filaments

Composite filaments were produced using PLA as the bulk matrix material and BG as a filler. 45S5 BG (composition: 45 wt% SiO_2−24.5 wt% CaO−24.5 wt% Na_2O−6 wt% P_2O_5, d50: (4.0 ± 1.0) μm, d95: $\leq 20\,\mu$m, Schott Vitryxx®, Schott AG, Germany) was used. A PLA powder was selected (PLA RXP 7503, Resinex GmbH, Germany). To prevent BG particle agglomeration, the glass was sieved through a 80 μm mesh (Mini-Sieve Micro Sieve Set, SP Scienceware—Bel-Art Products, USA) and treated with an anti-static ionizer (STABLO-AP, Shimadzu Cooperation, Japan) prior to mixing. PLA (100 g) was mixed with 0, 1, 2.5, 5, and 10%

(wt) of 45S5 BG by equal distribution in five 50 ml cell culture tubes (SARSTEDT AG & Co. KG, Germany) filling ∼25 ml of the tubes and subsequent rotationally mixing (Intelly-Mixer, ELMI, Latvia) at 60 rpm for 30 min. The powder was poured into the hopper of a desktop filament extruder (NEXT 2.0, 3Devo B.V., Netherlands). The material was fed in small portions of 10–20 g to reduce the time the material would spend in the hopper to prevent heat associated material agglomeration. The extrusion screw was always covered with layers of PLA-45S5 BG to ensure constant material intake. Cooling fans of the extruder were turned on as soon as the filament diameter reached a value $\geq$ 1 mm. After reaching a stable target diameter of 2.85 mm, the filament was collected on a spool. Filaments with a tolerance of ± 0.15 mm were considered suitable for final scaffold printing. The data produced by the optical sensor was monitored by a desktop computer connected to the extruder during filament production. Between each filament production process, the extruder was purged using high molecular weight polyethylene (HMWPE, 3Devo B.V., Netherlands) cleaning polymer. PLA filaments with varying BG contents were created ranging from 0, 1, 2.5, 5 up to 10 wt%. The final heating parameters were 110, 155, 155, and 145°C for heaters 4 to 1, respectively, with heater 4 being the heater closest to the hopper, heater 1 being the heater closest to the extrusion nozzle. Screw speed was set to 5.6 rpm, the fan speed was set to 50% of the maximum possible fan speed of the extruder.

Filament Characterization

Light Microscopy

Filament diameter, morphology and optical appearance were assessed using a Stemi 508 (Carl Zeiss, Jena) light microscope followed by Image processing via the ImageJ software package (Fiji, ImageJ 1.52i).

Scanning Electron Microscopy (SEM)

To assess BG particle distribution inside PLA-BG composite filaments, scanning electron microscopy (SEM) was performed (Auriga CrossBeam, Carl Zeiss microscopy GmbH, Germany). Fracture surfaces of PLA-BG filaments were prepared by immersion of the filaments in liquid nitrogen (LN2) at ∼-180°C and subsequently breaking them manually prior to SEM imaging.

Tensile Testing

The mechanical tensile properties of PLA-1, 2.5, 5, 10% (wt) BG composite filaments were determined using a universal testing machine (Zugfestigkeitsprüfmaschine Model FRANK, Karl Frank GmbH, Mannheim, Germany). Filaments ($n = 6$) were mounted using a 1kN sample holder at 3.5 bar, with tensile tests being recorded using a 1kN load cell and a constant deformation speed of 10 mm.s^{-1}, according to DIN53455.

Printability Assessment

To determine the accuracy of 3D printing using the fabricated PLA-BG composite filaments, a printability assessment was performed. A resolution tree was 3D printed to evaluate printing resolution using the manufactured PLA-BG filaments. In the resolution tree test, strut distances between 1 mm and 200 μm were examined, with the strut width set to 0.4 mm and strut distances reducing in increments of 100 μm and 10 μm to determine the zone of strut merging. Resolution trees were examined via a light microscope and images were processed using ImageJ. The strut width of $n = 6$ struts was measured as well as the position at which two struts would merge for the first time. The strut distance before merging was considered the resolution limit. To evaluate printability regarding 3D cylindrical open-porous scaffolds, samples ($n = 4$) were 3D printed and the porosity of the top and the side of the scaffold was assessed via ImageJ. Subsequently, the pore area ($n = 6$) was calculated and the deviation (d_{ev}) from the theoretical pore size given by CAD model (750 μm) was determined using the following equation, as described by Tappa and Jammalamadaka (2018):

$$d_{ev} = \frac{ARt - ARe}{ARt} * 100\%$$

where A_{Rt} is the theoretical pore area and A_{Re} is the experimental pore area measured from 3D printed scaffolds.

Scaffold Fabrication Using PLA-BG Filaments

Cylindrical scaffolds (diameter = 10 mm, height = 12 mm) were designed with an interconnected porosity and pore diameter of 750 μm using computer aided design software solid edge (Siemens AG, Germany) and the browser-based CAD tool tinkercad (Autodesk Inc., USA). PLA-BG filaments with 0, 1, 2.5, 5, and 10% (wt) BG content were fed into a FDM 3D printer (Ultimaker S5 Premium, Ultimaker B.V., Netherlands) and scaffolds were produced. The detail printing parameters can be found in **Supplementary Table 1**. The printer was equipped with an extrusion nozzle of diameter D = 400 μm, and a tempered glass building plate. No features of the 3D CAD design were smaller than the resolution limit of the FDM-printer of 0.4 mm.

Micro-CT (μCT) Imaging

To investigate the BG distribution and interconnectivity of porosity of 3D printed PLA-BG scaffolds, μCT analysis was performed. μCT tomograms of PLA-1%(wt) BG scaffolds were recorded on a Skyscan 1076 scanner (Bruker, Kontich, Belgium) applying a source voltage of 55 kV and a source current of 181 mA. To reduce beam hardening artifacts, a 0.5 mm aluminum filter was used. The scan resolution was set to 9 μm per voxel. For noise reduction, an average of 4 frames was recorded every 0.6 degree. The scans were reconstructed applying the cone beam algorithm in the NRecon software package (Bruker, Kontich, Belgium). High resolution 3D renderings were created using CTVox software (Bruker, Kontich, Belgium).

Mechanical Characterization

To evaluate the mechanical properties of the 3D printed scaffolds, compression strength tests were performed using an universal testing system (Instron 3300 Floor Model, Instron® GmbH, Germany). The tests were carried out with a speed of 1.3 mm.min^{-1} in accordance to ASTM D695 (ASTM D695-15, 2015). The starting distance was set close to the height of the scaffolds and the total compression displacement was set to 3 mm. Scaffold surface area was measured prior to the mechanical assessment. Images of the scaffolds ($n = 3$) for each group were taken using a light microscope (ZEISS Stemi 508, Zeiss AG, Germany). The area of each sample was calculated in ImageJ software using the polygon selection tool.

Bioactivity Study

For the bioactivity assessment of the PLA-BG scaffolds, simulated body fluid (SBF) was produced according to Kokubo and Takadama (2006) and as stated in ISO 23317 (ISO 23317:2014(E)H, 2014). A set of 3D printed PLA-BG squares of $6 \times 6 \times 0.4$ mm^3 ($n = 6$) was fabricated per group. The required amount of 9.6 ml of SBF was calculated using the formula stated by Kokubo and Takadama (2006). The equation describes the volume of SBF needed as:

$$Vs = \frac{Sa}{10}$$

where V_s is the volume of SBF in ml and S_a is the apparent surface area of the specimen in mm^2. The samples were placed in SBF and put in a shaking incubator (Heidolph Unimax 1010, Heidolph Instruments GmbH & CO. KG, Germany) at 37°C and 90 rpm. SBF was changed every 2 days. Sets of samples ($n = 3$) per group were removed after 14 and 28 days of incubation in SBF. Samples were washed with ultrapure water and dried under a fume hood at 22°C (room temperature, RT). Before and after the SBF incubation, light microscopy images were recorded. After drying, the samples were characterized using Fourier transformed infrared spectroscopy (FTIR), X-ray diffraction (XRD), and energy dispersed x-ray (EDX) analyses. The chemical composition of pristine and SBF incubated PLA-BG samples was characterized by FTIR (IRAffinity-1S, Shimadzu Europa GmbH). Absorbance spectra of PLA-BG were recorded after 0, 7 and 14 days of incubation in SBF. Samples were also tested with XRD (MiniFlex 600, Rigaku Corporation, Europe) to characterize the crystallinity of the surface layer after SBF incubation. Angles 2Θ of 20–80° were investigated, with 0.02° per step and a speed of 2° per minute. EDX was used to evaluate the composition of the surface of SBF incubated samples using an EDX system (X-Max^N, Oxford Instruments) fitted in a scanning electron microscope (Auriga Crossbeam, Carl Zeiss Microscopy GmbH, Germany). EDX spectra were recorded on non-sputtered samples at a working distance of 6 mm and an accelerating voltage of 10 keV to determine elemental surface composition. Map and point scans were performed at a dwell time of 10 µs.

Cell Culture Studies

Cell Culture

Mouse calvaria pre-osteoblast MC3T3E1 cells (Sigma Aldrich, Germany) were used to assess cytocompatibility of the 3D printed PLA-BG scaffolds. The cells were cultured in alpha-modified minimum essential medium (α-MEM) (Gibco®, Life Technologies™, Germany) containing 10% (v/v) fetal bovine serum (FBS, Sigma-Aldrich), 1% (v/v) penicillin/streptomycin (Sigma-Aldrich, Germany) and 1% (v/v) L-Glutamine (Thermo Fisher Scientific Inc., USA) media supplements. Cells were passaged in T75 cell culture flasks (Sarstedt, Germany) at 37°C and in a humidified atmosphere of 95% air and 5% CO_2 in an incubator (Galaxy® 170 R, Eppendorf AG, Germany). For cell detachment, Trypsin/EDTA (Sigma Aldrich, Germany) was used with cell counting performed using the trypan blue exclusion method using Neubauer chambers (Paul Marienfeld GmbH & Co.KG). To evaluate cell differentiation and gene expression on the composite materials, human adipose-derived stem cells were used (Lonza, CH). The cells were passaged in phenol-red free Dulbecco's modified eagle medium (DMEM) containing 10% (v/v) fetal calf serum (FCS, Corning, USA) and 1% (v/v) penicillin/streptomycin (Thermo Fisher, USA). Cells were harvested and counted using Trypsin/EDTA (Thermo Fisher, USA) and the trypan blue exclusion method. Human ASC at passage 4 (p4) were seeded on 3D printed PLA-1% BG scaffolds (150,000 cells/scaffolds) and cultured for 35 days in maintenance (-OS) and osteogenic (+OS) differentiation medium at 37°C in a humidified atmosphere of 95% air and 5% CO_2 in an incubator. Human ASC seeded on 3D printed PLA scaffolds without BG served as material controls. Osteogenic (+OS) medium consisted of phenol red DMEM containing 10% FCS, 1% penicillin/streptomycin, 50 μg.ml^{-1} ascorbic acid, 10 mM beta-glycerolphosphate, and 10 mM dexamethasone (all Sigma Aldrich). Non-osteogenic (-OS) medium contained phenol red DMEM, 10% FCS, and 1% penicillin/streptomycin.

In vitro Cytocompatibility

For the *in vitro* cytocompatibility assessment, two different structures of PLA-BG composites were 3D printed. Cylindrical scaffolds with three layers, a total height of 2.25 mm and a diameter of 10 mm with interconnected porosity as well as cell culture disks with a height of 4 mm and a diameter of 13 mm were produced. The disk surface was printed with a parallel line infill pattern. As a result, the disk featured an orientated topography to test the ability of directional guidance in cell growth. 3D PLA-BG scaffolds and cell-culture disk containing 0, 1, 2.5, 5, and 10% (wt) BG ($n = 6$) were printed and disinfected using UV light exposure. Wettability of the materials as well as pH development of cell culture medium (5 ml, $n = 3$ scaffolds) in contact with the scaffolds was recorded prior to cell culture. The scaffolds and cell culture disks were placed in 24-well-plates (Sarstedt, Germany) and MC3T3E1 cells were seeded with a concentration of 100,000 cells.ml^{-1} (Brooks et al., 2016). All samples were cultured for 24 h to assess initial cell attachment and *in vitro* cytocompatibility. Tissue culture polystyrene (PS) substrates served as additional controls to the cell-culture disks.

Cell Viability

To assess cell viability, a water-soluble tetrazolium salt (WST-8) assay was performed to indirectly determine the viability of cells on the different substrates by conversion of a water-soluble tetrazolium salt through cellular metabolism into an insoluble formazan. After 24 h, the medium was removed from the cells and the cells on scaffolds ($n = 6$) were incubated with cell culture medium containing 1% (v/v) WST solution (Cell

Counting Kit - 8, Sigma Aldrich, Germany) for 3 h according to manufacturer's instructions. An equally incubated WST-8 master stock solution served as control. After incubation, 100 µl aliquots (technical duplicates) were transferred into a 96-well-plate (Sarstedt, Germany) and the absorbance at 450 nm was recorded using a plate reader (type Phomo, Anthos Mikrosysteme GmbH, Krefeld, Germany).

LIVE/DEAD Staining

To determine the cellular viability on the 3D printed disk, a live/dead staining assay was performed. Viable cells were stained by calcein acetoxymethyl ester (Calcein AM), while apoptotic and necrotic cells were stained by propidium iodide (PI) (both Invitrogen^{TM}, Molecular probes by Life technologies^{TM}, USA), corresponding to live and dead cells, respectively. The samples were washed with phosphate buffered saline (DPBS, Thermo Fisher, USA) and incubated with 1 ml of DPBS stock solution containing 4 µl.ml^{-1} Calcein AM and 5 µl.ml^{-1} PI for 45 min. After incubation, the samples were washed with DPBS and fixed using 500 µl of fixing solution containing 0.1 M PIPES (Piperazine-N,N′-bis(2-ethanesulfonic acid), Merck, Germany), 1 mM EGTA (Ethylene glycol tetraacetic acid, Merck, Germany), 4% (w/v) polyethyleneglycol, and 3.7% (w/v) paraformaldehyde (all Sigma Aldrich, Germany), dissolved in HBSS. After 5 min of fixing, the samples were washed with DPBS and examined using a fluorescence microscope (FM) (Scope.A1, Carl Zeiss, Germany). Cell nuclei of fixed cells on 3D printed scaffolds were stained using Hank's buffered salt solution (HBSS) containing 1 µl.ml^{-1} DAPI (4′,6-diamidino-2-phenylindole, Invitrogen^{TM}, USA) for 5 min.

Gene Expression Analysis

For cDNA synthesis, total RNA was extracted from human ASC cultured on PLA and PLA-1% BG scaffolds ($n = 6$) using a RNeasy mini kit (Qiagen, Germany) according to the manufacturer's instructions. Cells were detached from the scaffolds using Trypsin/EDTA (ThermoFisher, USA), pelleted by centrifugation, and lysed using RLT buffer (RNeasy mini kit). RNA concentration and quality were quantified using a NanoDrop^{TM} One (ThermoFisher Scientific, USA) spectrophotometer. cDNA was reverse-transcribed from 150 µg RNA using iScript Advanced Reverse Transcription Supermix (Bio-Rad, Germany) according to the manufacturer's instructions. Real-time quantitative PCR (RT-qPCR) was performed on a CFX96 thermocycler (Bio-Rad, Germany) to measure levels of gene expression using SsoAdvanced Universal SYBR Green Supermix (Bio-Rad, Germany) on six replicate samples in technical duplicates with human primePCR validated specific primers (**Supplementary Table 2**). Relative gene expression was quantified by the $2^{-\Delta\Delta Cq}$ method and normalized using YWHAZ, HPRT1 and GAPDH multiple housekeeping genes. Relative gene expression of alkaline phosphatase (ALPL), Runt-related transcription factor 2 (RUNX2), collagen type I (COL1), osteocalcein (BGLAP) and vascular endothelial growth factor A (VEGF) was analyzed. Data analysis was conducted using the CFX Maestro software package (Bio-Rad, Germany). Light microscopy images were taken during and after 35 days of incubation to assess cellular growth on the scaffolds.

Statistical Analysis

All experiments were conducted using at least three replicate scaffolds per group. Statistical analyses were performed using one-way analysis of variances (ANOVA) with *post-hoc* Tukey test for multiple comparison of means between normally distributed groups and Welch's t-test for pairwise comparison between two groups using Origin 2019 software (OriginLab Corporation, Northhampton, USA). Data are expressed as mean ± SD except gene expression analysis where data are expressed as mean ± s.e.m. Number of samples per group were $n = 6$ (filament diameter), $n = 6$ (filament tensile testing), $n = 6$ (filament printability), $n \geq 4$ (scaffold characterization), $n = 6$ (scaffold mechanics), $n = 6$ (bioactivity assessment), $n = 3$ (pH), $n = 6$ (*in vitro* characterization), $n = 6$ (gene expression analyses). Differences were considered significant with $^{*}p < 0.05$, $^{**}p < 0.01$, $^{***}p < 0.001$, $^{****}p < 0.0001$.

RESULTS

Filament Production

Figure 1A depicts the production process of 3D printing filaments made by (I) mixing PLA and 45S5 BG particles, (II) filament extrusion using a desktop filament extruder and (III) 3D printing of the produced filaments using FDM. **Figure 1A**, II shows a final BG containing filament on a carrier spool ready for subsequent FDM printing. It was possible to produce filaments of PLA with increasing BG content of 1, 2.5, 5, and 10% (wt) BG (**Supplementary Figure 2**). We observed an increase of turbidity in the filaments with increasing amount of BG (**Figure 1B**). Scanning electron microscopy micrographs indicated a homogenous distribution of BG particles ($d_{50} = 4 \pm 1$ µm) inside PLA-BG filaments (**Figure 1C**). Melts of PLA-BG mixtures were extruded from the extruder and monitored live over time to assess the time point after which the goal filament diameter of $d = 2.85$ mm was achieved for each PLA-BG composition. The continuous monitoring allowed to assess the deviation in filament diameter from the filament extruder over time as a measure of the process stability. **Figure 1D** shows the filament diameter of the differently BG-laden PLA filaments over extrusion time. We found that with increasing BG content [>2.5% (wt) BG, **Figure 1D,** blue, green, purple graph], the deviation of filament diameter around the diameter aimed at ($d = 2.85$ mm) increased significantly in comparison to PLA-0% BG and PLA-1% BG filaments (**Figure 1E**). It was possible to produce filaments of all BG filler contents around the aimed filament diameter suitable for FDM using the herein utilized 3D printer. During filament extrusion, filament adhesion on the puller wheel (**Supplementary Figure 1**) of the NEXT 2.0 filament extruder was observed. A tool to be attached on NEXT 2.0 filament maker models to avoid this adhesion is provided (**Supplementary Figure 1**). (The file

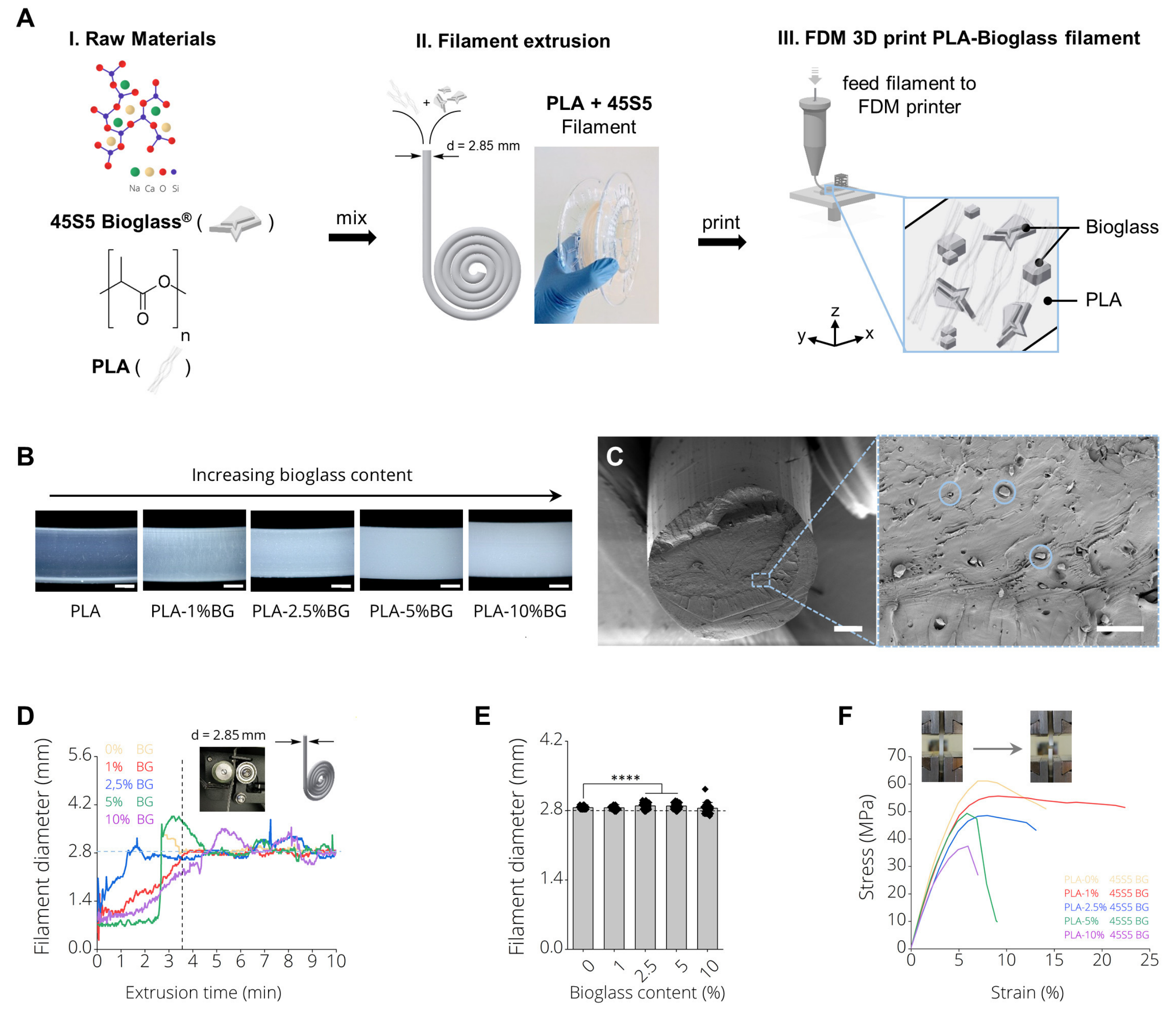

FIGURE 1 | PLA-45S5 BG filaments for fused deposition modeling. **(A)** Schematic diagram depicting the process pipeline to fabricate PLA-BG FDM printed scaffolds with (i) mixing of the raw materials PLA and 45S5 BG, (ii) filament production using a polymer extruder with an image of the final extruded and spooled 45S5 BG containing PLA filaments and (iii) FDM 3D printing by feeding the prior produced filaments into a FDM printer. **(B)** Light microscopy images of the final BG-laden PLA filaments of 0, 1, 2.5, 5, and 10% (wt) 45S5 BG content. An increase in turbidity with increasing BG content is observed. Scale bars: 500 µm. **(C)** SEM Micrograph of the filament cross section with 45S5 BG ($d_{50} = 4 \pm 1$ µm) particles homogeneously distributed inside the bulk PLA matrix. Scale bars: 500 µm (left), 15 µm (right). **(D)** Filament diameter monitored during filament extrusion illustrating the yield of filament as a function of the time required until a near constant filament diameter of d = 2.85 mm was extruded. It is visible that with increasing BG content, the time required to extrude filaments of a constant diameter increases. **(E)** Diameter of final filaments utilized for FDM printing (mean ± SD, $n = 6$; ****$p < 0.0001$ significant difference of mean diameter compared to pure PLA filaments determined by one-way ANOVA). **(F)** Tensile testing of the resulting PLA-45S5 BG filaments. Representative stress strain curves depicting the characteristic stress strain behavior of the resulting filaments with a decrease in ultimate tensile strength and elongation at break with increasing BG content.

is available in the **Supplementary Materials** to this article as an open source ready-to-print *.stl file). The mechanical properties of the BG containing PLA filaments were assessed via tensile testing. It was found that with BG contents exceeding 1% (wt), tensile strength and toughness decreased (**Figure 1F**), which is most likely associated to insufficient BG bonding to the PLA matrix, observed in SEM cross sections (**Figure 1C**).

Printability of PLA-BG Filaments

To assess the printability of PLA, PLA-1% BG, PLA-2.5% BG, PLA-5% BG, and PLA-10% BG filaments via FDM, resolution trees were fabricated from CAD models using the different filaments (**Figure 2A**). In light microscopy images, an increasing turbidity of the printed structures, indicative of the higher loading of BG particles, was observed (**Figure 2A**). PLA filaments provided by the 3D printer supplier

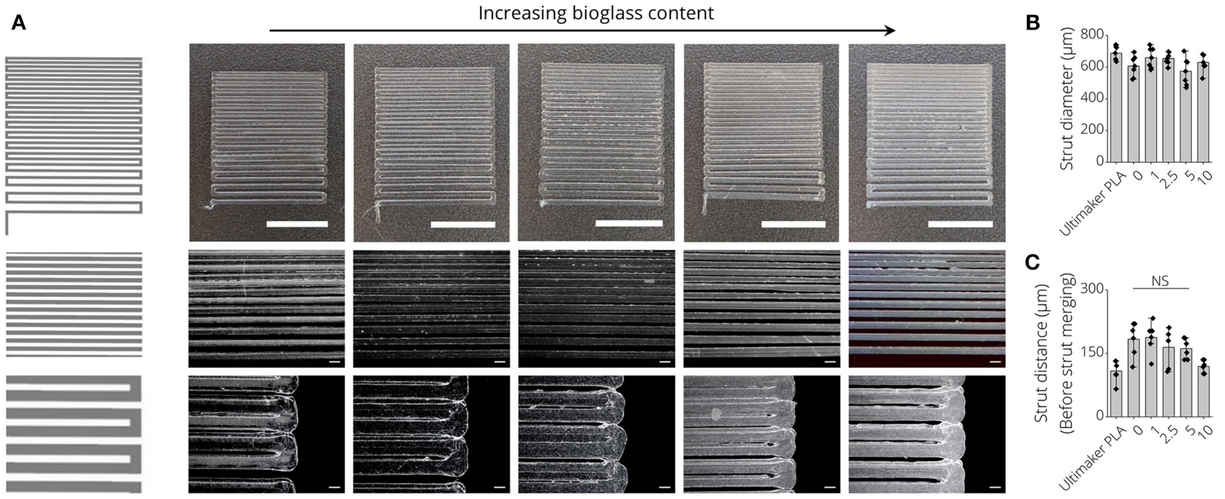

FIGURE 2 | Printability assessment of PLA-BG filaments. **(A)** CAD model (left) and light microscopy images (right) of the FDM printed BG-laden PLA filaments into meandering structures. Scale bars: 2000 µm (top row), 500 µm (mid row), 200 µm (bottom row). The light microscopy images indicate strut merging and increase in turbidity with increasing BG content. **(B)** Strut diameter achieved of 3D printed PLA-BG filaments with increasing BG content of 0, 1, 2.5, 5, and 10% (wt) BG in PLA, using a diameter = 400 µm FDM nozzle ($n = 7$, mean ± SD). **(C)** The distance between struts before strut merging occurred processing PLA-BG filaments. Strut distance before merging indicated the highest resolution possible between two struts for each material ($n = 6$, mean ± SD). NS indicates no significant difference comparing the different groups with $p < 0.05$ by one-way ANOVA test.

(Ultimaker) served as commercial PLA printing control. We found that the strut diameter of 3D printed resolution trees of all processed filaments was around 625 ± 68 µm without statistically significant differences between the groups (**Figure 2B**). Assessing the most narrow distance between struts that could be printed before strut merging occurred, the fabricated filaments in this study showed a maximal printing resolution of 163 ± 27 µm, with no significant difference between PLA-BG filaments of pristine PLA, 1, 2.5, and 5% BG loading (**Figure 2C**). Printing the commercially available PLA reference filament allowed a resolution of 108 ± 25 µm strut distance.

Scaffold Fabrication From PLA-BG Filaments

Open-porous three-dimensional structures were designed to produce biomaterial scaffolds from PLA-BG filaments (**Figure 3A**). It was possible to produce open porous scaffolds of height h = 12 mm, diameter d = 10 mm using all fabricated filaments in this study (**Figure 3B**). Light microscopy images indicated deviations from ideally rectangular pore geometries (**Figure 3B**, left, pristine PLA) when printing BG containing PLA filaments (**Figure 3B**). **Figure 3C** shows a top view light microscopy image of a 3D printed PLA-BG scaffold. The increase in turbidity with increasing BG content is visible, as well as material lumps deposited and defects introduced when fabricating higher BG content PLA-BG scaffolds from PLA-5% BG and PLA-10% BG filaments (**Supplementary Figure 3**). The strut diameter of the printed scaffolds varied negligibly from the theoretical strut diameter of 400 µm given by the 3D printers extrusion nozzle (**Figure 3D**). However, with increasing BG content, the variation in strut diameter increased, indicated by increasing standard deviation (SD) (**Figure 3D**). The mean strut diameter did not significantly change in comparison to 0% BG PLA scaffolds. Comparing to the CAD designed pore diameter (750 µm), the pore size of the top of the scaffolds prepared from PLA-BG did not significantly change except for PLA-2.5% BG scaffolds (**Figure 3E**). It was observed that with 5 and 10% BG containing PLA filaments, the SD of pore size increased, however not significantly altering the mean pore size. Regarding pore size assessed from the scaffold top, a reduction in pore size was observed with increasing BG content (**Figure 3F**). **Figure 3G** depicts the deviation of the pore size area in comparison to the theoretical pore size area designed in CAD (0.5625 mm^2). With increasing BG content in PLA-BG filaments, an increase in the deviation from the theoretical pore size was observed (**Figure 3G**), with significant deviation from the theoretical pore area for 2.5, 5, and 10% (wt) BG containing PLA-BG filaments (**$p < 0.01$). It was possible to predict and tailor the pore size based on the CAD model for PLA-BG filaments with low BG content (PLA-1% BG). In an attempt to assess the capacity to print more complex geometries, structures like e.g., an upscaled µCT derived model from a mouse femur, was successfully printed (**Figure 3H**) from PLA-1% BG filaments. µCT images derived from reconstructed tomograms of PLA-1% BG scaffolds confirmed the interconnected porosity of the PLA-BG scaffolds (**Figure 3I**, **Supplementary Video 1**). White arrows depicting areas of higher x-ray absorbance in the images indicate the presence and homogeneous distribution of bioactive glass particles in the 3D printed scaffolds due to higher x-ray absorbance in comparison to bulk PLA (**Figure 3I**, **Supplementary Video 2**).

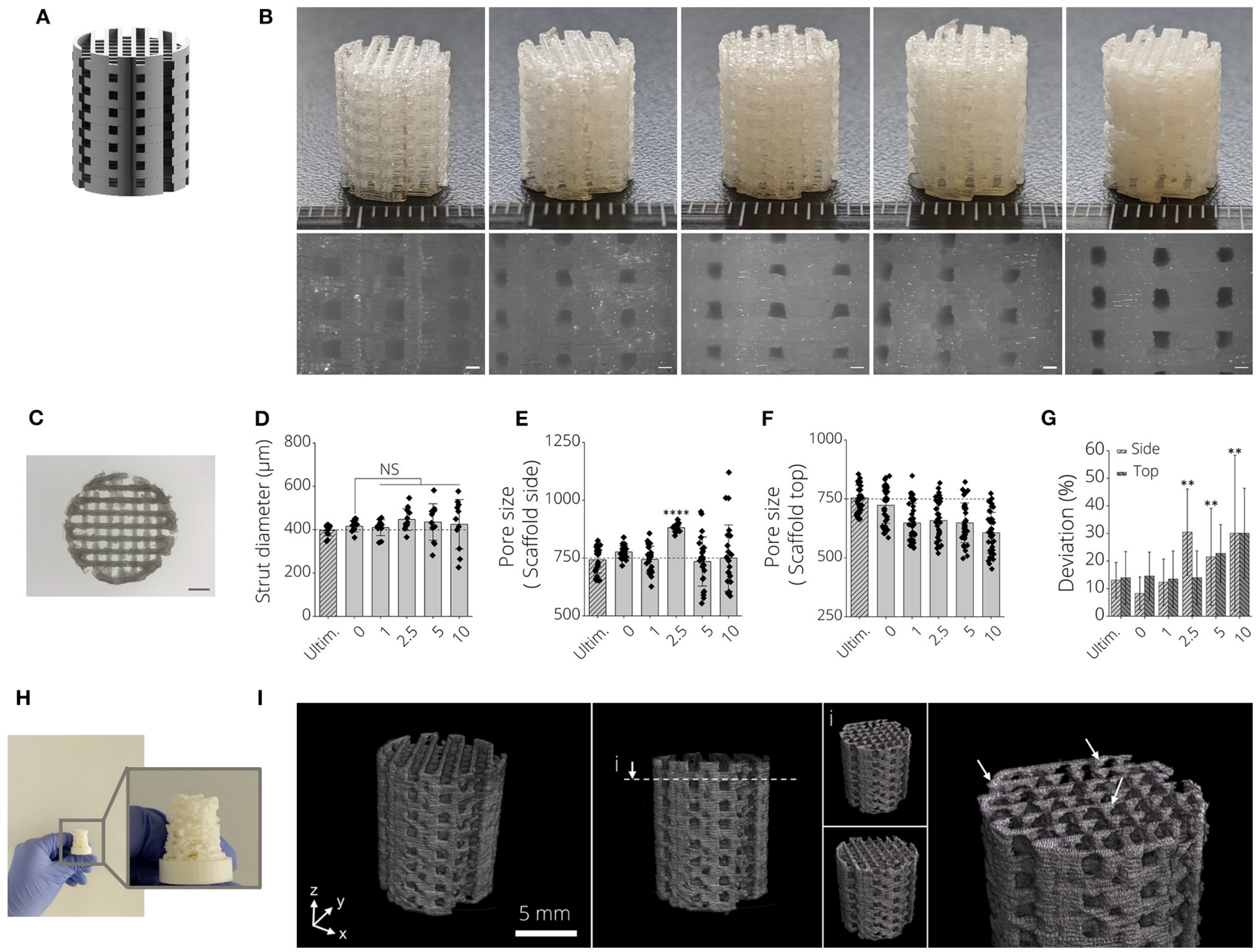

FIGURE 3 | 3D printed PLA-45S5 BG scaffolds. **(A)** CAD render of the aimed design for PLA-BG scaffolds with a pore size of width = 750 µm. **(B)** FDM 3D printed PLA-BG scaffolds from prior produced filaments. From left to right: PLA-0% (wt) BG, PLA-1%(wt) BG, PLA-2.5% (wt) BG, PLA-5% (wt) BG, and PLA-10% (wt) BG 45S5. Light microscopy images display the scaffold sides (bottom). Scale bars: 500 µm. **(C)** Top view light microscopy image of a PLA-BG scaffold. Scale bar: 2 mm. **(D–G)** Printability assessment and porosity analysis of PLA-BG scaffolds compared to Ultimaker PLA reference filaments depicting **(D)** strut diameter, **(E)** porosity at the side and top **(F)** of the scaffolds, as well as **(G)** the deviation of pore area from the theoretical pore area calculated from the CAD model as a measure of printing accuracy. $^{**}p < 0.01$, $^{****}p < 0.0001$ indicate statistical significant difference of means in comparison to 3D printed 0% BG PLA by one-way ANOVA or Welch's *t*-test in pairwise comparisons of scaffold side pore diameter. **(H)** Print of a complex shaped CAD model based on an upscaled MRI scan of a mouse femur. **(I)** µCT image of 3D printed PLA-1% BG scaffold showing the interconnected porosity and indicating even distribution of BG in the scaffolds (white arrows).

Mechanical Properties of PLA-BG Scaffolds

Figure 4A depicts representative images of scaffolds after compression tests, namely for PLA-1% BG and PLA-10% BG scaffolds. Differences in failure behavior from buckling (PLA-1% BG, **Supplementary Video 3**) to brittle fracture (PLA-10% BG) were observed (**Figure 4A**). Stress-strain diagrams show the decrease of work-of-fracture with increasing BG content in correspondence to those observations (**Figure 4B**). A multiple-stage failure process (black arrows) with regions of decreasing and increasing stress is visible for PLA-0% BG and PLA-1% BG scaffolds (**Figure 4B**), related to buckling and incremental failure of single struts observed during testing. For example, the compressive strength of PLA-BG scaffolds decreased from 18 ± 10 MPa (PLA) to 12 ± 4 MPa ($^{*}p < 0.05$; PLA-1% BG) and 3 ± 2 MPa ($^{****}p < 0.0001$; PLA-5% BG) with increasing BG content. We found a significant decrease in stiffness of BG-laden PLA scaffolds exceeding 1% (wt) BG (**Figure 4C**), with no significant difference in elastic modulus between pristine PLA (0% BG) and 1% (wt) PLA-BG scaffolds. A summary of the values of the 3D printed PLA-BG scaffolds can be found in **Table 1**. The elastic properties of PLA scaffolds loaded with 0–2.5% (wt) BG showed mechanical properties similar to the range of cancellous bone of human proximal tibias (Hvid et al., 1983; Rho et al., 1993).

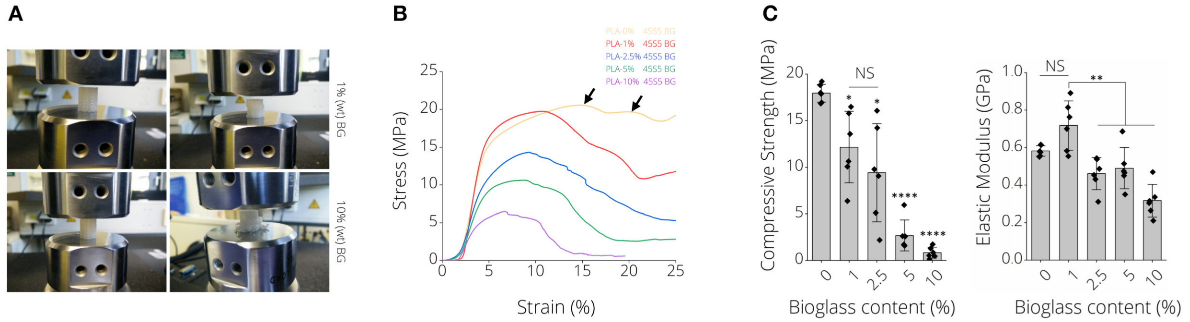

FIGURE 4 | Mechanical properties of 3D printed PLA-45S5 BG scaffolds. **(A)** Macroscopic images illustrating different failure modes of 1 and 10% (wt) BG loaded PLA-BG scaffolds indicating buckling and brittle failure, respectively. **(B)** Qualitative stress strain diagram from compression tests of PLA-0, 1, 2.5, 5, and 10%-BG laden 3D printed scaffolds. A loss in scaffold toughness with increasing BG content is visible. The consecutive failure of different layers inside the scaffolds during compression testing is indicated by stress hills (black arrow) inside the diagram after initial failure of a scaffold layer. **(C)** Compression strength and modulus of elasticity of 3D printed PLA-BG scaffolds with increasing BG content ($n = 6$). Data is shown as mean ± SD. $^*p < 0.05$, $^{**}p < 0.01$, and $^{***}p < 0.001$ indicate statistical significant differences of means in comparison to 3D printed pristine PLA scaffolds by one-way ANOVA or Welch's *t*-test pairwise comparisons.

TABLE 1 | Mechanical properties of PLA-BG scaffolds.

Sample	Elastic modulus (GPa)	Compressive strength (MPa)
0 BG	0.6	18 ± 10
1 BG	0.7 ± 0.1	12 ± 4
2.5 BG	0.5 ± 0.1	9 ± 5
5 BG	0.5 ± 0.1	3 ± 2
10 BG	0.3 ± 0.1	1 ± 1
Cortical Bone	18 GPa–30 (Rho et al., 1993; Mohamed and Shamaz, 2014)	100–203 (Mohamed and Shamaz, 2014)
Trabecular Bone	0.5–1.5 (Hvid et al., 1983); 13–20 (Ashman and Rho, 1988; Oftadeh et al., 2014)	2–12 (Hvid et al., 1983; Røhl et al., 1991; Mohamed and Shamaz, 2014)

Bioactivity of FDM Printed PLA-BG Filaments

Figure 5A depicts the formation of a white layer on the surface of PLA-1% BG rectangular plates after 28 days of incubation in SBF. SEM micrographs (**Figures 5B,C**) in combination with SEM-EDX analysis (**Figure 5D**) confirmed the formation of a calcium-phosphate layer with cauliflower-like structures visible after 14 days of incubation in SBF (**Figure 5C**). X-ray diffraction analysis indicated the formation of a crystalline layer for all PLA compositions incorporating BG after 28 days of SBF incubation (**Figure 5E**). Diffraction peaks at ∼26, 32, and 40° 2Θ were observed after incubation in SBF. Notably, diffraction peaks indicating layer crystallinity were observed after 14 days of SBF incubation for the highest BG incorporating (10% (wt)) PLA-BG composition (**Supplementary Figure 4**). FTIR absorbance spectra of PLA-BG plates after 0, 7, and 28 days of incubation in SBF (**Figure 5F**) showed the formation of absorbance peaks at ∼1,013, 600, and 555 cm^{-1}, initially for PLA-10% BG after 7 days of incubation in SBF, eventually occurring for all PLA-BG compositions after 28 days of incubation in SBF (**Figure 5F**).

Cytocompatibility of PLA-BG Scaffolds

Figures 6A,B show macroscopic images of 3D printed PLA-BG disks exhibiting a patterned surface for initial cytocompatibility assessment. Cell culture disks with increasing BG content showed similar increase in turbidity, analog to the observation made for the filaments (**Supplementary Figure 5**). The high quality of the produced scaffolds is to be expected when using additive manufacturing with strut distances of about 150 µm and strut diameter of 250 µm (**Figure 6C**). The hydrophobicity (water contact angle, **Figure 6D**) of the PLA surfaces did not change by adding BG, while only the pH value increased with the amount of BG over 24 h at 37°C (**Figure 6E**). In fact, the pH increase was dependent on BG content and changed over time, suggesting BG release (**Supplementary Figure 6**). The initial *in vitro* cytocompatibility studies of the different 2D surfaces performed via WST-8 assay showed no significant difference in viability with an increase of BG content (**Figure 6H**). Fluorescence microscopy images with Calcein AM (green) and propidium iodide (red) stainings show that the cells can be guided by the structures (**Figures 6F,G**). MC3T3-E1 cells expressed long, elongated and fibroblastic morphology after 24 h of incubation with PLA, which can be seen in **Figure 6G**. Fluorescence microscopy images of Calcein AM/DAPI (blue) stained MC3T3E1 cells on 3D printed PLA-BG scaffolds with 0, 1, 2.5, 5, and 10% BG are shown in **Figure 7**. Translating the results from 2D to 3D reveals no negative change in cell behavior, the MC3T3-E1 cells can grow well on all scaffold surfaces and the viability (indirect assay) is not dependent on the degree of filling of the polymer with BG (**Figure 7**).

Gene Expression of Human ASCs on FDM Printed PLA-BG Scaffolds

Since the most promising results regarding mechanical strength and printability were gained for PLA-1% BG scaffolds, osteogenic cell differentiation with and without osteo-induction stimulants was performed (**Figure 8**). The relative expression of ALP, RUNX2 as osteoblast markers, Col1, Osteocalcein as ECM

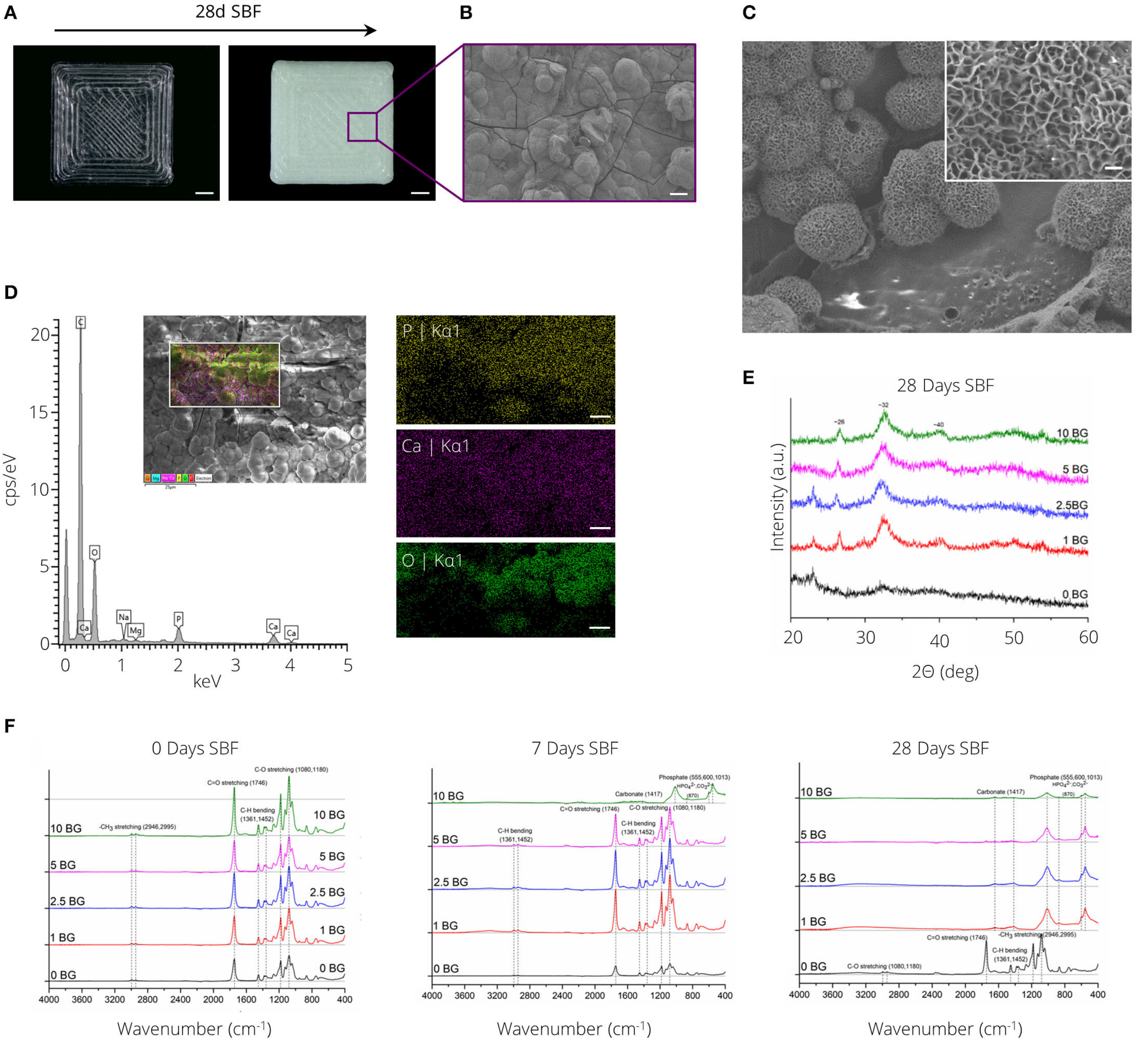

FIGURE 5 | Bioactivity assessment of PLA-BG materials. **(A)** Light microscopy images of 3D printed PLA-1% BG squares before (left) and after (right) incubation in simulated body fluid for 28 days. The precipitation of a white layer is apparent on the material surface. Scale bar = 2 mm. **(B)** SEM micrograph showing the formation of a solid layer with cauliflower-like structures present, indicating the formation of a ceramic hydroxy-carbonated apatite (HCA)-like layer. Scale bar: 20 μm. **(C)** SEM image of cauliflower like structure on PLA-BG after 14 days of incubation in SBF. Scale bar: 250 nm. **(D)** Energy dispersive x-ray spectrum of PLA-10% BG scaffolds incubated for 14 days in SBF, indicating the formation of phosphorus, calcium and oxygen species on the formed layer. Scale bar: 5 μm. **(E)** X-ray diffraction spectrum of the material surfaces of PLA-BG incubated for 28 days in SBF indicating the formation of crystalline species on the surface. **(F)** Fourier-transformed infrared spectroscopy analysis of PLA-0, 1, 2.5, 5, and 10% (wt) BG squares after 0, 7, and 28 days of incubation in SBF. The formation of new peaks indicative for carbonates and phosphates is shown over SBF incubation time.

expression markers, as well as VEGF as an angiogenesis marker in human ASC, cultured for 35 days, was detected. While it was not possible to increase the osteoblastic differentiation in the pure PLA samples in comparison to the BG containing samples, an increased expression of the ECM markers was shown (**Figure 8A**). BG also induced a significantly higher VEGF RNA-value. When osteoinduction stimulants were added, marked osteoblastic differentiation with increased ECM was detected on the BG-containing samples compared to the pure PLA scaffolds (**Figure 8B**). Cell growth inside the scaffolds after 35 days cultured in non-osteogenic (top) and osteogenic (bottom) medium is shown in **Figure 8C**. The white arrow indicates higher cell growth observed inside scaffold pores for human ASC cultured in non-osteogenic medium in comparison to +OS scaffolds, indicative of a higher proliferation on—OS scaffolds.

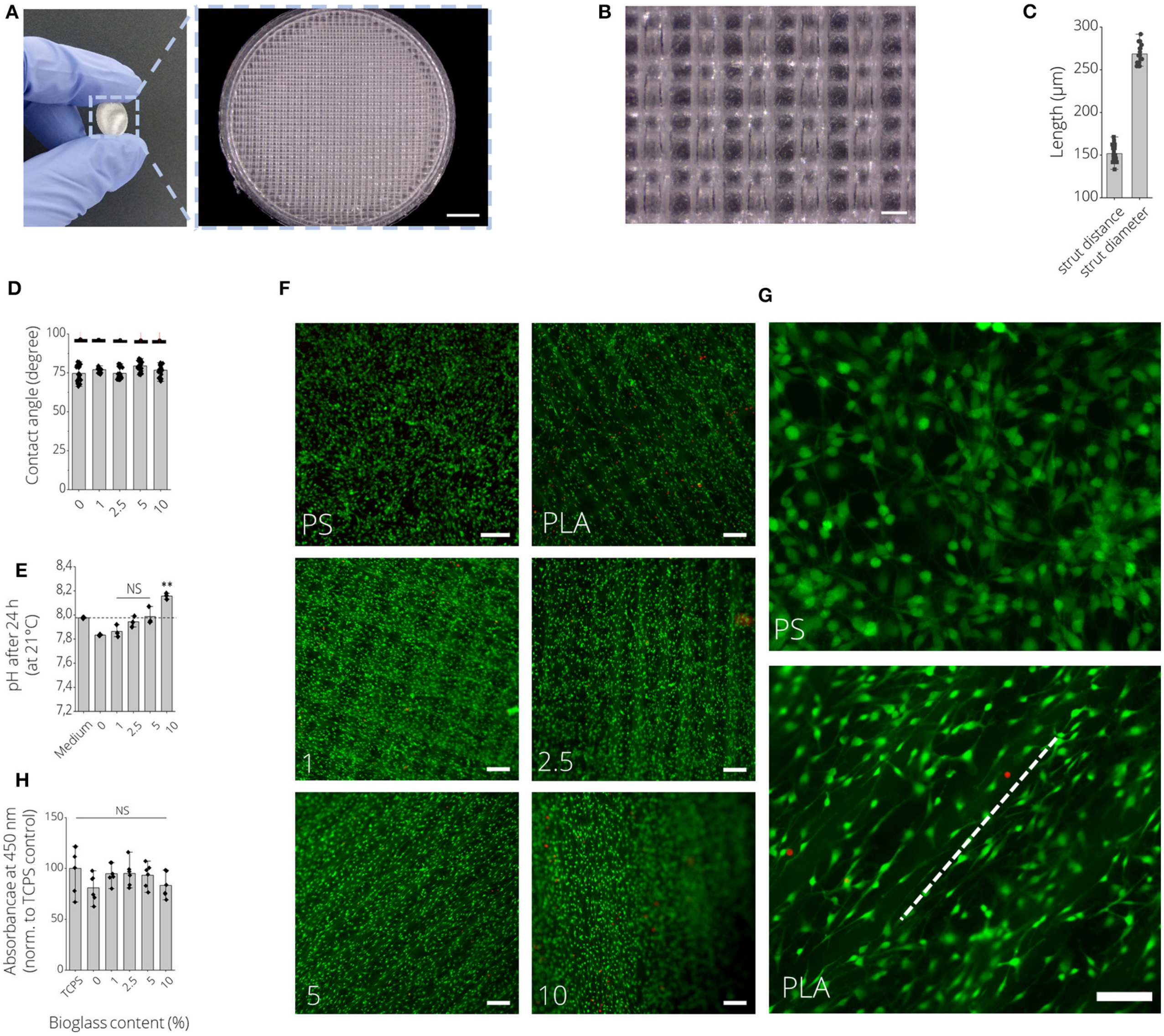

FIGURE 6 | 2D *in vitro* cytocompatibility assessment of FDM 3D printed PLA-BG disks. **(A)** Macroscopic image of a 3D printed PLA-BG disk used for initial cytocompatibility assessment. Light microscopy image illustrates the patterned surface of the FDM 3D printed PLA-BG disk. Scale bar: 2 mm. **(B)** Representative light microscopy image of the grit-like strut-by-strut surface structure of the cell-culture disk. Scale bar: 200 µm. **(C)** Corresponding quantification of distance between two struts and strut diameter. **(D)** Water contact angle as a measure of wettability of PLA-BG disks ($n = 6$). Data presented as mean ± SD. **(E)** Development of pH value of cell culture medium incubated with 3D printed PLA-BG disk of 0, 1, 2.5, 5, and 10% (wt) BG content over 24 h at 37°C, measured at 21°C. No significant increase in pH (NS) except for 10% (wt) BG-laden PLA disks was observed ($n = 6$). Data presented as mean ± SD. $^{**}p < 0.01$ compared to untreated cell culture medium by one-way ANOVA. **(F)** Fluorescence microscopy images of Calcein AM (green) and propidium iodide (red) stained MC3T3E1 cells after 24 h of incubation on PLA-BG disk and polystyrene reference substrates depicting LIVE/DEAD cells, respectively. Scale bars: 200 µm. **(G)** Cell orientation was present on PLA-BG disks (dashed white line) in comparison to PS cell culture well plates. Scale bar: 200 µm (both images). **(H)** Corresponding indirect viability WST-8 assay data with no significant (NS) difference in viability detected among the substrates.

DISCUSSION

In this study, we demonstrated the fabrication of PLA-BG 3D printing filaments for FDM, followed by presenting the scaffold fabrication using such composite filaments, and the characterization as well as *in vitro* assessment of the new materials. Wu et al. (2020) recently reported a feasibility study on producing PLA-HA scaffolds by FDM. Estrada et al. (2017) had previously shown the fabrication of PLA-BG by FDM, however the bioactivity of scaffolds was the main focus of the study (Estrada et al., 2017). In the present work, we demonstrate the characterization and screening of filaments with different BG contents, giving an insight into the production process and printability, the fabrication of open porous PLA-BG scaffolds

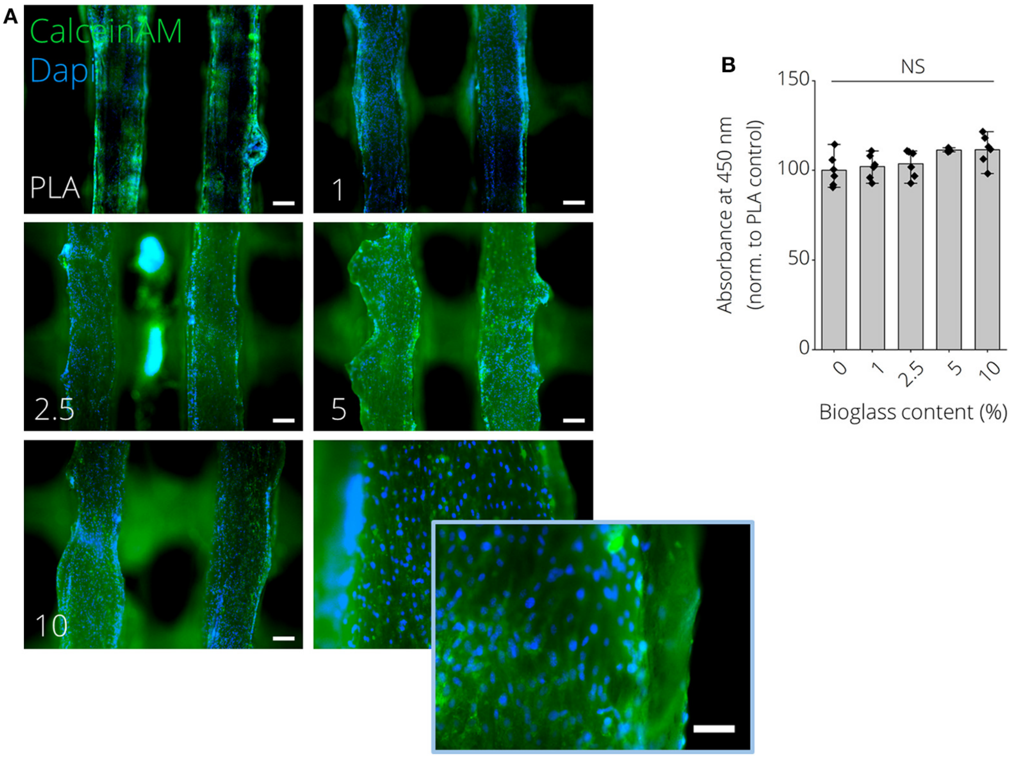

FIGURE 7 | MC3T3E1 pre-osteoblast cells cultured on 3D printed PLA-BG substrates for 24 h. **(A)** Fluorescence microscopy images of Calcein AM (green)/DAPI (blue) stained MC3T3E1 on 3D printed PLA-BG scaffolds with 0, 1, 2.5, 5, and 10% BG, respectively. Scale bars: 200 µm, 100 µm (insert, bottom right). **(B)** Indirect cell viability WST-8 test of MC3T3E1 cells on different substrates ($n = 6$), with no significant difference (NS) detected in WST conversion among the different groups.

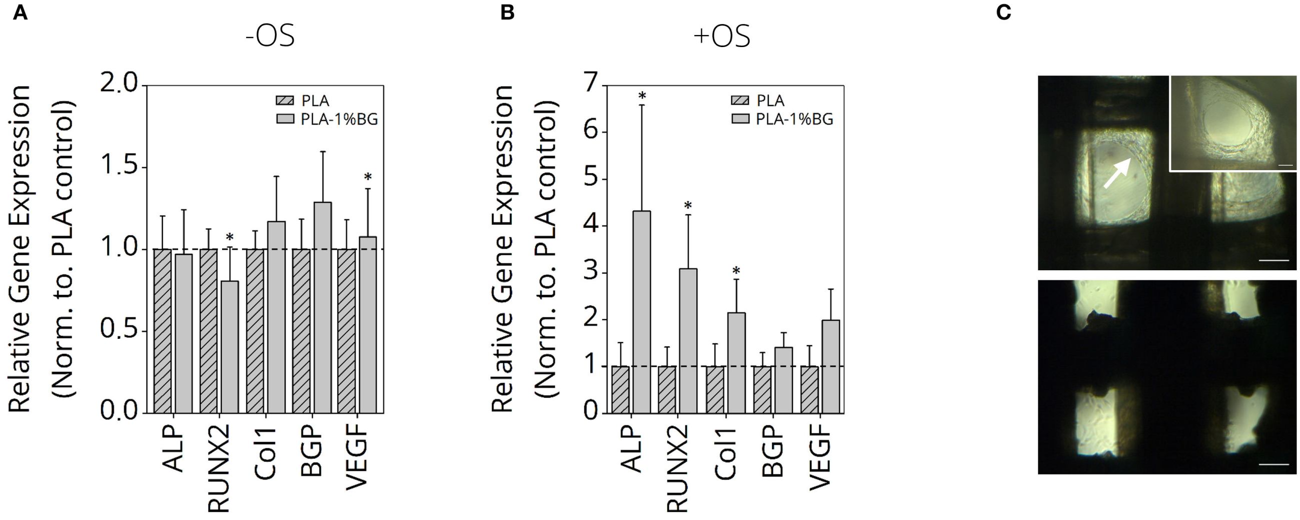

FIGURE 8 | Gene expression study of human ASC on PLA-1% BG scaffolds. Relative gene expression of Col1, VEGF, BGP, RUNX2, and ALP in human ASC cultured for 35 days on 3D printed 1% BG containing PLA scaffolds normalized to PLA scaffolds in **(A)** nonosteogenic and **(B)** osteogenic differentiation medium. Data is reported as mean ± s.e.m ($n = 4$). ANOVA with *post-hoc* Tukey -HSD test; $^*p \leq 0.05$. **(C)** Light microscopy images of ASC after 35 days cultured in non-osteogenic (top) and osteogenic (bottom) medium. The white arrow indicates higher cell growth observed inside scaffold pores for ASC cultured in nonosteogenic medium in comparison to +OS scaffolds, indicative for higher proliferation on –OS scaffolds. Scale bars: 200 µm, 100 µm (insert, top right).

from such filaments, and the control over scaffold porosity via CAD. In addition, We characterized the scaffold bioactivity, mechanical properties, and investigated the cytocompatibility by cell biology and gene expression studies. Gene expression results of human adipose-derived stem cells revealed the osteoinductive properties of FDM printed PLA-1% BG in comparison to pristine PLA. Our work provides cytocompatible and osteoinductive PLA-BG filaments that can be used in FDM to develop bioactive scaffolds for bone TE. Furthermore, FDM allows the high throughput printing of scaffolds (**Supplementary Figure 8**) by achieving a storable intermediate filament material which is fed in a FDM printer, which may be advantageous in comparison to solvent based approaches to fabricate PLA-BG scaffolds. The PLA-BG filaments in this study showed brittle fracture and a decrease of filament toughness and tensile strength with increasing BG content (**Figure 1F**). Those findings suggest the presence of a non-optimal interface bonding between BG particles and the bulk PLA. SEM images of filament cross sections (**Figure 1C**) reveal dark areas around the BG particles inside the PLA matrix, which indicates no strong bonding between the PLA bulk and the BG particles. This is in accordance with the hypothesis of improper interface adhesion. As a result, regardless of increasing BG content, strengthening of the PLA-BG scaffolds was not observed (**Figure 4C**), as it would be expected from composite theory of ceramic-laden polymer scaffolds with optimal interface bonding (Gerhard and Boccaccini, 2010). Instead, a decrease in stiffness and compressive strength was observed with increasing BG loading [$\geq$2.5% (wt)] (**Figure 4C**). Drummer et al. (2012) assessed PLA-βTCP FDM printed tensile specimens, showing no notable increase in elastic modulus with increasing βTCP content. Contrarily, a tendency of decreased stress at break when increasing βTCP filler content was observed, comparing specimens processed at the same temperature (Drummer et al., 2012). The group used βTCP particles with a diameter of $5.0 \pm 1.0\,\mu$m (Drummer et al., 2012), similar to the d_{50} ($4.0 \pm 1.0\,\mu$m) of 45S5 BG particles in the present study. We observed a similarly decreased tensile stress at break when increasing the filler content. It has been reported that the combination of hydrophobic bulk polymer and hydrophilic fillers leads to improper interface bonding, as observed in our study (Goda et al., 2013). Further work could focus on different surface modifications like particle roughness, size, and chemistry as well as bulk polymer chemistry to achieve an increased polymer/filler interface binding (Boccaccini et al., 2002, 2010; Goda et al., 2013). The properties of interface bonding might be assessed via AFM to get further insight of successful interface engineering (Goda et al., 2013). Barbeck et al. (2017) and Serra et al. (2013) recorded higher compressive strength of printed samples made from PLA/PEG/calcium-phosphate glasses via direct, solvent based printing when adding glass particles. Serra et al. reported compressive strength values of 9.11 ± 1.19 MPa (Serra et al., 2013) for PLA-5%PEG scaffolds, a value much higher than the one measured on the pure PLA scaffolds in the present study. It has to be noted that the manufacturing methods used in the previous studies (Serra et al., 2013; Barbeck et al., 2017) were direct printing processes, not having an intermediate step of FDM filament production. Second, glass filler contents of up to 50% were used, five times higher than the highest concentration of BG assessed in the current study. The differences in mechanical performance in comparison to our study could be caused by the different pore sizes and scaffold designs, as well as differences in the PLA material initially used. In combination, PEG could cause improved particle-to-bulk bonding due to its higher hydrophilicity [water content angle ~44° (Pan et al., 2015)] in comparison to PLA (~75°, **Figure 6D**), which could allow better interface adhesion to BG. Eqtesadi et al. infiltrated 3D printed BG scaffolds with PLA or PCL, which improved the toughness and strength of the scaffolds (Eqtesadi et al., 2014, 2016a,b). Serra et al. showed the reduction of hydrophobicity by PEG addition to PLA (Serra et al., 2013). The pore sizes in Serra et al.'s study were much smaller ($375 \pm 25\,\mu$m between struts) in comparison to the pore size in our work. Alongside with the different scaffold design, the change in porosity could lead to a better stress distribution in comparison to the scaffolds fabricated in our study. Drummer et al. (2012) highlighted the influence of specimen size used for mechanical characterization of FDM parts, observing that larger samples resulted in higher stiffness of the assessed material due to (i) the ability to print more homogenous specimens, being less susceptible to incorporate structural inhomogeneities and defects, and (ii) a reduced influence of the specimen surface roughness on the tensile testing in comparison to smaller specimens (Drummer et al., 2012). As a result, a combination of manufacturing related defects and potential improper binding at the BG-PLA interface might have led to the decrease in stiffness and strength of the present scaffolds, leaving room for improvement. It was intentional by the authors to choose specimens for tensile and compression testing similar to scaffolds used for *in vitro* characterization. However, a comparison of different blends of polymer and BG particles utilizing ISO tensile specimens may be a valid approach to assess polymer-filler material interaction, as demonstrated by Drummer et al. (2012). Strut diameters of around $625\,\mu$m were achieved with a $D = 400\,\mu$m nozzle. We found that the first layer deposited on the glass plate tended to have a higher strut diameter ($d = 635\,\mu$m) due to PLA wetting on the glass. This effect is not present when the polymer is deposited on existing struts (**Figure 6C**, cell culture disk, strut diameter $\sim 275\,\mu$m). Strut diameters could be tuned by using different printing nozzles, e.g., $D = 200\,\mu$m. The highest resolution of pure PLA and PLA-BG composites were strut distances of $163 \pm 27\,\mu$m (Ultimaker PLA control: $108 \pm 25\,\mu$m). Both materials feature similar SD ($\sim 25\,\mu$m), which can be attributed to the FDM printer. Thus, PLA and PLA-BG composites showed no statistically significant difference in printability. Pores of $\sim 165\,\mu$m were achieved by Barbeck et al. using PLA-bioactive glass and PEG (Barbeck et al., 2017). The resolution achieved here, with the advantage of using a solvent-free approach, is comparable to PLA-BG structures obtained by direct printing reported in literature (Barbeck et al., 2017). We observed increasing SD of strut diameter and pore size with increasing BG content. This can be an indicator of a loss in printing accuracy, producing lumps and defects. One reason for this behavior can be the higher variation in filament diameter during production (**Figure 1D**), which may lead to defects during scaffold manufacturing in FDM. Serra et al. (2013) demonstrated direct printing of PLA combined with PEG and 50 wt% BG particles ($44.5P_2O_5$-$44.5Ca_2O$-$6Na_2O$-$5TiO_2$ mol, $d < 40\,\mu m$, G5; Serra et al., 2013), independent of any filament quality. However, such direct printing approaches may require prior adjustment of polymer viscosity using solvents or plasticizers to allow 3D printing (Serra et al., 2013; Barbeck et al., 2017). Diomede et al. (2018) produced PLA scaffolds using filaments by FDM. They reported a pore size deviation of 24.1% (Diomede et al., 2018), comparable to pore size deviation of 0 and 1% BG-PLA scaffolds in our study. The study by Estrada et al. (2017), which is the closest to our work, cannot be compared regarding printability, as no similar data was reported. FTIR analyses at day 0 (**Figure 5F**, left) for PLA-BG depict absorbance peaks at 1,746 cm^{-1} [v(C=O)], 1,361 cm^{-1} [v(CH-CH3)], 1,452 cm^{-1} [v(CH3)], and 1,080, 1,180 cm^{-1} [v(C-O-C)], characteristic for PLA (Yuniarto et al., 2016). No characteristic peaks of BG were present. However, SEM images showing BG incorporated in PLA and positive bioactivity results indicate that BG particles are incorporated and surrounded by the bulk PLA matrix, which were not detectable by FTIR surface analysis. PLA-10% BG was the only composition showing silica peaks in EDX indicating BG on its surface. The result supports the hypothesis that BG was mostly surrounded by the PLA polymer when embedded in the polymer matrix by processing through filament making/3D printing, leaving BG particles undetectable for EDX surface analysis. However, for the highest BG composition (PLA-10% BG), a sufficient amount of BG particles was added to the matrix so that it was possible to detect BG by EDX. X-ray diffraction peaks at ∼26, 32, and 40° 2Θ after incubation of PLA-BG in SBF for 28 days suggest (002), (211), and (310) lattice diffraction of hydroxyapatite (HAP) (Takemoto et al., 2004; Meena et al., 2012; Shahabi et al., 2014). FTIR analysis shows stretching vibrations at 1,417 cm^{-1}, indicative of carbonate, and phosphate peaks [v(PO), v(CO)] at 555, 600, and 1,013 cm^{-1}(Rehman and Bonfield, 1997), suggesting a calcium-phosphate surface layer coverage. **Figure 5C** showing PLA-BG scaffolds after 14 days of SBF incubation (SEM images) indicates the presence of cauliflower like structures, while **Figure 5B** after 28 days in SBF depicts the growth of the initial cauliflower like structure to a dense HAP layer. Summarizing, XRD, FTIR, SEM, and EDX analyses indicate the formation of hydroxy-carbonated apatite, confirming scaffold bioactivity even for 1% BG content PLA. Hence, the filaments in this study were confirmed to be bioactive. The formation of a hydroxyapatite-like layer has been shown to be crucial for successful implant-bone bonding (Boccaccini et al., 2010). Estrada et al. (2017) demonstrated bioactivity of PLA-BG composites after 7 days of incubation in SBF (crystallinity at ∼20° 2Θ) (Estrada et al., 2017). We show the evolution of the calcium-phosphate layer on PLA-BG scaffolds toward higher detectable crystallinity at time points exceeding 7 days, maturating from day 14 (**Figure 5C**; **Supplementary Figure 4**) to day 28 of SBF incubation (**Figures 5B,E**). The results found by Estrada et al. (2017) are similar to the present XRD analysis after 14 days of incubation (**Supplementary Figure 4**). The wide peak forming at approx. 20° 2Θ is possibly due to semi-crystalline PLA with a slight additional peak at ∼23° 2Θ (Chieng et al., 2014; Nanaki et al., 2018). PLA-10% BG shows only a main peak of hydroxyapatite at ∼32° 2Θ after 14 days of incubation in SBF, suggesting accelerated bioactivity with higher BG content. The encapsulation of BG particles in the bulk PLA allows to reduce BG ion release. Therefore, the release of BG dissolution products could be controlled through BG filler content (**Supplementary Figure 6**), indicated by pH changes monitored over time. The ion release from, and bioactivity of the scaffolds can be controlled through the PLA resorption properties and BG filler content (**Supplementary Figure 7**) (Boccaccini and Maquet, 2003). *In vitro* cytocompatibility studies of PLA-BG composites in 2D showed cytocompatible surfaces independent of BG content. This result confirms that PLA-BG composite scaffolds made from extruded filaments are not cytotoxic. Kim et al. (2012) have shown that MSCs on PLA-BG composite exhibit higher cell viability after 3 days compared to pure PLA. Regarding structure compatibility, the fabricated strut-by-strut 3D-structures are well- known in TE and have already proven their potential on bone tissue scaffolds (Hollister et al., 2002; Detsch et al., 2008; Rottensteiner et al., 2014). We confirm that by 3D printing μm-range grooved patterns ($150\,\mu m$) an alignment of cells can be triggered (**Figure 6G**), as shown for groove widths of ∼$842\,\mu m$ (Blasiak et al., 2019). As a result, the printed PLA-BG plates could be used as platforms for cell guidance. PLA-BG scaffolds developed in this work exhibited hydrophobic surfaces independently of BG content (**Figure 6D**), which is the result of the intrinsic hydrophobicity of PLA caused by the presence of non-polar methyl groups (Cohn and Younes, 1988; Yang et al., 2002; Kim et al., 2006). This behavior corresponds to the fact that BG particles were incorporated in the PLA bulk and not present on the scaffold surface. PLA surface chemistry can be tailored by surface modifications or by adding hydrophilic polymers. Serra et al. (2013) showed an increase in the wettability of G5 BG containing scaffolds in contrast to our study. This difference could be attributed to the direct printing used, which might not lead to encapsulation of the BG particles in the bulk PLA compared to the FDM filaments fabricated here. Gene expression studies revealed that BG induces a higher expression of collagen and osteocalcin by human ASCs compared to pure PLA scaffolds (**Figure 8A**). Together, these two markers confirmed the osteogenic effectiveness of BG. The higher proliferation of non-stimulated cells is shown in **Figure 8C**, whereas the observed overgrowth of the squared pores is in correspondence with Rüdrich et al. (2019). They showed that scaffold pore design is of high importance for cell sensing during the initial step of cell adhesion and proliferation (Rüdrich et al., 2019). The use of +OS increased the expression of ALP and RUNX2 in cells grown on PLA-BG scaffolds, which are the characteristic markers for osteoblasts, thus confirming the potential of the PLA-BG scaffolds for bone tissue engineering.

CONCLUSIONS

We have shown the successful fabrication of PLA-BG composite filaments for the manufacturing of 3D scaffolds by fused deposition modeling. The filaments containing BG particles of size $4.0 \pm 1.0\,\mu m$ (d_{50}) exhibited bioactivity. It was possible to predict and control porosity and scaffold shape for PLA-1% BG filaments with similar accuracy to the commercially available

PLA FDM standard. The developed PLA-BG scaffolds triggered increased osteogenic differentiation of adipose derived human stem cells *in vitro*. By this approach, a high throughput, solvent free manufacturing route of PLA-BG composite scaffolds was demonstrated, which provides a versatile and potentially patient specific biomaterial platform for bone tissue engineering.

DATA AVAILABILITY STATEMENT

All 3D printing files generated for this study are included in the article/**Supplementary Material**.

AUTHOR CONTRIBUTIONS

TD, RD, and AB designed the experiments. TD and NF conducted main experiments and analyzed the data. TD, RD, NF, and AB wrote the manuscript. TD performed manuscript formatting and data visualization. CP and HS conducted and processed μCT experiments. TD and AG conducted gene expression experiments and analysis. TD, CP, HS, RD, and AB contributed to data interpretation and commented on the manuscript. AB supervised the overall project. All authors listed, contributed directly, and substantially and intellectually to the work. This work was approved by all authors for publication.

FUNDING

This research was funded by the Deutsche Forschungsgemeinschaft (DFG, German Research Foundation)—SFB 1270/1—299150580.

ACKNOWLEDGMENTS

The authors acknowledge the help of Dr. Judith Roether (Inst. of Polymer Materials, FAU) for scientific and practical support on mechanical testing of the composite filament materials. We acknowledge the support from the Core Facility Multimodal Small Animal Imaging (Rostock University Medical Center, Schillingallee 69a, 18057, Rostock, Germany) for access to the microCT.

SUPPLEMENTARY MATERIAL

The Supplementary Material for this article can be found online at: https://www.frontiersin.org/articles/10.3389/fbioe.2020.00552/full#supplementary-material

Supplementary Video 1 | μCT of PLA-1%BG Scaffold.

Supplementary Video 2 | μCT slicing of PLA-1%BG Scaffold.

Supplementary Video 3 | Compression Test of PLA-1% BG Scaffold.

REFERENCES

Ashman, R. B., and Rho, J. Y. (1988). Elastic modulus of trabecular bone material. *J. Biomech*. 21, 177–181. doi: 10.1016/0021-9290(88)90167-4

ASTM D695-15 (2015). *Standard Test Method for Compressive Properties of Rigid Plastics*. West Conshohocken, PA: ASTM International. Available online at: www.astm.org

Barba, M., Di Taranto, G., and Lattanzi, W. (2017). Adipose-derived stem cell therapies for bone regeneration. *Expert Opin. Biol. Ther*. 17, 677–689. doi: 10.1080/14712598.2017.1315403

Barbeck, M., Serra, T., Booms, P., Stojanovic, S., Najman, S., Engel, E., et al. (2017). Analysis of the *in vitro* degradation and the *in vivo* tissue response to bi-layered 3D-printed scaffolds combining PLA and biphasic PLA/bioglass components – Guidance of the inflammatory response as basis for osteochondral regeneration. *Bioact. Mater*. 2, 208–223. doi: 10.1016/j.bioactmat.2017.06.001

Bhattacharya, I., Ghayor, C., and Weber, F. E. (2016). The use of adipose tissue-derived progenitors in bone tissue engineering-a review. *Transfus. Med. Hemother*. 43, 336–343. doi: 10.1159/000447494

Blasiak, A., Guerin, T. H. M., Teh, D. B. L., Yang, I. H., Lahiri, A., and Thakor, N. V. (2019). Fibro-neuronal guidance on common, 3D-printed textured substrates. *IEEE Trans. Nanobiosci*. 18, 226–229. doi: 10.1109/TNB.2019.2905469

Boccaccini, A., R., Erol, M., Stark, W., Mohn, D., Hong, Z., and Mano, J. F. (2010). Polymer/bioactive glass nanocomposites for biomedical applications: a review. *Compos. Sci. Technol*. 70, 1764–1776. doi: 10.1016/j.compscitech.2010.06.002

Boccaccini, A. R., and Maquet, V. (2003). Bioresorbable and bioactive polymer/Bioglass® composites with tailored pore structure for tissue engineering applications. *Compos. Sci. Technol*. 63, 2417–2429. doi: 10.1016/S0266-3538(03)00275-6

Boccaccini, A. R., Roether, J. A., Hench, L. L., Maquet, V., and Jérome, R. (2002). "A composites approach to tissue engineering," in *26th Annual Conference on Composites, Advanced Ceramics, Materials, and Structures: B: Ceramic Engineering and Science Proceedings*, eds H. Lin and M. Singh (Westerville, OH), 805–817.

Bose, S., Darsell, J., Kintner, M., Hosick, H., and Bandyopadhyay, A. (2003). Pore size and pore volume effects on alumina and TCP ceramic scaffolds. *Mater. Sci. Eng. C*. 23, 479–486. doi: 10.1016/S0928-4931(02)00129-7

Bose, S., Suguira, S., and Bandyopadhyay, A. (1999). Processing of controlled porosity ceramic structures via fused deposition. *Scr. Mater*. 41, 1009–1014. doi: 10.1016/S1359-6462(99)00250-X

Bose, S., Vahabzadeh, S., and Bandyopadhyay, A. (2013). Bone tissue engineering using 3D printing. *Mater. Today* 16, 496–504. doi: 10.1016/j.mattod.2013.11.017

Brooks, E. K., Tobias, M. E., Yang, S., Bone, L. B., and Ehrensberger, M. T. (2016). Influence of MC3T3-E1 preosteoblast culture on the corrosion of a T6-treated AZ91 alloy. *J. Biomed. Mater. Res. B. Appl. Biomater*. 104, 253–262. doi: 10.1002/jbm.b.33378

Chen, Q., Roether, J. A., and Boccaccini, A. R. (2008). "Tissue engineering scaffolds from bioactive glass and composite materials," in *Topics in Tissue Engineering*, Vol 4, eds N. Ahsammakhi, R. Reis, and F. Chiellini (Oulu: Oulu University), 1–27.

Chieng, B. W., Ibrahim, N. A., Yunus, W. M. Z. W., Hussein, M. Z., Then, Y. Y., and Loo Y. Y. (2014). Effects of graphene nanoplatelets and reduced graphene oxide on poly(lactic acid) and plasticized poly(lactic acid): a comparative study. *Polymers* 6, 2232–2246. doi: 10.3390/polym6082232

Cohn, D., and Younes, H. (1988). Biodegradable PEO/PLA block copolymers. *J. Biomed. Mater. Res*. 22, 993–1009. doi: 10.1002/jbm.820221104

Crane, G. M., Ishaug, S. L., and Mikos, A., G. (1995). Bone tissue engineering. *Nat. Med*. 1, 1322–1324. doi: 10.1038/nm1295-1322

Czekanska, E. M., Stoddart, M. J., Richards, R. G., and Hayes, J. S. (2012). In search of an osteoblast cell model for *in vitro* research. *Eur. Cells Mater*. 24, 1–17. doi: 10.22203/eCM.v024a01

Detsch, R., Uhl, F., Deisinger, U., and Ziegler, G. (2008). 3D-Cultivation of bone marrow stromal cells on hydroxyapatite scaffolds fabricated by dispense-plotting and negative mould technique. *J. Mater. Sci. Mater. Med*. 19, 1491–1496. doi: 10.1007/s10856-007-3297-x

Diomede, F., Gugliandolo, A., Cardelli, P., Merciaro, I., Ettorre, V., Traini, T., et al. (2018). Three-dimensional printed PLA scaffold and human gingival stem cell-derived extracellular vesicles: a new tool for bone defect repair. *Stem Cell Res. Ther*. 9, 1–21. doi: 10.1186/s13287-018-0850-0

Drummer, D., Cifuentes-Cuéllar, S., and Rietzel, D. (2012). Suitability of PLA/TCP for fused deposition modelling. *Rapid Prototyp. J*. 18, 500–507. doi: 10.1108/13552541211272045

Du, J., Xie, P., Lin, S., Wu, Y., Zeng, D., Li, Y., et al. (2018). Time-phase sequential utilization of adipose-derived mesenchymal stem cells on mesoporous bioactive glass for restoration of critical size bone defects. *ACS Appl. Mater. Interfaces* 10, 28340–28350. doi: 10.1021/acsami.8b08563

Eqtesadi, S., Motealleh, A., Miranda, P., Pajares, A., Lemos, A., J., and Ferreira, J. M. F. (2014). Robocasting of 45S5 bioactive glass scaffolds for bone tissue engineering, J. *Eur. Ceram. Soc*. 34, 107–118. doi: 10.1016/j.jeurceramsoc.2013.08.003

Eqtesadi, S., Motealleh, A., Pajares, A., Guiberteau, F., and Miranda, P. (2016a). Improving mechanical properties of 13-93 bioactive glass robocast scaffold by poly (lactic acid) and poly (ε-caprolactone) melt infiltration. *J. Non. Cryst. Solids*. 432, 111–119. doi: 10.1016/j.jnoncrysol.2015.02.025

Eqtesadi, S., Motealleh, A., Perera, F. H., Pajares, A., and Miranda, P. (2016b). Poly-(lactic acid) infiltration of 45S5 Bioglass® robocast scaffolds: Chemical interaction and its deleterious effect in mechanical enhancement. *Mater. Lett*. 163, 196–200. doi: 10.1016/j.matlet.2015.10.073

Estrada, S. A. M., Olivas Armendáriz, I., Torres García, A., Francisco Hernández Paz, J., and Alejandra Rodríguez González, C. (2017). Evaluation of *in vitro* bioactivity of 45S5 bioactive glass / poly lactic acid scaffolds produced by 3D printing. *Int. J.* Compos. *Mater*. 7, 144–149. doi: 10.5923/j.cmaterials.20170705.03

Fu, C., Yang, X., Tan, S., and Song, L. (2017). Enhancing cell proliferation and osteogenic differentiation of MC3T3-E1 pre-osteoblasts by BMP-2 delivery in graphene oxide-incorporated PLGA/HA biodegradable microcarriers. *Sci. Rep*. 7, 1–13. doi: 10.1038/s41598-017-12935-x

Fu, Q., Saiz, E., Rahaman, M. N., and Tomsia, A. P. (2011). Bioactive glass scaffolds for bone tissue engineering: state of the art and future perspectives. *Mater Sci Eng C Mater Biol Appl*. 31, 1245–1256. doi: 10.1016/j.msec.2011.04.022

Garg, T., Singh, O., Arora, S., and R., Murthy, S. R. (2012). Scaffold: a novel carrier for cell and drug delivery. *Crit. Rev. Ther. Drug Carr. Syst*. 29, 1–63. doi: 10.1615/CritRevTherDrugCarrierSyst.v29.i1.10

Gerhard, L. C., and Boccaccini, A. R. (2010). Bioactive glass and glass-ceramic scaffolds for bone tissue engineering. *Materials* 3, 3867–3910. doi: 10.3390/ma3073867

Goda, K., Sreekala, M. S., Malhotra, S. K., Joseph, K., and Thomas, S. (2013). Advances in polymer composites: biocomposites-state of the art, new challenges, and opportunities. *Polym. Compos. Biocomposites* 3, 1–10. doi: 10.1002/9783527674220.ch1

Hench, L. L. (2006). The story of Bioglass®. *J. Mater. Sci. Mater. Med*. 17, 967–978. doi: 10.1007/s10856-006-0432-z

Hench, L. L., and Jones, J. R. (2015). Bioactive glasses: frontiers and challenges. *Front. Bioeng. Biotechnol*. 3:194. doi: 10.3389/fbioe.2015.00194

Hench, L. L., Splinter, R. J., Allen, W. C., and Greenlee, T. K. (1971). Bonding mechanisms at the interface of ceramic prosthetic materials. *J. Biomed. Mater. Res*. 5, 117–141. doi: 10.1002/jbm.820050611

Hill, N. M., Horne, G., and Devane, P., A. (1999). Donor site morbidity in the iliac crest bone graft. *Aust. N.Z. J. Surg*. 69, 726–728. doi: 10.1046/j.1440-1622.1999.01674.x

Hollister, S. J., Maddox, R. D., and Taboas, J. M. (2002). Optimal design and fabrication of scaffolds to mimic tissue properties and satisfy biological constraints. *Biomaterials* 23, 4095–4103. doi: 10.1016/S0142-9612(02)00148-5

Hutmacher, D. W. (2000). Scaffolds in tissue engineering bone and cartilage. *Biomaterials* 21, 2529–2543. doi: 10.1016/S0142-9612(00)00121-6

Hutmacher, D. W., Sittinger, M., and Risbud, M. (2004). Scaffold-based tissue engineering: rationale for computer-aided design and solid free-form fabrication systems. *Trends Biotechnol*. 22, 354–362. doi: 10.1016/j.tibtech.2004.05.005

Hvid, I., Christensen, P., Søndergaard, J., Christensen, P. B., and Larsen, C. G. (1983). Compressive strength of tibial cancellous bone: Instron® and osteopenetrometer measurements in an autopsy material. *Acta Orthop*. 54, 819–825. doi: 10.3109/17453678308992915

Iaquinta, M. R., Mazzoni, E., Bononi, I., Rotondo, J. C., Mazziotta, C., Montesi, M., et al. (2019). Adult stem cells for bone regeneration and repair. *Front. Cell Dev. Biol*. 7:268. doi: 10.3389/fcell.2019.00268

Ibrahim, A. (2017). "3D bioprinting bone," in *3D Bioprinting for Reconstructive Surgery: Techniques and Applications*, eds D. Thomas, Z. M. Jessop and I. S. Whitaker (Sawston: Elsevier Ltd; Woodhead Publishing), 245–275.

ISO 23317:2014(E) (2014). Implants for Surgery - *in vitro* Evaluation for Apatite-Forming Ability of Implant Materials.

Kim, J. J., Jin, G. Z., Yu, H. S., Choi, S. J., Kim, H. W., and Wall, I. B. (2012). Providing osteogenesis conditions to mesenchymal stem cells using bioactive nanocomposite bone scaffolds. *Mater. Sci. Eng. C* 32, 2545–2551. doi: 10.1016/j.msec.2012.07.038

Kim, S.-S., Sun Park, M., Jeon, O., Yong Choi, C., and Kim, B.-S. (2006). Poly(lactide-co-glycolide)/hydroxyapatite composite scaffolds for bone tissue engineering. *Biomaterials* 27, 1399−1409. doi: 10.1016/j.biomaterials.2005.08.016

Kokubo, T., and Takadama, H. (2006). How useful is SBF in predicting *in vivo* bone bioactivity? *Biomaterials* 27, 2907–2915. doi: 10.1016/j.biomaterials.2006.01.017

Kolan, K., Liu, Y., Baldridge, J., Murphy, C., Semon, J., Day, D., et al. (2017). Solvent based 3D printing of biopolymer/bioactive glass composite and hydrogel for tissue engineering applications. *Proc. CIRP*. 65, 38–43. doi: 10.1016/j.procir.2017.04.022

Kumar, G., and Narayan, B. (2014). "The biology of fracture healing in long bones," *Classic Papers in Orthopaedics Class,* eds P. Banaszkiewicz and D. Kader (London: Springer).

Langer, R., and Vacanti, J. P. (1993). Tissue engineering. *Science* 260, 920–926. doi: 10.1126/science.8493529

Linero Palacios, D., Lizuain Arroyo, M.C., Picón Olmos, C., Gracia Espeleta, A., De Blas Piñol, R. (2002). Radiosurgery techniques based on an electron lineal accelerator. Rotating tecnique with circular fields and irregular fixed fields. *Oncologia*. 25, 68–73. Available online at: https://www.scopus.com/inward/record.uri?eid=2-s2.0-0036200985&partnerID=40&md5=c83327388a2b72b3c9743a3761cfd33e

Liu, C. G., Zeng, Y. T., Kankala, R. K., Zhang, S. S., Chen, A. Z., and Bin Wang, S. (2018). Characterization and preliminary biological evaluation of 3D-printed porous scaffolds for engineering bone tissues. *Materials* 11, 1–20. doi: 10.3390/ma11101832

López-Álvarez, M., Rodríguez-Valencia, C., Serra, J., and González, P. (2013). Bio-inspired ceramics: promising scaffolds for bone tissue engineering. *Proc. Eng*. 59, 51–58. doi: 10.1016/j.proeng.2013.05.093

Mantalaris, A., Panoskaltsis, N., and J.,Wu, H. D. (2004). "Tissue engineering of bone marrow," in *Encyclopedia of Biomaterials and Biomedical Engineering, Vol. 4*, eds B. E. Wnek, and B. Gary L. (Boca Raton, FL: Taylor & Francis group), 2660. doi: 10.1201/9780429154065

Meena, R., Kesari, K. K., Rani, M., and Paulraj, R. (2012). Effects of hydroxyapatite nanoparticles on proliferation and apoptosis of human breast cancer cells (MCF-7). *J. Nanoparticle Res*. 14, 1–11. doi: 10.1007/s11051-011-0712-5

Mesimäki, K., Lindroos, B., Törnwall, J., Mauno, J., Lindqvist, C., Kontio, R., et al. (2009). Novel maxillary reconstruction with ectopic bone formation by GMP adipose stem cells. *Int. J. Oral Maxillofac. Surg*. 38, 201–209. doi: 10.1016/j.ijom.2009.01.001

Mohamed, S., and Shamaz, B. H. (2014). Bone tissue engineering and bony scaffolds. *Int. J. Dent*. 1, 15–20. doi: 10.25141/2471-657X-2015-1.0001

Mothersill, C., Seymour, C. B., and O'Brien, A. (1991). Induction of c-myc oncoprotein and of cellular proliferation by radiation in normal human urothelial cultures. *Anticancer Res*. 11, 1609–1612

Murphy, C., K., Kolan, K. C. R., Long, M., Li, W., Leu, M. C., Semon J. A., et al. (2016). "3D printing of a polymer bioactive glass composite for bone repair," in *Proceedings of the 27th Annual International Solid Freeform Fabrication Symposium* (Austin, TX), 1718–1731.

Nanaki, S., Barmpalexis, P., Iatrou, A., Christodoulou, E., Kostoglou, M., and Bikiaris, D. N. (2018). Risperidone controlled release microspheres based on poly(lactic acid)-poly(propylene adipate) novel polymer blends appropriate for long acting injectable formulations. *Pharmaceutics* 10, 1–21. doi: 10.3390/pharmaceutics10030130

Nauth, A., Schemitsch, E., Norris, B., Nollin, Z., and Watson, J. T. (2018). Critical-size bone defects: is there a consensus for diagnosis and treatment? *J. Orthop. Trauma*. 32, 7–11. doi: 10.1097/BOT.0000000000001115

Oftadeh, R., Perez-Viloria, M., Villa-Camacho, J. C., Vaziri, A., and Nazarian, A. (2014). Biomechanics and mechanobiology of trabecular bone: a review. *J. Biomech. Eng*. 137, 1–15. doi: 10.1115/1.4029176

Palmer, W., Crawford-Sykes, A., and Rose, R. (2008). Donor site morbidity following iliac crest bone graft. *West Indian Med. J*. 57, 490–492.

Pan, H., Xia, Y., Qin, M., Cao, Y., and Wang, W. (2015). A simple procedure to improve the surface passivation for single molecule fluorescence studies. *Phys. Biol*. 12:45006. doi: 10.1088/1478-3975/12/4/045006

Porter, J. R., Ruckh, T. T., and Popat, K. C. (2009). Bone tissue engineering: A review in bone biomimetics and drug delivery strategies. *Biotechnol. Prog*. 25, 1539–1560. doi: 10.1002/btpr.246

Rehman, I., and Bonfield, W. (1997). Characterization of hydroxyapatite and carbonated apatite by photo acoustic FTIR spectroscopy. *J. Mater. Sci. Mater. Med*. 8, 1–4. doi: 10.1023/A:1018570213546

Rho, J. Y., Ashman, R. B., and Turner, C. H. (1993). Young's modulus of trabecular and cortical bone material: ultrasonic and microtensile measurements. *J. Biomech*. 26, 111–119. doi: 10.1016/0021-9290(93)90042-D

Røhl, L., Larsen, E., Linde, F., Odgaard, A., and Jørgensen, J. (1991). Tensile and compressive properties of cancellous bone. *J. Biomech*. 24, 1143–1149. doi: 10.1016/0021-9290(91)90006-9

Rottensteiner, U., Sarker, B., Heusinger, D., Dafinova, D., Rath, S. N., Beier, J. P., et al. (2014). *In vitro* and *in vivo* biocompatibility of alginate dialdehyde/gelatin hydrogels with and without nanoscaled bioactive glass for bone tissue engineering applications. *Materials* 7, 1957–1974. doi: 10.3390/ma7031957

Rüdrich, U., Lasgorceix, M., Champion, E., Pascaud-Mathieu, P., Damia, C., Chartier, T., et al. (2019). Pre-osteoblast cell colonization of porous silicon substituted hydroxyapatite bioceramics: influence of microporosity and macropore design. *Mater. Sci. Eng. C* 97, 510–528. doi: 10.1016/j.msec.2018.12.046

Russias, J., Saiz, E., Deville, S., Gryn, K., Liu, G., Nalla, R. K., et al. (2007). Fabrication and *in vitro* characterization of three- dimensional organic/inorganic scaffolds by robocasting J. *Biomed. Mat. Res. Part A*. 83A, 443–445 doi: 10.1002/jbm.a.31237

Salgado, A. J., Coutinho, O. P., and Reis, R. L. (2004). Bone tissue engineering: state of the art and future trends. *Macromol. Biosci.* 4, 743–765. doi: 10.1002/mabi.200400026

Schemitsch, E. H. (2017). Size matters: defining critical in bone defect size! *J. Orthop. Trauma*. 31, 20–22 doi: 10.1097/BOT.0000000000000978

Serra, T., Planell, J. A., and Navarro, M. (2013). High-resolution PLA-based composite scaffolds via 3-D printing technology. *Acta Biomater*. 9, 5521–5530. doi: 10.1016/j.actbio.2012.10.041

Shahabi, S., Najafi, F., Majdabadi, A., Hooshmand, T., Haghbin Nazarpak, M., Karimi, B., et al. (2014). Effect of gamma irradiation on structural and biological properties of a PLGA-PEG-hydroxyapatite composite. *Sci. World J*. 2014:420616. doi: 10.1155/2014/420616

Simon, J. L., Michna, S., Lewis, J. A., Rekow, E. D., Thompson, V. P., Smay, J. E., et al. (2006). *In vivo* bone response to 3D periodic hydroxyapatite scaffolds assembled by direct ink writing. *J. Biomed. Mater. Res. Part A*. 83A, 28–31. doi: 10.1002/jbm.a.31329

Storti, G., Scioli, M. G., Kim, B. S., Orlandi, A., Cervelli, V., and De Francesco, F. (2019). Adipose-derived stem cells in bone tissue engineering: useful tools with new applications. *Stem Cells Int*. 2019:3673857. doi: 10.1155/2019/3673857

Takemoto, S., Kusudo, Y., Tsuru, K., Hayakawa, S., Osaka, A., and Takashima, S. (2004). Selective protein adsorption and blood compatibility of hydroxy-carbonate apatites. *J. Biomed. Mater. Res. Part A*. 69, 544–551. doi: 10.1002/jbm.a.30039

Tappa, K., and Jammalamadaka, U. (2018). Novel biomaterials used in medical 3D printing techniques. *J. Funct. Biomater*. 9, 1–16. doi: 10.3390/jfb9010017

Vishnubalaji, R., Al-Nbaheen, M., Kadalmani, B., Aldahmash, A., and Ramesh, T. (2012). Comparative investigation of the differentiation capability of bone-marrow- and adipose-derived mesenchymal stem cells by qualitative and quantitative analysis. *Cell Tissue Res*. 347, 419–427. doi: 10.1007/s00441-011-1306-3

Wu, D., Spanou, A., Diez-Escudero, A., and Persson, C. (2020). 3D-printed PLA/HA composite structures as synthetic trabecular bone: A feasibility study using fused deposition modelling. *J. Mech. Behav. Biomed. Mater*. 103:103608. doi: 10.1016/j.jmbbm.2019.103608

Xynos, I. D., Hukkanen, M. V. J., Batten, J. J., Buttery, L. D., Hench, L. L., and Polak, J. M. (2000). Bioglass ®45S5 stimulates osteoblast turnover and enhances bone formation *in vitro*: Implications and applications for bone tissue engineering. *Calcif. Tissue Int*. 67, 321–329. doi: 10.1007/s002230001134

Yang, J., Bei, J., and Wang, S. (2002). Enhanced cell affinity of poly (D,L-lactide) by combining plasma treatment with collagen anchorage, *Biomaterials* 23, 2607–2614. doi: 10.1016/S0142-9612(01)00400-8

Yang, S., Guo, S., Tong, S., and Sun, X. (2019). Promoting osteogenic differentiation of human adipose-derived stem cells by altering the expression of exosomal miRNA. *Stem Cells Int*. 2019:1351860. doi: 10.1155/2019/1351860

Yoshida, Y., Matsubara, H., Fang, X., Hayashi, K., Nomura, I., Ugaji, S., et al. (2019). Adipose-derived stem cell sheets accelerate bone healing in rat femoral defects. *PLoS ONE* 14:214488. doi: 10.1371/journal.pone.0214488

Yuniarto, K., Purwanto, Y. A., Purwanto, S., Welt, B. A., Purwadaria, H. K., and Sunarti, T. C. (2016). Infrared and Raman studies on polylactide acid and polyethylene glycol-400 blend. *AIP Conf. Proc*. 1725:020101. doi: 10.1063/1.4945555

Zang, X., He, L., Zhao, L., He, Y., Xiao, E., and Zhang, Y. (2019). Adipose-derived stem cells prevent the onset of bisphosphonate-related osteonecrosis of the jaw through transforming growth factor β-1-mediated gingival wound healing. *Stem Cell Res. Ther*. 10, 1–13. doi: 10.1186/s13287-019-1277-y

Zhang, X., Guo, J., Wu, G., and Zhou, Y. (2015). Effects of heterodimeric bone morphogenetic protein-2/7 on osteogenesis of human adipose-derived stem cells. *Cell Prolif.* 48, 650–660. doi: 10.1111/cpr.12218

Conflict of Interest: The authors declare that the research was conducted in the absence of any commercial or financial relationships that could be construed as a potential conflict of interest.

frontiers
in Bioengineering and Biotechnology

ORIGINAL RESEARCH
published: 24 July 2020
doi: 10.3389/fbioe.2020.00793

Melt Electrowriting of Complex 3D Anatomically Relevant Scaffolds

Navid T. Saidy[1,2], Tara Shabab[1], Onur Bas[1,3], Diana M. Rojas-González[4], Matthias Menne[5], Tim Henry[1], Dietmar W. Hutmacher[1,3,6], Petra Mela[4,7]*† and Elena M. De-Juan-Pardo[1,8,9]*†

[1] Centre in Regenerative Medicine, Institute of Health and Biomedical Innovation (IHBI), Queensland University of Technology (QUT), Kelvin Grove, QLD, Australia, [2] School of Dentistry, The University of Queensland, Herston, QLD, Australia, [3] ARC ITTC in Additive Biomanufacturing, Queensland University of Technology, Musk Avenue, Brisbane, QLD, Australia, [4] Medical Materials and Implants, Department of Mechanical Engineering, Technical University of Munich, Garching, Germany, [5] Department of Cardiovascular Engineering, Institute of Applied Medical Engineering, Helmholtz Institute, Medical Faculty, RWTH Aachen University, Aachen, Germany, [6] Institute for Advanced Study, Technical University of Munich, Garching, Germany, [7] Department of Biohybrid and Medical Textiles (BioTex), AME-Institute of Applied Medical Engineering, Helmholtz Institute, RWTH Aachen University, Aachen, Germany, [8] Translational 3d Printing Laboratory for Advanced Tissue Engineering (T3mPLATE), Harry Perkins Institute of Medical Research, QEII Medical Centre, Nedlands and Centre for Medical Research, The University of Western Australia, Perth, WA, Australia, [9] Department of Mechanical Engineering, School of Engineering, The University of Western Australia, Perth, WA, Australia

OPEN ACCESS

Edited by:
Luciano Vidal,
Institut National de la Santé et de la Recherche Médicale (INSERM), France

Reviewed by:
Antonio D'Amore,
University of Pittsburgh, United States
Lesley W. Chow,
Lehigh University, United States

****Correspondence:***
Petra Mela
petra.mela@tum.de
Elena M. De-Juan-Pardo
elena.juanpardo@uwa.edu.au

† These authors have contributed equally to this work

Specialty section:
This article was submitted to Biomaterials, a section of the journal Frontiers in Bioengineering and Biotechnology

Received: *10 April 2020*
Accepted: *22 June 2020*
Published: *24 July 2020*

Citation:
Saidy NT, Shabab T, Bas O, Rojas-González DM, Menne M, Henry T, Hutmacher DW, Mela P and De-Juan-Pardo EM (2020) Melt Electrowriting of Complex 3D Anatomically Relevant Scaffolds. Front. Bioeng. Biotechnol. 8:793. doi: 10.3389/fbioe.2020.00793

The manufacture of fibrous scaffolds with tailored micrometric features and anatomically relevant three-dimensional (3D) geometries for soft tissue engineering applications remains a great challenge. Melt electrowriting (MEW) is an advanced additive manufacturing technique capable of depositing predefined micrometric fibers. However, it has been so far inherently limited to simple planar and tubular scaffold geometries because of the need to avoid polymer jet instabilities. In this work, we surmount the technical boundaries of MEW to enable the manufacture of complex fibrous scaffolds with simultaneous controlled micrometric and patient-specific anatomic features. As an example of complex geometry, aortic root scaffolds featuring the sinuses of Valsalva were realized. By modeling the electric field strength associated with the MEW process for these constructs, we found that the combination of a conductive core mandrel with a non-conductive 3D printed model reproducing the complex geometry minimized the variability of the electric field thus enabling the accurate deposition of fibers. We validated these findings experimentally and leveraged the micrometric resolution of MEW to fabricate unprecedented fibrous aortic root scaffolds with anatomically relevant shapes and biomimetic microstructures and mechanical properties. Furthermore, we demonstrated the fabrication of patient-specific aortic root constructs from the 3D reconstruction of computed tomography clinical data.

Keywords: melt electrowriting, 3D printing, biomimetic, fused deposition modeling, personalized scaffolds

INTRODUCTION

Tissue engineering (TE) aims to develop methods of regenerating damaged tissues by combining cells and highly porous scaffolds to create biological substitutes that are capable of growth, remodeling and repair. Scaffolds aim to provide the 3D macro-geometry and micro-environment to guide cellular behavior toward the formation of a tissue, biologically and mechanically equivalent to the healthy native one (Hutmacher, 2001; O'Brien, 2011). To this end, the recapitulation of the fibrous nature of the ECM and the fiber architecture/alignment is crucial to achieve functional tissues (Ma, 2010). A number of techniques to fabricate fibrous scaffolds have been proposed for the bioengineering of soft tissues (Patterson et al., 2010; Capulli et al., 2016). However, the realization of a scaffold with controlled multiphasic microarchitecture and mechanical properties, and with anatomically relevant geometry and dimensions is still a challenge in biofabrication. Among the techniques to create fibrous scaffolds, melt electrowriting (MEW) has shown great potential because of its unique capability to deposit micron-sized fibers with ordered and pre-defined architectures. This advanced 3D printing technology combines principles of electrospinning and additive manufacturing (Brown et al., 2011; Muerza-Cascante et al., 2015; Bas et al., 2017; Wunner et al., 2017). In a typical MEW system, a molten polymer is extruded through a spinneret connected to a high voltage supply and deposited at the grounded collector, which is moving according to a predefined pattern. The net force between the surface tension and the attraction of the electrostatically charged droplet to the collector stabilizes the fluid column and prevents the jet from undergoing Raleigh Plateau instabilities (Stachewicz et al., 2017). The electric field plays a major role in MEW and governs important properties such as flight path of the polymeric jet and fiber diameter (Reneker et al., 2000). Once the printing conditions are established and maintained after an initial tuning phase, a robust printing process is achieved, however, changes in the electric field result in the breakage of the fluid column and accumulation of polymer at the spinneret with the consequent lack of control over fiber deposition. This determines the inability of MEW to print on complex 3D topographies that create continuous variations in the spinneret-to-collector distance. Thus, so far, melt electrowritten scaffolds have been exclusively fabricated on flat or cylindrical collectors, significantly restricting the potential of this technique for advanced tissue engineering and regenerative medicine applications.

The aim of this study was to overcome the technical boundaries of MEW in order to enable the manufacture of complex, anatomically relevant 3D fibrous scaffolds with tailored micrometric features for soft tissue engineering. Because of our interest in the cardiovascular field, we chose as an exemplary geometry the aortic root, as it features not only the irregular geometry of the sinuses of Valsalva (SV) but also a complex multiphasic histoarchitecture, including a unique tri-layered structure with a distinct collagen fiber distribution (Underwood, 2002; Tsamis et al., 2013). The aortic SV function as a supplementary component to the valve leaflets, by expanding a ring of flow vortices generated during systole, and promoting abrupt closure of leaflets (Toninato et al., 2016). Patients suffering from aortic root aneurysm or other valvular diseases present poor prognosis unless they receive root substitutes (Arabkhani et al., 2015). Inclusion and reconstruction of SV have been found instrumental in obtaining physiologically relevant structure-function relationship (Salica et al., 2016). Despite the long-recognized role of SV evident since the early 1990s (Robicsek, 1991), conventional aortic root replacements such as Dacron tubes do not include this important component leading to frequent long-term life-endangering complications (Robicsek and Thubrikar, 1999; De Paulis et al., 2001, 2002; Pisani et al., 2013). In addition, SV have been considered in very few tissue engineered heart valves where fine tuning fiber architecture and multiphasic properties across these constructs have been challenging (Lieshout et al., 2006; Nakayama et al., 2015; Capulli et al., 2017). Aortic root substitutes would ideally include not only the complex geometry of the SV but also their heterogeneous mechanical properties. However, the fabrication of such complex substitutes remains at best partial using current manufacturing techniques and requires further efforts toward root wall engineering to match the exquisite root properties (Butcher, 2018).

Here, we demonstrate that a two-component collector consisting of electrically conducting and non- conducting materials minimizes the electric field variations when printing a complex 3D geometry, thus allowing continuous controlled fiber deposition. Specifically, a metallic core enables the generation of the electric field, while a non-conductive polymeric shell reproduces the desired scaffold geometry without introducing variations in the electric field, which would otherwise result in jet instabilities. This solution does not require any modifications of existing set-ups and takes full advantage of the availability and versatility of 3D printing to realize any desired volumetric feature. We show that, by following this approach, we were able to produce real-size aortic roots with controlled fiber placement by MEW. We also demonstrate the capability to fabricate biomimetic tri-layered scaffolds mimicking the histoarchitecture and collagen fiber distribution of native aortic root and the potential of this technique for personalization and scalability.

MATERIALS AND METHODS

Design of Aortic Root Model

The aortic root model design was guided by idealized dimensions suggested by Thubrikar (1990) whereby setting the basis for the computer aided (CAD) design of the aortic root 3D model. In Solidworks (Dassault Systèmes, Vélizy-Villacoublay, France), the model was designed comprising a 25 mm cylinder representing the aortic wall, with the addition of three sinus structures with dimensions listed in **Supplementary Figure S1**. A two-part model was developed representing the ascending aorta and sinuses (1) and left ventricular side (2) to allow for easy removal of the scaffold from the mandrel (**Supplementary Figure S1**). The aortic root model was scaled down to 20, 15, and 10 mm to fabricate models over a range of relevant anatomies, highlighting the scalability of this fabrication platform.

Electric Field Simulation

The *in silico* electric field model was simulated in COSMOL Multiphysics software (version 5.3, COSMOL Inc., United States). The MEW setup was 3D modeled in Solidworks (Dassault Systèmes, Vélizy-Villacoublay, France) and imported to COSMOL along with the aortic root model. The electrical conductivity of the materials was defined according to the physical properties of materials established in the COSMOL Metaphysics (Aluminum mandrel: 3.774e7 [S/m], Titanium: 7.407e5 [S/m], Air: 5e-15 [S/m]) while the dielectric constant of 3D printed PLA was taken from previously published papers (die-electric constant:3.471) (Huber et al., 2016). The electric field strength (EFS) during the MEW process was modeled by defining the spinneret position at a collector distance of 10 mm from the wall for 10 kV, where voltage was kept constant for both mandrel models.

3D Printing of the PLA Aortic Root Model

The aortic root mold was fabricated via fused deposition modeling (FDM, WomBot, Keysborough, Australia) using polylactic acid (PLA, Bilby 3D, Australia) heated to 210–230°C. STL files of the aortic root model were imported into 3D Central (Simplified 3D, United States) to generate g-code with 0% infill, 6 perimeters, 0.2 mm layer height, 1200 mm/min. Following printing, the 3D printed models were smoothed using fine (320 grade) sand paper (Duramax, Australia) to minimize the surface roughness that could potentially damage the scaffolds. In the case of the patient-specific aortic root model, DICOM imaging slices collected from the CT scan of the patient's aorta (Office of Research Ethics and Integrity of the Queensland University of Technology, approval number QUT1900000599) were converted to a STL file using InVesalius software (Center for Information Technology Renato Archer, São Paulo, Brazil) for further processing. STL files were then smoothen and transformed into a straight configuration using Netfabb software (Autodesk, California, United States) to allow for the integration of the Al mandrel. This finalized model was used for 3D printing the personalized scaffold using MEW. Lastly the Titanium aortic root model was manufactured.

Scaffold Fabrication

Custom-made MEW Al-Ti and Al-PLA collectors were used to fabricate MEW scaffolds replicating the macroscopic geometry of aortic root including the sinuses of Valsalva. In this process, medical grade PCL pellets (Purasorb® PC 12, Purac Biomaterials, Netherlands) are heated at 80 (syringe) and 92°C (spinneret) in a plastic syringe. 2.0 bar air pressure pushes the molten polymer through a 23 G needle where high voltage drags the fiber down onto a rotating mandrel collector while translating the mandrel along its axis. The spinneret was kept at 10, 12 mm for Al-Ti and 10 mm for Al-PLA from the walls, positioning it at 7.5 mm from the highest point of the sinuses. The voltage was set at 6, 8, and 10 kV for the Al-Ti model and 10 kV for the Al-PLA model while other MEW parameters were kept constant. All scaffold groups were fabricated for 7500 cycles of collector translation moving at 1000 mm/min keeping the fiber collection time constant regardless of the scaffold architecture. Scaffolds were sprayed with Ethanol 70% and slipped of the two-part PLA model specifically designed to ease removal of the scaffolds.

Morphological Characterization

In-process MEW images were acquired using a handheld digital microscope (AM7115MZTL, Dino-Lite, Taiwan) and a handheld video camera recorder (HDR-PJ410, Sony, Tokyo, Japan) to monitor the MEW process when printing on the different mandrel models. Following printing and removal of scaffolds from the 3D printed model, macroscopic images were acquired with a microscope camera to illustrate the scaffold conformity to the model (Nikon DS-Fi2, Japan). For scanning electron microscopy (SEM), sections of aortic root scaffolds were taken from the walls and sinuses ($n = 3$) using an 8 mm biopsy punch (Kai medical, Australia) and mounted onto SEM stubs for gold sputter coating for 90 s. SEM images were taken from the inside of the scaffolds to ensure that potential roughness caused by the surface of the PLA mold could be detected. SEM images were acquired using a Mira3 SEM (TESCAN, Brno, Czechia) with 5 kV beam voltage, 200× magnification, 10.53 mm working distance. Fiber diameters were measured using SEM images using ImageJ and reported as average ± standard deviation for a total of $n = 81$ measurement points. Fiber diameter measurement was carried out for three independent complete scaffolds cut into three pieces (each containing a sinus) for each of three winding angle configurations. Nine measurements were taken from the wall and sinuses of each scaffold separately, to ensure fiber diameter consistency across every sample and different prints.

Fibrin Preparation and Polymerization

Fibrinogen was prepared as described previously (Moreira et al., 2016). In short, dissolved lyophilized fibrinogen (Calbiochem) was dialyzed against tris-buffered saline (TBS; pH 7.4) for 12 h utilizing a 6000–8000 molecular weight cut-off membrane (Novodirect). The obtained fibrinogen solution was sterilized by filtration (0.2 μm pore size, Corning®), and the concentration was defined by measuring the absorbance at 280 nm using an Infinite M200 spectrophotometer (Tecan Group Ltd.). The fibrin gel components of MEW/fibrin composite (5.0 mL in total) consisted of 2.5 mL fibrinogen solution (10 mg/mL), and the fibrin polymerization starting solution composed of 1.75 mL TBS, 0.375 mL 50 mM CaCl-2 (Sigma) in TBS, and 0.375 mL 40 U/mL thrombin (Sigma). The components were introduced into a 3D printed (Objet Eden350) square shaped mold of 225 mm^2 to composite the scaffolds for burst strength tests.

Burst Strength Test

Burst strength of the MEW fibrin composite scaffolds was obtained using a custom-made device equipped with a pressure gauge (Jumo Midas pressure transmitter, JUMO GmbH & Co. KG) and peristaltic pump (IPC Ismatic, IDEX Heath & Science GmbH), reported elsewhere (Moreira et al., 2016). Squared samples from the aortic wall and sinuses with 1.5 cm^2 area were mounted into the measuring device. Phosphate buffered saline (PSB) was pumped into the device with increasing pressure until structural failure occurred and the maximum pressure was measured. Burst strength samples were obtained either from the center of the sinuses or from the top of the root wall, and not on the overall scaffold.

Suture Retention Test

To assess the suture retention strength, MEW fibrin composite scaffolds ($n = 3$) were tested using an Instron tensile tester with a 100 N load cell (Zwick Roell, Ulm, Germany) according to ISO 7198. Samples were mounted into a pneumatic clamp and 4-0 suture line was threaded through the sample at a depth of 3 mm below the proximal surface of the aortic root wall and clamped. The suture line was then stretched until the sample was torn indicating failure where the maximum load was recorded as the suture retention strength.

Cell Seeding

Umbilical cords were kindly provided by the Department of Gynecology at the University Hospital Aachen in accordance with the human subjects' approval of the ethics committee (EK 2067). Human umbilical vein smooth muscle cells (HUVSMCs) were isolated by stripping out the umbilical cord vein, removing the remaining adherent connective tissue, cutting 1 mm tissue rings, and placing them in cell culture flasks. Outgrowth of HUVSMCs from the tissue rings onto the tissue culture plastic (TCP) was observed after 1 to 2 weeks. HUVSMCs were cultured in Dulbecco's modified Eagle medium (DMEM; Gibco) supplemented with 10% fetal calf serum (FCS; Gibco) in 5% CO2 and 95% humidity at 37°C up to a confluence of 80% to 90% and subsequently passaged. Cells in passage four were used for the seeding experiments.

Small pieces (1 cm × 1 cm) of MEW scaffolds from 60 degrees and tri-layered groups were cut from the scaffold root wall and used for the cell seeding experiments. MEW scaffolds were sterilized by dipping in 70% ethanol followed by evaporation inside the biosafety cabinet. After being completely dried, the scaffolds were washed with PBS and clamped into 48-well plate inserts (CellCrown, Scaffdex). HUVSMCs were enzymatically detached from the TCP by 0.25% trypsin/0.02% ethylenediaminetetraacetic acid (EDTA) solution (Gibco), collected in a conical tube (Sarstedt) and counted using a Neubauer chamber. Cells were centrifuged at 500 × *g* for 5 min and resuspended in cell culture medium at a concentration of 10 million cells per mL medium. The inserts were placed inside a 24-well plate (VWR international, Pennsylvania, United States) in a standing position with the scaffold facing upward. A direct seeding was performed by slowly pipetting 100 μL of cell suspension onto the surface of the MEW scaffolds. The constructs were incubated for 2 h at 37°C, 5% CO_2 and 95% humidity. After this, the cell crowns were laid onto their side and medium was added to the wells until the seeded surface was completely covered. The culture was maintained for 72 h.

Immunohistochemistry

To perform immunohistochemical analysis of the cell-seeded scaffolds, samples were fixed in methanol-free 4% PFA in PBS for 1 h at room temperature and washed with PBS afterward. Cell membranes were permeabilized using 0.1% Triton-PBS for 1 h at room temperature. Samples were incubated with 100 nM working solution of fluorescent phalloidin (Acti-stain^{TM} 488; Cytoskeleton, Inc.) for 1 h at 37°C, this was followed by a washing step with PBS and a nuclei counterstaining with DAPI (Molecular Probes). The stained samples were visualized using a Two photon laser scanning microscopy (TPLSM) setup consisting of an Olympus FluoView 1000MPE with a 25× water objective (NA 1.05, Olympus, Tokyo, Japan), a mode-locked MaiTai DeepSee Titanium-Sapphire Laser (Spectra-Physics, Stahnsdorf, Germany), and the FluoView FV10 4.2 acquisition software.

Micro-Computed Tomography

Disk shaped samples with 8mm diameter were biopsy punched from wall and sinuses of all scaffold groups and transferred into 9 mm μCT tubes. Microtomography (microCT) was carried out to provide information on the scaffold 3D morphology (microCT50, Scanco Medical, Bruettisellen, Switzerland – 9 mm tube, 3 μm voxel size, 45 kV, 200 μA). The lower threshold was set at 50 and the upper threshold was set at 1000 to isolate the PCL scaffold from the background for the evaluation of different morphological parameters. Scaffold fiber volume was evaluated by microCT software (Scanco Medical, Bruettisellen, Switzerland). Scaffold thickness was measured for every sample by first converting the CT scan files to DICOM format and calculating the number of stacked layers at five points of every selected sample using the free software package distribution Fiji, based on ImageJ v1.52c (National Institute of Health, United States). Accordingly, multiplying the number stacked layers and the voxel size of the micro CT machine (3 μm) determined the overall scaffold thickness. Finally, scaffold porosity was calculated from the scaffold fiber volume and true overall volume of an 8 mm disc, to ensure that the variability of thickness for every sample is considered.

Statistics

In order to compare the fiber diameter and winding angle, $n = 81$ points of measurement were taken from wall and sinuses from $n = 3$ scaffolds for every scaffold architecture and a one−way ANOVA test followed by a Tukey multiple comparison test was utilized to assess statistical significance (GraphPad, Prism 7). The asterisks above every candlestick column illustrate statistical significance with respect to all other columns, unless specified otherwise. Burst strength of scaffolds with both single layer and tri-layered architecture scaffolds were reported as mean ± standard deviation for $n = 3$ samples representing the wall and sinuses where one−way ANOVA test followed by Sidak's multiple comparison test was performed to control the familywise error rate. In addition, an unpaired *t*-test was performed for investigating the burst strength difference between wall and sinuses of the tri-layered scaffolds and the suture retention strength difference between 60° and tri-layered scaffolds. Lastly, fiber volume, thickness and porosity for every scaffold group was calculated $n = 3$ where these values are reported as mean ± standard deviation. A one−way ANOVA with Sidak's multiple comparison *post hoc* component was also used to test the statistical significance of this set of data. Values of $p < 0.05$ were considered significant. The level of significance was indicated with asterisks as follows: ($p < 0.0001$****, $0.0001 < p < 0.001$***, $0.001 < p < 0.01$**, $0.01 < p < 0.05$*.

RESULTS AND DISCUSSION

Fabrication of Anatomically Relevant Aortic Root Scaffolds

To maintain a stable polymer jet and, consequently, a reproducible printing process during MEW, it is essential to preserve a constant electric field (Wunner et al., 2018). Fast changes of working distance associated with 3D geometry of metallic collectors would cause electric field variabilities and consequent breakage of the fluid column, introducing printing defects. Here we hypothesized that a stable jet could be achieved by using a hybrid collector instead of a conventionally employed metallic one, as schematically shown in **Figures 1A,B**. Specifically, a conductive cylindrical Al mandrel would enable the formation of a constant electric field while a coaxial non-conductive PLA mold would collect the fibers into the desired macroscopic scaffold geometry without causing significant field variations (Al-PLA), thus avoiding the disruption of the printing process. Initially, computational simulations of the electric field strength (EFS) associated with the Al-PLA collector were performed. For comparison, two additional combinations of mandrel-mold collectors were also examined: Al mandrel combined with a coaxial conductive Ti mold (Al-Ti, fully conductive), and Al mandrel only (Al-only) (**Figures 1A,B**). The aortic root geometry was obtained by 3D printing based on literature as explained in **Supplementary Figure S1** (Thubrikar, 1990). Within a complete printing cycle, only small changes in the EFS associated to the translational (**Figure 1C**, left column) and rotational (**Figure 1C**, right column) movements were predicted for the Al-PLA collector (**Figure 1D**, Al-PLA) (**Supplementary Video 1** and **Supplementary Video 2**). This was in strong contrast with the EFS heterogeneities anticipated for the full metallic collector as shown in **Figure 1D**, Al-Ti and **Supplementary Videos 3, 4**. Quantitative assessment of EFS using this *in silico* model predicts a 45% rise in EFS as the spinneret moves toward the sinuses of the fully conductive collector (Al-Ti) during both translation and rotational movement, whereas this increase was not observed for the Al-PLA model (**Figure 1E**). Given the dielectric breakdown strength of air (3×10^6 V/m) and the humidity conditions (30–40%), we speculated that this significant increase in EFS could result in dielectric breakdown when printing on the Al-Ti mandrel. The Al cylindrical mandrel was modeled as a control group, which resulted in a stable field, confirming the capability of MEW to print plain cylindrical scaffolds.

Next, we fabricated aortic root scaffolds via MEW using collectors with the same geometry and materials as the ones used in the EFS model. The core conductive Al mandrel was fabricated by classical machining, whereas the molds featuring the SV were 3D printed in PLA and Ti. Once assembled, the double component collectors were easily coupled to the motorized stage without requiring any modifications of the existing set-up. The stability of the MEW process was first assessed by visual inspection of the jet and of the resulting printed samples, and subsequently further evaluated at the micrometric scale by scanning electron microscopy (SEM).

MEW performed on the Al-Ti collector resulted in unstable printing conditions, which were in agreement with the field inhomogeneity predicted by the simulations. In particular, for the 10 mm spinneret-to-collector distance, voltages equal or greater than 8 kV were sufficient to cause dielectric breakdown, confirming the prediction made using the *in silico* model of EFS (**Figure 2A** and **Supplementary Videos 5, 6**). A reduction of the voltage to 6 kV was enough to prevent the dielectric breakdown, but not to circumvent other undesirable events associated with unstable printing conditions, which were also detected at higher voltages and larger working distances (8 kV, 12 mm) (**Supplementary Videos 7, 8**). Specifically, accumulation of the polymer melt without the formation of a Taylor cone was observed at the spinneret when the applied voltage was too low (6 kV), and this caused a large mass of polymer melt to be dragged onto the collector, creating long beading defects (**Figures 2A,B**) (**Supplementary Video 9**) (Hochleitner et al., 2016). Printing at 12 mm collector-to-spinneret distance and 10 kV allowed to maintain a Taylor cone and a continuous flow jet without any visible dielectric breakdowns, permitting the fabrication of complete scaffolds (**Supplementary Video 10**) (Hochleitner et al., 2016). However, further analysis by SEM discovered substantial variability of the fiber diameters both on the wall and sinuses, which was a clear indication of fiber pulsing (**Figure 2**). Fiber pulsing is a common phenomenon that occurs as a result of imbalance of forces during MEW process, leading to inconsistencies in the extruded mass flow of polymer and consequently to inhomogeneous fiber diameters (Hochleitner et al., 2016). The occurrence of long bead defects and fiber pulsing renders the process uncontrollable and irreproducible.

In contrast, the Al-PLA collector facilitated the formation of a proper Taylor cone and regular fiber flight path resulting in a robust printing process at the same printing conditions that caused dielectric breakdown for the Al-Ti collector (optimal conditions found at 10 mm and 10 kV). In general, closer distances are sought in order to reach a better agreement between the programmed and the real fiber lay-down pattern. Snapshots of the fabrication process for both the Al-Ti and Al-PLA model were taken every 30 s to better capture the stability of the polymer jet when printing on the Al-PLA model (**Supplementary Figure S2**).

Previous studies had used a double-component collector in solution electrospinning for the manufacture of anatomically shaped heart valve scaffolds (D'Amore et al., 2018; Coyan et al., 2020). Contrarily to our concept and implementation, in these studies the collector surface was composed of two materials with different conductivity (as opposed to our conductive core and anatomically shaped non-conductive shell approach), to spatially control fiber deposition and avoid fiber accumulation in specific regions, which would affect the valve functionality.

Aortic root scaffolds were fabricated on the Al-PLA collector by keeping a constant translational speed of 1000 mm/min and

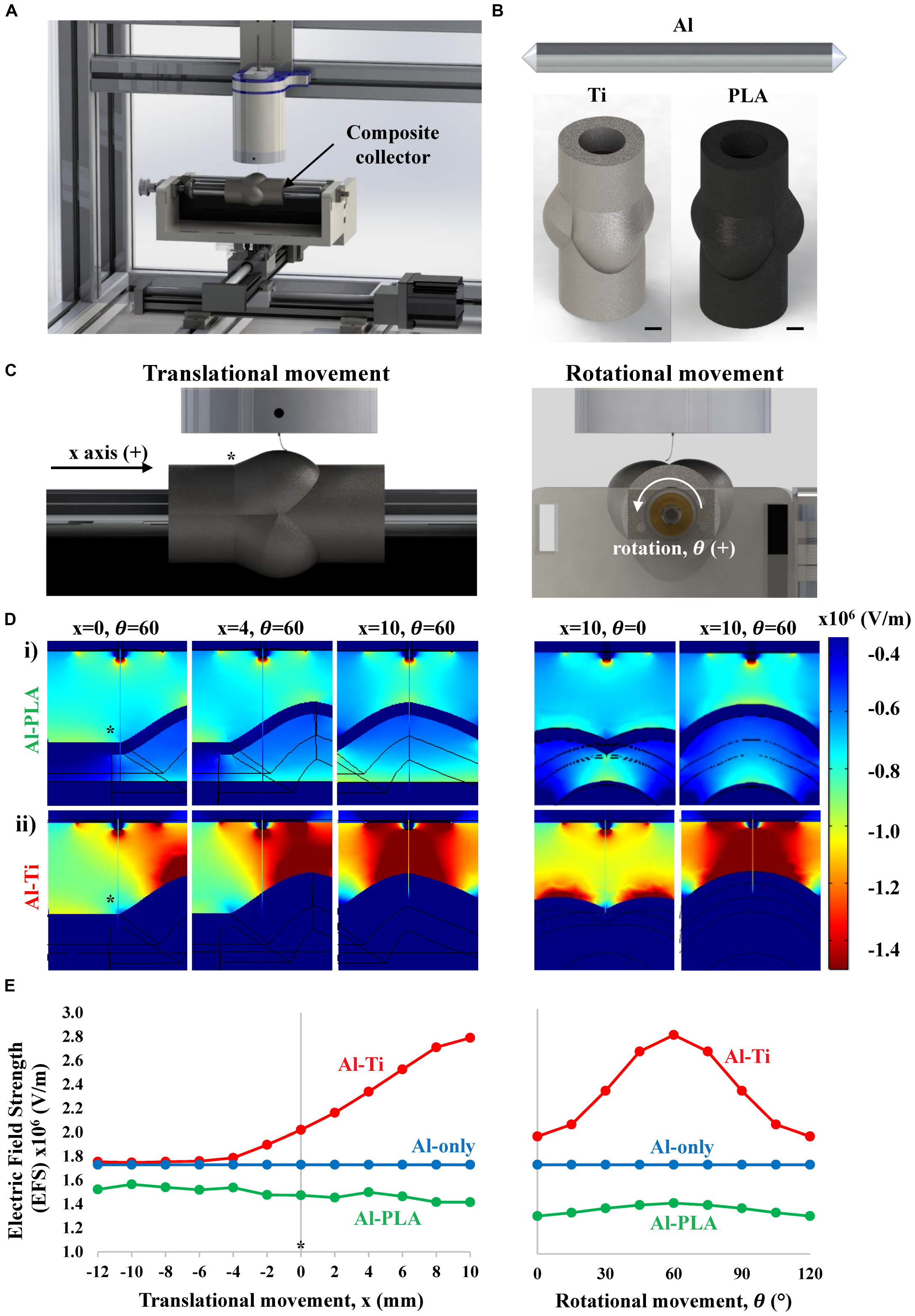

FIGURE 1 | Simulation of the electric field strength (EFS) (V/m) established between the spinneret and aortic root model during MEW. **(A)** Schematic representation of the mounted collector onto a standard MEW device. **(B)** Aluminum only (Al-only), Al-titanium (Al-Ti) and Al-polylactic acid (Al-PLA) mandrel models used for electric field simulation (scale bar = 5 mm). **(C)** Front (left) and side (right) plane views of the MEW setup used in this study, * indicates the point on the mandrel where *x* = 0 **(D)** Heat maps showing the EFS distribution when printing on i) Al-PLA and ii) Al-Ti collectors at different stages of the translational (left) and rotational (right) movements, **(E)** Quantitative EFS simulation results when printing on the different double component collectors: Al-Ti (red), Al-PLA (green) and Al-only (blue).

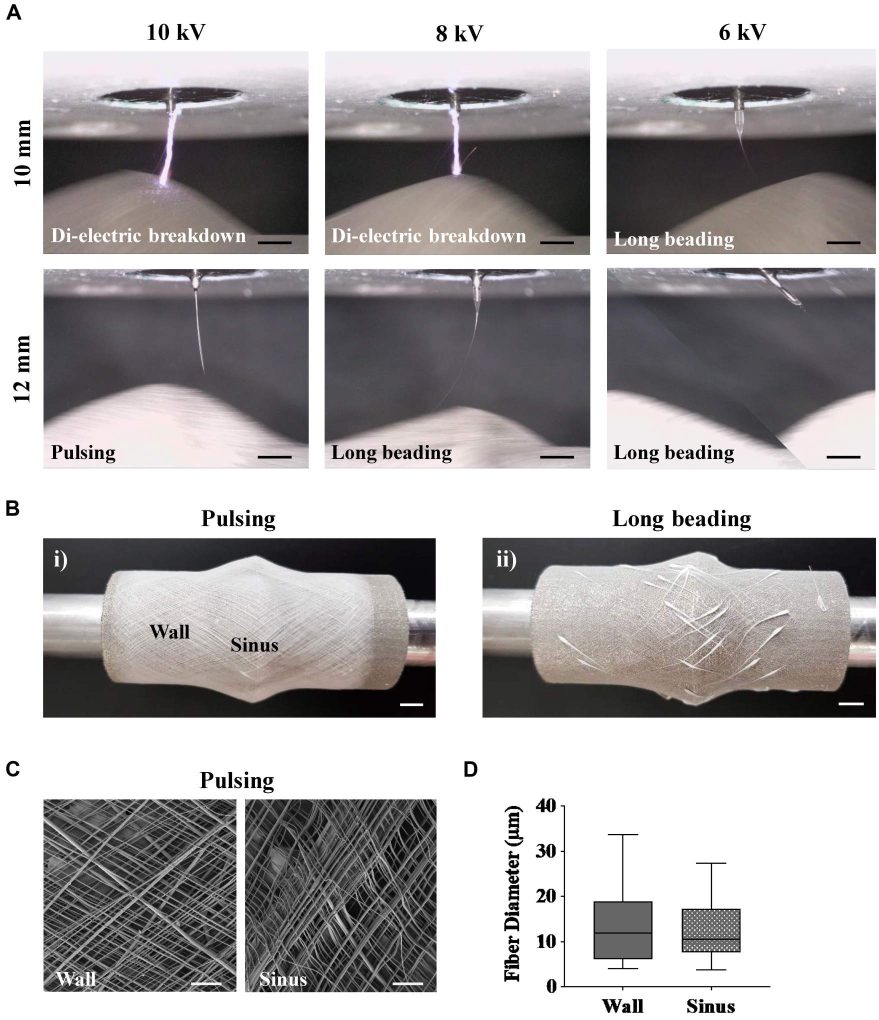

FIGURE 2 | MEW performed on the fully conductive Al-Ti. Taylor cone formation and fiber flight path were investigated as a function of collector-to-spinneret distance and applied voltage, while pressure, temperatures and speeds were kept constant. **(A)** Time lapse images of MEW process using an Al-Ti collector. **(B)** Representative images of scaffolds printed with (i) pulsing and (ii) long beading phenomena on the Al-Ti collector. **(C)** Representative SEM images of a scaffold successfully fabricated on the Al-Ti collector at 12 mm working distance and 10 kV. **(D)** Morphological analysis of scaffolds fabricated using the Al-Ti collector. (*n* = 3, *n* = 81 measurement points). (Scale bars: **(A,C)** = 2 mm; **(B)** = 5 mm).

varying the mandrel's rotational speed to obtain three different winding angles (Brown et al., 2012). All scaffolds conformed to the shape of the 3D printed PLA aortic root model (**Figure 3A**), with no apparent defects. We were able to obtain winding angles of 30, 45, and 60° on the scaffold wall, as estimated by analysis of SEM images (**Figures 3B,C**), by setting the rotational speed to 6.4, 11.0, and 19.1 rpm, respectively. For all scaffolds, fibers deposited on the sinuses presented higher winding angles than those deposited on the wall, which can be explained by the increased tangential speed as a result of the larger mandrel diameter at the SV. The direct relationship between tangential speed and winding angle observed in this experiment agrees with a study conducted by Jungst et al. (2015) on a simple non-complex mandrel.

Morphological analysis of these scaffolds by SEM revealed minimal variability of fiber diameters across the entire scaffold surface (**Figure 3D**) compared to those obtained with the Al-Ti collector (**Figure 2D**). A slight but significant reduction in fiber diameter caused by thinning of the polymer jet with increasing rotational speed (**Figure 3C**) was observed. Additionally, fibers were significantly thicker over the sinuses than on the wall, independent of the winding angle. This can be explained by the smaller thinning effect on the fibers associated to shorter spinneret-to-collector distances (**Figure 3C**). While regional heterogeneities in fiber diameter and winding angle can be beneficial for some applications, as we will next show for the aortic root scaffolds, these microarchitectural properties can be tuned and maintained by altering the rotational speed for applications that requires a homogeneous fiber structure, as shown in **Supplementary Figure S3**.

The burst strength of the scaffolds was measured to assess the effect of heterogeneous fiber diameters and winding angles across wall and sinuses on the mechanical properties. To this end, we

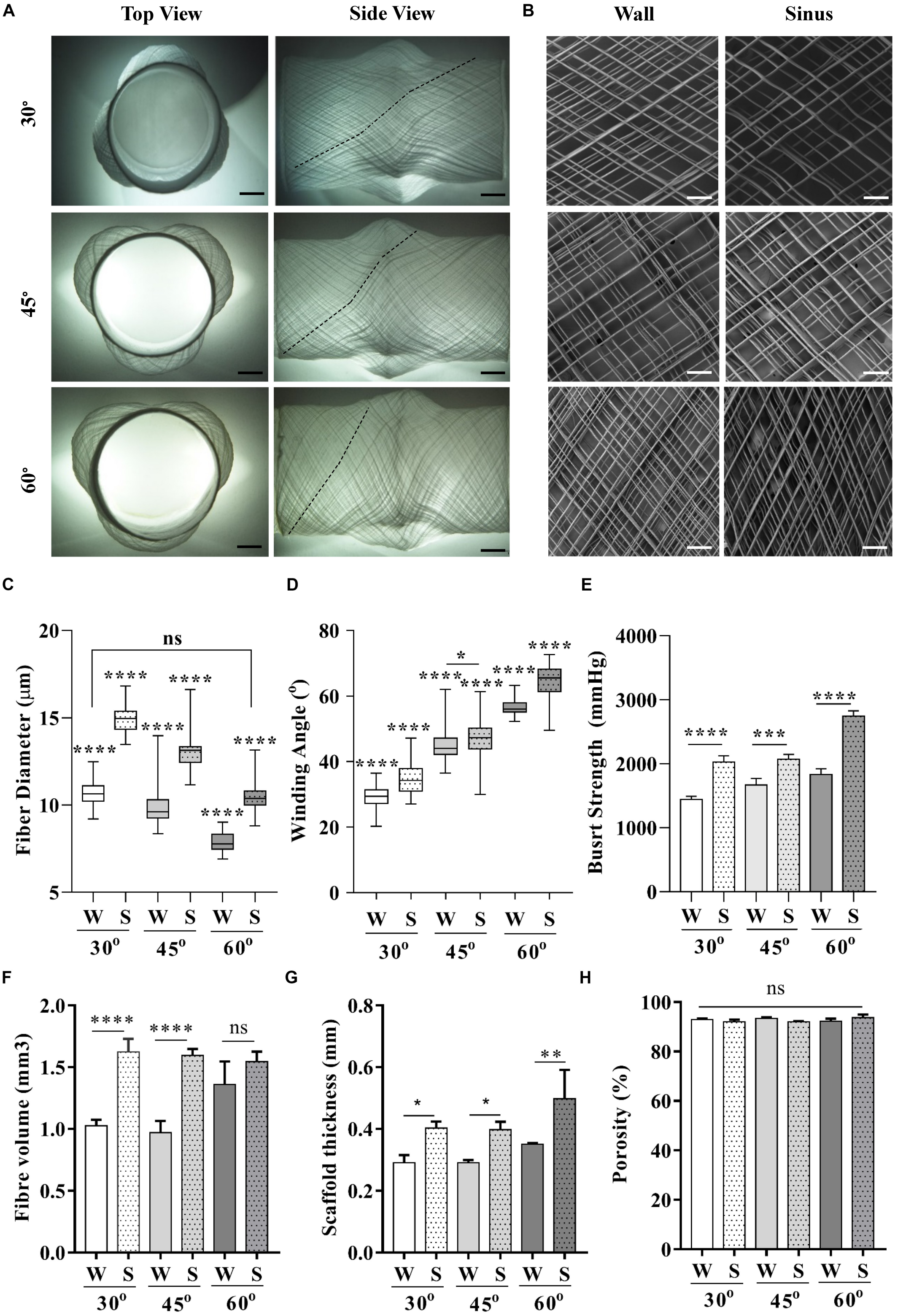

FIGURE 3 | Characterization of scaffolds printed at 30, 45, and 60° winding angle. **(A)** Macroscopic top and side view pictures of full scaffolds, **(B)** SEM images taken individually from the wall and sinuses. **(C)** Fiber diameter and **(D)** winding angle measurements on the wall and sinuses across all groups. **(E)** Burst strength of scaffolds with varying winding angles composited with fibrin hydrogel ($p < 0.05$ were considered significant). (Scale bars: **(A)** = 5 mm, **(B)** = 2 mm); (statistical analysis: **(C,D)** = One way ANOVA with Tukey multiple comparison; **(E–H)** = One way ANOVA with Sidak multiple comparison; $p < 0.0001$****, $0.0001 < p < 0.001$***, $0.001 < p < 0.01$**, $0.01 < p < 0.05$*).

composited the scaffolds with fibrin as an exemplary hydrogel. Fibrin is commonly used as cell carrier in tissue engineering applications, including cardiovascular ones (Jockenhoevel et al., 2001; Moreira et al., 2015, 2016; Toosi Saidy et al., 2019). Results showed a significant increase of burst strength on the sinuses compared to the walls for all scaffold groups (**Figure 3**). Although to the best of our knowledge, there are no data in the literature on the difference of burst strength between the wall and SV, higher tensile stiffness of SV (Azadani et al., 2012) suggests a higher burst strength according to a number of studies that correlate tensile stiffness to burst strength (Laterreur et al., 2014; Geelhoed et al., 2019). This is in agreement with our burst strength results presented for the wall and SV of MEW/fibrin scaffolds.

To further investigate the importance of other contributing factors such as fiber volume, sample thickness, and porosity toward this effect, we performed micro-computer tomography (μCT) analysis on 8 mm disk-shaped biopsies of both regions for all scaffold groups. Interestingly, μCT analysis revealed larger sample thickness and fiber volume over the sinuses across all samples. This could be explained based on the constant rotational speed and printing time kept for each of the scaffold groups, which caused higher fiber volume to be collected over the regions exposed to the fastest tangential speed, i.e., the sinuses. Enhanced fiber volume combined with increased fiber diameter over the sinuses directly contributed to larger sample thickness. The combination of increased sample thickness and fiber volume would suggest an increase of burst strength on the sinuses; however, the influence of larger fiber volumes over the sinuses superseded the contribution of fiber diameter to the overall thickness and total fiber volume collected. Intriguingly, there was no significant difference in terms of porosity among regions and scaffold groups (**Figure 3F**), which suggests that the fiber volume is the main contributing factor toward burst strength. These experiments confirmed the predicted *in silico* results suggesting that the quasi-uniform EFS distribution for the hybrid Al-PLA collector would be appropriate to achieve stable MEW printing conditions with controlled fiber deposition, thus validating the initial hypothesis.

There are other possible strategies that could be applied to keep the electric field constant during MEW of complex geometries. One of them would be to motorize the printer head and synchronize its vertical movement with the translation and rotation of the collector to keep the spinneret-to-collector distance constant. Altering the applied voltage during the printing process with a programmed module would be another approach to control the electric field during the course of MEW process. Recently, we demonstrated that the combination of both, a motorized print head and controlled incremental increase in applied voltage, safeguards a stable jet during the printing process of flat scaffolds, enabling to reach up to 7 mm scaffold thickness (Wunner et al., 2018). However, following a similar approach on a geometrical complex mandrel would require substantial additional programming and in-process control to adjust the voltage as the mandrel is rotating and translating. In addition, this requires fundamental understanding of electrostatic interactions and its influence on the forces imparted on the polymeric jet to predict the required voltage that retains these forces at different spinneret to collector distance, which is highly challenging. Another strategy would be to upgrade the MEW printer with the installation of a robotic arm to ensure a perpendicular and constant spinneret-to-collector distance. This approach, however, would require significant adjustments of both hardware and software to allow for the complex synchronization of the movements. Our proposed double component collector approach, on the contrary, presents a simple, cost-effective and robust method, which takes full advantage of the availability and versatility of 3D printing to realize any desired geometry.

Fabrication of Biomimetic Tri-Layered Aortic Root Scaffolds

Collagen fibers present a distinct and varying directionality within the tri-layered wall of native aortic roots (Schriefl et al., 2012). Given the influence of fiber arrangement and orientation on tissue mechanical properties, we manufactured tri-layered, anatomically relevant scaffolds mimicking the native collagen fiber orientation. Our design was guided by studies that have focused on microscopy and numerical modeling of collagen fibers in individual layers of the human coronary artery with fibers oriented at 50° in the intima, 65° in the media and 40° in the adventitia with respect to the central axis of the aorta (**Figure 4A**; Schriefl et al., 2012). The translational and rotational speeds were calculated accordingly to mimic these orientations in three superposed layers (**Supplementary Figure S3**) which were printed in a single print (**Figure 4B**). The morphological characterization of each individual layer by SEM confirmed the targeted winding angles (**Figure 4C**). While biomimetic design strategies based on the blueprint of the native tissue are highly desired, fabricating bioinspired multi-layered and multiphasic structures has been a major challenge due to the limitations associated with currently available fabrication technologies (Ma, 2010; Wang et al., 2016). Techniques such as solution electrospinning (Hasan et al., 2014; Liu et al., 2017; Akentjew et al., 2019) and jet spinning (Capulli et al., 2017) have been used to produce scaffolds with aligned fibers. However, predefining the angle of deposited fibers and fabrication of complex shaped scaffolds that mimic the individual layers of an aorta and includes the SV remains unexplored. The proposed MEW setup for the first time allows for the fabrication of complex shaped aortic root scaffold including SV with tri-layered fiber architecture mimicking that of a native coronary artery. The tunability of fiber deposition angle and alignment presented in **Figure 3** as a single architecture scaffold and in **Figure 4** as a tri-layered scaffold opens up avenues for the fabrication of scaffold for other soft tissues with hierarchical and heterogeneous collagen fiber architecture.

The tri-layered scaffolds composited with fibrin revealed a significant difference in burst strength between the sinus and the wall (**Figure 4D**), similarly to the scaffolds produced with just one winding angle (**Figure 4E**).

Suture retention is an important property for the implantability of the scaffolds (Pensalfini et al., 2018). Therefore, we next investigated the suture retention strength of the tri-layered scaffold and compared it to the 60° winding

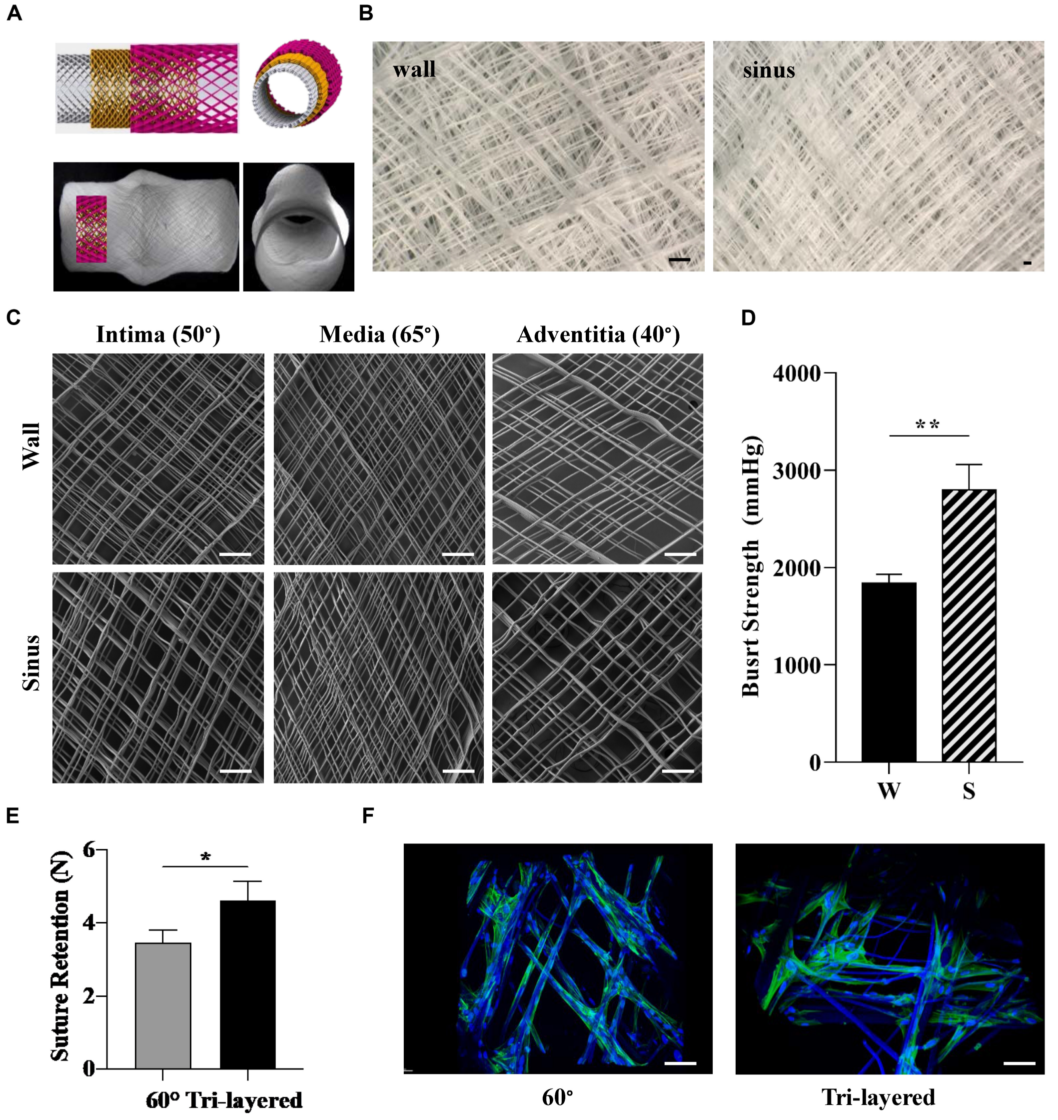

FIGURE 4 | Design and fabrication of biomimetic tri-layered aortic root scaffolds. **(A)** 3D illustration of the fibers at the defined angles across the three layers (top) and representative images of the scaffold (bottom). **(B)** Stereomicroscope images of tri-layered scaffold at the wall (left) and sinus (right). **(C)** SEM images of each of the individual layers forming the biomimetic scaffold: intima (50°), media (65°) and adventitia (40°) taken from the wall and sinus. **(D)** Burst strength of tri-layered scaffold measured at the wall and sinus. **(E)** Suture retention of tri-layered scaffold compared to scaffold with 60° winding angle, which presented similar burst strength. **(F)** Attachment and alignment of HUVSMC after 4 days of culture on scaffolds with 60° winding angle and tri-layered, measured by two-photon microscopy. (Scale bars: **(B,C,F)** = 200 μm); (statistical analysis: Unpaired *t*-test; $0.001 < p < 0.01$**, $0.01 < p < 0.05$*).

angle scaffold, as it presented a similar burst strength but a different fiber arrangement. The tri-layered scaffold displayed a significantly higher suture retention strength compared to the 60° scaffold (**Figure 4E**). Given that the printing time and number of printing loops were kept constant for both group of scaffolds, this is potentially associated with the difference in fiber arrangement.

To assess the potential of this biomimetic design approach for vascular tissue engineering, burst strength and suture retention of the tri-layered scaffolds where then compared to polytetrafluoroethylene (ePTFE) grafts, the gold-standard synthetic vascular grafts used in the clinic. Importantly, burst strength on both the wall and sinuses of the tri-layered MEW/fibrin scaffolds captured the reported values of ePTFE small caliber grafts (1323 ± 383 mmHg) generally used for aorta reconstruction (Kim et al., 2011), which is well above the pressure experienced by native aortic root under patho-physiological conditions (90–200 mmHg) (Rothwell et al., 2010). Moreover, MEW/fibrin scaffolds presented burst strength similar to that of the bovine arteries, native saphenous vein and internal mammary artery (Konig et al., 2009). The heterogeneity of burst strengths obtained for the tri-layered composite scaffold better captures the behavior of native aortic roots than the synthetic grafts that do not include SV. The suture retention strength

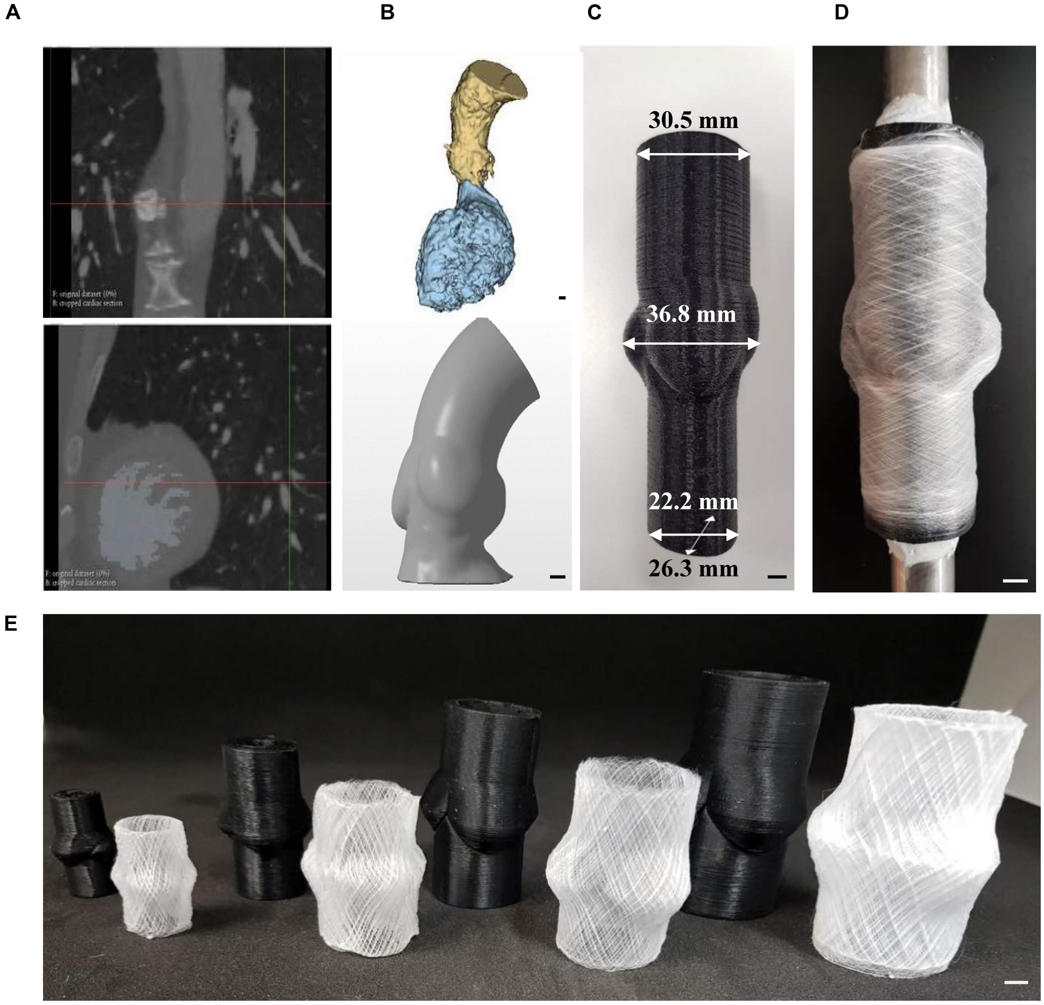

FIGURE 5 | Fabrication of personalized aortic root scaffolds. **(A)** CT scans of the patient's aorta. **(B)** DICOM to STL conversion using InVesalius software and smooth model of the personalized aorta. **(C)** PLA 3D printed model of the personalized aorta to be used as the substrate mandrel for MEW. **(D)** MEW performed on the 3D printed personalized mandrel. **(E)** 3D printed mandrel models and corresponding MEW scaffolds of 10, 15, 20, and 25 mm diameter. (Scale bar: 5 mm).

of the tri-layered composite scaffold was also significantly higher than that of the ePTFE (3.19 ± 1.49 N) (Kim et al., 2011), further highlighting its potential suitability for surgical implantation. High suture strength is also beneficial for the incorporation of aortic valve scaffolds in the root, given the importance of this property to enable successful integration. Scaffolds specifically designed for the aortic root with great suture retention and burst strength are also essential for heart valve tissue engineering given the growing body of literature on the importance of heterogeneous scaffolds specifically mimicking architecture and mechanical properties of aortic root and valve (Butcher, 2018).

Overall, the tri-layered scaffold not only performed comparably well in terms of suture retention and burst strength to the gold standard grafts but also incorporated the SV and heterogeneous fiber architecture across the wall and sinuses, both important characteristics of the native root that are not considered in the design of available grafts. To the best of our knowledge, this is the first report on the fabrication of a tri-layered aortic root fibrous scaffold that includes the SV.

Tri-layered scaffolds also supported HUVSMC attachment, with cells aligning to the PCL fibers, as demonstrated by DAPI-Phalloidin staining (**Figure 4F**).

MEW for Fabrication of Patient-Specific Scaffolds

Major developments have been undertaken in utilizing patient specific medical devices fabricated through 3D printing for different applications in the medical sector (Limmahakhun et al., 2017; Mohseni et al., 2019). Recently an exciting technology called personalized external aortic root support (PEARS) has emerged as a powerful pre-emptive operation to treat patients suffering from aortic root aneurysm (Treasure et al., 2014, 2016; Izgi et al., 2018). This technique takes advantage from the advancements in medical imaging and 3D printing to fabricate a personalized model of the patient's aorta, which is then used to fabricated a mesh sleeve that is purposed to restrict aortic root expansion. Given the laborious and time-consuming nature of this method to manually fit these supports to the models, we aimed to utilize the proposed MEW platform to introduce full automation, minimizing the complexity of this process. To highlight the capabilities of MEW to manufacture personalized scaffolds, we fabricated a customized 3D model using a patient-specific geometry obtained from a patient's aortic root CT scan (**Figures 5A–C**). This mold was readily incorporated into the versatile MEW platform where scaffolds were fabricated with an exemplary 30° winding angle according to the aforementioned process parameters discussed (**Figure 5D**). The stability of MEW printing on the personalized mold allowed to manufacture aortic root scaffolds including patient-specific anatomic features (**Figure 5C**). The ability of this platform to integrate with this exciting treatment approach elucidates the potential of MEW scaffolds for the PEARS procedure. In addition, the scalability of the process was investigated by fabricating hybrid collectors ranging from 10 to 25 mm in diameter. Scaffolds produced on these models demonstrated the capability of this platform to generate scaffolds suitable for patients of all ages (**Figure 5E**) (Roubertie et al., 2009; Yoganathan et al., 2013). The ability to fabricate anatomically relevant scaffolds at smaller scales has significant implications for the development of tissue engineered heart valves for pediatric patients.

CONCLUSION AND FUTURE OUTLOOK

In this study, we present a simple, cost-effective and robust method for the manufacture of scaffolds with anatomically relevant 3D geometries and controlled microarchitecture via MEW, here exemplified by the fabrication of biomimetic aortic root scaffolds featuring SV. This significantly expands the capabilities of this technology platform not only for cardiovascular tissue engineering but also for a much wider range of biomedical applications.

DATA AVAILABILITY STATEMENT

The raw data supporting the conclusions of this article will be made available by the authors, without undue reservation.

ETHICS STATEMENT

The studies involving human participants were reviewed and approved by University Hospital Aachen Local Ethics Committee (EK2067) and Office of Research Ethics and Integrity (OREI) of the Queensland University of Technology (QUT1900000599). The patients/participants provided their written informed consent to participate in this study.

AUTHOR CONTRIBUTIONS

NS, ED-J-P, PM, and DH designed the experiments and conceptualized the manuscript. NS conducted the majority of the experimental work, wrote the manuscript, and prepared the figures. ED-J-P and PM reviewed the manuscript. TS performed SEM and Micro CT. DR-G performed the biological evaluation. MM assisted in personalized scaffold design. OB and TH assisted the experimental work. All authors provided feedback. ED-J-P and PM supervised the project, share equal senior contribution, and finalized the manuscript together with NS. All authors approved the final version of the manuscript.

FUNDING

The authors gratefully acknowledge the financial support of the Australian Research Council (ARC ITTC in Additive Biomanufacturing, IC160100026), the Center in Regenerative Medicine (IHBI, QUT), and the German Research Foundation (DFG – Project number: 403170227 ArchiTissue). SEM imaging of MEW scaffolds was performed at the Central Analytical Research Facility operated by the Institute for Future Environments and supported by Science and Engineering Faculty at QUT.

SUPPLEMENTARY MATERIAL

The Supplementary Material for this article can be found online at: https://www.frontiersin.org/articles/10.3389/fbioe.2020.00793/full#supplementary-material

REFERENCES

Akentjew, T. L., Terraza, C., Suazo, C., Maksimcuka, J., Wilkens, C. A., Vargas, F., et al. (2019). Author Correction: rapid fabrication of reinforced and cell-laden vascular grafts structurally inspired by human coronary arteries. *Nat. Commun.* 10, 1–15. doi: 10.1038/s41467-019-11446-11449

Arabkhani, B., Mookhoek, A., Di Centa, I., Lansac, E., Bekkers, J. A., De Lind Van Wijngaarden, R., et al. (2015). Reported outcome after valve-sparing aortic root replacement for aortic root aneurysm: a systematic review and meta-analysis. *Ann. Thorac. Surg.* 100, 1126–1131. doi: 10.1016/j.athoracsur.2015.05.093

Azadani, A. N., Chitsaz, S., Matthews, P. B., Jaussaud, N., Leung, J., Tsinman, T., et al. (2012). Comparison of mechanical properties of human ascending aorta and aortic sinuses. *Ann. Thorac. Surg.* 93, 87–94. doi: 10.1016/j.athoracsur.2011.08.002

Bas, O., D'Angella, D., Baldwin, J. G., Castro, N. J., Wunner, F. M., Saidy, N. T., et al. (2017). An integrated design, material, and fabrication platform for engineering biomechanically and biologically functional soft tissues. *ACS Appl. Mater. Interf.* 9, 29430–29437. doi: 10.1021/acsami.7b08617

Brown, T. D., Dalton, P. D., and Hutmacher, D. W. (2011). Direct writing by way of melt electrospinning. *Adv. Mater.* 23, 5651–5657. doi: 10.1002/adma.201103482

Brown, T. D., Slotosch, A., Thibaudeau, L., Taubenberger, A., Loessner, D., Vaquette, C., et al. (2012). Design and fabrication of tubular scaffolds via direct writing in a melt electrospinning mode. *Biointerphases* 7, 1–16. doi: 10.1007/s13758-011-0013-17

Butcher, J. T. (2018). The root problem of heart valve engineering. *Sci. Transl. Med.* 10:eaat5850. doi: 10.1126/scitranslmed.aat5850

Capulli, A. K., Emmert, M. Y., Pasqualini, F. S., Kehl, D., Caliskan, E., Lind, J. U., et al. (2017). JetValve: rapid manufacturing of biohybrid scaffolds for biomimetic heart valve replacement. *Biomaterials*. 133, 229–241. doi: 10.1016/j.biomaterials.2017.04.033

Capulli, A. K., MacQueen, L. A., Sheehy, S. P., and Parker, K. K. (2016). Fibrous scaffolds for building hearts and heart parts. *Adv. Drug Deliv. Rev.* 96, 83–102. doi: 10.1016/j.addr.2015.11.020

Coyan, G. N., da Mota Silveira-Filho, L., Matsumura, Y., Luketich, S. K., Katz, W., Badhwar, V., et al. (2020). Acute in vivo functional assessment of a biodegradable stentless elastomeric tricuspid valve. *J. Cardiovasc. Transl. Res.* [Epub ahead of print]. doi: 10.1007/s12265-020-09960-z

D'Amore, A., Luketich, S. K., Raffa, G. M., Olia, S., Menallo, G., Mazzola, A., et al. (2018). Heart valve scaffold fabrication: bioinspired control of macro-scale morphology, mechanics and micro-structure. *Biomaterials* 150, 25–37. doi: 10.1016/j.biomaterials.2017.10.011

De Paulis, R., De Matteis, G. M., Nardi, P., Scaffa, R., Bassano, C., and Chiariello, L. (2002). Analysis of valve motion after the reimplantation type of valve-sparing procedure (David I) with a new aortic root conduit. *Ann. Thorac. Surg.* 74, 53–57. doi: 10.1016/S0003-4975(02)03583-X

De Paulis, R., De Matteis, G. M., Nardi, P., Scaffa, R., Buratta, M. M., and Chiariello, L. (2001). Opening and closing characteristics of the aortic valve after valve-sparing procedures using a new aortic root conduit. *Ann. Thorac. Surg.* 72, 487–494. doi: 10.1016/S0003-4975(01)02747-2743

Geelhoed, W. J., Lalai, R. A., Sinnige, J. H., Jongeleen, P. J., Storm, C., and Rotmans, J. I. (2019). Indirect burst pressure measurements for the evaluation of tissue engineered blood vessels. *Tissue Eng. Part C Methods* 25:ten.TEC.2019.0133. doi: 10.1089/ten.TEC.2019.0133

Hasan, A., Memic, A., Annabi, N., Hossain, M., Paul, A., Dokmeci, M. R., et al. (2014). Electrospun scaffolds for tissue engineering of vascular grafts. *Acta Biomater.* 10, 11–25. doi: 10.1016/j.actbio.2013.08.022

Hochleitner, G., Youssef, A., Hrynevich, A., Haigh, J. N., Jungst, T., Groll, J., et al. (2016). Fibre pulsing during melt electrospinning writing. *Bionano Mater.* 17, 159–171. doi: 10.1515/bnm-2015-2022

Huber, E., Mirzaee, M., Bjorgaard, J., Hoyack, M., Noghanian, S., and Chang, I. (2016). "Dielectric property measurement of PLA," in *Proceedings of the IEEE International Conference on Electro Information Technology*, New York, NY.

Hutmacher, D. W. (2001). Scaffold design and fabrication technologies for engineering tissues–state of the art and future perspectives. *J. Biomater. Sci. Polym. Edn.* 12, 107–124. doi: 10.1163/156856201744489

Izgi, C., Newsome, S., Alpendurada, F., Nyktari, E., Boutsikou, M., Pepper, J., et al. (2018). External aortic root support to prevent aortic dilatation in patients with marfan syndrome. *J. Am. Coll. Cardiol.* 72, 1095–1105. doi: 10.1016/j.jacc.2018.06.053

Jockenhoevel, S., Zund, G., Hoerstrup, S. P., Chalabi, K., Sachweh, J. S., Demircan, L., et al. (2001). Fibrin gel-advantages of a new scaffold in cardiovascular tissue engineering. *Eur. J. Cardio Thorac. Surg.* 19, 424–430. doi: 10.1016/S1010-7940(01)00624-628

Jungst, T., Muerza-Cascante, M. L., Brown, T. D., Standfest, M., Hutmacher, D. W., Groll, J., et al. (2015). Melt electrospinning onto cylinders: effects of rotational velocity and collector diameter on morphology of tubular structures. *Polym. Int.* 64, 1086–1095. doi: 10.1002/pi.4948

Kim, S. H., Hassan, K., Kim, S. H., Park, I., Lee, S. H., Kim, S. H., et al. (2011). Small diameter double layer tubular scaffolds using highly elastic PLCL copolymer for vascular tissue engineering. *Macromol. Res.* 19, 122–129. doi: 10.1007/s13233-011-0208-202

Konig, G., McAllister, T. N., Dusserre, N., Garrido, S. A., Iyican, C., Marini, A., et al. (2009). Mechanical properties of completely autologous human tissue engineered blood vessels compared to human saphenous vein and mammary artery. *Biomaterials* 30, 1542–1550. doi: 10.1016/j.biomaterials.2008.11.011

Laterreur, V., Ruel, J., Auger, F. A., Vallières, K., Tremblay, C., Lacroix, D., et al. (2014). Comparison of the direct burst pressure and the ring tensile test methods for mechanical characterization of tissue-engineered vascular substitutes. *J. Mech. Behav. Biomed. Mater.* 34, 253–263. doi: 10.1016/j.jmbbm.2014.02.017

Lieshout, M., Van Peters, G., Rutten, M., and Baaijens, F. (2006). A knitted, fibrin-covered polycaprolactone scaffold for tissue engineering of the aortic valve. *Tissue Eng.* 12, 481–487. doi: 10.1089/ten.2006.12.481

Limmahakhun, S., Oloyede, A., Sitthiseripratip, K., Xiao, Y., and Yan, C. (2017). 3D-printed cellular structures for bone biomimetic implants. *Addit. Manuf.* 15, 93–101. doi: 10.1016/j.addma.2017.03.010

Liu, K., Wang, N., Wang, W., Shi, L., Li, H., Guo, F., et al. (2017). A bio-inspired high strength three-layer nanofiber vascular graft with structure guided cell growth. *J. Mater. Chem. B.* 5, 3758–3764. doi: 10.1039/c7tb00465f

Ma, P. X. (2010). Biomimetic materials in tissue engineering. *Mater. Today* 13, 14–22. doi: 10.1016/S1369-7021(10)70013-70014

Mohseni, M., Bas, O., Castro, N. J., Schmutz, B., and Hutmacher, D. W. (2019). Additive biomanufacturing of scaffolds for breast reconstruction. *Addit. Manuf.* 30:100845. doi: 10.1016/j.addma.2019.100845

Moreira, R., Neusser, C., Kruse, M., Mulderrig, S., Wolf, F., Spillner, J., et al. (2016). Tissue-engineered fibrin-based heart valve with bio-inspired textile reinforcement. *Adv. Healthc. Mater.* 5, 2113–2121. doi: 10.1002/adhm.201600300

Moreira, R., Velz, T., Alves, N., Gesche, V. N., Malischewski, A., Schmitz-Rode, T., et al. (2015). Tissue-engineered heart valve with a tubular leaflet design for minimally invasive transcatheter implantation. *Tissue Eng. Part C Methods* 21, 530–540. doi: 10.1089/ten.tec.2014.0214

Muerza-Cascante, M. L., Haylock, D., Hutmacher, D. W., and Dalton, P. D. (2015). Melt electrospinning and its technologization in tissue engineering. *Tissue Eng. Part B Rev.* 21, 187–202. doi: 10.1089/ten.teb.2014.0347

Nakayama, Y., Takewa, Y., Sumikura, H., Yamanami, M., Matsui, Y., Oie, T., et al. (2015). In-body tissue-engineered aortic valve (Biovalve type VII) architecture based on 3D printer molding. *J. Biomed. Mater. Res. Part B Appl. Biomater.* 103, 1–11. doi: 10.1002/jbm.b.33186

O'Brien, F. J. (2011). Biomaterials & scaffolds for tissue engineering. *Mater. Today* 14, 88–95. doi: 10.1016/S1369-7021(11)70058-X

Patterson, J., Martino, M. M., and Hubbell, J. A. (2010). Biomimetic materials in tissue engineering. *Mater. Today* 13, 14–22.

Pensalfini, M., Meneghello, S., Lintas, V., Bircher, K., Ehret, A. E., and Mazza, E. (2018). The suture retention test, revisited and revised. *J. Mech. Behav. Biomed. Mater.* 77, 711–717. doi: 10.1016/j.jmbbm.2017.08.021

Pisani, G., Scaffa, R., Ieropoli, O., Dell'Amico, E. M., Maselli, D., Morbiducci, U., et al. (2013). Role of the sinuses of Valsalva on the opening of the aortic valve. *J. Thorac. Cardiovasc. Surg.* 145, 999–1003. doi: 10.1016/j.jtcvs.2012.03.060

Reneker, D. H., Yarin, A. L., Fong, H., and Koombhongse, S. (2000). Bending instability of electrically charged liquid jets of polymer solutions in electrospinning. *J. Appl. Phys.* 87:4531. doi: 10.1063/1.373532

Robicsek, F. (1991). Leonardo da vinci and the sinuses of valsalva. *Ann. Thorac. Surg.* 52, 328–335. doi: 10.1016/0003-4975(91)91371-91372

Robicsek, F., and Thubrikar, M. (1999). Are we implanting half-valves? The role of sinus wall compliance in aortic valve function. *Ann. Thorac. Surg.* 67:597.

Rothwell, P. M., Howard, S. H., Dolan, E., O'Brien, E., Dobson, E. J., Dahlöf, B., et al. (2010). Prognostic significance of visit-to-visit variability, maximum systolic blood pressure, and episodic hypertension. *Lancet* 375, 895–905. doi: 10.1016/s0140-6736(10)60308-x

Roubertie, F., Ali, W., Ben Raisky, O., Tamisier, D., Sidi, D., and Vouhé, P. R. (2009). Aortic root replacement in children: a word of caution about valve-sparing procedures. *Eur. J. Cardio Thoracic Surg.* 35, 136–140. doi: 10.1016/j.ejcts.2008.09.043

Salica, A., Pisani, G., Morbiducci, U., Scaffa, R., Massai, D., Audenino, A., et al. (2016). The combined role of sinuses of Valsalva and flow pulsatility improves energy loss of the aortic valve. *Eur. J. Cardio Thorac. Surg.* 49, 1222–1227. doi: 10.1093/ejcts/ezv311

Schriefl, A. J., Zeindlinger, G., Pierce, D. M., Regitnig, P., and Holzapfel, G. A. (2012). Determination of the layer-specific distributed collagen fibre orientations in human thoracic and abdominal aortas and common iliac arteries. *J. R. Soc. Interf.* 9, 1275–1286. doi: 10.1098/rsif.2011.0727

Stachewicz, U., Dijksman, J. F., Soudani, C., Tunnicliffe, L. B., Busfield, J. J. C., and Barber, A. H. (2017). Surface free energy analysis of electrospun fibers based on Rayleigh-Plateau/Weber instabilities. *Eur. Polym. J.* 91, 368–375. doi: 10.1016/j.eurpolymj.2017.04.017

Thubrikar, M. (1990). *The Aortic Valve*. Boca Raton, FL: CRC Press.

Toninato, R., Salmon, J., Susin, F. M., Ducci, A., and Burriesci, G. (2016). Physiological vortices in the sinuses of Valsalva: an in vitro approach for bio-prosthetic valves. *J. Biomech.* 49, 2635–2643. doi: 10.1016/j.jbiomech.2016.05.027

Toosi Saidy, N., Wolf, F., Bas, O., Hutmacher, D. W., Mela, P., De-Juan-Pardo, E. M., et al. (2019). Biologically-inspired scaffolds for heart valve tissue engineering via melt electrowriting. *Small* 15:1900873. doi: 10.1002/smll.201900873

Treasure, T., Petrou, M., Rosendahl, U., Austin, C., Rega, F., Pirk, J., et al. (2016). Personalized external aortic root support: a review of the current status. *Eur. J. Cardio Thorac. Surg.* 50, 400–404. doi: 10.1093/ejcts/ezw078

Treasure, T., Takkenberg, J. J. M., Golesworthy, T., Rega, F., Petrou, M., Rosendahl, U., et al. (2014). Personalised external aortic root support (PEARS) in Marfan syndrome: analysis of 1-9 year outcomes by intention-to-treat in a cohort of the first 30 consecutive patients to receive a novel tissue and valve-conserving procedure, compared with the publishe. *Heart* 100, 969–975. doi: 10.1136/heartjnl-2013-304913

Tsamis, A., Krawiec, J. T., and Vorp, D. A. (2013). Elastin and collagen fibre microstructure of the human aorta in ageing and disease: a review. *J. R. Soc. Interf.* 10:20121004. doi: 10.1098/rsif.2012.1004

Underwood, M. J. (2002). The aortic root: structure, function, and surgical reconstruction. *Heart* 83, 376–380. doi: 10.1136/heart.83.4.376

Wang, K., Wu, C., Qian, Z., Zhang, C., Wang, B., and Vannan, M. A. (2016). Dual-material 3D printed metamaterials with tunable mechanical properties for patient-specific tissue-mimicking phantoms. *Addit. Manuf.* 12, 31–37. doi: 10.1016/j.addma.2016.06.006

Wunner, F. M., Bas, O., Saidy, N. T., Dalton, P. D., Pardo, E. M. D.-J., and Hutmacher, D. W. (2017). Melt electrospinning writing of three-dimensional polycaprolactone scaffolds with controllable morphologies for tissue engineering applications. *J. Vis. Exp.* 13:5005. doi: 10.3791/56289

Wunner, F. M., Wille, M. L., Noonan, T. G., Bas, O., Dalton, P. D., De-Juan-Pardo, E. M., et al. (2018). Melt electrospinning writing of highly ordered large volume scaffold architectures. *Adv. Mater.* 30:1706570. doi: 10.1002/adma.201706570

Yoganathan, A. P., Fogel, M., Gamble, S., Morton, M., Schmidt, P., Secunda, J., et al. (2013). A new paradigm for obtaining marketing approval for pediatric-sized prosthetic heart valves. *J. Thorac. Cardiovasc. Surg.* 146, 879–886. doi: 10.1016/j.jtcvs.2013.04.016

Conflict of Interest: NS, OB, DH, PM, and ED-J-P declare that they have a pending patent (PCT/AU2020/050383) related to this research.

The remaining authors declare that the research was conducted in the absence of any commercial or financial relationships that could be construed as a potential conflict of interest.

frontiers
in Bioengineering and Biotechnology

REVIEW
published: 08 October 2020
doi: 10.3389/fbioe.2020.00924

Safety Considerations in 3D Bioprinting Using Mesenchymal Stromal Cells

Lucy Belk[1,2], Nazzar Tellisi[1,2,3], Hamish Macdonald[4], Ahmet Erdem[5,6,7,8], Nureddin Ashammakhi[5,6,9,10,11]* and Ippokratis Pountos[1,2,3]*

[1] Academic Department of Trauma and Orthopaedics, University of Leeds, Leeds, United Kingdom, [2] School of Medicine, University of Leeds, Leeds, United Kingdom, [3] Chapel Allerton Hospital, Leeds Teaching Hospitals, Leeds, United Kingdom, [4] Gloucester Royal Hospital, Gloucestershire Hospitals NHS Foundation Trust, Gloucester, United Kingdom, [5] Center for Minimally Invasive Therapeutics, University of California, Los Angeles, Los Angeles, CA, United States, [6] Department of Bioengineering, Henry Samueli School of Engineering, University of California, Los Angeles, Los Angeles, CA, United States, [7] Department of Chemistry, Kocaeli University, Kocaeli, Turkey, [8] Department of Biomedical Engineering, Kocaeli University, Kocaeli, Turkey, [9] Department of Radiological Sciences, David Geffen School of Medicine, University of California, Los Angeles, Los Angeles, CA, United States, [10] Institute for Quantitative Health Science and Engineering, Michigan State University, East Lansing, MI, United States, [11] Department of Biomedical Engineering, Michigan State University, East Lansing, MI, United States

Three-dimensional (3D) bioprinting has demonstrated great potential for the fabrication of biomimetic human tissues and complex graft materials. This technology utilizes bioinks composed of cellular elements placed within a biomaterial. Mesenchymal stromal cells (MSCs) are an attractive option for cell selection in 3D bioprinting. MSCs can be isolated from a variety of tissues, can pose vast proliferative capacity and can differentiate to multiple committed cell types. Despite their promising properties, the use of MSCs has been associated with several drawbacks. These concerns are related to the *ex vivo* manipulation throughout the process of 3D bioprinting. The herein manuscript aims to present the current evidence surrounding these events and propose ways to minimize the risks to the patients following widespread expansion of 3D bioprinting in the medical field.

Keywords: mesenchymal stromal cells, *ex vivo* expansion, bioprinting, additive manufacturing, 3D bioprinting

Edited by:
Julien Georges Didier Barthès,
PROTiP Medical, France

Reviewed by:
Daniela Duarte Campos,
Stanford University, United States
Jae-Won Shin,
University of Illinois at Chicago,
United States

***Correspondence:**
Nureddin Ashammakhi
n.ashammakhi@ucla.edu
Ippokratis Pountos
pountos@doctors.org.uk

Specialty section:
This article was submitted to Biomaterials, a section of the journal Frontiers in Bioengineering and Biotechnology

Received: *07 November 2019*
Accepted: *17 July 2020*
Published: *08 October 2020*

Citation:
Belk L, Tellisi N, Macdonald H, Erdem A, Ashammakhi N and Pountos I (2020) Safety Considerations in 3D Bioprinting Using Mesenchymal Stromal Cells. Front. Bioeng. Biotechnol. 8:924. doi: 10.3389/fbioe.2020.00924

INTRODUCTION

With an increasing aging population the need to regenerate diseased tissues or replace tissues and organs lost due to trauma or surgery is increasing (Colwill et al., 2008; International Population Reports, 2016). There is already a lack of supply of sufficient organ donations and tissue grafts which is likely to worsen in the future (Yanagi et al., 2017; American Transplant Foundation, 2018). Tissue engineering that was introduced in the last few decades generally employs the seeding of scaffolds with cells (Langer and Vacanti, 1993). This process is associated with inhomogeneous distribution of cells within the scaffold, which can also affect subsequent engineered construct survival, integration and function (Gao et al., 2014). It was previously hypothesized that inhomogeneous seeding could prevent some cells from nutrients and oxygen resulting in poor function (Melchels et al., 2010).

The recent advent of three-dimensional (3D) bioprinting has brought about new possibilities to advance tissue engineering and regenerative medicine. Three-dimensional bioprinting involves the use of cells that are mixed with a carrier material while in liquid form with subsequent solidification of such material by using one of a number of cross-linking techniques. This mixture, known as bioink may also include growth factors (Ashammakhi et al., 2019a,b) or other additives such as osteoconductive materials (Byambaa et al., 2017; Ashammakhi et al., 2019c). Three-dimensional bioprinting techniques and bioinks have evolved tremendously over the last two decades, to address the need to create complex biomimetic tissue constructs (Mandrycky et al., 2016; **Figure 1**).

Cells used in bioinks have represented one of the major challenges faced by tissue engineers because of their limited availability (Freimark et al., 2010), proliferation (Willerth and Sakiyama-Elbert, 2008), and differentiation potential (Tuszynski et al., 2014). While already differentiated cells could be ideal, their harvest can cause donor site morbidity while often perform poorly with ex vivo manipulation. Alternative cell sources of cells include embryonic or reprogrammed cells. These cell types are associated with many challenges (Bongso et al., 2008; Trounson and McDonald, 2015) and concerns. The biggest concern shared by physicians and other care providers, regulatory bodies and industry as a whole is the safety of stem cell therapeutics for use in patients (Goldring et al., 2011). Mesenchymal stem cells on the other hand, have gained popularity and represent a cell type of choice for many experimental and clinical studies in tissue engineering.

MSCs IN 3D BIOPRINTING

Mesenchymal stromal cells (MSCs) represent one of the most popular types of cells used in tissue engineering today. In fact, their clinical use is so strong today that are used in more than 700 clinical trials listed on US clinical trials. This is because MSCs have potential to differentiate into a wide variety of cell types (Sasaki et al., 2008) but also due of their wide availability from different sources such as the bone marrow (Gnecchi and Melo, 2009), adipose tissue (Katz et al., 2005), blood vessels (Kuznetsov et al., 2001), muscle (Young et al., 1995) as well as rather "embryonic" tissues such as amniotic fluid (Tsai et al., 2004) and cord blood (Bieback et al., 2004). MSCs actively participate in the regeneration of tissues and provide substitute cells for those that expire (Pintus et al., 2018). Following injury MSCs mobilize to distant sites and either provide reparative cells and/or secrete trophic factors to promote healing. In addition, MSCs pose anti-inflammatory and immunomodulatory capacity as can improve inflammation and restore or inhibit the functions of immune cells (Pintus et al., 2018). MSCs can be easily expanded *ex vivo* to provide clinically relevant numbers prior to use. Although their exact function is not fully elucidated, MSCs have been used widely in tissue engineering instead of pluripotent stem cells (embryonic or induced pluripotent stem cells) which possess their own concerns and more complex processing techniques (Porada et al., 2006).

In 3D bioprinting, MSCs remains a popular cell type for the use in bioink. Their use is not limited to bone (Ong et al., 2018), cartilage (Bae et al., 2018), and adipose tissue (Qi et al., 2018) but MSCs are considered and used in many other 3D bioprinting applications. In fact, in addition to bone and cartilage, MSCs were used in 3D bioprinting of muscle (Phillippi et al., 2008), aortic valve (Kang et al., 2017), cardiovascular tissue (Ryu et al., 2015), neural tissues (Jakab et al., 2010), tendons and ligaments (Rak Kwon et al., 2020), and others (Tasnim et al., 2018). Thus, the objective of this review is to examine the literature on 3D bioprinting that utilized MSCs and examine accumulated data pertaining to the safety of MSCs in 3D bioprinting in various pre-, intra-, and post-printing stages. Discussion of findings is included, challenges highlighted, and future directions are outlined.

PRE-PRINTING

The generation of reliable MSC-based 3D bioprinting products requires first an in-depth understanding of the MSC physiology. MSC physiology is complex and it is influenced by the local microenvironment. For example, some researchers have shown that MSCs have tumor-suppressing properties (Khakoo et al., 2006; Cousin et al., 2009; Ho et al., 2013). On the contrary, MSCs can also favor tumor progression by promoting tumor angiogenesis, maturation of tumor vasculature and expansion through the secretion of a wide range of bioactive biomolecules (Kucerova et al., 2010; Suzuki et al., 2011; Huang et al., 2013). The reason for such dual roles is largely obscure. Together with MSC physiology, the target tissue micro-architectural topography, physiology, mechanical properties have to be elucidated. This will dictate the porosity, stiffness, orientation of the scaffold components and depict the exact location of the cellular components (Daly et al., 2017).

In addition to robust understanding of MSC physiology, further work on developing methodologies that safeguard high viability and ensure safety of grafts is needed. Literature suggests that the success of potential application of MSCs is closely related to the number of MSCs (Hernigou et al., 2005a,b). The expansion of the cells raises several concerns involving the extent of the expansion (expansion induces deprivation of MSCs properties), the effect of culture conditions, culture media and tissue culture plastics on the cells as well as the effect of cryopreservation on MSCs (Sotiropoulou et al., 2006; Pountos et al., 2007). The need for supplementation of the culture media with cytokines and chemokines in high non-physiologic concentrations is unknown whether it can affect their long-term properties. Worrying reports are available suggesting, that *ex vivo* expansion of MSCs can induce spontaneous malignant transformation into cells with tumorigenic potential (Rubio et al., 2005). Even more disturbing are the reports of occasional sarcoma formation in patients receiving bone marrow treatment and those undergone autologous fat graft (Perrot et al., 2010).

PRINTING PROCESS

Characteristics of 3D Bioprinting Methods in Brief

There are several 3D printing techniques among which the most commonly used for 3D bioprinting are extrusion, laser-based (Catros et al., 2011), inkjet (Cui et al., 2010), stereolithography

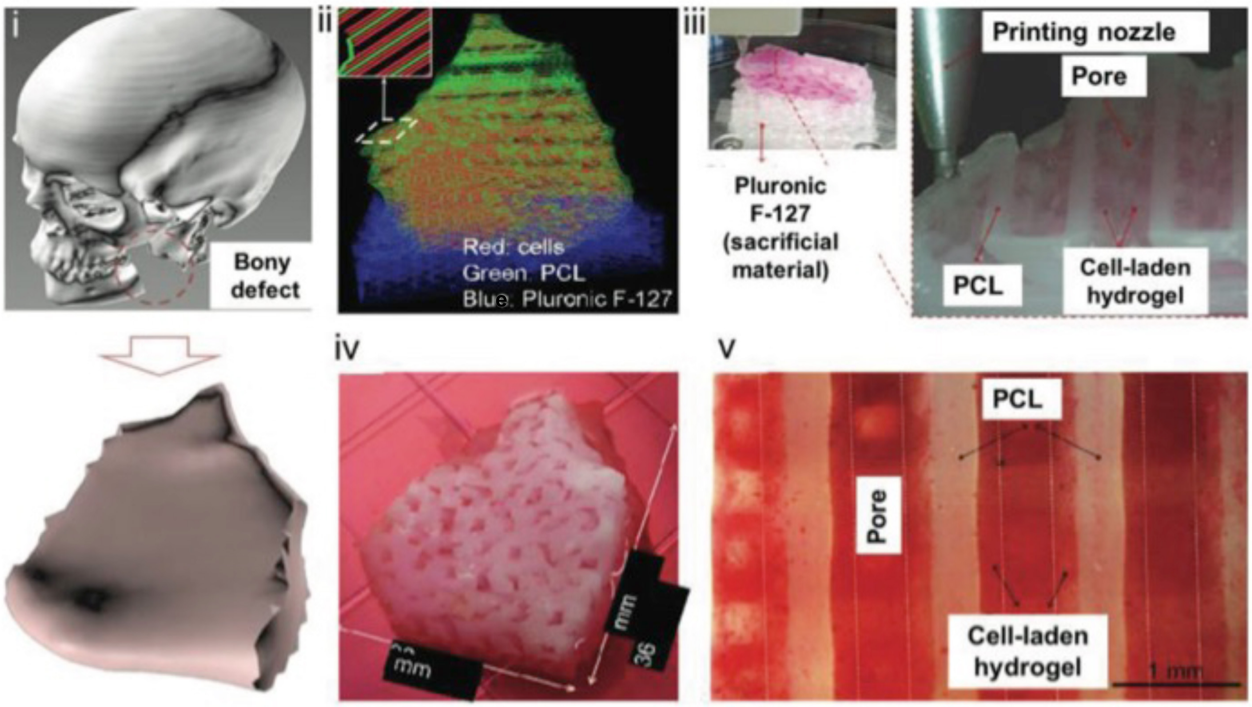

FIGURE 1 | The pathway of creating complex 3D printed structures. **(i)** Modeling of a mandibular defect with the use of patients CT scans. **(ii)** Construction of 3D architecture. **(iii)** 3D printing process. **(iv)** Culture of the graft. **(v)** Differentiation of the cells to osteoblasts. Reproduced with permission from Kang et al. (2016).

(Wang et al., 2015) and electrospinning-based printing (Khalil and Sun, 2009; Wüst et al., 2011; Dababneh and Ozbolat, 2014; **Figure 2**). The same technologies can be used to create smart 3D-bioprinted structures able to respond to the environment; commonly referred to as four-dimensional (4D) bioprinting (**Figure 3**). Extrusion 3D bioprinting or pressure-assisted bioprinting uses hydrogel bioinks extruded from a syringe in a continuous trace through a fine nozzle (Maher et al., 2009; Bhuthalingam et al., 2015; Irvine et al., 2015). In most extrusion bioprinters, the nozzle can move on y-z axes with the substrate collector plate moving in the *x*-axis to produce the final structure (Maher et al., 2009; Bhuthalingam et al., 2015; Irvine et al., 2015). Extrusion bioprinting delivers good homogeneity of bioinks, can deliver very high cell densities and does not require any specific environmental conditions (can be carried out at room temperature) (Atala and Yoo, 2015; Bishop et al., 2017). The overall resolution is rather poor compared to other techniques (minimum feature size is generally over 100 μm) (Leberfinger et al., 2017). Despite this, the technique has been used to create complex structures but MSCs survival was as low as 40% due to apoptosis and cell deformation.

Laser bioprinting uses a pulsed nanosecond or ultraviolet (UV) like wavelength laser as a source of energy to stimulate the upper surface of an energy absorbing metal film, which is usually made of a layer of titanium or gold (Catros et al., 2011). This metal film is coated with bioink on its lower surface and acts as a donor film. Stimulation of the upper surface of the metal film causes vaporization, creating a pressure bubble that drives the bioink from the donor film onto a substrate plate containing a biopolymer (Stolberg and McCloskey, 2009; Jana and Lerman, 2015; Irvine and Venkatraman, 2016; Li et al., 2016). The biopolymer functions to aid in sustaining growth and cellular adhesion of the cells after transfer from the donor film (Catros et al., 2011; Trombetta et al., 2017). The precise resolution is influenced by a number of factors including the energy emitted by the laser, printing speed, viscosity and thickness of the bioink layer on the donor film and its rheological properties, shape and organization of the structure and substrate wettability (Guillemot et al., 2010a,b; Li et al., 2016). Despite that, this is a scaffold-free technique reaching resolutions between 10 and 50 μm. Some studies managed to achieve a resolution of a single cell per droplet. This method negates the shearing stress experienced by cells during deposition down a narrow print head or nozzle (Murphy and Atala, 2014; Mandrycky et al., 2016; Keriquel et al., 2017). The potential of laser bioprinting has been demonstrated in a number of studies (Barron et al., 2004; Guillemot et al., 2010a,b).

Inkjet bioprinting arose from the adaptation of conventional desktop inkjet printers. It is a noncontact printing process where a droplet of bioink is deposited through the print head on demand, under the control of a thermal or piezoelectric actuator. This type of multi-cell printing is known as drop on demand (Irvine and Venkatraman, 2016). The resolution is in the region of up to 50 μm (Mandrycky et al., 2016). Thermal actuation is the more commonly used method for inkjet bioprinting where droplets of bioink are generated by an electric current. The

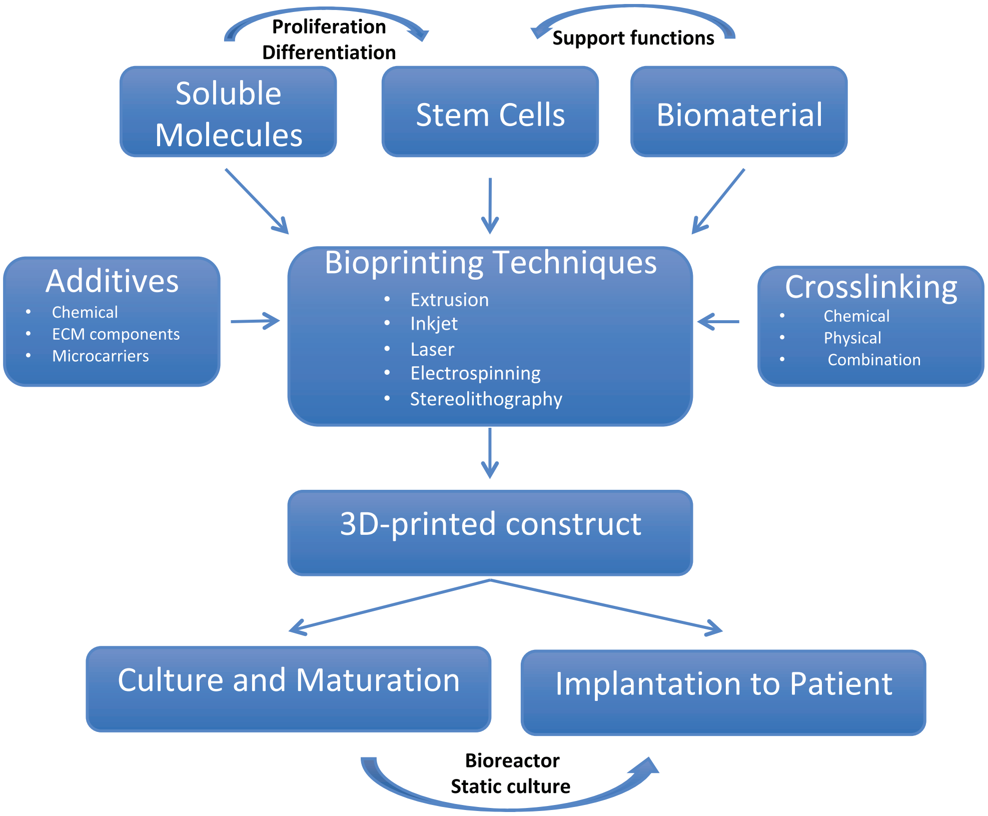

FIGURE 2 | The pathways and components of 3D bioprinting process.

thermal actuator element reaches temperatures in excess of up to 300°C, allowing a vapor bubble to generate sufficient pulse pressure to expel the bioink from the print head (Cui et al., 2010). This could potentially impart both shear and thermal stress on the cells (Irvine and Venkatraman, 2016; Li et al., 2016). The requirement to use low viscosity inks to prevent blockage of the print-head prevents the use of a number of efficacious bioinks. In contrast to the thermal, the piezoelectric actuation produces a transient pressure to eject the droplets on to the substrate. It produces more homogenous droplets than thermal actuation, but some authors reported greater levels of cell damage (Seetharam, 1991; Nakamura et al., 2005; Saunders et al., 2007).

Stereolithography is another 3D bioprinting technique that can be used to generate 3D constructs. This technique involves the solidification of a cell-laden photo-crosslinkable polymer solution in a layer-by-layer fashion, and it is controlled by a moveable stage along the *z*-axis (Murphy and Atala, 2014). In stereolithography, 3D complex structures can be produced without the need for a printhead that moves in x–y direction. In this process, a digital micromirror device (DMD) which allows highly precise patterns to be created, is used to control selectively crosslinking of bioink in z direction (Heinrich et al., 2019). This selective crosslinking method by light does not lead to any cell shear stress, making it possible to achieve higher cell viability in produced constructs. However, the use of transparent bioinks is required in stereolithography in order to achieve uniform crosslinking. This restricts the cell density that can be used in the bioink (Minteer et al., 2013). Despite this limitation, the technique has a great potential because of high speed, high resolution (∼1 µm) and controllability of the internal and external architecture of the resulting construct (Gruene et al., 2011a,b; Kang et al., 2017).

Electrospinning is a high-resolution fabrication method that can be used to produce thin fibers (Heinrich et al., 2019). During the process of electrospinning, a high voltage is applied to the ejected polymeric solution from the syringe. When the electrostatic repulsion starts to overcome the surface tension of the solution, the solution begins to evaporate and it is subsequently solidified during transit to form fibers (Ashammakhi et al., 2008; Bhardwaj and Kundu, 2010). Thin fiber-based constructs can be produced by this technique. Recently, this process technique has been modified for bioprinting by adding cells and controlling the process of fiber arrangement in the resulting structure. One of the primary features of electrospinning-based bioprinting (EBB) is the shorter collecting range of fibers (around 0.5–3 mm) in comparison to traditional electrospinning. This allows for more controllable deposition of electrospun materials with less applied voltage than usually used in conventional electrospinning (Heinrich et al., 2019). Visser et al., 2015; have recently used electrospinning-based bioprinting

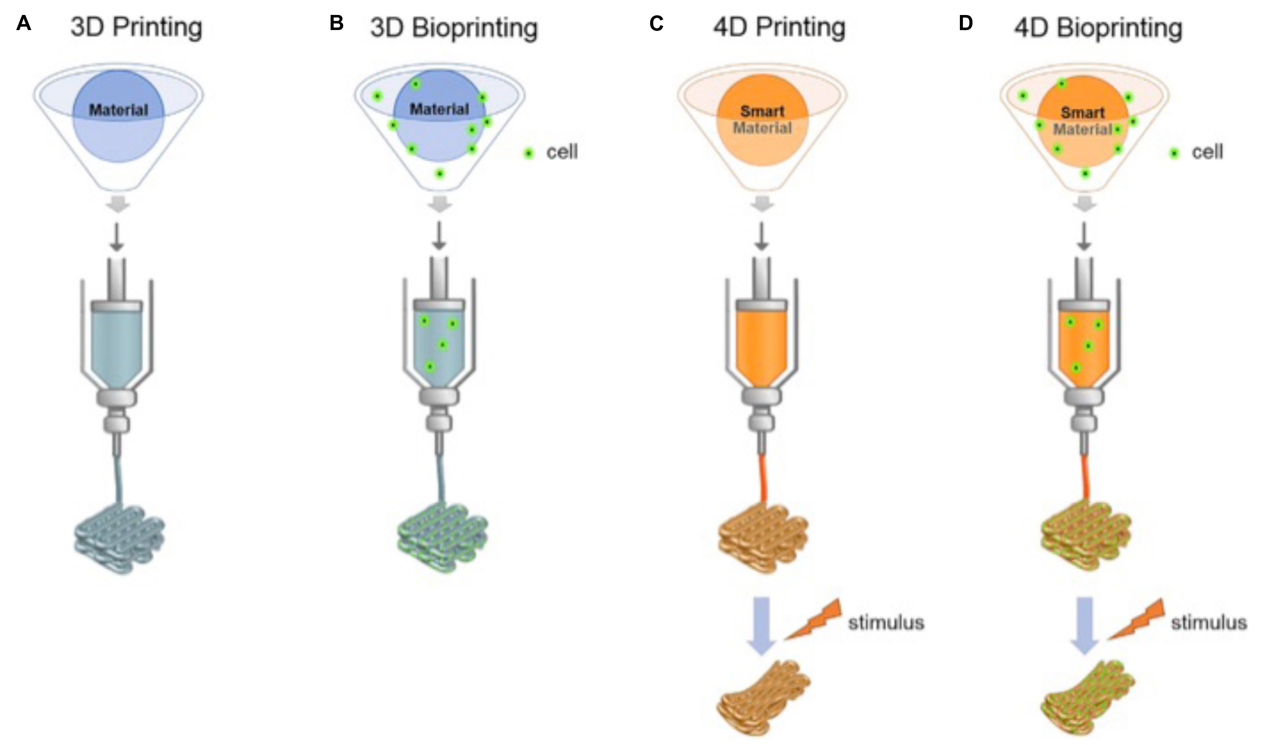

FIGURE 3 | The different printing technologies (3D, 3D bioprinting, 4D, and 4D bioprinting). **(A,B)** shows conventional 3D printing and bioprinting techniques. **(C,D)** For-dimensional bioprinting is defined as 3D printing of cell-laden materials in which the printed structures would be able to respond to external stimulus due to stimuli-responsive bioinks or internal cell forces. Reproduced with permission from Ashammakhi et al. (2018).

technology to enhance GelMA hydrogel mechanical strength by reinforcing high-porosity poly(ε-caprolactone) (Visser et al., 2015). The rigidity of GelMA hydrogels increased 30 times by 7–214 kPa while its elastic properties were preserved (Visser et al., 2015). However, the main restrictions of EBB are the fast spinning of fibers, resulting in a spatially unstable 3D structures and the high processing temperature and voltage, which is challenging to cells contained in the electrospun material.

Cell Death During 3D Bioprinting

The viability of the cells can be influenced by a number of factors. These include the storage of the cells in the printer, the thermal damage during the printing process and the mechanical forces exerted during bioprinting. **Table 1** shows documented survival rates following 3D bioprinting.

Cell storage and conditions during the printing process can potentially affect cell viability. During this process the cells are required to be stable and in media that could allow them to recover from the effects of cells-detaching solution (i.e., Trypsin, TrypLE, collagenase or others) and the stress exerted on them during the detachment process (i.e., centrifugation, washing, etc.). It is known that these methods can affect cell survival, phenotype and differentiation potential (Parvin et al., 2012; Tsuji et al., 2017). In addition, the effect of prolonged bioprinting protocols would require stable media and stable cell conditions. At present, there are limited studies in this field.

Thermal injury to cells is another area of concern. For example, during inkjet printing, where temperatures exceed 200 °, studies have shown that the bioink temperatures are raised by just 4–10° (Cui et al., 2010) and this does not significantly adversely affect the viability of mammalian cells (Suzuki et al., 2011). This heating effect is thought to be temporary (~5 μs), with less than 8% of the cells being lysed during bioprinting (Cui et al., 2010). Similar results were reported for the heat shock of the laser pulse where the cell survival, proliferation and differentiation were comparable to those of controls at 5 days in cell culture (Gruene et al., 2011b).

In addition to the potential thermal damage, the mechanical stress should be also taken into account. Cells are known to respond to mechanical stress by changing their gene expression and cell function. Among many cells' adaptation mechanisms activated, MSCs activates several intracellular signaling cascades, including kinases (PKB, MAPK, FAK), β-catenin, GTPases (Thompson et al., 2012). Chang et al. (2008), found that cellular viability is inversely related to extrusion pressure, with as little as 40% viability found at the extremes of high pressure. Mechanical pressure observed in inkjet printing has been demonstrated to promote the differentiation of MSCs toward bone and cartilage lineages (Shav and Einav, 2010). In contrast, the shear stress produced in extrusion techniques promotes differentiation toward both endothelial and bone tissues (Stolberg and McCloskey, 2009). The choice of the 3D technology is mostly done on the basis of required resolution and the target tissue as

TABLE 1 | Studies presenting the survival rates of cells used as bioink for 3D-bioprinting applications.

Author, year	3D Printer	Cell types	Survival rates	Comments/Other findings
Inkjet bioprinting				
Christensen et al. (2015)	Thermal inkjet printing	Chinese hamster ovary cells and primary embryonic motor neurons from ventral cords of 14-day embryos from pregnant Sprague-Dawley rats	Greater than 90% cellular viability after printing.	
Saunders et al. (2007)	Piezoelectric drop-on-demand inkjet printing	HT 1080 human fibroblasts	Cellular survival of 94–98%.	Survival rates decrease with increased printing pulse amplitude. Sampled printed at 40v demonstrated survival rates that could not be distinguished from unprinted control samples.
Cui et al. (2010)	Thermal inkjet printing	Green fluorescent protein expressing Chinese hamster ovary cells	Average cellular viability was 89%.	No significant difference in viability was observed in different cellular concentrations of ink. Printed cell number correlated with increasing cellular ink concentrations.
Christensen et al. (2015)	Inkjet based free form fabrication	NIH 3T3 mouse fibroblasts	Post printed cellular viability was 92.4% immediately after printing and 90.8% after 24 h of incubation.	
Levato et al. (2014)	Bioscaffolder system (Levato et al., 2014)	Mesenchymal stem cells from 2 to 4 weeks old Lewis rats	Post dispensing viability was 80% after 1 day and more than 90% after 3 days.	Pre-seeded particles suspended in the gels had the lowest number of viable cells (60%) after 1 day of culture, which increased to 90% after 3 days.
Du et al. (2015)	Inkjet with four independent *z*-axis-controlled ink reservoirs	Bone mesenchymal stem cells from 4-weeks-old male adult Sprague-Dawley rats	Cellular viability of > 90% was seen during printing	CBD-BMP2-collagen microfibers induced BMSC differentiation into osteocytes within 14 days more efficiently than the osteogenic medium.
Extrusion bioprinting				
Zhao et al. (2014)	Microextrusion printing	HeLa cells	Post printed viability of the HeLa cells in constructs was 94.9% ± 2.2% with parameters of 10 $\text{mm}^3\ \text{min}^{-1}$ extrusion speed, 250 μm nozzle inner diameter, 10°C chamber temperature and 25°C nozzle temperature.	Comparisons of 3D and 2D tumor models of HeLa cells show a higher cellular proliferation rate and more simulated tumor characteristics with 3D printing
Zhao et al., 2015	Four nozzle microextrusion printing	A549 cells	Cell survival rate was > 90% for all rheological conditions at a holding temperature of 20°	For all concentrations of bioink used in microextrusion printing, a holding temperature of 20° should be used. Optimum holding times were variable, dependent upon bioink concentration
Laser assisted bioprinting				
Barron et al. (2005)	BioLP$^{\text{TM}}$ Biological Laser Printing	Human osteosarcoma cells	After six days of incubation, cells demonstrated a 100% viability	
Koch et al. (2010)	Laser based printing based on laser assisted forward transfer (LIFT)	Skin cell lines (fibroblasts, keratinocytes); Human mesenchymal stem cells	98% ± 1% standard error of the mean (skin cells) and 90% ± 10% (hMSC).	No increase in apoptosis or DNA fragmentation was seen with the use of LIFT. hMSC phenotype was maintained as proven by fluorescence activated cell sorting analysis.
Hopp et al. (2012)	Femtosecond KrF laser in laser assisted forward transfer (LIFT)	Human neuroblastoma, chronic myeloid leukemia and osteogenic sarcoma cell lines and primary astroglial rat cells	Short-term and long-term survival for neuroblastoma and astroglial cells was 65–70%. Long term survival of osteosarcoma cells was low, while myeloid leukemia cells did not tolerate the procedure under the conditions.	

(Continued)

TABLE 1 | Continued

Author, year	3D Printer	Cell types	Survival rates	Comments/Other findings
Stereolithography bioprinting				
Arcaute et al. (2006)	Stereolithography bioprinting	Human dermal fibroblasts	Cell viability was at least 87% at 2 and 24 h following fabrication.	
Raman et al. (2016)	High-resolution projection stereolithography bioprinting	fibroblasts (3T3), myoblasts (C2C12), endothelial (C166), and bone marrow stromal (D1) cells	Cells encapsulated in the lower molecular weight polymer demonstrate a viability of 70% ± 10%, whereas cells encapsulated in the higher molecular weight polymer demonstrate a viability of 93% ± 3% on day 1 after printing for 3T3 cells. In the long term (2 weeks) cell viability in low molecular weight does not significantly change, but cell viability in high molecular weight significantly increases.	
Electrospinning-based bioprinting				
Visser et al. (2015)	Electrospinning-based bioprinting	Chondrocytes	Chondrocytes maintained high cell viability (~80%) on days 1 and 7.	

well as other factors. Lee et al. (2015) suggested that laser assisted and inkjet bioprinting may be preferable to extrusion bioprinting in most circumstances, but where circumstances necessitate the use of bioink with a high viscosity, extrusion bioprinting may be necessary. In these circumstances, the effects of sheer stress may be countered by modification of the bioink composition, e.g., by the inclusion of thinning polymers and the control of back pressure during the printing process (Mackay et al., 1998).

Bioink Characteristics and Cellular Adhesion

The primary aim in preparing a bioink is the biomimicry of the extracellular matrix, which creates a microenvironment that is optimal for cellular adhesion, proliferation and differentiation. An ideal bioink will maintain its printed structure integrity, be crosslinkable and can undergo degradation. It must accommodate cells, and sustain their integrity and viability throughout the printing process (Irvine and Venkatraman, 2016; Grungor-Ozkerim et al., 2018). It should also have the specific mechanical, physicochemical, rheological and biological properties needed for printability and for the preservation of cellular phenotype (Byambaa et al., 2017). Skardal and Atala (2015) highlighted that most biocompatible bioinks which were able to bear the vertical weight of emerging structures either produced toxic macromolecules during the setting process or required a toxic solvent for setting itself.

Porosity and interconnectivity are also two essential factors. Pore size, shape and volume are all influential in the behavior of cells following adhesion to the scaffold structure. Matsiko et al. (2015), found that pore size correlates with cellular organization, mineralization and the development and assembly of collagen I. Greater porosity and more interconnectivity allow for better matrix deposition and transportation of oxygen and other essential substrates into the center of the scaffold, promoting better ingrowth of tissue. Domingos et al. (2013), concluded that the morphology of printed cells did not appear to be influenced by the topology of pores, but that cell viability and proliferation were strongly affected by the size and shape of the pores, with large quadrangular pores resulting in the best viability and proliferation of human MSCs.

Scaffold stiffness has also been noted to play an integral role in the terminal differentiation of cells. MSCs have been observed to differentiate into cell types that best fit the microenvironment supported by the mechanical properties of the attachment surface or matrix. Differentiation toward an osteogenic lineage is observed in cells adhering to a rigid surface (34 kPa), compared with a more elastic surface (0.1–1 kPa), where MSCs display a tendency to differentiate toward a neuronal lineage (Engler et al., 2006; Lane et al., 2014). In relatively soft hydrogels (2.5–5 kPa), a differentiation toward adipogenesis is observed (Arany et al., 2010). This offers the possibility for the modification of bioink matrices and scaffolds to induce a specific lineage differentiation. Gao et al. (2015), produced a bioink that was optimized for bone and cartilage regeneration. The ink, made from a hybrid of polyethylene glycol and gel dimethylacrylate, had a compressive modulus of 1–2 MPa when printed, significantly stiffer than previously used hydrogels. MSCs printed in this hydrogel demonstrated a greater propensity toward osteocyte and chondrocyte lineage (Gao et al., 2015), but only in the context of specific extracellular matrix (Rowlands et al., 2008) and cross-linking conditions (Das et al., 2015).

It has been previously suggested that a scaffold can guide MSCs toward a specific lineage. In cases where the aim is to maintain stemness, bioinert hydrogels should be used. This avoids creating an environment that may be favorable to one particular lineage of cells. One such example of a bioinert hydrogel is alginate (Irvine and Venkatraman, 2016) which retains the stemness of printed stem cells (Blaeser et al., 2016). However, caution must be exercised when using bioinert hydrogels, as proliferative capabilities and movement are reduced, which may promote anoikis (Carrow et al., 2015), however, this may be overcome by the addition of the integrin binding peptide arginyl-glycyl-aspartic acid (RGD) moieties to bioinert alginates which increases cellular interaction whilst maintaining stemness (Carrow et al., 2015). Hyaluronic acid is an alternative to alginate, with proven clinical efficacy (Ozbolat and Hospodiuk, 2015). In contrast to alginate, hyaluronic acid promotes MSC attachment and maintains multipotency and proliferation through CD44 receptors (Cao et al., 2016), with the added benefit of adaptation to promote a specific lineage differentiation. One such example is the use of hyaluronic acid in cardiogenesis (Mairim et al., 2012). Where bioinert inks have been used, MSCs can be differentiated by incubation with soluble factors that direct maturation to a specific lineage in a similar fashion to culture additives (Irvine and Venkatraman, 2016). To remove reliance on extrinsic factors, additives can be included in bioink. For example, alginate bioinks have been modified with the addition of hydroxyapatite in the context of bone regeneration (Wüst et al., 2014). *In vivo* murine models of alginate scaffolds containing biphasic calcium phosphate particles (consisting of hydroxyapatite and β-tricalcium phosphate) displayed greater osteogenic differentiation than scaffolds having no biphasic calcium triphosphate (Wang et al., 2007).

The Effect of Cross-Linking

Three-dimensionally bioprinted extracellular matrix may lack the required stability and integrity to support contained cells. Crosslinking is often an essential step and a number of physical, biological and chemical crosslinking techniques have been proposed over the years. The aim of these techniques is to enhance the mechanical and biological properties of the grafts preventing the cell-mediated contraction. Crosslinking induces chemical or physical links between the polymer chains of the scaffold and can be achieved by using UV light, dehydrothermal treatment, or treatment with sodium citrate, sodium tripolyphosphate, sulfosuccinic acid, oxalic acid, glutaraldehyde, genipin, or carbodiimide (Lew et al., 2007; Pfeiffer et al., 2008; Jóźwiak et al., 2017; Vining et al., 2019).

Crosslinking can affect several of the cellular functions, including proliferation, differentiation and cellular ability to attach to a scaffold (Davidenko et al., 2015). Kim et al., investigated the effect of different crosslinking techniques on immortalized human corneal epithelial cells, human skin fibroblasts, primary bovine corneal endothelial cells and immortalized human retinal pigment epithelial cells (Kim et al., 2014). The authors reported different toxicity levels with the least toxic being with mononitroalcohols and glyceraldehide, intermediate toxicity being with nitrodiol and nitrotriol, and highest toxicity being with glutaraldehyde, paraformaldehyde, genipin, and bronopol. Several studies have also defined the critical concentration over which the agent induces cytotoxic effect (Wang and Stegemann, 2011; Muzzarelli et al., 2015). On the contrary, some studies suggest that crosslinking can have a positive effect on cellular function. Raucci et al. (2015), studies the effect of citric acid crosslinked cellulose containing hydrogel on the osteogenic differentiation of MSCs. The authors revealed enhanced hydrophilicity and roughness of the hydrogel together with a stimulation of osteogenic differentiation as demonstrated by enhanced expression of bone markers such as osteopontin and osteocalcin. In addition to the direct effect of the crosslinking on MSCs, the physical properties of the extracellular matrix can regulate the response and phenotypes of the cells (Kyle et al., 2019).

Despite many promising studies, to date, there is no gold standard method for cross-linking 3D printed biomimetic materials. In cases where multiple bioinks are used, tuning the scaffold microstructure through crosslinking of multiple biomaterials without affecting its properties will require significant improvement in our 3D printing technology. In tissues where biodegradation or regeneration is required, like for example in 3D bioprinting of bone, the mechanical properties of scaffolds are negatively correlated with their biodegradation profile (Oryan et al., 2018). Finally, one major concern is the potential inflammatory reaction following implantation. It is shown that the cross-linking methods can induce an immune reaction, initiate M1 macrophage response and inhibition of M2 macrophage polarization, reduced cell infiltration, increased proinflammatory cytokine expression and peri-implantation fibrosis (Delgado et al., 2015), which should be carefully considered and solutions devised.

POST-PRINTING

Following 3D printing, cell-laden scaffolds will require incubation prior to implantation. This raises the question of how the nutrients and wastes will be exchanged to support the cells until implantation. For a thin construct, this can be done through a static culture through diffusion; however, functioning vasculature will be required for larger constructs. Dynamic culturing can provide continuous infiltrating flow of medium and/or compressive/tensile loading, which is most beneficial for cartilage and bone tissue engineering (Butler et al., 2009). In case the technology reaches the stage of creating vasculature (Shahabipour et al., 2020), research would be needed to determine if blood would be an adequate medium to facilitate nutrients and waste exchange.

In addition to the nutrient supply, cells will require time to attach onto the scaffold. It has been previously shown that post-fabrication incubation for long periods can increase the mechanical strength of the construct due the function of the cells and further tissue development (Butler et al., 2009). If photopolymerization is used to harden the bioink, it is unknown whether it can cause cytotoxicity due to the photoinitiators and ultraviolet light. Visible light-sensitive photoinitiators are reported to cause less cytotoxicity but this area is poorly explored (Lim et al., 2016; Mondschein et al., 2017).

Future Directions and Conclusion

Three-dimensional bioprinting technology has achieved growing popularity for its favorable potential. There is impressive progress with the pertinent techniques supporting the view that in the near future organ manufacturing will be a reality. Three-dimensional bioprinting can find application in organ and graft transplantation by overcoming the issues of immune rejection and reducing the cost of grafts and could be used to establish platforms for research and drug screening.

MSCs are one of the most popular cell type in tissue engineering and are involved in more than half of the clinical trials since 2000 (Yuan et al., 2019). These cells are most likely to be the main component of 3D bioprinting. In order to preserve and deliver MSCs advantages, it is essential to mimic there *in vivo* microenvironment throughout the 3D biofabrication process (Baker and Chen, 2012). In addition, the availability of nutrients and oxygen remains high and similar to that in the body (Melchels et al., 2010; Ashammakhi et al., 2020). This seems to be the only way for the cells retain their phenotype, adhesion, metabolism, and response signaling (Baker and Chen, 2012).

Despite the great progress we have seen in understanding the biology of target tissues in humans, our knowledge is still based on animal biology. Understanding MSC biology is also crucial and it is in fact the most difficult challenge. This will allow us to direct the efforts creating more physiologically relevant structures. MSCs for example could be used in high densities when creating biomimetic cartilage and bone tissues or in lower densities as supporting cells in other applications. Before, however, we are in a position to discuss such matters we would have to decode our biology in health and disease in humans raises significant ethical issues. Once 3D bioprinting reaches a position of manufacturing complex biomimetic tissues, such as organs and large grafts, an appropriate regulatory framework will be required. Hints that this is imminent are shown in many studies which produced complex grafts. Ethical issues include the ownership of prototypes, the harvesting and type of cells and biomaterials, research as well as commercialization of produced constructs. Regulation in terms of safety is also needed including the biocompatibility of bioinks, long-term safety of grafts and the *ex vivo* manipulation of cells.

The optimal *ex vivo* conditions prior to printing should be established. In our view, minimizing the *ex vivo* journey of the cells is crucial. Harvesting and printing the cells in the same sitting could only be done with knowledge of specific markers for MSC, which we lack at present. This is feasible for other cell types with, such as for example the hematopoietic stem cells, which are currently used without manipulation in cancer patients following whole body irradiation (Bazinet and Popradi, 2019). For MSCs however, at present there is a lack of robust techniques for cell isolation and purification that do not affect MSCs biology and then cell preservation strategies. To this end, one of the major drawbacks is the unavailability of reliable culture media, as current research is merely based on animal derived sera. Serum free media or the use of autologous serum can be an alternative but further research is needed in this matter. In addition, the identification of biomimetic matrices mimicking the native tissue composition and allowing cellular growth and differentiation is required. Finally, conditions under which the 3D constructs will survive following printing potentiate dangers and can jeopardize the whole process. A solution would include developing new bioinks and bioprinters that allow high-resolution fabrication process would diminish the need for post-fabrication culture. Only addressing the aforementioned challenges will safeguard the feasibility and safety of 3D bioprinting for regenerative medicine applications.

AUTHOR CONTRIBUTIONS

LB, NT, HM, AE, NA, and IP contributed to the research, writing, editing and formatting of the manuscript. All authors contributed to the article and approved the submitted version.

FUNDING

AE acknowledges funding from TUBITAK-2219 (1059B19170 0093).

REFERENCES

American Transplant Foundation (2018). *American Transplant Foundation*. Available at: www.americantransplantfoundation.org (accessed November 7, 2019).

Arany, P. R., Shvartsman, D., Huebsch, N., Mao, A. S., Ali, O. A., Bencherif, S. A., et al. (2010). Harnessing traction-mediated manipulation of the cell/matrix interface to control stem-cell fate. *Nat. Mater*. 9, 518–526. doi: 10.1038/nmat2732

Arcaute, K., Mann, B., and Wicker, R. (2006). Stereolithography of three-dimensional bioactive poly(ethylene glycol) constructs with encapsulated cells. *Ann. Biomed. Eng*. 34, 1429–1441. doi: 10.1007/s10439-006-9156-y

Ashammakhi, N., Ahadian, S., Darabi, M. A., El Tahchi, M., Lee, J., Suthiwanich, K., et al. (2019a). Minimally invasive and regenerative therapeutics. *Adv. Mater*. 31:e1804041.

Ashammakhi, N., Hasan, A., Kaarela, O., Byambaa, B., Sheikhi, A., Gaharwar, A. K., et al. (2019b). Advancing frontiers in bone bioprinting. *Adv. Healthc. Mater*. 8:e1801048.

Ashammakhi, N., Ahadian, S., Xu, C., Montazerian, H., Ko, H., Nasiri, R., et al. (2019c). Bioinks and bioprinting technologies to make heterogeneous and biomimetic tissue constructs. *Mater. Today Bio* 1:100008. doi: 10.1016/j.mtbio.2019.100008

Ashammakhi, N., Ahadian, S., Zengjie, F., Suthiwanich, K., Lorestani, F., Orive, G., et al. (2018). Advances and future perspectives in 4D bioprinting. *Biotechnol. J*. 13:e1800148.

Ashammakhi, N., Darabi, M. A., Kehr, N. S., Erdem, A., Hu, S. K., Dokmeci, M. R., et al. (2020). Advances in controlled oxygen generating biomaterials for tissue engineering and regenerative therapy. *Biomacromolecules* 21, 56–72.

Ashammakhi, N., Ndreu, N., and Wimpenny, Y. (2008). Advancing tissue engineering by using electrospun nanofibers. *Regen. Med.* 3, 547–574. doi: 10.2217/17460751.3.4.547

Atala, A., and Yoo, J. J. (2015). *Essentials of 3D Biofabrication and Translation [Internet]*. San Diego, CA: Elsevier Scienc.

Bae, S. W., Lee, K. W., Park, J. H., Lee, J., Jung, C. R., Yu, J., et al. (2018). 3D bioprinted artificial trachea with epithelial cells and chondrogenic-differentiated bone marrow-derived mesenchymal stem cells. *Int. J. Mol. Sci.* 19:1624. doi: 10.3390/ijms19061624

Baker, B. M., and Chen, C. S. (2012). Deconstructing the third dimension – how 3D culture microenvironments alter cellular cues. *J. Cell. Sci.* 125(Pt 13), 3015–3024. doi: 10.1242/jcs.079509

Barron, J., Krizman, D., and Ringeisen, B. (2005). Laser printing of single cells: statistical analysis. *Cell Viabil. Stress* 33, 121–130. doi: 10.1007/s10439-005-8971-x

Barron, J., Wu, P., Ladouceur, H., and Ringeisen, B. (2004). Biological laser printing: a novel technique for creating heterogeneous 3-dimensional cell patterns. *Biomed. Microdev.* 6, 139–147. doi: 10.1023/b:bmmd.0000031751.67267.9f

Bazinet, A., and Popradi, G. (2019). A general practitioner's guide to hematopoietic stem-cell transplantation. *Curr. Oncol.* 26, 187–191.

Bhardwaj, N., and Kundu, S. C. (2010). Electrospinning: a fascinating fiber fabrication technique. *Biotechnol. Adv.* 28, 325–347. doi: 10.1016/j.biotechadv.2010.01.004

Bhuthalingam, R., Lim, P. Q., Irvine, S., Agrawal, A., Mhaisalkar, P., An, J., et al. (2015). A novel 3D printing method for cell alignment and differentiation. *Int. J. Bioprint.* 1, 57–65.

Bieback, K., Kern, S., Klüter, H., and Eichler, H. (2004). Critical parameters for the isolation of mesenchymal stem cells from umbilical cord Blood. *Stem Cells* 22, 625–634. doi: 10.1634/stemcells.22-4-625

Bishop, E. S., Mostafa, S., Pakvasa, M., Luu, H. H., Lee, M. J., Wolf, J. M., et al. (2017). 3-D bioprinting technologies in tissue engineering and regenerative medicine: current and future trends. *Genes Dis.* 4, 185–195. doi: 10.1016/j.gendis.2017.10.002

Blaeser, A., Duarte Campos, D. F., Puster, U., Richtering, W., Stevens, M. M., and Fischer, H. (2016). Controlling shear stress in 3D bioprinting is a key factor to balance printing resolution and stem cell integrity. *Adv. Healthc. Mater.* 5, 326–333. doi: 10.1002/adhm.201500677

Bongso, A., Fong, C.-Y., and Gauthaman, K. (2008). Taking stem cells to the clinic: major challenges. *J. Cell. Biochem.* 105, 1352–1360. doi: 10.1002/jcb.21957

Butler, D. L., Goldstein, S. A., Guldberg, R. E., Guo, X. E., Kamm, R., Laurencin, C. T., et al. (2009). *The Impact of Biomechanics in Tissue Engineering and Regenerative Medicine*. Larchmont, NY: Mary Ann Liebert, Inc.

Byambaa, B., Annabi, N., Yue, K., Trujillo-de Santiago, G., Alvarez, M. M., Jia, W., et al. (2017). Bioprinted osteogenic and vasculogenic patterns for engineering 3D bone tissue. *Adv. Healthc. Mater.* 6:1700015. doi: 10.1002/adhm.201700015

Cao, H., Heazlewood, S. Y., Williams, B., Cardozo, D., Nigro, J., Oteiza, A., et al. (2016). The role of CD44 in fetal and adult hematopoietic stem cell regulation. *Haematologica* 101, 26–37. doi: 10.3324/haematol.2015.135921

Carrow, J. K., Kerativitayanan, P., Jaiswal, M. K., Lokhande, G., and Gaharwar, A. K. (2015). "Chapter 13-polymers for bioprinting," in *Essentials of 3D Biofabrication and Translation*, ed. M. Haley (Amsterdam: Elsevier Inc).

Catros, S., Fricain, J.-C., Guillotin, B., Pippenger, B., Bareille, R., Remy, M., et al. (2011). Laser-assisted bioprinting for creating on-demand patterns of human osteoprogenitor cells and nano-hydroxyapatite. *Biofabrication* 3:025001. doi: 10.1088/1758-5082/3/2/025001

Chang, R., Nam, J., and Sun, W. (2008). Effects of dispensing pressure and nozzle diameter on cell survival from solid freeform fabrication–based direct cell writing. *Tissue Eng. Part A* 14, 41–48. doi: 10.1089/ten.2007.0004

Christensen, K., Xu, C., Chai, W., Zhang, Z., Fu, J., and Huang, Y. (2015). Freeform inkjet printing of cellular structures with bifurcations. *Biotechnol. Bioeng.* 112, 1047–1055. doi: 10.1002/bit.25501

Colwill, J. M., Cultice, J. M., and Kruse, R. L. (2008). Will generalist physician supply meet demands of an increasing and aging population? *Health Aff.* 27, w232–w241.

Cousin, B., Ravet, E., Poglio, S., De Toni, F., Bertuzzi, M., Lulka, H., et al. (2009). Adult stromal cells derived from human adipose tissue provoke pancreatic cancer cell death both in vitro and in vivo. *PLoS One* 4:e6278. doi: 10.1371/journal.pone.0006278

Cui, X., Dean, D., Ruggeri, Z. M., and Boland, T. (2010). Cell damage evaluation of thermal inkjet printed Chinese hamster ovary cells. *Biotechnol. Bioeng.* 106, 963–969. doi: 10.1002/bit.22762

Dababneh, A. B., and Ozbolat, I. T. (2014). Bioprinting technology: a current state-of-the-art review. *J. Manufact. Sci. Eng.* 136:61016.

Daly, A. C., Freeman, F. E., Gonzalez-Fernandez, T., Critchley, S. E., Nulty, J., and Kelly, D. J. (2017). 3D bioprinting for cartilage and osteochondral tissue engineering. *Adv. Healthc. Mater.* 6:1700298. doi: 10.1002/adhm.201700298

Das, S., Pati, F., Choi, Y.-J., Rijal, G., Shim, J.-H., Kim, S. W., et al. (2015). Bioprintable, cell-laden silk fibroin–gelatin hydrogel supporting multilineage differentiation of stem cells for fabrication of three-dimensional tissue constructs. *Acta Biomater.* 11, 233–246. doi: 10.1016/j.actbio.2014.09.023

Davidenko, N., Schuster, C. F., Bax, D. V., Raynal, N., Farndale, R. W., Best, S. M., et al. (2015). Control of crosslinking for tailoring collagen-based scaffolds stability and mechanics. *Acta Biomater.* 25, 131–142. doi: 10.1016/j.actbio.2015.07.034

Delgado, L. M., Bayon, Y., Pandit, A., and Zeugolis, D. I. (2015). To cross-link or not to cross-link? Cross-linking associated foreign body response of collagen-based devices. *Tissue Eng. Part B Rev.* 21, 298–313. doi: 10.1089/ten.teb.2014.0290

Domingos, M., Intranuovo, F., Russo, T., De Santis, R., Gloria, A., Ambrosio, L., et al. (2013). The first systematic analysis of 3D rapid prototyped poly(ε-caprolactone) scaffolds manufactured through BioCell printing: the effect of pore size and geometry on compressive mechanical behaviour and in vitro hMSC viability. *Biofabrication* 5:045004. doi: 10.1088/1758-5082/5/4/045004

Du, M., Chen, B., Meng, Q., Liu, S., Zheng, X., Zhang, C., et al. (2015). 3D bioprinting of BMSC-laden methacrylamide gelatin scaffolds with CBD-BMP2-collagen microfibers. *Biofabrication* 7:044104. doi: 10.1088/1758-5090/7/4/044104

Engler, A. J., Sen, S., Sweeney, H. L., and Discher, D. E. (2006). Matrix elasticity directs stem cell lineage specification. *Cell* 126, 677–689. doi: 10.1016/j.cell.2006.06.044

Freimark, D., Pino-Grace, P., Pohl, S., Weber, C., Wallrapp, C., Geigle, P., et al. (2010). Use of encapsulated stem cells to overcome the bottleneck of cell availability for cell therapy approaches. *Trans. Med. Hemother.* 37, 66–73.

Gao, G., Schilling, A., Hubbell, K., Yonezawa, T., Truong, D., Hong, Y., et al. (2015). Improved properties of bone and cartilage tissue from 3D inkjet-bioprinted human mesenchymal stem cells by simultaneous deposition and photocrosslinking in PEG-GelMA. *Biotechnol. Lett.* 37, 2349–2355. doi: 10.1007/s10529-015-1921-2

Gao, G., Schilling, A. F., Yonezawa, T., Wang, J., Dai, G., and Cui, X. (2014). Bioactive nanoparticles stimulate bone tissue formation in bioprinted three-dimensional scaffold and human mesenchymal stem cells. *Biotechnol. J.* 9, 1304–1311. doi: 10.1002/biot.201400305

Gnecchi, M., and Melo, L. G. (2009). Bone marrow-derived mesenchymal stem cells: Isolation, expansion, characterization, viral transduction, and production of conditioned medium. *Methods Mol. Biol.* 482, 281–294. doi: 10.1007/978-1-59745-060-7_18

Goldring, C. E., Duffy, P. A., Benvenisty, N., Andrews, P. W., Ben-David, U., Eakins, R., et al. (2011). Assessing the safety of stem cell therapeutics. *Cell Stem Cell* 8, 618–628. doi: 10.1016/j.stem.2011.05.012

Gruene, M., Deiwick, A., Koch, L., Schlie, S., Unger, C., Hofmann, N., et al. (2011a). Laser printing of stem cells for biofabrication of scaffold-free autologous grafts. *Tissue Eng. Part C Methods* 17, 79–87. doi: 10.1089/ten.tec.2010.0359

Gruene, M., Pflaum, M., Deiwick, A., Koch, L., Schlie, S., Unger, C., et al. (2011b). Adipogenic differentiation of laser-printed 3D tissue grafts consisting of human adipose-derived stem cells. *Biofabrication* 3:015005. doi: 10.1088/1758-5082/3/1/015005

Guillemot, F., Souquet, A., Catros, S., Guillotin, B., Lopez, J., Faucon, M., et al. (2010a). High-throughput laser printing of cells and biomaterials for tissue engineering. *Acta Biomater.* 6, 2494–2500. doi: 10.1016/j.actbio.2009.09.029

Guillemot, F., Souquet, A., Catros, S., and Guillotin, B. (2010b). Laser-assisted cell printing: principle, physical parameters versus cell fate and perspectives in tissue engineering. *Nanomedicine* 5, 507–515. doi: 10.2217/nnm.10.14

Grungor-Ozkerim, P. S., Inci, I., Zhang, Y. S., Khademhosseini, A., and Dokmeci, M. R. (2018). Bioinks for 3D bioprinting: an overview. *Biomater. Sci.* 6, 915–946.

Heinrich, M. A., Liu, W., Jimenez, A., Yang, J., Akpek, A., Liu, X., et al. (2019). 3D bioprinting: from benches to translational applications. *Small* 15:e1805510.

Hernigou, P., Poignard, A., Beaujean, F., and Rouard, H. (2005a). Percutaneous autologous bone-marrow grafting for nonunions: influence of the number and concentration of progenitor cells. *J. Bone Joint Surg. Am.* 87, 1430–1437. doi: 10.2106/00004623-200507000-00003

Hernigou, P., Poignard, A., Manicom, O., Mathieu, G., and Rouard, H. (2005b). The use of percutaneous autologous bone marrow transplantation in nonunion and avascular necrosis of bone. *J. Bone Joint Surg. Br.* 87, 896–902. doi: 10.1302/0301-620x.87b7.16289

Ho, I. A., Toh, H. C., Ng, W. H., Teo, Y. L., Guo, C. M., Hui, K. M., et al. (2013). Human bone marrow-derived mesenchymal stem cells suppress human glioma growth through inhibition of angiogenesis. *Stem Cells* 31, 146–155. doi: 10.1002/stem.1247

Hopp, B., Smausz, T., Szabó, G., Kolozsvári, L., Kafetzopoulos, D., Fotakis, C., et al. (2012). Femtosecond laser printing of living cells using absorbing film-assisted laser-induced forward transfer. *Opt. Eng.* 51:014302. doi: 10.1117/1.oe.51.1.014302

Huang, W.-H., Chang, M.-C., Tsai, K.-S., Hung, M.-C., Chen, H.-L., and Hung, S.-C. (2013). Mesenchymal stem cells promote growth and angiogenesis of tumors in mice. *Oncogene* 32, 4343–4354. doi: 10.1038/onc.2012.458

Hyeong, J. L., Yong, B. K., Seung, H. A., Ji-Seon, L., Jang, c., Yoon, H., et al. (2015). *A New Approach for Fabricating Collagen/ECM-Based Bioinks Using Preosteoblasts and Human Adipose Stem Cells*. Weinheim: Wiley Subscription Services, Inc.

International Population Reports (2016). *Aging World : 2015: International Population Reports. Series WP;2016 ASI 2546-17.21;Census P95/16-1*. Available online at: https://statistical.proquest.com/statisticalinsight/result/pqpresultpage.previewtitle?docType=PQSI&titleUri=/content/2016/2546-17.21.xml (accessed November 7, 2019).

Irvine, S., Agrawal, A., Lee, B., Chua, H., Low, K., Lau, B., et al. (2015). Printing cell-laden gelatin constructs by free-form fabrication and enzymatic protein crosslinking. *Biomed. Microdev.* 17, 1–8.

Irvine, S. A., and Venkatraman, S. S. (2016). Bioprinting and differentiation of stem cells. *Molecules* 21:1188. doi: 10.3390/molecules21091188

Jakab, K., Norotte, C., Marga, F., Murphy, K., Vunjak-Novakovic, G., Forgacs, G., et al. (2010). Tissue engineering by self-assembly and bio-printing of living cells. *Biofabrication* 2:022001. doi: 10.1088/1758-5082/2/2/022001

Jana, S., and Lerman, A. (2015). Bioprinting a cardiac valve. *Biotechnol. Adv.* 33, 1503–1521. doi: 10.1016/j.biotechadv.2015.07.006

Jóźwiak, T., Filipkowska, U., Szymczyk, P., Rodziewicz, J., and Mielcarek, A. (2017). Effect of ionic and covalent crosslinking agents on properties of chitosan beads and sorption effectiveness of Reactive Black 5 dyeReactive and Functional Polymers. *Reacti. Funct. Polym.* 114, 58–74. doi: 10.1016/j.reactfunctpolym.2017.03.007

Kang, H.-W., Lee, S. J., Ko, I. K., Kengla, C., Yoo, J. J., and Atala, A. (2016). A 3D bioprinting system to produce human-scale tissue constructs with structural integrity. *Na.t Biotechnol.* 34, 312–319. doi: 10.1038/nbt.3413

Kang, L., Armstrong, P., Lee, L., Duan, B., Kang, K., and Butcher, J. (2017). Optimizing photo-encapsulation viability of heart valve cell types in 3D printable composite hydrogels. *Ann. Biomed. Eng.* 45, 360–377. doi: 10.1007/s10439-016-1619-1

Katz, A. J., Tholpady, A., Tholpady, S. S., Shang, H., and Ogle, R. C. (2005). Cell surface and transcriptional characterization of human adipose-derived adherent stromal (hADAS) cells. *Stem Cells* 23, 412–423. doi: 10.1634/stemcells.2004-0021

Keriquel, V., Oliveira, H., Rémy, M., Ziane, S., Delmond, S., Rousseau, B., et al. (2017). In situ printing of mesenchymal stromal cells, by laser-assisted bioprinting, for in vivo bone regeneration applications. *Sci. Rep.* 7:1778.

Khakoo, A. Y., Pati, S., Anderson, S. A., Reid, W., Elshal, M. F., Rovira, I. I., et al. (2006). Human mesenchymal stem cells exert potent antitumorigenic effects in a model of Kaposi's sarcoma. *J. Exp. Med.* 203, 1235–1247. doi: 10.1084/jem.20051921

Khalil, S., and Sun, W. (2009). Bioprinting endothelial cells with alginate for 3D tissue constructs. *J. Biomech. Eng.* 131:111002.

Kim, M., Takaoka, A., Hoang, Q. V., Trokel, S. L., and Paik, D. C. (2014). Pharmacologic alternatives to riboflavin photochemical corneal cross-linking: a comparison studyof cell toxicity thresholds. *Invest. Ophthalmol. Vis. Sci.* 55, 3247–3257. doi: 10.1167/iovs.13-13703

Koch, L., Kuhn, S., Sorg, H., Gruene, M., Schlie, S., Gaebel, R., et al. (2010). Laser printing of skin cells and human stem cells. *Tissue Eng. Part C Methods* 16, 847–854. doi: 10.1089/ten.tec.2009.0397

Kucerova, L., Matuskova, M., Hlubinova, K., Altanerova, V., and Altaner, C. (2010). Tumor cell behaviour modulation by mesenchymal stromal cells. *Mol. Cancer* 9:129. doi: 10.1186/1476-4598-9-129

Kuznetsov, S. A., Mankani, M. H., Gronthos, S., Satomura, K., Bianco, P., and Robey, P. G. (2001). Circulating skeletal stem cells. *J. Cell Biol.* 153, 1133–1140.

Kyle, H. V., Stafford, A., and Mooney, D. J. (2019). Sequential modes of crosslinking tune viscoelasticity of cell-instructive hydrogels. *Biomaterials* 188, 187–197. doi: 10.1016/j.biomaterials.2018.10.013

Lane, S. W., Williams, D. A., and Watt, F. M. (2014). Modulating the stem cell niche for tissue regeneration. *Nat. Biotechnol.* 32, 795–803. doi: 10.1038/nbt.2978

Langer, R., and Vacanti, J. P. (1993). Tissue engineering. *Science* 260, 920–926.

Leberfinger, A. N., Ravnic, D. J., Dhawan, A., and Ozbolat, I. T. (2017). Concise review: bioprinting of stem cells for transplantable tissue fabrication. *pISSN* 6, 1940–1948. doi: 10.1002/sctm.17-0148

Lee, H. J., Kim, Y. B., Ahn, S. H., Lee, J., Jang, C. H., Yoon, H., et al. (2015). A new approach for fabricating collagen/ECM-based bioinks using preosteoblasts and human adipose stem cells. *Adv. Healthc. Mater.* 4, 1359–1368. doi: 10.1002/adhm.201500193

Levato, R., Visser, J., Planell, J. A., Engel, E., Malda, J., and Mateos-Timoneda, M. A. (2014). Biofabrication of tissue constructs by 3D bioprinting of cell-laden microcarriers. *Biofabrication* 6:035020. doi: 10.1088/1758-5082/6/3/035020

Lew, D. H., Liu, P. H., and Orgill, D. P. (2007). Optimization of UV cross-linking density for durable and nontoxic collagen gag dermal substitute. *J. Biomed. Mater. Res. B Appl. Biomater.* 82, 51–56. doi: 10.1002/jbm.b.30704

Li, J., Chen, M., Fan, X., and Zhou, H. (2016). Recent advances in bioprinting techniques: approaches, applications and future prospects. *J. Transl. Med.* 14:271.

Lim, K. S., Schon, B. S., Mekhileri, N. V., Brown, G. C. J., Chia, C. M., Prabakar, S., et al. (2016). New visible-light photoinitiating system for improved print fidelity in gelatin-based bioinks. *ACS Biomater. Sci. Eng.* 2, 1752–1762. doi: 10.1021/acsbiomaterials.6b00149

Mackay, A. M., Beck, S. C., Murphy, J. M., Barry, F. P., Chichester, C. O., Pittenger, M. F., et al. (1998). Chondrogenic differentiation of cultured human mesenchymal stem cells from marrow. *Tissue Eng.* 4, 415–428.

Maher. P., Keatch, R., Donnelly, K., Mackay, R., and Paxton, J. (2009). Construction of 3D biological matrices using rapid prototyping technology. *Rapid Prototyp. J.* 15, 204–210. doi: 10.1108/13552540910960307

Mairim, A. S., Chen, Y. H., Wong, T. Y., Bittencourt, V., Lin, Y. C., and Huang, L. (2012). Hyaluronan regulates cell behavior: A potential niche matrix for stem cells. *Biochem. Res. Int.* 2012:346972-11. doi: 10.1155/2012/346972

Mandrycky, C., Wang, Z., Kim, K., and Kim, D. -H. (2016). 3D bioprinting for engineering complex tissues. *Biotechnol. Adv.* 34, 422–434. doi: 10.1016/j.biotechadv.2015.12.011

Matsiko, A., Gleeson, J. P., and O'Brien, F. J. (2015). Scaffold mean pore size influences mesenchymal stem cell chondrogenic differentiation and matrix deposition. *Tissue Eng. Part A* 21, 486–497. doi: 10.1089/ten.tea.2013.0545

Melchels, F. P., Barradas, A. M., van Blitterswijk, C. A., de Boer, J., Feijen, J., Grijpma, D. W., et al. (2010). Effects of the architecture of tissue engineering scaffolds on cell seeding and culturing. *Acta Biomater.* 6, 4208–4217. doi: 10.1016/j.actbio.2010.06.012

Minteer, D., Marra, K. G., and Rubin, J. P. (2013). Adipose-derived mesenchymal stem cells: biology, and potential applications. *Adv. Biochem. Eng. Biotechnol.* 129, 59–71. doi: 10.1007/10_2012_146

Mondschein, R. J., Kanitkar, A., Williams, C. B., Verbridge, S. S., Long, T. E., et al. (2017). Polymer structure-property requirements for stereolithographic 3D printing of soft tissue engineering scaffolds. *Biomaterials* 140, 170–188. doi: 10.1016/j.biomaterials.2017.06.005

Murphy, S. V., and Atala, A. (2014). 3D bioprinting of tissues and organs. *Nat. Biotechnol.* 32, 773–785. doi: 10.1038/nbt.2958

Muzzarelli, R. A., El Mehtedi, M., Bottegoni, C., Aquili, A., and Gigante, A. (2015). Genipin-crosslinked chitosan gels and scaffolds for tissue engineering and regeneration of cartilage and bone. *Mar. Drugs* 13, 7314–7338. doi: 10.3390/md13127068

Nakamura, M., Kobayashi, A., Takagi, F., Watanabe, A., Hiruma, Y., Ohuchi, K., et al. (2005). Biocompatible inkjet printing technique for designed seeding of individual living Cells. *Tissue Eng.* 11, 1658–1666. doi: 10.1089/ten.2005.11.1658

Ong, C. S., Yesantharao, P., Huang, C. Y., Mattson, G., Boktor, J., Fukunishi, T., et al. (2018). 3D bioprinting using stem cells. *Pediatr. Res.* 83, 223–231. doi: 10.1038/pr.2017.252

Oryan, A., Kamali, A., Moshiri, A., Baharvand, H., and Daemi, H. (2018). Chemical crosslinking of biopolymeric scaffolds: current knowledge and future directions of crosslinked engineered bone scaffolds. *Int. J. Biol. Macromol.* 107(Pt A):678–688. doi: 10.1016/j.ijbiomac.2017.08.184

Ozbolat, I. T., and Hospodiuk, M. (2015). Current advances and future perspectives in extrusion-based bioprinting. *Biomaterials* 76, 321–343. doi: 10.1016/j.biomaterials.2015.10.076

Parvin, S., Noorjahan, B. A., Abdul, M. A., Abdul, R. O., Maryam, M., Ehsan, J., et al. (2012). Comparison of different methods for the isolation of mesenchymal stem cells from human umbilical cord Wharton's jelly. *In Vitro Cell Dev. Biol. Anim.* 48, 75–83. doi: 10.1007/s11626-011-9480-x

Perrot, P., Rousseau, J., Bouffaut, A. L., Rédini, F., Cassagnau, E., Deschaseaux, F., et al. (2010). Safety concern between autologous fat graft, mesenchymal stem cell and osteosarcoma recurrence. *PLoS One* 5:e10999. doi: 10.1371/journal.pone.0010999

Pfeiffer, E., Vickers, S. M., Frank, E., Grodzinsky, A. J., and Spector, M. (2008). The effects of glycosaminoglycan content on the compressive modulus of cartilage engineered in type II collagen scaffolds. *Osteoarthr. Cartil.* 16, 1237–1244. doi: 10.1016/j.joca.2008.02.014

Phillippi, J. A., Miller, E., Weiss, L., Huard, J., Waggoner, A., Campbell, P., et al. (2008). Microenvironments engineered by inkjet bioprinting spatially direct adult stem cells toward muscle- and bone-like subpopulations. *Stem Cells* 26, 127–134. doi: 10.1634/stemcells.2007-0520

Pintus, E., Baldassarri, M., Perazzo, L., Natali, S., Ghinelli, D., Buda, R., et al. (2018). Stem cells in osteochondral tissue engineering. *Adv. Exp. Med. Biol.* 1058, 359–372. doi: 10.1007/978-3-319-76711-6_16

Porada, C., Zanjani, E. D., and Almeida-Porad, G. (2006). Adult mesenchymal stem cells: a pluripotent population with multiple applications. *Stem Cell Res. Ther.* 1, 365–369. doi: 10.2174/157488806778226821

Pountos, I., Corscadden, D., Emery, P., and Giannoudis, P. V. (2007). Mesenchymal stem cell tissue engineering: Techniques for isolation, expansion and application. *Injury* 38:S33. doi: 10.1016/S0020-1383(08)70006-8

Qi, D., Wu, S., Kuss, M. A., Shi, W., Chung, S., Deegan, P. T., et al. (2018). Mechanically robust cryogels with injectability and bioprinting supportability for adipose tissue engineering. *Acta Biomater.* 74, 131–142. doi: 10.1016/j.actbio.2018.05.044

Rak Kwon, D., Jung, S., Jang, J., Park, G. Y., Suk Moon, Y., Lee, S. C., et al. (2020). A 3-dimensional bioprinted scaffold with human umbilical cord blood-mesenchymal stem cells improves regeneration of chronic full-thickness rotator cuff tear in a rabbit model. *Am. J. Sports Med.* 48, 947–958. doi: 10.1177/0363546520904022

Raman, R., Bhaduri, B., Mir, M., Shkumatov, A., Lee, M. K., Popescu, G., et al. (2016). High-resolution projection microstereolithography for patterning of neovasculature. *Adv. Healthcare Mater.* 5, 610–619. doi: 10.1002/adhm.201500721

Raucci, M. G., Alvarez-Perez, M. A., Demitri, C., Giugliano, D., De Benedictis, V., Sannino, A., et al. (2015). Effect of citric acid crosslinking cellulose-based hydrogels on osteogenic differentiation. *J. Biomed. Mater. Res. A.* 103, 2045–2056. doi: 10.1002/jbm.a.35343

Rowlands, A. S., George, P. A., and Cooper-White, J. J. (2008). Directing osteogenic and myogenic differentiation of MSCs: interplay of stiffness and adhesive ligand presentation. *Am. J. Physiol. Cell Physiol.* 295, 1037–1044. doi: 10.1152/ajpcell.67.2008

Rubio, D., Garcia-Castro, J., Martin, M. C., de la Fuente, R., Cigudosa, J. C., Lloyd, A. C., et al. (2005). Spontaneous human adult stem cell transformation. *Cancer Res.* 65, 3035–3039. doi: 10.1158/0008-5472.CAN-04-4194

Ryu, S., Yoo, J., Jang, Y., Jin, H., Jung, SY., Park, J., et al. (2015). Nanothin coculture membranes with tunable pore architecture and thermoresponsive functionality for transfer-printable stem cell-derived cardiac sheets. *ACS Nano* 9, 10186–10202. doi: 10.1021/acsnano.5b03823

Sasaki, M., Abe, R., Fujita, Y., Ando, S., Inokuma, D., and Shimizu, H. (2008). Mesenchymal stem cells are recruited into wounded skin and contribute to wound repair by trans differentiation into multiple skin cell type. *J. Immunol.* 180, 2581–2587. doi: 10.4049/jimmunol.180.4.2581

Saunders, R. E., Gough, J. E., and Derby, B. (2007). Delivery of human fibroblast cells by piezoelectric drop-on-demand inkjet printing. *Biomaterials* 29, 193–203. doi: 10.1016/j.biomaterials.2007.09.032

Seetharam, R. (1991). "Purification and analysis of recombinant proteins," in *Bioprocess Technology* (New York, NY: Dekker).

Shav, D., and Einav, S. (2010). The effect of mechanical loads in the differentiation of precursor cells into mature cells. *Ann. N. Y. Acad. Sci.* 1188, 25–31. doi: 10.1111/j.1749-6632.2009.05079.x

Shahabipour, F., Ashammakhi, N., Oskuee, R. K., Bonakdar, S., Hoffman, T., Shokrgozar, M. A., et al. (2020). Key components of engineering vascularized 3-dimensional bioprinted bone constructs. *Transl Res.* 216, 57–76 doi: 10.1016/j.trsl.2019.08.010

Skardal, A., and Atala, A. (2015). Biomaterials for Integration with 3-D Bioprinting. *Biomed. Eng.* 43, 730–746. doi: 10.1007/s10439-014-1207-1

Sotiropoulou, P. A., Perez, S. A., Salagianni, M., Baxevanis, C. N., and Papamichail, M. (2006). Characterization of the optimal culture conditions for clinical scale production of human mesenchymal stem cells. *Stem Cells* 24, 462–471. doi: 10.1634/stemcells.2004-0331

Stolberg, S., and McCloskey, K. E. (2009). Can shear stress direct stem cell fate? *Cell Culture Tissue Eng.* 25, 10–19. doi: 10.1002/btpr.124

Suzuki, K., Sun, R., Origuchi, M., Kanehira, M., Takahata, T., Itoh, J., et al. (2011). "Mesenchymal stromal cells promote tumor growth through the enhancement of neovascularization," in *Molecular Medicine,* Vol. 17 (Cambridge, MA), 579–587. doi: 10.2119/molmed.2010.00157

Tasnim, N., De la Vega, L., Kumar, S. A., Abelseth, L., Matthew Alonzo, M., et al. (2018). 3D bioprinting stem cell derived tissues. *Cell Mol. Bioeng.* 11, 219–240. doi: 10.1007/s12195-018-0530-2

Thompson, W. R., Rubin, J., and Rubin, C. T. (2012). Mechanical regulation of signaling pathways in bone. *Gene* 503, 179–193. doi: 10.1016/j.gene.2012.04.076

Trombetta, R., Inzana, J., Schwarz, E., Kates, S., and Awad, H. (2017). 3D printing of calcium phosphate ceramics for bone tissue engineering and drug delivery. *Ann. Biomed. Eng.* 45, 23–44. doi: 10.1007/s10439-016-1678-3

Trounson, A., and McDonald, C. (2015). Stem cell therapies in clinical trials: Progress and challenges. *Cell Stem Cell* 17, 11–22. doi: 10.1016/j.stem.2015.06.007

Tsai, M. S., Lee, J. L., Chang, Y. J., and Hwang, S. M. (2004). Isolation of human multipotent mesenchymal stem cells from second-trimester amniotic fluid using a novel two-stage culture protocol. *Hum. Reprod.* 19, 1450–1456. doi: 10.1093/humrep/deh279

Tsuji, K., Ojima, M., Otabe, K., Horie, M., Koga, H., Sekiya, I., et al. (2017). Effects of different cell-detaching methods on the viability and cell surface antigen expression of synovial mesenchymal stem cells. *Cell Transplant.* 26, 1089–1102. doi: 10.3727/096368917X694831

Tuszynski, M. H., Wang, Y., Graham, L., Gao, M., Wu, D., Brock, J., et al. (2014). Neural stem cell dissemination after grafting to CNS injury sites. *Cell* 156, 388–389. doi: 10.1016/j.cell.2014.01.016

Vining, K. H., Stafford, A., and Mooney, D. J. (2019). Sequential modes of crosslinking tune viscoelasticity of cell-instructive hydrogels. *Biomaterials* 188, 187–197. doi: 10.1016/j.biomaterials.2018.10.013

Visser, J., Melchels, F., and Jeon, J. (2015). Reinforcement of hydrogels using three-dimensionally printed microfibres. *Nat. Commun.* 6:6933. doi: 10.1038/ncomms7933

Wang, H. L., Zuo, Y., Li, Y., Ma, J., and Cheng, S. L. (2007). Biocompatibility and osteogenesis of biomimetic nano-hydroxyapatite/polyamide composite scaffolds for bone tissue engineering. *Biomaterials* 28, 3338–3348. doi: 10.1016/j.biomaterials.2007.04.014

Wang, L., and Stegemann, J. P. (2011). Glyoxal crosslinking of cell-seeded chitosan/collagen hydrogels for bone regeneration. *Acta Biomater*. 7, 2410–2417. doi: 10.1016/j.actbio.2011.02.029

Wang, Z., Abdulla, R., Parker, B., Samanipour, R., Ghosh, S., and Kim, K. (2015). A simple and high-resolution stereolithography-based 3D bioprinting system using visible light crosslinkable bioinks. *Biofabrication* 7:045009. doi: 10.1088/1758-5090/7/4/045009

Willerth, S. M., and Sakiyama-Elbert, S. (2008). Cell therapy for spinal cord regeneration. *Drug. Deliv. Rev.* 60, 263–276. doi: 10.1016/j.addr.2007.08.028

Wüst, S., Godla, M. E., Müller, R., and Hofmann, S. (2014). Tunable hydrogel composite with two-step processing in combination with innovative hardware upgrade for cell-based three-dimensional bioprinting. *Acta Biomater.* 10, 630–640. doi: 10.1016/j.actbio.2013.10.016

Wüst, S., Müller, R., and Hofmann Boss, S. S. (2011). Controlled positioning of cells in biomaterials – approaches towards 3D tissue printing. *J. Funct. Biomater.* 2:119.

Xu, T., Jin, J., Gregory, C., Hickman, J. J., and Boland, T. (2005). Inkjet printing of viable mammalian cells. *Biomaterials* 26, 93–99. doi: 10.1016/j.biomaterials.2004.04.011

Yanagi, Y., Nakayama, K., Taguchi, T., Enosawa, S., Tamura, T., Yoshimaru, K., et al. (2017). *In vivo* and *ex vivo* methods of growing a liver bud through tissue connection. *Sci. Rep.* 7:14085. doi: 10.1038/s41598-017-14542-2

Young, H. E., Mancini, M. L., Wright, R. P., Smith, J. C., Black, A. C. Jr, Reagan, C. R., et al. (1995). Mesenchymal stem cells reside within the connective tissues of many organs. *Dev. Dyn.* 202, 137–144. doi: 10.1002/aja.1002020205

Yuan, X., Logan, T. M., and Ma, T. (2019). Metabolism in human mesenchymal stromal cells: A missing link between hMSC Biomanufacturing and therapy? *Front. immunol.* 10:977. doi: 10.3389/fimmu.2019.00977

Zhao, Y., Li, Y., Mao, S., Sun, W., and Yao, R. (2015). The influence of printing parameters on cell survival rate and printability in microextrusion-based 3D cell printing technology. *Biofabrication* 7:045002. doi: 10.1088/1758-5090/7/4/045002

Zhao, Y., Yao, R., Ouyang, L., Ding, H., Zhang, T., Zhang, K., et al. (2014). Three-dimensional printing of Hela cells for cervical tumor model *in vitro*. *Biofabrication* 6:035001. doi: 10.1088/1758-5082/6/3/035001

Conflict of Interest: The authors declare that the research was conducted in the absence of any commercial or financial relationships that could be construed as a potential conflict of interest.

frontiers in Bioengineering and Biotechnology

ORIGINAL RESEARCH
published: 23 October 2020
doi: 10.3389/fbioe.2020.557215

3D Printed Polyurethane Scaffolds for the Repair of Bone Defects

Megan E. Cooke[1,2†], **Jose L. Ramirez-GarciaLuna**[2,3†], **Karla Rangel-Berridi**[2,3], **Hyeree Park**[4], **Showan N. Nazhat**[4], **Michael H. Weber**[1,2], **Janet E. Henderson**[2,3] and **Derek H. Rosenzweig**[1,3*]

[1] Biofabrication Laboratory, Research Institute of McGill University Health Centres, McGill University, Montreal, QC, Canada, [2] Department of Surgery, McGill University, Montreal, QC, Canada, [3] Bone Engineering Labs, Injury, Repair & Recovery Program, Research Institute McGill University Health Centres, McGill University, Montreal, QC, Canada, [4] Department of Mining and Materials Engineering, McGill University, Montreal, QC, Canada

Critical-size bone defects are those that will not heal without intervention and can arise secondary to trauma, infection, and surgical resection of tumors. Treatment options are currently limited to filling the defect with autologous bone, of which there is not always an abundant supply, or ceramic pastes that only allow for limited osteo-inductive and -conductive capacity. In this study we investigate the repair of bone defects using a 3D printed LayFomm scaffold. LayFomm is a polymer blend of polyvinyl alcohol (PVA) and polyurethane (PU). It can be printed using the most common method of 3D printing, fused deposition modeling, before being washed in water-based solutions to remove the PVA. This leaves a more compliant, micro-porous PU elastomer. *In vitro* analysis of dental pulp stem cells seeded onto macro-porous scaffolds showed their ability to adhere, proliferate and form mineralized matrix on the scaffold in the presence of osteogenic media. Subcutaneous implantation of LayFomm in a rat model showed the formation of a vascularized fibrous capsule, but without a chronic inflammatory response. Implantation into a mandibular defect showed significantly increased mineralized tissue production when compared to a currently approved bone putty. While their mechanical properties are insufficient for use in load-bearing defects, these findings are promising for the use of polyurethane scaffolds in craniofacial bone regeneration.

Keywords: mandibular defect, bone regeneration, polyurethane, 3D printing, layfomm, fused depositing modeling (FDM)

OPEN ACCESS

Edited by:
Luciano Vidal,
Institut National de la Santé et de la Recherche Médicale (INSERM), France

Reviewed by:
Pinar Yilgor Huri,
Ankara University, Turkey
Patricia Diaz-Rodriguez,
University of La Laguna, Spain

***Correspondence:**
Derek H. Rosenzweig
derek.rosenzweig@mcgill.ca

[†] *These authors have contributed equally to this work*

Specialty section:
This article was submitted to Biomaterials, a section of the journal Frontiers in Bioengineering and Biotechnology

Received: *29 April 2020*
Accepted: *18 September 2020*
Published: *23 October 2020*

Citation:
Cooke ME, Ramirez-GarciaLuna JL, Rangel-Berridi K, Park H, Nazhat SN, Weber MH, Henderson JE and Rosenzweig DH (2020) 3D Printed Polyurethane Scaffolds for the Repair of Bone Defects. Front. Bioeng. Biotechnol. 8:557215. doi: 10.3389/fbioe.2020.557215

1. INTRODUCTION

Critical sized bone defects are those that will not heal spontaneously, without intervention (Lichte et al., 2011). They can arise through trauma, poor fracture healing, and bone removal following severe infection or tumor resection. The current gold standard of treatment is to reconstruct the defect with autologous bone from a different region of the skeleton and to stabilize with ridged implants fixed to the bone. This has limitations including the amount of bone available for transfer without causing donor site morbidity, and increased risk of infection (Fairag et al., 2019). An alternative strategy for long term implantation, which has been used clinically, is to fill the defects with ceramic or resin-based pastes and to then secure them with implantable plates and screws (Williams, 2008). While pastes solidify to provide structural support for surrounding tissues, they are very dense materials and allow limited (if any) growth of new bone into the defect for repair

(Lichte et al., 2011). The ideal scaffold is one which will provide initial structural support to the defect site and then be gradually degraded and replaced by newly formed bone.

The use of additive manufacturing (AM) is rapidly increasing in healthcare, particularly in the fields of dentistry and orthopedics (Liu et al., 2014; Dawood et al., 2015; Rosenzweig et al., 2015; Fairag et al., 2019). A key benefit of this approach is the potential for personalized implants. By reconstructing 3D scans of bony defects and reverse-engineering the damaged site, an implant can be produced of exact dimensions to repair the defect (Cox et al., 2016). There are numerous techniques and materials available such that metals, ceramics, and polymers can all be additively manufactured for orthopedic applications (Ahangar et al., 2019). This study investigates the use of fused deposition modeling (FDM) for bone reconstruction. This technique uses thermoplastics, usually supplied in filament form, that are heated directly before extrusion and then quickly cooled to solidify on the print bed (Zein et al., 2002). The hardware and materials for FDM are now readily available at relatively low cost and represent an economically viable technique to produce customized implants. A further advantage is the level of control over design parameters. For example, materials, macro-porosity and infill geometry can all be refined such that the scaffold can be tuned in terms of cell adhesion, cell infiltration, and stiffness, respectively (Nyberg et al., 2016).

LayFomm (PoroLay) is a polymer blend of polyvinyl alcohol (PVA) and polyurethane (PU). It is commercially available in 1.75 mm filament and can be printed at 215–225 °C . Following printing, washing in water removes the water-soluble PVA, leaving a highly porous PU elastomer (Belka et al., 2017; Ahangar et al., 2018). This material has been used previously by our group to deliver therapeutic agents (Ahangar et al., 2018; Akoury et al., 2019). In this study we first investigated the use of LayFomm as a scaffolding material for the *in vitro* differentiation of dental pulp stem cells (DPSCs) and subsequent production of bone-like matrix. We then implanted the same material subcutaneously to determine the foreign body response to the material. Finally, scaffolds were implanted into mandibular defects in an *in vivo* rodent model to determine the potential for bony ingrowth and healing of the defect compared to a commercially available Norian cement used in craniofacial defects.

2. MATERIALS AND METHODS

2.1. Preparation of Scaffolds

Scaffold blanks measuring 3 × 3 × 50 mm were designed in TinkerCAD (Autodesk, San Rafael, CA). For *in vitro* assessment and subcutaneous implantation they were designed with a central cavity of 750 μm with macropores in the walls measuring 750 μm in diameter every 5 mm. For mandibular implantation, there were no macropores. The models were exported as .stl files and sliced using Slicr3D. The blanks were printed with LayFomm60 (PoroLay Filaments, Germany) using a Duplicator i3 (Wanhao, China) using the following parameters: nozzle diameter 0.4 mm; nozzle temperature 215°C; print bed temperature 45°C; layer height 0.2 mm, print speed 10 mm.s^{-1}. Following printing, individual scaffolds were cut from the blank to 5 mm lengths before being washed in dH$_2$O four times to remove the water-soluble PVA. For cell seeding and implantation, scaffolds were disinfected by submersion in 70% ethanol for 4 h, followed by UV light exposure to each side for 20 min.

2.2. Scaffold Characterization

2.2.1. LayFomm Filament Characterization

The composition of the LayFomm60 material is proprietary so to estimate the percentage of PVA and PU present, small pieces of filament were cut, weighed and then incubated at 37°C in dH$_2$O for up to 28 days ($n = 4$ for each timepoint). Following incubation, excess water was removed using a kimwipe before weighing to determine "wet" weight to account for swelling. They were then dried for 24 h at 37°C before the "dry" weight was recorded. The change in weight was then calculated to determine when there was no further change.

2.2.2. Mechanical Testing

3 mm long samples were loaded, perpendicular to the long fiber orientation, in unconfined compression at a rate of 0.045 mm.s^{-1} to 40% strain using a Mini Bionix 858 (MTS, Eden Prairie, MN). Compressive modulus was then calculated between 8 and 10% strain in the linear region of the curve.

2.2.3. Scanning Electron Microscopy

Acellular samples were dehydrated through increasing concentrations of ethanol (70-80-90-95-100%) and then hexamethyldisilazane (HDMS, Sigma Aldrich, Oakville, ON) to dry overnight. Cell-seeded samples were fixed with 4% paraformaldehyde (PFA, Sigma Aldrich) for 1 h and then dehydrated through ethanol as above before being critical point dried using CO$_2$ in a 030 CPD (Leica Microsystems, Richmond Hill, ON). Samples were coated with a 4 nm layer of platinum using a ACE600 high resolution sputter coater (Leica Microsystems) before being imaged using an FEI Quanta 450 ESEM (Thermo Fisher, Saint Laurent, QC).

2.3. *In vitro* Analysis of Scaffolds

2.3.1. Seeding of Dental Pulp Stem Cells (DPSCs)

After disinfecting, as described previously, scaffolds were placed in sterile phosphate buffered saline (PBS, Sigma Aldrich) to maintain hydration. As previously reported (Fairag et al., 2019), 4 × 10^5 DPSCs were suspended in 500 μL media and placed in a capped 3 mL syringe with two scaffolds. They were turned every 30 min for 2 h to ensure even coating of the scaffolds. After 2 h, scaffolds were moved into well plates, the excess media was centrifuged and cells that did not adhere were counted using a haemocytometer to determine seeding efficiency. Cell-seeded scaffolds were cultured in non-adherent multi-well plates with either control [high glucose DMEM (Sigma Aldrich) with pyruvate, glutamine and sodium bicarbonate with 1% Penicillin-Streptomycin (Gibco, Thermo Fisher), 10% heat-inactivated fetal bovine serum (Gibco) and 50 μg/ml ascorbic acid (Sigma Aldrich)] or osteogenic, OG (control media supplemented with 10 nM dexamethasone and 5 mM β-glycerol-2-phosphate) media. Cells were cultured on scaffolds for 21 days and media was changed twice weekly.

2.3.2. Live/Dead Assay

After 21 days of culture, scaffolds were removed from media and washed with PBS. A 2 μM Calcein-AM, 4 μM Ethidium homodimer-1 (Invitrogen, Thermo Fisher) solution was prepared in PBS and applied to each scaffold for 15 min. Scaffolds were transferred to glass slides and imaged using an EVOS M5000 imaging system (ThermoFisher). Composite images were produced using ImageJ (NIH, Bethesda, MD).

2.3.3. Crysectioning and Histology

Following live/dead imaging, samples were washed in PBS and then fixed in 4% PFA for 1 hr. They were then submerged in increasing concentrations of sucrose (10-20-30%) before being embedded in OCT (TissueTek, Sakura, Canada). When confident there were no bubbles in samples, they were snap frozen at -80°C. Gelatin-coated slides were prepared by dipping clean slides in a solution of 5% gelatin with 0.05% chromium potassium sulfate dodecadhydrate (Sigma Aldrich) before drying overnight. 10 μm sections were prepared using a CM1950 cryostat (Leica). Von Kossa, Alizarin Red (1% solution, Sigma Aldrich) and Safranin-O/Fast Green staining were then performed. Samples were mounted with Permount (Fisher Scientific) and imaged using an Axioskop 40 microscope with a high-resolution camera (Carl Zeiss, ON, Canada).

2.4. *In vivo* Implantation of Scaffolds

2.4.1. Animal Maintenance

Live animal procedures were conducted in accordance with a protocol approved by the Facility Animal Care Committee of McGill University (AUP-7815) in keeping with the guidelines of the Canada Council on Animal Care, as previously described (Jabbour et al., 2014). Six- to eight-month-old male Sprague Dawley rats (Charles River laboratories, Senneville, QC, Canada) were caged individually and weighed weekly with unrestricted access to food and water.

2.4.2. Subcutaneous Scaffold Implantation and Analysis

3 mm long × 2mm tall × 1 mm wide LayFomm scaffolds with 750 μm pores were 3D printed and disinfected as described previously (section 2.1). The scaffolds were inserted subcutaneously in the dorsum of four anesthetized rats between the shoulder blades through a 1 mm incision 5 mm away from the scaffold's final resting site. The incision was sutured using 4-0 PDS-II thread and the animals received 20 mg/kg/24 h carprofen for pain control for 3 days postoperatively. The scaffold was left undisturbed in place for 6 weeks after insertion.

Animals were euthanized by CO_2 asphyxiation under anesthesia before the scaffolds, surrounding tissue and overlying skin were collected. They were fixed overnight with 4% PFA at 4°C, washed three times with cold PBS and embedded in paraffin for histological analysis. Five micron thick sections were prepared from the mid-sagittal point of the scaffold and stained with hematoxylin–eosin (H&E, Thermofisher - cat SH26-500D and cat 245-658, Waltham, MA, USA) to assess general morphology, and immunostained with alpha-smooth muscle actin (α-SMA, 1:300, abcam - cat 5694, ON, Canada), CD34 (1:300, abcam - cat ab23830), CD86 (1:300, abcam - cat ab238468) and Arginase-1 (1:300, Santa cruz - cat sc 271430, USA) to visualize fibrous tissues, vascular channels, M1 and M2 macrophages, respectively, using previously described methodology (Ramirez-Garcia-Luna et al., 2019). Images were captured with a Zeiss Axioskop 40 microscope (Carl Zeiss).

2.5. Mandibular Scaffold Implantation and Analyses

After 1-week of acclimatization, rats ($n = 6$) were anesthetized and the first molar was extracted on both sides. After a 4-week healing period, rats were randomly assigned to either LayFomm or Norian CRS putty (Kensey Nash, PA) implantation on each hemi-mandible. Norian CRS putty is a calcium phosphate bone cement clinically used for cranial repair and as such was deemed a clinically relevant comparator. The animals were again anesthetized to generate defects measuring 5 mm (sagittal) × 2 mm (frontal) × 3 mm (transverse) in the left and right mandibles using a 1 mm spherical burr (Stryker, Canada). All surgical procedures were performed with minimal trauma to preserve as much as possible the integrity of soft and hard tissues. Bone shards were washed away with gentle irrigation and either a 5 × 2 × 3 mm LayFomm scaffold (printed without macropores) or Norian CRS putty was inserted into the defects. A total volume of 100 μL per defect were used to fill the void by press fitting the putty into it. The residual cement was gently wiped with gauze, ensuring the void remained full. LayFomm scaffolds were press-fitted into the defects. In both cases, the gums were sutured to maintain the materials in place. All rats were given soft food (DietGel Recovery, ClearH2O, ME) *ad libitum* and 20 mg/kg/24 h carprofen for pain control for 3 days postoperatively. Rats were then switched back to regular chow and maintained for 6 weeks. Immediately after animal euthanasia, by CO_2 asphyxiation under anesthesia, the region of interest of the mandibles was carefully extracted and excess soft tissue removed before fixation for 24 h in 4% PFA at 4°C . The 6-week post-implantation time point was selected because it lays in the coupled-remodeling stage of bone healing. Moreover, from our previous experience, defects that at this point have not been filled with bone will most likely develop fibrous non-unions, thereby being a good time point to assess long-term outcomes (Ramirez-Garcialuna et al., 2017).

2.5.1. Micro-CT Analyses

Rat mandibles with inserted scaffolds were carefully dissected free of soft tissue, fixed for 24 h in 4% paraformaldehyde at 4°C and then rinsed thoroughly with sterile PBS prior to micro-computed tomography (μCT) analysis. A skyscan 1172 (Bruker, Milton, 139 ON) was used with 9 μm/pixel resolution, using a 1.0 mm aluminum filter at a voltage of 59 kV and a 140 current of 167 μA. 2D projections were reconstructed into slices using NRecon (Bruker) and analyzed using CTAn v.1.16.4.1 (Bruker). 3D reconstructions were visualized using CTVol (Bruker). Quantitative data for bone regeneration was recorded in a region of interest (ROI) measuring 5 mm long × 3 mm wide × 2 mm deep, in the middle of the bone window defect, encompassing the defect and scaffold. Quantitative data for mineralized tissue includes bone quantity (BV/TV), trabecular number (Tb.N), trabecular thickness (Tb.Th), separation of trabeculae (Tb.Sp), connective density (Conn.Dn), total porosity (Po.Tot), and structure model index (SMI) (Drager et al., 2017).

2.5.2. Histological Analyses

Following micro CT, mandibles were decalcified in 10% EDTA for 21 days before embedding in paraffin as previously described (Ramirez-Garcialuna et al., 2017). Serial 5 μm sections were cut in the sagittal plane in the implant region. Sections were probed for alkaline phosphatase (ALP) activity in osteogenic cells, tartrate resistant acid phosphatase (TRAP) activity in catabolic cells (Abcam, Cambridge UK). Samples were imaged using an Axioskop 40 microscope with a high-resolution camera (Zeiss).

2.6. Statistical Analysis

Non-linear curves were fit to the dry and change in weight of filament samples, while a spline fit (7 knots) was used to fit a line to the wet weights. Error bars or line fills indicate standard deviation from the mean. Paired t-tests were performed between compressive moduli and microCT data. Values of $P < 0.05$ were deemed statistically significant. All statistical analyses were performed using GraphPad Prism v8.

3. RESULTS

3.1. Characterization of LayFomm Material and Acellular Scaffolds

The percentages of PVA and PU were estimated by incubating small pieces of LayFomm60 filament in water at 37°C for up

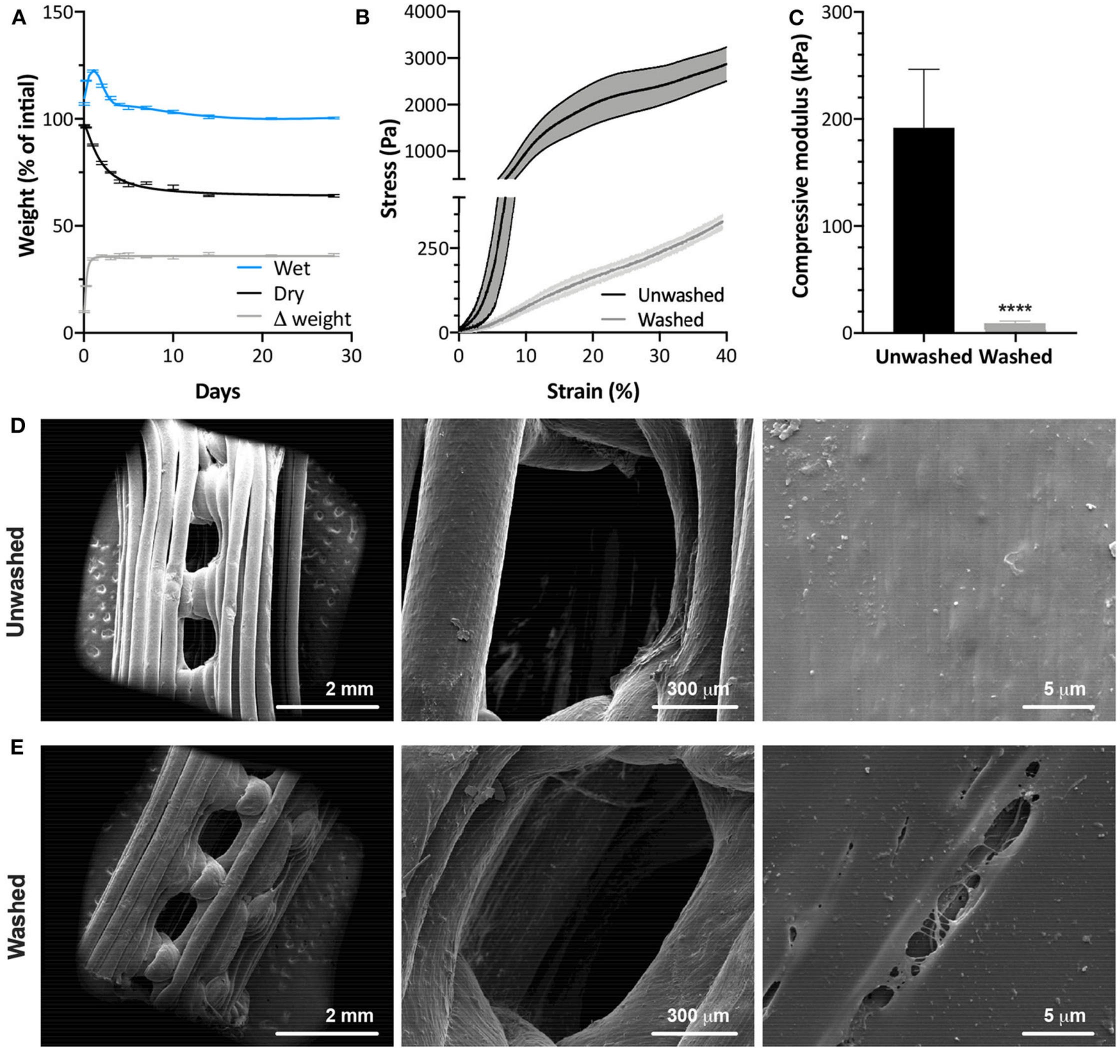

FIGURE 1 | (A) Temporal change in scaffold weight with removal of PVA by washing in dH_2O ($N = 4$). Mechanical compression data of washed and unwashed scaffolds showing **(B)** deformation behavior and **(C)** compressive modulus between 8 and 10% strain ($N = 5$). SEM images of **(D)** washed and **(E)** unwashed LayFomm scaffolds, showing the appearance of micropores (arrowheads) following removal of PVA by washing in dH_2O. Error bars **(A,C)** and fill between lines **(B)** indicates standard deviation. For **(A)**, lines are as follows: wet—smoothing spline, 7 knots; dry and Δ weight—non-linear fit, $R^2 = 0.9907$ and 0.9892, respectively. $^{****}P < 0.0001$.

to 28 days. As shown in **Figure 1A**, after the initial swelling phase, there is a consistent difference (Δ) in dry and wet weights of 36% between 4 and 28 days. The initial removal of water-soluble PVA happens quickly, with the dry mass decreasing by 4% after just 1h and continuing to decrease, down to a plateau of 64% of the original mass between 14 and 28 days (mean d14 = 64.01, d21 = 64.08, d28 = 64.01%). This plateau suggests that all PVA has been removed and there was no degradation of PU between 14 and 28 days.

Compression testing shown in **Figures 1B,C** reveals that removal of the PVA causes a significant reduction in the mechanical strength of the scaffolds. The stress-strain curves in **Figure 1B**, show that before washing, there is a steep gradient to the curve in the elastic region and evidence of a yield point prior to the region of plastic deformation. Following washing, however, there is clear elastomeric behavior. There is a small decrease in gradient of the curve around 15% strain, likely when the pores of the scaffold have been completely compressed, but no clear yield point. The gradient then increases again without plateauing

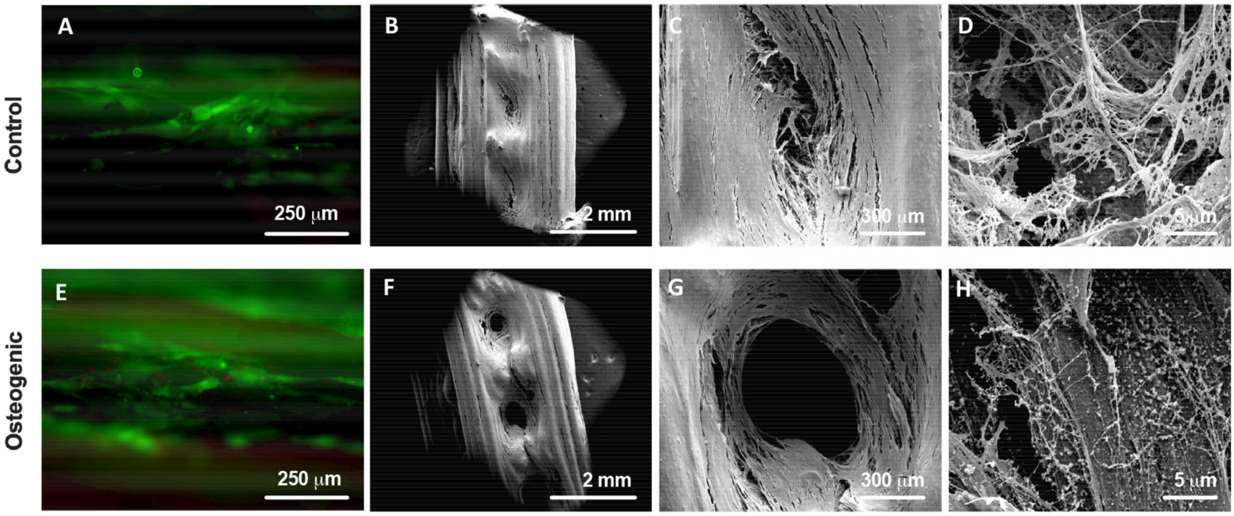

FIGURE 2 | Live/Dead staining **(A,E)** showing good viability of DPSCs on the scaffolds. SEM images of DPSC-seeded scaffolds after 21 days of culture in either control **(A–D)** or osteogenic **(E–H)** media showing cells and matrix filling the macropores of the scaffolds.

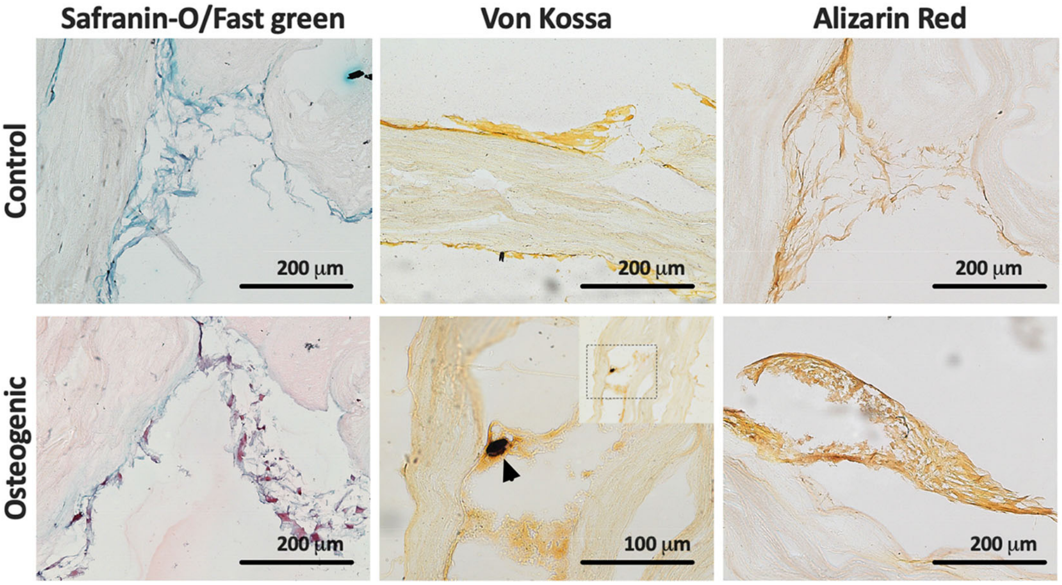

FIGURE 3 | Histology of DPSCs cultured on LayFomm scaffolds in either control or osteogenic media for 21 days. Safranin-O/Fast green staining indicates formation of collagenous matrix in both conditions; Von Kossa staining for phosphate, arrows indicate phosphate-rich nodules formed in osteogenic media; Alizarin Red staining for calcium shows increased straining in osteogenic media.

up to 40% strain. **Figure 1C** shows a significant reduction in compressive modulus following washing. Removal of the PVA had no effect on the macrostructure of the LayFomm scaffolds. It did, however, result in micropores ranging from approximately 200 nm to 20 μm visible on the surface (**Figures 1D,E**).

3.2. *In vitro* Analyses

Initial seeding had a 68% adhesion success, resulting in approximately 1.36×10^5 cells seeded onto each scaffold (data not shown). After 21 days of culture, DPSCs in both control and osteogenic media proliferated, showed very good viability (**Figures 2A,E**) and produced matrix that filled the pores of scaffold (**Figures 2B,C,F,G**). DPSCs cultured in osteogenic media, showed some evidence of mineralized matrix formation, with small crystals visible under SEM (**Figure 2H**) compared to control media (**Figure 2D**).

Histological evaluation of LayFomm scaffolds cultured with DPSCs for 21 days is presented in **Figure 3**. In all staining, the produced matrix is clearly visible. Safranin O/Fast green staining shows production of collagen-rich matrix in both conditions as would be expected. Von Kossa staining shows some evidence of phopsphate-rich nodules as indicated by the arrowhead in **Figure 3** when DPSCs were cultured in osteogenic media. Alizarin Red S staining is slightly increased

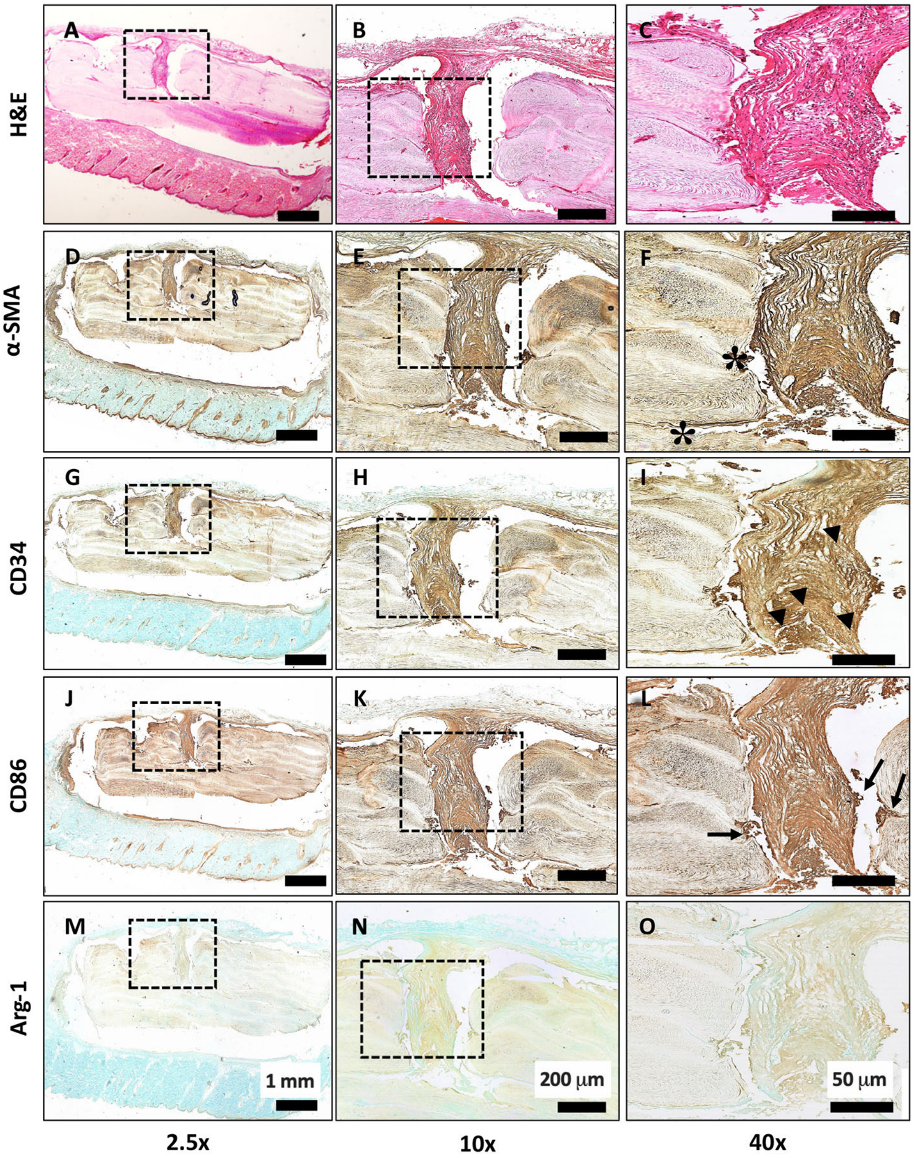

FIGURE 4 | Histological evaluation of subcutaneous implantation of LayFomm scaffold. **(A–C)** H&E staining of overall tissue morphology; **(D–F)** α-smooth muscle actin shows formation of fibrous tissue around and directly next to (*) the implanted scaffold; **(G–I)** CD34 shows positive staining for haematopoietic stem cells, indicating vascularization (arrowheads); **(J–L)** CD86 staining shows few clusters of M1 macrophages at the scaffold-tissue interface (arrows); **(M–O)** Arg-1 staining for M2 macrophages is negative.

with osteogenic media, indicating increased production of calcium-rich matrix.

3.3. *In vivo* Subcutaneous Implantation

Scaffolds were first implanted subcutaneously for 6 weeks to determine any local inflammatory response. In **Figures 4A–C**, H & E staining shows the overall morphology and presence of fibrous tissue growing into the pores of the scaffold. There were no necrotic regions observed. Strong staining of α-smooth muscle actin (α-SMA) in **Figures 4D–F** confirms the activation of a fibrotic response to the LayFomm scaffold. **Figures 4G–I** show positive staining for CD-34, showing the presence of haematopoietic stem cells that indicates blood vessel formation. CD86 staining in **Figures 4J–L** shows clusters of M1 macrophages at the implant-tissue interface, showing that the material is not biologically inert and there is a mild inflammatory response. Finally, in **Figures 4M–O**, negative arginase-1 staining confirms the absence of M2 macrophages in the fibrous tissue formed. This shows that the scaffold did not promote a chronic inflammatory response.

3.4. *In vivo* Mandibular Implantation and Bone Ingrowth

Following molar extraction and a 4 week recovery period a 5 mm defect was drilled in the mandible. **Figure 5** shows the pre- (**Figure 5A**) and post-operative (**Figure 5B**) *in vivo* MicroCT of the molar extraction and scaffold implantation. LayFomm is polymeric and thus radio-translucent so not visible by CT. Toluidine Blue staining in **Figure 5C** shows the scaffold in place, regions of repaired tissue in the scaffold is marked by an asterisk (*) and the bony interface is shown by a hash (#).

Histological staining of the recovered tissues was performed to investigate bone formation in the implanted scaffolds. Alkaline phosphatase staining was positive in both the Norian CRS putty and LayFomm groups (**Figures 5D–G**). Stronger staining in the LayFomm group indicates increased levels of osteogenesis (**Figures 5F,G**). TRAP staining for osteoclast activity was much higher at the bone interface in the Norian putty (**Figure 5I**), such that the putty appears to have been resorbed away from the native bone. In the LayFomm group however, the interface between the scaffold and native bone is constant (**Figures 5J,K**). This indicates that there is a less of an inflammatory response with the implantation of LayFomm compared to the Norian putty.

Finally, analysis of the microCT reconstructions was performed (**Figure 6** and **Table 1**). Quantitative μCT analysis showed a significantly increased amount of mineralized tissue (BV/TV) in the mandibles implanted with LayFomm scaffolds compared with those implanted with Norian CRS Putty. This increase in bone mass was reflected by significantly higher trabecular thickness (Tb.Th) that exhibited less separation (Tb.Sp), and a significantly different geometry (SMI).

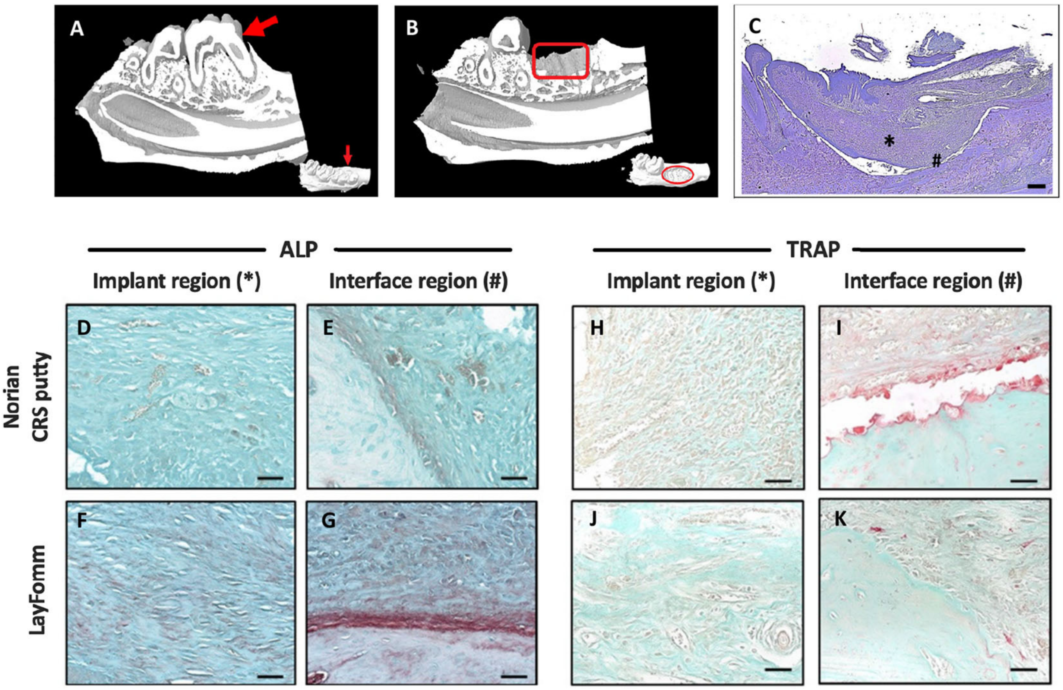

FIGURE 5 | MicroCT reconstruction of rat mandible pre **(A)** and post **(B)** implantation of LayFomm scaffold; LayFomm is radio-translucent so not visible. **(C)** Toluidine Blue staining of the scaffold following implantation. *Implant region and #bone interface region in **(D–K)**. ALP **(D–G)** and TRAP **(H–K)** staining of repaired tissue and the bone interface following 6 weeks of either Norian putty or LayFomm implantation. Scale bar = 50 μm.

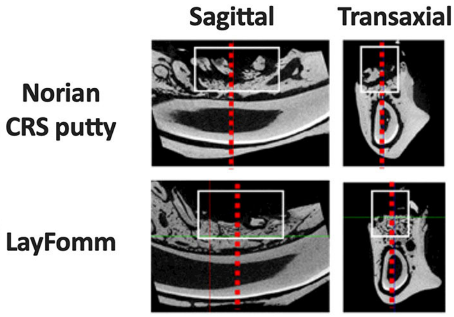

FIGURE 6 | MicroCT reconstructions of implanted scaffolds compared to Norian CRS putty. The white box marks the analyzed ROI that corresponds to data in **Table 1**. Dashed red lines represent the corresponding transaxial and sagittal views.

TABLE 1 | Bone volume (BV), Bone volume/Tissue volume (BV/TV), numbers of trabeculae (Tb.N), trabecular thickness (Tb.Th), trabecular separation (Tb.Sp), Total porosity (Po.Tot), Connective Density (Conn.Dn), Structure Model Index (SMI).

Parameter	Norian CRS Putty (*n* = 6)	LayFomm (*n* = 6)	*P*-value
BV/TV (%)	14.33 ± 7.94	30.26 ± 9.46	0.02
Tb.Th (μm)	140.5 ± 14.3	201.7 ± 33.4	<0.001
Tb.Sp (μm)	1456.0 ± 226.9	685.5 ± 113.3	<0.001
Tb.N (no./mm)	1.66 ± 0.65	1.58 ± 0.58	0.69
Po(Tot) (%)	76.92 ± 8.56	69.74 ± 9.46	0.16
Conn.Dn (1/μm)	0.09 ± 0.06	0.11 ± 0.04	0.55
SMI	−3.92 ± 1.18	−0.30 ± 1.68	<0.001

Data was analyzed using paired t-*tests (*n = *6 rats).*

4. DISCUSSION

Critical-sized bone defects are a challenging scenario for clinicians and patients. A scaffolding material that allows for bony regrowth while providing structural support to the bone has the potential to help millions of patients around the world annually. The rapidly increasing availability of additive manufacturing hardware is likely to have a huge impact on the medical field. FDM printers are already becoming available in hospitals for surgical planning and education but the use of AM in surgical practice remains limited. This is due in part to the lack of highly qualified personnel to perform the computational tasks that convert patient scans to 3D models for printing. As technological developments enable the automation of this critical step, implantable devices will be designed, manufactured and sterilized within the confines of surgical units.

A large range of materials are currently available for additive manufacturing, that include metals, ceramics and polymers. Metallic implants have commonly been used in orthopedic applications due to their inherent stiffness; they have traditionally been used for long-term structural applications but recent studies are seeking to increase their biological applications (Cox et al., 2016, 2017; Burton et al., 2019). A number of additively manufactured titanium implants have now been FDA approved, such as the FastForward device for correction of hallux valgus deformities (Smith et al., 2016). Polymers are a group of materials that have many different characteristics including cell adhesion, degradation rate and mechanism. Multiple polymers can be blended or co-polymerized to alter their properties. The material used in this study, LayFomm, is a blend of PU and PVA. The PVA acts as a stiffener, such that the blend can be extruded into filament and then printed using FDM. The water-soluble PVA can then be washed away leaving just the highly swollen functional elastomer, PU.

The PU used in this study allowed for rapid cell attachment, as seen by a 68% seeding efficiency after just 3 h. This may be attributed to the hydrophilicity of the material and also its microporosity (Marzec et al., 2017). Microporosity gives a larger surface area and has been shown to increase protein adhesion, cell adhesion and proliferation as well as playing a critical role in osteogenesis in bone scaffolds (Muschler et al., 2004; Liu et al., 2013; Zhang et al., 2018). This microporosity in LayFomm has previously been exploited as a means to enable uptake and also deliver small molecules. We have shown the ability for LayFomm to uptake and then release chemotherapeutics over a period of 14 days (Ahangar et al., 2018), while other groups have used LayFomm in separation science. Konieczna et al. (2018) used LayFomm to entrap small molecules such as steroids from human plasma prior to analysis in mass spectroscopy. As such, it would be possible to load osteoinductive factors such as bone morphogenic proteins (BMPs) into these scaffolds prior to implantation. This concept has been shown to promote bone formation *in vivo*; Bouyer et al. showed complete bridging of critical-sized defects in a rat models with BMP-2 coated PLGA and PCL scaffolds (Sawyer et al., 2009; Bouyer et al., 2016).

Dental pulp stem-cells were used in this study for *in vitro* analysis due to their fast proliferation rate and ability to undergo osteogenic differentiation in the presence of the appropriate factors (Gronthos et al., 2000; Zhang et al., 2006). In this study they were able to proliferate, differentiate and produce matrix, filling the 750 μm macropores in the scaffold; pores of this size-range have been shown to favor cell migration *in vitro* (Karageorgiou and Kaplan, 2005; Fairag et al., 2019). Similarly, after subcutaneous implantation *in vivo*, fibrous tissue was shown growing into the macropores of the scaffold. A mild inflammatory response is required for the integration of a foreign material into a biological system. A fibrotic response was seen here by the positive staining of α-smooth muscle actin. A mild inflammatory response was observed by the positive staining of M1 macrophage marker CD-86, while there was no chronic inflammation as evidenced by the absence of M2 macrophages. Macrophages play a pivotal role in the foreign body response (Klopfleisch, 2016), they have been shown to be responsible for the recruitment of vascular cells, enabling angiogenesis (Spiller et al., 2014). Formation of a vascular network is critical in bone regeneration, as seen in the healthy fracture healing response (Marsell and Einhorn, 2011). Subcutaneous implantation showed evidence of vascularization in the fibrous tissue formed around the implant (by CD34 staining). In the mandibular defect model, there was limited evidence of CD34 staining; a possible reason for the lack of vascularization is the lack of porosity in the scaffolds used (these scaffolds were printed with 100% infill density). It has been shown previously that without macropores, there is a lack of interconnectivity for growth of a vascular network (Hutmacher, 2000; Liu et al., 2013).

Formation of calcified matrix on the PU scaffold was shown both *in vitro* using SEM and also histologically, by the presence of phosphate-rich nodules in Von Kossa staining. *In vitro*, osteogenic media was required to promote this response despite DPSCs having many bone-like biochemical markers (Gronthos et al., 2000). Mineralized matrix formation *in vivo* was shown by micro-CT; the significant increase in BV/TV compared to the Norian putty is promising for its use as a 3D printed scaffold for bone regeneration. Polyurethanes have previously been shown to promote calcification *in vivo* and the mechanism has been proposed as by the interaction of PU with calcium and phosphate in the blood and other fluids (Marzec et al., 2017). PU is hydrophilic and has polar groups resulting in high affinity for CaP binding (Jie and Yubao, 2004). The composition of PU in the LayFomm filament was estimated by a 28-day washing study, with a plateau in dry mass at 64% of the initial weight after 14 days. An important limitation of this method to determine the amount of PU/PVA in the LayFomm filament is that it does not differentiate between degradation of PU and solubilization of PVA in this time frame. The plateau in dry mass between days 14 and 28, however, suggests that there is no degradation in this time. The formation of bone-like tissue is encouraging, however, a key limitation of LayFomm as a bone scaffold is its low mechanical stiffness. This is an important reason for the use of a mandibular defect rodent model in this study, rather than a load-bearing critical defect model.

This is the first study to characterize LayFomm as a potential material for bone regeneration both *in vitro* and *in vivo*. The successful formation of mineralized matrix is promising for this as a bone repair strategy. As an elastomer, the mechanical stiffness of this scaffold is not high enough to be utilized as a scaffold in a load bearing application but may be useful in craniofacial defect repair. An interesting avenue for further investigation is in delivery of therapeutics within the micropores of the material to further enhance its capacity for bone formation.

DATA AVAILABILITY STATEMENT

The raw data supporting the conclusions of this article will be made available by the authors, without undue reservation.

ETHICS STATEMENT

The animal study was reviewed and approved by Animal Care Committee of McGill University (AUP-7815).

AUTHOR CONTRIBUTIONS

DR and JH: conception of study. MC: manuscript preparation. MC, KR-B, JR-G, and HP: experimental work and data analysis. DR, JH, and SN: supervision. All authors contributed to the article and approved the submitted version.

FUNDING

MC and JH acknowledged the financial support of Fonds de Recherche Québec Santé - Réseau de Recherche en Santé Buccodentaire et Osseuse (FRQS-RSBO). MC also acknowledged funding from MITACS, Canada. The work was performed in the Bone Engineering Labs at the Montreal General Hospital campus of the Research Institute-McGill University Health Center (RI-MUHC), which is an FRQ-S sponsored Center de Recherche. KR-B and JR-G were scholars of the Mexican National Council for Science and Technology (CONACYT). JR-G holds a doctoral studentship from FRQ-S. SN acknowledged funding from NSERC, FRQNT, and McGill's Faculty of Engineering MEDA fellowship for HP.

REFERENCES

Ahangar, P., Akoury, E., Ramirez Garcia Luna, A., Nour, A., Weber, M., and Rosenzweig, D. (2018). Nanoporous 3D-printed scaffolds for local doxorubicin delivery in bone metastases secondary to prostate cancer. *Materials* 11:1485. doi: 10.3390/ma11091485

Ahangar, P., Cooke, M. E., Weber, M. H., and Rosenzweig, D. H. (2019). Current biomedical applications of 3D printing and additive manufacturing. *Appl. Sci.* 9:1713. doi: 10.3390/app9081713

Akoury, E., Weber, M. H., and Rosenzweig, D. H. (2019). 3D-printed nanoporous scaffolds impregnated with zoledronate for the treatment of spinal bone metastases. *MRS Advances* 4, 1245–1251. doi: 10.1557/adv.2019.156

Belka, M., Ulenberg, S., and Baczek, T. (2017). Fused deposition modeling enables the low-cost fabrication of porous, customized-shape sorbents for small-molecule extraction. *Anal. Chem.* 89, 4373–4376. doi: 10.1021/acs.analchem.6b04390

Bouyer, M., Guillot, R., Lavaud, J., Plettinx, C., Olivier, C., Curry, V., et al. (2016). Surface delivery of tunable doses of BMP-2 from an adaptable polymeric scaffold induces volumetric bone regeneration. *Biomaterials* 104, 168–181. doi: 10.1016/j.biomaterials.2016.06.001

Burton, H. E., Eisenstein, N. M., Lawless, B. M., Jamshidi, P., Segarra, M. A., Addison, O., et al. (2019). The design of additively manufactured lattices to increase the functionality of medical implants. *Mater. Sci. Eng. C* 94, 901–908. doi: 10.1016/j.msec.2018.10.052

Cox, S. C., Jamshidi, P., Eisenstein, N. M., Webber, M. A., Burton, H., Moakes, R. J., et al. (2017). Surface finish has a critical influence on biofilm formation and mammalian cell attachment to additively manufactured prosthetics. *ACS Biomater. Sci. Eng.* 3, 1616–1626. doi: 10.1021/acsbiomaterials.7b00336

Cox, S. C., Jamshidi, P., Eisenstein, N. M., Webber, M. A., Hassanin, H., Attallah, M. M., et al. (2016). Adding functionality with additive manufacturing: fabrication of titanium-based antibiotic eluting implants. *Mater. Sci. Eng. C* 64, 407–415. doi: 10.1016/j.msec.2016.04.006

Dawood, A., Marti, B. M., Sauret-Jackson, V., and Darwood, A. (2015). 3D printing in dentistry. *Brit. Dental J.* 219, 521–529. doi: 10.1038/sj.bdj.2015.914

Drager, J., Ramirez-Garcialuna, J. L., Kumar, A., Gbureck, U., Harvey, E. J., and Barralet, J. E. (2017). Hypoxia biomimicry to enhance monetite bone defect repair. *Tissue Eng A* 23, 1372–1381. doi: 10.1089/ten.tea.2016.0526

Fairag, R., Rosenzweig, D. H., Ramirez-Garcialuna, J. L., Weber, M. H., and Haglund, L. (2019). Three-dimensional printed polylactic acid scaffolds promote bone-like matrix deposition *in vitro. ACS Appl. Mater. Interfaces* 11, 15306–15315. doi: 10.1021/acsami.9b02502

Gronthos, S., Mankani, M., Brahim, J., Robey, P. G., and Shi, S. (2000). Postnatal human dental pulp stem cells (DPSCs) *in vitro* and *in vivo. Proc. Natl. Acad. Sci. U.S.A*. 97, 13625–13630. doi: 10.1073/pnas.240309797

Hutmacher, D. W. (2000). Scaffolds in tissue engineering bone and cartilage. *Biomaterials* 21, 175–189. doi: 10.1016/B978-008045154-1.50021-6

Jabbour, Z., El-Hakim, M., Henderson, J. E., and De Albuquerque, R. F. (2014). Bisphosphonates inhibit bone remodeling in the jaw bones of rats and delay healing following tooth extractions. *Oral Oncol*. 50, 485–490. doi: 10.1016/j.oraloncology.2014.02.013

Jie, W., and Yubao, L. (2004). Tissue engineering scaffold material of nano-apatite crystals and polyamide composite. *Eur. Polymer J*. 40, 509–515. doi: 10.1016/j.eurpolymj.2003.10.028

Karageorgiou, V., and Kaplan, D. (2005). Porosity of 3D biomaterial scaffolds and osteogenesis. *Biomaterials* 26, 5474–5491. doi: 10.1016/j.biomaterials.2005.02.002

Klopfleisch, R. (2016). Macrophage reaction against biomaterials in the mouse model–Phenotypes, functions and markers. *Acta Biomater*. 43, 3–13. doi: 10.1016/j.actbio.2016.07.003

Konieczna, L., Belka, M., Okońska, M., Pyszka, M., and Bączek, T. (2018). New 3D-printed sorbent for extraction of steroids from human plasma preceding LC-MS analysis. *J. Chromatogr. A* 1545, 1–11. doi: 10.1016/j.chroma.2018.02.040

Lichte, P., Pape, H. C., Pufe, T., Kobbe, P., and Fischer, H. (2011). Scaffolds for bone healing: concepts, materials and evidence. *Injury* 42, 569–573. doi: 10.1016/j.injury.2011.03.033

Liu, X., Zhao, K., Gong, T., Song, J., Bao, C., Luo, E., et al. (2014). Delivery of growth factors using a smart porous nanocomposite scaffold to repair a mandibular bone defect. *Biomacromolecules* 15, 1019–1030. doi: 10.1021/bm401911p

Liu, Y., Lim, J., and Teoh, S.-H. H. (2013). Review: development of clinically relevant scaffolds for vascularised bone tissue engineering. *Biotechnol. Adv*. 31, 688–705. doi: 10.1016/j.biotechadv.2012.10.003

Marsell, R., and Einhorn, T. A. (2011). The biology of fracture healing. *Injury* 42, 551–555. doi: 10.1016/j.injury.2011.03.031

Marzec, M., Kucińska-Lipka, J., Kalaszczyńska, I., and Janik, H. (2017). Development of polyurethanes for bone repair. *Mater. Sci. Eng. C* 80, 736–747. doi: 10.1016/j.msec.2017.07.047

Muschler, G. F., Nakamoto, C., and Griffith, L. G. (2004). Engineering principles of clinical cell-based tissue engineering. *J. Bone Joint Surg. Ser. A* 86, 1541–1558. doi: 10.2106/00004623-200407000-00029

Nyberg, E., Rindone, A., Dorafshar, A., and Grayson, W. L. (2016). Comparison of 3D-printed poly–caprolactone scaffolds functionalized with tricalcium phosphate, hydroxyapatite, bio-oss, or decellularized bone matrix. *Tissue Eng. A* 23, 503–514. doi: 10.1089/ten.tea.2016.0418

Ramirez-Garcialuna, J. L., Chan, D., Samberg, R., Abou-Rjeili, M., Wong, T. H., Li, A., et al. (2017). Defective bone repair in mast cell-deficient Cpa3Cre/+ mice. *PLoS ONE* 12:e0174396. doi: 10.1371/journal.pone.0174396

Ramirez-Garcia-Luna, J. L., Wong, T. H., Chan, D., Al-Saran, Y., Awlia, A., Abou-Rjeili, M., et al. (2019). Defective bone repair in diclofenac treated C57Bl6 mice with and without lipopolysaccharide induced systemic inflammation. *J. Cell. Physiol*. 234, 3078–3087. doi: 10.1002/jcp.27128

Rosenzweig, D. H., Carelli, E., Steffen, T., Jarzem, P., and Haglund, L. (2015). 3D-printed ABS and PLA scaffolds for cartilage and nucleus pulposustissue regeneration. *Int. J. Mol. Sci*. 16, 15118–15135. doi: 10.3390/ijms160715118

Sawyer, A. A., Song, S. J., Susanto, E., Chuan, P., Lam, C. X., Woodruff, M. A., et al. (2009). The stimulation of healing within a rat calvarial defect by mPCL-TCP/collagen scaffolds loaded with rhBMP-2. *Biomaterials* 30, 2479–2488. doi: 10.1016/j.biomaterials.2008.12.055

Smith, K. E., Dupont, K. M., Safranski, D. L., Blair, J. W., Buratti, D. R., Zeetser, V., et al. (2016). "Use of 3D printed bone plate in novel technique to surgically correct hallux valgus deformities," in *Techniques in Orthopaedics*, Vol. 31 (Rockville, MD: Lippincott Williams and Wilkins), 181–189. doi: 10.1097/BTO.0000000000000189

Spiller, K. L., Anfang, R. R., Spiller, K. J., Ng, J., Nakazawa, K. R., Daulton, J. W., et al. (2014). The role of macrophage phenotype in vascularization of tissue engineering scaffolds. *Biomaterials* 35, 4477–4488. doi: 10.1016/j.biomaterials.2014.02.012

Williams, D. F. (2008). On the mechanisms of biocompatibility. *Biomaterials* 29, 2941–2953. doi: 10.1016/j.biomaterials.2008.04.023

Zein, I., Hutmacher, D. W., Tan, K. C., and Teoh, S. H. (2002). Fused deposition modeling of novel scaffold architectures for tissue engineering applications. *Biomaterials* 23, 1169–1185. doi: 10.1016/S0142-9612(01)00232-0

Zhang, K., Fan, Y., Dunne, N., and Li, X. (2018). Effect of microporosity on scaffolds for bone tissue engineering. *Regenerat. Biomater*. 5, 115–124. doi: 10.1093/rb/rby001

Zhang, W., Walboomers, X. F., Shi, S., Fan, M., and Jansen, J. A. (2006). Multilineage differentiation potential of stem cells derived from human dental pulp after cryopreservation. *Tissue Eng*. 12, 2813–2823. doi: 10.1089/ten.2006.12.2813

Conflict of Interest: The authors declare that the research was conducted in the absence of any commercial or financial relationships that could be construed as a potential conflict of interest.

Advantages of publishing in Frontiers

OPEN ACCESS
Articles are free to read
for greatest visibility
and readership

FAST PUBLICATION
Around 90 days
from submission
to decision

HIGH QUALITY PEER-REVIEW
Rigorous, collaborative,
and constructive
peer-review

TRANSPARENT PEER-REVIEW
Editors and reviewers
acknowledged by name
on published articles

Frontiers
Avenue du Tribunal-Fédéral 34
1005 Lausanne | Switzerland

Visit us: www.frontiersin.org
Contact us: frontiersin.org/about/contact

REPRODUCIBILITY OF RESEARCH
Support open data
and methods to enhance
research reproducibility

DIGITAL PUBLISHING
Articles designed
for optimal readership
across devices

FOLLOW US
@frontiersin

IMPACT METRICS
Advanced article metrics
track visibility across
digital media

EXTENSIVE PROMOTION
Marketing
and promotion
of impactful research

LOOP RESEARCH NETWORK
Our network
increases your
article's readership